

**Non-rare earth-based new class of inorganic phosphors for
lighting, medical imaging and security applications**

by

THEJAS K. K.

Registration No: 10PP19J39002

A thesis submitted to the
Academy of Scientific & Innovative Research
for the award of the degree of
DOCTOR OF PHILOSOPHY

in

SCIENCE

Under the supervision of

Dr. Subrata Das



**CSIR-National Institute for Interdisciplinary Science and
Technology (CSIR-NIIST)
Thiruvananthapuram-695019**



**Academy of Scientific and Innovative Research
AcSIR Headquarters, CSIR-HRDC campus
Sector 19, Kamla Nehru Nagar,
Ghaziabad, U.P. – 201 002, India**

April-2024

Thesis is dedicated to my beloved family...

National Institute for Interdisciplinary Science and Technology (NIIST)



Council of Scientific & Industrial Research (CSIR)
Ministry of Science and Technology, Government of India
Industrial Estate P. O., Trivandrum - 695 019
Kerala, INDIA



Dr. Subrata Das
Principal Scientist,
Materials Science and Technology Division

Tel: 91-471-2515360 (O), 7407825435 (M)
Email: subratadas@niist.res.in
physubrata@gmail.com

CERTIFICATE

This is to certify that the work incorporated in this Ph.D. thesis entitled, “*Non-rare earth-based new class of inorganic phosphors for lighting, medical imaging and security applications*”, submitted by **Mr. Thejas K. K.** to the Academy of Scientific and Innovative Research (AcSIR) in fulfillment of the requirements for the award of the Degree of *Doctor of Philosophy in Science*, embodies original research work carried-out by the student. We, further certify that this work has not been submitted to any other University or Institution in part or full for the award of any degree or diploma. Research material(s) obtained from other source(s) and used in this research work has/have been duly acknowledged in the thesis. Image(s), illustration(s), figure(s), table(s) etc., used in the thesis from other source(s), have also been duly cited and acknowledged.

Thejas K. K.


Dr. Subrata Das

(Research Supervisor)

Thiruvananthapuram
April 2024

STATEMENTS OF ACADEMIC INTEGRITY


I Thejas K. K., a Ph.D. student of the Academy of Scientific and Innovative Research (AcSIR) with Registration No. 10PP19J39002 hereby undertake that, the thesis entitled “*Non-rare earth-based new class of inorganic phosphors for lighting, medical imaging and security applications*” has been prepared by me and that the document reports original work carried out by me and is free of any plagiarism in compliance with the UGC Regulations on “Promotion of Academic Integrity and Prevention of Plagiarism in Higher Educational Institutions (2018)” and the CSIR Guidelines for “Ethics in Research and in Governance (2020)”.


16/4/24
Thejas K. K.

Thiruvananthapuram

April 2024

It is hereby certified that the work done by the student, under my/our supervision, is plagiarism-free in accordance with the UGC Regulations on “Promotion of Academic Integrity and Prevention of Plagiarism in Higher Educational Institutions (2018)” and the CSIR Guidelines for “Ethics in Research and in Governance (2020)”.


Dr. Subrata Das

Thiruvananthapuram

April 2024

DECLARATION

I Thejas K. K., bearing AcSIR Registration No. 10PP19J39002 declare: that my thesis entitled, “*Non-rare earth-based new class of inorganic phosphors for lighting, medical imaging and security applications*” is plagiarism free in accordance with the UGC Regulations on “Promotion of Academic Integrity and Prevention of Plagiarism in Higher Educational Institutions (2018)” and the CSIR Guidelines for “Ethics in Research and in Governance (2020)”.

I would be solely held responsible if any plagiarised content in my thesis is detected, which is violative of the UGC regulations 2018.

 15/4/24

Thejas K. K.

Thiruvananthapuram

April 2024

ACKNOWLEDGEMENTS

First and foremost, I have great pleasure to express my heartfelt gratitude towards Dr. Subrata Das, research supervisor, for suggesting the research problem, as well as his constant guidance, freedom and timely support during the course of my research led to the successful completion of this work on time.

My sincere thanks to:

- Dr C. Anandharamkrishnan and Dr A. Ajayaghosh, present and former Directors of the CSIR-National Institute for Interdisciplinary Science and Technology, for letting me avail the laboratory facilities.
- Dr. Jayamurthy P., Dr K. Karunakaran, Dr C.H Suresh and Dr Luxmi Varma, present and former AcSIR program coordinators at CSIR-NIIST, for the help during the academic procedures of AcSIR.
- Dr. S. Ananthakumar, Dr M. Ravi, Dr S Savithri and Dr. Harikrishna Bhatt, present and former Heads of MSTD, for allowing me to conduct my research at MSTD.
- DAC members (Dr K. N. Narayanan Unni, Dr K. P. Surendran, and Dr. Saju Pillai) for their valuable suggestions and constant support throughout my research programme.
- Dr. Vasundhara M., for her guidance and support during the first six months of my Ph.D.
- Dr. Kaustab Kumar maithy, Dr. Maria Tchernycheva, Dr. Arup K. Kunti, and Dr. Shahzad Ahammed for their valuable suggestions and collaborations.
- All Scientists in MSTD for fruitful discussion, advise and help during the period of research work.
- Mr. A Peer Muhammed for XPS characterization, Mr. Harish Raj V for SEM analysis, Mr. Kiran Mohan for HRTEM, Ms Anjali for PXRD analysis.
- My labmates, Dr Sariga C. Lal, Malini Abraham, Ranjith P., Sreevalsa S., Shisina S, Meera Sebastian, Dr. Revathy J. S., Dr. Divya Saraswathy for their advices, suggestions, support and friendly atmosphere in the laboratory.
- Special mention to Dr. K. V. Devadas and Dr. Joshy George who brought me to the world of research.

- Dr. Nishanth K.G. and their students, Dr. Thejus P. K., Nithyaa J., Dr. Krishnapriya K V, Dr. Roshima K., and Ms. Dipannita Ganguly for their advice, suggestions and excellent companionship.
- Thanks to Dr. Akshay V. R., Dr. Arun B., Vishnu K., Dr. Aswathy K., Dr. Revathy R., Rojerce Brown Job, Chinnu V. Devan, Shabeer Ali P.C, Syamili and all other members of the Magnetism group.
- Thanks to all my friends in Anju Cottege, Sree Kailash and Football NIIST for their excellent companionship. I would like to acknowledge Rishad, students of Dr. K. N. Narayanan Unni and Dr. K. P. Surendran.
- Mr. C. K. Chandrakanth, for his constant motivation and inspiration during my course of Ph.D. work.
- All my wonderful inspiring teachers from schools to the present for molding my character and attitude.
- Technical and non-technical staffs, friends from CSIR-NIIST for their support and help during this journey.
- Council of Scientific and Industrial Research (CSIR) for the financial assistance and Academy of Scientific and Innovative Research (AcSIR) for academic facilities. I will be eternally grateful to my dear Achan and Amma, who have been the backbone of my life with immense support, drive, love and prayers. My brother Athul K. K. who always gave me the confidence to take up the challenges in my professional and personal life. My friend Mukesh Murali has been by my side as a consistent shoulder in times of disappointment and failure, always ready to support me. I also greatly acknowledge my whole family and cousins for their constant support, love and encouragement to achieve my goals. Above all, I am grateful to the Almighty for all the blessings which hold my hands in every moment of my life.

Thejas K. K.

Table of contents

Certificate	i
Statement of Academic Integrity	ii
Declaration	iii
Acknowledgement	iv-v
Table of contents	vi-ix
List of Abbreviations	x
List of Figures	xi-xiv
List of Tables	xx
Preface	xxi-xxv
1. Introduction	1-75
1.1 Abstract	2
1.2 Review on deep red-emitting rare-earth free germanates and their efficiency as well as adaptability for various applications.	2
1.2.1 Introduction	2
1.2.2 Basic ionic configurations of Mn ⁴⁺ and Cr ³⁺ ions	7
1.2.2.1 Simplified Tanabe-Sugano (T-S) energy level diagrams of Mn ⁴⁺ and Cr ³⁺	9
1.2.2.2 Crystal field analysis	11
1.2.2.3 Configuration Coordinate model	14
1.2.3 Mn ⁴⁺ -activated deep red-emitting germanate phosphors	15
1.2.3.1 Alkali metal-based germanate system	20
1.2.3.2 Alkaline-earth metal-based germanate systems	27
1.2.3.3 Lanthanum-based germanate systems	32
1.2.3.4 Non-Ge ⁴⁺ site occupancy of germanates	34
1.2.4 Cr ³⁺ -activated deep red/NIR emitting germanate phosphors	36
1.2.5 Amplification of deep red/NIR emission	39
1.2.5.1 Effect of synthesis methods and particle morphology	39
1.2.5.2 Cationic modifications and co-doping	41
1.2.5.3 Energy transfer mechanisms	43
1.2.6 Thermal stability enhancement	44

1.2.7 Potential applications of Mn ⁴⁺ /Cr ³⁺ activated oxide phosphors	44
1.2.7.1 W-LED applications	45
1.2.7.2 Long-glow applications	47
1.2.7.3 Security applications	49
1.2.7.4 Display applications	50
1.2.7.5 Plant growth applications	51
1.2.7.6 Thermometry applications	52
1.2.7.7 Solar energy applications	53
1.3 Self-activated persistent oxide phosphor: mechanism, overview, and applications	55
1.4 Summary, future and perspective	58
1.5 Objectives of the thesis	59
1.6 References	60
2. Enriching the deep red emission in (Mg, Ba)₃M₂GeO₈: Mn⁴⁺ (M = Al, Ga) compositions for light-emitting diodes	76-130
2.1 Abstract	77
2.2 Introduction	77
2.3 Experimental	79
2.3.1 Material synthesis	79
2.3.2 Characterization	79
2.4 Results and discussion	80
2.4.1 Elucidation of structural information	80
2.4.2 Effect of Ba ²⁺ doping in the crystal structure of Mg ₃ M ₂ GeO ₈ (M = Al, Ga)	83
2.4.3 UV-Vis absorption, photoluminescence and cathodoluminescence properties of (Mg, Ba) ₃ M ₂ GeO ₈ : Mn ⁴⁺ (M = Al, Ga)	89
2.4.3.1 Comparative PL analysis	95
2.4.3.2 Estimation of Mn ⁴⁺ energy level diagram and, evaluation of spectroscopic parameters	98
2.4.3.3 Low-temperature photoluminescence of MAG: Mn ⁴⁺ , 0.27Ba ²⁺ and MGG: Mn ⁴⁺ , 0.13Ba ²⁺	101
2.4.3.4 Cathodoluminescence properties of optimum MAG: Mn ⁴⁺ , 0.27Ba ²⁺ and MGG: Mn ⁴⁺ , 0.13Ba ²⁺	104

2.4.4 Applications in WLEDs and red LEDs	107
2.5 Conclusions	110
2.6 Supporting Information	111
2.7 References	122
3. Compositionally engineered (Mg, Sr)₃(Al, Ga)₂GeO₈:Cr³⁺ phosphors with tuned emission from ultra-sharp red to ultra-broad NIR band for LEDs and in vitro cell imaging applications	131-165
3.1 Abstract	132
3.2 Introduction	132
3.3 Experimental	134
3.3.1 Materials and Synthesis	134
3.3.2 Sample characterization	135
3.3.3 In vitro cell imaging	135
3.3.3.1 Culturing of cells	135
3.3.3.2 Assessment of cell viability	135
3.3.3.3 Cellular internalization studies	136
3.4 Results and discussion	136
3.4.1 Structural, compositional and morphological characterization	136
3.4.2 UV-Vis DRS and photoluminescence studies of MAG: Cr ³⁺ and effect of alkaline earth metal ions' substitution	141
3.4.3 Structural properties of Ga ³⁺ co-doped MAG: Cr ³⁺ , 0.1Sr ²⁺ , yGa ³⁺ samples	145
3.4.4 UV-Vis DRS and photoluminescence of Ga ³⁺ co-doped MAG: Cr ³⁺ , 0.1Sr ²⁺ , yGa ³⁺ samples	146
3.4.5 Temperature-dependent PL emission	149
3.4.6 Phosphor-converted LEDs for display, plant growth, and night vision surveillance	152
3.4.7 in vitro cell imaging	155
3.5 Conclusions	157
3.6 Supporting information	158
3.7 References	159
4. Inducing defects to boost the persistent luminescence in novel cyan emitting rare-earth free strontium zirconium silicate for dynamic anti-	166-197

counterfeiting and plant growth LED applications	
4.1 Abstract	167
4.2 Introduction	167
4.3 Experimental	170
4.3.1 Materials synthesis	170
4.3.2 Characterization	170
4.4 Results and discussion	171
4.4.1 Structural and optical properties of CZSO4 and SZSO4	171
4.4.2 Structural, elemental and morphological characterization of SZSO6	173
4.4.2.1 XRD analysis	173
4.4.2.2 HRTEM analysis	174
4.4.2.3 Elemental and morphological studies of SZSO6: 12 wt% NH ₄ Cl, 0.02 Bi ³⁺	175
4.4.2.4 XPS analysis of SZSO6: 12wt% NH ₄ Cl and SZSO6: 12wt% NH ₄ Cl, 0.02 Bi ³⁺	176
4.4.3 UV-Vis DRS and photoluminescence properties of SZSO6, SZSO6: 12wt% NH ₄ Cl and SZSO6: 12 wt% NH ₄ Cl, 0.02 Bi ³⁺	177
4.4.3.1 UV-Vis DRS and bandgap	177
4.4.3.2 Persistent Luminescence	178
4.4.3.2.1 PL and PersL properties of SZSO6 and effect of NH ₄ Cl addition	178
4.4.3.2.2 Enhancing the PersL via Bi ³⁺ co-doping and post-annealed vacuum treatment	181
4.4.4 Anti-counterfeiting and plant-growth LED applications	185
4.5 Conclusions	188
4.6 Supporting Information	188
4.7 References	191
5. Summary and future scope of the thesis	198-201
Abstract	202
Thesis outcome	203-204
Abstracts for conference presentations	205-206
Attachment of the publications	

List of abbreviations

LEDs	- Light-emitting diodes
NIR	- Near-infrared
CRI	- Colour rendering index
W-LEDs	- White light-emitting diodes
LCDs	- Liquid-crystal displays
LS terms	- Electrostatic terms
T-S	- Tanabe-Sugano
NR	- Non-radiative transition
ECM	- Exchange Charge Model
PLE	- Photoluminescence excitation
PL	- Photoluminescence
DFT	- Density functional theory
ZPL	- Zero-phonon line
CIE	- <i>commission internationale de l'éclairage</i>
XRD	- X-ray diffraction
NUV	- Near ultra-violet
MMCT	- Metal-to-metal charge transfer
CCT	- Correlated colour temperature
EL	- Electroluminescence
NTSC	- National television standard committee
WLED	- White light-emitting diode
XPS	- X-ray photoelectron spectroscopy
PXRD	- Powder X-ray Diffraction
JCPDS	- Joint committee on Powder Diffraction Standards
HR-TEM	- High-resolution transmission electron microscope
SEM	- Scanning electron microscopy
UV-Vis DRS	- Ultraviolet-visible diffuse reflectance spectroscopy
QE	- Quantum efficiency
CL	- Cathodoluminescence
CCD	- Charge-coupled device
EL	- Electroluminescence
CTB	- Charge transfer band
EQE	- External quantum efficiency
CT	- Charge transfer
FWHM	- Full width at half maximum
pc-LEDs	- Phosphor-converted light-emitting diodes
UCN	- Up-converted nanoparticles
QY	- Quantum yield
r-FFT	- Reduced FFT
IQE	- Internal quantum efficiency
Hela	- Human cervical cancer cells
HEPG2	- human hepato cellular carcinoma
FBS	- Fetal Bovine Serum
HBSS	- Hanks balanced Salt solution
MEM	- Minimum Essential Media
PersL	- Persistent luminescence
2D-FFT	- 2D- fast Fourier transform

List of Figures

Fig.1.1 Development scheme of deep red-emitting phosphor	6
Fig.1.2 Energy levels diagram of the free V^{2+} , Cr^{3+} , Mn^{4+} , and Fe^{5+} ions by taking the energy of ground state energy as zero	9
Fig.1.3 Simplified T-S diagram in the octahedral crystal field for ions having d^3 electronic configuration	9
Fig.1.4 (a) General energy level diagram for Mn^{4+} and Cr^{3+} . (b) Typical energy level diagram of Mn^{4+} showing excitation and emission (NR representing non-radiative transition).	10
Fig.1.5 Typical energy level diagram for Cr^{3+} . (NR representing non-radiative transition)	11
Fig.1.6 Configuration coordinate model representing typical PL emission and absorption transition along with the schematic representation for the PL and PLE spectra of the Mn^{4+} -activated oxide phosphor (S = Stokes; a-S = anti-Stokes)	15
Fig.1.7 Chart showing the available literature on different Mn^{4+} activated (a) hosts and (b) oxide hosts. (Based on the literature collected from the Web of Science published during January 2000-December 2020).	16
Fig.1.8 Structure of trigonal crystal structure with the occupation of Mn^{4+} in octahedral and tetrahedral sites drawn using the VESTA software	16
Fig.1.9 (a) and (b) Crystal structure of $LiNaGe_4O_9:0.05\%Mn^{4+}$ (orthorhombic-Pcca) viewed along a and b; (c) Comparison of PL emission intensities of $LiNaGe_4O_9:Mn^{4+}$ and $MFG:Mn^{4+}$.	21
Fig.1.10 (a) Crystal structure of $K_2BaGe_8O_{18}:Mn^{4+}$ (hexagonal-P3c1); (b) PL excitation and emission spectra of $K_2BaGe_8O_{18}:0.002Mn^{4+}$.	25
Fig.1.11 (a) Design of the phosphor-composition search space; (b) Comparison of PL emission spectra of $Li_3RbGe_8O_{18}:0.005Mn^{4+}$ with $L_2Ge_4O_9:Mn^{4+}$, $K_2Ge_4O_9:Mn^{4+}$ and $Rb_2Ge_4O_9:Mn^{4+}$; (c) Crystal structure of $Li_3RbGe_8O_{18}$ (trigonal-P31m); (d) Comparison of PL emission spectra of $Li_3RbGe_8O_{18}:0.005Mn^{4+}$ with $K_2SiF_6:Mn^{4+}$.	26
Fig.1.12 (a) Crystal structure of $Mg_{14}Ge_{5(1-0.2\%)}O_{24}:0.2\%Mn^{4+}$ (orthorhombic-Pbam); (b) The change of emission intensity and quantum yields as a function of Mn^{4+} concentration.	28

Fig.1.13 Low-temperature PL emission spectra of MGO ($\text{Mg}_{14}\text{Ge}_5\text{O}_{24}:\text{Mn}^{4+}$) and cation substituted MGSO ($\text{Mg}_{14}\text{Ge}_5\text{O}_{24}:\text{Mn}^{4+}, \text{Si}^{4+}$), MGTO ($\text{Mg}_{14}\text{Ge}_5\text{O}_{24}:\text{Mn}^{4+}, \text{Ti}^{4+}$), and MGNO ($\text{Mg}_{14}\text{Ge}_5\text{O}_{24}:\text{Mn}^{4+}, \text{Sn}^{4+}$) samples.	29
Fig.1.14 Comparison of PL emission spectra of $\text{Ba}_2\text{Ti}_{0.994}\text{Ge}_2\text{O}_8:0.006\text{Mn}^{4+}$ and $\text{Ba}_2\text{TiGe}_{1.994}\text{O}_8:0.006\text{Mn}^{4+}$	30
Fig.1.15 The temperature depended PL (a) excitation, and (b) emission spectra of $\text{BaGe}_4\text{O}_9:0.005\text{Mn}^{4+}$.	32
Fig.1.16 (a) Crystal structure of $\text{La}_3\text{GaGe}_5\text{O}_{16}:0.0025\text{Mn}^{4+}$ (trigonal-P321); (b) PL excitation and emission spectra; (c) Low temperature PL of $\text{La}_3\text{GaGe}_5\text{O}_{16}:0.0025\text{Mn}^{4+}$ phosphor.	34
Fig.1.17 (a) Crystal structure of $\text{Mg}_3\text{Ga}_2\text{GeO}_8$ (orthorhombic-Imma); (b) PL emission spectra of $\text{Mg}_3\text{Ga}_2\text{GeO}_{12}:0.005\text{Mn}^{4+}$ with different Mn^{4+} sources and different dopant sites	35
Fig.1.18 (a) Crystal structure of $\text{Mg}_2\text{Ti}_{0.65}\text{Ge}_{0.35}\text{O}_4:0.001\text{Mn}^{4+}$ (cubic-Fd3m); (b) PL emission spectra showing the effect of Ge substitution	36
Fig.1.19 (a) Normalized transmission spectra of NIR light after penetrating water and (b) sugar solutions	37
Fig.1.20 PL excitation and emission spectrum of $\text{Zn}_3\text{Al}_2\text{Ge}_2\text{O}_{10}:0.01\text{Cr}^{3+}$	38
Fig.1.21 Schematic representation of microwave-assisted sol-gel synthesis	40
Fig.1.22 Emission spectrum of $\text{Mg}_2\text{TiO}_4:\text{Mn}^{4+}$ for different concentration of Ag@SiO ₂ nanoparticles having 40 nm Ag cores	41
Fig.1.23 Energy level diagrams and energy transfer process between (a) Bi^{3+} and Mn^{4+} (b) Sm^{3+} and Cr^{3+} Adapted from ref. [136]. [(NR representing non-radiative relaxation)	43
Fig.1.24 Representation of different applications of Mn^{4+} and Cr^{3+} activated phosphors	45
Fig.1.25 (a) EL spectra of the W-LEDs fabricated with the various mixing ratios of YAG: Ce^{3+} and $\text{Li}_3\text{RbGe}_8\text{O}_{18}:0.005\text{Mn}^{4+}, \text{Mg}^{2+}$ ((i) 1:0, (ii) 1:1, (iii) 2:3, and (iv) 3:7), combined with 460 nm blue InGaN chip. (b) The digital images of the W-LEDs ((i) 1:0, (ii) 1:1, (iii) 2:3, and (iv) 3:7). (c) CIE plot showing the change in CCT values for different mixing ratio	46
Fig.1.26 <i>In-vivo</i> images of the mouse after injection of $\text{Zn}_{2.94}\text{Ga}_{1.96}\text{Ge}_2\text{O}_{10}:\text{Cr}^{3+}, \text{Pr}^{3+}$ phosphor	48

Fig.1.27 Red emission images of $\text{La}_3\text{GaGe}_{5+x}\text{O}_{16-x}:0.01\text{Cr}^{3+}$ ($-0.005 < x < 0.05$) at different PersL time with same exposure time	49
Fig.1.28 Images of latent fingerprints stained with $\text{Mg}_2\text{TiO}_4:\text{Mn}^{4+}$ phosphor on (a) glass, (b) Si wafer, and (c) plastic; regions squared in images, 1: termination; 2: bridge; 3: eyes; 4: island; 5: whorl; 6: bifurcation; 7: hook	50
Fig.1.29 CIE and CCT diagram of $\text{MgAl}_2\text{O}_4:0.05\text{Cr}^{3+}$	51
Fig.1.30 The PL emission, excitation spectra and CIE diagram of $\text{Ba}_2\text{TiGe}_2\text{O}_8:0.006\text{Mn}^{4+}$	52
Fig.1.31 PL emission spectrum of $\text{Mg}_{14}\text{Ge}_{4.5}\text{Ti}_{0.5}\text{O}_{24}:\text{Mn}^{4+}$ by varying temperature from (a) 6.9–303 K and (b) 303–473 K	53
Fig.1.32 Schematic representation of (a) a potential gain for down- and upconversion for a silicon solar cell; (b) solar cell with down converter	54
Fig.1.33 Excitation and emission spectrum of $\text{La}_3\text{GaGe}_5\text{O}_{16}:0.03\text{Cr}^{3+}$ phosphor applicable in luminescence solar concentrator	55
Fig.1.34 (a) Energy level diagram showing fluorescence and phosphorescence in an activator ion-based phosphor material (b) Energy level diagram in a self-activated persistent phosphor showing persistent emission.	56
Fig.1.35 (a) Graph showing the no. of publication in persistent phosphors from 1960 to 2020. (b) Schematic diagram of applications of persistent phosphors.	57
Fig.2.1 Rietveld refinement patterns of (a) MAG) (b) MGG. (c) Representation of an orthorhombic crystal arrangement for $\text{Mg}_3\text{M}_2\text{GeO}_8$ ($\text{M} = \text{Al}, \text{Ga}$) with the corresponding polyhedrons of (d) MAG and (e) MGG.	82
Fig.2.2 HRTEM images of (a) MAG sample with a magnified version of three different regions denoted as (i) (ii) and (iii), and (b) MGG sample with a magnified version of two different regions denoted as (i) and (ii).	83
Fig.2.3 Refinement patterns of (a) $\text{MAG}:\text{Mn}^{4+}, 0.03\text{Ba}^{2+}$ and (b) $\text{MGG}:\text{Mn}^{4+}, 0.10\text{Ba}^{2+}$. Schematic representation of variation in the octahedrons of (c) MAG and (d) MGG after Ba^{2+} incorporation.	86
Fig.2.4 (a) XRD patterns of $\text{MAG}:\text{Mn}^{4+}, x\text{Ba}^{2+}$ ($x = 0.0$ to 0.3) samples. (b) XRD patterns of synthesized $\text{MGO}:\text{Mn}^{4+}$, $\text{BMG}:\text{Mn}^{4+}$, $\text{MAG}:\text{Mn}^{4+}, 0.1\text{Ba}^{2+}$ and $\text{MAG}:\text{Mn}^{4+}, 0.27\text{Ba}^{2+}$ with corresponding JCPDS.	87
Fig.2.5 (a) Raman spectra of $\text{MAG}:\text{Mn}^{4+}$ and $\text{MAG}:\text{Mn}^{4+}, x\text{Ba}^{2+}$ ($x = 0.03, 0.27$) samples. (b) XPS survey spectrum of the sample $\text{MAG}:\text{Mn}^{4+}, 0.27\text{Ba}^{2+}$. Inset	89

figures show the XPS core-level spectra of Mg 2p and O 1s for the samples MAG: Mn⁴⁺ and MAG: Mn⁴⁺, 0.27Ba²⁺.

Fig.2.6 (a) UV-DRS spectra of MAG and MAG: Mn⁴⁺, xBa²⁺ (x = 0.0 and 0.27), (i) 91
Overlapping of the host absorption and the Mn⁴⁺ - O²⁻ CTB (ii) ⁴A_{2g} → ⁴T_{1g}, and (iii)
⁴A_{2g} → ⁴T_{2g} transitions. **(b)** Tauc's plots for bandgap calculation **(c)** PLE (λ_{EM}: 659
nm) and PL emission spectra (λ_{EX}: 284 nm) of MAG: Mn⁴⁺, xBa²⁺ (x = 0.0 to 0.37).
(d) Corresponding PL images under UV excitation and bar diagram showing the
variation of PL intensity with Ba²⁺ concentration under UV and blue excitation.

Fig.2.7 (a) Comparison of PL emission spectra (λ_{ex} = 284 nm) of (i) MGG: Mn⁴⁺, 98
(ii) MGG: Mn⁴⁺, 0.13Ba²⁺, (iii) MAG: Mn⁴⁺ and (iv) MAG: Mn⁴⁺, 0.27Ba²⁺ samples
with the **(b)** corresponding PL images, PL intensity (line with symbol) and colour
purity (bar). **(c)** CIE diagram and the colour coordinates of the above 4 samples.
XPS spectra of **(d)** Ga 2P and **(e)** O 1s for MGG: Mn⁴⁺. XPS spectra of **(f)** Al 2p
and **(g)** O 1s for MAG: Mn⁴⁺.

Fig.2.8 (a) Deconvoluted PL excitation spectra of **(i)** MGG: Mn⁴⁺ **(ii)** MGG: Mn⁴⁺, 100
0.13Ba²⁺ **(iii)** MAG: Mn⁴⁺ and **(iv)** MAG: Mn⁴⁺, 0.27Ba²⁺. **(b)** Plots of normalized
emission intensity vs temperature and Arrhenius plots for the samples MGG: Mn⁴⁺,
0.13Ba²⁺ and MAG: Mn⁴⁺, 0.27Ba²⁺. **(c)** Tanabe–Sugano energy illustration of Mn⁴⁺
ions in an octahedron and representation of Dq/B values of MGG: Mn⁴⁺, xBa²⁺ (x =
0.0, 0.13) and MAG: Mn⁴⁺, xBa²⁺ (x = 0.0, 0.27). **(d)** Configuration coordinate
diagram for activation energy calculation. **(e)** Bar diagram showing variation of CIE
coordinates with temperature along with variation of peak intensities (positioning at
659 nm and 630 nm) with temperature for the sample MAG: Mn⁴⁺, 0.27 Ba²⁺.

Fig.2.9 (a) Low-temperature PL spectra of MAG: Mn⁴⁺, 0.27 Ba²⁺ and 103
corresponding **(b)** Arrhenius plot (inset shows the variation of peak intensities with
temperature) **(c)** Low-temperature PL spectra of MGG: Mn⁴⁺, 0.13 Ba²⁺ (inset shows
the enlarged portion of green emission) and corresponding **(d)** Arrhenius plot (inset
shows the variation of peak intensities with temperature).

Fig.2.10 (a) Normalized CL spectra with respect to the green emission peak of 104
MAG: Mn⁴⁺, 0.27Ba²⁺ sample. **(b, b')** SEM images, **(b1, b'1)** panchromatic overall
intensity mapping, and filtered maps for the **(b2, b'2)** green (from 450 to 570 nm)
and **(b3, b'3)** red emission (from 570 and 800 nm) recorded for different sized
particles in MAG: Mn⁴⁺, 0.27Ba²⁺ sample. **(c)** Normalized CL spectra with respect

to the green emission peak of MGG: Mn⁴⁺, 0.13Ba²⁺ sample. (d, d') SEM images, (d1, d'1) panchromatic overall intensity mapping, and filtered maps for the (d2, d'2) green (from 450 to 570 nm) and (d3, d'3) red emission (from 570 and 800 nm) band recorded for different sized particles in MGG: Mn⁴⁺, 0.13Ba²⁺ sample.

Fig.2.11 Comparative (a) PLE and (b) PL spectra of the optimum MAG: Mn⁴⁺, 0.27Ba²⁺ sample with commercial BAM: Eu²⁺ (blue), YAG: Ce³⁺ (yellow) and Y₂O₃: Eu³⁺ (red) phosphors. (c) PLE spectra of MAG: Mn⁴⁺, 0.27Ba²⁺ and emission spectra of YAG: Ce³⁺ showing spectral overlap. (d) PLE spectra of MAG: Mn⁴⁺, 0.27Ba²⁺ with the PL spectra of BAM: Eu²⁺ and CMA: Tb³⁺ showing spectral overlap. 109

Fig.2.12 (a) EL spectra for the WLED fabricated by combing blue LED chip with YAG: Ce³⁺ and MAG: Mn⁴⁺, 0.27Ba²⁺ (b) EL spectra for the WLED fabricated by combing red MAG: Mn⁴⁺, 0.27Ba²⁺ phosphor with commercial green and blue phosphors using 280 nm UV LED chip. (c) EL spectra for the red LED fabricated using LED chips of different wavelengths. 110

Fig.2.S1. (a) XPS survey spectra of MAG: Mn⁴⁺ sample. (b) EDX compositional analysis, (c) SEM image and elemental mapping of Mg, Al, Ge, O, and Mn for MAG: Mn⁴⁺. 111

Fig.2.S2. EDX composition analysis and SEM image of MGG: Mn⁴⁺ with EDX elemental mapping images of Mg, Ga, Ge, O and Mn. 112

Fig.2.S3. XRD patterns of MGG, MGG: Mn⁴⁺, MGG: Mn⁴⁺, xBa²⁺ (x = 0.03 to 0.15) samples. 113

Fig.2.S4. XPS survey spectrum of the sample MGG: Mn⁴⁺, 0.13Ba²⁺. The inset shows the XPS core-level spectra of Mg 2p and O 1s for the samples MGG: Mn⁴⁺ and MGG: Mn⁴⁺, 0.13Ba²⁺. 114

Fig.2.S5. (a) UV-DRS spectra of MGG and MGG: Mn⁴⁺, xBa²⁺ (x = 0.0, 0.13), (i) Overlapping of the host absorption and the Mn⁴⁺- O²⁻ CTB (ii) ⁴A_{2g} → ⁴T_{1g}, and (iii) ⁴A_{2g} → ⁴T_{2g} transitions. (b) Tauc's plots for bandgap calculation (c) PLE spectra (λ_{em}: 659 nm) and PL emission spectra (λ_{ex}: 315 nm) of MGG: Mn⁴⁺, xBa²⁺ (x = 0.0 to 0.15). Inset shows the variation of PL intensity with Ba²⁺ concentration under UV and blue excitation. 115

Fig.2.S6. PL emission spectra of BMG: Mn⁴⁺ and MGO: Mn⁴⁺ samples under the UV excitation of 284 nm. 116

Fig.2.S7. SEM images of (a) MAG: Mn ⁴⁺ and (b) MAG: Mn ⁴⁺ , 0.27Ba ²⁺ samples.	116
Fig.2.S8. SEM images of MAG: Mn ⁴⁺ , 0.27Ba ²⁺ samples synthesized at various sintering temperatures (a) 700 °C (b) 800°C (c) 900 °C and (d) 1300 °C.	117
Fig.2.S9. PL emission spectra (λ_{ex} : 284) of MAG: Mn ⁴⁺ , 0.27Ba ²⁺ samples synthesized at various sintering temperatures (700 °C, 800°C, 900 °C and 1300 °C).	117
Fig.2.S10. PL emission decay curves of (a) MAG: Mn ⁴⁺ and MAG: Mn ⁴⁺ , 0.27Ba ²⁺ (b) MGG: Mn ⁴⁺ and MGG: Mn ⁴⁺ , 0.13Ba ²⁺ recorded at $\lambda_{\text{Em}} = 659$ nm and $\lambda_{\text{Exc}} = 284$ nm.	118
Fig.3.1 Retvield refinement patterns of (a) MAG: Cr ³⁺ and (b) MAG: Cr ³⁺ , 0.05Sr ²⁺ . (c) Representation of orthorhombic crystal structure for MAG sample and corresponding polyhedrons. (d) Bar diagram showing the variation in lattice parameter values and cell volume for sample 1 (MAG), Sample 2 (MAG: Cr ³⁺) and Sample 3 (MAG: Cr ³⁺ , 0.1Sr ²⁺).	137
Fig.3.2 (a) Schematic representation of structural distortion in [(Mg/Al)O ₆] octahedrons after Sr ²⁺ ions' doping (b) The powder XRD patterns of MAG: 0.01Cr ³⁺ , xSr ²⁺ (x = 0.0 to 0.15) samples and the (c) enlarged portion of the patterns between 2 θ ~ 34° to 38°	139
Fig.3.3 (a) and (b) HRTEM images of MAG: Cr ³⁺ , 0.1Sr ²⁺ sample with a magnified version of four different regions and the corresponding reduced FFT	140
Fig. 3.4 (a) UV-Vis DRS spectra of the undoped MAG, MAG: Cr ³⁺ and MAG: Cr ³⁺ , 0.1M ²⁺ (M = Ca, Sr, Ba) and (b) Tauc's plot for bandgap calculation (c) UV-Vis DRS spectra of MAG: Cr ³⁺ , 0.1Sr ²⁺ and ZnGa ₂ O ₄ : Cr ³⁺ .	142
Fig.3.5 (a) PLE (λ_{em} : 693 nm) and emission (λ_{ex} : 400 nm) spectra of alkaline earth metal ions co-doped MAG: 0.01Cr ³⁺ , 0.1 M ²⁺ (M = Ca ²⁺ , Sr ²⁺ , and Ba ²⁺) samples. (b) simplified energy level diagram of Cr ³⁺ ions in d ³ electronic configuration (strong crystal field environment) (c) PLE (λ_{em} : 693 nm) and emission spectra (λ_{ex} : 400 nm) of MAG: 0.01Cr ³⁺ , xSr ²⁺ (x = 0.0 to 0.13) (d) Bar diagram showing the variation of PL emission intensity under blue and green excitation.	144
Fig.3.6 The (a) PLE (λ_{em} : 693 nm) and (b) emission spectra of the MAG: Cr ³⁺ , 0.1Sr ²⁺ and ZnGa ₂ O ₄ : 0.01Cr ³⁺ sample	145
Fig.3.7 (a) Powder XRD patterns of MAG: Cr ³⁺ , 0.1Sr ²⁺ , yGa ³⁺ (y = 0.0 to 1.5) samples and (b) enlarged portion of XRD pattern from 35.5° to 37°. (c) TEM image and EDX elemental mapping of various elements in MAG: Cr ³⁺ , 0.1Sr ²⁺ , 1.5Ga ³⁺	146

sample. **(d)** HRTEM image showing the lattice planes of MAG: Cr³⁺, 0.1Sr²⁺, 1.5 Ga³⁺ sample and the r-FFT of a small portion.

Fig.3.8 **(a)** UV-Vis spectra of MAG: Cr³⁺ and MAG: Cr³⁺, 0.1Sr²⁺, xGa³⁺ (x = 0.0 to 0.15) samples **(b)** PLE (λ_{em} : 693 nm) and emission (λ_{ex} : 400 nm) spectra of MAG: Cr³⁺ and MAG: Cr³⁺, 0.1Sr²⁺, xGa³⁺ (x = 0.0 to 0.15) samples and the corresponding **(c)** emission spectra under 450 nm excitation. **(d)** Graph showing the variation of FWHM and emission intensity for different Ga co-doped samples under different excitations. **(e)** Energy level diagram of Cr³⁺ ions in d³ electronic configuration showing emission from both weak and strong crystal field environments. 149

Fig.3.9 Temperature-dependent PL emission spectra of **(a)** MAG: Cr³⁺, 0.1Sr²⁺ and corresponding **(b)** contour plot. Temperature-dependent PL emission spectra of **(c)** MAG: Cr³⁺, 0.1Sr²⁺, 1.0Ga³⁺, and **(d)** corresponding PL plot. 151

Fig.3.10. Plots of normalized emission intensity vs temperature and Arrhenius plots for the samples **(a)** MAG: Cr³⁺, 0.1Sr²⁺ and **(b)** MAG: Cr³⁺, 0.1Sr²⁺, 1Ga³⁺. **(c)** Configuration coordinate diagram for activation energy calculation **(d)** The comparison of luminescence thermal stability at 423 K and internal quantum efficiency (IQE) 152

Fig.3.11 **(a)** The EL spectrum of the fabricated LED for display application by combing 410 nm LED with MAG: Cr³⁺, 0.1Sr²⁺. **(b)** The EL spectrum of the fabricated LED for plant growth application by combing 410 nm LED with MAG: Cr³⁺, 0.1Sr²⁺, 1.0Ga³⁺ 153

Fig.3.12 EL spectra of **(a)** NIR pc-LED1 (fabricated using 410 nm LED with MAG: Cr³⁺, 0.1Sr²⁺, 1.5Ga³⁺) and **(b)** NIR pc-LED2 (fabricated using 450 nm LED with MAG: Cr³⁺, 0.1Sr²⁺, 1.5Ga³⁺). Images of CSIR NIIST logo and QR code **(c)** under indoor light and **(d)** under fabricated NIR LEDs 155

Fig. 3.13 Effect of MAG: Cr³⁺, 0.1Sr²⁺ on cell viability of **(a)** HeLa cells and **(b)** HepG2 cells. **(c)** Cellular uptake of MAG: Cr³⁺, 0.1Sr²⁺ by HeLa cells. 156

Fig. 3.14 Time dependent internalisation of MAG: Cr³⁺, 0.1Sr²⁺ by HeLa cells. 157

Fig.3.S1 **(a)** The EDX spectra and **(b)** EDX elemental mapping of Mg, Sr, Al, Ge, O and Cr for MAG: Cr³⁺, 0.1Sr²⁺ sample. 158

Fig.3.S2 PL emission spectra of MAG: Cr³⁺ sample for under 280 nm excitation. 158

Fig.3.S3. The EDX spectra of MAG: Cr³⁺, 1.5 Ga³⁺, 0.1Sr²⁺ sample showing the presence of Mg, Al, Ge, Ga, Sr and Cr elements in the sample. 159

Fig.4.1. PLE and PL spectra of (a) CZSO ₄ , SZSO ₄ and (b) SZSO ₄ : x wt% NH ₄ Cl (x = 0 to 15 wt%).	172
Fig.4.2 (a) Rietveld refinement pattern of SZSO ₆ phosphor and the corresponding (b) monoclinic crystal structure	173
Fig.4.3 (a-b) HRTEM images of SZSO ₆ sample with magnified versions (inset) and reduced FFT (inset) showing the planes corresponding to different phases.	175
Fig.4.4 (a) XPS survey spectra of SZSO ₆ : 12wt% NH ₄ Cl. Insets: core level XPS spectra of (a1) Sr 3d, (a2) Zr 3d, (a3) Si 2p and (a4) O 1s. (b) XPS survey spectra of the SZSO ₆ : 12wt% NH ₄ Cl, 0.02Bi ³⁺ . Insets core level XPS spectra of (b1) Sr 3d, (b2) Zr 3d, (b3) Si 2p, (b4) O 1s and (b5) Bi 4f.	177
Fig.4.5 The (a) UV- vis diffuse reflectance spectra and (b) Tauc plots for SZSO ₆ , SZSO ₆ : 12wt% NH ₄ Cl and SZSO ₆ : 12 wt% NH ₄ Cl, 0.02 Bi ³⁺ .	178
Fig.4.6 (a) A comparison of PLE and PL spectra of SZSO ₄ and SZSO ₆ . (b) PLE and PL spectra of SZSO ₆ : x wt% NH ₄ Cl (x = 0, 4, 8, 12, 15,18, 20), (c) CIE diagram of SZSO ₆ : 12 wt% NH ₄ Cl phosphor and (d) PL decay curves of SZSO ₆ and SZSO ₆ : 12 wt% NH ₄ Cl	180
Fig.4.7 (a) PL images of CZSO ₄ , SZSO ₄ and SZSO ₄ : 12 wt% NH ₄ Cl sample under 254 nm excitation. PersL images of (b) CZSO ₄ , SZSO ₄ , SZSO ₄ : 12 wt% NH ₄ Cl, and (c) SZSO ₆ and SZSO ₆ : 12 wt% NH ₄ Cl samples after illuminating under 254 nm irradiation for one minute.	181
Fig.4.8 (a) PLE and PL spectra of the xBi ³⁺ doped SZSO ₆ : 12 wt% NH ₄ Cl (x = 0.01, 0.02, 0.03 and 0.04), (b) PersL images of the SZSO ₆ :12 wt% NH ₄ Cl, SZSO ₆ : 12 wt% NH ₄ Cl, 0.02 Bi ³⁺ and post annealed vacuum treated SZSO ₆ : 12 wt% NH ₄ Cl, 0.02 Bi ³⁺ sample (c) PLE and PL spectra of the SZSO ₆ : 12 wt% NH ₄ Cl, 0.02 Bi ³⁺ and post annealed vacuum treated SZSO ₆ : 12 wt% NH ₄ Cl, 0.02 Bi ³⁺ sample (d) deconvoluted core-level spectra of O 1s for the post annealed vacuum treated SZSO ₆ : 12 wt% NH ₄ Cl, 0.02 Bi ³⁺ phosphor and (e) PersL decay curves of SZSO ₆ : 12 wt% NH ₄ Cl, 0.02 Bi ³⁺ and post annealed vacuum treated SZSO ₆ : 12 wt% NH ₄ Cl, 0.02 Bi ³⁺ phosphor.	184
Fig.4.9 Digital photographs of dip pen writing on (a) currency note and (b) QR code under 365 nm, 254 nm and after irradiation stops.	186
Fig.4.10 (a) PLE spectrum of MAG: Mn ⁴⁺ , 0.27Ba ²⁺ and PL spectrum of SZSO ₆ : 12wt% NH ₄ Cl and (b) EL spectrum of the MAG: Mn ⁴⁺ , 0.27Ba ²⁺ / SZSO ₆ : 12wt%	187

NH₄Cl mixture and the absorption spectra of phytochrome (P_r) and Chlorophyll a, b, and carotenoids.

Fig.4.S1 (a) XRD patterns of CZSO₄ and SZSO₄ (b) XRD pattern of SZSO₄: x wt% NH₄Cl (x = 0, 4, 8, 12, 15). 188

Fig.4.S2. XRD patterns of (a) SZSO₆: x wt% NH₄Cl (x = 0, 4, 8, 12, 15, 18 wt%) samples and (b) SZSO₆: 12 wt% NH₄Cl, yBi³⁺ (y = 0, 0.01, 0.02, 0.03, 0.04). 189

Fig.4.S3. (a-b) HRTEM images of undoped SZSO₆ with magnified versions (inset) and reduced FFT (inset) showing the planes corresponds to different phases. 189

Fig.4.S4 (a) SEM image and (b) TEM image of SZSO₆: 12wt% NH₄Cl, 0.02Bi³⁺ sample. (c) The EDAX spectrum and atomic percentage of elements in SZSO₆: 12 wt% NH₄Cl, 0.02Bi³⁺. (d) EDAX elemental mapping of Sr, Zr, Si, O and Bi for SZSO₆: 12 wt% NH₄Cl, 0.02Bi³⁺ phosphor. 190

Fig.4.S5 Persistent luminescence mechanism of SZSO₆: 12wt%NH₄Cl, 0.02 Bi³⁺. 191

Fig.4.S6 PLE spectrum of MAG: Mn⁴⁺, 0.27Ba²⁺ (λ_{em}: 659 nm) and PL emission (λ_{ex}: 284 nm) spectrum of SZSO₆: 12wt% NH₄Cl.

List of tables

Table 1.1 Energies of eight electrostatic terms (LS terms) in the d^3 system in terms of B and C taking the energy of ground-level 4F as zero.	8
Table 1.2 The Racah parameters values of free ions having d^3 electronic configuration.	8
Table 1.3 Splitting of LS terms of the d^3 (or d^7) configuration in the O_h or T_d group.	8
Table 1.4 Synthesis parameters, crystal structure and space groups of Mn^{4+} -doped germanate phosphors.	18
Table 1.5 Spectroscopic properties of some of the important germanates	19
Table 2.1 Spectroscopic parameter values obtained from PL emission and excitation spectra	101
Table 2.S1: The lattice parameters of the following refined samples	118
Table 2.S2: Rietveld refined atomic coordinates and fraction of occupancies of MAG and MGG samples.	119
Table 2.S3: Rietveld refined atomic coordinates and fraction of occupancies of MAG: $0.03Ba^{2+}$ and MGG: Mn^{4+} , $0.1Ba^{2+}$ samples.	120
Table 2.S4: Calculated bond lengths (\AA) and average bond lengths (\AA) in the following samples.	121

Preface

The innovation of various kinds of phosphor material paved the way for the generation of energy-efficient light-emitting diodes (LEDs). Further, these materials started to replace many of the conventional functional materials available for various optoelectronic, bioimaging, sensors, security applications, etc. The synthesis and tuning of the emission wavelength to the desired wavelength with high quantum efficiency without using rare earth activators (Eu^{2+} , Eu^{3+} , Tb^{3+} , Dy^{3+} , etc.) is still challenging in this field. The rare earth-free inorganic phosphor materials are highly recommended due to their low cost. Meanwhile, oxide materials possess many advantages, such as being chemically and thermally stable. The use of transition metal ion activators (such as Mn^{4+} and Cr^{3+}), Bi^{3+} ions, and self-activated phosphors are suitable solutions for replacing rare earth activators. The Mn^{4+} and Cr^{3+} ions possess $3d^3$ electronic configuration and show excellent optical, magnetic and electronic properties. The Bi^{3+} ions are excellent in enhancing the properties of self-activated phosphors, and Bi^{3+} activators are capable of producing emission from ultraviolet (UV) to near infra-red (NIR) region depending upon the host material.

Designing and producing phosphor material with a suitable wavelength range for the desired application is very crucial. Here, our primary efforts are to solve the issues related to the currently available white light-emitting diode (WLED). Commercial WLEDs produce cool white light emissions due to the lack of red components. The commercially available red phosphors activated by Mn^{4+} ions are fluorides and not thermally stable under the working temperatures of LEDs. An efficient rare earth-free deep red-emitting phosphor is required to supplement this issue. Moreover, the demand for red LEDs matching the absorption range of chlorophylls and phytochrome (P_r) is increasing. Hence, efficient deep red phosphors can also supplement this demand. The second goal of the thesis work is the development of tuneable deep red to NIR emitting phosphors excitable with visible radiation for various LEDs and displays and suitable for bio-imaging applications. The highly efficient rare earth-free deep red to NIR emitting LEDs are still lacking. The above LEDs can be used for night vision surveillance, red light therapy, plant growth, display and bioimaging applications. The currently available phosphors used for bioimaging are based on rare earth activators, and $\text{NaYF}_4: \text{Nd}^{3+}$ -based cell imaging requires continuous exposure to an NIR laser, which in turn can cause cell damage in cells. Many of the currently available phosphors are activated by UV light, and UV light exposure is also not suitable for bioimaging. Hence, a visible light excitable

deep red to NIR emitting phosphors is highly recommended to solve this issue. Moreover, there is a scarcity of self-activated cyan emitting persistent phosphors. Most of the reported persistent cyan emitting persistent phosphors are activated by rare earth ions. Further, there exists a high demand for cyan-emitting persistent phosphors for security applications. Hence, developing persistent cyan emitting phosphor with high quantum yield and better lifetime is highly required for information storage and anticounterfeiting applications. This thesis focuses on developing rare earth-free inorganic oxide phosphors for WLEDs, deep red to NIR LEDs, cell imaging, display, plant growth and security applications.

The thesis is divided into five chapters. In Chapter 1, we discuss the theory, mechanisms and significance of the Mn^{4+} and Cr^{3+} activated deep red and NIR emitting phosphors. The various methods for improving red/NIR emission and the potential applications of the above phosphors are also described. Further, the mechanism, overview and various applications of recently reported self-activated persistent phosphors are elaborated in the final part of the chapter 1.

Chapter 2: Enriching the deep-red emission in $(\text{Mg}, \text{Ba})_3\text{M}_2\text{GeO}_8: \text{Mn}^{4+}$ ($\text{M} = \text{Al}, \text{Ga}$) compositions for light-emitting diodes.

Chapter 2 deals with the development of transition metal ions (Mn^{4+}) activated deep red-emitting phosphors. In this chapter, innovative deep red-emitting $(\text{Mg}, \text{Ba})_3\text{Al}_2\text{GeO}_8: \text{Mn}^{4+}$ phosphor was developed from its analogue of $\text{Mg}_3\text{Ga}_2\text{GeO}_8: \text{Mn}^{4+}$. Initial replacement of Ga^{3+} by Al^{3+} yielded $\text{Mg}_3\text{Al}_2\text{GeO}_8: \text{Mn}^{4+}$, which showed much more intense red emission than $\text{Mg}_3\text{Ga}_2\text{GeO}_8: \text{Mn}^{4+}$ due to the strong preference of Mn^{4+} to the $[\text{AlO}_6]$ octahedrons compared to $[\text{GaO}_6]$ octahedrons. The co-existing phases of MgAl_2O_4 and Mg_2GeO_4 in $\text{Mg}_3\text{Al}_2\text{GeO}_8$ also contributed to the Mn^{4+} luminescence by providing more preferable octahedral sites for Mn^{4+} occupancy. These sites reduced the natural reduction probability of Mn^{4+} to Mn^{2+} in the tetrahedral sites, which was confirmed by the low-temperature photoluminescence and cathodoluminescence studies for the first time. Eventually, the partial substitution of larger Ba^{2+} ions in Mg^{2+} sites caused structural distortions and generated new Ba impurity phases, which improved the Mn^{4+} photoluminescence further. Under UV and violet-blue exposure, the optimum composition $\text{Mg}_{2.73}\text{Ba}_{0.27}\text{Al}_2\text{GeO}_8: \text{Mn}^{4+}$ exhibited deep red emission at 659 nm, which was 35 folds greater in intensity than the base composition of $\text{Mg}_3\text{Ga}_2\text{GeO}_8: \text{Mn}^{4+}$. The emission matched with the absorption of chlorophylls liable for plants' photosynthesis. The

intense red emission with 100% colour purity of the optimised composition makes it a suitable red phosphor to enhance the colour rendering of commercial white LEDs.

Chapter 3: Compositionally engineered (Mg, Sr)₃(Al, Ga)₂GeO₈: Cr³⁺ phosphors with tuned emission from ultra-sharp red to ultra-broad NIR for LEDs and *in vitro* cell imaging applications.

In Chapter 3, we demonstrate the various applications of a novel tuneable deep red to NIR-emitting phosphor. At first, a novel Mg₃Al₂GeO₈: 0.01Cr³⁺ phosphor with ultra-sharp band emission peaking at 693 nm having full width at half maximum (FWHM) of around 4 nm has been developed. The emission intensity, as well as the FWHM of the phosphor, has been increased by the substitution of alkaline earth metal ions. The optimum Mg_{2.9}Al₂GeO₈: 0.01Cr³⁺, 0.1Sr²⁺ exhibits three times greater emission intensity than Mg₃Al₂GeO₈: 0.01Cr³⁺ sample, and the FWHM increased to ~12 nm. The additional [MgO₆] sites contributed from the newly generated Sr impurity phase and the structural distortion in the Cr³⁺ occupied sites are responsible for the emission enhancement. In addition, a series of Ga³⁺ co-doped Mg_{2.9}(Al_{2-y}Ga_y)GeO₈: 0.01Cr³⁺, 0.1Sr²⁺ (y = 0, 0.5, 1, 1.5) samples have been developed. The partial Ga³⁺ substitution created some weak crystal field environment [GaO₆] suitable for Cr³⁺ ions to occupy. The combined emission from the strong and weak crystal field environment resulted in a broadband emission (600 nm to 1050 nm) with an FWHM of ~154 nm covering the first biological window region effectively. Hence, the developed phosphors are suitable for bio-imaging applications. Finally, various phosphor-converted LEDs have been fabricated using commercial 410 nm and 450 nm LEDs. The sharp red emitting LED produced by combining 410 nm LED with Mg_{2.9}Al₂GeO₈: 0.01Cr³⁺, 0.1Sr²⁺ phosphor having 100% colour purity can be used for display application. The 410 nm LED combined with Mg_{2.9}(AlGa)GeO₈: 0.01Cr³⁺, 0.1Sr²⁺ phosphor can be used for plant growth application since the absorption range of phytochrome P_{fr} matches well with the emission range of the developed LED. Moreover, the NIR LED produced from Mg_{2.9}(Al_{0.5}Ga_{1.5})GeO₈: 0.01Cr³⁺, 0.1Sr²⁺ phosphor having increased FWHM finds potential application in night vision surveillance.

Chapter 4: Inducing defects to boost the persistent luminescence in novel cyan emitting rare-earth free strontium zirconium silicate for dynamic anti-counterfeiting and plant growth LED applications

Chapter 4 reports a novel cyan-emitting persistent phosphor suitable for security and plant growth applications. Initially, a self-activated $\text{Sr}_2\text{Zr}(\text{SiO}_3)_4$ phosphor is developed from the reported $\text{Ca}_2\text{Zr}(\text{SiO}_3)_4$. The persistence emission and photoluminescence intensity of the above phosphors are enhanced with NH_4Cl concentration. The XRD pattern of the synthesised sample matches with monoclinic- $\text{Sr}_3\text{Y}_2\text{Si}_6\text{O}_{18}$ (JCPDS 00-065-0204), and this led to the development of a novel self-activating persistent cyan emitting $\text{Sr}_2\text{Zr}_2(\text{SiO}_3)_6$ phosphor. The Sr^{2+} and Zr^{4+} ions share six, seven, and eight co-ordinate environments in the host. The XRD analysis revealed the presence of a secondary orthorhombic $\text{Sr}_3\text{Zr}_2\text{O}_7$ phase with some impurity peaks of precursor materials. The various planes in the host lattice were confirmed from the HRTEM analysis. The optimised $\text{Sr}_2\text{Zr}_2(\text{SiO}_3)_6$: 12 wt% NH_4Cl phosphor material with high intensity and persistent luminescence shows potential application in information storage due to its self-activated property. The presence of oxygen vacancies in these samples was identified from the XPS analysis. The Bi^{3+} co-doping and the vacuum treatment increased the cation vacancies and oxygen vacancies in the sample. Interestingly, an orange-red emission is observed around 620 nm due to Bi^{3+} incorporation. The oxygen-vacancy-induced electronic localisation around the Bi^{3+} ions are the main reason for the orangish-red luminescence peak. The optimised vacuum-treated $\text{Sr}_2\text{Zr}_2(\text{SiO}_3)_6$: 12 wt% NH_4Cl , 0.02 Bi^{3+} sample with high persistence luminescence has been used for information storage. The designed QR code using the above phosphor mixed with rare earth-free deep red phosphor stores the information CSIR NIIST, which can be read out and found suitable for security applications. Further, the material is used for anti-counterfeiting applications. Here, the vacuum-treated $\text{Sr}_2\text{Zr}_2(\text{SiO}_3)_6$: 12 wt% NH_4Cl , 0.02 Bi^{3+} material is incorporated with rare earth-free deep red phosphor. Meanwhile the high intense $\text{Sr}_2\text{Zr}_2(\text{SiO}_3)_6$: 12 wt% NH_4Cl phosphor has been mixed with deep red emitting phosphor and combined with 280 nm LED and 410 nm LED for the plant growth applications.

Chapter 5: Conclusions

The phosphor materials received a lot of attention owing to their ability to produce light in various wavelength ranges. The thesis focused on the development of various inorganic oxide phosphors with high quantum yield through the crystal field engineering of the currently available phosphors. The thesis can shed light on the various methods to improvise and tune the properties of the phosphor material for the desired application. Structural and optical studies of each compound have been studied in detail, and these studies were correlated with suitable

experimental proofs. The developed deep red phosphor was used for the WLED and plant growth application. The crystal field and engineering and activator ion modifications done on the above phosphor could produce deep red to NIR emitting phosphors, and these phosphors find potential application in the deep red/NIR LEDs and in *In vitro* bioimaging applications. The third chapter deals with the self-activated persistent cyan-emitting phosphors that can be used for security and plant growth applications.

Chapter 1
Introduction

1.1 Abstract

Deep red/NIR emitting phosphors are becoming the hot area of research during these times owing to their wide variety of applications in various fields, including lighting, display, imaging, and many others. The transition metal ions, especially Mn^{4+} and Cr^{3+} activated oxide phosphors possess admirable merits such as high chemical and thermal stability, eco-friendly preparation, and emission in the deep-red/NIR region. It is important to mention that Mn^{4+} doped oxides usually show emission spectra peaking above 650 nm. Thanks to this emissive property, $\text{Mn}^{4+}/\text{Cr}^{3+}$ doped germanates can be the best choice for lighting, display, sensing, bioimaging etc. Moreover, the emission of these phosphors can be extended to the near-infrared region. Most of the reports on Mn^{4+} activated phosphors concentrate on the white light-emitting diode applications. Whereas the reports on Cr^{3+} activated phosphors are focused on their deep red to near-infrared emission. This chapter mainly focused on the Mn^{4+} and Cr^{3+} -activated deep red/near-infrared emitting oxide phosphors, especially germanates. The octahedral sites in germanate oxides are ideal for accommodating these transition metal ions and thoroughly discussed the crystal structure-dependent luminescence behaviour of the reported germanate phosphors. In addition to that, we have also discussed various methods for improving the luminescence properties of these phosphors. Finally, we have presented possible potential applications of the reviewed phosphors. We believe that this review will give the insight to develop new deep red/ near-infrared emitting phosphors and it will be helping the researchers to improve the luminescence properties of different existing phosphors. After all, it will be good to make a better understanding of the reported work in this area in a short time. Meanwhile an overview of the self-activated persistent phosphor mechanism and a detailed description of the cyan emitting persistent phosphors and its application in various areas are elaborated in the final part of this chapter.

1.2 Review on deep red-emitting rare-earth free germanates and their efficiency as well as adaptability for various applications.

1.2.1 Introduction

Red emitting phosphors have crucial roles in the areas of solid-state lighting, field emission displays, thermal sensors, solar cells, plant cultivation, bio-imaging, and many others.¹⁻⁶ The activators used in the red-emitting phosphors can be sharp band red-emitting rare-earth ions (Eu^{3+} , Pr^{3+} , Sm^{3+}), broad-band red-emitting rare-earth ions (Eu^{2+} , Ce^{3+}), and the sharp band deep red-emitting transition metals (Mn^{4+} , Cr^{3+}). The sharp-band red-emitting

phosphors produce a red colour with high quantum efficiency, which is eye sensitive for humans. However, the absence of a wide excitation band in the ultra-violet (UV) or blue region limits their applications in light-emitting diodes (LEDs).⁷ The broad-band red-emitting phosphors such as nitrides, oxynitrides, silicates, aluminates, which are mostly activated by Eu^{2+} ions, have better LED applications while comparing with that of Eu^{3+} doped phosphors. Nitrides hosts such as $\text{CaAlSiN}_3:\text{Eu}^{2+}$ and $\text{Sr}_2\text{Si}_5\text{N}_8:\text{Eu}^{2+}$ are known as efficient phosphors owing to their broad absorption band, high luminescence intensity, and low thermal quenching.^{8, 9} However, these broad red-emitting phosphors possess either harsh synthesis conditions, high production cost, toxicity, or poor chemical and thermal stability.¹⁰ Moreover, the inability of Eu^{2+} ions in producing emissions beyond 650 nm in the visible region and non-radiative loss due to the re-absorption phenomena further restrict their practical utility in several fields including agriculture.¹¹ Eventually, the focus of the research community recently moved to the development of red-emitting phosphors activated by transition metal ions such as Mn^{4+} , Mn^{2+} , Cr^{3+} , and Bi^{2+} .¹²⁻¹⁵ In addition, a strong interest is grown in producing phosphors, which exhibit broad absorption in the UV and blue regions and are able to emit sharp-band red or deep-red lights and emission.^{12, 16, 17}

Among all the transition metal ions, Mn^{4+} ions may be the better choice for red-emitting phosphors since the spectral position of the red emission (600-790 nm) can be tuned by appropriate modification in their crystal field environment as the position of their emission peaks depends upon the host employed.^{16, 17} The intense absorption band in the UV and blue region is attributed to the spin-allowed ${}^4\text{A}_{2g} \rightarrow {}^4\text{T}_{1g}$, ${}^4\text{T}_{2g}$ transitions. The excited electrons in the ${}^4\text{T}_{1g}$ and ${}^4\text{T}_{2g}$ states non-radiatively relax to the ${}^2\text{E}_g$ state leading to a spin forbidden ${}^2\text{E}_g \rightarrow {}^4\text{A}_{2g}$ transition, which is responsible for the red emission. Generally, Mn^{4+} ions prefer to occupy the octahedral site as they possess strong crystal field stabilization energy in an octahedral environment.^{16, 17} The Mn^{4+} ions can be very well substituted for Ga^{3+} ¹⁸, Al^{3+} ¹¹, Ge^{4+} ⁶, Ti^{4+} ¹⁹, Sb^{5+} ²⁰, Si^{4+} ²¹, Sn^{4+} ²², Zr^{4+} ²³, Ta^{5+} ²⁴, Te^{6+} ²⁵, Sc^{3+} ²⁶, Nb^{5+} ²⁷, W^{6+} ²⁸ etc. in the unit cell, and thus, the covalency of Mn^{4+} -ligand bonding can be altered.

Another deep red-emitting transition metal under consideration is Cr^{3+} for synthesizing deep red-emitting phosphors. Although the Cr^{3+} ion has the essentially same electronic configuration as the Mn^{4+} ion (i.e., $3d^3$), their electronic transitions are quite different.²⁹ In fact, Mn^{4+} -doped oxide and fluoride phosphors emit only red light caused by the ${}^2\text{E}_2 \rightarrow {}^4\text{A}_2$ transitions (strong crystal field)³⁰, but Cr^{3+} -doped oxide phosphors can emit red light caused

by the ${}^2E_2 \rightarrow {}^4A_2$ transitions or deep red/far-red/near-infrared light caused by the ${}^4T_2 \rightarrow {}^4A_2$ transitions (weak crystal field).³¹ Similarly, Cr^{3+} -doped fluoride phosphors emit only deep red or far-red/near-infrared light due to the ${}^4T_2 \rightarrow {}^4A_2$ transitions.³² Comparing to Mn^{4+} activated hosts, Cr^{3+} activated hosts have some other merits such as emission in deep red and near-infrared (NIR) region, long persistence, etc. The emission of Cr^{3+} doped phosphors in the NIR region generates its applications in near-infrared bio-imaging, dark glow signage, photodynamic tumour therapy, night vision surveillance, etc.³³⁻³⁵ On the other hand, its emission in the deep-red region could facilitate the applications in solid-state lighting, plant photo-morphogenesis, solar concentrator, display etc.³⁶⁻³⁸

Fluorides, oxides, and oxyfluorides are the three types of hosts where the Mn^{4+} ions can be doped efficiently. In particular, Mn^{4+} doped fluoride hosts are getting huge attention owing to their ability in producing intense red emission in the region of 600 to 640 nm, high colour purity, broad excitation bands in the UV and blue regions.^{39, 40} Because of the eye-sensitive red-emitting nature below 640 nm, these materials are promising candidates for improving the colour rendering index (CRI) of white light-emitting diodes (W-LEDs).⁴¹ Eventually, these phosphors can be efficiently used for the backlighting in liquid-crystal displays (LCDs) and LEDs since the transmittance spectrum of the optical filters matches well with that of the narrow red emission produced by these phosphors.⁴² Among the various fluoride compositions having the empirical formula of $A_2MF_6:Mn^{4+}$ fluoride phosphors (A = alkali metal; M = Ge, Ti, Si, etc.), $K_2SiF_6:Mn^{4+}$ and $K_2TiF_6:Mn^{4+}$ are the popular phosphors for the W-LEDs application.^{43, 44} But the synthesis of these phosphors requires a highly corrosive HF solution. In addition, the obtained fluorides are suffering from low stability and have considerable moisture sensitivity, which makes them inadequate for high-temperature applications. Furthermore, the red emission from the Mn^{4+} -activated fluorides usually gets saturated at a certain excitation power, which restricts their commercial utility.³⁹ Eventually, the highly electronegative fluoride environment is also not favourable for tuning the red emission peak above 650 nm.⁴⁵

Meanwhile, the researchers have started to focus on oxyfluoride hosts, which combine the advantage of fluorides as well as oxides. In comparison with other hosts, oxyfluoride may possess non-centrosymmetric structures as the incorporation of the fluorine into the oxide sites will lead to a distortion of polyhedron coordination.⁴⁶ Furthermore, due to the similar ionic radii of the F^- and O^{2-} ions,⁴⁷ the formation of a stable anionic sub-lattice is possible in

oxyfluorides, owing to which, oxyfluorides show excellent absorption and emission properties. These phosphors are widely applicable in W-LEDs also in the areas of catalysts, batteries, UV shielding properties, etc.⁴⁸⁻⁵¹ The most researched oxyfluoride material is Sr₃AlO₄F due to its easy synthesis, its better stability, and its excellent luminescence property. However, this host can be optically activated by Eu³⁺ ions only for producing red-orange emissions which have their own drawbacks including the lack of broadband absorption and emission nature, as mentioned earlier.⁴⁹⁻⁵¹ Hence the studies on Mn⁴⁺ doped oxyfluorides have gathered some attention for the last few years. Few red-emitting Mn⁴⁺ doped oxyfluorides phosphors such as BaNbOF₅:Mn⁴⁺⁵², Cs₂NbOF₅:Mn⁴⁺⁵³, Na₂WO₂F₄:Mn⁴⁺⁵⁴, Rb₂NbOF₅:Mn⁴⁺⁵⁵, and Cs₂WO₂F₄:Mn⁴⁺⁵⁶ have been reported recently. Even though these phosphors exhibit satisfactory luminescence properties, they could not eliminate the usage of HF solution during their synthesis, make them imperfect in large-scale eco-friendly production.

The oxide hosts bear more advantages due to the excellent thermal and chemical stability and outstanding material properties including hardness, larger transparency, etc.⁵⁷ Compared with the oxyfluoride hosts, the oxide hosts exhibit stronger covalence, weaker polarizability, and lesser thermal vibration which make them favourable for attaining intense red emission.⁵⁸ Chen *et al.* reported that the Mn⁴⁺ ions in fluoride hosts are associated with the ²E_g value ranging from 626 nm to 635 nm.¹⁷ While in oxide hosts, its range becomes wider from 652 nm to 713 nm owing to the high covalency of oxides, and considerable shifting of energy levels due to the nephelauxetic effect.^{17, 59, 60} Such a wide spectral range of Mn⁴⁺ ions in oxides can extend their application by taking the advantage of deep red emission. Furthermore, a solid-state synthesis is an easiest and adaptable method for synthesizing various Mn⁴⁺-activated oxides since it includes simplified stoichiometric mixing, grinding, and high-temperature heating.¹⁰ In the various oxide hosts, Mn⁴⁺ can easily be stabilized in aluminates, germanates, titanates, zirconates, niobates, arsenate, etc.¹⁶ Germanate-based phosphors are a promising host as they provide the most optimal octahedral sites for Mn⁴⁺ ions due to the same ionic radii and charge of Ge⁴⁺ and Mn⁴⁺ ions.⁴⁷ The recent rising of germanates as the suitable hosts of Mn⁴⁺ ions for producing deep red emission above 650 nm attracted our focus to accomplish a detailed review of their progress as the prominent deep red-emitting phosphor systems. The development scheme of deep red-emitting phosphors from nitrides to Mn⁴⁺/Cr³⁺ activated germanates and gallates is represented in **Fig. 1.1**

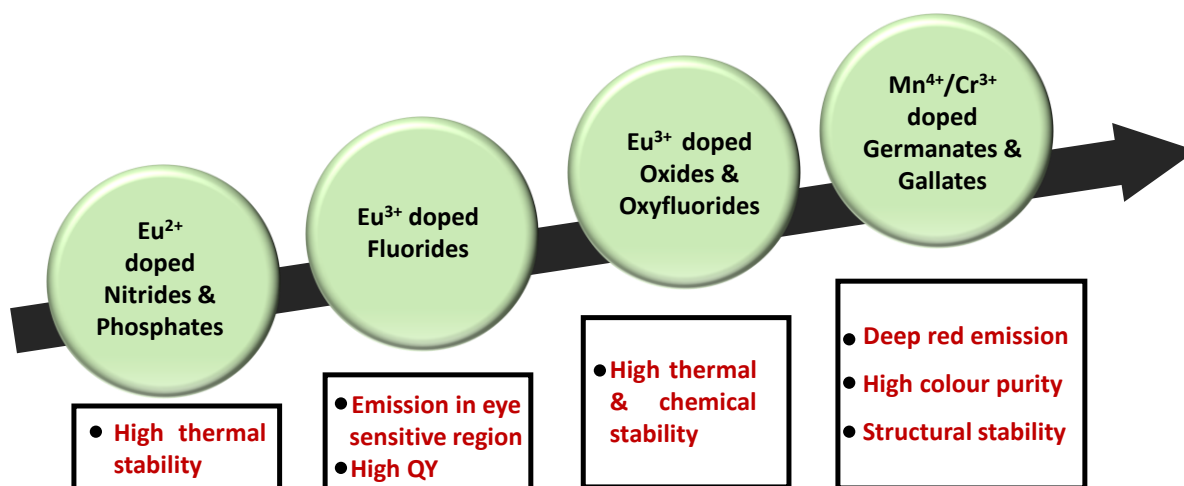


Fig.1.1 Development scheme of deep red-emitting phosphor.

This chapter focuses on the Mn⁴⁺ and Cr³⁺ activated germanates with deep red/ NIR emission above 650 nm. Such deep red emission systems are highly capable of providing a larger colour gamut and thereby accomplish the parameter values for ultra-high-definition television systems according to ITU-R BT.2020-2 recommendations.⁶ So far, some interesting germanate host systems have been proposed from the formulas of A–Ge–O and M–Ge–O (A = Alkali metal; M = alkaline-earth metal), which can emit deep red emissions in the desired wavelength region under UV and blue excitation. Although these germanates are generated using the same chemical formula, however, their crystal arrangements are not similar. This is because of the fact that the crystal structure mainly depends on the size of the monovalent cations at the A or divalent cations at the M site as well as on the bond length of Ge–O. Hence, there are decent possibilities for finding new phosphors based on the alkali- or alkaline-earth germanate system depending upon a suitable search for one or a combination of alkali or alkaline-earth metal ions. Therefore, we emphasize the structural and spectroscopic properties of Mn⁴⁺ and Cr³⁺ activated deep-red/NIR emitting germanates for some of their special characteristic features, which are discussed in sections 1.4 and 1.5 of this review. Additionally, we have also discussed the various techniques employed to enhance the red emission like synthesis methodologies, crystal structure, the role of activator, dopant concentration, temperature, etc. Simultaneously, the electronic properties of transition metal ions of these germanate phosphors have also been presented. Also, some of the important applications and future perspectives of these germanate phosphors are discussed. Meanwhile, the last part of this chapter describes the self-activated persistence luminescence mechanism. Moreover, a

brief description of the currently available cyan persistent phosphor and persistent phosphor applications are displayed.

1.2.2 Basic ionic configurations of Mn⁴⁺ and Cr³⁺ ions

The general electronic configuration of both Mn⁴⁺ and Cr³⁺ is 1s²2s²2p⁶3s²3p⁶3d³, while their ground state valence electronic configuration in an octahedral environment is t_{2g}³e_g⁰. This half-filled t_{2g}³ orbital provides extra stability to manganese and chromium in their +4 and +3 oxidation state, respectively. Moreover, the fascinating electronic, magnetic, and spectroscopic properties of these metal ions are possible due to their favourable electronic configuration. There will be 8 LS terms originating from the Coulomb interaction that occurs between the electrons in the unfilled d orbitals and they were generally denoted by ^{2S+1}L. Here “L” represents the total angular momentum while “S” stands for the total spin. The eight LS terms denoted by ⁴F, ⁴P, ²G, ²P, ²D₍₁₎, ²F, ²D₍₂₎, and ²H are consisting of two spin quarters, and six spin doublets. According to Hund’s rule, the first term ⁴F corresponds to the ground state while the remaining terms correspond to the excited states.^{61, 62} Further, each term is found to be degenerate to (2S+1)(2L+1) states and the number of degenerate states for all the 8 terms will give rise to 120 possible combinations. Hence, the three electrons can be distributed in the 3d orbitals in 120 ways.^{61, 62} The energy values of the LS coupling terms in the d³ electronic configuration are provided in terms of the Racah parameters B and C in **Table 1.1**.^{61, 62} By substituting the Racah parameter values of Cr³⁺, Mn⁴⁺, Fe⁵⁺, and V²⁺ free ions given in **Table 1.2**, the energy values for 8 LS terms for each of these ions having a d³ system are estimated and illustrated in an energy level diagram in **Fig. 1.2**. The splitting of LS terms and energy position of the split sublevels highly depend on the strength and symmetry of the crystal field. The splitting of LS terms of Mn⁴⁺, Cr³⁺, and all other ions having d³ or d⁷ electronic configuration is listed in **Table 1.3**.⁶²

Table 1.1 Energies of eight electrostatic terms (LS terms) in the d^3 system in terms of B and C taking the energy of ground-level 4F as zero. Adapted from ref. ⁶²

Term(s)	Energy
4F	0
4P	$15B$
2P	$9B+3C$
$^2D_{(1)}, ^2D_{(2)}$	$20B+5C \pm \sqrt{193B^2 + 8BC + 4C^2}$
2F	$24B+3C$
2G	$4B+3C$
2H	$9B+3C$

Table 1.2 The Racah parameters values of free ions having d^3 electronic configuration. Adapted from ref. ⁶²

Ion	B (cm^{-1})	C (cm^{-1})
V^{2+}	766	2855
Cr^{3+}	918	3850
Mn^{4+}	1160	4303
Fe^{5+}	1210	5066

Table 1.3 Splitting of LS terms of the d^3 (or d^7) configuration in the O_h or T_d group. Adapted from ref. ⁶²

The electrostatic terms	T_d or O_h groups irreducible representation
P-term (L=1)	T_1
D-term (L=2)	T_2+E
F-term (L=3)	$A_2+T_1+T_2$
G-term (L=4)	$A_1+E+T_1+T_2$
H-term (L=5)	$E+2T_1+T_2$

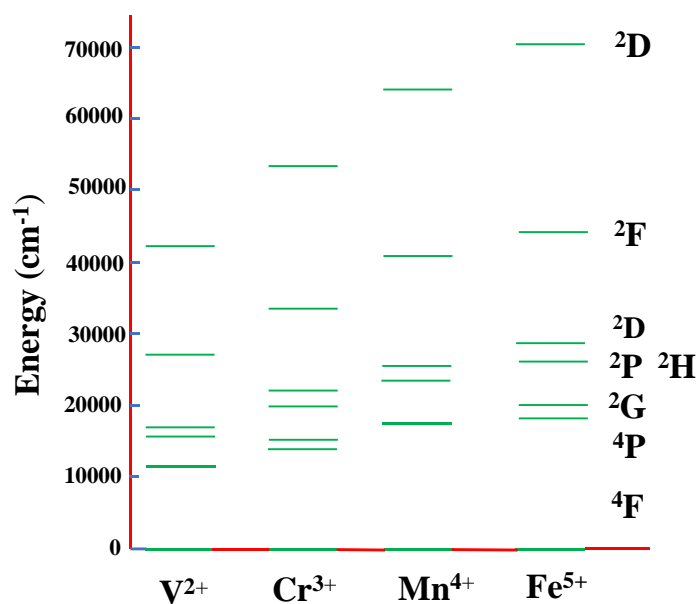


Fig.1.2 Energy levels diagram of the free V^{2+} , Cr^{3+} , Mn^{4+} , and Fe^{5+} ions by taking the energy of ground state energy as zero. Adapted from ref. ⁶²

1.2.2.1 Simplified Tanabe-Sugano (T-S) energy level diagrams of Mn^{4+} and Cr^{3+}

The simplified T-S diagram shown in **Fig.1.3** represents the splitting of the energy levels of Mn^{4+} and Cr^{3+} ions in an ideal octahedral environment. The energy difference between the ground state ${}^4A_{2g}$ and the excited state ${}^4T_{2g}$ is $10D_q$ (D_q is the crystal field intensity). For a Dq/B value less than 2.1, the first excited state is ${}^4T_{2g}$, and after that 2E_g becomes the first excited state, as represented in **Fig.1.3**. The strong and weak crystal fields can be distinguished in the T-S diagram by a point at which the ${}^4T_{2g}$ and 2E_g levels intersect, as marked in **Fig.1.3**.

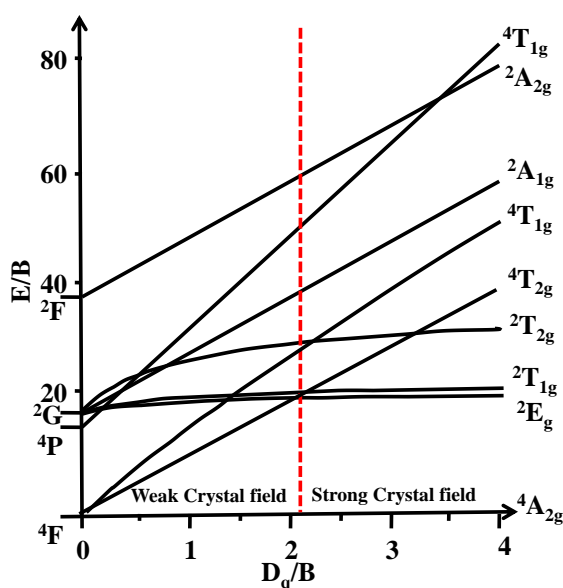


Fig.1.3 Simplified T-S diagram in the octahedral crystal field for ions having d^3 electronic

configuration. Adapted from ref. ⁵⁷

The separation between the $^4A_{2g}$ ground state and the 2E_g and $^2T_{1g}$ states is practically independent of crystal field strength Dq . While Cr^{3+} ion can experience both strong as well as weak field environments, Mn^{4+} ion, on the other hand, experiences only a strong field environment because of its larger positive charge.^{62, 63} A general energy level diagram of Mn^{4+} and Cr^{3+} in a strong field environment is shown in **Fig.1.4 (a)** The bands arising from the ground state, $^4A_{2g} \rightarrow ^2E_g$, $^2T_{1g}$, $^4T_{2g}$, $^2T_{2g}$, $^4T_{1g}$ are called R line, R' line, U band, B, line, and Y band, respectively. The ions from the higher excited states come down to 2E_g excited state through non-radiative transition, and then their transition from the 2E_g state to the ground state results in emission.⁶³ In the case of Mn^{4+} ion, as already discussed, the sharp emission peak corresponds to the spin forbidden $^2E_g \rightarrow ^4A_{2g}$ transition. Depending upon the crystal field environment, the spectral position of this transition can vary over a wide range of 620 to 723 nm. Also, the two broad excitation bands correspond to the spin-allowed transitions of $^4A_{2g} \rightarrow ^4T_{1g}$ (4F) and $^4A_{2g} \rightarrow ^4T_{2g}$. Another spin allowed transition is $^4A_{2g} \rightarrow ^4T_{1g}$ (4P), however, it is generally covered by the host absorption as well as the charge transfer.^{17, 59, 60} For a case study, we used Mn^{4+} doped $NaMgGdTeO_6$ phosphor,⁶⁴ and the energy level diagram

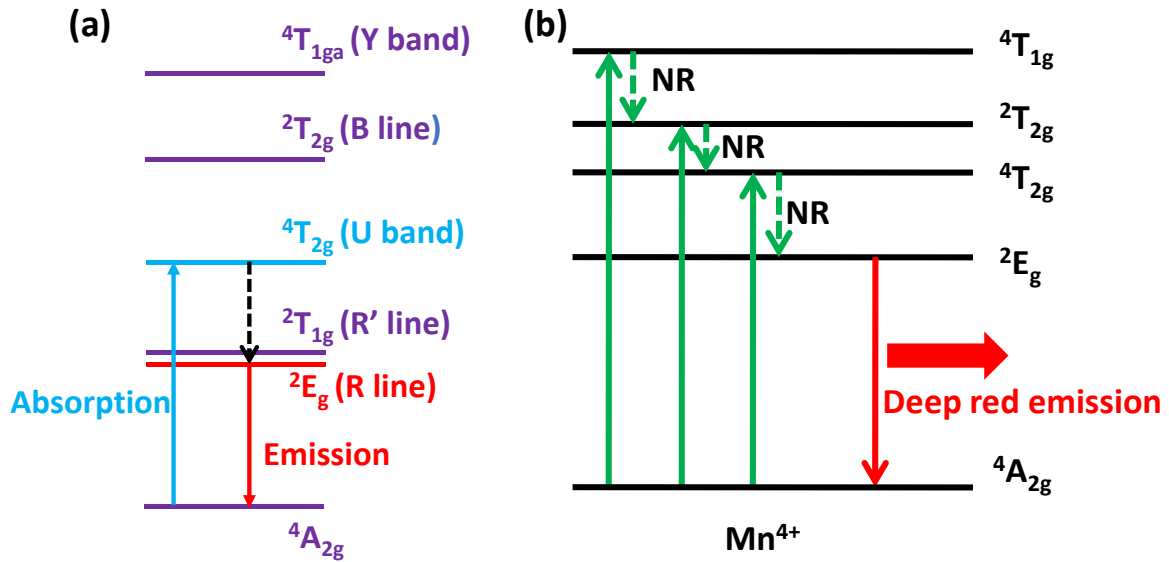


Fig.1.4 (a) General energy level diagram for Mn^{4+} and Cr^{3+} . Adapted from ref.⁶³; **(b)** Typical energy level diagram of Mn^{4+} showing excitation and emission (NR representing non-radiative transition). Adapted from ref ⁶⁴

consisting of all possible transitions in Mn^{4+} is shown in **Fig.1.4 (b)**. Here the electrons from the higher excited ${}^4T_{1g}$, ${}^2T_{2g}$, and ${}^4T_{2g}$ states may relax to the lower excited 2E_g state through a non-radiative transition and then completely transfer to the ground state resulting in a deep red emission.^{17, 64} Similarly, for Cr^{3+} ion, let us consider an example of Cr^{3+} -doped $ZnGa_2O_4$ phosphor with the energy level diagram consisting of all possible transitions in Cr^{3+} shown in **Fig.1.5**⁶⁵. Here the substitution of Al^{3+} ions in the Ga sites does not make any changes in the diagram except a slight upward shift in the conduction band (represented in green colour). The excitation of electrons from the ground state to excited states or 4T_1 (4P) in the conduction band leads to its trapping which facilitates the persistence in these phosphors. The non-radiative relaxation occurs to the 2E_g state and the transition from this state to the ground state results in a red emission.⁶⁵

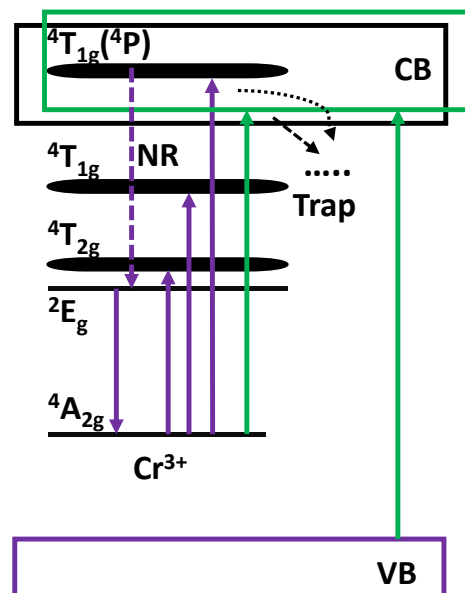


Fig.1.5 Typical energy level diagram for Cr^{3+} . (NR representing non-radiative transition)
Adapted from ref.⁶⁵

1.2.2.2 Crystal field analysis

As we already discussed, the Racah parameters B and C are the characteristics of an oxide ion within a metal oxide compound. The introduction of the Mn^{4+} and Cr^{3+} ions in the crystal field results in the formation of the chemical bond between the metal 3d orbitals and the ligands resulting in the nephelauxetic effect. Subsequently, the hybridization between these metal ions and ligands becomes maximized resulting in the reduction of the Racah parameters. Irrespective of the same Mn^{4+} and/or Cr^{3+} ionic doping, the reduction in the Racah parameters are found to be different for each host, causing a wide variation in the energy value of their

emission peak.⁵⁹ Considering the case of Mn⁴⁺-activated fluoride phosphors, the emission peak lies in the range of 620-640 nm owing to the comparatively weak hybridisation effect.⁶⁶ However, in the case of oxides, the emission peak lies above 650 nm due to a strong hybridisation effect.⁶⁶ Hence, it can be concluded that the position of the ²E_g level of Mn⁴⁺ and Cr³⁺ highly depends on the covalency, nature of ligands, and bond angle in chemical bonds.^{59, 60, 67, 68} The energy level difference between ⁴A_{2g} and ⁴T_{2g} of Mn⁴⁺ and Cr³⁺ is 10D_q, which can be represented as follows,⁶⁷

$$10D_q = \frac{K}{R^n} \quad (1.1)$$

here R is the bond length between the cation and the ligand, while n and K are the fitting parameters. The value of power 'n' depends on the nature of ligands, the geometry of the complex, etc. Depending upon the systems, it varies from 3.5 to 7.3 – as was shown by many quantum-chemical calculations.^{67, 69, 70, 71} Ogasawara *et al.* estimated the value of n and K for CrO₆ and MnO₆ clusters and observed that the value 'n' for Cr³⁺ is greater than Mn⁴⁺ showing that the 10D_q value of Cr³⁺ ions is more sensitive to bond length in comparison with Mn⁴⁺ ions.⁶³ The nephelauxetic ratio (β_1) can be introduced for predicting the position of the emission spectrum since the ²E_g level (generally for Mn⁴⁺) can be written as the linear function of this parameter. The nephelauxetic ratio can be estimated using the following equation.^{59, 72, 73}

$$\beta_1 = \sqrt{\left(\frac{B}{B_0}\right)^2 + \left(\frac{C}{C_0}\right)^2} \quad (1.2)$$

where B_0 and C_0 represent the values of Racah parameters of free Mn⁴⁺ ions.

The value of D_q can also be estimated from the absorption spectrum using the equation,

$$D_q = E(4A_{2g} \rightarrow 4T_{2g}) / 10 \quad (1.3)$$

The Racah parameter B can be obtained from the absorption spectra by considering the peak energy difference between the two transitions ⁴A_{2g} → ⁴T_{1g} and ⁴A_{2g} → ⁴T_{2g}. The equation used for calculation^{64, 73}

$$\frac{D_q}{B} = \frac{15(x-8)}{x^2-10x} \quad (1.4)$$

where the parameter x is given by

$$x = [E(4A_{2g} \rightarrow 4T_{1g}) - E(4A_{2g} \rightarrow 4T_{2g})] / D_q \quad (1.5)$$

The Racah parameter C can also be calculated from the emission spectrum using the peak energy value from the ²E_g → ⁴A_{2g} transition and the obtained B value.^{64, 73}

$$E(^2E_g \rightarrow ^4A_{2g}) / B = 3.05C / B + 7.9 - 1.8B / D_q \quad (1.6)$$

The T-S diagram is used for interpreting the optical spectra and the splitting of energy levels however it is not applicable for crystal fields having lower symmetry than cubic. Hence a method can be used by finding the eigenvalues of the crystal field Hamiltonian. The eigenvalues of the following crystal field Hamiltonian can be used for representing the energy levels of impurity ions with the d -electron shell ($p = 2, 4$) and f -electron shell ($p = 2, 4, 6$) (in our case, Mn^{4+} and Cr^{3+} ions having d^3 electronic configuration) in a crystal field of arbitrary symmetry.⁷⁴

$$H = \sum_{p=2} \sum_{k=-p}^p B_p^k O_p^k \quad (1.7)$$

where the B_p^k represents the crystal field parameters which are obtained from the crystal structure data and the O_p^k is the linear combination of appropriately selected tensor operators which were acting on the angular part of the dopant ion's wave function. Thus, it can be concluded that these parameters include all the geometrical and structural characteristics of the host lattice. The crystal field parameters B_p^k , with reference to the Exchange Charge Model (ECM), can be written as,⁷⁵

$$B_p^k = B_{p,q}^k + B_{p,s}^k \quad (1.8)$$

$$B_{p,q}^k = -K_p^k e^2 \langle r^p \rangle \sum_i q_i \frac{V_p^k(\theta_i, \varphi_i)}{R_i^{p+1}} \quad (1.9)$$

$$B_{p,s}^k = K_p^k e^2 \frac{2(2p+1)}{5} \sum_i (G_s S(s)_i^2 + G_\sigma S(\sigma)_i^2 + \gamma_p G_\pi S(\pi)_i^2) \frac{V_p^k(\theta_i, \varphi_i)}{R_i} \quad (1.10)$$

The term $B_{p,q}^k$ describes the electrostatic interaction between the dopant valence electrons and the host metal ions while the term $B_{p,s}^k$ represents the overlap integral of wave functions of the dopant ion and the ligands. The summations are performed over the lattice ions i with charge q_i ; R_i , θ_i , and φ_i denote the spherical polar coordinates of the i^{th} ion of the crystal lattice in the reference system centered at the dopant ion. Here, the average $\langle r^p \rangle$ of the p^{th} power of electron radial coordinate (r) can be calculated using the radial parts of the wave function of 3d orbitals. The values of the various constants like K_p^k , γ_p , and V_p^k are provided in reference.⁷⁵ The overlapping integrals between d -functions of the dopant ion, and the s - and p -functions of the ligands having different ' l ' and ' m ' quantum numbers are defined in terms of S_s , S_σ , and S_π ; where (in $\langle lm|l'm' \rangle$ notation) $S_s = \langle d0|s0 \rangle$, $S_\sigma = \langle d0|p0 \rangle$ and $S_\pi = \langle d1|p1 \rangle$. G_s ,

G_σ , and G_π represent the dimensionless adjustable parameters obtained from the positions of the first three absorption bands of the given crystal. It is possible to approximate $G_s = G_\sigma = G_\pi = G$, thereby reducing the number of parameters which is a key feature of the ECM approach. The value of G could be obtained by fitting the position of the calculated first absorption band to the observed first absorption band. The superiority of the ECM is that if the G parameter is determined to fit the first absorption band, the other higher energy levels will also fit experimental spectra quite well.⁷⁴ Brik *et al.* carried out the crystal field analysis for $\text{KAl}(\text{MoO}_4)_2:\text{Cr}^{3+}$ ⁷⁴ Here the Cr^{3+} ion is entering into the octahedral Al^{3+} site. The energy value obtained for ${}^2\text{E}_g({}^2\text{G})$ from ECM is 13516 cm^{-1} which is very close to the experimental value (13512 cm^{-1}). All other energy values obtained using ECM are also well matching with the experimental data.⁷⁴

1.2.2.3 Configuration Coordinate model

The electron-phonon interaction of Cr^{3+} and Mn^{4+} ions with the lattice vibrations can very well be analysed using the configurational coordinate model. The model assumes that the local environment of Cr^{3+} and Mn^{4+} ions vibrate harmonically about their mean position. **Fig.1.6** shows the potential energies of the electronic states expressed as a function of the vibrational coordinate for the case of a strong crystal field. The electron-phonon interaction plays a vital role in the absorption and emission processes taking place at the impurity centre. Consequently, the photoluminescence excitation (PLE) and photoluminescence (PL) spectra of Cr^{3+} and Mn^{4+} in solids can be explained using Frank-Condon analysis with the configurational coordinate model. Here the positions of excitation and emission lines are given as,^{57, 76, 77}

$$h\nu_{\text{ex}} = E_{\text{ZPL}} + kh\nu_{\text{p,ex}} \quad (1.11)$$

$$h\nu_{\text{em}} = E_{\text{ZPL}} - lh\nu_{\text{p,em}} \quad (1.12)$$

where, $h\nu_{\text{p,ex}}$ and $h\nu_{\text{p,em}}$ represent the lattice vibrational quanta for the excited and ground state, respectively. The absorption and emission bands could be considered as consisting of several lines representing the transitions between the vibrational levels, for example, the vibrational level l of the ground electronic state, and k of the excited electronic state. Using the Configurational Coordinate model, the spectral distribution of the excitation and emission spectra could be illustrated as,⁵⁷

$$I_{\text{PLE}}(E) = \sum_n I_n^{\text{ex}}(n) \exp \left[-\frac{(E - E_{\text{ZPL}} - nh\nu_{\text{p,ex}})^2}{2\sigma_{\text{ex}}^2} \right] \quad (1.13)$$

$$I_{\text{PL}}(E) = \sum_n I_n^{\text{em}}(n) \exp \left[-\frac{(E - E_{\text{ZPL}} + nh\nu_{\text{p,em}})^2}{2\sigma_{\text{em}}^2} \right] \quad (1.14)$$

$$\text{where, } I_n^{ex}(n) = I_0^{ex} \exp(-S) \frac{S^n}{n!} \quad (1.15)$$

$$I_n^{em}(n) = I_0^{em} \exp(-S) \frac{S^n}{n!} \quad (1.16)$$

where, I_0^{ex} and I_0^{em} represent the ZPL intensity, S , the mean local vibrational number, and σ_{ex} and σ_{em} represent the broadening energy of each Gaussian component.⁵⁷

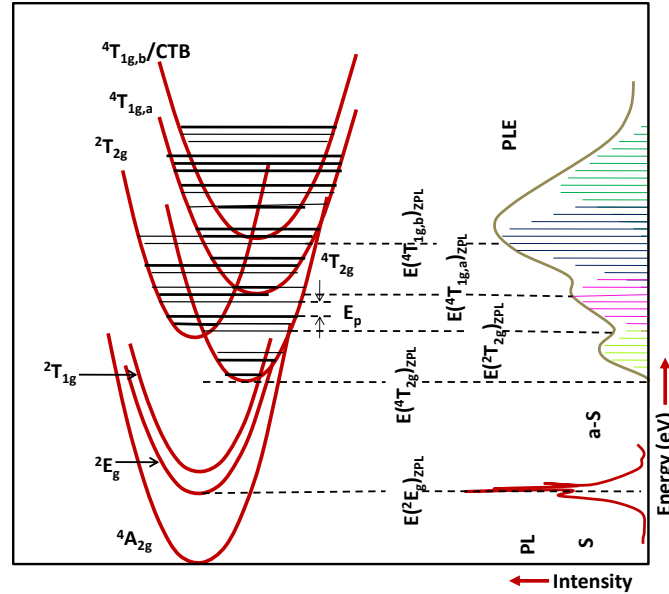


Fig.1.6 Configuration coordinate model representing typical PL emission and absorption transition along with the schematic representation for the PL and PLE spectra of the Mn^{4+} -activated oxide phosphor (S = Stokes; a-S = anti-Stokes). Adapted from ref.⁵⁷

1.2.3 Mn^{4+} -activated deep red-emitting germanate phosphors

The literature available on different Mn^{4+} -activated hosts is represented in **Fig.1.7 (a)**. Since the red-emitting fluoride host has some unavoidable drawbacks (mentioned earlier), the search for a new efficient phosphor ends up with Mn^{4+} -activated red-emitting oxide hosts. Nowadays, major studies on oxides are taking place in between aluminates,¹¹ titanites,⁶¹ germanates,⁶ pyro-silicates,⁶¹ Perovskites,²⁸ double perovskites,^{24, 57} etc. (**Fig. 1.7 (b)**). Among the different oxide hosts, aluminates, titanates, and germanates are getting more research interests because of the similar ionic radii of Al^{3+} (Al^{VI} : 0.535 Å), Ti^{4+} (Ti^{VI} : 0.605 Å), and Ge^{4+} (Ge^{VI} : 0.530 Å) with that of Mn^{4+} (Mn^{VI} : 0.530 Å) in an octahedral environment.⁴⁷ In an octahedral environment, the d -orbital splits into three-fold degenerate t_{2g} and two-fold degenerate e_g states, and the three valance electrons of Mn^{4+} occupy the lower t_{2g} energy level. The crystal field splitting creates a large energy splitting between t_{2g} and e_g states leading to

the crystal field stabilization of Mn^{4+} in the octahedral environment.⁷⁸ **Fig.1.8** shows the trigonal crystal structure considering the occupation of Mn^{4+} in the tetrahedral and octahedral

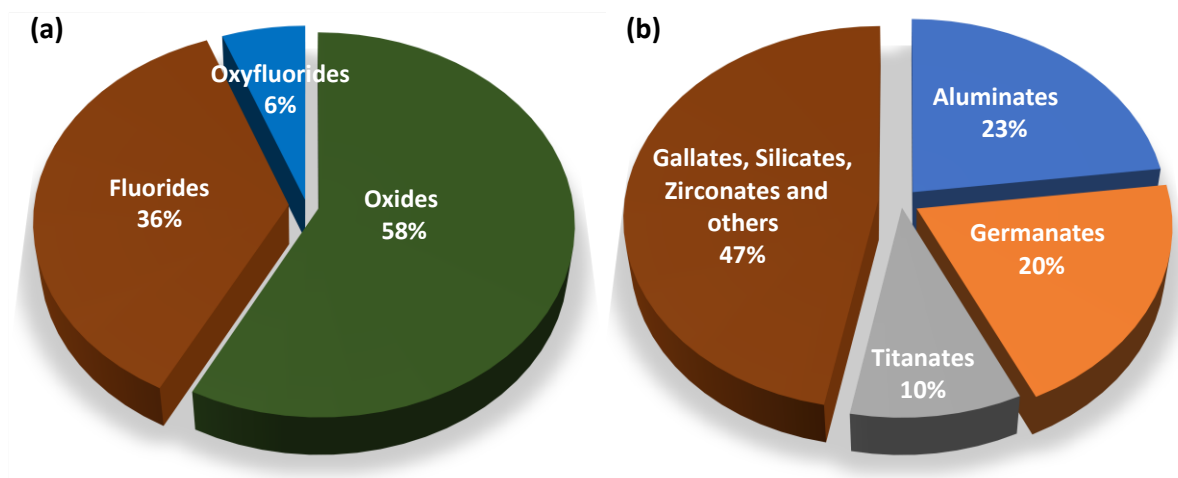


Fig.1.7 Chart showing the available literature on different Mn^{4+} activated (a) hosts and (b) oxide hosts. (Based on the literature collected from the Web of Science published during January 2000-December 2020).

environments. Here Ge^{4+} ions coordinate with four oxygen atoms to form a tetrahedron and coordinates with six oxygen atoms to form the octahedron. Mostly Mn^{4+} occupies the octahedral sites provided by the Ge^{4+} .

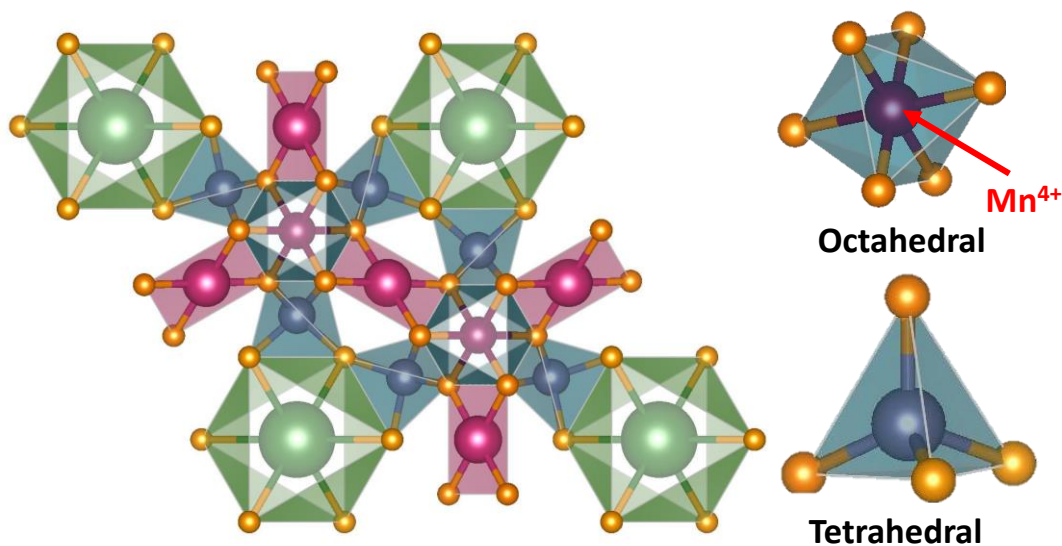


Fig.1.8 Structure of trigonal crystal structure with the occupation of Mn^{4+} in octahedral and tetrahedral sites drawn using the VESTA software.⁷⁹

Comparing to titanites, aluminates, and even other Mn^{4+} doped oxide hosts, germanates are even more superior due to their structural stability. Even though the octahedral sites of Mn^{4+} can be easily replaced by the Al^{3+} ions, these systems require the use of a charge compensator owing to the ionic mismatch between Al^{3+} and Mn^{4+} ions. The charge imbalance between these two ions promotes some electronic defects which not only reduce the intensity of emission but also affect the emission profile of Mn^{4+} . Considering aluminates, their covalency is higher (greater than germanates) which leads to the decrease of interactions among electrons and results in the spread out of electrons over wide orbitals.⁸⁰ Since charge defects are unfavourable for luminescence intensity, high temperature and long calcination time are required during their synthesis although it is not economically favourable.^{80, 81} On the other hand, Mn^{4+} and Ti^{4+} have the same ionic charges, and this charge equivalency helps in eliminating electronic defects as well as the incorporation of charge compensator. However, small differences in their ionic sizes (0.065 Å) are sufficient to perturb the symmetry distortion in their crystal lattice thereby lowering the stability of the titanium host. In comparison with the Al^{3+} and Ti^{4+} , Ge^{4+} ion has the same ionic radii and charge as that of Mn^{4+} ion, and thus doping of Mn^{4+} does not make any charge imbalance and symmetry distortion of the crystal lattice. This charge equivalency helps in eliminating electronic defects as well as the incorporation of charge compensator. Further, the use of energy-consuming experimental conditions can also be avoided due to the lack of these charge defects. To confirm the site suitability in germanates mathematically, a parameter called effective compensating factor can be used in six coordinated environments which can be defined as $\varphi = z/r$ where z is the ionic charge, and the r is the ionic radius in that octahedral environment. This value for Mn^{4+} and Ge^{4+} is found to be the same (7.54).^{47, 81} The emission intensity of Mn^{4+} -activated phosphors highly depends upon its local symmetry, that is presence or absence of an inversion centre at the Mn^{4+} site.⁸² Ji *et al.* reported Mn^{4+} -activated double-perovskite structural $\text{La}_4\text{Ti}_3\text{O}_{12}$, which possesses a slightly- and highly-distorted $\text{Ti}(1)\text{O}_6$ and $\text{Ti}(2)\text{O}_6$ octahedra, respectively.⁸³ The Mn^{4+} ion occupying $\text{Ti}(1)$ site possesses a centre of inversion with symmetry of C_{3i} , while the Mn^{4+} ion occupying $\text{Ti}(2)$ site has a reduced symmetry of C_3 . High distortion in $\text{Ti}(2)\text{O}_6$ octahedra makes $\text{MnTi}(2)$ less stable than the $\text{MnTi}(1)$ by 0.09 eV as calculated from the density functional theory (DFT). As a result, the ratio of the zero-phonon line (ZPL) with vibronic emission intensity of $\text{MnTi}(2)$ is larger than those of $\text{MnTi}(1)$.⁸³ The list of synthesis parameters, crystal structure and space groups of most of the recently reported germanates are tabulated in **Table 1.4**, and their spectroscopic parameters are tabulated in **Table 1.5**.

Table 1.4 Synthesis parameters, crystal structure and space groups of Mn⁴⁺-doped germanate

Germanates	Temp. (°C)	Holding time (h)	Optimal Mn conc. (mol%)	Crystal structure	Space group	Ref
K ₂ BaGe ₈ O ₁₈	1050	6	0.2	Hexagonal	P3c1	66,151
BaAl ₂ Ge ₂ O ₈	1200	2	0.1	Monoclinic	12/C	105
BaGe ₄ O ₉	1100	10	2	Trigonal	P321	107
BaGe ₄ O ₉	1100	6	0.5	Trigonal	P321	106
Ba ₂ GeO ₄	1400	4	0.6	Orthorhombic	Pnma	102
Ba ₂ MgGe ₂ O ₇	1000	6	1.3	Tetragonal	P42m	104
Ba ₂ TiGe ₂ O ₈	1050	6	0.6	Orthorhombic	Cmm2	103
K ₂ Ge ₄ O ₉	850	4	0.08	Trigonal	P $\bar{3}$ c1	91
K ₂ Ge ₄ O ₉	800	4	0.4	Trigonal	P $\bar{3}$ c1	94
K ₂ Ge ₄ O ₉	900	6	0.1	Trigonal	P $\bar{3}$ c1	90
K ₂ Ge ₄ O ₉	900	6	0.2	Trigonal	P $\bar{3}$ c1	93
K ₂ MgGeO ₄	920	8	0.4	Orthorhombic	Pnma	95
La ₃ GaGe ₅ O ₁₆	1300	12	0.25	Triclinic	p2 ₁ /c	110
La ₂ MgGeO ₆	1400	6	0.2	Hexagonal	R3H	109
LiAlGe ₂ O ₆	900	8	0.6	Trigonal	P-3m1	112
LiGaGe ₂ O ₆	900	8	0.6	Monoclinic	P21/c	112
Li ₂ MgGeO ₄	920	8	0.4	Orthorhombic	Pnma	95
Li ₂ Ge ₄ O ₉	900	6	0.2	Orthorhombic	P21ca	93
Li ₂ Ge ₄ O ₉	800	6	0.3	Orthorhombic	Pcca	86
LiNaGe ₄ O ₉	900	6	0.2	Orthorhombic	Pcca	93
Li ₃ RbGe ₈ O ₁₈	800	4	0.5	Trigonal	P $\bar{3}$ 1m	6
Mg ₃ Ga ₂ GeO ₈	1300	6	0.5	Orthorhombic	Imma	111
Mg ₇ Ga ₂ GeO ₁₂	1400	10	0.5	Orthorhombic	Cmmm	113
Mg ₂ GeO ₄	1250	5	0.1	Orthorhombic	Pnma	98
Mg ₁₄ Ge ₅ O ₂₄	1300	8	1	Orthorhombic	Pbam	80
Mg _{3.5} Ge _{1.25} O ₆	1000	3	0.5	Orthorhombic	Pbam	132
Mg ₃ Y ₂ Ge ₃ O ₁₂	1350	6	1	Cubic	Ia $\bar{3}$ d	115
Mg ₆ ZnGa ₂ GeO ₁₂	1400	5	1	Orthorhombic	Cmmm	114
Rb ₂ Ge ₄ O ₉	800	4	0.4	Trigonal	P $\bar{3}$ C1	94
SrGe ₄ O ₉	1100	6	0.5	Trigonal	P321	106

Table 1.5 Spectroscopic properties of some of the important germanates

Germanates	CIE	QE (%)	λ_{em} (nm)	λ_{exc} (nm)	2E_g (cm^{-1})	${}^4T_{2g}$ (cm^{-1})	${}^4T_{1g}$ (cm^{-1})	D_q (cm^{-1})	B (cm^{-1})	C (cm^{-1})	Ref
$K_2BaGe_8O_{18}$	(0.702, 0.298)	32.9	666	468	15015	21645	28571	2164	654	3345	66
$BaAl_2Ge_2O_8$	(0.720, 0.279)	28	668	288	15345	19443	26543	1945	690	3390	105,151
$BaGe_4O_9$	--	61	666	335,465	15015	20408	29411	2040	740	2980	107
Ba_2GeO_4	0.7187, 0.281	22.5	667	290	14990	19847	26624	1985	650	3360	102,151
$Ba_2MgGe_2O_7$	(0.721, 0.279)	14.3	660	289	15563	22025	30255	2205	805	3190	104,151
$Ba_2TiGe_2O_8$	(0.719, 0.281)	35.6	666	300	14990	20492	25414	2050	445	3820	103,151
$K_2Ge_4O_9$	(0.719, 0.280)	57.8	664	300,450	15060	22271	31250	2227	900	2821	93
K_2MgGeO_4	--	--	667	310,470	15232	18556	24365	1855	545	3675	95
$La_3GaGe_5O_{16}$	--	68	660	330	15151	21413	30303	2141	856	2947	110
La_2MgGeO_6	--	--	708	320	14124	21551	29761	2155	807	2719	109
$LiAlGe_2O_6$	(0.72, 0.27)	32	671	289	14885	18879	23558	1890	425	3840	112,151
$LiGaGe_2O_6$	(0.72, 0.27)	15	669	289	14942	18395	23881	1840	510	3660	112,151
$Li_2Ge_4O_9$	(0.723, 0.277)	30.7	669	330,450	14947	22522	29069	2252	608	3423	93
Li_2MgGeO_4	(0.699, 0.300)	--	671	323,470	15167	17749	21783	1775	365	4080	95,151
$LiNaGe_4O_9$	(0.723, 0.278)	58.9	661	330,450	15128	22371	28571	2237	571	3566	93
$Li_3RbGe_8O_{18}$	--	--	667	460	14998	19201	23558	1920	390	3950	6,151
$Mg_3Ga_2GeO_8$	(0.295, 0.677)	64.7	659	419	15401	21138	25817	2115	420	4015	111,151
$Mg_7Ga_2GeO_{12}$	(0.713, 0.287)	28.1	660	420	15426	20815	24920	2080	365	4150	113,151
Mg_2GeO_4	--	--	659	303,420	15635	20654	25252	2065	415	4110	98,151
$Mg_{14}Ge_5O_{24}$	(0.62, 0.29)	81	659	422	15603	20331	24607	2035	380	4170	80,151
$Mg_{3.5}Ge_{1.25}O_6$	--	--	660	405,450	15522	20573	25414	2055	435	4015	132,151
$Mg_3Y_2Ge_3O_{12}$	--	64	658	288,421	15595	21944	27269	2195	480	3930	115,151
$Mg_6ZnGa_2GeO_{12}$	(0.717, 0.283)	--	660	420	15385	21380	25978	2140	410	4030	114,151
$Rb_2Ge_4O_9$	--	--	657	345	15240	18475	23800	1850	495	3800	94
$SrGe_4O_9$	(0.71, 0.29)	46	670	430	15240	19766	26785	1975	680	3380	106,151

1.2.3.1 Alkali metal-based germanate system

The alkali germanate systems can be represented as A-Ge-O, where A represents the alkali metals such as Li, K, and Rb. Initially, the studies were concentrated on the $A_2Ge_4O_9$ alkali germanate system. In 2015, Kunitomo and co-workers synthesized red-emitting orthorhombic $Li_2Ge_4O_9:Mn^{4+}$ using a glass-ceramic route.⁸⁴ It has a slightly distorted GeO_6 octahedron connected with $[GeO_3]_n$ -chains to form a three-dimensional framework and shows a sharp emission peak at a wavelength of 670 nm.⁸⁴ But the thermal quenching even below 100°C makes $Li_2Ge_4O_9:Mn^{4+}$ inappropriate for several practical applications. Odawara *et al.* prepared nanocrystals of $Li_2Ge_4O_9:Mn^{4+}$ by employing a modified glass-ceramic route wherein they used YAG laser irradiation operated at 1064 nm.⁸⁵ Cao *et al.* used a conventional solid-state method with the usage of flux to synthesize this $Li_2Ge_4O_9:0.003Mn^{4+}$ phosphor for W-LED application with a high quantum yield and deep red emission.⁸⁶ All the raw materials along with the flux were taken in the stoichiometric ratio and grounded and heated at a temperature of 800°C for 6 h. The obtained phosphor has a quantum yield of 80.3%, and good thermal stability better than the $K_2SiF_6:Mn^{4+}$ sample. At 300°C, $Li_2Ge_4O_9:0.003Mn^{4+}$ could maintain 42% of its initial room temperature intensity. But at the same temperature, the emission intensity of $K_2SiF_6:Mn^{4+}$ dropped to 18% of its initial intensity.⁸⁶ Further, they have also studied the water resistance property of $Li_2Ge_4O_9:0.003Mn^{4+}$ and compared the outcomes with $K_2SiF_6:Mn^{4+}$. Under the same experimental condition, the red emission of $K_2SiF_6:Mn^{4+}$ reduced from 100% to 32% but no change in intensity is reported in the case of $Li_2Ge_4O_9:0.003Mn^{4+}$ showing its superior moisture resistance.⁸⁶

The luminescence spectrum of tetra germanate $LiNaGe_4O_9:Mn^{4+}$ phosphor is initially studied by Omel'chenko and co-workers wherein they observed a strong red and weak yellow-green emission.⁸⁷ Later, Suzuki *et al.* studied the effect of Na substitution on the luminescence properties of $LiNaGe_4O_9:Mn^{4+}$ phosphors.⁸⁸ They have prepared $Li_{2-x}Na_xGe_4O_9:Mn^{4+}$ samples using a glass-ceramic technique by melting the raw materials in the required stoichiometric ratio at 1200°C for 30 min. The substitution of Na at the Li site helps in improving the quenching temperature as well as the quantum yield of the obtained phosphor. The same research group has also prepared $LiNaGe_4O_9:Mn^{4+}$ by the solid-state method which shows greater quantum yield and better colour purity.⁸⁸ This might be due to the suppression of crystal defects when prepared through solid-state synthesis at high temperatures resulting in the reduction of non-radiative transition.⁸⁸ Solid-state synthesized $LiNaGe_4O_9:0.05\%Mn^{4+}$ with a

high quantum yield of 78% has been reported by Li and co-workers.⁸⁹ To get the best performance of the phosphor they optimised synthesis condition at 850°C for 3 h with 0.05% Mn⁴⁺. The emission peak consists of the strongest peak at 661 nm in the deep-red region along with some shoulder peaks centred at 666, 676, 682, and 687 nm. These peaks are attributed to the ²E_g → ⁴A_{2g} transition of Mn⁴⁺ ions in the octahedral environment and its vibronic sidebands. The broad excitation spectrum is observed in the UV and blue region and peaks were centred at 295 nm due to the spin allowed ⁴A_{2g} → ⁴T_{1g} and 462 nm due to spin allowed ⁴A_{2g} → ⁴T_{2g} transitions, respectively. The emission intensity of this phosphor is about four times higher than that of commercially available 3.5MgO•0.5MgF₂•GeO₂:Mn⁴⁺ [MFG: Mn⁴⁺]. The main reason behind its better emission intensity is its crystal structure which is shown in **Fig.1.9 (a)** and **(b)**. The PL plots of LiNaGe₄O₉:Mn⁴⁺ and MFG: Mn⁴⁺ samples are shown in **Fig.1.9 (c)**. Here Mn⁴⁺ is efficiently doped into the GeO₆ octahedra. The layer of the GeO₆ group is separated by the layer of GeO₄ and each GeO₆ is connected to the three GeO₄ polyhedra by sharing common corners. Also, none of the GeO₆ is connected to each other showing the good isolation of the GeO₆ octahedra. Since Mn⁴⁺ ions are occupying these octahedral sites, the interactions between these Mn⁴⁺ ions are weakened or blocked leading to stronger luminescence and higher quantum yield.⁸⁹

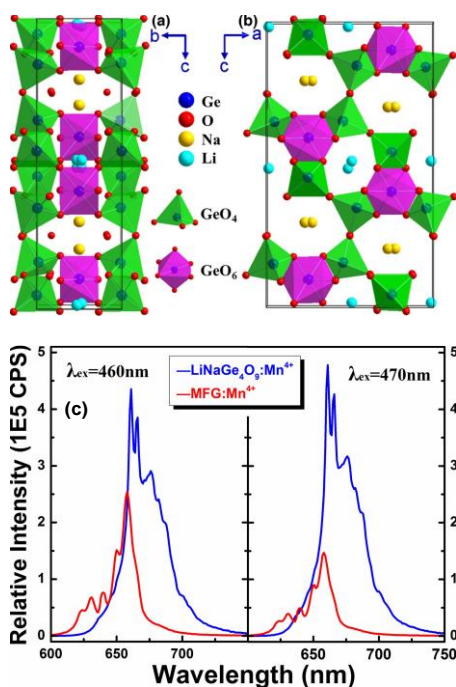


Fig.1.9 (a) and (b) Crystal structure of LiNaGe₄O₉:0.05%Mn⁴⁺ (orthorhombic-Pcca) viewed along a and b; (c) Comparison of PL emission intensities of LiNaGe₄O₉:Mn⁴⁺ and MFG: Mn⁴⁺. Reproduced with permission from ref. ⁸⁹

Ding *et al.* reported novel trigonal $\text{K}_2\text{Ge}_4\text{O}_9:0.001\text{Mn}^{4+}$ (KGO: Mn^{4+}) prepared using solid-state reaction.⁹⁰ The unit cell of trigonal $\text{K}_2\text{Ge}_4\text{O}_9$ is composed of both octahedral and tetrahedral sites wherein the octahedral site is preferred by the Mn^{4+} . Here the concentration of Mn^{4+} is optimised to be 0.1 mol% and the concentration quenching mechanism of the sample is explained by the energy transfer mechanism involved between the Mn^{4+} ions. The emission spectrum of the sample under blue excitation is centred at 663 nm and the corresponding *commission internationale de l'éclairage* (CIE) values are found to be (0.702, 0.296) which is close to that of commercialised MFG: Mn^{4+} . This phosphor could be applied in W-LEDs owing to its satisfactory luminescence intensity and CIE values. But the major problem depicted for this phosphor is its low thermal quenching. The thermal quenching property has been explained using the configurational coordinate diagram, where at high temperature the electrons absorb an energy from the lattice vibration and come back to the ground state through a non-radiative transition. The easy path provided by the charge transfer band $\text{Mn}^{4+}-\text{O}^{2-}$ is the main reason for the lower thermal stability of the sample.⁹⁰

Li *et al.* predicted the energy levels of Mn^{4+} ion in the same phosphor by crystal field calculation based on the ECM which is well matching with the phosphor prepared using similar experimental conditions.⁹¹ The calculation result shows the red emission peak at 663 nm and 450-470 nm wavelength range of blue absorption. From the calculation, both Ge1 and Ge2 octahedral sites are found to be favourable for the Mn^{4+} . Here an important observation made from the structural analysis is that there are two octahedral germanium sites and that the mean bond lengths of Ge-O are 1.8937 Å and 1.8988 Å.^{91, 92} These shorter bond lengths indicate the higher covalence around Mn^{4+} , which is favourable for longer emission and excitation wavelength and this is also matching with the experimental results.⁹¹

Li *et al.* prepared partial alkali substituted $\text{K}_x\text{Rb}_{2-x}\text{Ge}_4\text{O}_9: 0.02\%\text{Mn}^{4+}$ to enhance its photoluminescent properties.⁴⁵ Structural analysis of $\text{Rb}_2\text{Ge}_4\text{O}_9: \text{Mn}^{4+}$ suggested that Mn^{4+} ions prefer to occupy GeO_6 octahedral sites, which are surrounded by GeO_4 tetrahedrons. Surrounding GeO_4 tetrahedrons can favour structural isolation of Mn^{4+} from local perturbations and also it can weaker interaction among Mn^{4+} ions. Due to the partial substitution of K for Rb, a slight shifting of X-ray diffraction (XRD) peaks towards a higher diffraction angle and a decrease in interplanar spacing have also been observed. The contraction of crystal lattice upon the substitution of K^+ ion indicates the presence of higher crystal field strength. From the PL analysis, it is observed that $\text{Rb}_2\text{Ge}_4\text{O}_9:\text{Mn}^{4+}$ shows a comparatively lower intensity than

$\text{K}_2\text{Ge}_4\text{O}_9:\text{Mn}^{4+}$ but the partial substitution of K in this compound helps to increase the luminous intensity. It is observed that the $\text{K}_{1.5}\text{Rb}_{0.5}\text{Ge}_8\text{O}_{18}:\text{Mn}^{4+}$ sample shows a significantly larger intensity than the $\text{K}_2\text{Ge}_4\text{O}_9:\text{Mn}^{4+}$ sample. The blue excitation peak observed for $\text{Rb}_2\text{Ge}_4\text{O}_9:\text{Mn}^{4+}$ shifts gradually from 480 nm to 462 nm with the increase of potassium content but no change in the UV excitation peak indicates that the incorporation of potassium content affects the ${}^4\text{T}_2$ energy level but not the ${}^4\text{T}_1$ energy level. This effect can be efficiently used for designing a new material having tailored blue excitation. The strongest emission peak of Mn^{4+} is shifted from 666 nm to 663 nm while moving from $\text{Rb}_2\text{Ge}_4\text{O}_9:\text{Mn}^{4+}$ to $\text{K}_{1.5}\text{Rb}_{0.5}\text{Ge}_8\text{O}_{18}:\text{Mn}^{4+}$. The presence of potassium increases the energy of the ${}^2\text{E}_g$ level because of the decreased covalency of the Mn–O bond in MnO_6 octahedra since potassium ion possesses lower polarizability than Rb^+ ion. The emission lifetime is observed to increase gradually with potassium substitution. The quantum yield value of $\text{K}_{1.5}\text{Rb}_{0.5}\text{Ge}_8\text{O}_{18}:\text{Mn}^{4+}$ is higher than that of $\text{K}_2\text{Ge}_4\text{O}_9:\text{Mn}^{4+}$, and it is much greater than $\text{Rb}_2\text{Ge}_4\text{O}_9:\text{Mn}^{4+}$. The emission lifetime and thermal stability are also much shorter in $\text{Rb}_2\text{Ge}_4\text{O}_9:\text{Mn}^{4+}$ and it is found to be enhanced with the partial K^+ substitution.⁴⁵

A detailed study on the influence of alkali ions on the luminescence property of Mn^{4+} -activated $\text{MGe}_4\text{O}_9:\text{Mn}^{4+}$ ($\text{M} = \text{Li}_2, \text{Li-Na}, \text{and K}_2$) as a function of various alkali ions has been carried out by Xue and co-workers.⁹³ They have also adopted a similar milder solid-state methodology for the syntheses of these samples. Apart from the already discussed results, the calculated D_q/B values for these three phosphors are found to be greater than 2.2 indicating that Mn^{4+} is experiencing a stronger crystal field. As the energy of the emission spectrum is mainly influenced by the nephelauxetic effect, their obtained β_1 value is found to be distinct for the three different phosphors showing that the nephelauxetic effect is varying with different phosphors according to the type of host. As expected, the phosphor having smaller ${}^2\text{E}_g$ value has smaller β_1 indicating the host experiencing comparatively strong nephelauxetic and emit lights in the lower wavelength region.⁹³

Another study on $\text{K}_2\text{Ge}_4\text{O}_9:\text{Mn}^{4+}$ and $\text{Rb}_2\text{Ge}_4\text{O}_9:\text{Mn}^{4+}$ phosphors has been carried out in order to get a clear insight on the dependence of their optical properties on the chemical compositions and the temperature.⁹⁴ In these germanates, Mn^{4+} ions occupy two germanate octahedral sites, but the Mn–O bond length is dissimilar for these two sites. Usually, Mn^{4+} ions occupying Ge–O sites with larger bond length experience smaller crystal field splitting and the corresponding ${}^4\text{T}_{2g}$ band locates at a lower energy region. Owing to the smaller Mn–O distance

in $\text{K}_2\text{Ge}_4\text{O}_9$ comparing to $\text{Rb}_2\text{Ge}_4\text{O}_9$ results in stronger crystal field splitting for $\text{K}_2\text{Ge}_4\text{O}_9$. Meanwhile, Mn^{4+} ions occupying a site with a smaller Mn–O bond length show a higher thermal quenching temperature. As we know, the Racah parameter, B , is the measure of inter electronic repulsion in $3d$ orbitals, and the maximum value is achieved for free Mn^{4+} ions, which is equal to 1160 cm^{-1} . The redshift observed in the emission spectrum with increasing temperature may be due to the decrease of D_q , B , or C . But the magnitude of these parameters with temperature clearly shows that the value of B increases with the temperature while the decrease in D_q value is minor. These results strongly suggest that the redshift in the spectrum is due to the considerable decrease of C value with an increase in temperature. This shows the strong influence of Racah parameter C on the luminescent properties of these phosphors. The Racah parameters B and C can be related through the Slater-Condon parameters F_2 and F_4 .⁹⁴

$$B = F_2 - 5F_4 \quad \text{and} \quad C = 35 F_4 \quad (17)$$

Here the parameters F_2 and F_4 describe the electrostatic interaction between the electrons in the unfilled shell of Mn^{4+} ions. Therefore, the covalent character of M–O bonds mainly affects the parameter F_2 . These two equations indicate that the decrease in F_4 is the reason for the decrease in the C value and the increase in the B value. However, it is quite difficult to generate a simple relation between B and C , which hinders the exact prediction of the position of the emission wavelength of these phosphors. In fact, the bond angle $\text{Mn}^{4+}\text{--O--M}^{n+}$ (M stands for neighbouring cations) has a strong influence on the parameter C and less effect on B . Brik *et al.* demonstrated a correlation between the energy position of the Mn^{4+} and the $\text{Mn}^{4+}\text{--O}^{2-}\text{--M}^{n+}$ bond angle in the materials possessing a perovskite structure.⁵⁹ A bond angle close to 180° results in a small value for C . Hence, a highly ionic host with a bond angle that deviates more from 180° B as well as C coefficients should have larger values resulting in a blue shift. In $\text{K}_2\text{Ge}_4\text{O}_9$ and $\text{Rb}_2\text{Ge}_4\text{O}_9$, the decrease in crystal field strength and increase in B value with the increase in temperature is due to the thermal expansion of the host which results in a reduction in the covalent interaction between Mn^{4+} and O^{2-} .⁹⁴

Li *et al.* reported a novel red-emitting $\text{K}_2\text{BaGe}_8\text{O}_{18}:0.002\text{Mn}^{4+}$ for W-LEDs application with an emission spectrum centred at 666 nm .⁶⁶ They adopted the conventional solid-state method for synthesis with a calcination temperature of 1050°C for 6 h. The crystal structure of this compound consists of four octahedral Ge^{4+} sites (Ge1-Ge4) and three tetrahedral Ge^{4+} sites

(Ge5-Ge7) (**Fig.1.10 (a)**). However, the PL origin is only due to the occupancy of Mn^{4+} at octahedral Ge sites. Here the obtained excitation spectrum is deconvoluted into four Gaussian curves centred at 313 nm, 350 nm, 391 nm, and 462 nm and these are attributed to the Mn^{4+} - O^{2-} charge transfer band, spin allowed ${}^4\text{A}_2 \rightarrow {}^4\text{T}_1$, spin forbidden ${}^4\text{A}_2 \rightarrow {}^2\text{T}_2$, and spin allowed ${}^4\text{A}_2 \rightarrow {}^4\text{T}_2$ transitions, respectively (**Fig.1.10 (b)**). To understand the energy transfer mechanism involved in the concentration quenching, critical distance has been calculated to 35.75 Å. As the exchange interaction plays a significant role only when the critical distance value is less than 5 Å, further evaluation was carried out wherein the dominant energy transfer mechanism is caused by the electric dipole-dipole interactions. While increasing the Mn^{4+} concentrations from the optimum leads to the reduction of emission lifetime, which implies the faster decay of the emission because of the energy transfer among the Mn^{4+} - Mn^{4+} pairs. The crystal field analysis is also carried out and the obtained value of Dq/B (3.31) is high enough since Mn^{4+} ions experience a stronger crystal field in the GeO_6 octahedra compared to other germanates. As the ${}^2\text{E}_g \rightarrow {}^4\text{A}_{2g}$ transition depends mainly on the nephelauxetic effect rather than on the strength of the crystal, the nephelauxetic ratio (0.9604) was also estimated.⁶⁶

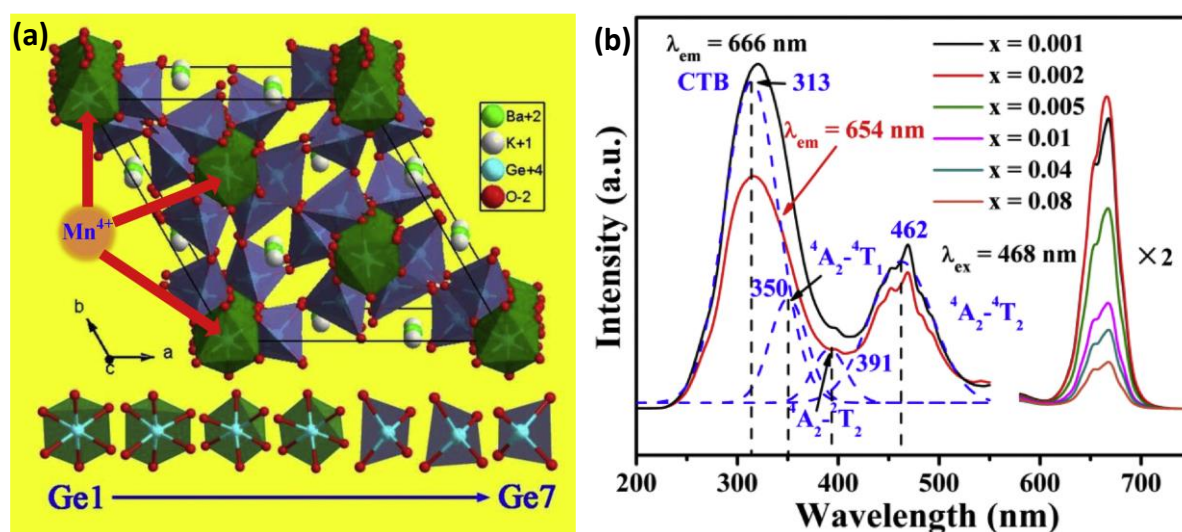


Fig.1.10 (a) Crystal structure of $\text{K}_2\text{BaGe}_8\text{O}_{18}:\text{Mn}^{4+}$ (hexagonal- $\text{P}3\text{c}1$); **(b)** PL excitation and emission spectra of $\text{K}_2\text{BaGe}_8\text{O}_{18}:0.002\text{Mn}^{4+}$. Reproduced with permission from ref.⁶⁶

Cao *et al.* introduced two red-emitting phosphors $\text{Li}_2\text{MgGeO}_4:0.004\text{Mn}^{4+}$ and $\text{K}_2\text{MgGeO}_4:0.004\text{Mn}^{4+}$ and found that the former one has greater intensity while the latter one easily deliquesces at room temperature.^{95,96} The shift in the emission position between these phosphors may be attributed to the difference in the ionic radii of Li^+ and K^+ .⁹⁵ Another novel deep red-emitting phosphor $\text{Li}_3\text{RbGe}_8\text{O}_{18}:0.005\text{Mn}^{4+}$ was reported by Singh and co-workers

which shows better emission intensity greater than other available alkali tetra germanate hosts.⁶ Here a combinatorial chemistry approach is used for finding the best emitting phosphors among A–Ge–O systems where A can be alkali metals such as Li, Rb, K, or their combination. At first, the ratio between A:Ge was fixed as 2:4, then 21 compositions based on this ratio were prepared as shown in **Fig.1.11 (a)** and studies were extended with four other ratios (A: Ge = 2.25:4, 2.5:4, 2.75:4, 3:4). Then out of the total 105 prepared samples, the sample $\text{Li}_3\text{RbGe}_8\text{O}_{18}:\text{Mn}^{4+}$ was found to show maximum emission intensity **Fig.1.11 (b)**. The crystal structure of $\text{Li}_3\text{RbGe}_8\text{O}_{18}:\text{Mn}^{4+}$ shown in **Fig.1.11 (c)** consists of GeO_4 tetrahedra and GeO_6 octahedra. While the bond length of all Ge–O bonds in the GeO_6 octahedra are identical, two values are observed for the bond length of Ge–O bonds in the GeO_4 tetrahedra.

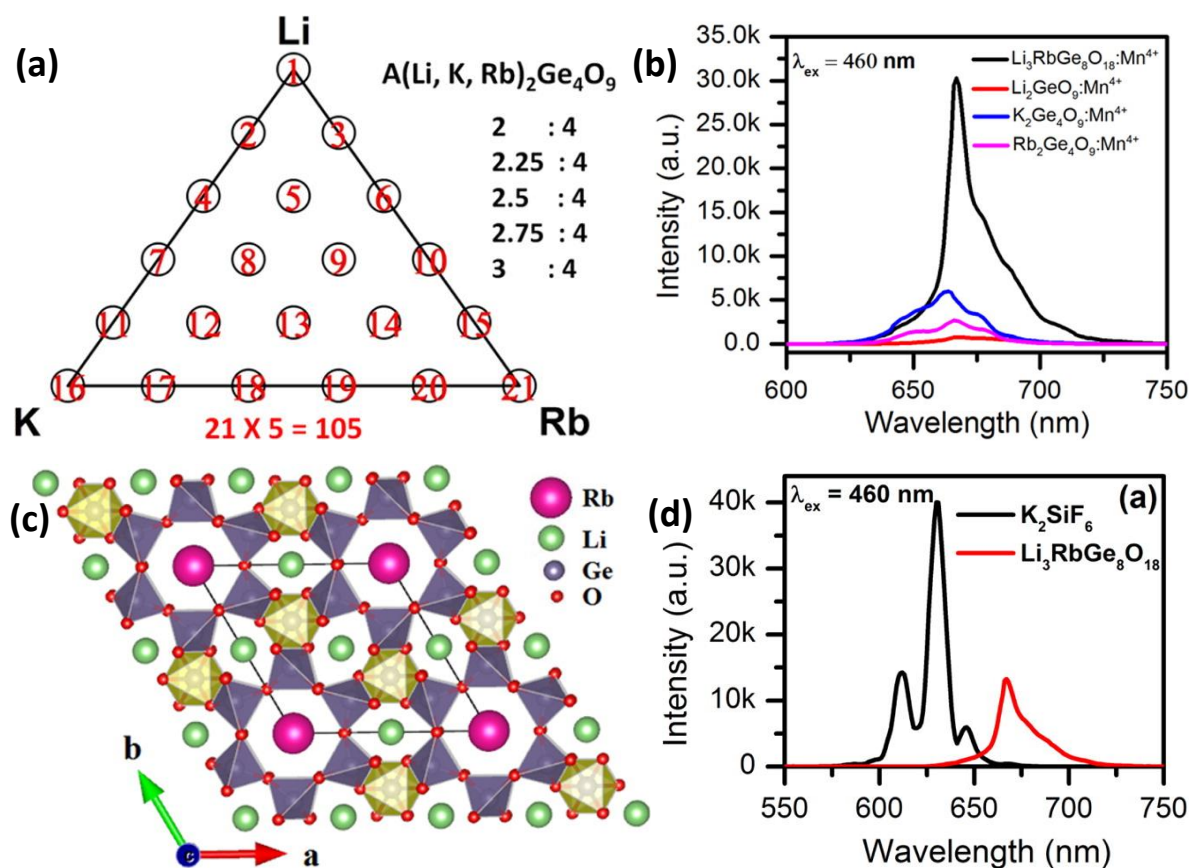


Fig.1.11 (a) Design of the phosphor-composition search space; **(b)** Comparison of PL emission spectra of $\text{Li}_3\text{RbGe}_8\text{O}_{18}:\text{Mn}^{4+}$ with $\text{Li}_2\text{Ge}_4\text{O}_9:\text{Mn}^{4+}$, $\text{K}_2\text{Ge}_4\text{O}_9:\text{Mn}^{4+}$ and $\text{Rb}_2\text{Ge}_4\text{O}_9:\text{Mn}^{4+}$; **(c)** Crystal structure of $\text{Li}_3\text{RbGe}_8\text{O}_{18}$ (trigonal-P31m); **(d)** Comparison of PL emission spectra of $\text{Li}_3\text{RbGe}_8\text{O}_{18}:\text{Mn}^{4+}$ with $\text{K}_2\text{SiF}_6:\text{Mn}^{4+}$. Reproduced with permission from ref.⁶

Although its emission intensity is observed to be lower than $\text{K}_2\text{SiF}_6:\text{Mn}^{4+}$ as shown in **Fig. 1.11 (d)**, its PL spectrum falls in the deep-red region.⁶ Recently a novel deep red-emitting phosphor $\text{Li}_3\text{Cs}_{1-y}\text{Rb}_y\text{Ge}_8\text{O}_{18}:0.01\text{Mn}^{4+}$ was also prepared using a similar methodology as described for the $\text{Li}_3\text{RbGe}_8\text{O}_{18}:0.005\text{Mn}^{4+}$ sample.⁹⁷ The PL intensity of $\text{Li}_3\text{Cs}_{1-y}\text{Rb}_y\text{Ge}_8\text{O}_{18}:0.01\text{Mn}^{4+}$ phosphor increased to about 1.75 times compared to its corresponding rubidium phosphor, while its internal quantum efficiency is also increased by 1.57 times.⁹⁷

1.2.3.2 Alkaline-earth metal-based germanate systems

Xue and co-workers discovered a long persistent phosphor $\text{Mg}_2\text{GeO}_4:0.001\text{Mn}^{4+}$ and reported its long glow luminescence properties.⁹⁸ The emission of the $\text{Mg}_2\text{GeO}_4:0.001\text{Mn}^{4+}$ lasted for 30 min, which can be observed with the naked eye. This phosphor is a well-suited deep red long-lasting or storage phosphor for many applications. The persistence luminescence (PersL) of this phosphor is enhanced by the substitution of Ln^{3+} ions ($\text{Ln}^{3+} = \text{Pr}^{3+}, \text{Er}^{3+}, \text{Yb}^{3+},$ and Nd^{3+}) at the Mg^{2+} sites. The addition of these Ln^{3+} ions with larger ionic radii (as compared to the Mg^{2+}) caused cationic distortions which create some additional defects. Among the various co-doped samples, the persistent emission from the phosphor composition of $\text{Mg}_2\text{GeO}_4: 0.001\text{Mn}^{4+}, 0.005\text{Yb}^{3+}$ lasts for 2 h. The performance of the persistent emission depends highly on the carriers captured in the trapping centres. Compare to other co-doped samples, the trapping centres introduced by Yb^{3+} ions in $\text{Mg}_2\text{GeO}_4:0.001\text{Mn}^{4+}, 0.005\text{Yb}^{3+}$ significantly enhanced the persistence behaviour of this composition, and making this material good for room temperature long persistent emission. Here the substitution of Yb^{3+} ions in the Mg^{2+} sites may lead to the formation of defects and the positive defects are acting as the electron traps whereas the negative defects act as the hole traps.⁹⁸

Liang *et al.* reported $\text{Mg}_{14}\text{Ge}_{5(1-0.2\%)}\text{O}_{24}: 0.2\%\text{Mn}^{4+}$ phosphor having a high quantum yield of 81%.⁸⁰ Crystal structure analysis of this compound revealed that the Ge^{4+} ions occupied two tetrahedral and one octahedral site. The octahedral site occupies the centre of lattice faces as well as the vertex of the crystal lattice (**Fig.1.12 (a)**). Further, these octahedrons are connected to each other by sharing the same vertices, and Mn^{4+} ions occupy these six coordinated octahedral sites and act as the luminescence centres. As seen from **Fig.1.12 (b)**, the highest PL intensity, as well as quantum yield is reported for 1 mol% Mn^{4+} -doped $\text{Mg}_{14}\text{Ge}_5\text{O}_{24}$ phosphor. This is because of the fact that this composition possesses high crystallinity without any defects. Also the lattice distortion is found to be negligible due to well-matched ionic radii and the charge between Ge^{4+} and Mn^{4+} . Meanwhile, this composition

also exhibited appreciable emission intensity at elevated temperatures as it maintained 64% PL intensity at 60 °C relative to the PL intensity at 20 °C.⁸⁰

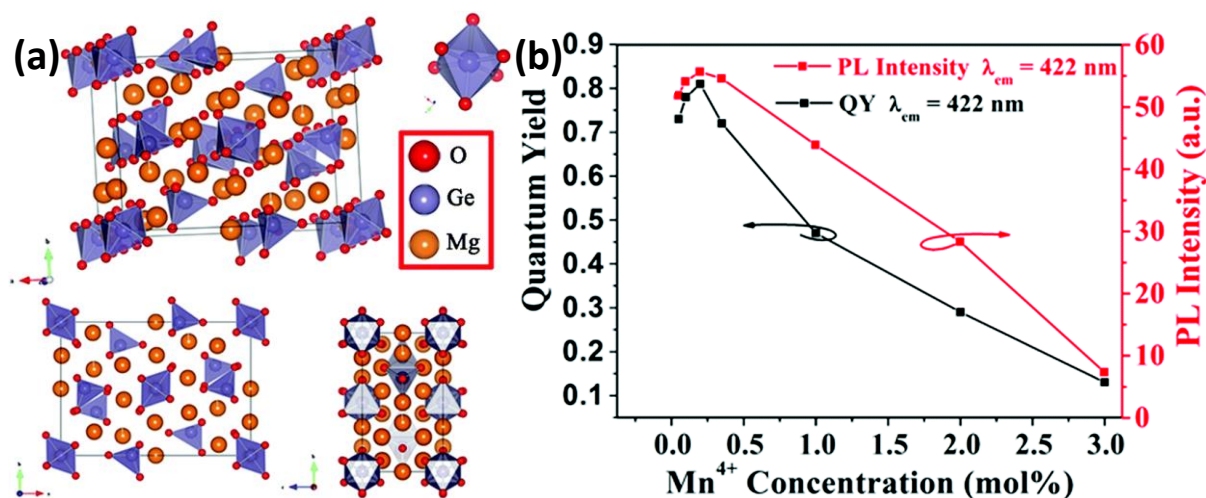


Fig.1.12 (a) Crystal structure of $\text{Mg}_{14}\text{Ge}_5(1-0.2\%)\text{O}_{24}:0.2\%\text{Mn}^{4+}$ (orthorhombic-Pbam); (b) The change of emission intensity and quantum yields as a function of Mn^{4+} concentration.

Reproduced with permission from ref.⁸⁰

The emission intensity of this phosphor is enhanced by Zn^{2+} substitution in the Mg^{2+} site since this substitution makes some ionic rearrangement in the crystal. The difference in ionic radii between Zn^{2+} and Mg^{2+} leads to the lattice distortion of the crystal.⁹⁹ Q. Huang *et al.* reported Bi^{3+} and Mn^{4+} co-doped $\text{Mg}_{14}\text{Ge}_5\text{O}_{24}$ phosphor for optical agriculture application.¹⁰⁰ Comparing with the single Mn^{4+} doped phosphor, the Bi^{3+} co-doped one has enhanced emission because of the energy transfer mechanism involved between Bi^{3+} and Mn^{4+} .¹⁰⁰ Another detailed study on this phosphor was carried out by Liang and co-workers who substituted cations such as Ti^{4+} , Sn^{4+} , and Si^{4+} for the Ge^{4+} site since the cation substitution is the better way to tune or enhance the emission in matrix sensitive activator such as Mn^{4+} doped phosphors.¹⁰¹ In the PL emission spectra, the peak located at 639 nm is identified as the ZPL. The peaks located at lower energy (above 639 nm) are the Stokes shift emission peak whereas the peak located at higher energy (below 639 nm) is the anti-Stokes shift emission peak. The Ti^{4+} substituted $\text{Mg}_{14}\text{Ge}_{4.5}\text{Ti}_{0.5}\text{O}_{24}:\text{Mn}^{4+}$ has higher emission intensity which is about 2.49 times greater than the $\text{Mg}_{14}\text{Ge}_5\text{O}_{24}:\text{Mn}^{4+}$. The addition of these cations leads to the formation of energy or electron trapping defects which helps in increasing the emission intensity.

The change in the intensity of the ZPL is also observed with the cationic substitution. The ZPL is very sensitive to lattice distortion hence, the degree of lattice distortion is calculated by the polyhedron distortion index. The quantum yield of the optimized $\text{Mg}_{14}\text{Ge}_4.5\text{Ti}_{0.5}\text{O}_{24}:\text{Mn}^{4+}$ sample is 94% which could maintain up to 85% of the initial intensity at 473 K.

The low-temperature emission spectrum of $\text{Mg}_{14}\text{Ge}_5\text{O}_{24}:\text{Mn}^{4+}$ with cation substitution and without cation substitution was carried out at 6.9 K (**Fig.1.13**). Here the emission intensity gets significantly increased manifolds with Ti^{4+} and Sn^{4+} substitution while comparing with PL spectra recorded at room temperature. Moreover, the substitution of the three cations (Ti^{4+} , Sn^{4+} , and Si^{4+}) leads to a slight redshift in their emission peaks, and the shifting increases with the increase in ionic radii of cations since these substitutions weaken the crystal field strength. The crystal field strength Dq has an inverse relation ($Dq = Ze^2r^4/6R^5$) between the bond length (R) of the central ion with the ligand.¹⁰¹ Here the XRD refinement result indicates that with an increase in ionic radii of cations, the bond length is also found to be increased which weakens the crystal field strength resulting in a slight shift (redshift) in their emission peaks.¹⁰¹

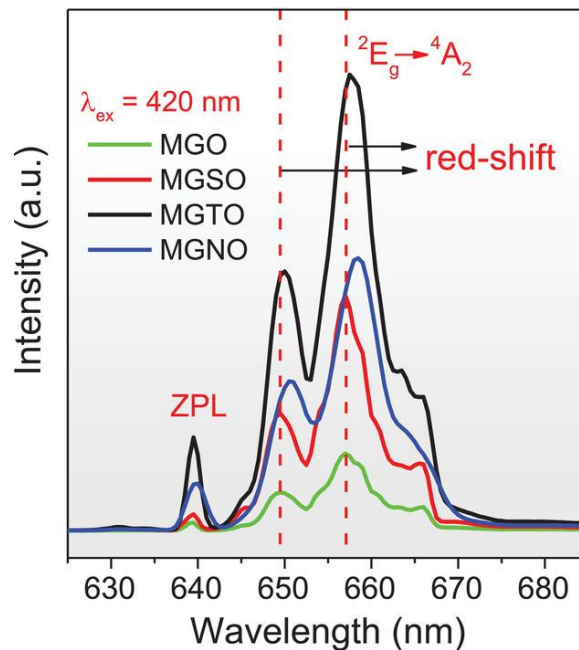


Fig.1.13 Low-temperature PL emission spectra of MGO ($\text{Mg}_{14}\text{Ge}_5\text{O}_{24}:\text{Mn}^{4+}$) and cation substituted MGSO ($\text{Mg}_{14}\text{Ge}_5\text{O}_{24}:\text{Mn}^{4+}, \text{Si}^{4+}$), MGTO ($\text{Mg}_{14}\text{Ge}_5\text{O}_{24}:\text{Mn}^{4+}, \text{Ti}^{4+}$), and MGNO ($\text{Mg}_{14}\text{Ge}_5\text{O}_{24}:\text{Mn}^{4+}, \text{Sn}^{4+}$) samples. Reproduced with permission from ref.¹⁰¹

Another class of alkaline-earth based germanate material is $\text{Ba}_2\text{GeO}_4:0.006\text{Mn}^{4+}$.¹⁰² Owing to its deep red-emitting ability peaking at 667 nm, $\text{Ba}_2\text{GeO}_4:0.006\text{Mn}^{4+}$ can be used as

a red LED for indoor plant cultivation. This wavelength range is very close to the absorption peaks of the chlorophyll, and therefore suitable for the photosynthesis and photoperiodic effects of indoor plants. A novel thermally stable red-emitting $\text{Ba}_2\text{TiGe}_2\text{O}_8:0.006\text{Mn}^{4+}$ is also reported by Cao and co-workers for plant growth application.¹⁰³ In this phosphor structure, a Ba^{2+} ion combines with the eight oxygens to form the BaO_8 polyhedral, whereas a Ti^{4+} ion combines with the five oxygens to form the TiO_5 polyhedral. On the other hand, a Ge^{4+} ion combines with four oxygens as well as with six oxygens to form GeO_4 tetrahedra and GeO_6 octahedra, respectively. Importantly, Mn^{4+} ions are expected to occupy the Ge^{4+} site in the GeO_6 octahedra. To confirm this, Mn^{4+} has been doped into two different sites Ge^{4+} and Ti^{4+} separately. It is observed that Mn^{4+} ions occupied the Ge^{4+} sites have greater intensity showing the site suitability of Mn^{4+} in GeO_6 octahedra (**Fig.1.14**).¹⁰³

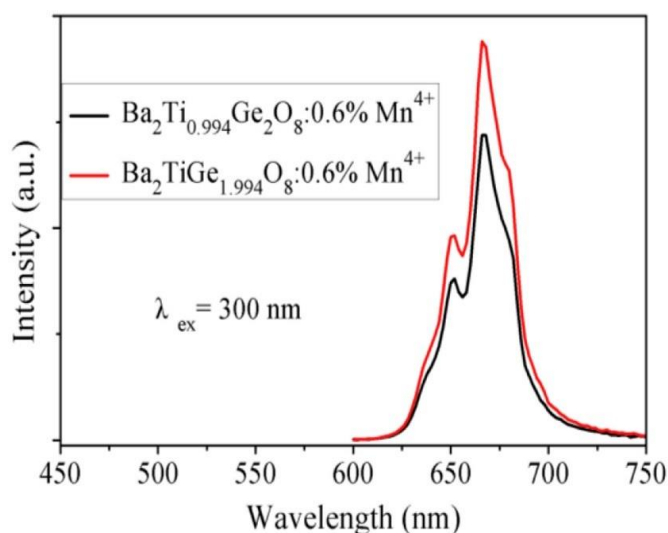


Fig.1.14 Comparison of PL emission spectra of $\text{Ba}_2\text{Ti}_{0.994}\text{Ge}_2\text{O}_8:0.006\text{Mn}^{4+}$ and $\text{Ba}_2\text{TiGe}_{1.994}\text{O}_8:0.006\text{Mn}^{4+}$. Reproduced with permission from ref.¹⁰³

Lu *et al.* reported deep red-emitting double perovskite $\text{Ba}_2\text{MgGe}_2\text{O}_7:0.013\text{Mn}^{4+}$ phosphors prepared by a conventional solid-state methodology.¹⁰⁴ These phosphors show a strong red emission band centred at 660 nm, while the maximum emission intensity is observed at 0.013 mol of Mn^{4+} concentration. The dipole-dipole interaction among the Mn^{4+} ions led to luminescence quenching.¹⁰⁴ Fu *et al.* reported $\text{BaAl}_2\text{Ge}_2\text{O}_8:0.001\text{Mn}^{4+}$ phosphors for the plant growth application.¹⁰⁵ In this composition, Mn^{4+} ions occupy either Al^{3+} or Ge^{4+} sites in the AlO_4 and GeO_4 tetrahedra. The results of temperature-dependence emission spectra and the calculated activation energy ($\Delta E = 0.36$ eV) suggested that this phosphor composition is thermally stable.¹⁰⁵

Two alkaline-earth metal-based materials, $\text{SrGe}_4\text{O}_9:0.005\text{Mn}^{4+}$ and $\text{BaGe}_4\text{O}_9:0.005\text{Mn}^{4+}$ have been reported by Liang and co-workers for W-LED applications.¹⁰⁶ The crystal structure of these hosts has a great impact on their luminescence properties. Both BaGe_4O_9 and SrGe_4O_9 matrices are isostructural and consist of three different types of coordination environments: BaO_8 polyhedral, GeO_4 tetrahedral, and GeO_6 octahedral. The GeO_4 tetrahedra and GeO_6 octahedra are connected, and Mn^{4+} ions are occupying the Ge^{4+} sites of GeO_6 octahedra. As observed from the PL analysis, the emission intensity of $\text{BaGe}_4\text{O}_9:0.005\text{Mn}^{4+}$ is higher than that of the $\text{SrGe}_4\text{O}_9:0.005\text{Mn}^{4+}$ sample. Even though SrGe_4O_9 and BaGe_4O_9 are isostructural, the excitation peak position and shape of their emission spectra are different. This observation can be attributed to the change in the microstructure around Mn^{4+} ions, which might be occurred due to the difference in ionic radii between Ba^{2+} and Sr^{2+} . Hence the crystal field strength and nephelauxetic effect may also be different for these two phosphors leading to the aforementioned difference in their spectra. Meanwhile, the PL emission intensities of $\text{BaGe}_4\text{O}_9:0.005\text{Mn}^{4+}$ and $\text{SrGe}_4\text{O}_9:0.005\text{Mn}^{4+}$ are observed to reduce half of the room temperature PL intensity at 180 °C and 100 °C, respectively, indicated that both phosphors have appreciable thermal stability. However, the absolute quantum efficiency of these phosphors is not even higher than 50.¹⁰⁶

Zhang *et al.* carried out the detailed crystal field studies on $\text{BaGe}_4\text{O}_9:0.005\text{Mn}^{4+}$, and the obtained $D_q/B = 2.7$ value indicates that Mn^{4+} ions experience a strong crystal field in this host.¹⁰⁷ The temperature-dependent PL analysis, including the low-temperature PL studies, is also carried out (**Fig.1.15**). The change in the PL excitation spectra at a temperature greater than 300 K is attributed to the activation of vibronic modes in the luminescence centres. While the PL intensity is found to be increasing with the decrease in temperatures. From the PL emission spectra, surprisingly, the ZPL identified at 666 nm has a relatively strong intensity over the temperature range of 10-300 K. No spectral shift is observed with temperature variation, but the peaks get broadened while increasing the temperature from 10-400 K. The broadening of peaks with temperature manifests the involvement of phonon in these transitions. The visibility of the ZPL is very much sensitive to the local symmetry of Mn^{4+} ions. The peak centred at 666 nm can be ascribed to the ZPL of the transition at the C_3 site since this transition is much stronger than the ZPL of the transition at the centrosymmetric D_3 site. At an ultra-low temperature of 10 K, the emission peak at 666 nm split into two peaks which may be appeared due to the formation of Kramer's doublets since Mn^{4+} ion belongs to the d^3 system.¹⁰⁷

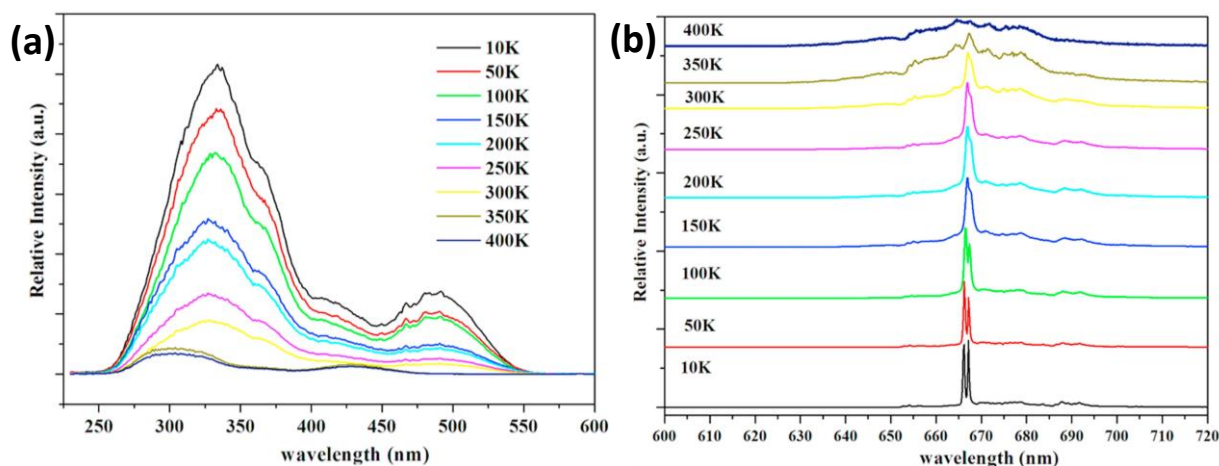


Fig.1.15 The temperature depended PL (a) excitation, and (b) emission spectra of $\text{BaGe}_4\text{O}_9:0.005\text{Mn}^{4+}$. Reproduced with permission from ref. ¹⁰⁷

Another Sr-based novel $\text{Sr}_2\text{MgGe}_2\text{O}_7:0.007\text{Mn}^{4+}$ phosphor is reported by Chen and co-workers.¹⁰⁸ The crystal structure of this phosphor consists of MgO_4 tetrahedra and Ge_2O_7 double tetrahedra which are connected through oxygen. It is believed that Mn^{4+} ions occupy the Ge^{4+} sites in Ge_2O_7 double tetrahedra. The crystal field studies show that the Dq/B value is approximately equal to 2.86 showing that Mn^{4+} experiences a strong crystal field, and the calculated nephelauxetic ratio is 0.9747. Also, $\text{Sr}_2\text{MgGe}_2\text{O}_7:0.007\text{Mn}^{4+}$ phosphor could maintain 60.3% of the room temperature emission intensity at 145°C .¹⁰⁸

1.2.3.3 Lanthanum-based germanate systems

The reports on lanthanum-based germanate phosphors are comparatively less numerous. The double perovskite $\text{La}_2\text{MgGeO}_6:\text{Mn}^{4+}$ is a long persisting germanate producing deep red emission centred at 708 nm under UV excitation.¹⁰⁹ The crystal structural analysis of this compound reveals that a La^{3+} ion is coordinated with 12 oxygen atoms. Although there exist both GeO_6 and MgO_6 octahedral, Mn^{4+} ions prefer GeO_6 octahedral sites mostly. The alternatively arranged GeO_6 and MgO_6 octahedral help in increasing the distance between Mn^{4+} ions, owing to which intense deep red emission is observed. Based on the value of Dq/B (2.67), it is concluded that Mn^{4+} ions are experiencing a strong crystal field in the above host.¹⁰⁹

Another lanthanum-based germanate system is $\text{La}_3\text{GaGe}_5\text{O}_{16}:0.0025\text{Mn}^{4+}$, which can also be efficiently used in phosphor-converted W-LEDs.¹¹⁰ The crystal structure of this phosphor consists of GeO_6 octahedra, GeO_4 tetrahedra, and GaO_4 tetrahedra (**Fig.1.16 (a)**).

Each octahedron is connected to six tetrahedrons while each tetrahedron is connected to two octahedrons, thereby forming the chains of composition $[\text{Ge}(\text{GaGeO}_4)_3]$. The PLE spectrum recorded at 659 nm shows three excitation bands originating from ${}^4\text{A}_{2g} \rightarrow {}^4\text{T}_{1g}$, ${}^2\text{T}_{2g}$, ${}^4\text{T}_{2g}$ transitions of Mn^{4+} , while the PL spectrum recorded at 330 nm shows one sharp peak corresponds to the ${}^2\text{E}_g \rightarrow {}^4\text{A}_{2g}$ transitions of Mn^{4+} (**Fig.1.16 (b)**). From the low-temperature PL analysis (**Fig.1.16 (c)**), two sharper peaks named B and D with one shoulder peak C, are observed at a temperature of 10 K. The intensity of these peaks gets reduced with the increase in temperature. However, the intensity of the anti-Stokes shoulder peak A gets increased with the increase in temperature. This abnormality is due to the thermal vibration in the host. Since the ${}^2\text{E}_g \rightarrow {}^4\text{A}_{2g}$ transition is spin forbidden, therefore, the ${}^2\text{E}_g$ state life time is rather long. Because of the increase in temperature and the thermal vibration, the electrons are coupled to the lattice. The electrons can jump from the lower vibrational energy level to higher and thereby making the balance in electron distribution in these two levels.¹¹⁰ Because of this, the shoulder peak appears and grows with the increase in temperature. But the PL intensity of other peaks decreases with an increase in temperature.

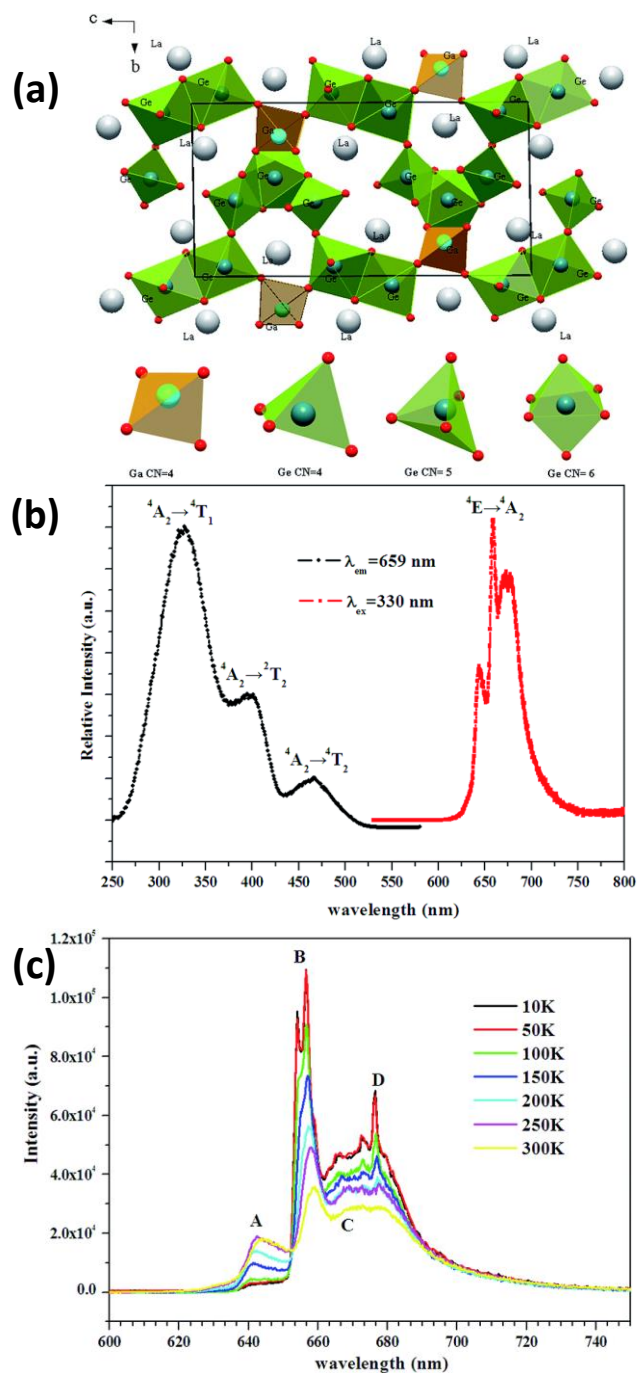


Fig.1.16 (a) Crystal structure of $\text{La}_3\text{GaGe}_5\text{O}_{16}:0.0025\text{Mn}^{4+}$ (trigonal-P321); (b) PL excitation and emission spectra; (c) Low temperature PL of $\text{La}_3\text{GaGe}_5\text{O}_{16}:0.0025\text{Mn}^{4+}$ phosphor.

Reproduced with permission from ref.¹¹⁰

1.2.3.4 Non-Ge⁴⁺ site occupancy of germanates

There are some other germanate phosphors where the Ge sites may not accommodate Mn^{4+} ions. $\text{Mg}_3\text{Ga}_2\text{GeO}_8:0.005\text{Mn}^{4+}$ is one of the best examples of such phosphors.¹¹¹ Since Mn^{4+} ions stabilized in the octahedral environment. Herein, Mn^{4+} ions prefer to occupy octahedral sites provided by Mg^{2+} and Ga^{3+} ions instead of the tetrahedral sites of Ge^{4+} ions

(Fig.1.17 (a)). The variation in PL emission intensity with different Mn^{4+} sources doped in different sites is shown in Fig.1.17 (b), which ascertained the occupancy of the Mn^{4+} at Mg^{2+}/Ga^{3+} sites.¹¹¹ In addition, maximum emission intensity is seen when the source of the activator ion is MnO_2 . This observation reveals the octahedral preference of Mn^{4+} ions, and also indicates that Mn^{4+} ions have high crystal field stabilization energy in the octahedral environment. Cao *et al.* reported a deep red-emitting $LiRGe_2O_6:0.006Mn^{4+}$ ($R = Al$ or Ga) composition where Mn^{4+} ions occupy the octahedral sites provided by Al^{3+} and Ga^{3+} ions. The emission intensity of the $LiAlGe_2O_6:0.006Mn^{4+}$ and $LiGaGe_2O_6:0.006Mn^{4+}$ are found to be different. After the occupation of the Mn^{4+} ions in Al^{3+} and Ga^{3+} sites of the host lattice, the bond of Mn-O in the GaO_6 octahedral is become stronger than that in the AlO_6 octahedral due to the different ionic radii of Al^{3+} and Ga^{3+} ions. Due to this, the PL intensity of $LiAlGe_2O_6:0.006Mn^{4+}$ is found to be greater than that of $LiGaGe_2O_6:0.006Mn^{4+}$ under UV excitations.¹¹²

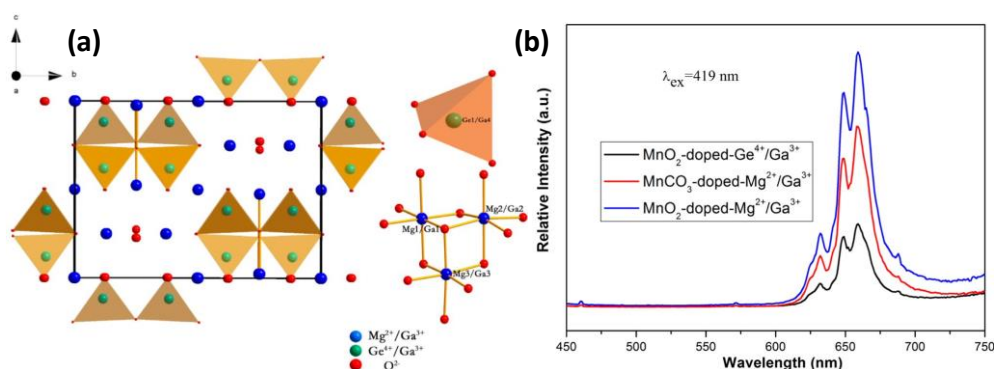


Fig.1.17 (a) Crystal structure of $Mg_3Ga_2GeO_8$ (orthorhombic- $Imma$); **(b)** PL emission spectra of $Mg_3Ga_2GeO_{12}:0.005Mn^{4+}$ with different Mn^{4+} sources and different dopant sites.

Reproduced with permission from ref.¹¹¹

Another reported germanate is $Mg_7Ga_2GeO_{12}:Mn^{4+}$ where Mn^{4+} ions prefer Ga^{3+} sites.¹¹³ In this host, Mn^{4+} ions conveniently occupy Mg^{2+} , Ga^{3+} and Ge^{4+} sites of $Mg_7Ga_2GeO_{12}:0.005Mn^{4+}$ and it was found that Mn^{4+} doped in the Ga^{3+} site has higher emission intensity as compared to when it is doped at the Mg^{2+} site. Further, this phosphor can be efficiently excited by blue light. In the case of $Mg_6ZnGeGa_2O_{12}:0.01Mn^{4+}$ phosphor, the XRD, as well as PL analysis reveals that Mn^{4+} ions occupy the octahedral ($Mg^{2+}(Zn^{2+})/Ga^{3+}$) sites.¹¹⁴ This phosphor is a promising red-emitting candidate excited by near ultra-violet (NUV) chips.¹¹⁴ Jansen *et al.* reported a novel $Mg_3Y_2Ge_3O_{12}:0.01Mn^{4+}, 0.015Li^+$ phosphor prepared by a sol-gel method.¹¹⁵ Here, Mn^{4+} ions occupy the Mg^{2+} sites, and Li^+ is incorporated for charge

compensation. This phosphor shows extraordinary thermal quenching behaviour since its $T_{1/2}$ value is above 800 K, which is greater than the thermal quenching temperature $T_{1/2}$ of red-emitting $\text{Mg}_{14}\text{Ge}_5\text{O}_{24}:\text{Mn}^{4+}$. Because of these properties, this phosphor is a potential red candidate in phosphor blends of high-power W-LEDs.¹¹⁵

Dong *et al.* reported novel orange red-emitting $\text{Ca}_3\text{M}_2\text{Ge}_3\text{O}_{12}:\text{Mn}^{2+}$, Mn^{4+} ($\text{M} = \text{Al}$, Ga)¹¹⁶. Here, Mn^{2+} ions occupying Ca^{2+} sites produce the orange emission, whereas Mn^{2+} and Mn^{4+} ions occupying $\text{Al}^{3+}/\text{Ga}^{3+}$ sites produce red and deep red emission.¹¹⁶ Lingling *et al.* reported the PL of $\text{Mg}_2\text{Ti}_{0.65}\text{Ge}_{0.35}\text{O}_4:0.001\text{Mn}^{4+}$ by substituting Ge^{4+} ions in Ti^{4+} sites.¹¹⁷ The incorporation of Ge^{4+} ions enhance the emission intensity. When Ge^{4+} is incorporated, there are two sites for Mn^{4+} to occupy and it is believed that replacement of Ge^{4+} by Ti^{4+} accelerates the translation of a greater number of TiO_6 octahedral to contorted GeO_6 octahedral and separation of adjacent TiO_6 octahedral. As a result of this, the distance between isolated Mn^{4+} ions as well as the $\text{Mn}^{4+}-\text{Mn}^{4+}$ distance enhanced, which can decrease the energy transfer rate in the host thereby increasing the PL intensity. The PL emission spectra and the crystal structure are shown in **Fig.1.18**.¹¹⁷

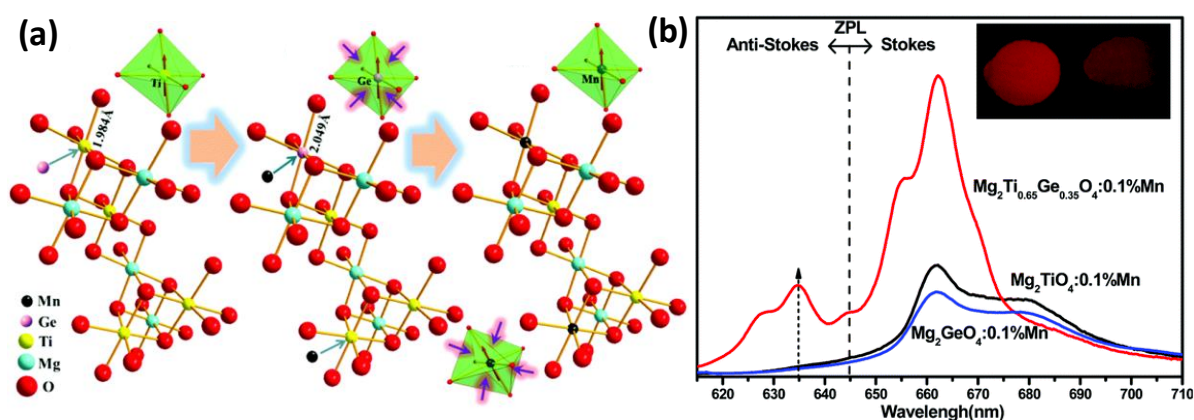


Fig.1.18 (a) Crystal structure of $\text{Mg}_2\text{Ti}_{0.65}\text{Ge}_{0.35}\text{O}_4:0.001\text{Mn}^{4+}$ (cubic-Fd3m); (b) PL emission spectra showing the effect of Ge substitution. Reproduced with permission from ref.¹¹⁷

1.2.4 Cr^{3+} -activated deep red/NIR emitting germanate phosphors

Detailed description on the ionic configuration of Cr^{3+} ion and its related luminescence properties in the various host materials can be found in Refs.^{31,32} As we have already discussed in the introduction part, the studies on Cr^{3+} -activated phosphors are mainly taking place in oxide hosts owing to their admirable merits comparing to fluorides. In comparison with Mn^{4+} activated phosphors, the Cr^{3+} activated phosphors have some advantages such as their

capability in producing light in deep red and NIR region, long persistence, etc. Hence apart from the various display applications, these phosphors can extend their use in sensors, biomedical imaging, decoration, night vision surveillance, dark glow signage, security, etc.¹¹⁸ Most of the studies on Cr³⁺-doped phosphors are based on gallates since Ga³⁺ can efficiently provide the octahedral site for Cr³⁺ because of their similar ionic radii and charge. The ionic radius of Cr³⁺ (Cr^{VI}: 0.615 Å) is quite close to the ionic radius of Ga³⁺ (Ga^{VI}: 0.620 Å) in an octahedral environment.⁴⁷ It is noteworthy to discuss the Cr³⁺-doped NIR emitting phosphors. Some of the important NIR emitting gallates and gallo-germanates are Zn₃Ga₂GeO₈:Cr³⁺¹¹⁹, ZnGa₂O₄:0.005Cr³⁺¹²⁰ Mg₄Ga₄Ge₃O₁₆:0.005Cr³⁺¹²¹ and Ca₃Ga₂Ge₃O₁₂:0.01Cr³⁺¹²²

Zhou *et al.* reported Cr³⁺-doped NIR emitting gallo-germanate garnet La₃GaGe₅O₁₆:0.03Cr³⁺ for the luminescent solar concentrator, which can convert the photons from sunlight to the required deep or NIR radiation.¹²³ Wang *et al.* reported Cr³⁺-doped NIR emitting Mg₃Ga₂GeO₈:0.05Cr³⁺ phosphor for light source application in food analysis.¹²⁴ This phosphor exhibits a broad emission band in the range of 650-1200 nm, which is matching with the overtones of vibration of molecules present in the food components, hence the details of water content or sugar content, as well as the damages in food materials, can be analysed by making use of these phosphors in the light source of food analyser (**Fig.1.19**).¹²⁴

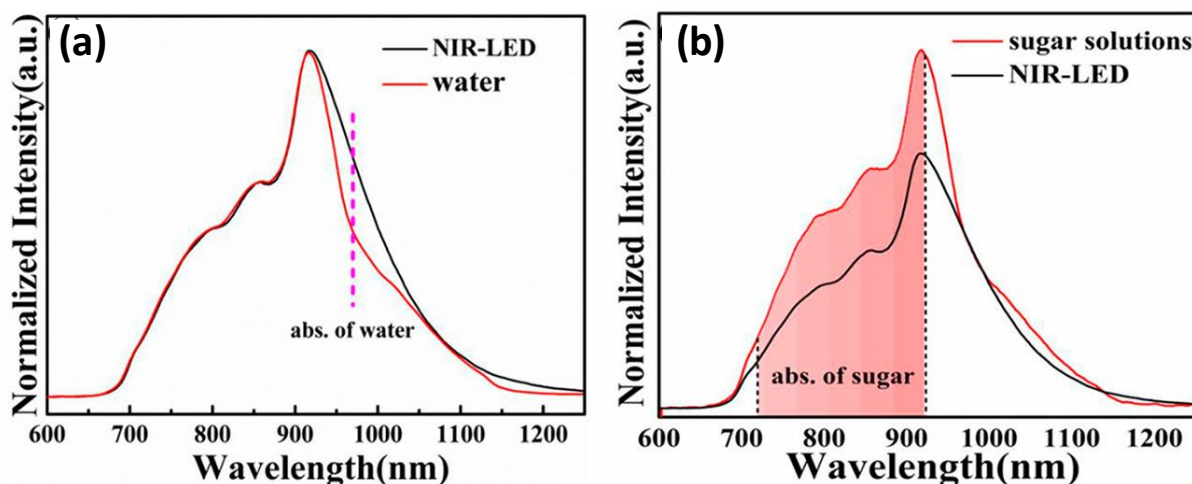


Fig.1.19 (a) Normalized transmission spectra of NIR light after penetrating water and (b) sugar solutions. Reproduced with permission from ref.¹²⁴

Besides these NIR emitting phosphors, some of the efficient Cr³⁺-activated deep red-emitting phosphors are MgY₂Al₄SiO₁₂:0.02Cr³⁺,¹²⁵ Zn(GaAl)₂O₄:0.005Cr³⁺,0.01Bi³⁺,⁶⁵

MgGa₂O₄:Cr³⁺,¹²⁶ etc. Chi *et al.* synthesized MgAl₂O₄:0.012Cr³⁺ by co-precipitation method which produces deep red emission centred at 687 nm.¹⁴ Further, a W-LED has fabricated by combining this phosphor with blue InGaN chip commercial YAG:Ce³⁺, and the produced W-LED exhibited a CRI value of 3481 K and a CRI value of 78.¹⁴ Katayama *et al.* reported long persisting Cr³⁺-doped deep red-emitting phosphor LaAlO₃:0.005Cr³⁺ having emission band centred at 734 nm for *in-vivo* imaging application.¹²⁷ The intensity of this phosphor is found to be greater than Cr³⁺-doped persistent phosphor ZnGa₂O₄:Cr³⁺, which shows an emission peak at 694 nm. The PersL properties and luminescence intensity of LaAlO₃:0.005Cr³⁺ phosphors are found to increase with Sm³⁺-doping.¹²⁷ There are different reports on the various types of Cr³⁺ activated phosphors but the focus of our review is deep red-emitting Cr³⁺ activated germanate phosphors. The reports on these categories of phosphors are comparatively less in number. Bai *et al.* prepared Ca₃Al₂Ge₂O₁₀:0.07Cr³⁺ phosphor by a solid-state method and it shows a broad emission band in the range of 650-750 nm peaking at 697 nm.³⁸ The optimum concentration for Cr³⁺ in this phosphor is 0.07 mol. Bai *et al.* synthesized Zn₃Al₂Ge₂O₁₀:0.01Cr³⁺ phosphor by solid-state methodology.¹²⁸ The heating condition required for the preparation of this sample in a box furnace is 1200°C for 2.5 h. The phosphor can produce deep red emission in the range of 650-750 nm with an emission peak centred at 694 nm under the excitation of 400 nm (**Fig.1.20**). Further, the introduction of Ca²⁺ ions in the Zn²⁺ sites of this phosphor could induce PersL properties and bluish-white light emission.¹²⁸

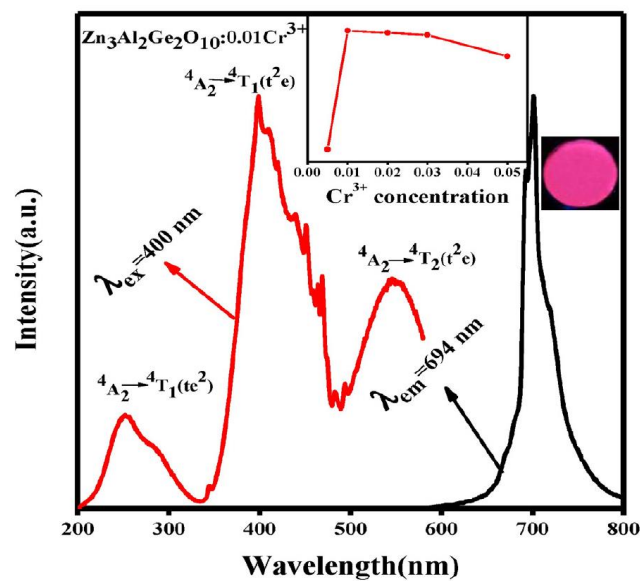


Fig.1.20 PL excitation and emission spectrum of Zn₃Al₂Ge₂O₁₀:0.01Cr³⁺. Reproduced with permission from ref.¹²⁸

1.2.5 Amplification of deep red/NIR emission

1.2.5.1 Effect of synthesis methods and particle morphology

Methods adopted for the synthesis of phosphors have a great impact on their luminescence properties and potential applications. Phosphors prepared through different methods can produce different structures such as spherical, core-shell, nanoflakes, etc., and these may have pure or tuneable emission properties.¹²⁹ As we already discussed the glass-ceramic routes were used for the synthesis of nanocrystals of $\text{Li}_2\text{Ge}_4\text{O}_9:\text{Mn}^{4+}$ and $\text{LiNaGe}_4\text{O}_9:\text{Mn}^{4+}$.^{84, 85, 88} Even though they could make samples even in the nano range, the phosphor $\text{LiNaGe}_4\text{O}_9:\text{Mn}^{4+}$ prepared by the solid-state reaction possesses greater colour purity as well as quantum yield compared to the sample prepared through the glass-ceramic route. The tetragermanate phase obtained for $\text{LiNaGe}_4\text{O}_9:\text{Mn}^{4+}$ through the glass-ceramic route contains more defects than the solid-state sample.⁸⁸ Suppression of defects that are acting as non-radiative centres during solid-state synthesis is the reason for improved quantum yield.^{84, 85, 88, 97-102.}

While discussing the effect of synthesis on deep red-emitting phosphor, the Mn^{4+} and Cr^{3+} sources have some relevance. The phosphor $\text{Mg}_3\text{Ga}_2\text{GeO}_8:0.005\text{Mn}^{4+}$ is prepared using two different sources of Mn, which are MnCO_3 and MnO_2 . Then it is observed that phosphor prepared using MnO_2 has better intensity. In the MnCO_3 compound, Mn is divalent, and after calcination, many of the Mn^{2+} ions will not oxidize to Mn^{4+} , some may be just oxidized to Mn^{3+} . Hence the actual contribution of Mn^{4+} from MnCO_3 is less than MnO_2 . (**Fig.1.17 (b)**).¹¹¹ In solid-state synthesis, fluxes can be used for lowering the sintering and reaction time along with improved crystallinity without making any reaction with raw materials. The lower melting point of flux compared to final calcination temperature can assure the liquid face during sintering which can further increase the mobility and homogeneity of solid reactants. The cationic radius of flux is large enough to avoid atomic substitution. The luminescence intensity and morphology of $\text{Sr}_2\text{MgAl}_{22}\text{O}_{36}:0.012\text{Mn}^{4+}$ phosphor are increased with the usage of flux H_3BO_3 since the addition of flux stimulate the ionic diffusion inducing enhanced red emission.^{130, 131} Most of the germanates mentioned in this article are prepared through the solid-state method. But this method requires higher calcination temperature, and the chances for forming impurity phases are relatively high. The red emission of these phosphors and their morphology can be improved by implementing the sol-gel technique with a lower calcination time. $\text{Mg}_2\text{TiO}_4:\text{Mn}^{4+}$ is one of the best examples that we can provide since the sample prepared through the sol-gel technique shows 2.24-fold emission enhancement in comparison with the

solid-state sample.^{129, 132} The microwave-assisted sol-gel technique is one method that we can suggest for red emission enhancement and nanoscale production of germanates. Our research group used the microwave-assisted sol-gel method efficiently to enhance the red emission of $\text{Li}_3\text{RbGe}_8\text{O}_{18}:0.005\text{Mn}^{4+}$ nanophosphor.¹³³ Here the raw materials were taken in the stoichiometric ratio. The carbonates (Li_2CO_3 , Rb_2CO_3 , and MnCO_3) were dissolved in HNO_3 to obtain their corresponding nitrates and then separate solutions of GeO_2 and citric acid were mixed into this solution. The obtained resultant solution was placed in a microwave at different temperatures and microwave power for optimization (**Fig.1.21**). The microwave energy in the microwave-assisted method couples directly with the ions in the reaction medium. This results in effective internal volumetric heating, rapid and homogeneous heating of reaction medium, with minimal thermal variations. This method leads to uniform nucleation, producing uniform-sized crystalline nanoparticles with better performance.

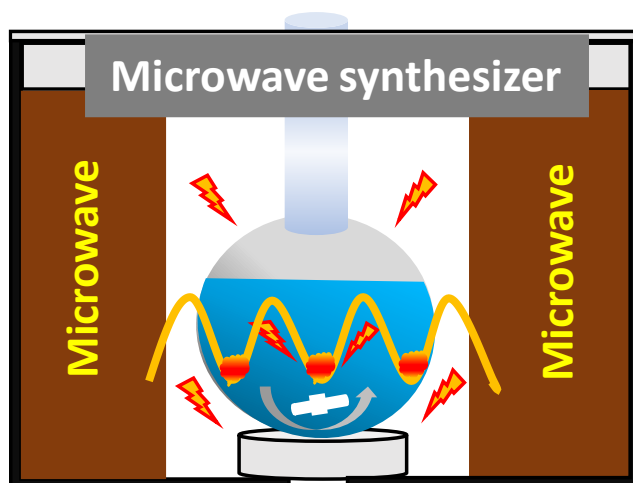


Fig.1.21 Schematic representation of microwave-assisted sol-gel synthesis. Adapted from ref.¹³³

Morphology has a great influence on photoluminescence property, and it is very important for some specific applications. Phosphor with spherical size can minimize the scattering, thereby elevating the luminescence properties. Also, phosphors with nano-size are highly desirable since particle with smaller size is preferred for higher resolution.⁸⁰ But the greater surface effects of the nanoparticle may reduce the luminescence efficiency since the unsaturated bonds on the surfaces are capable to quench the luminescence centres on or near the surface. Hence, a method that can be adapted for red emission enhancement for germanate, that we can suggest is the synthesis of nanophosphor with a core-shell structure. Here surface coating with the non-metals can be used for reducing the surface effects, or metal shells can be

used to coat over the nanoparticle for metal enhanced luminescence. In the former case if we are using sensitizers in the shell additional luminescence enhancement may be visible. In the latter case, there may be an increased radiative transition and enhanced luminescence only if the distance between luminescence species and the metal surface is between 5-20 nm.¹³⁴ A combination of noble metal nanoparticles with luminescence species is collectively called plasmons. The oscillation of surface electrons in the nanoparticle can interact with the incident light leading to increased light absorption cross-section. Dolgov and co-workers prepared $\text{Mg}_2\text{TiO}_4:\text{Mn}^{4+}$ with core-shell $\text{Ag}@\text{SiO}_2$ nanoparticles, and the luminescence intensity is observed to increase due to the core-shell structure (**Fig.1.22**).¹³⁵ This approach can be used in the case of germanates.

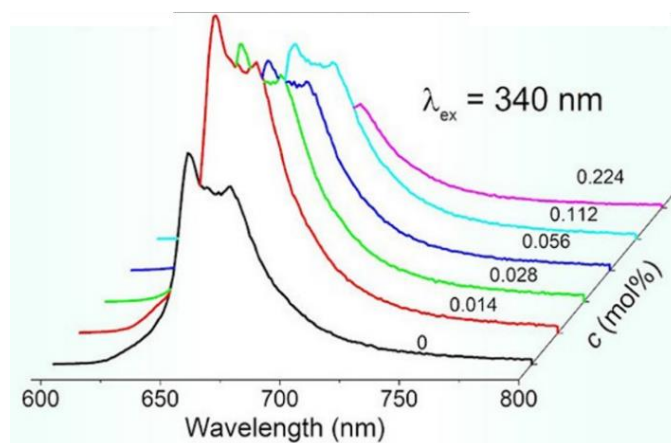


Fig.1.22 Emission spectrum of $\text{Mg}_2\text{TiO}_4:\text{Mn}^{4+}$ for different concentration of $\text{Ag}@\text{SiO}_2$ nanoparticles having 40 nm Ag cores. Reproduced with permission from ref.¹³⁵

1.2.5.2 Cationic modifications and co-doping

It is known that Cr^{3+} and Mn^{4+} ions are host-sensitive activators and the phosphors activated by these ions include $3d-3d$ transitions. Hence, the cationic substitution is one of the most efficient methods utilized for improving and modulating the emission intensity of these phosphors.¹⁰¹ It is already mentioned that partial substitution of K^+ in the Rb^+ site of $\text{Rb}_2\text{Ge}_4\text{O}_9:\text{Mn}^{4+}$ phosphor can lead to emission enhancement.⁴⁵ Also, the partial substitution of Rb^+ ions in the Cs^+ sites of $\text{Li}_3\text{CsGe}_8\text{O}_{18}:0.01\text{Mn}^{4+}$ phosphor improved its quantum efficiency from 37% to 55%.⁹⁷ The optimized sample with the most efficient optical properties is $\text{Li}_3\text{Cs}_{0.5}\text{Rb}_{0.5}\text{Ge}_8\text{O}_{18}:0.01\text{Mn}^{4+}$. Also, a slight red shift is observed in the emission spectra with Rb substitution which can be attributed to the local crystal structure variation and stronger crystal field strength with Rb substitution. Structural rigidity has a great role in luminescence

property. Phosphor having greater structural rigidity shows greater emission. The substitution of Rb^+ in the Cs^+ site can alter the degree of distortion of $\text{Ge}(1)\text{O}_6$ octahedra where Mn^{4+} ions are going to be incorporated.⁹⁷ The change in the degree of distortion occurs because of the difference in the ionic radii of Rb^+ and Cs^+ . From the calculation of the degree of distortion of $\text{Ge}(1)\text{O}_6$ octahedra for different Rb substituted samples, the optimized sample $\text{Li}_3\text{Cs}_{0.5}\text{Rb}_{0.5}\text{Ge}_8\text{O}_{18}:0.01\text{Mn}^{4+}$ has the smallest value showing its high structural rigidity thus greater emission.⁹⁷ While discussing how cationic modification enhancing red emission, the Ti^{4+} , Sn^{4+} , and Si^{4+} substituted $\text{Mg}_{14}\text{Ge}_5\text{O}_{24}:\text{Mn}^{4+}$ phosphor is worth mentioning even though it is mentioned in the alkali earth metal-based germanates in section 3.2. Here the substitution of Ti^{4+} at the Ge^{4+} site could enhance the emission intensity by 2.49 times. The enhancement of PL emission in the Ti^{4+} substituted phosphors can be attributed to the resonance effect. As we know the emission spectrum of Mn^{4+} is dominated by energy differences of some vibronic bands which involved allowed transition. During their vibronic transitions, the energy waves travelling in the lattice obey the periodic function given by,¹⁰¹

$$I = 4I_o \cos^2 \left(\frac{\pi d}{\lambda} \right) \quad (1.18)$$

where I represent the relative intensity and d is the distance between Mn^{4+} ions. The increase in d value due to the cation substitution can alter the intensities of emission. In addition, the intensity of the emission peak will be higher when d is an integral multiple of λ . This phenomenon is called the resonance emission enhancement effect, which plays a significant role in the enhancement of emission intensity in Ti^{4+} ions substituted $\text{Mg}_{14}\text{Ge}_5\text{O}_{24}:\text{Mn}^{4+}$ phosphor.¹⁰¹

Although in some cases, co-doping is carried out for charge compensation, this compensation is also found to be one of the efficient ways to tune the optical properties. In the case of $\text{Mg}_3\text{Ga}_2\text{GeO}_8:0.005\text{Mn}^{4+}$ phosphor, the emission intensity gets increased with the co-doping of Li^+ ions.¹¹¹ Here as already discussed Mn^{4+} ions are substituting at $\text{Mg}^{2+}/\text{Ga}^{3+}$ sites. If Mn^{4+} ions are substituting at the Mg^{2+} sites, then the extra positive charges developed could be balanced by co-doping of Li^+ ions at the Mg^{2+} sites leading to charge compensation as well as emission enhancement.¹¹¹ The persistent red luminescence of the Cr^{3+} activated $\text{ZnGa}_2\text{O}_4:0.005\text{Cr}^{3+}$ phosphor is enhanced by substituting the co-dopant Bi^{3+} at the Zn^{2+} site.¹²⁰ Similarly, the Sm^{3+} co-doping in $\text{LaAlO}_3:0.005\text{Cr}^{3+}$ could also enhance the persistent red

emission.¹²⁷ Consequently, it can be concluded that co-doping and cationic modification is an efficient way of enhancing persistence and luminescence in Cr³⁺ and Mn⁴⁺ doped phosphors.

1.2.5.3 Energy transfer mechanisms

The energy transfer mechanism involved between the co-dopant and the activator-like Cr³⁺ and Mn⁴⁺ can also alter the intensity of red emission. In some cases, the co-dopant is found to act as a sensitizer. One of the best examples for the red emission enhancement via sensitizer is Bi³⁺ and Mn⁴⁺ co-doped Mg₁₄Ge₅O₂₄. Usually, Bi³⁺ ion is known for its metal-to-metal charge transfer (MMCT) character between its outer 6s² orbital and host metal cations with d⁰ or d¹⁰ system. The energy transfer mechanism involved between Bi³⁺ and Mn⁴⁺ is represented schematically (**Fig.1.23 (a)**). Under the excitation of UV light, the electrons in the ¹S₀ state get excited to MMCT, ¹P₁ or ³P₁ states. After that, these electrons may relax to lower excited ³P_{1,0} states of Bi³⁺ by the non-radiative process, followed by energy transfer to excited state ²E_g of Mn⁴⁺ ion, as shown in **Fig.1.23 (a)**. Under UV and blue excitations, electrons in the ground state of Mn⁴⁺ get excited to ⁴T_{1,2} states. After that, these electrons may relax to a lower excited ²E_g state and produce amplified deep red emission about 10.6 times greater than without Bi³⁺ sample.¹⁰⁰ Xu *et al.* enhanced the red emission CaAl₁₂O₁₉:Cr³⁺ by Sm³⁺ co-doping. Here the energy transfer mechanism is involved between the Sm³⁺ and Cr³⁺ (**Fig.1.23(b)**). Hence the energy transfer mechanism is one of the efficient methods for enhancing red emission.¹³⁶

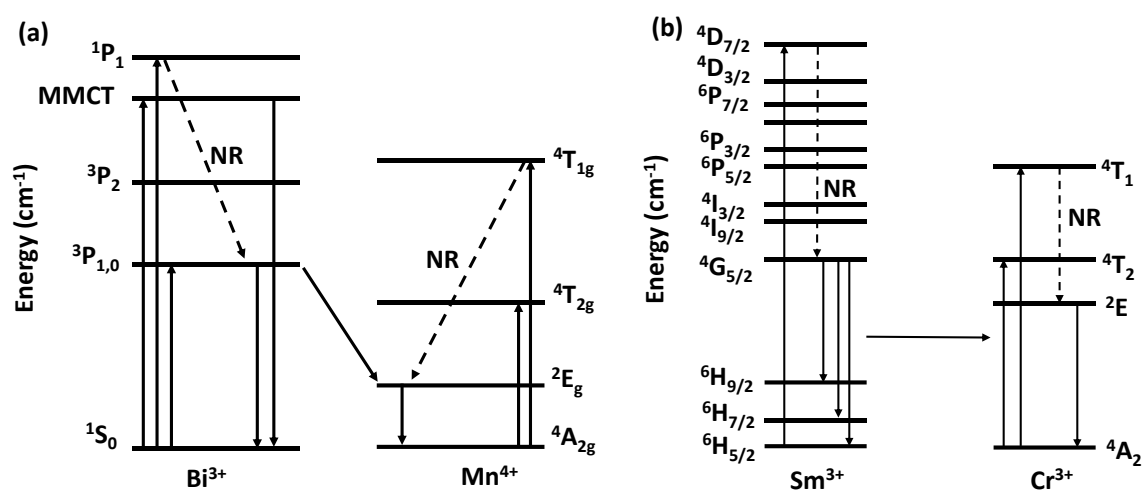


Fig.1.23 Energy level diagrams and energy transfer process between (a) Bi³⁺ and Mn⁴⁺ Adapted from ref. ¹⁰⁰ (b) Sm³⁺ and Cr³⁺ Adapted from ref. ¹³⁶ [(NR representing non-radiative relaxation)]

1.2.6 Thermal stability enhancement

Thermal stability is an important requirement of phosphors during their practical applications in particular, in solid-state lighting. Taking the LED application of phosphor as an example, the operating temperature of LED can exceed 150°C due to the high input power density imparted in the chip. This heat may transfer to the phosphor.¹³⁷ Thermal stability of the efficient germanate $\text{Mg}_{14}\text{Ge}_5\text{O}_{24}:\text{Mn}^{4+}$ which is capable of maintaining 75% of its initial intensity at 473 K is increased by the substitution of Ti^{4+} cations to 85% at 473 K of its room-temperature emission intensity. Here, cation substitution leads to an increase in lattice distortion which can induce traps (defects acting as electron trapping centres). These traps may be able to capture and store the phonon energy at room temperature from the excited state, and it will release the captured phonons to maintain the emission loss at high temperatures. The increased activation energy due to cation substitution can suppress the non-radiative transition and enhance thermal stability.¹⁰¹ An alternative to a cationic substitution for enhancing thermal stability that can be suggested is the preparation of core-shell morphology to protect the phosphor particles via shell. Already some graphite-like carbon nitride has been used as a coating shell on $\text{Y}_2\text{O}_3:\text{Eu}^{3+}, \text{Tb}^{3+}$ and $\text{Ca}_{9.5}\text{Na}_2(\text{PO}_4)_7:\text{Eu}^{2+}$. At the elevated temperature, the outer shell can be able to isolate the luminescence centres from external effects (moisture, temperature, etc.) and significantly reduce the surface defects. The coating layer combined with the phosphor favours the decrease of dangling bonds and defects on the surface of $\text{Y}_2\text{O}_3:\text{Eu}^{3+}$ thereby modifying the surface micro-structure effectively leading to enhanced thermal stability.¹³⁸

1.2.7 Potential applications of $\text{Mn}^{4+}/\text{Cr}^{3+}$ activated oxide phosphors

In this section, the important present and some future applications of Mn^{4+} and Cr^{3+} activated deep red-emitting phosphors including W-LEDs, plant growth, security, night vision surveillance, decoration, *in-vivo* imaging, display, biomarking, etc. (illustrated in **Fig.1.24**) have been highlighted. Some of the applications can be achieved only if these phosphors exhibit long persistent nature. Even though these wide varieties of applications are available for Cr^{3+} and Mn^{4+} activated phosphors, we are focusing mainly on deep red-emitting Mn^{4+} and Cr^{3+} germanate phosphors.

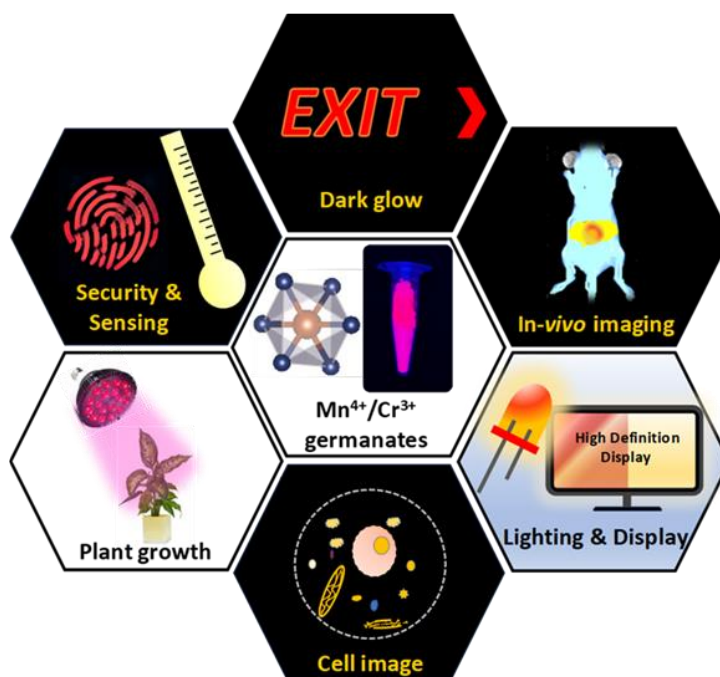


Fig.1.24 Representation of different applications of Mn^{4+} and Cr^{3+} activated phosphors.

1.2.7.1 W-LED applications

Most of the reports on Mn^{4+} -activated germanates are aiming for providing an efficient red component for the commercial W-LEDs. A famous commercialized method to produce white light is to combine broad yellow emitting $\text{Y}_3\text{Al}_5\text{O}_{12}:\text{Ce}^{3+}$ (YAG: Ce^{3+}) phosphor along with blue InGaN LED. However, due to the deficiency of the red component and higher correlated colour temperature (CCT) value, this commercially available W-LED faces a severe CRI problem.⁴⁸ To resolve the colour rendering issue of this system, Mn^{4+} -activated phosphors perhaps are a good solution as Mn^{4+} ions can be activated by the blue excitations. Li *et al.* used optimized $\text{LiNaGe}_4\text{O}_9:0.05\%\text{Mn}^{4+}$ for warm W-LED fabrication.⁸⁹ They fabricated a W-LED by combining blue InGaN LED chip, $\text{LiNaGe}_4\text{O}_9:0.05\%\text{Mn}^{4+}$, and YAG: Ce^{3+} and able to produce warm white light with a CCT value of 3353 K and CRI value of 69.2. But these systems do not have competing luminous efficiency, which shows the urge for another Mn^{4+} -doped phosphor for this application.⁸⁹ Ding *et al.* fabricated a W-LED using 455 nm InGaN LED chip, YAG: Ce^{3+} , and $\text{K}_2\text{Ge}_4\text{O}_9:0.001\text{Mn}^{4+}$ phosphor in various empirical ratios. While increasing the weight ratio of $\text{K}_2\text{Ge}_4\text{O}_9:\text{Mn}^{4+}$, the CCT values decrease from 6343 K to 3119 K, while the CRI value increases from 65.4 to 84.1. After tuning the weight ratio, the optimized white LED has a CIE value of (0.405, 0.356), and a CCT value of 3119 K, and a CRI of 84.1.⁹⁰

Yan *et al.* fabricated three W-LEDs using the three different deep red-emitting phosphors ($\text{Li}_3\text{RbGe}_8\text{O}_{18}:0.01\text{Mn}^{4+}$, $\text{Li}_3\text{CsGe}_8\text{O}_{18}:0.01\text{Mn}^{4+}$, and $\text{Li}_3\text{Cs}_{0.5}\text{Rb}_{0.5}\text{Ge}_8\text{O}_{18}:0.01\text{Mn}^{4+}$) by combining each one of them separately with the blue emitting InGaN chip, and the yellow emitting YAG:Ce³⁺.⁹⁷ Among these W-LEDs, the W-LED fabricated using $\text{Li}_3\text{Cs}_{0.5}\text{Rb}_{0.5}\text{Ge}_8\text{O}_{18}$ phosphor has good CRI (90.8) and CCT (4474 K) values. Our research group recently reported W-LEDs by combining the red-emitting Mn⁴⁺, Mg²⁺ co-doped $\text{Li}_3\text{RbGe}_8\text{O}_{18}:\text{Mg}^{2+},0.005\text{Mn}^{4+}$ nanophosphor and YAG:Ce³⁺ using blue InGaN chip.¹³³ The electroluminescence (EL) spectra of W-LED for various mixing ratio of YAG:Ce³⁺ yellow phosphor and red nanophosphor along with their digital images and CIE plots are depicted in **Fig.1.25 (a)-(c)**. The transition of cool white light (with a CCT of 6952 and CRI of 71) to the natural white light (with CCT of 5025 and CRI of 92) with the increment in red phosphor component can be easily identified from the digital images,¹³³ as well as from the CIE diagram, as shown in **Fig.1.25**.

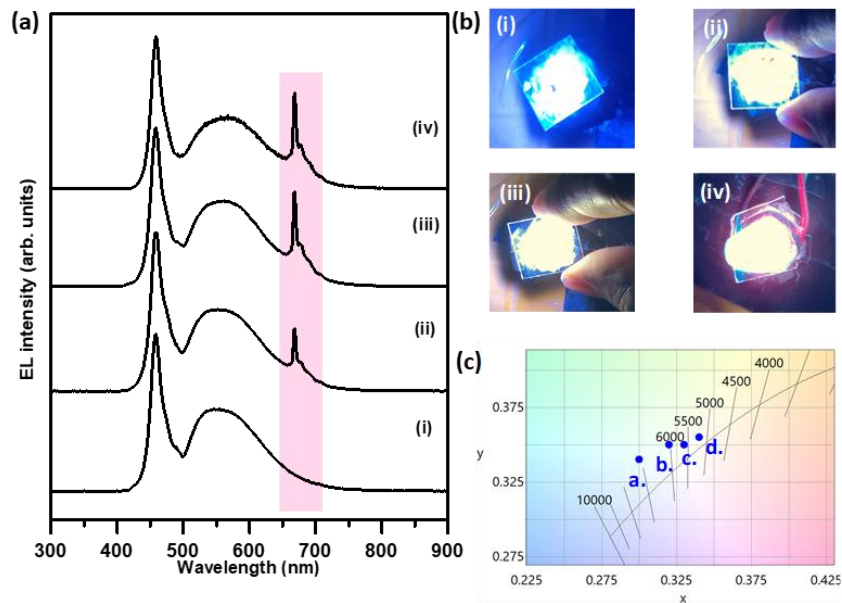


Fig.1.25 (a) EL spectra of the W-LEDs fabricated with the various mixing ratios of YAG:Ce³⁺ and $\text{Li}_3\text{RbGe}_8\text{O}_{18}:0.005\text{Mn}^{4+},\text{Mg}^{2+}$ ((i) 1:0, (ii) 1:1, (iii) 2:3, and (iv) 3:7), combined with 460 nm blue InGaN chip. **(b)** The digital images of the W-LEDs ((i) 1:0, (ii) 1:1, (iii) 2:3, and (iv) 3:7. **(c)** CIE plot showing the change in CCT values for different mixing ratio. Reproduced with permission from ref.¹³³

Liang *et al.* fabricated W-LED by combining the blue InGaN chip with the yellow emitting YAG:Ce³⁺ and $\text{Mg}_{14}\text{Ge}_5\text{O}_{24}:0.002\text{Mn}^{4+}$.⁸⁰ The CCT, CRI, and CIE values of the

fabricated W-LED are observed to be 2864 K, 80.6, and (0.36, 0.38), respectively. These results are found to be much better than the LED fabricated without the $\text{Mg}_{14}\text{Ge}_5\text{O}_{24}:0.002\text{Mn}^{4+}$ phosphor suggesting its suitability for solving the deficiency of red component in W-LEDs.⁸⁰ As cationic substitution in this phosphor ($\text{Mg}_{14}\text{Ge}_5\text{O}_{24}:\text{Mn}^{4+}$) could increase the emission intensity, the W-LED is also fabricated using the optimized cationic substituted $\text{Mg}_{14}\text{Ge}_{4.5}\text{Ti}_{0.5}\text{O}_{24}:\text{Mn}^{4+}$ 440 nm blue chip, and $\text{YAG}:\text{Ce}^{3+}$.¹⁰¹ The CCT value, CRI value, and CIE coordinate of the optimized cationic substituted W-LED are 3566 K, 87.3, and (0.45, 0.35), respectively. Moreover, the luminescence efficiency and the R_a value of this optimized W-LED are 109.42 lm/W and 93, respectively, showing the enhanced red spectral saturation.¹⁰¹

Other important phosphors used for the fabrication of W-LED are $\text{SrGe}_4\text{O}_9:0.005\text{Mn}^{4+}$ and $\text{BaGe}_4\text{O}_9:0.005\text{Mn}^{4+}$.¹⁰⁶ W-LED was fabricated by combining the blue InGaN chip with YAG and the respective phosphors. The obtained CRI and CCT values for W-LED fabricated using $\text{BaGe}_4\text{O}_9:\text{Mn}^{4+}$ is 92.1 and 3082 K, respectively, whereas these values for W-LED fabricated using $\text{SrGe}_4\text{O}_9:\text{Mn}^{4+}$ is 89.1 and 3440 K. Thus, based on the obtained results, $\text{BaGe}_4\text{O}_9:0.005\text{Mn}^{4+}$ provides a better deep red component for W-LED than $\text{SrGe}_4\text{O}_9:0.005\text{Mn}^{4+}$.¹⁰⁶ $\text{Mg}_3\text{Ga}_2\text{GeO}_8:0.005\text{Mn}^{4+}$ is another phosphor that can be efficiently used for W-LED. Here the ratio of the blue-emitting $\text{BaMgAl}_{10}\text{O}_{17}:\text{Eu}^{2+}$ (BAM: Eu^{2+}), green-emitting $\text{Sr}_2\text{SiO}_4:\text{Eu}^{2+}$, and red-emitting $\text{Mg}_3\text{Ga}_2\text{GeO}_8:0.005\text{Mn}^{4+}$ are tuned and combined with the GaN NUV chip to fabricate W-LED. The optimized fabricated W-LED produces white light with a CIE value of (0.316,0.375) and a CCT value of 3340 K.¹¹¹ Likewise, Mn^{4+} ions, Cr^{3+} activated red-emitting phosphors are also used for W-LED application. A W-LED was fabricated by combining the red-emitting $\text{Y}_3\text{Al}_5\text{O}_{12}:\text{Cr}^{3+}$ with the blue InGaN chip and YAG: Ce^{3+} . The fabricated W-LED has a CRI value of 76.4 and a CCT value of 5236 K.¹³⁹

1.2.7.2 Long-glow applications

The long glow or dark glow phosphors have crucial applications in the areas of optical memory, decoration, *in-vivo* imaging, traffic signs, imaging storage, etc. Deep red-emitting phosphor plays a crucial role in traffic signs and other important dark glow applications due to its higher wavelength emission. According to Rayleigh scattering, the scattering of light is inversely proportional to the fourth power of wavelength. Deep red light greater than 650 nm undergoes the least scattering during the cloudy atmosphere, fog time, and translucent situation. Generally, Cr^{3+} -activated phosphors serve the purpose of long red PersL emission. Few Mn^{4+} -activated red PersL phosphors including $\text{Mg}_2\text{GeO}_4:0.001\text{Mn}^{4+}$ are also reported.⁹⁸ Previously

mentioned $\text{ZnGa}_2\text{O}_4: 0.005\text{Cr}^{3+}\text{-Bi}^{3+}$,¹²⁰ $\text{Zn}(\text{Ga}_{1-x}\text{Al}_x)_2\text{O}_4: 0.005\text{Cr}^{3+}, 0.01\text{Bi}^{3+}$,⁶⁵ and $\text{LaAlO}_3: 0.005\text{Cr}^{3+}$ perovskite¹²⁷ are the best examples for long persistent phosphors emitting deep red light. Some of these phosphors are also found to be used *in-vivo* imaging. Deep red to NIR range corresponds to the higher transmittance wavelength range of biological tissue called biological optical window.¹²⁷ Cr^{3+} activated NIR emitting $\text{Zn}_{2.94}\text{Ga}_{1.96}\text{Ge}_2\text{O}_{10}: \text{Cr}^{3+}, \text{Pr}^{3+}$ phosphor is successfully used for *in-vivo* imaging, and its *in-vivo* images are shown in **Fig.1.26**. Before injecting the phosphor into the body of the mouse, it is irradiated with a 254 nm UV lamp. After that *in-vivo* images were collected for more than 450 min without any excitation.¹⁴⁰ Eventually, $\text{La}_3\text{GaGe}_5\text{O}_{16}: 0.01\text{Cr}^{3+}$ can also be used for *in-vivo* imaging, medical imaging, night vision due to its emission range (650-750 nm) and better PersL time (more than 30 min).¹⁴¹ The red emission images of this phosphor for different PersL time by varying Ge/O content is shown in **Fig.1.27** and it clearly shows that Ge/O content deficiency can improve the PersL time. This observation can be attributed to the close relationship between persistent luminescence of this phosphor with oxygen or germanium deficiency in the host.¹⁴¹

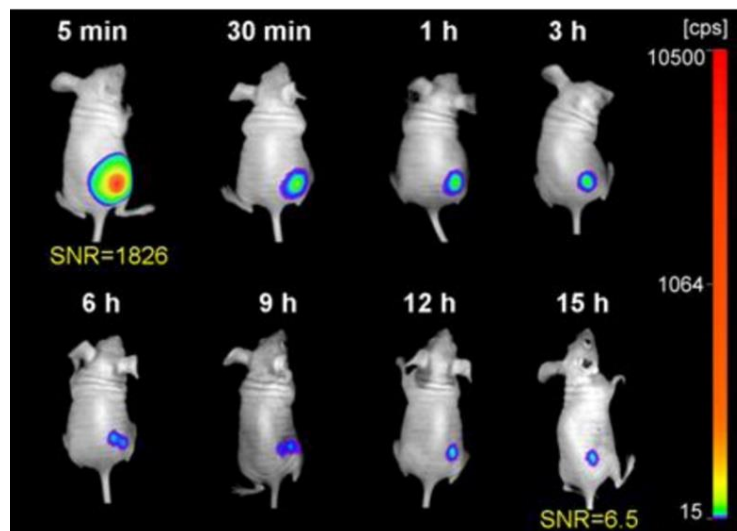


Fig.1.26 *In-vivo* images of the mouse after injection of $\text{Zn}_{2.94}\text{Ga}_{1.96}\text{Ge}_2\text{O}_{10}: \text{Cr}^{3+}, \text{Pr}^{3+}$ phosphor. Reproduced with permission from ref.¹⁴⁰

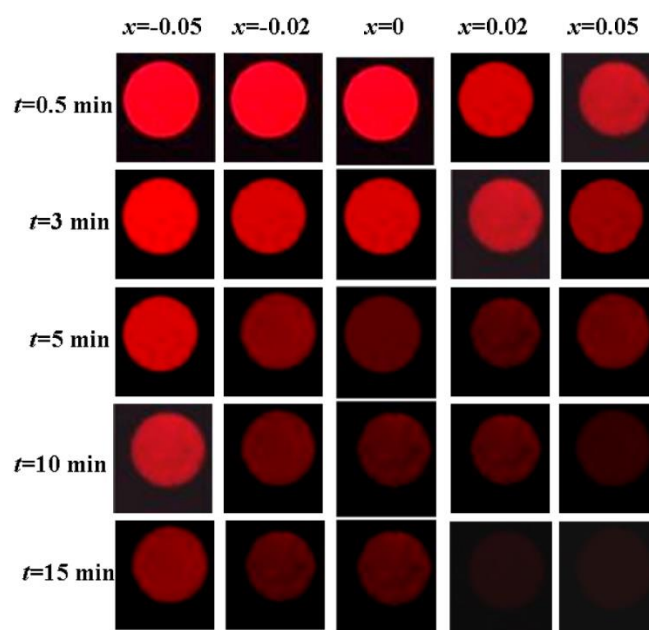


Fig.1.27 Red emission images of $\text{La}_3\text{GaGe}_{5+x}\text{O}_{16-x}:0.01\text{Cr}^{3+}$ ($-0.005 < x < 0.05$) at different PersL time with same exposure time. Reproduced with permission from ref.¹⁴¹

1.2.7.3 Security applications

The $\text{Mn}^{4+}/\text{Cr}^{3+}$ activated deep red-emitting phosphors have a significant role in security and forensic applications, including latent fingerprint visualisation. The development of fluorescent nanomaterials for the detection of latent fingerprints requires good contrast with minimal background interference. Pavitra *et al.* reported $\text{Ba}_2\text{LaNbO}_6:0.25\text{Mn}^{4+}$ nanophosphor to visualize all the features such as to individualize the minute fingerprint details such as termination, bifurcation, core, and ridge clearly and to identify partial or damaged fingerprints on various nonporous surfaces.¹⁴² The $\text{Ba}_2\text{LaNbO}_6:0.25\text{Mn}^{4+}$ nanorod-like particles exhibited good adhesion with the fingerprint ridges on all the nonporous surfaces without any background staining and displayed a well-defined pattern, which is clearly visible to the naked eye.¹⁴² Yang *et al.* reported $\text{Mg}_2\text{TiO}_4:\text{Mn}^{4+}$ for the same application.¹²⁹ Fluorescent images of latent fingerprints stained using this phosphor on glass and other substrates are shown in **Fig.1.28**.¹²⁹

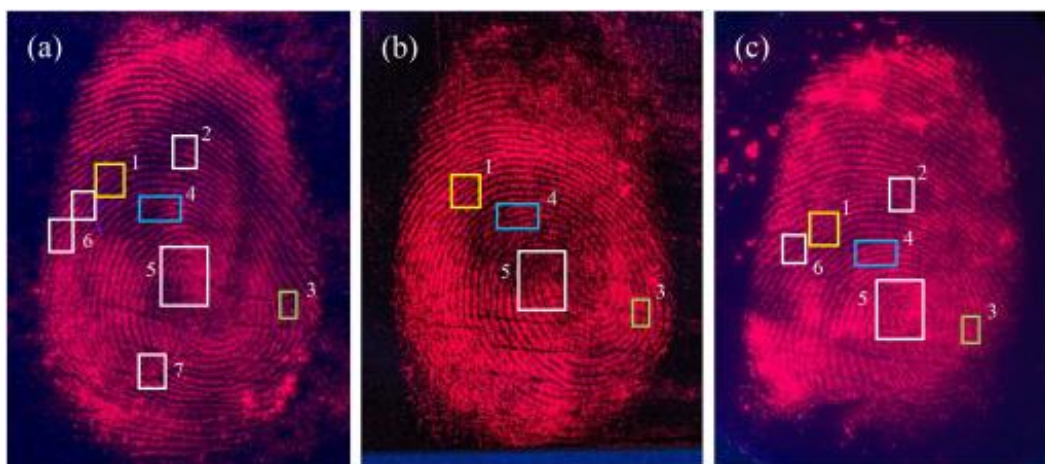


Fig.1.28 Images of latent fingerprints stained with $\text{Mg}_2\text{TiO}_4:\text{Mn}^{4+}$ phosphor on (a) glass, (b) Si wafer, and (c) plastic; regions squared in images, 1: termination; 2: bridge; 3: eyes; 4: island; 5: whorl; 6: bifurcation; 7: hook. Reproduced with permission from ref.¹²⁹

King and co-workers used NIR emitting persistent $\text{Zn}_3\text{Ga}_2\text{Ge}_2\text{O}_{10}:0.5\%\text{Cr}^{3+}$ phosphor activated by sunlight for finger-mark visualization. Since the background patterns and textures make no transmission at higher wavelengths imaging of substrates in the NIR region of the spectra can mute these background patterns and textures.¹⁴³ Most of the $\text{Mn}^{4+}/\text{Cr}^{3+}$ activated germanates are having emissions above 650 nm but in the visible region. So that these deep red-emitting phosphors can take the advantage of its higher wavelength for muting the background and textures. At the same time, it can use its emission in the eye sensitive region for latent fingerprint visualization.

1.2.7.4 Display applications

Apart from lighting applications, deep red-emitting phosphors can be efficiently used for various display applications. Recently Mn^{4+} activated fluoride phosphor K_2NaScF_6 with narrow-band red emission peaking at 630 nm were reported.¹⁴⁴ But phosphor with deep-red emission 650 nm or greater are highly preferred for providing a wide colour gamut in UHD TV according to ITU-R BT.2020-2 recommendations.⁶ Reportedly, $\text{Li}_3\text{RbGe}_8\text{O}_{18}:0.005\text{Mn}^{4+}$ phosphor with emission spectra peaking at 667 nm (**Fig.1.11(b)**) is one of the best examples for display application that can be used for providing a wide colour gamut in UHD TV⁶. Another efficient Mn^{4+} doped phosphor showing application as wide gamut backlight is $\text{Mg}_{14}\text{Ge}_{4.5}\text{Ti}_{0.5}\text{O}_{16}:\text{Mn}^{4+}$.¹⁰¹ Among different Cr^{3+} activated phosphors, $\text{MgAl}_2\text{O}_4:0.05\text{Cr}^{3+}$ finds potential applications in solid-state displays and lasers due to its suitable CCT and CIE value. The CIE coordinates ($x = 0.633$, $y = 0.366$) of this phosphor is very much close to the

standard value given by NSTC (National television standard committee) and its CCT value is 2109 K (Fig.1.29).¹⁴⁵

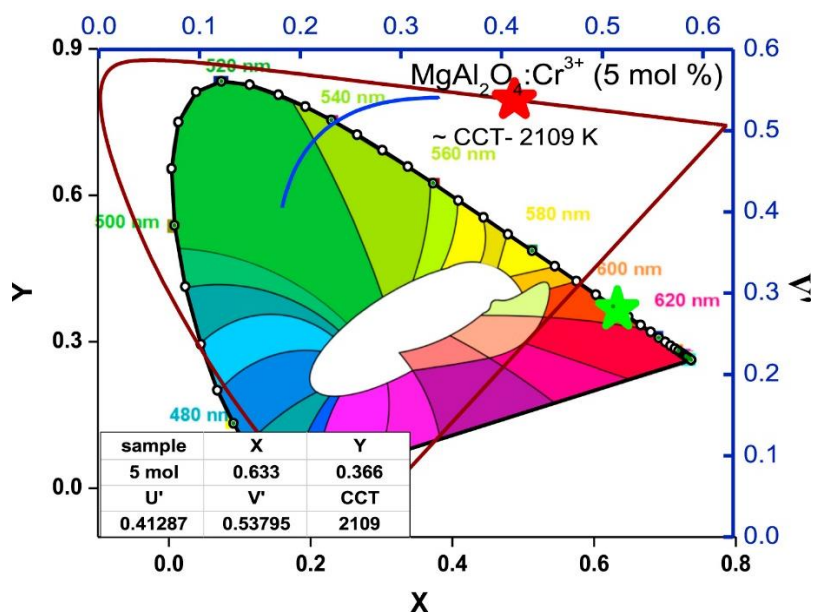


Fig.1.29 CIE and CCT diagram of $\text{MgAl}_2\text{O}_4:0.05\text{Cr}^{3+}$. Reproduced with permission from ref.¹⁴⁵

1.2.7.5 Plant growth applications

Comparing to the traditional horticulture lighting available for plant growth, LEDs possess greater advantages owing to their durability, compact size, and long liveness. Many of the reported germanate phosphors show their promising application in optical agriculture and indoor planting as these deep red-emitting phosphors can convert the unwanted UV light to deep red light. The wavelength of deep red light emitted by germanates matches with the absorption range of chlorophylls responsible for photosynthesis in plants and thus this range of wavelengths helps in the photoperiodic effects in plants. Consequently, germanates are potential candidates for agriculture sunlight spectrum converter and LEDs, which can be used for indoor plant cultivation.^{100, 102, 105} Some of the reported Mn^{4+} -activated germanates for plant growth applications are $\text{Mg}_{3.5}\text{Ge}_{1.25}\text{O}_6: 0.0125 \text{ Bi}^{3+}, 0.01\text{Mn}^{4+}$,¹⁰⁰ $\text{Ba}_2\text{GeO}_4: 0.006\text{Mn}^{4+}$ ¹⁰² $\text{Ba}_2\text{TiGe}_2\text{O}_8: 0.006\text{Mn}^{4+}$,¹⁰³ and $\text{BaAl}_2\text{Ge}_2\text{O}_8: 0.001\text{Mn}^{4+}$.¹⁰⁵ The emission wavelength of these phosphors is matching well with the absorption spectrum of chlorophylls. The PL emission spectrum of $\text{Ba}_2\text{TiGe}_2\text{O}_8: 0.006\text{Mn}^{4+}$ and its potential application in plant growth is illustrated in Fig.1.30. This phosphor has a CIE value of (0.7188, 0.2811) which is in the deep-

red region.¹⁰³ One of the potential Cr^{3+} activated red-emitting phosphors that can be used for plant growth LEDs is $\text{BaMgAl}_{10}\text{O}_{17}: 0.01\text{Cr}^{3+}$.¹⁴⁶

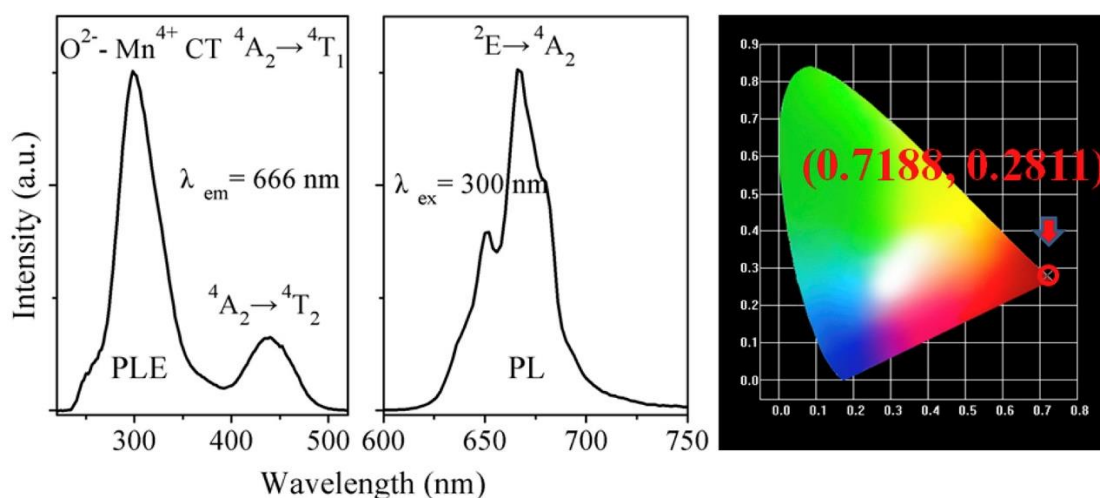


Fig.1.30 The PL emission, excitation spectra and CIE diagram of $\text{Ba}_2\text{TiGe}_2\text{O}_8: 0.006\text{Mn}^{4+}$.

Reproduced with permission from ref.¹⁰³

1.2.7.6 Thermometry applications

Luminescence temperature sensors are grasping more attention during these times owing to their fast response, better spatial resolution, and comparatively low perturbation of sample temperature during measurement.¹⁴⁷ Germanates phosphors can effectively be used for optical thermometry applications. The currently available phosphor-converted optical thermometry has some disadvantages such as narrow temperature range, energy loss in multiple activators due to the energy transfer process and relatively low sensitivity, etc. A single activator doped phosphor with high sensitivity and relatively high-temperature range is required for thermometry application. Reportedly, $\text{Mg}_{14}\text{Ge}_{4.5}\text{Ti}_{0.5}\text{O}_{24}: \text{Mn}^{4+}$ finds potential application in optical thermometry as it shows an abnormal variation in the intensity of Stokes and anti-Stokes lines with temperature.¹⁰¹ The lattice distortion induced by the cation ($\text{Ti}^{4+} \rightarrow \text{Ge}^{4+}$) substitution has a significant effect on temperature-dependent luminescence. Here the emission spectrum of the sample is recorded by varying the temperature from 6.9–303 K and 303–473 K.

It is observed that the emission intensity of Stokes lines increases with the increase in temperature whereas the intensity of anti-Stokes lines decreases with an increase in temperature (**Fig.1.31**). This high-temperature dependence behaviour makes this phosphor a potential

candidate for optical thermometry. To evaluate the performance of this phosphor as a thermometer the absolute sensitivity (S_a) as well as relative sensitivity (S_r) were calculated in the temperature range 6.9 K to 303 K. The maximum S_r value is 2.71% K^{-1} and the maximum S_a value is 0.00152 K^{-1} which are calculated at temperatures 97 K and 215 K, respectively. This maximum S_r value is comparatively greater than that of most of the reported optical thermometry materials. The converse change in Stokes and anti-Stokes peaks, broad temperature range, and higher relative sensitivity make this phosphor suitable for thermometry application.¹⁰¹

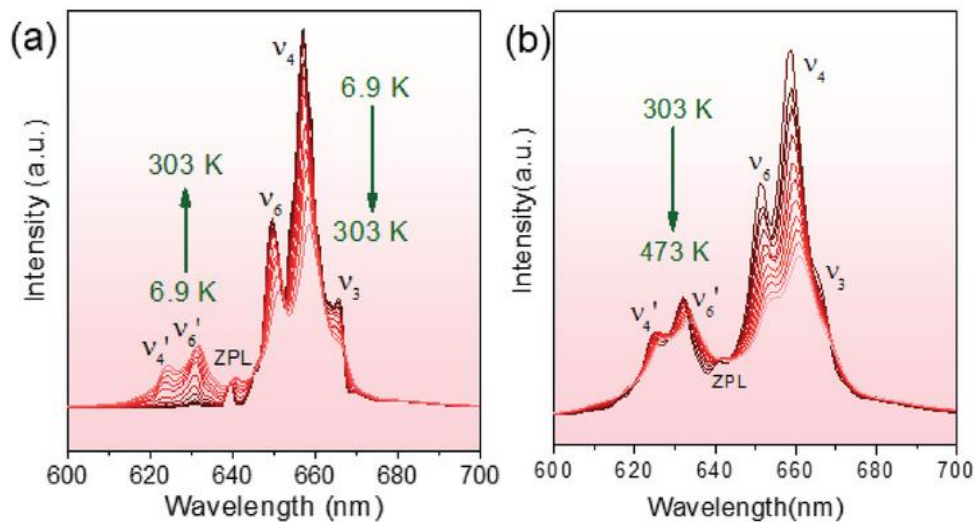


Fig.1.31 PL emission spectrum of $Mg_{14}Ge_{4.5}Ti_{0.5}O_{24}: Mn^{4+}$ by varying temperature from (a) 6.9–303 K and (b) 303–473 K. Reproduced with permission from ref.¹⁰¹

One of the best examples of Cr^{3+} -activated phosphor for the thermometry application is $LaGaO_3: 0.005Cr^{3+}$ phosphor.¹⁴⁸ It can be used as an optical nano-thermometer for sensing temperature below room temperature as well as at above room temperature. Here the temperature-dependent peak intensity, as well as the lifetime changes with the temperature, are used for sensing.¹⁴⁸ Another important phosphor coming under this category is Cr^{3+} -activated $Sr_2MgAl_2O_6: 0.02Cr^{3+}$ phosphor.¹⁴⁹

1.2.7.7 Solar energy applications

Fig.1.32 (a) represents the spectral mismatch between the bandgap of silicon solar cell and incident photon energy coming from sunlight that causes difficulty in converting the solar energy to electricity. The bandgap of the Si cell is appropriate for absorbing deep red and NIR

region, but the incident solar energy contains the UV content. Hence luminescent solar concentrator or a downconverter capable of collecting solar photons and converting them into matching bandgap energy of Si cells is highly required.¹²³ The Solar spectrum showing a potential gain from the downconversion of UV rays for a silicon solar cell is represented in **Fig. 1.32 (a)**. As seen from **Fig.1.32 (b)**, a transparent layer of downconverters is situated on the top of the solar cell. They are used for converting UV photons to a red-rich spectrum.¹⁵⁰ Mn⁴⁺ doped germanates are suitable for down-converting applications. Comparing to fluorides these phosphors are accomplished with emission in the deep-red region (greater than 650 nm) and strong absorption in UV. J. Zhou *et al.* reported that Cr³⁺-activated La₃GaGe₅O₁₆: 0.03Cr³⁺ phosphor in luminescence solar concentrator can significantly enhance the efficiency of Si cell due to its UV absorption as well as deep red and NIR emission.¹²³ The emission peak of this phosphor is centred at 700 nm (**Fig.1.33**).¹²³

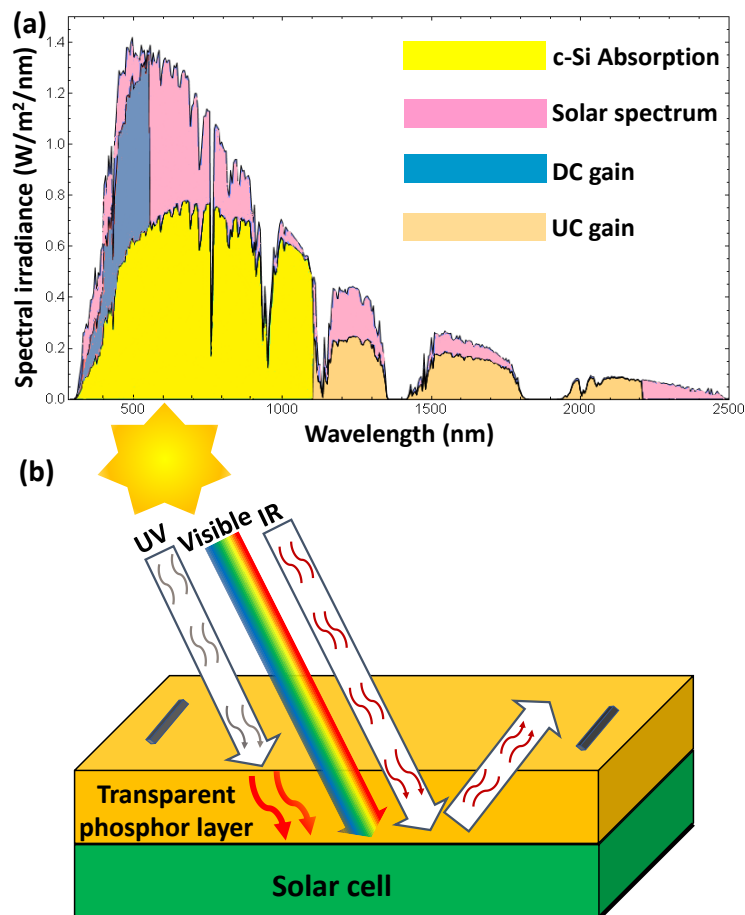


Fig.1.32 Schematic representation of (a) a potential gain for down- and upconversion for a silicon solar cell; (b) solar cell with down converter. Adapted from ref.¹⁵⁰

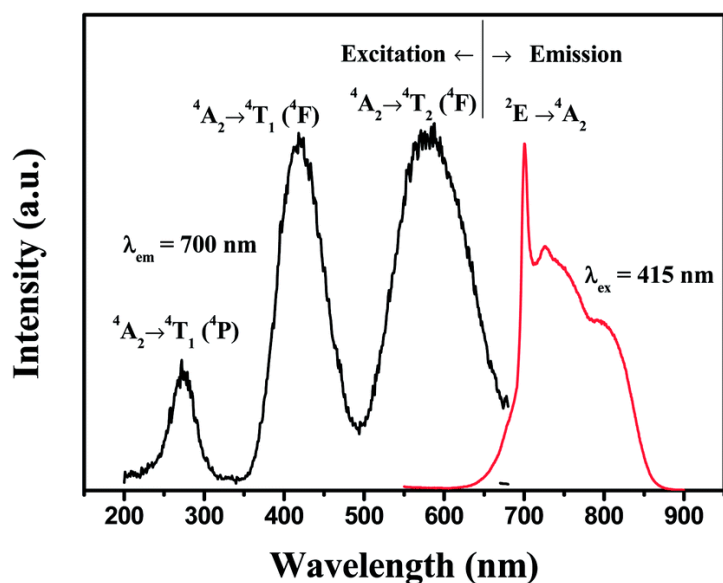


Fig.1.33 Excitation and emission spectrum of $\text{La}_3\text{GaGe}_5\text{O}_{16}: 0.03\text{Cr}^{3+}$ phosphor applicable in luminescence solar concentrator. Reproduced with permission from ref.¹²³

1.3 Self-activated persistent oxide phosphor: mechanism, overview, and applications

The persistent luminescence materials are capable of producing light even after the removal of the source of excitations.¹⁵² There are basically two types of persistent luminescence in the case of inorganic materials. One is due to the activator ion present in the sample (**Fig.1.34 (a)**) and the second one is due to the various kinds of trapping centres in the host materials (**Fig.1.34 (b)**).¹⁵³

The process of fluorescence and phosphorescence in an inorganic material activated by an activator ion can be explained with Jablonski energy level diagram shown in **Fig.1.34 (a)**. The material will be irradiated with suitable source of excitation. The activator ion will be jumped to higher energy states by absorbing the excitation energy. This will be followed by the relaxation of activator ion from the higher energy excited state to lower energy level of excited state. Finally, activator ion will return to its ground state by a radiative transition with lower energy photon emission. The emission from the singlet state S1 will result in phenomenon of fluorescence. But fluorescence phenomenon exhibits a short time duration of decay levels. Meanwhile the emission from the triplet T1 states results in phosphorescence. Since T1 is a metastable state the phosphorescence emission will persist for more time even after the removal of source of excitation as shown in **Fig.1.34 (a)**.^{154, 155}

The second kind of persistence is from the host itself. This kind of material showing persistent luminescence without the help of any activator ion is called the self-activated persistent phosphor. Here the luminescence is assigned to the complex groups and/or defects present in the host material. The self-activated persistent luminescence mechanism is schematically represented in **Fig.1.34 (b)**. Here, the electrons will be trapped in the trapping centres and will delay the fluorescence emission, leading to persistence emission.

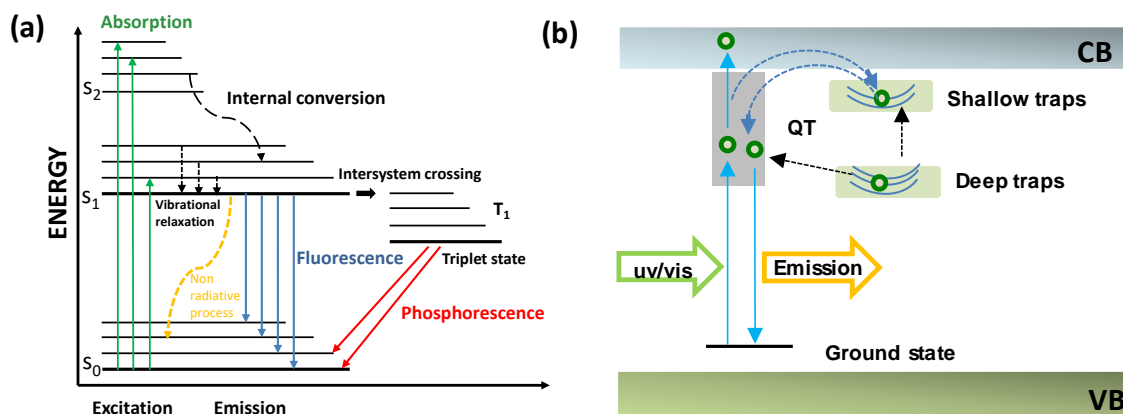


Fig.1.34 (a) Energy level diagram showing fluorescence and phosphorescence in an activator ion based phosphor material.^{154, 155} **(b)** Energy level diagram in a self-activated persistent phosphor showing persistent emission.¹⁵³

Recently, PersL phosphors have played a great roles in various fields, including security, safety signage, drug delivery, *in vivo* imaging, energy saving, 3D printing, etc.¹⁵⁶

Fig.1.35 (a) shows the increase in the no of reports of persistent phosphors, and the reports are found to be higher after 2000. **Fig.1.35 (b)** represents the various applications of persistent phosphors and it is classified into three categories such as established, in progress and challenging. Applications such as road making, AC LEDs, bioimaging, etc. are not well explored. Some of the applications, such as solar and photocatalysis, are still challenging in this field.¹⁵⁶

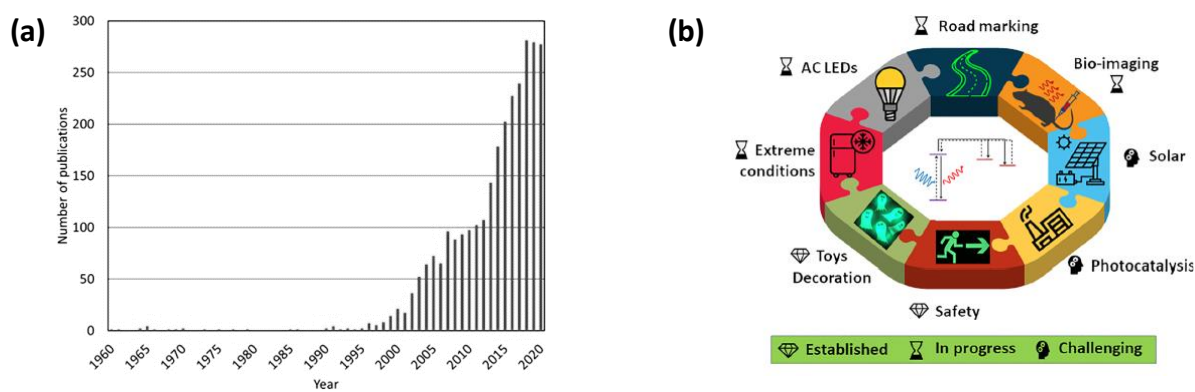


Fig.1.35 (a) Graph showing the no. of publication in persistent phosphors from 1960 to 2020. (b) Schematic diagram of applications of persistent phosphors.¹⁵⁶

The presently available PerSL phosphors are $\text{SrAl}_2\text{O}_4: \text{Eu}^{2+}, \text{Dy}^{3+}$ (green), $\text{CaAl}_2\text{O}_4: \text{Eu}^{2+}, \text{Nd}^{3+}$ (blue), and $\text{Y}_2\text{O}_2\text{S}: \text{Eu}^{3+}, \text{Ti}^{3+}, \text{Mg}^{2+}$ (red). However, these PersL materials have some drawbacks, such as low moisture resistance of aluminates and poor stability of sulphides.¹⁵⁷ Moreover, the above phosphors used rare earth ions. Recently, W. Yuan *et al.* reported a new cyan emitting persistent $\text{BaLu}_2\text{Al}_2\text{Ga}_2\text{SiO}_{12}: \text{Ce}^{3+}, \text{Bi}^{3+}$ phosphors for AC-LEDs via defect modulation.¹⁵⁸ Won Bin Im and co-workers reported non- Eu^{2+} based $\text{Na}_3\text{ScSi}_3\text{O}_9: \text{Ce}^{3+}, \text{Dy}^{3+}$ blue persistent phosphors.¹⁵⁹ Erin Finley *et al.* reported $(\text{Sr}_{1-\delta}\text{Ba}_\delta)_2\text{MgSi}_2\text{O}_7: \text{Eu}^{2+}, \text{Dy}^{3+}$ sample through solid solution method for use in Point-of-Care Diagnostics method.¹⁶⁰ Even though the above phosphors are non- Eu^{2+} based, the above phosphors couldn't avoid the usage of rare earth ions.

The self-activated oxide persistent phosphors can effectively replace the rare earth based persistence phosphors. The self-activated persistent oxide phosphors have other advantages also, including activator-free, high thermal and chemical stability, non-toxic and cost-effective, etc. Among the different self-activated persistent phosphors Zirconate based phosphors are not explored well and the number of reports are found to be less.

Here, in zirconates, the electron can be excited from oxygen to empty 4d orbits of Zr^{4+} ions which luminescence is mostly attributed to the charge transfer transition luminescence.¹⁶¹ However, of Zirconate based phosphor materials aren't utilized effectively. LI Xiaochen *et al.*

reported a novel undoped SrZrSi₂O₇ phosphor with persistent emission. However, the persistent emission is only observed for the sample synthesized under reduced atmosphere.¹⁶²

Lattice defects, such as cation or anion vacancies, have always been present in materials. These vacancies have the ability to produce local potentials, resulting in the trapping of electrons or holes. Altering the atmospheric conditions, introducing inequivalent substitutions, or adding flux like NH₄Cl during the material preparation can modify the production of vacancies. For example, oxide-based phosphor materials can easily generate oxygen vacancies that trap electrons in a low oxygen atmosphere.¹⁶³

1.4 Summary, future and perspective

In this introduction chapter, we have reviewed the spectroscopic properties of the Mn⁴⁺/Cr³⁺ activated deep red/NIR emitting oxide phosphors, in particular germanates. According to our literature review, Mn⁴⁺ activated germanates can be classified into three categories: alkali metal-based germanates, alkaline-earth metal-based germanates, and lanthanum-based germanates. Further, a study on the crystal structure-dependent luminescence behaviour of these Mn⁴⁺/Cr³⁺ deep red/NIR emitting phosphors is also discussed. From the detailed analysis of the crystal structures, it is concluded that for the efficient optical properties, Mn⁴⁺ ions should possess a well isolated octahedral geometry. The Cr³⁺ activated phosphors are capable of giving long persistent character and emission in NIR region. However, it is difficult for Mn⁴⁺ activated phosphors to produce the same. The majority of the phosphors discussed here have comparatively low quantum efficiency. Moreover, a detailed description of various other methods that can be used for enhancing the red/NIR emission as well as the thermal stability of red-emitting phosphor is discussed. We have presented the possible and potential application of these phosphors in the last part of the review. Most of the reports discussed here focus on the W-LED application. The next generation of oxide phosphors will be Cr³⁺ and Mn⁴⁺ activated deep red to NIR emitting phosphors. So that in addition to W-LEDs, the applications can be extended to wide areas including medical diagnosis, *in-vivo* imaging, night vision surveillance, security, etc.

Nowadays self-activated oxide phosphors are also seeking much attention due to its persistent emission, economic preparation, thermal and chemical stability, activator free synthesis etc. The cyan emitting persistent phosphors, especially zirconates, has not been much

explored to date. Hence the mechanism, overview and applications of the self-activated persistent phosphor are also elaborated in the final part of this introduction chapter.

Acknowledgement: We would like to thank all the publishers for granting permission to reproduce the images in this chapter.

1.5 Objectives of the thesis

- Designing Mn^{4+} activated deep red emitting phosphor (> 650 nm) and improving emission intensity and red fabrications.
- Combining optimum red phosphor with yellow emitting YAG: Ce^{3+} and blue InGaN chip for the WLED fabrications.
- Developing Cr^{3+} activated deep red to NIR emitting phosphor and improving emission under visible light excitations.
- Utilization of structurally modified different Cr^{3+} activated phosphors for in vitro bioimaging, display, plant growth and NIR LEDs.
- Developing self-activated cyan emitting persistent phosphor and improving persistent time and intensity.
- Usage of developed persistent phosphors for anti-counterfeiting and plant growth applications.

Taking into account the challenges and focusing on the objectives, the current thesis provided three working chapters, which are organized as follows,

Non-rare earth-based new class of inorganic phosphors for lighting, medical imaging and security applications

Chapter 2

Enriching the deep-red emission in $(\text{Mg}, \text{Ba})_3\text{M}_2\text{GeO}_8 : \text{Mn}^{4+}$ ($\text{M} = \text{Al}, \text{Ga}$) compositions for light-emitting diodes.

Chapter 3

Compositionally engineered $(\text{Mg}, \text{Sr})_3(\text{Al}, \text{Ga})_2\text{GeO}_8 : \text{Cr}^{3+}$ phosphors with tuned emission from ultra-sharp red to ultra-broad NIR for LEDs and in vitro cell imaging applications.

Chapter 4

Inducing defects to boost the persistent luminescence in novel cyan emitting rare-earth free strontium zirconium silicate for dynamic anti-counterfeiting and plant growth LED applications

1.6 References

- [1] Yang, Z.; Wei, Q.; Rong, M.; Yang, Z.; Wang, Z.; Zhou, Q.; Wang, Q. Novel red-emitting phosphors $A_2HfF_6:Mn^{4+}$ ($A = Rb^+, Cs^+$) for solid-state lighting. *Dalt. Trans.* **2017**, 46, 9451–9456. <https://doi.org/10.1039/c7dt01842h>.
- [2] Du, P.; Huang, X.; Yu, J.S. Facile synthesis of bifunctional Eu^{3+} -activated $NaBiF_4$ red-emitting nanoparticles for simultaneous white light-emitting diodes and field emission displays. *Chem. Eng. J.* **2018**, 337, 91–100. <https://doi.org/10.1016/j.cej.2017.12.063>.
- [3] Wang, X.; Liu, Q.; Bu, Y.; Liu, C.S.; Liu, T.; Yan, X. Optical temperature sensing of rare-earth ion doped phosphors. *RSC Adv.* **2015**, 5, 86219–86236. <https://doi.org/10.1039/c5ra16986k>.
- [4] Min, X.; Huang, Z.; Fang, M.; Liu, Y.G; Tang, C.; Wu, X. Energy transfer from Sm^{3+} to Eu^{3+} in red-emitting phosphor $LaMgAl_{11}O_{19}:Sm^{3+},Eu^{3+}$ for solar cells and near-ultraviolet white light-emitting diodes. *Inorg. Chem.* **2014**, 53, 6060–6065. <https://doi.org/10.1021/ic500412r>.
- [5] Liang, J.; Sun, L.; Devakumar, B.; Wang, S.; Sun, Q.; Guo, H.; Li, B.; Huang, X. Novel Mn^{4+} -activated $LiLaMgWO_6$ far-red emitting phosphors: High photoluminescence efficiency, good thermal stability, and potential applications in plant cultivation LEDs. *RSC Adv.* **2018**, 8, 27144–27151. <https://doi.org/10.1039/c8ra05669b>.
- [6] Singh, S.P.; Kim, M.; Park, W. B.; Lee, J.W.; Sohn, K.S. Discovery of a Red-Emitting $Li_3RbGe_8O_{18}:Mn^{4+}$ Phosphor in the Alkali-Germanate System: Structural Determination and Electronic Calculations. *Inorg. Chem.* **2016**, 55, 10310–10319. <https://doi.org/10.1021/acs.inorgchem.6b01576>.
- [7] Li, Y.; Qi, S.; Li, P.; Wang, Z. Research progress of Mn doped phosphors. *RSC Adv.* **2017**, 7, 38318–38334. <https://doi.org/10.1039/c7ra06026b>.
- [8] Piao, X.; Machida, K.I.; Horikawa, T.; Hanzawa, H.; Shimomura, Y.; Kijima, N. Preparation of $CaAlSiN_3:Eu^{2+}$ phosphors by the self-propagating high-temperature synthesis and their luminescent properties. *Chem. Mater.* **2007**, 19, 4592–4599. <https://doi.org/10.1021/cm070623c>.
- [9] Xie, R.J.; Hirosaki, N.; Suehiro, T.; Xu, F.F.; Mitomo, M. A simple, efficient synthetic route to $Sr_2Si_5N_8:Eu^{2+}$ -based red phosphors for white light-emitting diodes. *Chem. Mater.* **2006**, 18, 5578–5583. <https://doi.org/10.1021/cm061010n>.
- [10] Shisina, S.; Das, S.; Som, S.; Ahmad, S.; Vinduja, V.; Structure and optoelectronic properties of palmierite structured $Ba_2Y_{0.67}\delta_{0.33}V_2O_8:Eu^{3+}$ red phosphors for n-UV and blue diode based warm white light systems. *J. Alloys Compd.* **2019**, 802, 723–732

- <https://doi.org/10.1016/j.jallcom.2019.05.355>.
- [11] Hu, J.; Huang, T.; Zhang, Y.; Lu, B.; Ye, H.; Chen, B.; Xia, H.; Ji, C. Enhanced deep-red emission from $\text{Mn}^{4+}/\text{Mg}^{2+}$ co-doped CaGdAlO_4 phosphors for plant cultivation. *Dalt. Trans.* **2019**, 48, 2455–2466. <https://doi.org/10.1039/c8dt04955f>.
- [12] Song, E.; Wang, J.; Shi, J.; Deng, T.; Ye, S.; Peng, M.; Wang, J.; Wondraczek, L.; Zhang, Q.; Highly Efficient and Thermally Stable $\text{K}_3\text{AlF}_6:\text{Mn}^{4+}$ as a Red Phosphor for Ultra-High-Performance Warm White Light-Emitting Diodes. *ACS Appl. Mater. Interfaces.* **2017**, 9, 8805–8812. <https://doi.org/10.1021/acsami.7b00749>.
- [13] Zhang, Z.; Ma, C.; Gautier, R.; Molocheev, M.S.; Liu, Q.; Xia, Z. Structural Confinement toward Giant Enhancement of Red Emission in Mn^{2+} -Based Phosphors. *Adv. Funct. Mater.* **2018**, 28, 2–8. <https://doi.org/10.1002/adfm.201804150>.
- [14] Chi, N.T.K.; Quang, N. V.; Tuan, N.T.; Trung, D.Q.; Huy, P.T.; Tam, P.D.; Nguyen D.H. Deep Red Emitting $\text{MgAl}_2\text{O}_4:\text{Cr}^{3+}$ Phosphor for Solid State Lighting. *J. Electron. Mater.* **2019**, 48, 5891–5899. <https://doi.org/10.1007/s11664-019-07358-5>.
- [15] Cao, R.; Cao, Y.; Fu, T.; Jiang, S.; Li, W.; Luo, Z.; Fu, J. Synthesis and luminescence properties of novel red-emitting $\text{R}_3\text{P}_4\text{O}_{13}:\text{Bi}^{2+}$ (R=Sr and Ba) phosphors. *J. Alloys Compd.* **2016**, 661, 77–81. <https://doi.org/10.1016/j.jallcom.2015.11.176>.
- [16] Cao, R.; Lv, X.; Ran, Y.; Xu, L.; Chen, T.; Guo, S.; Ao, H.; Yu, X. Rare-earth-free $\text{Li}_5\text{La}_3\text{Ta}_2\text{O}_{12}:\text{Mn}^{4+}$ deep-red-emitting phosphor: Synthesis and photoluminescence properties. *J. Am. Ceram. Soc.* **2019**, 102, 5910–5918. <https://doi.org/10.1111/jace.16447>.
- [17] Chen, D.; Zhou, Y.; Zhong, J. A review on Mn^{4+} activators in solids for warm white light-emitting diodes. *RSC Adv.* **2016**, 6, 86285–96. <https://doi.org/10.1039/c6ra19584a>.
- [18] Zhong, Y.; Gai, S.; Xia, M.; Gu, S.; Zhang, Y.; Wu, X.; Wang, J.; Zhou, N.; Zhou, Z. Enhancing quantum efficiency and tuning photoluminescence properties in far-red-emitting phosphor $\text{Ca}_{14}\text{Ga}_{10}\text{Zn}_6\text{O}_{35}:\text{Mn}^{4+}$ based on chemical unit engineering. *Chem. Eng. J.* **2019**, 374, 381–391. <https://doi.org/10.1016/j.cej.2019.05.201>.
- [19] Zhang, M.; Jia, M.; Sheng, T.; Fu, Z. Multifunctional optical thermometry based on the transition metal ions doped down-conversion $\text{Gd}_2\text{ZnTiO}_6:\text{Bi}^{3+}, \text{Mn}^{4+}$ phosphors, *J. Lumin.* **2021**, 229, 117653–117658. <https://doi.org/10.1016/j.jlumin.2020.117653>.
- [20] Liang, J.; Devakumar, B.; Sun, L.; Wang, S.; Sun, Q.; Guo, H.; Huang, X. Deep-red-emitting $\text{Ca}_2\text{LuSbO}_6:\text{Mn}^{4+}$ phosphors for plant growth LEDs: Synthesis, crystal structure, and photoluminescence properties. *J. Alloys Compd.* **2019**, 804, 521–526. <https://doi.org/10.1016/j.jallcom.2019.06.312>.

- [21] Fu, A.; Zhou, L.; Wang, S.; Li, Y. Preparation, structural and optical characteristics of a deep red-emitting $\text{Mg}_2\text{Al}_4\text{Si}_5\text{O}_{18}:\text{Mn}^{4+}$ phosphor for warm w-LEDs. *Dye. Pigment.* **2018**, 148, 9–15. <https://doi.org/10.1016/j.dyepig.2017.08.050>.
- [22] Cao, R.; Liu, X.; Bai, K.; Chen, T.; Guo, S.; Hu, Z.; Xiao, F.; Luo, Z. Photoluminescence properties of red-emitting $\text{Li}_2\text{ZnSn}_2\text{O}_6:\text{Mn}^{4+}$ phosphor for solid-state lighting. *J. Lumin.* **2018**, 197, 169–174. <https://doi.org/10.1016/j.jlumin.2018.01.023>.
- [23] Cao, R.; Shi, Z.; Quan, G.; Chen, T.; Guo, S.; Hu, Z.; Liu, P.; Preparation and luminescence properties of $\text{Li}_2\text{MgZrO}_4:\text{Mn}^{4+}$ red phosphor for plant growth. *J. Lumin.* **2017**, 188, 577–581. <https://doi.org/10.1016/j.jlumin.2017.05.002>.
- [24] Cao, R.; Chen, T.; Ren, Y.; Chen, T.; Ao, H.; Li, W.; Zheng, G. Synthesis and photoluminescence properties of $\text{Ca}_2\text{LaTaO}_6:\text{Mn}^{4+}$ phosphor for plant growth LEDs. *J. Alloys Compd.* **2019**, 780, 749–755. <https://doi.org/10.1016/j.jallcom.2018.12.027>.
- [25] Li, K.; Lian, H.; Van Deun, R.; Brik, M.G. A far-red-emitting $\text{NaMgLaTeO}_6:\text{Mn}^{4+}$ phosphor with perovskite structure for indoor plant growth. *Dye. Pigment.* **2019**, 162, 214–221. <https://doi.org/10.1016/j.dyepig.2018.09.084>.
- [26] Cao, R.; Ouyang, X.; Jiao, Y.; Wang, X.; Hu, Q.; Chen, T.; Liao, C.; Li, Y. Deep-red-emitting $\text{SrLa}_2\text{Sc}_2\text{O}_7:\text{Mn}^{4+}$ phosphor: Synthesis and photoluminescence properties. *J. Alloys Compd.* **2019**, 795, 134–140. <https://doi.org/10.1016/j.jallcom.2019.04.220>.
- [27] Cao, R.; Jiao, Y.; Wang, X.; Ouyang, X.; Wan, H.; Chen, T.; Zheng, G.; Xie, S. Far-red emitting $\text{Mg}_2\text{La}_3\text{NbO}_9:\text{Mn}^{4+}$ powder phosphor: Synthesis and luminescence properties. *Adv. Powder Technol.* **2020**, 31, 4045–4052. <https://doi.org/10.1016/j.apt.2020.08.009>.
- [28] Cao, R.; Zhang, W.; Chen, T.; Zheng, T.; Ao, H.; Luo, Z.; Xie, S.; Wan, H. Perovskite tungstate $\text{Ba}_2\text{La}_2\text{ZnW}_2\text{O}_{12}:\text{Mn}^{4+}$ phosphor: Synthesis, energy transfer and tunable emission. *Mater. Res. Bull.* **2021**, 137, 111200–111206. <https://doi.org/10.1016/j.materresbull.2020.111200>.
- [29] Adachi, S. Review— Mn^{4+} vs Cr^{3+} : A Comparative Study as Activator Ions in Red and Deep Red-Emitting Phosphors. *ECS J. Solid State Sci. Technol.* **2020**, 9, 026003-026014. <https://doi.org/10.1149/2162-8777/ab6ea6>.
- [30] Adachi, S. Crystal-field and Racah parameters of Mn^{4+} ion in red and deep red-emitting phosphors: Fluoride versus oxide phosphor. *J. Lumin.* **2020**, 218, 116829-116827. <https://doi.org/10.1016/j.jlumin.2019.116829>.
- [31] Adachi, S. Review—Photoluminescence Properties of Cr^{3+} -Activated Oxide Phosphors. *ECS J. Solid State Sci. Technol.* **2021**, 10, 026001-026021. <https://doi.org/10.1149/2162-8777/abdc01>.

- [32] Adachi, S. Review—Photoluminescence Properties of Cr³⁺-Activated Fluoride Phosphors. *ECS J. Solid State Sci. Technol.* **2021**, 10, 036001-036020. <https://doi.org/10.1149/2162-8777/abdfb7>.
- [33] Shi, J.; Sun, X.; Zheng, S.; Song, L.; Zhang, F.; Madl, T.; Zhang, Y.; Zhang, H.; Hong, H. Tin-Doped Near-Infrared Persistent Luminescence Nanoparticles with Considerable Improvement of Biological Window Activation for Deep Tumor Photodynamic Therapy. *ACS Appl. Bio Mater.* **2020**, 3, 5995–6004. <https://doi.org/10.1021/acsabm.0c00644>.
- [34] Shi, J.; Sun, X.; Li, H.; Man, H.; Shen, J.; Yu, Y.; Zhang, H.; Multifunctional near infrared-emitting long-persistence luminescent nanoprobe for drug delivery and targeted tumor imaging. *Biomaterials.* **2015**, 37, 260–270. <https://doi.org/10.1016/j.biomaterials.2014.10.033>.
- [35] Pan, Z.; Lu, Y. Y.; Liu, F.; Sunlight-activated long-persistent luminescence in the near-infrared from Cr³⁺-doped zinc gallogermanates. *Nat. Mater.* **2012**, 11, 58–63. <https://doi.org/10.1038/nmat3173>.
- [36] Pratapkumar, C.; Prashantha, S. C.; Nagabhushana, H.; Jnaneshwara, D. M. Photoluminescence and photometric studies of low temperature prepared red emitting MgAl₂O₄:Cr³⁺ nanophosphors for solid state displays. *J. Sci. Adv. Mater. Devices.* **2018**, 3, 464–470. <https://doi.org/10.1016/j.jsamd.2018.09.002>.
- [37] Yu, D.; Zhou, Y.; Ma, C.; Melman, J. H.; Baroudi, K. M.; LaCapra, M.; Riman, R. E. Non-Rare-Earth Na₃AlF₆:Cr³⁺ Phosphors for Far-Red Light-Emitting Diodes. *ACS Appl. Electron. Mater.* **2019**, 1, 2325–2333. <https://doi.org/10.1021/acsaelm.9b00527>.
- [38] Bai, Q.; Wang, Z.; Li, P.; Li, T.; Xu, S.; Yang, Z.; Luminescence properties of novel deep-red-emitting Ca₃Al₂Ge₂O₁₀:Cr³⁺ phosphors. *Luminescence.* **2016**, 31, 1277–1282. <https://doi.org/10.1002/bio.3103>.
- [39] Senden, T.; Geitenbeek, R. G.; Meijerink, A. Co-precipitation synthesis and optical properties of Mn⁴⁺-doped hexafluoroaluminate w-LED phosphors. *Materials (Basel).* **2017**, 10, 1322-1335. <https://doi.org/10.3390/ma10111322>.
- [40] Jin, Y.; Fang, M. H.; Grinberg, M.; Mahlik, S.; Lesniewski, T.; Brik, M. G.; Luo, G.; Lin, J. G.; Liu, R. S. Narrow Red Emission Band Fluoride Phosphor KNaSiF₆:Mn⁴⁺ for Warm White Light-Emitting Diodes. *ACS Appl. Mater. Interfaces.* **2016**, 8, 11194–11203. <https://doi.org/10.1021/acsami.6b01905>.
- [41] Lin, C. C.; Meijerink, A.; Liu, R. S. Critical Red Components for Next-Generation White LEDs. *J. Phys. Chem. Lett.* **2016**, 7, 495–503.

- <https://doi.org/10.1021/acs.jpcclett.5b02433>.
- [42] Wang, Z.; Wang, N.; Yang, Z.; Yang, Z.; Wei, Q.; Zhou, Q.; Liang, H. Luminescent properties of novel red-emitting phosphor Na_3TaF_8 with non-equivalent doping of Mn^{4+} for LED backlighting. *J. Lumin.* **2017**, *192*, 690–694. <https://doi.org/10.1016/j.jlumin.2017.07.064>.
- [43] Huang, L.; Liu, Y.; Yu, J.; Zhu, Y.; Pan, F.; Xuan, T.; Brik, M.G.; Wang, C.; Wang, J. Highly Stable $\text{K}_2\text{SiF}_6:\text{Mn}^{4+}@\text{K}_2\text{SiF}_6$ Composite Phosphor with Narrow Red Emission for White LEDs. *ACS Appl. Mater. Interfaces.* **2018**, *10*, 18082–18092. <https://doi.org/10.1021/acsami.8b03893>.
- [44] Huang, D.; Zhu, H.; Deng, Z.; Zou, Q.; Lu, H.; Yi, X.; Guo, W.; Lu, C.; Chen, X. Moisture-Resistant Mn^{4+} -Doped Core–Shell-Structured Fluoride Red Phosphor Exhibiting High Luminous Efficacy for Warm White Light-Emitting Diodes. *Angew. Chemie.* **2019**, *131*, 3883–3887. <https://doi.org/10.1002/ange.201813363>.
- [45] Li, P.; Wondraczek, L.; Peng, M.; Zhang, Q.; Setlur, A. Tuning Mn^{4+} Red Photoluminescence in $(\text{K,Rb})_2\text{Ge}_4\text{O}_9:\text{Mn}^{4+}$ Solid Solutions by Partial Alkali Substitution. *J. Am. Ceram. Soc.* **2016**, *99*, 3376–3381. <https://doi.org/10.1111/jace.14363>.
- [46] Xia, Z.; Molokeev, M.S.; Oreshonkov, A.S.; Atuchin, V.; Liu, R.S.; Dong, C. Crystal and local structure refinement in $\text{Ca}_2\text{Al}_3\text{O}_6\text{F}$ explored by X-ray diffraction and Raman spectroscopy. *Phys. Chem. Chem. Phys.* **2014**, *16*, 5952–5957. <https://doi.org/10.1039/c3cp53816h>.
- [47] Shannon, R.D. Revised Effective Ionic Radii and Systematic Studies of Interatomic Distances in Halides and Chalcogenides BY, *Acta Crystallogr. Sect. A.* **1976**, *32*, 751–766. <https://doi.org/10.1023/A:1018927109487>.
- [48] Ranjith, P.; Sreevalsa, S.; Tyagi, J.; Jayanthi, K.; Jagannath, G.; Patra, P.; Ahmad, S.; Annapurna, K.; Allu, A.R.; Das, S.; Elucidating the structure and optimising the photoluminescence properties of $\text{Sr}_2\text{Al}_3\text{O}_6\text{F}:\text{Eu}^{3+}$ oxyfluorides for cool white-LEDs. *J. Alloys Compd.* **2020**, *826*, 154015–154025. <https://doi.org/10.1016/j.jallcom.2020.154015>.
- [49] Bandi, V.R.; Grandhe, B.K.; Woo, H.J.; Jang, K.; Shin, D.S.; Yi, S.S.; Jeong, J.H. Luminescence and energy transfer of Eu^{3+} or/and Dy^{3+} co-doped in $\text{Sr}_3\text{AlO}_4\text{F}$ phosphors with NUV excitation for WLEDs. *J. Alloys Compd.* **2012**, *538*, 85–90. <https://doi.org/10.1016/j.jallcom.2012.05.057>.
- [50] Shang, M.; Li, G.; Kang, X.; Yang, D.; Geng, D.; Lin, J. Tunable luminescence and

- energy transfer properties of $\text{Sr}_3\text{AlO}_4\text{F}:\text{RE}^{3+}$ (RE=Tm/Tb, Eu, Ce) phosphors. *ACS Appl. Mater. Interfaces*. **2011**, 3, 2738–2746. <https://doi.org/10.1021/am200534u>.
- [51] Chen, W. Effect of composition on the luminescence of Ce^{3+} activated $\text{Sr}_3\text{AlO}_4\text{F}$ phosphor for light-emitting diode. *J. Alloys Compd.* **2013**, 550, 320–325. <https://doi.org/10.1016/j.jallcom.2012.10.159>.
- [52] Dong, X.; Pan, Y.; Li, D.; Lian, H.; Lin, J. A novel red phosphor of Mn^{4+} ion-doped oxyfluoroniobate BaNbOF_5 for warm WLED applications. *CrystEngComm*. **2018**, 20, 5641–5646. <https://doi.org/10.1039/c8ce01304g>.
- [53] Ming, H.; Zhang, J.; Liu, L.; Peng, J.; Du, F.; Ye, X.; Yang, Y.; Nie, H. A novel $\text{Cs}_2\text{NbOF}_5:\text{Mn}^{4+}$ oxyfluoride red phosphor for light-emitting diode devices. *Dalt. Trans.* **2018**, 47, 16048–16056. <https://doi.org/10.1039/c8dt02817f>.
- [54] Hu, T.; Lin, H.; Cheng, Y.; Huang, Q.; Xu, J.; Gao, Y.; Wang, J.; Wang, Y. A highly-distorted octahedron with a: C 2v group symmetry inducing an ultra-intense zero phonon line in Mn^{4+} -activated oxyfluoride $\text{Na}_2\text{WO}_2\text{F}_4$. *J. Mater. Chem. C*. **2017**, 5, 10524–10532. <https://doi.org/10.1039/c7tc03655h>.
- [55] Wang, Z.; Yang, Z.; Yang, Q.; Wei, Q.; Zhou, L.; Wang, X.; Red Phosphor $\text{Rb}_2\text{NbOF}_5:\text{Mn}^{4+}$ for Warm White Light-Emitting Diodes with a High Color-Rendering Index. *Inorg. Chem.* **2019**, 58, 456–461. <https://doi.org/10.1021/acs.inorgchem.8b02676>.
- [56] Cai, P.; Qin, L.; Chen, C.; Wang, J.; Seo, H.J.; Luminescence, energy transfer and optical thermometry of a novel narrow red emitting phosphor: $\text{Cs}_2\text{WO}_2\text{F}_4:\text{Mn}^{4+}$. *Dalt. Trans.* **2017**, 46, 14331–14340. <https://doi.org/10.1039/c7dt02751f>.
- [57] Adachi, S. Photoluminescence properties of Mn^{4+} -activated oxide phosphors for use in white-LED applications: A review. *J. Lumin.* **2018**, 202, 263–281. <https://doi.org/10.1016/j.jlumin.2018.05.053>.
- [58] Chen, L.; Xue, S.; Chen, X.; Bahader, A.; Deng, X.; Zhao, E.; Jiang, Y.; Chen, S.; Chan, T.S.; Zhao, Z.; Zhang, W.; The site occupation and valence of Mn ions in the crystal lattice of $\text{Sr}_4\text{Al}_{14}\text{O}_{25}$ and its deep red emission for high color-rendering white light-emitting diodes. *Mater. Res. Bull.* **2014**, 60, 604–611. <https://doi.org/10.1016/j.materresbull.2014.08.055>.
- [59] Brik, M.G.; Camardello, S.J.; Srivastava, A.M.; Influence of Covalency on the $\text{Mn}^{4+} {}^2\text{E}_g \rightarrow {}^4\text{A}_{2g}$ Emission Energy in Crystals. *ECS J. Solid State Sci. Technol.* **2015**, 4, R39–R43. <https://doi.org/10.1149/2.0031503jss>.
- [60] Brik, M.G.; Srivastava, A.M. On the optical properties of the Mn^{4+} ion in solids, *J.*

- Lumin.* **2013**, 133, 69–72. <https://doi.org/10.1016/j.jlumin.2011.08.047>.
- [61] Zhou, Q.; Dolgov, L.; Srivastava, A.M.; Zhou, L.; Wang, Z.; Shi, J.; Dramićanin, M.D.; Brik, M.G.; Wu, M. Mn²⁺ and Mn⁴⁺ red phosphors: Synthesis, luminescence and applications in WLEDs. A review, *J. Mater. Chem. C.* **2018**, 6, 2652–2671. <https://doi.org/10.1039/c8tc00251g>.
- [62] Brik, M.G.; Srivastava, A.M. Critical Review—A Review of the Electronic Structure and Optical Properties of Ions with d³ Electron Configuration (V²⁺, Cr³⁺, Mn⁴⁺, Fe⁵⁺) and Main Related Misconceptions. *ECS J. Solid State Sci. Technol.* **2018**, 7, R3079–R3085. <https://doi.org/10.1149/2.0041801jss>.
- [63] Ogasawara, K.; Alluqmani, F.; Nagoshi, H. Multiplet Energy Level Diagrams for Cr³⁺ and Mn⁴⁺ in Oxides with O_h Site Symmetry Based on First-Principles Calculations. *ECS J. Solid State Sci. Technol.* **2016**, 5, R3191–R3196. <https://doi.org/10.1149/2.0231601jss>.
- [64] Li, K.; Lian, H.; Van Deun, R. Site occupancy and photoluminescence properties of a novel deep-red-emitting phosphor NaMgGdTeO₆:Mn⁴⁺ with perovskite structure for w-LEDs. *J. Lumin.* **2018**, 198, 155–162. <https://doi.org/10.1016/j.jlumin.2018.02.035>.
- [65] Zhuang, Y.; Ueda, J.; Tanabe, S. Tunable trap depth in Zn(Ga_{1-x}Al_x)₂O₄:Cr, Bi red persistent phosphors: Considerations of high-temperature persistent luminescence and photostimulated persistent luminescence. *J. Mater. Chem. C.* **2013**, 1, 7849–7855. <https://doi.org/10.1039/c3tc31462f>.
- [66] Li, K.; Zhu, D.; Van Deun, R. Photoluminescence properties and crystal field analysis of a novel red-emitting phosphor K₂BaGe₈O₁₈:Mn⁴⁺. *Dye. Pigment.* **2017**, 142, 69–76. <https://doi.org/10.1016/j.dyepig.2017.03.007>.
- [67] Brik, M.G.; Ogasawara, K. Microscopic analysis of the crystal field strength and lowest charge transfer energies in the elpasolite crystals Cs₂NaYX₆ (X=F, Cl, Br) doped with Cr³⁺, *Phys. Rev. B - Condens. Matter Mater. Phys.* **2006**, 74, 045105–045113. <https://doi.org/10.1103/PhysRevB.74.045105>.
- [68] Sviridov, D.T.; Sviridova, R.K.; Kulik, N.; Glasko, V.B. Optical spectra of the isoelectronic ions V²⁺, Cr³⁺, and Mn⁴⁺ in an octahedral coordination. *J. Appl. Spectrosc.* **1979**, 30, 334–337. <https://doi.org/10.1007/BF00608274>.
- [69] Moreno, M.; Aramburu, J.A. The Huang-Rhys factor S (a_{1g}) for transition-metal impurities: a microscopic insight. *J. Phys. Condens. Matter.* **1992**, 4, 9481–9488. <https://doi.org/10.1088/0953-8984/4/47/027>.
- [70] M. Moreno, Barriuso, M.T.; Aramburu, J.A. The dependence of 10Dq upon the metal–

- ligand distance, R, for transition-metal complexes. What is its microscopic origin?, *Int. J. Quantum Chem.* **1994**, 52, 829–835. <https://doi.org/10.1002/qua.56052041>
- [71] Wissing, K.; Aramburu, J.A.; Barriuso, M.T.; Moreno, X.; Optical properties due to Cr⁴⁺ in oxides: Density functional study. *Solid State Commun.* **1998**, 108, 1001–1005. [https://doi.org/10.1016/S0038-1098\(98\)00479-7](https://doi.org/10.1016/S0038-1098(98)00479-7).
- [72] Srivastava, A.M.; Brik, M.G. Crystal field studies of the Mn⁴⁺ energy levels in the perovskite, LaAlO₃. *Opt. Mater. (Amst)*. **2013**, 35, 1544–1548. <https://doi.org/10.1016/j.optmat.2013.03.021>.
- [73] Brik, M.G.; Srivastava, A.M. Electronic Energy Levels of the Mn⁴⁺ Ion in the Perovskite, CaZrO₃. *ECS J. Solid State Sci. Technol.* **2013**, 2, R148–R152. <https://doi.org/10.1149/2.020307jss>.
- [74] Brik, M.G.; Avram, C.N. Exchange charge model and analysis of the microscopic crystal field effects in KAl(MoO₄)₂:Cr³⁺. *J. Lumin.* **2011**, 131, 2642–2645. <https://doi.org/10.1016/j.jlumin.2011.06.034>.
- [75] Malkin, B.Z.; Macfarlane, R.M.; Kaplyanskii, A.A. Spectroscopy of Solids Containing Rare-earth Ions, *Elsevier Science Publishers B.V.*, North-Holland, Amsterdam, **1987**.
- [76] Fitchen, D.B. W.B.F. (Ed.), *Physics of Color Centers*, Academic, New York, **1968**.
- [77] Brik, M.G.; Crystal field analysis, electron-phonon coupling and spectral band shape modeling in MgO:Cr³⁺. *Zeitschrift Für Naturforsch. A.* **2005**, 60, 437–443. <https://doi.org/10.1515/zna-2005-0609>.
- [78] Du, M.H. Chemical trends of Mn⁴⁺ emission in solids. *J. Mater. Chem. C.* **2014**, 2, 2475–2481. <https://doi.org/10.1039/c4tc00031e>.
- [79] Momma, K.; Izumi, F. VESTA: a Three-Dimensional Visualization System for Electronic and Structural Analysis. *J. Appl. Crystallogr.* **2011**, 44, 1272–1276.
- [80] Liang, S.; Shang, M.; Lian, H.; Li, K.; Zhang, Y.; Lin, J. An efficient rare-earth free deep red emitting phosphor for improving the color rendering of white light-emitting diodes. *J. Mater. Chem. C.* **2017**, 5, 2927–2935. <https://doi.org/10.1039/c6tc05499d>.
- [81] Zhang, Y.; Wu, Z.; Geng, D.; Kang, X.; Shang, M.; Li, X.; Lian, H.; Cheng, Z.; Lin, J.; Full Color Emission in ZnGa₂O₄: Simultaneous Control of the Spherical Morphology, Luminescent, and Electric Properties via Hydrothermal Approach. *Adv. Funct. Mater.* **2014**, 24, 6581–6593. <https://doi.org/10.1002/adfm.201402092>.
- [82] Brik, M.G.; Beers, W.W.; Cohen, W.; Payne, S.A.; Cherepy, N.J.; Piasecki, M.; Srivastava, A.M. On the Mn⁴⁺ R-line emission intensity and its tunability in solids. *Opt. Mater. (Amst)*. **2019**, 91, 338–343. <https://doi.org/10.1016/j.optmat.2019.03.046>.

- [83] Ji, H.; Ueda, J.; Brik, M.G.; Du, M.H.; Chen, D.; Tanabe, S. Intense deep-red zero phonon line emission of Mn^{4+} in double perovskite $La_4Ti_3O_{12}$. *Phys. Chem. Chem. Phys.* **2019**, 21, 25108–25117. <https://doi.org/10.1039/c9cp04007b>.
- [84] Kunitomo, J.; Suzuki, R.; Takahashi, Y.; Miyazaki, T.; Terakado, N.; Fujiwara, T. Red-emissive Mn-doped $Li_2Ge_4O_9$ phase synthesized via glass-ceramic route. *J. Ceram. Soc. Japan.* **2014**, 122, 725–727. <https://doi.org/10.2109/jcersj2.122.725>.
- [85] Odawara, Y.; Takahashi, Y.; Yamazaki, Y.; Terakado, N.; Fujiwara, T. Synthesis of nanocrystals from glass-ceramics by YAG-laser irradiation: Mn^{4+} -doped $Li_2Ge_4O_9$ deep-red nanophosphor. **2017**, 125, 378–381.
- [86] Cao, Y.; Fang, Y.; Zhang, G.; Zhao, G.; Liu, Y.; Zou, J.; Vainos, N.; Hou, J. High quantum yield red-emission phosphor $Li_2Ge_4O_9:Mn^{4+}$ for WLEDs application. *Opt. Mater. (Amst.)* **2019**, 98, 109442-109447. <https://doi.org/10.1016/j.optmat.2019.109442>.
- [87] Omel'chenko, K.S.; Khmelenko, O. V.; Panchenko, T. V.; Volnyanskii, M.D. Photoluminescence of manganese-doped $LiNaGe_4O_9$ crystals. *Phys. Solid State.* **2014**, 56, 751–756. <https://doi.org/10.1134/S1063783414040246>.
- [88] Suzuki, R. ; Kunitomo, J. ; Takahashi, Y.; Nakamura, K.; Osada, M.; Terakado, V; Fujiwara, T. Mn-doped $LiNaGe_4O_9$ as a rare-earth free phosphor: Impact of Na-substitution on emission in tetragermanate phase. *J. Ceram. Soc. Japan.* **2015**, 123, 888–891. <https://doi.org/10.2109/jcersj2.123.888>.
- [89] Li, P.; Tan, L.; Wang, L.; Zheng, J.; Peng, M. ; Wang, Y. Synthesis, Structure, and Performance of Efficient Red Phosphor $LiNaGe_4O_9:Mn^{4+}$ and Its Application in Warm WLEDs. *J. Am. Ceram. Soc.* **2016**, 99, 2029–2034. <https://doi.org/10.1111/jace.14168>.
- [90] Ding, X.; Wang, Q.; Wang, Y. Rare-earth-free red-emitting $K_2Ge_4O_9:Mn^{4+}$ phosphor excited by blue light for warm white LEDs. *Phys. Chem. Chem. Phys.* **2016**, 18, 8088–8097. <https://doi.org/10.1039/c6cp00168h>.
- [91] Li, P. ; Brik, M.G.; Li, L.; Han, J. ; Li, Peng, M. Prediction on Mn^{4+} -Doped Germanate Red Phosphor by Crystal Field Calculation on Basis of Exchange Charge Model: A Case Study on $K_2Ge_4O_9:Mn^{4+}$. *J. Am. Ceram. Soc.* **2016**, 99, 2388–2394. <https://doi.org/10.1111/jace.14236>.
- [92] Vollenkle, H.; Wittmann, A.; Die Kristallstruktur des Kaliumtetragermanats $K_2[Ge_4O_9]$, *Monatsh. Chem.* **1971**, 102, 1245–1254. <https://doi.org/10.1007/BF00917178>.
- [93] Xue, J.; Ran, W.; Noh, H.M. ; Choi, B.C.; Park, S.H. ; Jeong, J.H; Kim, J.H. Influence of alkaline ions on the luminescent properties of Mn^{4+} -doped MGe_4O_9 ($M = Li_2, LiNa$

- and K₂) red-emitting phosphors. *J. Lumin.* **2017**, 192, 1072–1083. <https://doi.org/10.1016/j.jlumin.2017.08.036>.
- [94] Baur, F.; Jüstel, T. Dependence of the optical properties of Mn⁴⁺ activated A₂Ge₄O₉ (A=K, Rb) on temperature and chemical environment. *J. Lumin.* **2016**, 177, 354–360. <https://doi.org/10.1016/j.jlumin.2016.04.046>.
- [95] Cao, R. ; Ceng, D. ; X. Yu, S. Guo, Y. Wen, G. Zheng, Synthesis and luminescence properties of novel deep red emitting phosphors Li₂MgGeO₄:Mn⁴⁺. *Funct. Mater. Lett.* **2015**, 8, 1550046–1550049. <https://doi.org/10.1142/S1793604715500460>.
- [96] Zhu, H. ; Lin, C.C.; Luo, W. ; Shu, S.; Liu, Z.; Liu, Y.; Kong, J.; Chen, X. Highly efficient non-rare-earth red emitting phosphor for warm white light-emitting diodes. *Nat. Commun.* **2014**, 5, 1-10. <https://doi.org/10.1038/ncomms5312>.
- [97] Yan, W.; Yun, X. ; Yang, H. ; Wei, Y.; Li, G. A novel Mn⁴⁺-activated Li₃CsGe₈O₁₈ red phosphor and cation substitution induced photoluminescence improvement. *J. Lumin.* **2020**, 225, 117323–117333. <https://doi.org/10.1016/j.jlumin.2020.117323>.
- [98] Xue, F.; Hu, Y.; Chen, L.; Wu, H.; Ju, G.; Wang, T.; Yang, L. A novel rare-earth free red long-persistent phosphor: Mg₂GeO₄:Mn⁴⁺. *Ceram. Int.* **2017**, 43, 15141–15145. <https://doi.org/10.1016/j.ceramint.2017.08.044>.
- [99] Huang, Q.; Ye, W.; Hu, G. ; Jiao, X.; Liu, X. Deep red emission enhancement in Mg₂₈Ge₁₀O₄₈:Mn⁴⁺ phosphor by Zn substitution. *J. Lumin.* **2018**, 194, 557–564. <https://doi.org/10.1016/j.jlumin.2017.08.049>.
- [100] Huang, Q.; Ye, W. ; Hu, G. ; Liu, X. Strong red emission in Bi³⁺ and Mn⁴⁺ codoped Mg_{3.5}Ge_{1.25}O₆ phosphors applied in optical agriculture. *J. Lumin.* **2019**, 210, 89–95. <https://doi.org/10.1016/j.jlumin.2019.01.047>.
- [101] Liang, S.; Li, G. ; Dang, V.; Wei, Y.; Lian, H.; Lin, J. Cation Substitution Induced Adjustment on Lattice Structure and Photoluminescence Properties of Mg₁₄Ge₅O₂₄:Mn⁴⁺: Optimized Emission for w-LED and Thermometry Applications. *Adv. Opt. Mater.* **2019**, 7, 1900093–1900107. <https://doi.org/10.1002/adom.201900093>.
- [102] Cao, R. ; Luo, W.; Xiong, Q.; Jiang, S.; Luo, Z.; Fu, J. Synthesis and photoluminescence properties of Ba₂GeO₄:Mn⁴⁺ novel deep red-emitting phosphor. *Chem. Lett.* **2015**, 44, 1422–1424. <https://doi.org/10.1246/cl.150578>.
- [103] Cao, R.; Ye, Y.; Peng, Q.; Zheng, G.; Ao, H. ; Fu, J. ; Guo, Y. ; Guo, B. Synthesis and luminescence characteristics of novel red-emitting Ba₂TiGe₂O₈:Mn⁴⁺ phosphor. *Dye. Pigment.* **2017**, 146, 14–19. <https://doi.org/10.1016/j.dyepig.2017.06.061>.
- [104] Lu, V.; Fu, A.; Gao, F.; Zhang, X.; Zhou, L. Synthesis and luminescence properties of

- double perovskite Ba₂MgGe₂O₇:Mn⁴⁺ deep red phosphor. *J. Lumin.* **2018**, 203, 420–426. <https://doi.org/10.1016/j.jlumin.2018.06.061>.
- [105] Fu, S.; Tian, L. A novel deep red emission phosphor BaAl₂Ge₂O₈:Mn⁴⁺ for plant growth LEDs. *Optik (Stuttg.)* **2019**, 183, 635–641. <https://doi.org/10.1016/j.ijleo.2019.02.131>.
- [106] Liang, S. .; Shang, M.; Lian, H.; Li, K.; Zhang, Y. ; Lin, J. Deep red MGe₄O₉:Mn⁴⁺ (M = Sr, Ba) phosphors: Structure, luminescence properties and application in warm white light emitting diodes. *J. Mater. Chem. C.* **2016**, 4, 6409–6416. <https://doi.org/10.1039/c6tc01813k>.
- [107] Zhang, S.; Hu, Y. Photoluminescence spectroscopies and temperature-dependent luminescence of Mn⁴⁺ in BaGe₄O₉ phosphor. *J. Lumin.* **2016**, 177, 394–401. <https://doi.org/10.1016/j.jlumin.2016.05.020>.
- [108] Chen, W.; Cheng, Y. ; Shen, L. ; Shen, C.; Liang, X. .; Xiang, W. Red-emitting Sr₂MgGe₂O₇:Mn⁴⁺ phosphors: Structure, luminescence properties, and application in warm white light emitting diodes. *J. Alloys Compd.* **2018**, 762, 688–696. <https://doi.org/10.1016/j.jallcom.2018.05.264>.
- [109] Zhang, X. .; Nie, J.; Liu, S.; Li, Y.; Qiu, J. Deep-red photoluminescence and long persistent luminescence in double perovskite-type La₂MgGeO₆:Mn⁴⁺. *Int. J. Lab. Hematol.* **2018**, 101, 1576–1584. <https://doi.org/10.1111/ijlh.12426>.
- [110] Zhang, S. .; Hu, Y.; Duan, H. .; Chen, L. .; Fu, Y.; He, M. Novel La₃GaGe₅O₁₆:Mn⁴⁺ based deep red phosphor: A potential color converter for warm white light. *RSC Adv.* **2015**, 5, 90499–90507. <https://doi.org/10.1039/c5ra18163a>.
- [111] Ding, X. .; Zhu, G.; Geng, W.; Wang, Q.; Wang, Y. Rare-Earth-Free High-Efficiency Narrow-Band Red-Emitting Mg₃Ga₂GeO₈:Mn⁴⁺ Phosphor Excited by Near-UV Light for White-Light-Emitting Diodes. *Inorg. Chem.* **2016**, 55, 154–162. <https://doi.org/10.1021/acs.inorgchem.5b02048>.
- [112] Cao, R.; Luo, W.; Xiong, Q.; A. Liang, Jiang, S.; Xu, Y. Synthesis and luminescence properties of novel red phosphors LiRGe₂O₆:Mn⁴⁺ (R = Al or Ga), *J. Alloys Compd.* **2015**, 648, 937–941. <https://doi.org/10.1016/j.jallcom.2015.07.080>.
- [113] Wu, C.; Li, J.; Xu, H.; Wu, J.; Zhang, J.; Ci, Z.; Feng, L.; Cao, C.; Zhang, Z. .; Wang, Y. Preparation, structural and photoluminescence characteristics of novel red emitting Mg₇Ga₂GeO₁₂:Mn⁴⁺ phosphor. *J. Alloys Compd.* **2015**, 646, 734–740. <https://doi.org/10.1016/j.jallcom.2015.06.166>.
- [114] Ding, X. .; Wang, Y. Structure and photoluminescence properties of rare-earth free narrow-band red-emitting Mg₆ZnGeGa₂O₁₂:Mn⁴⁺ phosphor excited by NUV light. *Opt.*

- Mater. (Amst)*. **2017**, 64, 445–452. <https://doi.org/10.1016/j.optmat.2017.01.003>.
- [115] Jansen, T.; Gorobez, J.; Kirm, M.; Brik, M.G.; Vielhauer, S.; Oja, M.; Khaidukov, N.M.; Makhov, V.N.; Jüstel, T. Narrow Band Deep Red Photoluminescence of $\text{Y}_2\text{Mg}_3\text{Ge}_3\text{O}_{12}:\text{Mn}^{4+}$. Li^+ Inverse Garnet for High Power Phosphor Converted LEDs, *ECS J. Solid State Sci. Technol.* **2018**, 7, R3086–R3092. <https://doi.org/10.1149/2.0121801jss>.
- [116] Dong, L.; Zhang, L.; Jia, Y.; Shao, B.; Zhao, S.; You, H. Site Occupation and Luminescence of Novel Orange-Red $\text{Ca}_3\text{M}_2\text{Ge}_3\text{O}_{12}:\text{Mn}^{2+}$, Mn^{4+} (M = Al, Ga) Phosphors. *ACS Sustain. Chem. Eng.* **2020**, 8, 3357–3366. <https://doi.org/10.1021/acssuschemeng.9b07281>.
- [117] Peng, L.; Chen, W.; Cao, S.; Liu, B.; Han, T.; Zhao, L.; Zhao, C.; Li, F.; Li, X. Enhanced photoluminescence and thermal properties due to size mismatch in $\text{Mg}_2\text{Ti}_x\text{Ge}_{1-x}\text{O}_4:\text{Mn}^{4+}$ deep-red phosphors. *J. Mater. Chem. C*. **2019**, 7, 2345–2352. <https://doi.org/10.1039/c8tc05743e>.
- [118] Van den Eeckhout, K.; Poelman, D.; Smet, P.F. Persistent Luminescence in Non-Eu²⁺-Doped Compounds: A Review. *Materials (Basel)*. **2013**, 6, 2789–2818. <https://doi.org/10.3390/ma6072789>.
- [119] Liu, F.; Chen, Y.; Liang, Y.; Pan, Z. Phonon-assisted upconversion charging in $\text{Zn}_3\text{Ga}_2\text{GeO}_8:\text{Cr}^{3+}$ near-infrared persistent phosphor. *Opt. Lett.* **2016**, 41, 954–957. <https://doi.org/10.1364/ol.41.000954>.
- [120] Zhuang, Y.; Ueda, J.; Tanabe S. Enhancement of red persistent luminescence in Cr^{3+} -doped ZnGa_2O_4 phosphors by Bi_2O_3 codoping. *Appl. Phys. Express*. **2013**, 6 052602–052605. <https://doi.org/10.7567/APEX.6.052602>.
- [121] Zhan, Y.; Y. Jin; Wu, H.; Yuan, G; Ju, Hu, Y.; Cr^{3+} -doped $\text{Mg}_4\text{Ga}_4\text{Ge}_3\text{O}_{16}$ near-infrared phosphor membrane for optical information storage and recording. *J. Alloys Compd.* **2019**, 777, 991–1000. <https://doi.org/10.1016/j.jallcom.2018.11.065>.
- [122] Lin, H.; Bai, G.; Yu, T. T.; Tsang, M.K.; Zhang, Q.; Hao, J. Site Occupancy and Near-Infrared Luminescence in $\text{Ca}_3\text{Ga}_2\text{Ge}_3\text{O}_{12}:\text{Cr}^{3+}$ Persistent Phosphor. *Adv. Opt. Mater.* **2017**, 5, 1700227–1700235. <https://doi.org/10.1002/adom.201700227>.
- [123] Zhou, J.; Xia, Z. Synthesis and near-infrared luminescence of $\text{La}_3\text{GaGe}_5\text{O}_{16}:\text{Cr}^{3+}$ phosphors. *RSC Adv.* **2014**, 4, 46313–46318. <https://doi.org/10.1039/c4ra09793a>.
- [124] Wang, C.; Wang, X.; Zhou, Y.; Zhang, S.; Li, C.; Hu, D.; Xu, L.; Jiao, H. An Ultra-Broadband Near-Infrared Cr^{3+} -Activated Gallogermanate $\text{Mg}_3\text{Ga}_2\text{GeO}_8$ Phosphor as Light Sources for Food Analysis. *ACS Appl. Electron. Mater.* **2019**, 1, 1046–1053.

- <https://doi.org/10.1021/acsaelm.9b00219>.
- [125] Kim, I.W.; Kaur, S.; Yadav, A.; Rao, A.S.; Saravanakumar, S.; Rao, J.L.; Singh, V. Structural, luminescence and EPR properties of deep red emitting $\text{MgY}_2\text{Al}_4\text{SiO}_{12}:\text{Cr}^{3+}$ garnet phosphor. *J. Lumin.* **2020**, *220*, 116975-116981. <https://doi.org/10.1016/j.jlumin.2019.116975>.
- [126] Basavaraju, N.; Sharma, S.; Bessière, A.; Viana, B.; Gourier, D.; Priolkar, K.R. Red persistent luminescence in $\text{MgGa}_2\text{O}_4:\text{Cr}^{3+}$; A new phosphor for in vivo imaging. *J. Phys. D. Appl. Phys.* **2013**, *46*, 375401–375405. <https://doi.org/10.1088/0022-3727/46/37/375401>.
- [127] Katayama, Y.; Kobayashi, H.; Tanabe, S. Deep-red persistent luminescence in Cr^{3+} -doped LaAlO_3 perovskite phosphor for in vivo imaging. *Appl. Phys. Express.* **2015**, *8*, 0121010–0121023. <https://doi.org/10.7567/APEX.8.012102>.
- [128] Bai, Q.; Li, P.; Wang, Z.; Li, T.; Xu, S.; Yang, Z. Using Ca^{2+} ions to induce the long afterglow and bluish white emission of red emitting phosphor $\text{Zn}_3\text{Al}_2\text{Ge}_2\text{O}_{10}:\text{Cr}^{3+}$. *Mater. Des.* **2016**, *91*, 28–36. <https://doi.org/10.1016/j.matdes.2015.11.061>.
- [129] Yang, S.H.; Hung, Y.C.; Tseng,.; Lee, H.Y. Versatile deep-red $\text{Mg}_2\text{TiO}_4:\text{Mn}^{4+}$ phosphor for photoluminescence, thermometry, and latent fingerprint visualization. *J. Alloys Compd.* **2019**, *801*, 394–401. <https://doi.org/10.1016/j.jallcom.2019.06.028>.
- [130] Zhao, X.; Wang, X.; Chen, B.; Meng, Q.; Di, W.; Ren, G.; Yang, Y. Novel Eu^{3+} -doped red-emitting phosphor $\text{Gd}_2\text{Mo}_3\text{O}_9$ for white-light-emitting-diodes (WLEDs) application. *J. Alloys Compd.* **2007**, *433*, 352–355. <https://doi.org/10.1016/j.jallcom.2006.06.096>.
- [131] Zhang, H.; Zhang, H.; Zhuang, J.; Dong, H.; Zhu, Y.; Ye, X.; Liu, Y.; Lei, B. Effect of H_3BO_3 flux on the morphology and optical properties of $\text{Sr}_2\text{MgAl}_{22}\text{O}_{36}:\text{Mn}^{4+}$ red phosphors for agricultural light conversion films. *Ceram. Int.* **2016**, *42*, 13011–13017. <https://doi.org/10.1016/j.ceramint.2016.05.076>
- [132] Lee, S.J. ; Jung, J.; Park, J.Y.; Jang, H.M. ; Kim, Y.R.; Park, J.K. Application of red light-emitting diodes using $\text{Mg}_{3.5}\text{Ge}_{1.25}\text{O}_6:\text{Mn}^{4+}$ phosphor. *Mater. Lett.* **2013**, *111*, 108–111. <https://doi.org/10.1016/j.matlet.2013.08.098>.
- [133] Abraham, M.; Kunti,A.K.; Thejas, K. K.; Amador-Mendez, N.; Gogneau, N.; Nishanth, K.G.; Tchernycheva, M.; Das, S. The elevated colour rendering of white-LEDs by microwave-synthesized red-emitting $(\text{Li}, \text{Mg})_3\text{RbGe}_8\text{O}_{18}:\text{Mn}^{4+}$ nanophosphors. *Dalton. Trans.* **2021**, *50*, 3044–3059. <https://doi.org/10.1039/d0dt04309e>.
- [134] Xie, D.; Peng, H.; Huang, S.; You, F. Core-shell structure in doped inorganic nanoparticles: Approaches for optimizing luminescence properties. *J. Nanomater.* **2013**

- 1–10. <https://doi.org/10.1155/2013/891515>.
- [135] Dolgov, L.; Hong, J.; Zhou, L.; Li, X.; Li, J.; Djordjevic, V.; Dramicanin, M.; Shi, J.; Wu, M. Efficient Luminescence Enhancement of $\text{Mg}_2\text{TiO}_4:\text{Mn}^{4+}$ Red Phosphor by Incorporating Plasmonic $\text{Ag}@\text{SiO}_2$ Nanoparticles. *ACS Appl. Mater. Interfaces*. **2019**, 11, 21004–21009. <https://doi.org/10.1021/acsami.9b05781>.
- [136] Xu, Y.; Zhang, L.; Wang, L.; Shi, M.; Liu, L.; Chen, Y. Red emission enhancement for $\text{CaAl}_{12}\text{O}_{19}:\text{Cr}^{3+}$ and $\text{CaAl}_{12}\text{O}_{19}:\text{Mn}^{4+}$ phosphors. *J. Mater. Sci. Mater. Electron*. **2017**, 28, 12032–12038. <https://doi.org/10.1007/s10854-017-7014-3>.
- [137] Nair, G.B.; Dhoble, S.J. Fundamentals of LEDs. *Fundam. Appl. Light. Diodes*. **2020**, 35–57. <https://doi.org/10.1016/b978-0-12-819605-2.00002-1>.
- [138] Zhu, Y.; Li, X.; Zhu, B.; Liang, Y. Design of core-shell phosphors with tunable luminescence and improved thermal stability by coating with g- C_3N_4 . *Inorg. Chem. Front*. **2020**, 7, 3126–3135. <https://doi.org/10.1039/d0qi00498g>.
- [139] Xu, T.; Yuan, L.; Chen, Y.; Zhao, Y.; Ding, L.; Liu, J.; Xiang, W.; Liang, X. $\text{Y}_3\text{Al}_5\text{O}_{12}:\text{Ce}^{3+}$ single crystal and red-emitting $\text{Y}_3\text{Al}_5\text{O}_{12}:\text{Cr}^{3+}$ single crystal for high power W-LEDs. *Opt. Mater. (Amst)*. **2019**, 91, 30–34. <https://doi.org/10.1016/j.optmat.2019.03.010>.
- [140] Abdukayum, A.; Chen, J.T.; Zhao, Q.; Yan, X.P. Functional near infrared-emitting $\text{Cr}^{3+}/\text{Pr}^{3+}$ Co-doped zinc gallogermanate persistent luminescent nanoparticles with superlong afterglow for in vivo targeted bioimaging. *J. Am. Chem. Soc*. **2013**, 135, 14125–14133. <https://doi.org/10.1021/ja404243v>.
- [141] Zhang, S.; Hu, Y.; Chen, L.; Fu, Y.; Ju, G. $\text{La}_3\text{GaGe}_5\text{O}_{16}:\text{Cr}^{3+}$ phosphor: the near-infrared persistent luminescence. *Opt. Mater. Express*. **2016**, 6, 1247–1255. <https://doi.org/10.1364/ome.6.001247>.
- [142] Pavitra, E.; Raju, G.S.R.; Park, J.Y.; Hussain, S.K.; Chodankar, N.R.; Rao, G.M.; Han, Y.K.; Huh, Y.S. An efficient far-red emitting $\text{Ba}_2\text{LaNbO}_6:\text{Mn}^{4+}$ nanophosphor for forensic latent fingerprint detection and horticulture lighting applications. *Ceram. Int*. **2020**, 46, 9802–9809. <https://doi.org/10.1016/j.ceramint.2019.12.253>.
- [143] King, R.S.P.; Skros, D.A. Sunlight-activated near-infrared phosphorescence as a viable means of latent fingermark visualisation. *Forensic Sci. Int*. **2017**, 276, e35–e39. <https://doi.org/10.1016/j.forsciint.2017.04.012>.
- [144] Ming, H.; Liu, L.; He, S.; Peng, J.; Du, F.; Fu, J.; Yang, F.; Ye, X. An ultra-high yield of spherical $\text{K}_2\text{NaScF}_6:\text{Mn}^{4+}$ red phosphor and its application in ultra-wide color gamut liquid crystal displays. *J. Mater. Chem. C*. **2019**, 7, 7237–7248.

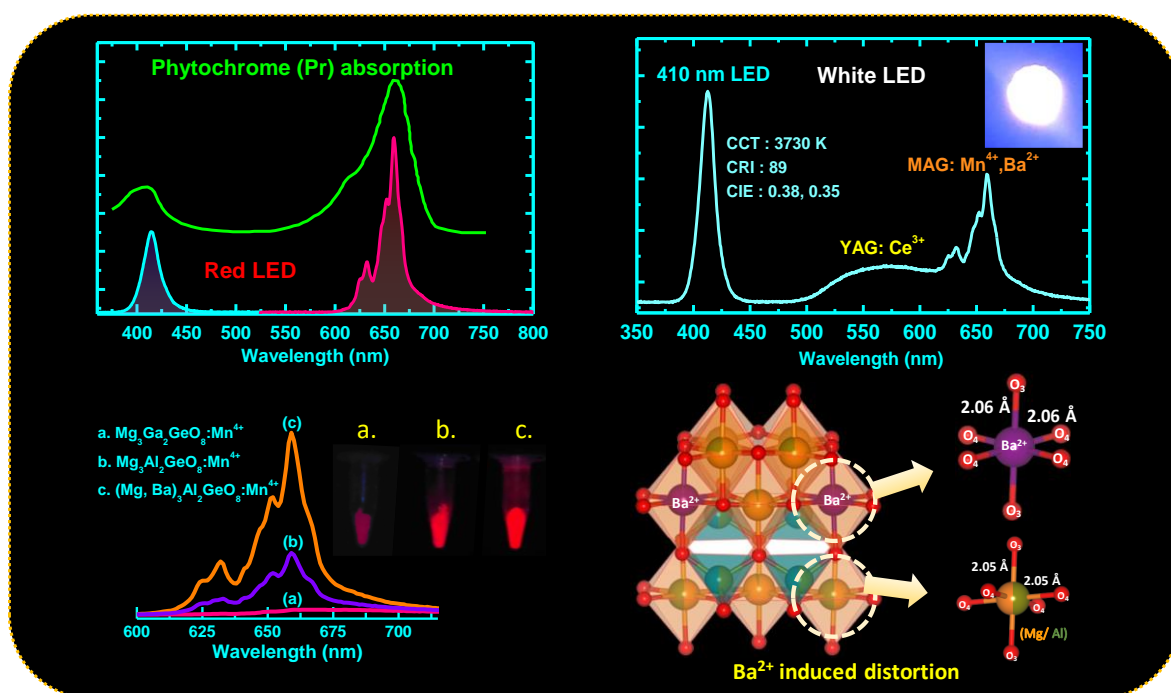
<https://doi.org/10.1039/c9tc02295c>.

- [145] Pratapkumar, C.; Prashantha, S.C.; Nagabhushana, H.; Jnaneshwara, D.M. Photoluminescence and photometric studies of low temperature prepared red emitting $\text{MgAl}_2\text{O}_4:\text{Cr}^{3+}$ nanophosphors for solid state displays. *J. Sci. Adv. Mater. Devices*. **2018**, *3*, 464–470. <https://doi.org/10.1016/j.jsamd.2018.09.002>.
- [146] Huyen, N.T.; Tu, N.; Tung, D.T.; Trung, D.Q.; Anh, D.D.; Duc, T.T.; Nga, T.T.T.; Huy, P.T. Photoluminescent properties of red-emitting phosphor $\text{BaMgAl}_{10}\text{O}_{17}:\text{Cr}^{3+}$ for plant growth LEDs. *Opt. Mater. (Amst)*. **2020**, *108*, 110207–110213. <https://doi.org/10.1016/j.optmat.2020.110207>.
- [147] Getz, M.N.; Nilsen, O.; Hansen, P.A. Sensors for optical thermometry based on luminescence from layered $\text{YVO}_4:\text{Ln}^{3+}$ (Ln = Nd, Sm, Eu, Dy, Ho, Er, Tm, Yb) thin films made by atomic layer deposition. *Sci. Rep.* **2019**, *9*, 1–11. <https://doi.org/10.1038/s41598-019-46694-8>.
- [148] Mondal, A.; Manam, J. Structural, optical and temperature dependent photoluminescence properties of Cr^{3+} -activated LaGaO_3 persistent phosphor for optical thermometry. *Ceram. Int.* **2020**, *46*, 23972–23984. <https://doi.org/10.1016/j.ceramint.2020.06.174>.
- [149] Wang, Q.; Liang, Z.; Luo, J.; Yang, Y.; Mu, Z.; Zhang, X.; Dong, H.; Wu, F.; Ratiometric optical thermometer with high sensitivity based on dual far-red emission of Cr^{3+} in $\text{Sr}_2\text{MgAl}_{22}\text{O}_{36}$. *Ceram. Int.* **2020**, *46*, 5008–5014. <https://doi.org/10.1016/j.ceramint.2019.10.241>.
- [150] van Sark, W.G.J.H.M.; Meijerink, A.; Schropp, R.E.I. Solar Spectrum Conversion for Photovoltaics Using Nanoparticles. in: V. Fthenakis (Ed.), *Third Gener. Photovoltaics, InTechOpen, Croatia*, **2012**: pp. 1–28. <https://doi.org/10.1201/9781420076752>.
- [151] S. Adachi, Review— Mn^{4+} -Activated Red and Deep Red-Emitting Phosphors. *ECS J. Solid State Sci. Technol.* **2020**, *9*, 16001–16034. <https://doi.org/10.1149/2.0022001jss>.
- [152] Kang, F.; Sun, G.; Boutinaud, P.; Wu, H.; Ma, F. X.; Lu, J.; Gan, J.; Bian, H.; Gao, F.; Xiao, S. Recent Advances and Prospects of Persistent Luminescent Materials as Inner Secondary Self-Luminous Light Source for Photocatalytic Applications. *Chem. Eng. J.* **2021**, *403*. <https://doi.org/10.1016/j.cej.2020.126099>.
- [153] Liang, L.; Chen, J.; Shao, K.; Qin, X.; Pan, Z.; Liu, X. Controlling Persistent Luminescence in Nanocrystalline Phosphors. *Nat. Mater.* **2023**, *22* (3), 289–304. <https://doi.org/10.1038/s41563-022-01468-y>.
- [154] Jabłoński, A. Über den Mechanismus der Photolumineszenz von Farbstoffphosphoren.

- Z. Physik* , **1935**, 38–46 . <https://doi.org/10.1007/BF01330795>
- [155] Schweizer, T.; Kubach, H.; Koch, T. Investigations to Characterize the Interactions of Light Radiation, Engine Operating Media and Fluorescence Tracers for the Use of Qualitative Light-Induced Fluorescence in Engine Systems. *Automot. Engine Technol.* **2021**, *6* (3–4), 275–287. <https://doi.org/10.1007/s41104-021-00092-3>
- [156] Poelman, D.; Van Der Heggen, D.; Du, J.; Cosaert, E.; Smet, P. F. Persistent Phosphors for the Future: Fit for the Right Application. *J. Appl. Phys.* **2020**, *128* (24). <https://doi.org/10.1063/5.0032972>.
- [157] Feng, P.; Zhang, J.; Wu, C.; Liu, X.; Wang, Y. Self-Activated Afterglow Luminescence of Un-Doped $\text{Ca}_2\text{ZrSi}_4\text{O}_{12}$ Material and Explorations of New Afterglow Phosphors in a Rare Earth Element-Doped $\text{Ca}_2\text{ZrSi}_4\text{O}_{12}$ System. *Mater. Chem. Phys.* **2013**, *141* (1), 495–501. <https://doi.org/10.1016/j.matchemphys.2013.05.049>.
- [158] Yuan, W.; Pang, R.; Wang, S.; Tan, T.; Li, C.; Wang, C.; Zhang, H. Enhanced Blue-Light Excited Cyan-Emitting Persistent Luminescence of $\text{BaLu}_2\text{Al}_2\text{Ga}_2\text{SiO}_{12}:\text{Ce}^{3+}, \text{Bi}^{3+}$ Phosphors for AC-LEDs via Defect Modulation. *Light Sci. Appl.* **2022**, *11* (1). <https://doi.org/10.1038/s41377-022-00868-8>.
- [159] Viswanath, N. S. M.; Grandhi, G. K.; Kim, H. J.; Zhuang, Y.; Xie, R. J.; Im, W. Bin. A New Persistent Blue-Emitting Phosphor: Tailoring the Trap Density for Enhancing the Persistent Time. *Appl. Mater. Today* **2020**, *18*, 100518. <https://doi.org/10.1016/j.apmt.2019.100518>.
- [160] Erin F.; Angelica C.; Anna D.; Andrew P.; and Jakoah B.; Optimizing Blue Persistent Luminescence in $(\text{Sr}_{1-\delta}\text{Ba}_\delta)_2\text{MgSi}_2\text{O}_7:\text{Eu}^{2+}, \text{Dy}^{3+}$ via Solid Solution for Use in Point-of-Care Diagnostics. *ACS Appl. Mater. Interfaces* **2016**, *8*, 40, 26956–26963 <https://doi.org/10.1021/acsami.6b10303>
- [161] Xiong, P.; Zheng, C.; Peng, M.; Zhou, Z.; Xu, F.; Qin, K.; Hong, Y.; Ma, Z. Self-Activated Persistent Luminescence from $\text{Ba}_2\text{Zr}_2\text{Si}_3\text{O}_{12}$ for Information Storage. *J. Am. Ceram. Soc.* **2020**, *103* (12), 6922–6931. <https://doi.org/10.1111/jace.17412>.
- [162] Li, X.; Zou, Z.; Wang, Z.; Wu, C.; Zhang, J.; Wang, Y. A Novel Un-Doped Long Lasting Phosphorescence Phosphor: $\text{SrZrSi}_2\text{O}_7$. *J. Rare Earths* **2015**, *33* (1), 37–41. [https://doi.org/10.1016/S1002-0721\(14\)60380-X](https://doi.org/10.1016/S1002-0721(14)60380-X).
- [163] Sreevalsa, S.; Ranjith, P.; Ahmad, S.; Sahoo, S. K.; Som, S.; Pandey, M. K.; Das, S. Host Sensitized Photoluminescence in $\text{Sr}_{2.9-3x/2}\text{Ln}_x\text{AlO}_4\text{F}: 0.1\text{Eu}^{3+}$ ($\text{Ln} = \text{Gd}, \text{Y}$) for Innovative Flexible Lighting Applications. *Ceram. Int.* **2020**, *46* (13), 21448–21460. <https://doi.org/10.1016/j.ceramint.2020.05.243>.

Chapter 2

Enriching the deep red emission in $(\text{Mg}, \text{Ba})_3\text{M}_2\text{GeO}_8:\text{Mn}^{4+}$ ($\text{M} = \text{Al}, \text{Ga}$) compositions for light-emitting diodes



2.1 Abstract

Red emission from Mn^{4+} -containing oxides inspired the development of high colour rendering and cost-effective white LEDs (WLEDs). Aiming this fact, a series of new crystallographic site modified $(\text{Mg}, \text{Ba})_3\text{M}_2\text{GeO}_8: \text{Mn}^{4+}$ ($\text{M} = \text{Al}, \text{Ga}$) compositions were developed with strong deep red emission in reaction to UV and blue lights. $\text{Mg}_3\text{Al}_2\text{GeO}_8$ host is composed of three phases, orthorhombic- $\text{Mg}_3\text{Ga}_2\text{GeO}_8$, orthorhombic- Mg_2GeO_4 , and cubic- MgAl_2O_4 . Whereas $\text{Mg}_3\text{Ga}_2\text{GeO}_8$ secured orthorhombic crystal structure. Interestingly, $\text{Mg}_3\text{Al}_2\text{GeO}_8: \text{Mn}^{4+}$ showed 13 folds intense emission than $\text{Mg}_3\text{Ga}_2\text{GeO}_8: \text{Mn}^{4+}$ since Mn^{4+} occupancy was preferable to $[\text{AlO}_6]$ sites compared to $[\text{GaO}_6]$. The co-existing phases of MgAl_2O_4 and Mg_2GeO_4 in $\text{Mg}_3\text{Al}_2\text{GeO}_8: \text{Mn}^{4+}$ contributed to the Mn^{4+} luminescence by providing additional $[\text{AlO}_6]$ and $[\text{MgO}_6]$ octahedrons for Mn^{4+} occupancy. Further, these sites reduced the natural reduction probability of Mn^{4+} to Mn^{2+} in $[\text{AlO}_4]$ tetrahedrons, which was confirmed using cathodoluminescence analysis for the first time. A cationic substitution strategy was employed on $\text{Mg}_3\text{M}_2\text{GeO}_8: \text{Mn}^{4+}$ to improve the luminescence and $\text{Mg}_{3-x}\text{Ba}_x\text{M}_2\text{GeO}_8: \text{Mn}^{4+}$ ($\text{M} = \text{Al}, \text{Ga}$) phosphors were synthesized. Partial substitution of larger Ba^{2+} ions in Mg^{2+} sites caused structural distortions and generated a new Ba impurity phase, which improved the photoluminescence. Compositionally tuned $\text{Mg}_{2.73}\text{Ba}_{0.27}\text{Al}_{1.993}\text{GeO}_8: 0.005\text{Mn}^{4+}$ exhibited 35 folds higher emission than that of $\text{Mg}_3\text{Ga}_{1.993}\text{GeO}_8: 0.005\text{Mn}^{4+}$. Additionally, this could retain 70% of its ambient emission intensity at 453 K. A warm WLED with CCT of 3730 K and CRI of 89 was fabricated by combining the optimized red component with $\text{Y}_3\text{Al}_5\text{O}_{12}: \text{Ce}^{3+}$ and 410 nm blue-LED. By tuning the ratio of blue ($\text{BaMgAl}_{10}\text{O}_{17}: \text{Eu}^{2+}$), green ($\text{Ce}_{0.63}\text{Tb}_{0.37}\text{MgAl}_{11}\text{O}_{19}$), and red ($\text{Mg}_{2.73}\text{Ba}_{0.27}\text{Al}_2\text{GeO}_8: 0.005\text{Mn}^{4+}$) phosphors, another WLED was developed using 280 nm UV-LED chip. This showed natural white emission with a CRI of 79 and CCT of 5306 K. Meanwhile, three red LEDs were also fabricated using $\text{Mg}_{2.73}\text{Ba}_{0.27}\text{Al}_{1.993}\text{GeO}_8: 0.005\text{Mn}^{4+}$ phosphor with commercial sources. These could be potential pc-LEDs for plant growth applications.

2.2 Introduction

Deep red-emitting Mn^{4+} -activated oxides are gathering extensive attention as the suitable replacement for expensive rare-earth-based phosphors for the potential applications in white light-emitting diode (WLED), security, sensing, plant growth, bio detectors, etc. Several, Mn^{4+} -doped fluorides are recently commercialized due to their eye-sensitive red peak at ~630 nm.¹⁻³ Regrettably, these phosphors are unstable and require the use of highly corrosive HF for synthesis.¹⁻³ While, Mn^{4+} -activated oxide phosphors have advantages such as eco-friendly

preparation, higher thermal as well as chemical stability, and deep-red emission ($\lambda_{em} > 650$ nm). Moreover, Mn^{4+} ions can be stabilized in the Al^{3+} ($r_{AlO_6} = 0.535$ Å) and Ge^{4+} ($r_{GeO_6} = 0.53$ Å) octahedrons due to close ionic sizes with Mn^{4+} ($r_{MnO_6} = 0.53$ Å).³⁻⁸ The recently reported potential hosts such as $Li_3RbGe_8O_{18}$,⁴ $Mg_{14}Ge_5O_{24}$,⁹ Mg_2TiO_4 ,¹⁰ $Mg_3Ga_2GeO_8$,¹¹ $BaGe_4O_9$,¹² etc. are observed to be suitable for Mn^{4+} ions to generate deep red emission. However, the red emission intensity of these samples needs to be enhanced further for commercial lighting and display applications.

Q. Huang *et al.* have intensified the deep red emission of $Mg_{14}Ge_5O_{24}: Mn^{4+}$ by Bi^{3+} co-activation,¹³ which sensitized Mn^{4+} ions effectively. Liang *et al.* boosted the deep red emission of this phosphor by 2.49 times via substituting Ti^{4+} and Sn^{4+} in the Ge^{4+} octahedrons, and it introduced some resonance effect due to the multiple luminescence centers.¹⁴ Likewise, the emission intensity of $Mg_2TiO_4: Mn^{4+}$ was immensely improved via the Ge^{4+} ion substitution in the Ti^{4+} sites. Such replacement enhanced the conversion of more $[TiO_6]$ octahedrons to $[GeO_6]$, which separated adjacent Mn^{4+} ions and interrupts the energy migrations among Mn^{4+} ionic pairs within the lattice.¹⁵ Recently, Mg^{2+} co-doping in the Li sites was employed to increase the emission intensity of $Li_3RbGe_8O_{18}: Mn^{4+}$ by reducing surface defects (conversion of the surface oxygen to lattice oxygen).¹⁶

Since Mn^{4+} is a matrix-sensitive activator, cation substitution can induce a considerable impact on luminescence properties. Due to this fact, Mn^{4+} -activated $Mg_3Ga_2GeO_8$ ¹¹ was chosen for a case study and the emission intensity could be intensified via suitable cationic modifications. A major advantage of this phosphor is its multiple luminescence centers. According to Ding *et al.*, Mn^{4+} ions can occupy both $[MgO_6]$ and $[GaO_6]$ octahedrons and produce deep red emission at 659 nm. Synthesizing mixed phased hosts could be another promising strategy for improving luminescence efficiency. Y. Wu *et al.* developed Mn^{4+} -activated red phosphor composed of $CaAl_{12}O_{19}$ and $MgAl_2O_4$ phases,¹⁷ where the coexisting phase $MgAl_2O_4$ acted as a flux throughout the sintering process and increases the crystallinity and red emission intensity.

Herein, a new class of deep red emitting $Mg_3M_2GeO_8: Mn^{4+}$ ($M = Al, Ga$) compositions were developed. In particular, the $Mg_3Al_2GeO_8: Mn^{4+}$ emission is higher than that of $Mg_3Ga_2GeO_8: Mn^{4+}$. The substitution of Ba^{2+} ions in the Mg^{2+} sites enhanced the deep

red emission substantially. The presence of a new impurity phase tetragonal-Ba₂MgGe₂O₇ was identified with Ba²⁺ substitution in Mg₃Al₂GeO₈: Mn⁴⁺ and Mg₃Ga₂GeO₈: Mn⁴⁺ samples. The emission intensity of the compositionally tuned Mg_{2.73}Ba_{0.27}Al₂GeO₈: 0.005Mn⁴⁺ was found to be 3 folds and 35 folds greater than Mg₃Al₂GeO₈: Mn⁴⁺ and Mg₃Ga₂GeO₈: Mn⁴⁺, respectively. The optimized Mg_{2.73}Ba_{0.27}Al₂GeO₈: 0.005Mn⁴⁺ phosphor showed an extensive choice of absorption features reaching from UV to blue and emitting intense red light maxima at 659 nm. This emission wavelength is well matching with the chlorophylls' absorption choice accountable for plants' photosynthesis, and accordingly could be effective for indoor plant cultivation.¹⁸ Moreover, the intense red emission with 100% colour purity of the optimized composition makes it a suitable red phosphor candidate to enhance the colour rendering and reduce the correlated colour temperature of the commercial phosphor-based white-LEDs.

2.3 Experimental

2.3.1 Material synthesis

The phosphors Mg₃Al_(2-4/3×0.005)GeO₈: 0.005Mn⁴⁺ (MAG: Mn⁴⁺), Mg₃Ga_(2-4/3×0.005)GeO₈: 0.005Mn⁴⁺ (MGG: Mn⁴⁺), and a series of Ba²⁺ substituted Mg_{3-x}Al_(2-4/3×0.005)GeO₈: 0.005Mn⁴⁺, xBa²⁺ (MAG: Mn⁴⁺, xBa²⁺) and Mg_{3-x}Ga_(2-4/3×0.005)GeO₈: 0.005Mn⁴⁺, xBa²⁺ (MGG: Mn⁴⁺, xBa²⁺) compositions were prepared via the solid-state synthesis method. MgO (99.99%), Ga₂O₃ (99.99%), Al₂O₃ (99.6%), GeO₄ (99.998%), MnO₂ (>99%), BaCO₃ (99.8%) and 0.25wt% H₃BO₃ (99.999%) are the raw materials (purchased from Sigma-Aldrich) used for synthesis. Required raw materials for the synthesis of different compositions are weighed and taken in a stoichiometric ratio. These raw materials were mixed with ethanol in an agate mortar and ground for 30 minutes. After drying, white powder was obtained and it is preheated in the air furnace at 600 °C for 2 h followed by sintering at 1300 °C for 6 h with intermediate grinding. 5 °C/min is the heating rate applied for calcination. After cooling the final powder is ground and used for further characterization.

2.3.2 Characterization

The crystal structures of the obtained samples were analyzed by collecting the X-ray powder diffraction (XRD) patterns using Malvern PANalytical B.V. EMPYREAN 3 diffractometer with Ni filtered Cu-K α radiation ($\lambda = 1.54 \text{ \AA}$). Rietveld refinement analysis was carried out using GSAS2 software. Micro-Raman spectroscopy was performed using ALPHA 300 R, WITec Spectra PRO Raman spectrometer using a laser power of 10 W. The X-ray photoelectron spectroscopy (XPS) analysis was accomplished with a PHI 5000 VersaProbe II

equipped with a micro-focused (200 μm , 15 kV) monochromatic Al-K α X-ray source (1486.6 eV). The structural properties were identified using a high-resolution transmission electron microscope (HR-TEM), JEOL JEM-F200. The morphology including elemental investigation of the prepared samples was examined using scanning electron microscopy (JEOL JSM-5600 LV SEM). The UV-Vis diffuse reflectance spectra (DRS) measurements were recorded using the Shimadzu UV-VIS-NIR spectrophotometer (UV 3600). The photoluminescence (PL) excitation, emission, quantum efficiency (QE) and lifetime were investigated using a Yvon Fluorolog 3 spectrofluorimeter having a 450 W Xenon irradiation source. The cathodoluminescence (CL) spectral analysis was performed by an Attolight Chronos CL-scanning electron microscope. The CL spectra were achieved with an achromatic reflective objective (numerical aperture 0.72) that delivers persistent recording capacity over a diameter field view of $\sim 150 \mu\text{m}$. The electron beam acceleration voltage and current were fixed to 6 kV, and 2 nA, respectively. The CL emission spectra were dispersed with a Horiba diffraction grating (150 grooves/mm) and taken with an Andor Newton charge-coupled device (CCD) camera (1024 \times 256 pixels, pixel width 26 μm). The resultant spectral dispersion was 0.53 nm/pixel.

For evaluating the device performances, the optimum red component was mixed with $\text{Y}_3\text{Al}_5\text{O}_{12}:\text{Ce}^{3+}$ (YAG: Ce^{3+}), and the mixture was incorporated with poly (methyl methacrylate) (PMMA; Sigma Aldrich). With the above mixture, acralyn cold-curing liquid (Asian Acrylates, India) was added during stirring to make a thick paste. The paste was then deposited on a 410 nm violet-blue InGaN LED, which functioned at 300 mA. The electroluminescence (EL) behaviours of the phosphor-LED system were recorded using a CCD spectrophotometer (Ocean Optics Maya 2000 Pro). Another WLED was fabricated by mixing the optimum red component with the commercial blue and green components in an appropriate ratio. The EL spectra for these WLED and red LEDs were measured using the same spectrophotometer with 280 nm LEDs at a 1A current.

2.4 Results and discussion

2.4.1 Elucidation of structural information

The XRD pattern of the inactivated $\text{Mg}_3\text{Al}_2\text{GeO}_8$ (MAG) has been Rietveld refined with three phases *viz.* orthorhombic- $\text{Mg}_3\text{Ga}_2\text{GeO}_8$ (o-MGG, space group *Imma*), orthorhombic Mg_2GeO_4 (o-MGO, space group *Pnma*), and cubic- MgAl_2O_4 (c-MAO, space group *Fd-3m*). The refinement pattern of this mixed phase composition is shown in **Fig.2.1 (a)**, where MAG,

an analogue of the orthorhombic $\text{Mg}_3\text{Ga}_2\text{GeO}_8$ phase (space group *Imma*) appears as the main phase. The refinement results are tabulated in supporting information (**Table 2.S1 and 2.S2**) and the corresponding crystal structure, drawn using *Vesta* software, is shown in **Fig.2.1 (c)**. The crystal assembly of the MAG phase consists of octahedral and tetrahedral units captured by the $\text{Mg}^{2+}/\text{Al}^{3+}$ ions and $\text{Ge}^{4+}/\text{Al}^{3+}$ ions, respectively. Here, Mn^{4+} ions preferentially occupy any of the three octahedrons provided by (Mg1/Al1), (Mg2/Al2), and (Mg3/Al3) sites, as shown in **Fig.2.1 (c)**, due to the strong ligand field stabilization energy of Mn^{4+} ions in the octahedral sites.^{19,20} Meanwhile, the Rietveld analysis of $\text{Mg}_3\text{Ga}_2\text{GeO}_8$ (MGG) indicated that this host is crystallized in the orthorhombic arrangement with the space group of *Imma* (**Fig.2.1 (b)**). A small fraction of impurity phase o-MGO is also observed in this structure. According to Ding and co-workers, the activator Mn^{4+} ions can reliably occupy the $[\text{MgO}_6]$ and $[\text{GaO}_6]$ octahedrons rather than the $[\text{GeO}_4]$ or $[\text{GaO}_4]$ tetrahedrons in this host.¹¹

The calculated lattice parameters of MAG and MGG samples are listed in **Table 2.S1** and the obtained metal-oxygen bond lengths for their structures are presented in **Table 2.S4**. The lower value of the lattice volume of MAG host (534.06 \AA^3) in comparison with that of MGG (569.13 \AA^3) can be attributed to the smaller ionic radii of Al^{3+} ($r_{\text{AlO}_6} = 0.53 \text{ \AA}$) ions compared to Ga^{3+} ($r_{\text{GaO}_6} = 0.62 \text{ \AA}$) ions in the subsequent octahedral coordination. The $[(\text{Mg}/\text{Al})\text{O}_6]$ octahedrons and $[\text{AlO}_4]$ tetrahedrons in the MAG sample are found to be more contracted and distorted relative to the $[(\text{Mg}/\text{Ga})\text{O}_6]$ octahedrons and $[\text{GaO}_4]$ tetrahedrons in the MGG sample, as can be seen in **Fig.2.1 (d)** and **(e)**, respectively.¹⁵ Such contraction can be ascribed to the smaller Al-O bond lengths of the MAG compared to the Ga-O bond lengths in the MGG (**Table 2.S4**). Similar kinds of lattice volume reduction and bond length contraction are reported previously for the $\text{Ca}_3\text{Ga}_2\text{Ge}_3\text{O}_{12}$ and $\text{LiGaGe}_2\text{O}_6$ hosts due to Al substitution in Ga sites.^{21,22}

The high-resolution microscopic analysis was also carried out for the samples MAG and MGG to verify the presence of different phases present in both samples by identifying the interplanar spacing of adjacent lattice fringes. **Fig.2.2 (a)** and **(b)** depicted the HRTEM images of MAG and MGG host matrices, respectively. **Fig.2.2 (a-i)** presents the magnified version of a region of the HRTEM image of MAG. The interplanar distance of the fringe pattern of this section is calculated to be 2.56 \AA , which is attributed to the (1 3 2) lattice planes of the orthorhombic-MGG phase (JCPDS 039-1108). Likewise, the other two insets **Fig.2.2 (a-ii)** and

Fig.2.2 (a-iii), depicted the two different regions of the HRTEM image of MAG. The interplanar distances of the fringe arrangements in these two magnified regions are calculated to be 2.88 Å and 3.06 Å, respectively, which are corresponding to the (2 2 0) and (2 1 1) planes of the cubic-MAO (JCPDS 086-0096) and orthorhombic-MGO (JCPDS 078-2316) phases, respectively. However, only one existing phase has been identified in the HRTEM image of the MGG host, in which the interplanar distances of 2.67 Å and 4.77 Å (**Fig.2.2 (b-i)** and **Fig. 2.2 (b-ii)**, respectively) correspond to the (2 1 1) and (1 0 1) planes of the orthorhombic-MGG phase (JCPDS 039-1108).

Existence of all the major elements in the MAG: Mn⁴⁺ sample including Mg, Al, Ge, O, and Mn⁴⁺ are confirmed from the XPS survey spectra, as revealed in **Fig.2.S1 (a)**. The EDX spectra (**Fig.2.S1 (b)**) and elemental mapping (**Fig.2.S1 (c)**) further confirmed the existence of the above elements with stoichiometric homogeneity. Meanwhile, the SEM images of MAG: Mn⁴⁺, shown in **Fig.2.S1 (c)**, exhibited irregular granular morphology and the sizes is in the micron range. The XPS and EDX results of the MGG: Mn⁴⁺ sample are also presented in the supporting information (**Fig.2.S2**).

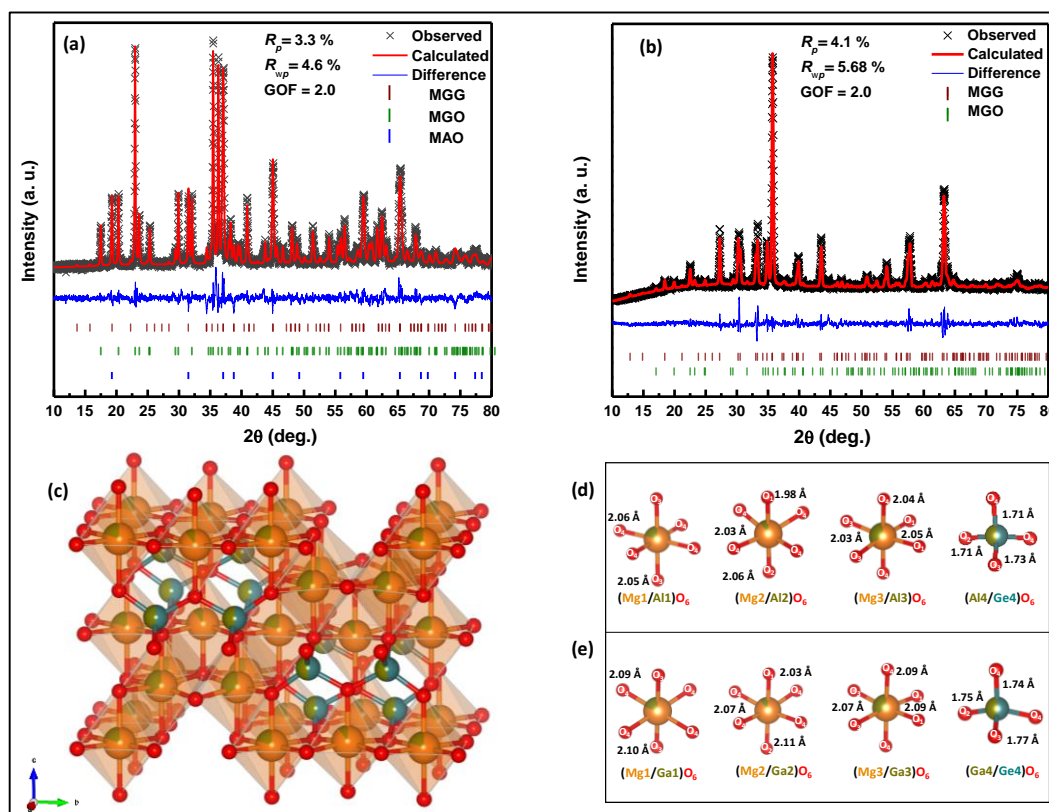


Fig.2.1 Rietveld refinement patterns of (a) MAG) (b) MGG. (c) Representation of an orthorhombic crystal arrangement for Mg₃M₂GeO₈ (M = Al, Ga) with the corresponding polyhedrons of (d) MAG and (e) MGG.

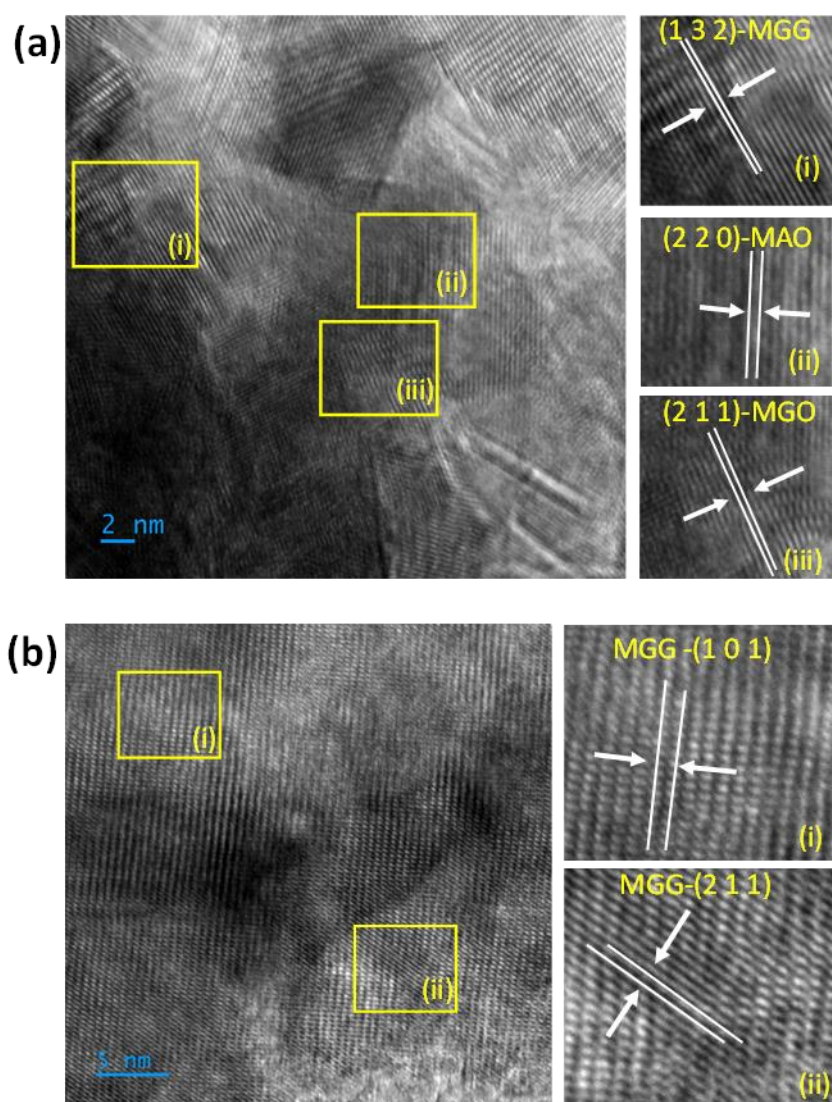


Fig.2.2 HRTEM images of **(a)** MAG sample with a magnified version of three different regions denoted as (i) (ii) and (iii), and **(b)** MGG sample with a magnified version of two different regions denoted as (i) and (ii).

2.4.2 Effect of Ba^{2+} doping in the crystal structure of $\text{Mg}_3\text{M}_2\text{GeO}_8$ ($\text{M} = \text{Al}, \text{Ga}$)

The recorded XRD patterns of $\text{MAG}: 0.005\text{Mn}^{4+}$ and $\text{MGG}: 0.005\text{Mn}^{4+}$ samples including their structural parameters cannot be differentiated from the respective patterns and parameters of MAG and MGG samples. Because of this reason, the Rietveld refinement analysis of $\text{MAG}: 0.005\text{Mn}^{4+}$ and $\text{MGG}: 0.005\text{Mn}^{4+}$ samples are not included. However, to realize the effect of cationic substitution by larger-sized Ba^{2+} ions ($r_{\text{BaO}_6} = 1.35 \text{ \AA}$) on the crystal structure of $\text{Mg}_3\text{M}_2\text{GeO}_8$ ($\text{M} = \text{Al}, \text{Ga}$), the Rietveld refinement analysis of $\text{MAG}: \text{Mn}^{4+}$,

0.03Ba²⁺ and MGG: Mn⁴⁺, 0.1Ba²⁺ samples are carried out and the resultant plots are given in **Fig.2.3 (a)** and **Fig.2.3 (b)**, respectively. The XRD pattern of the MAG: Mn⁴⁺, 0.03Ba²⁺ has been Rietveld refined using four reference phases *viz.* o-MGG, o-MGO, c-MAO and tetragonal-Ba₂MgGe₂O₇ (t-BMG, space group *P-421m*) whereas the refinement of MGG: Mn⁴⁺, 0.1Ba²⁺ has been carried out with three phases *viz.* o-MGG, o-MGO and t-BMG. The calculated refinement parameters are tabulated in **Table 2.S1** and **Table 2.S3** of the supporting information. Due to the doping of 0.03Ba²⁺ in MAG: Mn⁴⁺ sample, the cell volume is observed to be increased from 534.06 Å³ to 540.17 Å³ (**Table 2.S1**). The values of the estimated metal-oxygen bond lengths are also listed in **Table 2.S4** of the supporting information. Eventually, the increment in the metal-oxygen bond lengths (**Table 2.S4**) in the various octahedral coordination are supporting the above cell volume extension after Ba²⁺ ions' incorporation in MAG: Mn⁴⁺ sample. Such probable expansion due to the Ba²⁺ ions' substitution in the various [(Mg/Al)O₆] octahedral sites has been elaborated schematically in **Fig.2.3 (c)**. Among the different octahedral coordination, the volume enhancement of [(Mg1/Al1)O₆] sites is comparatively higher after Ba²⁺ ions' doping (**Table 2.S4**). This might be due to the more suitability of the (Mg1/Al1) sites for the larger-sized Ba²⁺ ions' occupation.²³

Meanwhile, the changes in [(Mg/Al)-O] bond lengths are also indicating that the incorporation of larger Ba²⁺ ions caused structural distortion in the symmetry of [(Mg/Al)O₆] octahedrons. Slight variation in the bond lengths of adjacent [(Al/Ge)O₄] tetrahedrons has also been observed (**Fig.2.3 (d)**). In the case of the MGG: Mn⁴⁺, 0.1 Ba²⁺ sample, the Ba²⁺ ions' substitution in the [(Mg/Ga)O₆] octahedral sites caused an increase in cell volume from 569.13 to 580.46 Å³ and similar type of changes in the metal-oxygen bond lengths, as depicted schematically in **Fig.2.3 (d)**. The detailed structural parameters evaluated for MGG: Mn⁴⁺, 0.1 Ba²⁺ sample are supplemented in **Table 2.S1**, **Table 2.S3** and **Table 2.S4**.

The XRD plots of a series of MAG: Mn⁴⁺, xBa²⁺ (x = 0.0 to 0.3) samples are presented in **Fig.2.4 (a)**. As can be seen from **Fig.2.4 (a)**, the XRD patterns of MAG: Mn⁴⁺, xBa²⁺ are not much altered below a certain amount of Ba²⁺ concentration (x < 0.1). With the further increase in Ba²⁺ ions' concentration to x = 0.1 and above, the XRD peaks of Mg impurity phase o-MGO (at 2θ = 22.6 ° and 35.1 °) and o-MGG (at 2θ = 36 °) are observed to be decreased gradually. Eventually, a new peak at 2θ = 28.7 ° attributed to t-BMG,^{24,25} is generated with the Ba²⁺ doping, which becomes prominent when the Ba²⁺ ions' concentration reached to x = 0.10. According to Ozturk, the major structure can be able to tolerate the size mismatch between

Ba²⁺ and Mg²⁺ up to a certain limit of Ba²⁺ substitution into the Mg²⁺ sites.²⁶ Hence, at higher Ba²⁺ ionic concentrations ($x > 0.1$), the substitution of Ba²⁺ ions in Mg²⁺ sites becomes ineffective owing to the large dissimilarity in the ionic radii of Mg²⁺ ($r_{MgO_6} = 0.72\text{\AA}$) and Ba²⁺ ($r_{BaO_6} = 1.35\text{\AA}$) in their octahedral coordination.²⁷ Because of this reason, a new Ba compound phase (t-BMG) has been generated.^{24, 25}

The t-BMG phase consists of [MgO₄] tetrahedrons, [Ge₂O₇] double tetrahedrons, and [BaO₈] dodecahedrons.²⁵ The higher concentration of Ba²⁺ ions could form more [BaO₈] dodecahedrons and utilized Mg²⁺ and Ge⁴⁺ ions from the respective octahedral and tetrahedral sites belonging to MGG and MGO phases for the formation of the t-BMG phase. Because of this reason might be, the MGG and MGO phases are suppressed significantly at higher Ba²⁺ concentrations. The newly generated t-BMG might also cause severe structural distortion in the host. To confirm the above prediction, the identified impurity phases such as o-MGO and t-BMG samples have been chosen and synthesized further via the solid-state method, and their XRD patterns are illustrated in **Fig.2.4 (b)** along with the XRD of MAG: Mn⁴⁺, xBa²⁺ ($x = 0.1$ and 0.27) samples. From **Fig.2.4 (b)**, the existence of both o-MGO and t-BMG phases in MAG: Mn⁴⁺, 0.1Ba²⁺ samples can be easily identified by the corresponding JCPDS data included in the figure. Moreover, a higher amount of Ba²⁺ ions' doping (MAG: Mn⁴⁺, 0.27Ba²⁺) led to intensified XRD peaks of the t-BMG phase, while the main XRD peaks of MGO and MGG phases decreased significantly. The XRD analysis has also been carried out for a series of MGG: Mn⁴⁺, xBa²⁺ ($x = 0.0$ to 0.15), which are given in **Fig.2.S3** of the supporting information. Here also the same impurity phase t-BMG is identified to be prominent at the higher doping concentration of Ba²⁺ ions (**Fig.2.S3**).

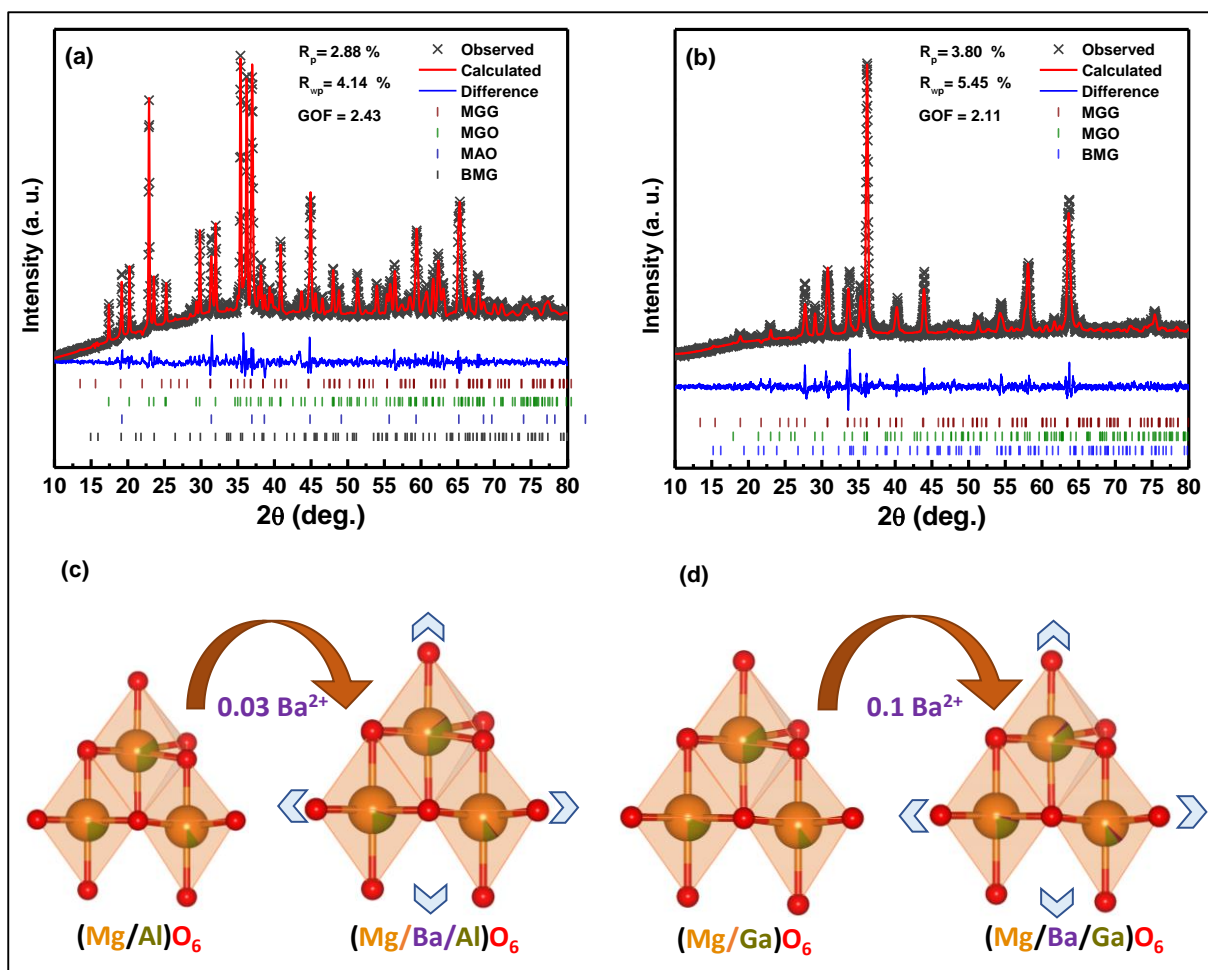


Fig.2.3 Refinement patterns of (a) MAG: Mn^{4+} , 0.03 Ba^{2+} and (b) MGG: Mn^{4+} , 0.10 Ba^{2+} . Schematic representation of variation in the octahedrons of (c) MAG and (d) MGG after Ba^{2+} incorporation.

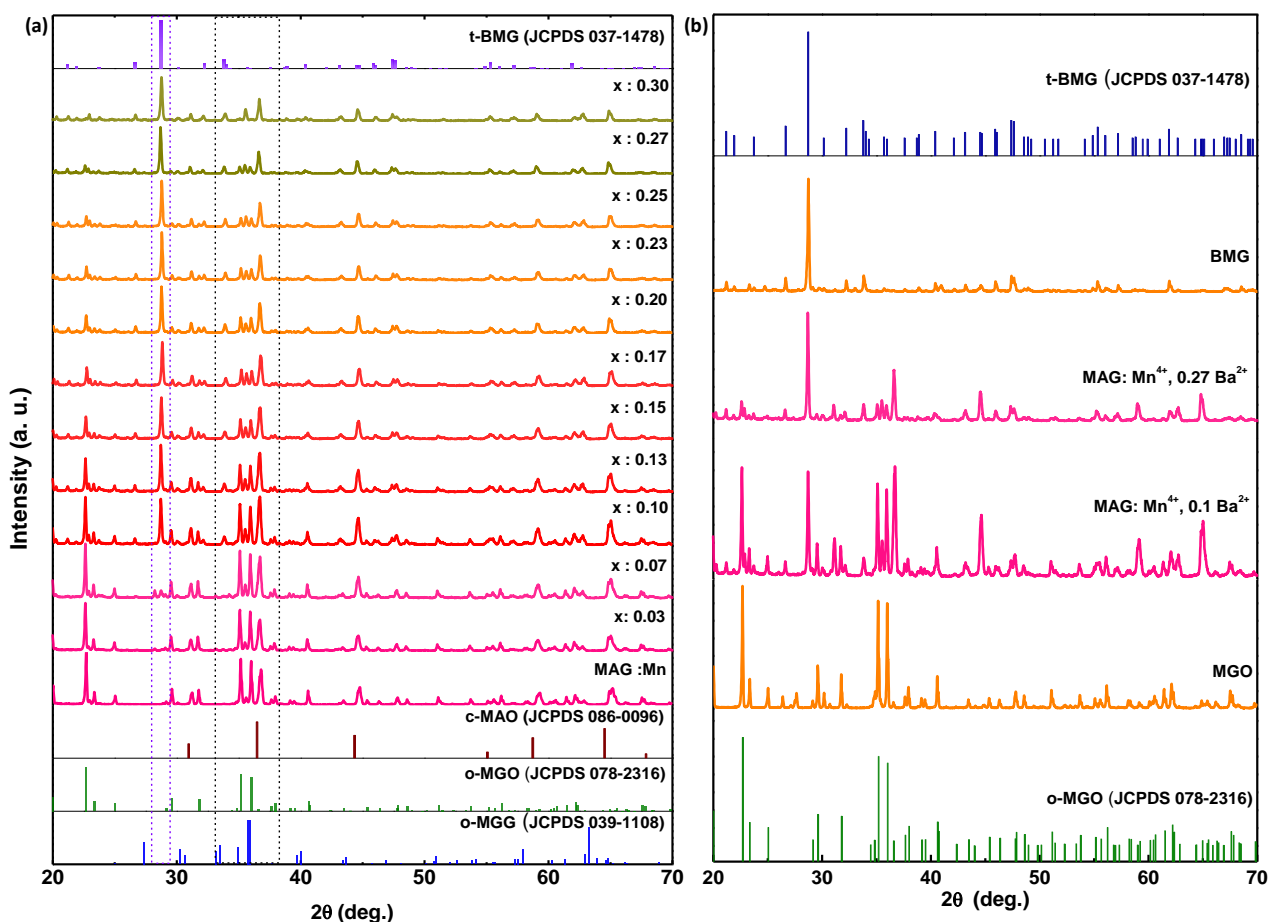


Fig.2.4 (a) XRD patterns of MAG: Mn⁴⁺, xBa²⁺ (x = 0.0 to 0.3) samples. **(b)** XRD patterns of synthesized MGO: Mn⁴⁺, BMG: Mn⁴⁺, MAG: Mn⁴⁺, 0.1Ba²⁺ and MAG: Mn⁴⁺, 0.27Ba²⁺ with corresponding JCPDS.

The change in the microstructure of MAG: Mn⁴⁺ due to the Ba²⁺ ions' incorporation could also be realized from the Raman analyses of MAG: Mn⁴⁺ and MAG: Mn⁴⁺, xBa²⁺ (x = 0.03, 0.27) samples. In the obtained Raman spectra of the above samples, as illustrated in **Fig. 2.5 (a)**, the main band that appeared at ~645 cm⁻¹ can be attributed to the stretching vibration of [Al-O] bonds corresponding to [AlO₆] octahedrons.²⁸ Meanwhile, the band at around 358 cm⁻¹ could be attributed to the stretching vibrations of [MgO₆] octahedrons.²⁹ The stretching vibrations corresponding to the above octahedrons become stronger in Ba²⁺ co-doped MAG: Mn⁴⁺, xBa²⁺ (x = 0.03, 0.27) samples. This might be because of the reduced symmetry of structurally distorted [(Mg/Al)O₆] octahedrons and increased [(Mg/Al)-O] bond lengths due to Ba²⁺ co-doping as discussed in the XRD analysis of MAG: Mn⁴⁺ and MAG: Mn⁴⁺, 0.03Ba²⁺ samples previously.²⁰ The average [(Mg/Al)-O] bond lengths are calculated to be 2.039 Å and

2.047 Å for MAG: Mn⁴⁺ and MAG: Mn⁴⁺, 0.03Ba²⁺ samples, respectively (**Table 2.S4**). Wang *et al.*²⁰ also reported a similar kind of larger ionic substitution in Ca₂MgWO₆ which resulted in increased [W-O] bond lengths of [WO₆] octahedrons. The stretching vibration corresponds to the [WO₆] octahedrons reportedly becoming stronger due to the above substitution as visible in the present case also. The other peaks in **Fig. 2.5 (a)** located around 450 cm⁻¹,³⁰ 793 cm⁻¹,³¹ and 813 cm⁻¹³² can be assigned to the stretching vibration of [GeO₄] tetrahedrons and the peak at ~830 cm⁻¹³³ can be attributed to the stretching vibration of [AlO₄] tetrahedrons.

Fig.2.5 (b) presents the XPS survey spectrum of MAG: Mn⁴⁺, 0.27Ba²⁺, which confirmed the peaks of Ba, Mg, Al, Ge, O, and Mn exactly where they were predicted to be. The Mg 2p core spectrum of MAG: Mn⁴⁺ is deconvoluted into two peaks at 49.86 eV and 51.37 eV (**Fig.2.5 (b): (i)**). The higher binding energy peak (51.37 eV) corresponds to Mg²⁺ ions has disappeared in MAG: Mn⁴⁺, 0.27Ba²⁺ (**Fig.2.5 (b): (ii)**), indicating that Ba²⁺ might have created some structural distortion in the Mg²⁺ sites. The core-level spectra of O 1s for the samples MAG: Mn⁴⁺ and MAG: Mn⁴⁺, 0.27Ba²⁺ are deconvoluted into O₁ (lattice oxygen) and O₂ (surface oxygen), which are positioned at 531 and 532.8 eV (**Fig.2.5 (b): (iii) and (iv)**). The content of surface oxygen (O₂) in MAG: Mn⁴⁺, 0.27Ba²⁺ is reduced compared to that in MAG: Mn⁴⁺. Moreover, the lattice oxygen content (O₁) is found to be higher in MAG: Mn⁴⁺, 0.27 Ba²⁺ sample compared to MAG: Mn⁴⁺.

The formation t-BMG phase at a higher concentration (x > 0.1 mol) of Ba²⁺ ions might be responsible for the conversion of more non-lattice oxygen to lattice oxygen for the formation of Ba-O bonds. The enhanced lattice oxygen (O₁) content for MAG: Mn⁴⁺, 0.27Ba²⁺ sample might help to create additional octahedral sites for occupying Mn⁴⁺ ions. Moreover, due to higher lattice oxygen content, the structural stability should be increased.⁸ The enhanced structural stability and octahedral sites due to the Ba²⁺ ions' substitution could be effective to intensify Mn⁴⁺ ions' emission.¹⁶ The XPS spectra of MGG: Mn⁴⁺, xBa²⁺ (x = 0.0, 0.13) are shown in **Fig.2.S4**. In this case also, reduction of Mg²⁺ content is observed because of Ba²⁺ inclusion (**Fig.2.S4 (i) and (ii)**). Meanwhile, the substitution of Ba²⁺ ions in the Mg²⁺ sites led to a substantial reduction in surface oxygen peak (O₂) with the coinciding increase in lattice oxygen peak (O₁) is observed (**Fig.2.S4 (iii) and (iv)**).

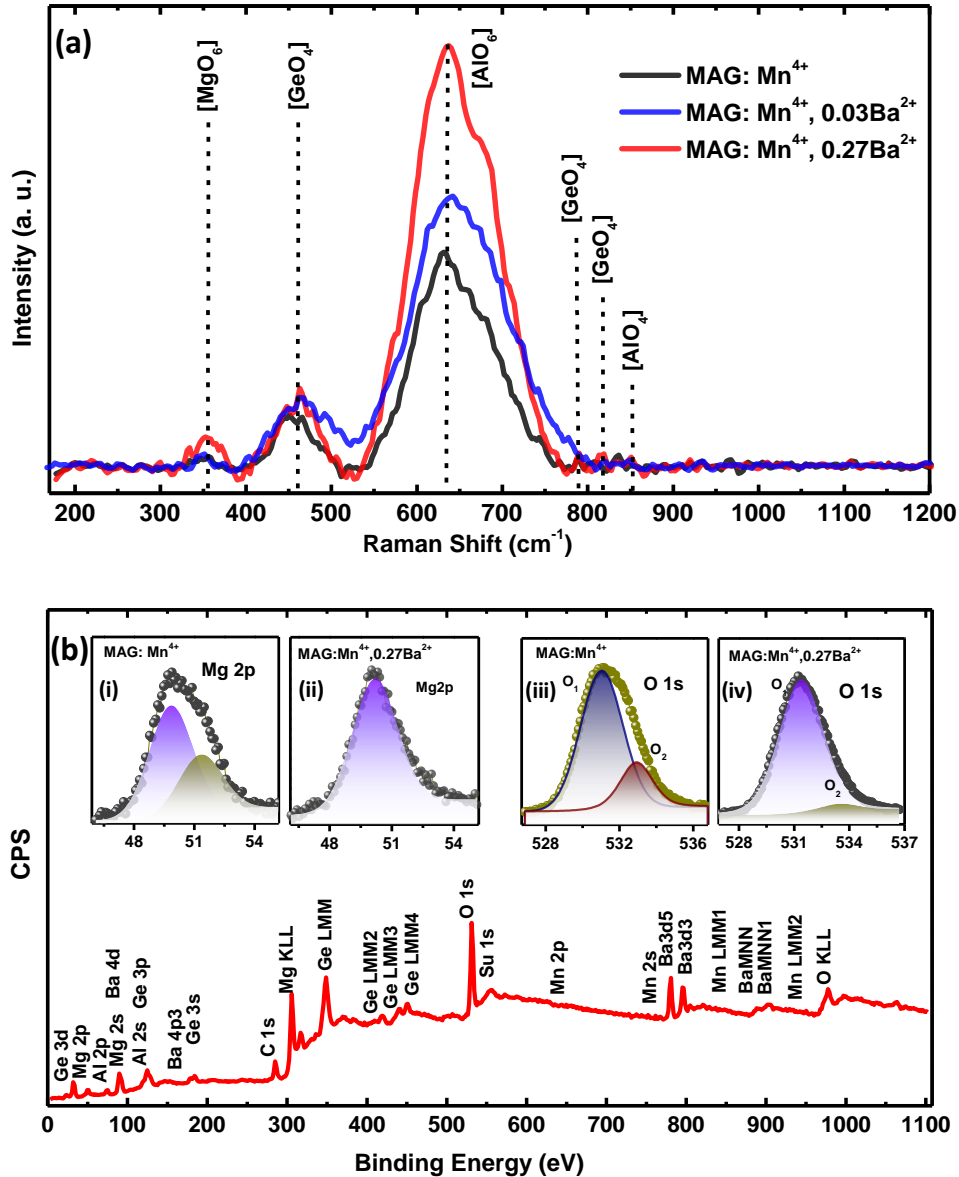


Fig.2.5 (a) Raman spectra of MAG: Mn⁴⁺ and MAG: Mn⁴⁺, xBa²⁺ (x = 0.03, 0.27) samples. **(b)** XPS survey spectrum of the sample MAG: Mn⁴⁺, 0.27Ba²⁺. Inset figures show the XPS core-level spectra of Mg 2p and O 1s for the samples MAG: Mn⁴⁺ and MAG: Mn⁴⁺, 0.27Ba²⁺.

2.4.3 UV-Vis absorption, photoluminescence and cathodoluminescence properties of (Mg, Ba)₃M₂GeO₈: Mn⁴⁺ (M = Al, Ga)

The UV-DRS spectra of undoped MAG, MAG: Mn⁴⁺, and MAG: Mn⁴⁺, 0.27Ba²⁺ samples are shown in **Fig.2.6 (a)**. The MAG host has shown optical absorption at ~250 nm owing to the host absorption ((i) of **Fig.2.6 (a)**).³⁴ In the MAG: Mn⁴⁺ and MAG: Mn⁴⁺, 0.27Ba²⁺ samples, the absorption peak at 250 nm becomes more prominent owing to the overlapping of the O²⁻- Mn⁴⁺ charge transfer band (CTB) and the host absorption. In addition,

two more absorption deeps are observed at ~300 nm and 421 nm because of the ${}^4A_{2g} \rightarrow {}^4T_{1g}$ and ${}^4A_{2g} \rightarrow {}^4T_{2g}$ transitions of Mn^{4+} ions ((ii) and (iii) of Fig.2.6 (a)). Eventually, the mentioned Mn^{4+} absorption peaks are intensified owing to the Ba^{2+} co-doping in MAG: Mn^{4+} sample (Fig.2.6 (a)). The band gap values obtained for MAG, MAG: Mn^{4+} and MAG: Mn^{4+} , $0.27Ba^{2+}$ samples are calculated via using the Tauc plots³⁵ (Fig.2.6 (b)), and the resultant values are 5.97 eV, 5.91 eV, and 5.67 eV, respectively. Because of the lower electronegativity of Mn^{4+} ions than Al^{3+} ions, the required energy for the band-to-band transitions is reduced after Mn^{4+} doping. The band gap energy further decreased in MAG: Mn^{4+} , $0.27Ba^{2+}$ might be due to the lower electronegativity of Ba^{2+} ions than Mn^{4+} and Al^{3+} ions.³⁶

The UV-Vis DRS spectra of MGG and MGG: Mn^{4+} , xBa^{2+} ($x = 0.0, 0.13$) samples are also analysed as supporting evidence (Fig.2.S5 of the supporting information). Broad absorption bands are observed in the UV and blue regions for the MGG: Mn^{4+} and MGG: Mn^{4+} , $0.13Ba^{2+}$ samples. The absorption is higher in the case of MGG: Mn^{4+} , $0.13Ba^{2+}$ sample for all transitions. The obtained bandgap values for MGG, MGG: Mn^{4+} and MGG: Mn^{4+} , $0.13Ba^{2+}$ samples (5.0, 4.96, and 4.89 eV, respectively) followed a similar trade with undoped and doped MAG compositions. It is worth mentioning that Mn^{4+} ions are having strong ligand field stabilization energy in the octahedral sites.^{19,37} In the MAG host, both Mg^{2+} and Al^{3+} ions are providing the octahedral sites for Mn^{4+} ions due to matching ionic radii. Also, some of the Mn^{4+} ions can occupy $[MgO_6]$ and $[AlO_6]$ octahedrons provided by the o-MGO and c-MAO phases,³⁸ respectively, which could elevate the Mn^{4+} emission.

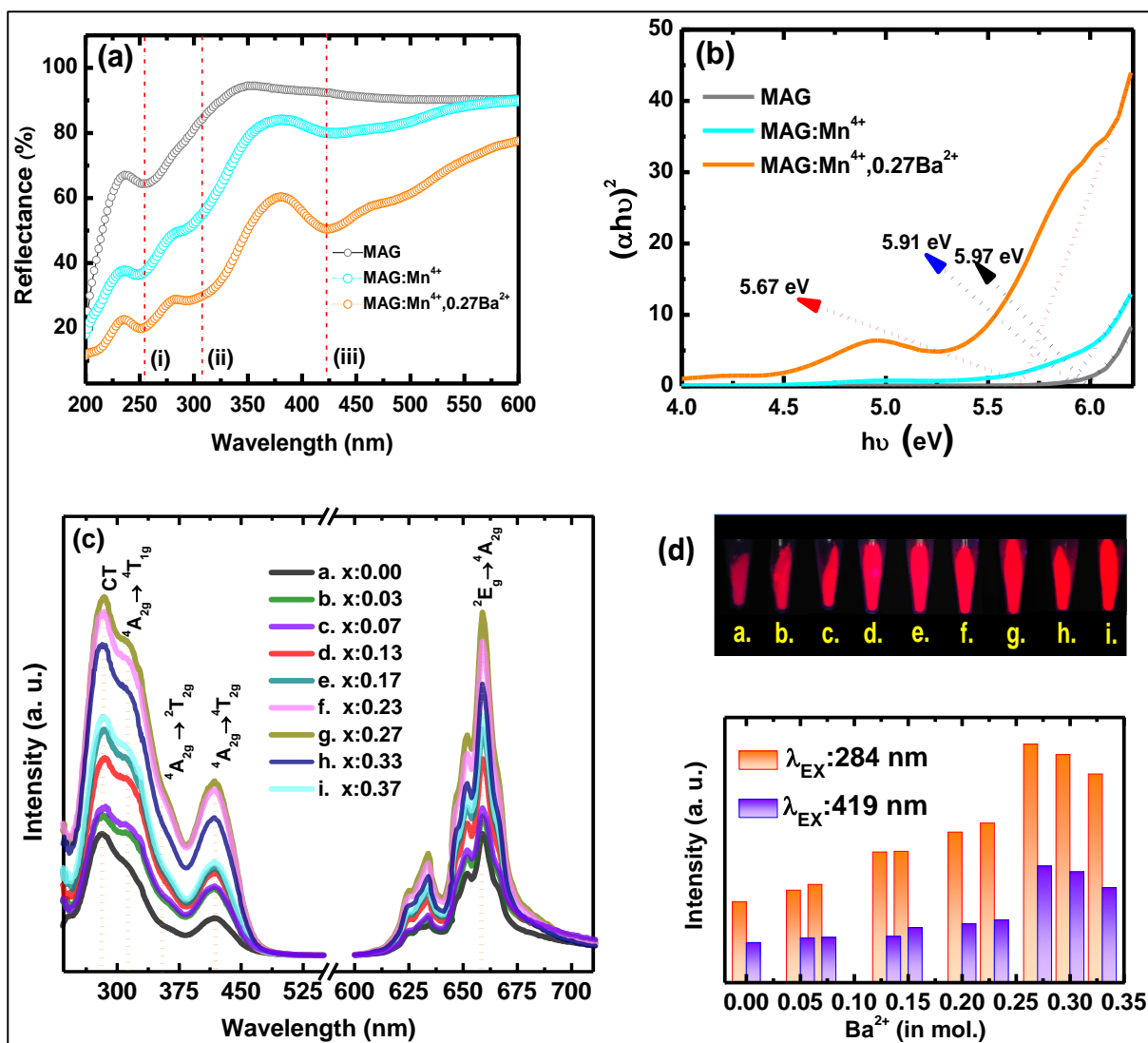


Fig.2.6 (a) UV-DRS spectra of MAG and MAG: Mn⁴⁺, xBa²⁺ (x = 0.0 and 0.27), (i) Overlapping of the host absorption and the Mn⁴⁺-O²⁻ CTB (ii) $^4A_{2g} \rightarrow ^4T_{1g}$, and (iii) $^4A_{2g} \rightarrow ^4T_{2g}$ transitions. (b) Tauc's plots for bandgap calculation (c) PLE (λ_{EM} : 659 nm) and PL emission spectra (λ_{EX} : 284 nm) of MAG: Mn⁴⁺, xBa²⁺ (x = 0.0 to 0.37). (d) Corresponding PL images under UV excitation and bar diagram showing the variation of PL intensity with Ba²⁺ concentration under UV and blue excitation.

The photoluminescence excitation (PLE, λ_{em} : 659 nm) and emission (λ_{ex} : 284 nm) spectra of MAG: Mn⁴⁺, xBa²⁺ (x = 0.0 to 0.37) samples are shown in **Fig.2.6** (c). The PLE spectrum of all these samples exhibits broad excitation bands having peaks at 284 nm and 419 nm. The excitation band ranging from 230 to 380 nm which is identical to the UV chips, can be ascribed to Mn⁴⁺-O²⁻ CTB and $^4A_{2g} \rightarrow ^4T_{1g}$, $^2T_{2g}$ transitions of Mn⁴⁺ (as assigned in **Fig.2.6** (c)). The excitation band in the blue region (380 to 480 nm) is well-fitted with the commercial

blue-chip, which can be attributed to the spin-allowed ${}^4A_{2g} \rightarrow {}^4T_{2g}$ transition of Mn^{4+} ions.¹⁶ A slight redshift appeared in the spectra due to the addition of Ba^{2+} in the MAG: Mn^{4+} since Ba^{2+} incorporation increases the bond length between the Mn^{4+} and the ligands, thereby decreasing the energy of the $Mn^{4+}-O^{2-}$ CTB.³⁹ Further, PL spectra for each sample resulted in a sharp emission peak at 659 nm due to the ${}^2E_g \rightarrow {}^4A_{2g}$ transition and the other weak emissions arise due to vibrational sidebands.⁴⁰ The emission intensity of the phosphors gets increased due to partial Ba^{2+} ions' substitutions and maximized at $xBa^{2+} = 0.27$ mol, which is 3 folds greater than that of the MAG: Mn^{4+} sample. The external quantum efficiency (EQE) value obtained for MAG: Mn^{4+} sample is 29.44%, however, it is calculated to be 49.35% for MAG: Mn^{4+} , $0.27Ba^{2+}$ sample. Further, increase in Ba^{2+} ions' concentration quenched the PL intensity. The variations in the emission intensity as a function of Ba^{2+} ions' concentrations can be understood via the PL images of these samples (**Fig.2.6 (d)**), which are arranged in the increasing order of Ba^{2+} content.

The possible reasons for the red emission enhancement due to the Ba^{2+} ions' incorporation can be explained using three different aspects as follows: (i) structural distortion occurred in MAG: Mn^{4+} sample due to larger-sized Ba^{2+} ionic substitution and contribution of luminescent centres provided by the newly generated barium phase, (ii) increase in the particle sizes of MAG: Mn^{4+} sample due to the inclusion of Ba^{2+} ions, and (iii) replacement of $Mn^{4+}-Mn^{4+}$ pairs by the $Ba^{2+}-Mn^{4+}$ pairs in Ba^{2+} co-doped samples.

(i) The most probable reason for the enhanced red emission intensity could be the structural distortion occurred due to the Ba^{2+} ions' substitution in MAG: Mn^{4+} sample. At the lower Ba^{2+} - doping concentrations ($<0.1 Ba^{2+}$), smaller Mg^{2+} ions might be substituted by larger Ba^{2+} ions, which resulted in a distorted lattice, as explained during interpreting the XRD results. Such lattice distortion, created due to the substitution of larger Ba^{2+} ions, possibly further reduced the site symmetry of $[(Mg/Al)O_6]$ octahedrons which are preferably accommodating Mn^{4+} ions and thereby enhanced the red emission.^{14-16,41-43} Since the 3d–3d forbidden transition probability of Mn^{4+} ions with the $3d^3$ configuration is largely determined by the local symmetry of $[MnO_6]$ octahedrons, the decrease of the octahedral symmetry usually leads to the relaxation of the selection rule of Mn^{4+} ions occupied at these octahedral sites. Similar results are reported by Wang *et al.*²⁰ Here the luminous intensity of $Ca_2MgWO_6: Mn^{4+}$ is reported to be increased by the larger cation pair ($Na^+ - La^{3+}$) substitution in Ca^{2+} sites. This substitution makes severe lattice distortion in the $[WO_6]$ sites (preferential for the Mn^{4+}

occupation) by changing the [W-O] bond length, which led to a higher emission. Recently, Wang and co-workers also introduced Ba²⁺ in the Mg²⁺ sites of the Mg₂Y₂Al₂Si₂O₁₂: Ce³⁺ for increasing its emission intensity.⁴⁴ Fang *et al.* reported enhanced Mn⁴⁺ emission by introducing larger K⁺ ions in the Ba²⁺ sites of BaTiF₆: Mn⁴⁺, which led to the increase of [Ba/K-F] bond lengths and distortion the [TiF₆] octahedral sites preferential for Mn⁴⁺ ions' occupation.⁴⁵

Meanwhile, after a certain amount of Ba²⁺ ions' doping (> 0.1Ba²⁺), a new phase tetragonal-Ba₂MgGe₂O₇ (t-BMG) has been observed in the Ba²⁺ co-doped MAG: Mn⁴⁺ samples. This newly generated phase might have supplied the additional luminescent centers for Mn⁴⁺ ions owing to which the emission of MAG: Mn⁴⁺, Ba²⁺ could be intensified further. Z. Lu *et al.*²⁴ have been reported the emission properties of Mn⁴⁺-doped t-BMG synthesized via the solid-state route. Herein, Mn⁴⁺ ions are reported to be substituted at the Ge⁴⁺ sites of t-BMG. The t-BMG crystal structure consists of [MgO₄] tetrahedrons, [Ge₂O₇] double tetrahedrons and [BaO₈] dodecahedrons.^{24,25} Substituting Mn⁴⁺ ions in the Ge⁴⁺ sites of t-BMG exhibited red emission at 660 nm due to the Mn⁴⁺: ²E_g → ⁴A_{2g} transitions.²⁴ The optimized composition Ba₂MgGe₂O₇: 0.013Mn⁴⁺, reported by Z. Lu *et al.*,²⁴ has been re-synthesized to confirm the reported red emission Mn⁴⁺ ions located at the Ge-tetrahedral sites. The PL emission spectrum of the Ba₂MgGe₂O₇: 0.013Mn⁴⁺ sample is supplemented in **Fig.2.S6**, of the supporting information. The PL emission spectrum of the UV irradiated Ba₂MgGe₂O₇: 0.013Mn⁴⁺ sample shows identical emission features as reported in ref.²⁴. Meanwhile, the peak position has been noted at 660 nm, which is well matching with that of MAG: Mn⁴⁺, xBa²⁺ (x = 0.0 to 0.3) samples. Since the structure of MAG: Mn⁴⁺, xBa²⁺ samples are containing the t-BMG phase, therefore, it can be predicted that the t-BMG phase could supply additional luminescent centres for intensifying the Mn⁴⁺ ions' emission. Peng *et al.* recently reported the enhancement in the PL intensity of the Sr₄Al₁₄O₂₅: Mn⁴⁺ sample due to the additional luminescent centres contributed by the supplementary phases such as SrAl₂O₄ and SrAl₁₂O₁₉.⁴⁶ However, some advanced studies are still required to establish this phenomenon.

(ii) The increase in phosphor particle size due to the Ba²⁺ ions' incorporation could be another probable reason for the observed PL enhancement in MAG: Mn⁴⁺, xBa²⁺ samples. To observe the effect of Ba²⁺ co-doping on the morphology, the SEM analyses are carried out for MAG: Mn⁴⁺ and MAG: Mn⁴⁺, 0.27Ba²⁺ samples (**Fig.2.S7**, supporting information). It is detected that because of the inclusion of Ba²⁺ ions, the particle sizes are found to be increased,

as can be seen in the SEM results of MAG: Mn⁴⁺ and MAG: Mn⁴⁺, 0.27Ba²⁺ samples (**Fig.2.S7**). Generally, the surface-associated defects are decreasing with the increase in particle size, which may also be able to reduce the non-radiative transitions, and enhance the emission subsequently.⁴⁷ Similar interpretations are reported recently, where the K⁺ ions' substitution in the Ba²⁺ sites of Ba₂TiF₆:Mn⁴⁺⁴⁵ and the Mg²⁺-doping at the Sr²⁺ sites of Sr₄Al₁₄O₂₅: Mn⁴⁺⁴⁶ enhanced the particle sizes as well as the PL intensity of the respective phosphors. In the present case, the precursor material BaCO₃ melted earlier (melting point ~811 °C) and might act as a flux throughout the sintering process thereby increasing the crystallinity and particle sizes.^{17,46} To reconfirm the effect of particle sizes of MAG: Mn⁴⁺, 0.27Ba²⁺ sample on its emission intensity, this sample was also synthesized at various sintering temperatures (700 °C, 900 °C, 1100 °C and 1300 °C). The corresponding SEM images and PL emission spectra are given in **Fig.2.S8** and **Fig.2.S9**, respectively, of supporting information, respectively. The PL intensity, as well as the particle sizes of the samples, were found to be increased with increasing annealing temperature.⁴⁷ The increase in PL emission intensity with the increase of particle size can be ascribed to the already explained reduction in non-radiative transition for the larger-sized particle.⁴⁷

(iii) To verify the role of Mn⁴⁺-Ba²⁺ pairs in enhancing the PL emission intensity in Ba²⁺ co-doped samples, PL emission decay lifetime measurements are also performed by monitoring the emission at 659 nm upon the UV excitation of 284 nm. The resultant PL decay curves for the samples MAG: Mn⁴⁺ and MAG: Mn⁴⁺, 0.27 Ba²⁺ are shown in **Fig.2.S10 (a)** of the supporting information. All the curves were well-fitted with a second-order exponential function and the average lifetime values are calculated by following the procedures reported elsewhere.^{11,46,48} Most importantly, the double exponential fitting indicates the presence of multiple luminescence centres in these hosts. The average lifetime values for MAG: Mn⁴⁺ and MAG: Mn⁴⁺, 0.27 Ba²⁺ are calculated to be 2.14 ms and 2.27 ms, respectively. The slightly higher emission lifetime value for MAG: Mn⁴⁺, 0.27Ba²⁺ is related to its brighter emission compared to that of MAG: Mn⁴⁺ sample.⁴⁶ This elongation of emission lifetime because of the Ba²⁺ ions' doping in MAG: Mn⁴⁺ sample might also indicate a possible reduction in the content of Mn⁴⁺-Mn⁴⁺ pairs due to the formation of Mn⁴⁺-Ba²⁺ pairs. Such newly formed Mn⁴⁺-Ba²⁺ pairs might reduce the non-radiative energy migration probabilities between two neighbouring Mn⁴⁺ ions by reducing the non-radiative depopulation in the ²E_g level of Mn⁴⁺ and thereby enhancing the PL emission intensity.^{46,49}

The photoluminescence of a series of MGG: Mn⁴⁺, xBa²⁺ (x = 0.0 to 0.15) samples is also recorded to confirm the effectiveness of larger ionic substitution to enhance the Mn⁴⁺ ions' emission, as shown in **Fig.2.S5 (c)** of the supporting information. Also, in this case, a similar kind of luminescence behaviour is observed with the Ba²⁺ ions' incorporation as seen in MAG: Mn⁴⁺, xBa²⁺ due to their isomorphic structure. The PL intensity is maximum when the Ba²⁺ concentration is 0.13 mol, which is 5 folds' greater than the emission intensity of MGG: Mn⁴⁺. The PL images captured as a function of various Ba²⁺ ions' concentrations are shown in the inset of **Fig.2.S5 (c)**. The XRD of MGG: Mn⁴⁺, xBa²⁺ (x = 0.0 to 0.15) samples, shown in **Fig.2.S3** of the supporting information, indicated an impurity phase of t-BMG due to Ba²⁺ ions' substitution which possibly helped to enhance the Mn⁴⁺ ions' emission in MGG: Mn⁴⁺, xBa²⁺ as in the case of MAG: Mn⁴⁺, xBa²⁺. The average lifetime values obtained (from **Fig.2.S10 (b)**) for MGG: Mn⁴⁺ and MGG: Mn⁴⁺, 0.13Ba²⁺ samples are 0.48 ms and 0.70 ms respectively. However, these values are much less than the lifetime values of the MAG: Mn⁴⁺, 0.27Ba²⁺ sample.^{46,49,50}

2.4.3.1 Comparative PL analysis

From the comparative photoluminescence emission spectra of MAG: Mn⁴⁺, xBa²⁺ (x = 0.0, 0.27) and MGG: Mn⁴⁺, xBa²⁺ (x = 0.0, 0.13) samples, shown in **Fig.2.7 (a)**, it has been observed that replacing Ga³⁺ by Al³⁺ enhanced the PL intensity by 13 folds. The PL intensity of MAG: Mn⁴⁺ has been further enhanced 3 times by the Ba²⁺ ions' substitution (**Fig.2.7 (b)**), which effectively created a more appropriate crystal environment for Mn⁴⁺ occupancy in the MAG host. The preferential sites for Mn⁴⁺ occupancy in MGG are [MgO₆] ($r_{MgO_6} = 0.72 \text{ \AA}$) and [GaO₆] ($r_{GaO_6} = 0.62 \text{ \AA}$), whereas that for MAG are [MgO₆] and [AlO₆] ($r_{AlO_6} = 0.535 \text{ \AA}$). However, the ionic size of Al³⁺ in MAG is more closely to that of Mn⁴⁺ ($r_{MnO_6} = 0.53 \text{ \AA}$) than that of Ga³⁺ in MGG, which indicates that [AlO₆] octahedrons could be more favourable than [GaO₆] for Mn⁴⁺ ions' occupancy. To know the site suitability, a parameter known as the effective compensating factor ($\varphi = z/r$) can be employed in octahedral surroundings, where z and r are the charge and radius of an ion located in that octahedron. The z/r ratio of Mg²⁺, Ga³⁺, Al³⁺ and Mn⁴⁺ in octahedral sites are 2.77, 4.84, 5.607, and 7.547, respectively.⁵¹ From these values, it is well clear that the z/r ratio of Al³⁺ is closer to Mn⁴⁺ in comparison with other sites. Hence MAG is expected to provide more suitable [AlO₆] sites for Mn⁴⁺ ions leading to greater intensity of MAG: Mn⁴⁺. Some Mn⁴⁺ ions could replace divalent Mg²⁺ ions at [MgO₆]

octahedrons because of which Mn^{4+} valance could reduce to Mn^{2+} valance to account for the charge compensation.

However, the more preferential $[\text{AlO}_6]$ sites in MAG efficiently reduce the probability of Mn^{4+} ions' occupancy in $[\text{MgO}_6]$ sites. Hence the natural reduction probability of Mn^{4+} to Mn^{2+} for charge compensation is lesser in the MAG host compared to the MGG host will be less. This prediction is also supported by the cathodoluminescence studies (discussed later in this paper) for the first time for any Mn^{4+} activated samples.

In addition to the ionic similarities, the detailed XRD and HRTEM analysis of the MAG sample confirmed the presence of the co-existing phases such as o-MGO and c-MAO. The intense red emission identified in the MAG: Mn^{4+} might be due to the additional luminescence centres of Mn^{4+} ions provided by the above co-existing phases. Xue *et al.* synthesized $\text{Mg}_2\text{GeO}_4: 0.001\text{Mn}^{4+}$ sample through the high-temperature solid-state method and observed deep red emission peaking at 659 nm due to the Mn^{4+} ions occupancy in the $[\text{MgO}_6]$ sites.³⁸ The emission spectrum of the UV irradiated $\text{Mg}_2\text{GeO}_4: \text{Mn}^{4+}$ sample, which was synthesized via adopting the method as reported by Xue *et al.*, is shown in **Fig.2.S6** of the supporting information.

Another co-existing phase observed in the MAG host is c-MAO, which is also containing octahedral coordination for accommodating Mn^{4+} ions. Wang *et al.* described the luminescence performance of the $\text{MgAl}_2\text{O}_4: \text{Mn}^{4+}$ sample prepared via the molten salt method.⁵² According to this report, Mn^{4+} ions are occupying the $[\text{AlO}_6]$ octahedrons and producing deep red emission at 651 nm. Analogous emission properties of $\text{MgAl}_2\text{O}_4: \text{Mn}^{4+}$ prepared through the co-precipitation method are also reported by Ji *et al.*⁴⁰ Nonetheless, no report so far illustrated the photoluminescence of the $\text{MgAl}_2\text{O}_4: \text{Mn}^{4+}$ sample prepared via the high-temperature solid-state route. Therefore, we have synthesized $\text{MgAl}_2\text{O}_4: \text{Mn}^{4+}$ through the solid-state method at a sintering temperature of 1300 °C. However, the solid-state synthesized sample have not showed any Mn^{4+} ions' emission. In the present case, the MgAl_2O_4 phase probably acted as a flux and helped in enhancing the red emission intensity by improving the crystallinity. Recently, various literatures have been published by studying the advantages of co-existing phases on the red emission enhancement of Mn^{4+} -activated oxide phosphors. For example, Wu *et al.* improved the emission intensity of $\text{CaAl}_{12}\text{O}_{19}: \text{Mn}^{4+}$ by introducing co-

existing MgAl_2O_4 phase as a flux.¹⁷ Similarly, Gu *et al.* also reported the advantages of co-existing non-luminescent MgAl_2O_4 phase on the increased red emission intensity of $\text{SrMgAl}_{10-y}\text{Ga}_y\text{O}_{17}:\text{Mn}^{4+}$.⁵³ Meanwhile the co-existing phases SrAl_2O_4 and $\text{SrAl}_{12}\text{O}_{19}$ are reported to be helpful for improvising the emission intensity of $\text{Sr}_4\text{Al}_{14}\text{O}_{25}:\text{Mn}^{4+}$.⁴⁶

The average [Al-O] bond length (2.06 Å) in the octahedral sites of $\text{MAG}:\text{Mn}^{4+}$ is found to be less than the average [Ga-O] bond length in the octahedral sites of $\text{MGG}:\text{Mn}^{4+}$ (2.08 Å). These structural changes may also be the root for the higher red emission of $\text{MAG}:\text{Mn}^{4+}$ compared to $\text{MGG}:\text{Mn}^{4+}$.¹⁵ The digital PL images, the plots of emission intensity and colour purity for $\text{MGG}:\text{Mn}^{4+}$, $x\text{Ba}^{2+}$ ($x = 0.0, 0.13$) and $\text{MAG}:\text{Mn}^{4+}$, $x\text{Ba}^{2+}$ ($x = 0.0, 0.27$) samples are revealed in **Fig.2.7 (b)**. All four samples exhibit excellent red colour purity ~100% under the response of both UV and blue irradiations. The CIE coordinates for these samples are in the deep-red zone (shown in **Fig.2.7 (c)**). The CIE coordinates obtained for the brighter red emitting $\text{MAG}:\text{Mn}^{4+}$, 0.27Ba^{2+} sample are situated in the deeper red region (0.716, 0.283).

A try has been made to support the above justifications for enhanced red emission in $\text{MAG}:\text{Mn}^{4+}$ sample compared to $\text{MGG}:\text{Mn}^{4+}$ with the help of XPS analysis. The core-level XPS spectra (**Fig.2.7 (d)** and **(f)**) measured for Ga and Al strongly suggest their 3+ oxidation states in $\text{MGG}:\text{Mn}^{4+}$ and $\text{MAG}:\text{Mn}^{4+}$, respectively. While comparing the O1s spectra recorded for $\text{MGG}:\text{Mn}^{4+}$ and $\text{MAG}:\text{Mn}^{4+}$ samples (**Fig.2.7 (e)** and **(g)**), the lattice oxygen (O_1) content is higher in the case of $\text{MAG}:\text{Mn}^{4+}$. The higher lattice oxygen content in the $\text{MAG}:\text{Mn}^{4+}$ may help to form more octahedral bonds in $\text{MAG}:\text{Mn}^{4+}$ compared to $\text{MGG}:\text{Mn}^{4+}$. Also, the structural stability will be higher in $\text{MAG}:\text{Mn}^{4+}$ due to this higher lattice oxygen content.⁸ These factors can lead to higher emission intensity of $\text{MAG}:\text{Mn}^{4+}$.

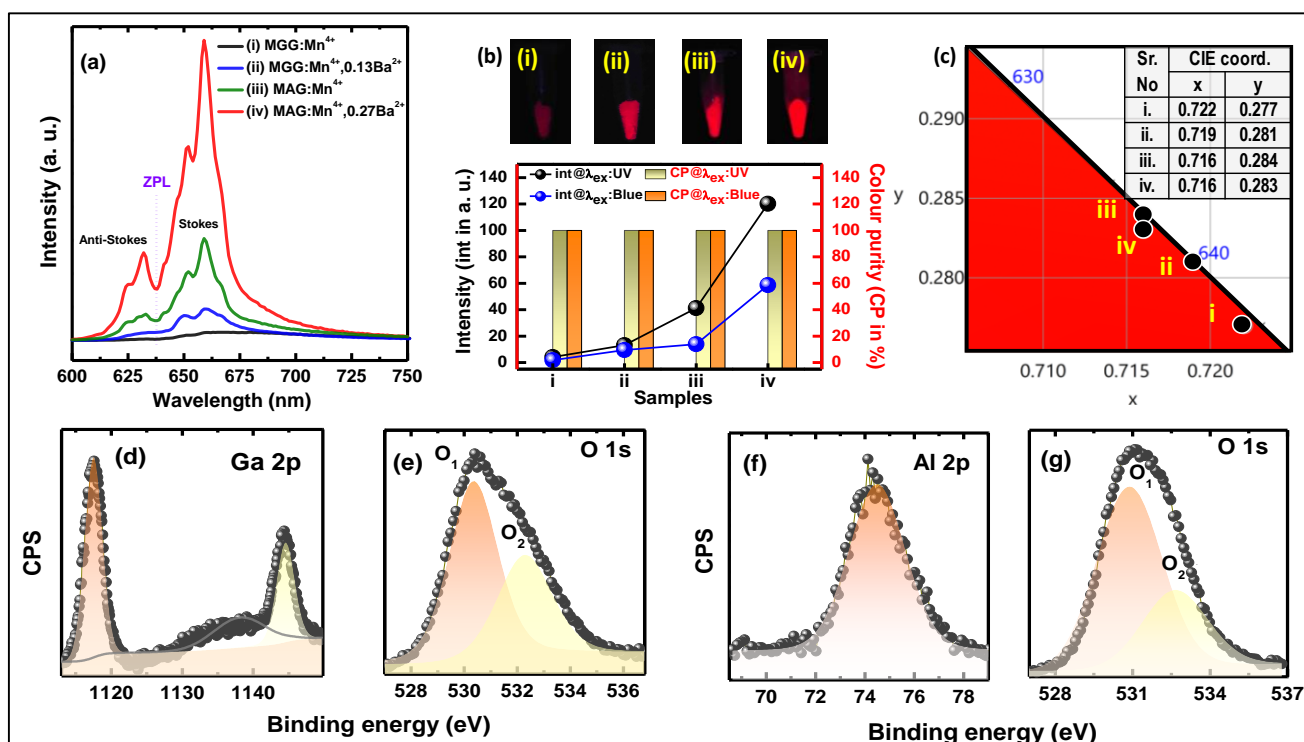


Fig.2.7 (a) Comparison of PL emission spectra ($\lambda_{ex} = 284$ nm) of (i) MGG: Mn^{4+} , (ii) MGG: Mn^{4+} , $0.13Ba^{2+}$, (iii) MAG: Mn^{4+} and (iv) MAG: Mn^{4+} , $0.27Ba^{2+}$ samples with the (b) corresponding PL images, PL intensity (line with symbol) and colour purity (bar). (c) CIE diagram and the colour coordinates of the above 4 samples. XPS spectra of (d) Ga 2P and (e) O 1s for MGG: Mn^{4+} . XPS spectra of (f) Al 2p and (g) O 1s for MAG: Mn^{4+} .

2.4.3.2. Estimation of Mn^{4+} energy level diagram and, evaluation of spectroscopic parameters

The PLE spectra of MGG: Mn^{4+} , xBa^{2+} ($x = 0.0, 0.13$) and MAG: Mn^{4+} , xBa^{2+} ($x = 0.0, 0.27$) samples can be deconvoluted into 4 Gaussian peaks (**Fig.2.8 (a)**).^{54,55} The peaks located around 280 nm, 320 nm, 360 nm, and 420 nm resemble the $Mn^{4+}-O^{2-}$ CTB, ${}^4A_{2g} \rightarrow {}^4T_{1g}$, ${}^4A_{2g} \rightarrow {}^2T_{2g}$, and ${}^4A_{2g} \rightarrow {}^4T_{2g}$ transitions of Mn^{4+} ions, respectively. The Tanabe Sugano energy level illustration of Mn^{4+} ions in an octahedron is displayed in **Fig.2.8 (c)**. The strong and weak crystal fields are distinguished by a line passing through the intersection of ${}^4T_{2g}$ and 2E_g . The ratio of octahedral field strength (Dq) and Racah parameter (B) for MGG: Mn^{4+} , xBa^{2+} ($x = 0.0, 0.13$) and MAG: Mn^{4+} , xBa^{2+} ($x = 0.0, 0.27$) samples are greater than 2.1 indicating that Mn^{4+} experiences a strong crystal field in all these hosts. To compare the effect of the host structure crystal field splitting energy value ($10 Dq$) and Racah parameter values B and C for the samples MGG: Mn^{4+} , xBa^{2+} ($x = 0.0, 0.13$) and MAG: Mn^{4+} , xBa^{2+} ($x = 0.0, 0.27$) are also

calculated and listed in **Table 2.1**. It is obvious from **Fig.2.8 (a)** that the $\text{Mn}^{4+}\text{-O}^{2-}$ CTB of MAG: Mn^{4+} is slightly blue-shifted compared to the MGG: Mn^{4+} since Mn^{4+} ions in the smaller Al^{3+} sites require a larger charge transfer (CT) energy than for the Mn^{4+} in the Ga^{3+} sites.³⁹ The slight reduction in the Dq/B values of MAG: Mn^{4+} compared to MGG: Mn^{4+} can be attributed to the lower average Al-O bond length of MAG: Mn^{4+} .⁴⁹

The high-temperature PL analysis has been carried out for the two compositions $\text{MAG: Mn}^{4+}, 0.27\text{Ba}^{2+}$ and $\text{MGG: Mn}^{4+}, 0.13\text{Ba}^{2+}$. The temperature is varied from 300 K to 453 K and the PL emission spectra are recorded under the UV excitation. Even at 453 K, $\text{MAG: Mn}^{4+}, 0.27\text{Ba}^{2+}$ sample could retain 70% of its initial room temperature intensity. However, the $\text{MGG: Mn}^{4+}, 0.13\text{Ba}^{2+}$ could retain less than 60% of its room temperature intensity (**Fig.2.8 (b)**). The quenching temperature increases when Ga^{3+} is replaced with Al^{3+} in $\text{MAG: Mn}^{4+}, 0.27\text{Ba}^{2+}$ sample. The ionic size of the Mn^{4+} ion in the octahedral coordination is 0.53 Å, which is closer to that of Al^{3+} ($r_{\text{AlO}_6} = 0.535$ Å) in MAG: Mn^{4+} samples rather than that of Ga^{3+} ($r_{\text{GaO}_6} = 0.62$ Å) in MGG: Mn^{4+} samples. Using the Arrhenius plot,¹⁵ the activation energy has been calculated for both samples, which is calculated to be 156 meV for $\text{MAG: Mn}^{4+}, 0.27\text{Ba}^{2+}$, and 149 meV for $\text{MGG: Mn}^{4+}, 0.13 \text{Ba}^{2+}$.

The higher activation energy in $\text{MAG: Mn}^{4+}, 0.27\text{Ba}^{2+}$ sample than that in $\text{MGG: Mn}^{4+}, 0.13\text{Ba}^{2+}$ can be explained with the configuration coordinate diagram, as presented in **Fig.2.8 (d)**. With UV excitation, free electrons jump first from the ${}^4\text{A}_{2g}$ ground state to the excited states (${}^2\text{E}_g$, ${}^4\text{T}_{1g}$, or ${}^4\text{T}_{2g}$) and then non-radiatively relax to the ${}^2\text{E}_g$ states. The radiative emission towards the ${}^4\text{A}_{2g}$ state from the ${}^2\text{E}_g$ state results in deep red emission. While increasing the temperature number of electrons in the ${}^2\text{E}_g$ state increase and gain more energy. The thermally excited electrons could reach the intersection point of ${}^4\text{A}_{2g}$ and ${}^2\text{E}_g$ (Cross over point) and relax to the ground state (${}^4\text{A}_{2g}$) non-radiatively. The position of cross over points may be different for these two samples and $\text{MAG: Mn}^{4+}, 0.27\text{Ba}^{2+}$ might requires more energy for reaching this point leading to its higher activation energy. Hence the different activation energy is that Mn^{4+} in the above two samples experiences different quenching barriers considering the structural difference as well as the ${}^4\text{T}_{1g}$, ${}^2\text{T}_{2g}$ energy and $\text{Mn}^{4+}\text{-O}^{2-}$ CTB energy.⁵⁶ The variation of peak intensities (positioning at 659 nm and 630 nm) with temperature for $\text{MAG: Mn}^{4+}, 0.27\text{Ba}^{2+}$ is shown in **Fig.2.8 (e)**. The absorbed energy in this process is called activation energy.^{57,58} Meanwhile, the CIE coordinates are not affected much due to the increase in temperature

indicating strong ligand field stabilization energy in the octahedral sites of MAG: Mn^{4+} , 0.27Ba^{2+} where Mn^{4+} ions are situated (**Fig.2.8** (e)).

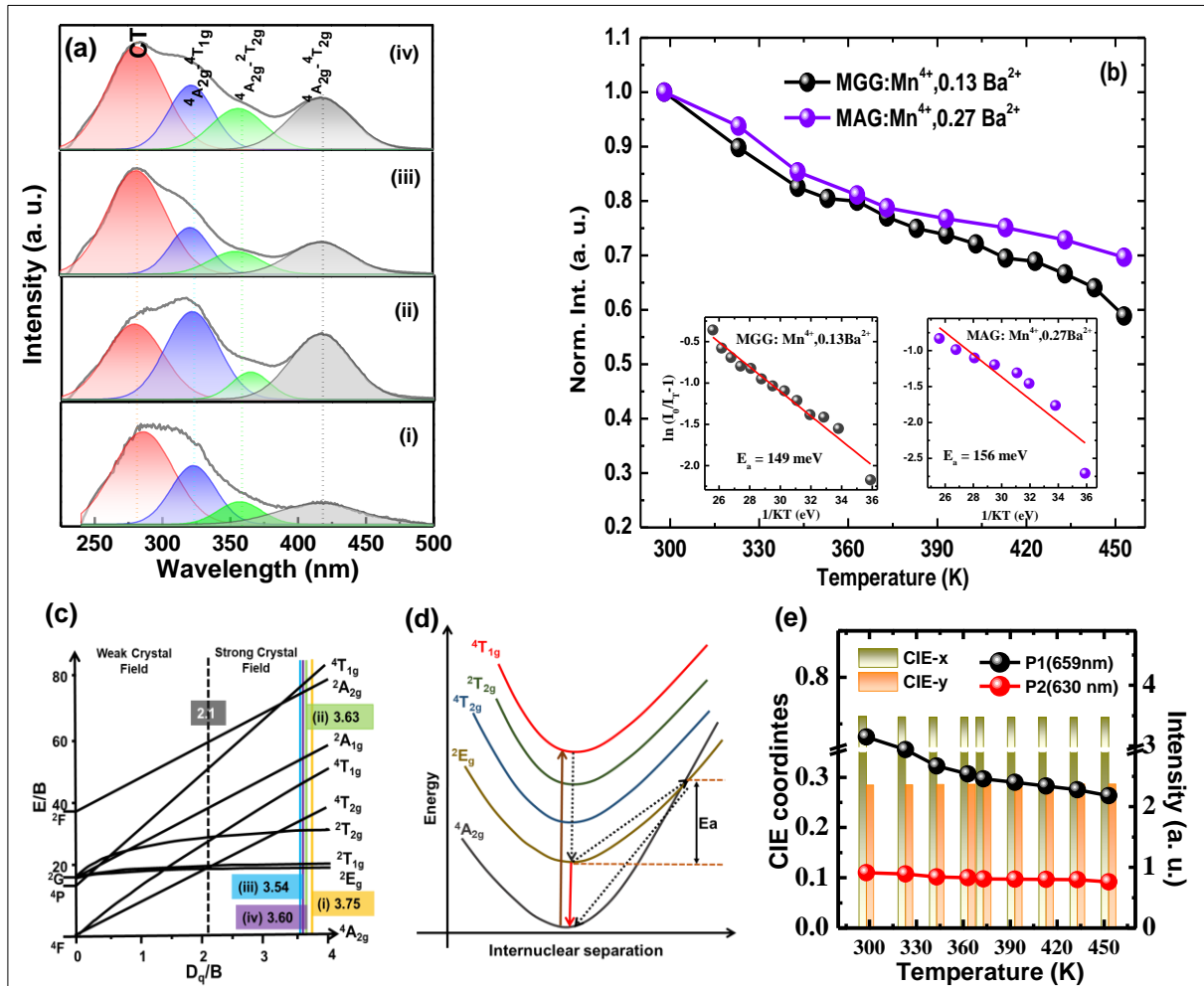


Fig.2.8 (a) Deconvoluted PL excitation spectra of (i) MGG: Mn^{4+} (ii) MGG: Mn^{4+} , 0.13Ba^{2+} (iii) MAG: Mn^{4+} and (iv) MAG: Mn^{4+} , 0.27Ba^{2+} . (b) Plots of normalized emission intensity vs temperature and Arrhenius plots for the samples MGG: Mn^{4+} , 0.13Ba^{2+} and MAG: Mn^{4+} , 0.27Ba^{2+} . (c) Tanabe–Sugano energy illustration of Mn^{4+} ions in an octahedron and representation of Dq/B values of MGG: Mn^{4+} , $x\text{Ba}^{2+}$ ($x = 0.0, 0.13$) and MAG: Mn^{4+} , $x\text{Ba}^{2+}$ ($x = 0.0, 0.27$). (d) Configuration coordinate diagram for activation energy calculation. (e) Bar diagram showing variation of CIE coordinates with temperature along with variation of peak intensities (positioning at 659 nm and 630 nm) with temperature for the sample MAG: Mn^{4+} , 0.27Ba^{2+} .

Table 2.1. Spectroscopic parameter values obtained from PL emission and excitation spectra.

Phosphor	4T_1	4T_2	2E_g	Dq	Dq/B	B	C
	(cm^{-1})	(cm^{-1})	(cm^{-1})				
MGG: Mn^{4+}	30960	24038	15175	2404	3.75	642	3414
MGG: Mn^{4+} , 0.13 Ba^{2+}	31153	24038	15175	2404	3.63	662	3367
MAG: Mn^{4+}	31153	23923	15175	2392	3.54	676	3338
MAG: Mn^{4+} , 0.27 Ba^{2+}	31055	23923	15175	2392	3.60	664	3362

2.4.3.3 Low-temperature photoluminescence of MAG: Mn^{4+} , 0.27 Ba^{2+} and MGG: Mn^{4+} , 0.13 Ba^{2+}

Low-temperature PL spectra for the two optimum samples MAG: Mn^{4+} , 0.27 Ba^{2+} and MGG: Mn^{4+} , 0.13 Ba^{2+} are investigated with the excitation of a 266 nm laser source operated at 10 mW to compare the activation energy of these phosphors. To elucidate the influence of $[\text{AlO}_6]$ octahedrons in activation energy and photoluminescence, the PL spectra of these two samples are probed by varying the temperature from 10 K to 300 K (**Fig.2.9 (a)**). The activation energy is calculated from the low-temperature PL spectra using the Arrhenius plot, as revealed in **Fig.2.9 (b)** for MAG: Mn^{4+} , 0.27 Ba^{2+} .

Generally, electronic transitions between 2E_g and ${}^4A_{2g}$ states of Mn^{4+} ions are forbidden because of the same parity. In these phosphors, Mn^{4+} ions occupy the $\text{Al}^{3+}/\text{Ga}^{3+}$ octahedral sites without inversion symmetry which helps to partially break the selection rules for this transition. The PL spectra of the ${}^2E_g \rightarrow {}^4A_{2g}$ transition show several emissions bands between 600 to 700 nm. The zero phonon line (ZPL) at 639 nm and sidebands are prominently observable at 10 K. The Stokes bands are highly intense whereas anti-Stokes bands are less intense. As the temperature increased, the intensity of the stokes bands at 659 nm (P1) and 647 nm (P2), and ZPL decrease, whereas, that of the anti-Stokes band at 630 nm (P3) increased. This can be attributed to the participation of more restricted phonon vibrations at higher temperatures.¹⁵ On increasing the temperature, the anti-Stokes bands are thermally depopulated from the Stokes band until the thermal equilibrium is reached. This substantiates the increase in intensity with the rise in temperature. Also, Boltzmann's law should be obeyed in the intensity ratio of anti-

Stokes and Stokes bands as phonon-coupled sidebands are considered as a couple of adjacent levels.¹⁵

The variation of peak intensities with temperature is shown in the inset of **Fig.2.9 (b)**. This can be attributed to the thermal vibration developed in the host.⁵⁹ The temperature-dependent emission spectra show a typical trend of spectral broadening and a redshift of the emission band. As the temperature increases, the emission bands become broader and the peaks are shifted to higher wavelength regions because of photon reabsorption and increased acoustic electron interaction following the Varshni equation. The redshift of the emission bands with increasing temperature is due to the expansion of activator-ligand distance leading to a lower crystal field splitting. Furthermore, ZPL intensity decreases with increasing temperature can be ascribed to the loss of phonon energy via non-radiative transition.¹⁶

The low-temperature PL spectra and intensity variation of P1, P2, and P3 with temperature and Arrhenius plots of MGG: Mn⁴⁺, 0.13Ba²⁺ are shown in **Fig.2.9 (c)** and **(d)**, respectively. A similar kind of temperature-dependent emission behaviour is observed for P1 (~659 nm), P2 (~650 nm), and P3 (~631 nm) peaks in the MGG: Mn⁴⁺, 0.13Ba²⁺ sample (inset of **Fig.2.9 (d)**).

While comparing low-temperature PL spectra for these two optimum samples, the shape of the emission spectra has been changed due to the replacement of Ga³⁺ with Al³⁺. This might be due to the preferential occupancy of Mn⁴⁺ in [AlO₆] octahedrons (in MAG: Mn⁴⁺, 0.27Ba²⁺) rather than [GaO₆] octahedra (in MGG: Mn⁴⁺, 0.13Ba²⁺). Since the shape of the emission spectra depends on the coordination environment of Mn⁴⁺. The activation energy obtained for MAG: Mn⁴⁺, 0.27Ba²⁺ is 119.83 meV, which is greater than the calculated activation energy of MGG: Mn⁴⁺, 0.13Ba²⁺ (102.85 meV). The Mn-O bond in [AlO₆] octahedrons is weaker than the same situated in [GaO₆] octahedrons due to the lower size of Al³⁺ ions than Ga³⁺ ions. These differences in their bond-length causes difference in the energies of ⁴T_{1g} and Mn⁴⁺-O²⁻ CTB. Hence, these two samples experience different quenching barriers and it could be the reason for the higher activation energy of MAG: Mn⁴⁺, 0.27Ba²⁺ compared to MGG: Mn⁴⁺, 0.13Ba²⁺.^{22,56,60} The ZPL (P2) intensity mainly depends on the Mn⁴⁺ ions' coordination environment. Therefore, more sharpness and higher intensity of the ZPL in MAG: Mn⁴⁺, 0.27Ba²⁺ compared to MGG: Mn⁴⁺, 0.13 Ba²⁺ might be due to the lower symmetry of the [AlO₆] octahedrons than the [GaO₆] octahedrons.⁶¹

An interesting fact to note is that a very weakly intense broad green emission band peaked at 505 nm is observed for MGG: Mn⁴⁺, 0.13Ba²⁺ sample at lower temperatures, which is however not seen in the low-temperature PL of MAG: Mn⁴⁺, 0.27Ba²⁺. The magnified portion below 600 nm of the low-temperature PL spectra of MGG: Mn⁴⁺, 0.13Ba²⁺ sample is shown in the insets of **Fig.2.9** (c). To predict the origin of a such broad peak, the cathodoluminescence analysis of MAG: Mn⁴⁺, 0.27Ba²⁺ and MGG: Mn⁴⁺, 0.13 Ba²⁺ samples are carried out further.

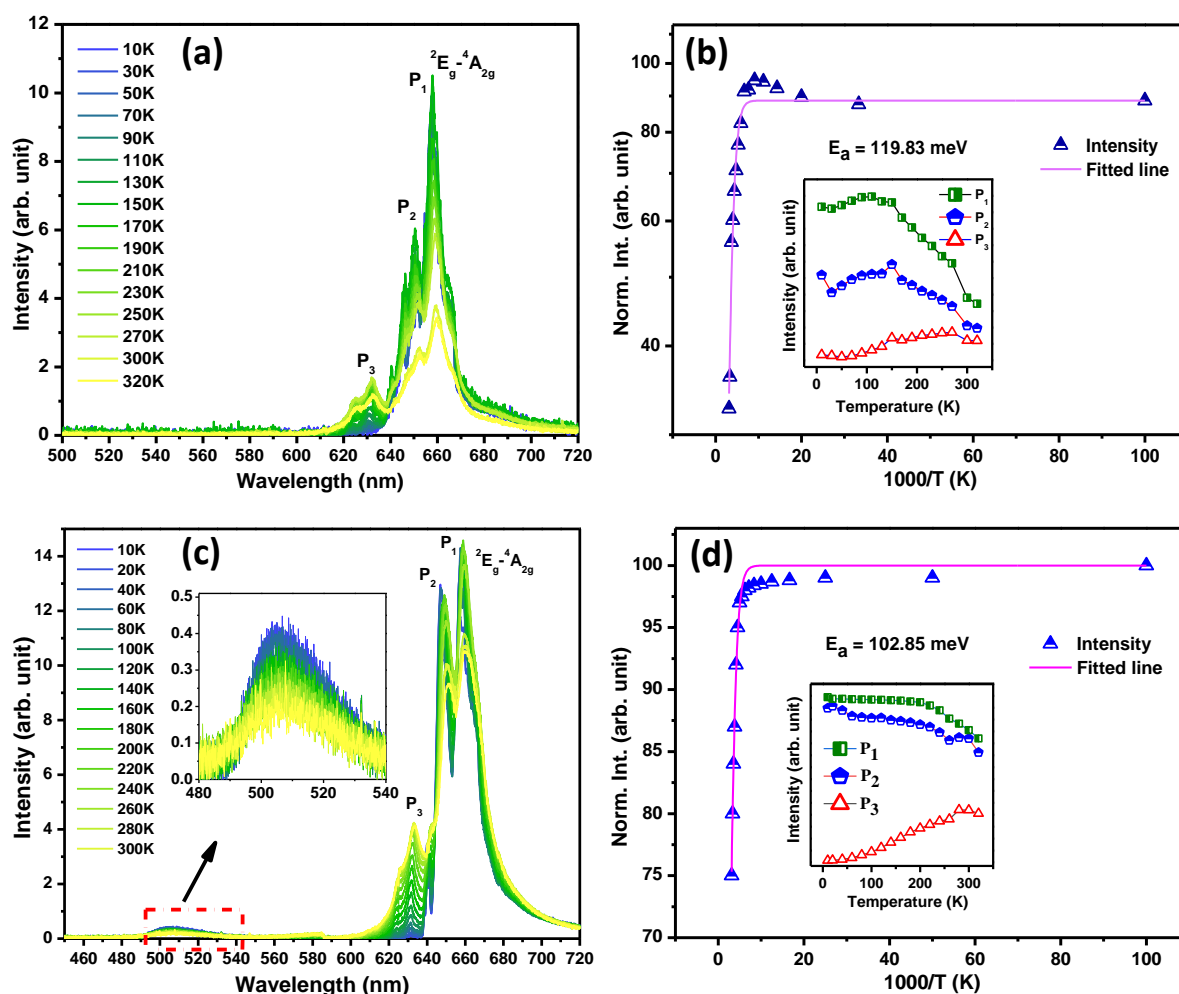


Fig.2.9 (a) Low-temperature PL spectra of MAG: Mn⁴⁺, 0.27 Ba²⁺ and corresponding (b) Arrhenius plot (inset shows the variation of peak intensities with temperature) (c) Low-temperature PL spectra of MGG: Mn⁴⁺, 0.13 Ba²⁺ (inset shows the enlarged portion of green emission) and corresponding (d) Arrhenius plot (inset shows the variation of peak intensities with temperature).

2.4.3.4. Cathodoluminescence properties of optimum MAG: Mn⁴⁺, 0.27Ba²⁺ and MGG: Mn⁴⁺, 0.13Ba²⁺

Apart from the ${}^2E_g \rightarrow {}^4A_{2g}$ transitions of Mn⁴⁺ ions, a weakly intense broad green emission is observed at 505 nm in low-temperature PL spectra of MGG: Mn⁴⁺, 0.13Ba²⁺ sample (Fig.2.9 (c)). However, no such green emission is observed for MAG: Mn⁴⁺, 0.27Ba²⁺ sample (Fig.2.9 (a)). To investigate the origin of the green emission, the cathodoluminescence (CL) spectra, as well as the spectral maps, are collected for MAG: Mn⁴⁺, 0.27Ba²⁺ and MGG: Mn⁴⁺, 0.13Ba²⁺ samples. Unlike the UV photons' excitation in PL, the excitation with high-energy electrons in CL can produce almost all the possible transitions to the higher energy state. Hence, it could be more useful to identify the various emission centers in any kind of luminescent materials.⁶²

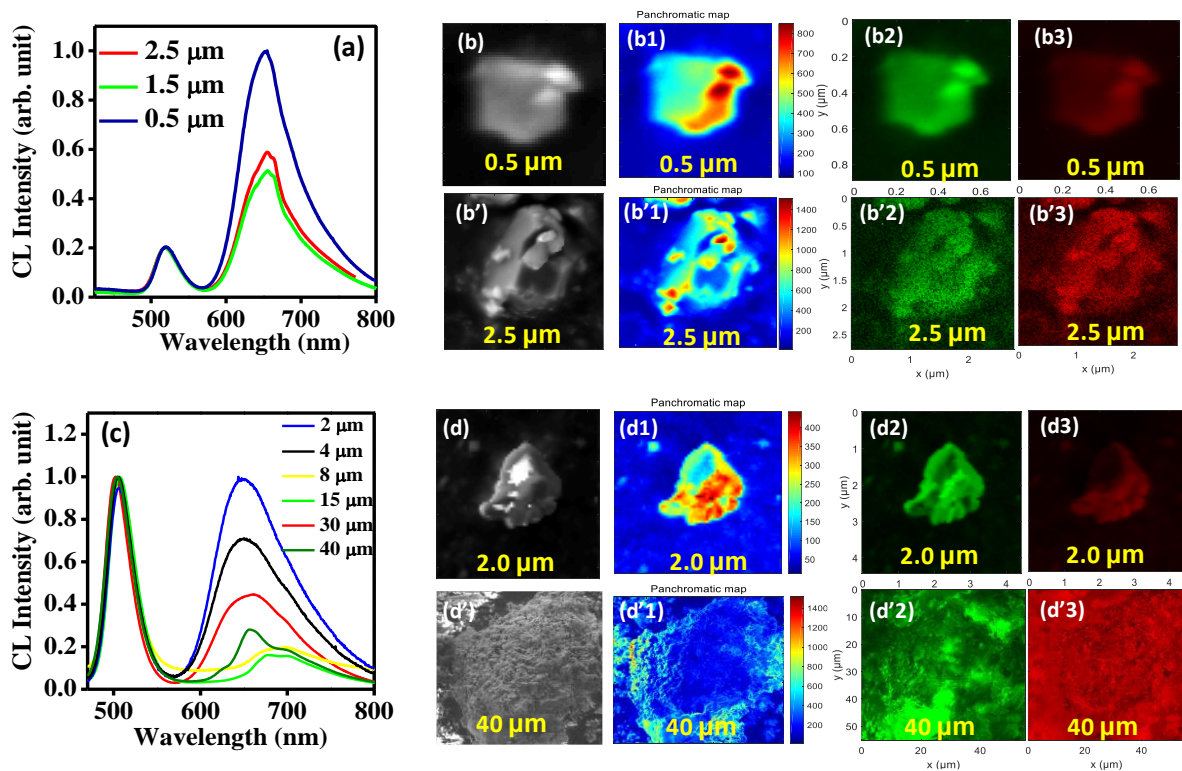


Fig.2.10 (a) Normalized CL spectra with respect to the green emission peak of MAG: Mn⁴⁺, 0.27Ba²⁺ sample. (b, b') SEM images, (b1, b'1) panchromatic overall intensity mapping, and filtered maps for the (b2, b'2) green (from 450 to 570 nm) and (b3, b'3) red emission (from 570 and 800 nm) recorded for different sized particles in MAG: Mn⁴⁺, 0.27Ba²⁺ sample. (c) Normalized CL spectra with respect to the green emission peak of MGG: Mn⁴⁺, 0.13Ba²⁺ sample. (d, d') SEM images, (d1, d'1) panchromatic overall intensity mapping, and filtered

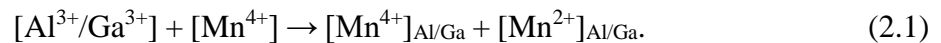
maps for the (d2, d'2) green (from 450 to 570 nm) and (d3, d'3) red emission (from 570 and 800 nm) band recorded for different sized particles in MGG: Mn⁴⁺, 0.13Ba²⁺ sample.

The CL spectra are recorded at room temperature for MAG: Mn⁴⁺, 0.27Ba²⁺ and MGG: Mn⁴⁺, 0.13Ba²⁺ samples focusing on individual grains having different sizes (**Fig.2.10 (a) and (c)**). Compared to the sharp PL emission spectra, the CL spectra of these samples show a broader emission band centered at 650 nm, which might be attributed to the red emission originating from the emission centers of both Mn⁴⁺ and Mn²⁺ ions since the occupancy of Mn²⁺ ions in the [MgO₆] octahedrons can also produce broad orange-red emission.⁶³ Interestingly, broad green emission bands centered at 518 nm and 504 nm is observed for MAG: Mn⁴⁺, 0.27Ba²⁺ and MGG: Mn⁴⁺, 0.13Ba²⁺, respectively, which are attributed to the *d-d* transitions of Mn²⁺ ions. Unlike the PL spectra, the green emission band in both samples are observed to be prominent in their CL spectra. Since the *d-d* transitions of Mn²⁺ ions are forbidden in view of spin and parity, therefore, it requires high energy pumping or the help of sensitizers (Ce³⁺, Eu²⁺) to be intensified.⁶⁴⁻⁶⁶ In the present case, the high energy electronic irradiations during the CL spectral measurements could effectively pump the *d-d* transitions of Mn²⁺ ions owing to which the broad Mn²⁺ emission bands are detected. The CL spectra normalized with respect to the intensity of the green emission bands observed in various-sized grains in both these samples are presented in **Fig.2.10 (a)** and **Fig.2.10 (c)**. These could be helpful to observe the effect of particle sizes on the emission features of manganese ions having 2+ and 4+ valance.

The relative intensity of the red emission of MAG: Mn⁴⁺, 0.27Ba²⁺ and MGG: Mn⁴⁺, 0.13Ba²⁺ samples varies with the particle sizes, as can be seen in **Fig.2.10 (a)** and **Fig.2.10 (c)**, respectively. Meanwhile, the red emission is dominant in the case MAG: Mn⁴⁺, 0.27Ba²⁺ sample irrespective of the particle size. However, no consistent trend of CL emission variation with the particle size could be identified in both of these samples. A similar kind of result showing the independency of particle size on CL efficiency is reported by L. E. Shea *et al.*⁶⁷ Though the variations appear to be uncorrelated with the parcel size, interestingly in the present case, the red-to-green emission proportion is seen to be dependent on the compositions of the materials. The red-to-green CL peak ratio in MGG: Mn⁴⁺, 0.13Ba²⁺ particles is lower than that observed in MAG: Mn⁴⁺, 0.27Ba²⁺ particles.

The existence of sharp red (from Mn^{4+}), and broad red (from Mn^{2+}) as well as broad green (from Mn^{2+}) emission bands can be identified from the spectrally filtered SEM micrographs of different particles having different sizes in these two samples. **Fig.2.10 (b, b')** and **Fig.2.10 (d, d')** are representing the general SEM images of different-sized particles to be studied in MAG: Mn^{4+} , 0.27Ba^{2+} and MGG: Mn^{4+} , 0.13Ba^{2+} samples, respectively. Whereas, **Fig.2.10 (b1, b'1)** and **Fig.2.10 (d1, d'1)** are representing the overall panchromatic intensity maps of the respective particles shown in **Fig.2.10 (b, b')** and **Fig.2.10 (d, d')**. In the illustrated panchromatic intensity maps, the CL signal is averaged over all visible wavelengths that fall within the specific detection range. The red and green emission regions can be easily visualized from the respective panchromatic maps of both samples. The spectrally filtered maps of the small and big particles in MAG: Mn^{4+} , 0.27Ba^{2+} and MGG: Mn^{4+} , 0.13Ba^{2+} samples are also presented in **Fig.2.10 (b2, b3, and b'2, b'3)** and **Fig.2.10 (d2, d3, and d'2, d'3)**, respectively. These filtered maps are further helpful for the precise visualization and the spatial distribution of the green emission (from 450 nm to 570 nm), and the red emission (from 570 nm to 800 nm) intensities observed in the overall panchromatic maps.

The origin of green emissions can be attributed to the reduction of Mn^{4+} ions to Mn^{2+} ions and their occupancy in tetrahedral sites.⁶³ The reduction can be explained in two ways. One is self-reduction resulting from site occupation and the other is caused by the electron beam during CL measurement. Here the generated Mn^{2+} ions (r_{MnO_4} : 0.66 Å) can occupy the Al^{3+} (r_{AlO_4} : 0.39 Å) and Ga^{3+} (r_{GaO_4} : 0.47 Å) tetrahedral sites of MAG: Mn^{4+} , 0.27Ba^{2+} and MGG: Mn^{4+} , 0.13Ba^{2+} , respectively. When a tetravalent ion is doped at the trivalent site, a divalent ion can be generated to maintain charge neutrality. In this case, an Mn^{4+} ion can substitute one Al^{3+} (or Ga^{3+}) ion at the octahedrons, and other Mn^{4+} ions might be reduced to Mn^{2+} and occupy an Al^{3+} (or Ga^{3+}) tetrahedrons to maintain the charge neutrality²¹ according to the following equation:



If some of the Mn^{4+} ions are substituted in the $[\text{MgO}_6]$ sites instead of Al^{3+} (or Ga^{3+}) octahedral sites, the self-reduction of Mn^{4+} to Mn^{2+} may enhance. The number of Mn^{4+} ions going to $[\text{MgO}_6]$ sites of MAG: Mn^{4+} , 0.27Ba^{2+} are less due to the availability of more suitable $[\text{AlO}_6]$ sites of MAG host for Mn^{4+} ions' occupancy. Hence, the self-reduction of Mn^{4+} to Mn^{2+} is

expected to be lesser in MAG: Mn⁴⁺, 0.27Ba²⁺ compare to MGG: Mn⁴⁺, 0.13Ba²⁺.^{68,69} Also, compared to [AlO₄] tetrahedrons [GaO₄] tetrahedrons are more suitable for Mn²⁺ to occupy. Therefore, the Mn²⁺ green emission is relatively lower in MAG: Mn⁴⁺, 0.27Ba²⁺ compared to MGG: Mn⁴⁺, 0.13Ba²⁺. Moreover, the full width at half maximum (FWHM) of the electrons' irradiated red emission in MGG: Mn⁴⁺, 0.13Ba²⁺ is much higher due to more contribution of Mn²⁺ ions in red emission. Further studies are required for the exact confirmation of these observations.

2.4.4 Applications in WLEDs and red LEDs

The PLE and PL emission intensity of optimum MAG: Mn⁴⁺, 0.27Ba²⁺ phosphor has been compared with commercial blue-emitting BaMgAl₁₀O₁₇: Eu²⁺ (BAM: Eu²⁺), yellow-emitting Y₃Al₅O₁₂: Ce³⁺ (YAG: Ce³⁺) and red-emitting (Y₂O₃: Eu³⁺) phosphors, as displayed in **Fig.2.11 (a)** and **(b)**, respectively. The emission intensity of the optimum red phosphor is higher than the commercial blue and yellow phosphors. It exhibited almost the same emission intensity but more width (FWHM~18 nm) than the commercial red phosphor (FWHM~2 nm) (**Fig.2.11 (b)**). **Fig.2.11 (c)** represents the excitation spectrum of MAG: Mn⁴⁺, 0.27Ba²⁺ and emission spectra of YAG: Ce³⁺. The trivial overlapping of the emission spectra of YAG: Ce³⁺ and excitation spectra of MAG: Mn⁴⁺, 0.27Ba²⁺ is indicating that the probability of photons' reabsorption is negligible. Therefore, MAG: Mn⁴⁺, 0.27Ba²⁺ composition can be a suitable red component to enhance the colour rendering (CRI) and to reduce the correlated colour temperature (CCT) of a YAG: Ce³⁺ based WLEDs. Likewise, **Fig.2.11 (d)** represents the excitation spectra of MAG: Mn⁴⁺, 0.27Ba²⁺ with the emission spectra of blue-emitting BAM: Eu²⁺ and green-emitting CeMgAl₁₁O₁₉: Tb³⁺ (CMA: Tb³⁺) phosphors. In this case, the overlapping region between excitation spectra of MAG: Mn⁴⁺, 0.27Ba²⁺ phosphor and emission spectra of the green phosphor (CMA: Tb³⁺) is negligible. Also, the overlapping between the excitation spectra and emission spectra of MAG: Mn⁴⁺, 0.27Ba²⁺ and BAM: Eu²⁺ phosphors, respectively, is marginal. This result supports the suitability of MAG: Mn⁴⁺, 0.27Ba²⁺ composition as a red component for the tricolour phosphors-based WLEDs.

Therefore, WLEDs have been fabricated by two different approaches. At first, MAG: Mn⁴⁺, 0.27Ba²⁺ phosphor has been mixed with YAG: Ce³⁺ with a ratio of 6:4. This phosphor mixture is then incorporated with poly (methyl methacrylate) by grinding. Then the mixture is stirred thoroughly with acryline to make a thick paste. The resulting paste has been coated on

a blue InGaN chip of 410 nm wavelength to produce WLED. The EL spectrum and corresponding digital image of the resultant WLED are shown in **Fig.2.12 (a)**. This combination produces warm white light with a CCT of 3730 K, CRI of 89, and CIE coordinates of (0.38, 0.35). Using a 280 nm UV LED chip, another WLED has been fabricated by mixing optimum MAG: Mn⁴⁺, 0.27Ba²⁺ red phosphor with commercial blue (BAM: Eu²⁺) and green (CMA: Tb³⁺) phosphors with a mixing ratio of 7:3:2. This combination produces natural white light with a CCT of 5306 K, a CRI of 79, and a CIE coordinate of (0.34, 0.34). The EL spectrum and the corresponding digital image of the fabricated WLED are shown in **Fig.2.12 (b)**. The obtained values of CCT and CRI strongly suggest that MAG: Mn⁴⁺, 0.27Ba²⁺ is a promising red component for blue and UV-based phosphor-converted WLEDs used in indoor lighting.

Furthermore, three red LEDs are developed by combining the red phosphor with 280 nm, 365 nm UV LED, and 410 nm blue LED chips. The corresponding EL spectra with the direct red LED images are shown in **Fig.2.12 (c)**. The emission peak centered at 659 nm is well matching with the absorption peak of chlorophyll A and Chlorophyll B responsible for photosynthesis and photoperiodic effects in plant leaves.^{18,70} The red LED developed by combining red phosphors with blue LED has two emission bands at 410 nm and 659 nm. Hence this LED can cover the absorption spectrum of phytochrome Pr since its absorption spectrum exhibits major bands at 405 nm and 655 nm.⁷¹ L. Shi *et al.* developed red LED for plant growth application by combining Ca₂LaSbO₆: Mn⁴⁺ with a near UV LED chip and it showed an emission peak at 695 nm with a CRI of 26.6.⁷² S. Gu *et al.* developed red LEDs by combining SrMgAl_{10-y}Ga_yO₁₇: Mn⁴⁺ phosphor with blue LEDs and its CIE coordinate values varies from (0.146, 0.036) to (0.578, 0.229).⁵³ Here we fabricated three red LEDs and the corresponding CRI (35, 47, and 49) and CIE values (0.472, 0.174), (0.624, 0.327), and (0.705, 0.286) are found to be suitable for artificial lighting for plant growth.^{18,70}

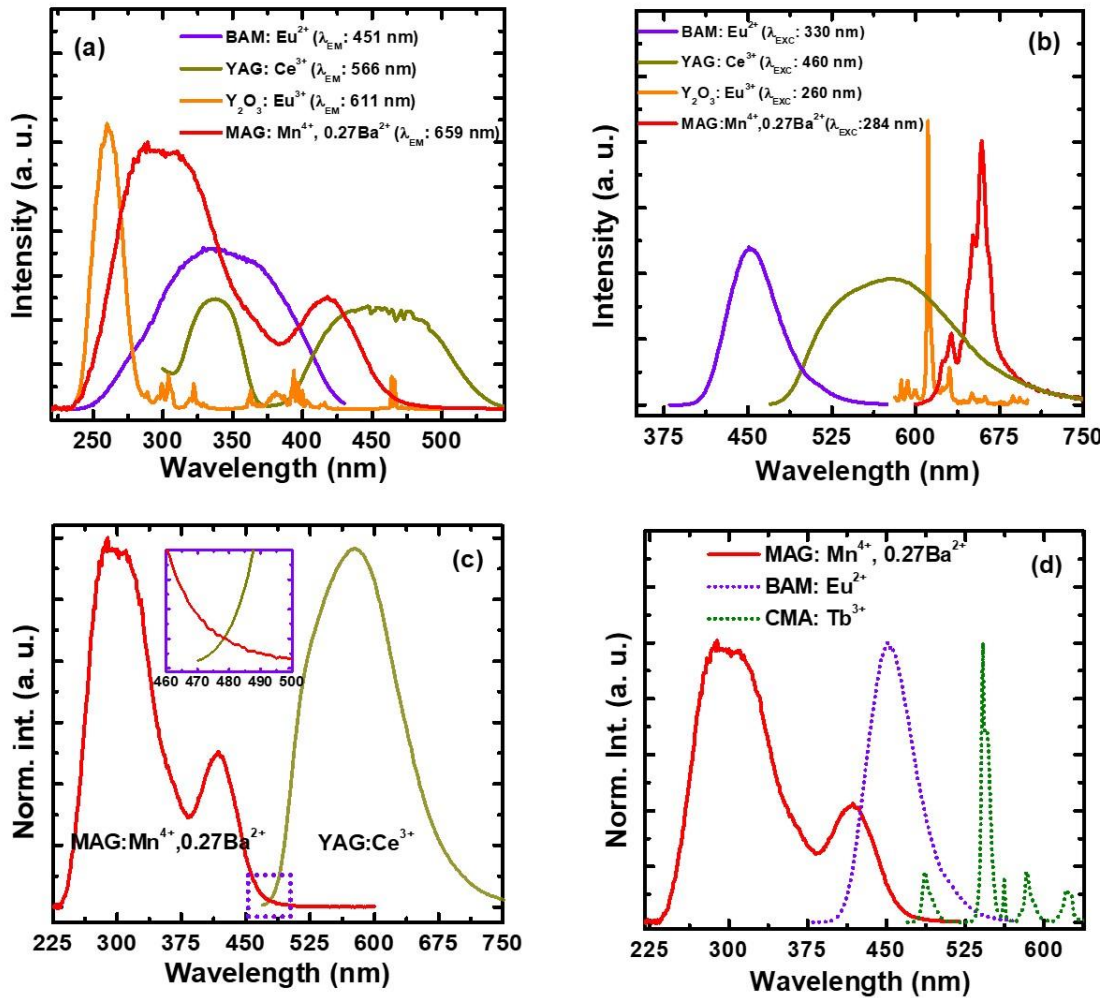


Fig.2.11 Comparative (a) PLE and (b) PL spectra of the optimum MAG: Mn⁴⁺, 0.27Ba²⁺ sample with commercial BAM: Eu²⁺ (blue), YAG: Ce³⁺ (yellow) and Y₂O₃: Eu³⁺ (red) phosphors. (c) PLE spectra of MAG: Mn⁴⁺, 0.27Ba²⁺ and emission spectra of YAG: Ce³⁺ showing spectral overlap. (d) PLE spectra of MAG: Mn⁴⁺, 0.27Ba²⁺ with the PL spectra of BAM: Eu²⁺ and CMA: Tb³⁺ showing spectral overlap.

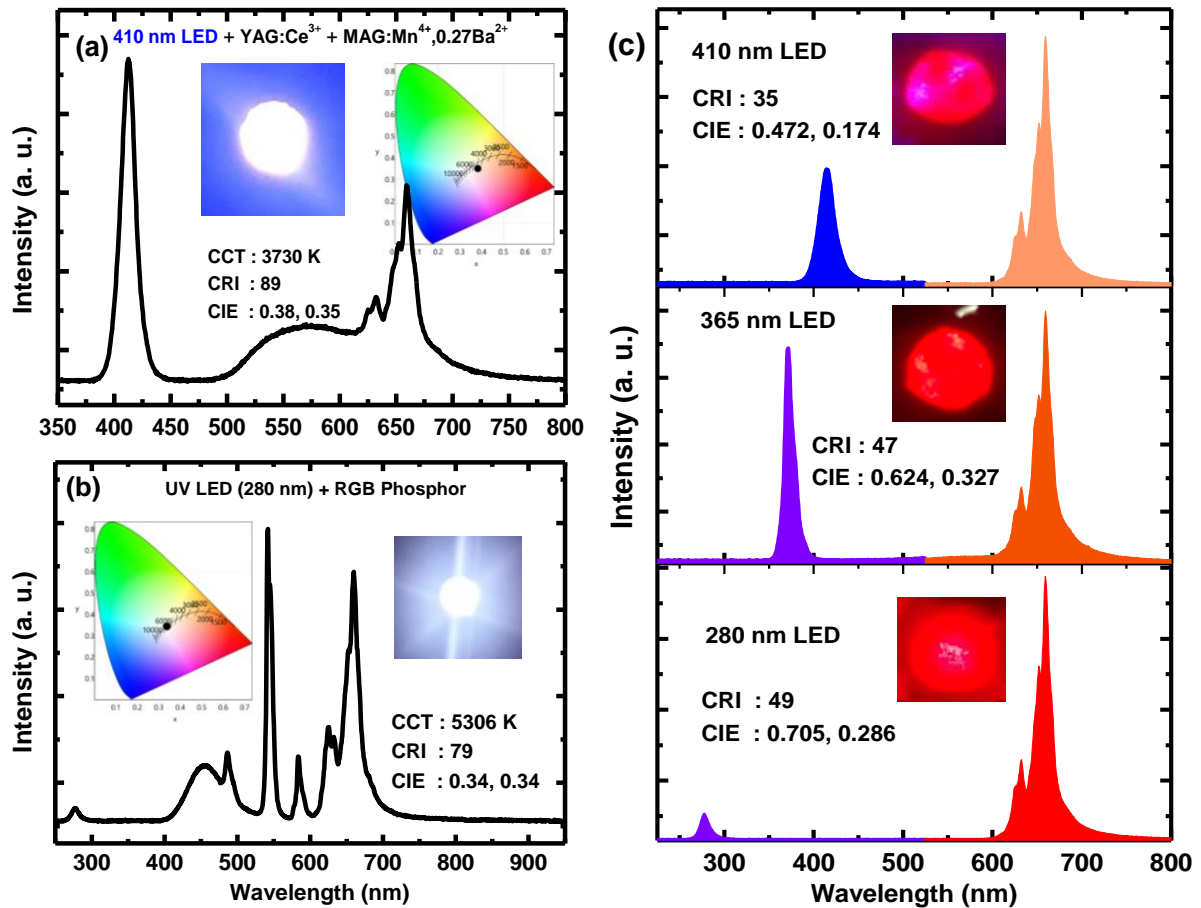


Fig.2.12 (a) EL spectra for the WLED fabricated by combining blue LED chip with YAG: Ce^{3+} and MAG: Mn^{4+} , 0.27Ba^{2+} (b) EL spectra for the WLED fabricated by combining red MAG: Mn^{4+} , 0.27Ba^{2+} phosphor with commercial green and blue phosphors using 280 nm UV LED chip. (c) EL spectra for the red LED fabricated using LED chips of different wavelengths.

2.5 Conclusions

In the present research, innovative deep red-emitting $(\text{Mg}, \text{Ba})_3\text{Al}_2\text{GeO}_8$: Mn^{4+} phosphor was evaluated from its analogue of $\text{Mg}_3\text{Ga}_2\text{GeO}_8$: Mn^{4+} . Initial replacement of Ga^{3+} by Al^{3+} yielded $\text{Mg}_3\text{Al}_2\text{GeO}_8$: Mn^{4+} , which showed much more intense red emission than $\text{Mg}_3\text{Ga}_2\text{GeO}_8$: Mn^{4+} due to the strong preference of Mn^{4+} to the $[\text{AlO}_6]$ octahedrons compared to $[\text{GaO}_6]$ octahedrons. The co-existing phases of MgAl_2O_4 and Mg_2GeO_4 in $\text{Mg}_3\text{Al}_2\text{GeO}_8$: Mn^{4+} also contributed to the Mn^{4+} luminescence by providing more preferable octahedral sites for Mn^{4+} occupancy. These sites reduced the natural reduction probability of Mn^{4+} to Mn^{2+} in the tetrahedral sites, which was confirmed by the low-temperature photoluminescence and cathodoluminescence studies for the first time. Eventually, the partial substitution of larger Ba^{2+} ions in Mg^{2+} sites caused structural distortions and generated new Ba impurity phases,

which improved the Mn^{4+} photoluminescence further. Under UV and violet-blue exposure, the optimum composition $\text{Mg}_{2.73}\text{Ba}_{0.27}\text{Al}_2\text{GeO}_8:\text{Mn}^{4+}$ exhibited deep red emission at 659 nm, which was 35 folds greater in intensity than the base composition of $\text{Mg}_3\text{Ga}_2\text{GeO}_8:\text{Mn}^{4+}$. The emission was matching with the absorption of chlorophylls liable for plants' photosynthesis. The intense red emission with 100% colour purity of the optimized composition makes it a suitable red phosphor to enhance the colour rendering of commercial white-LEDs.

2.6 Supporting Information

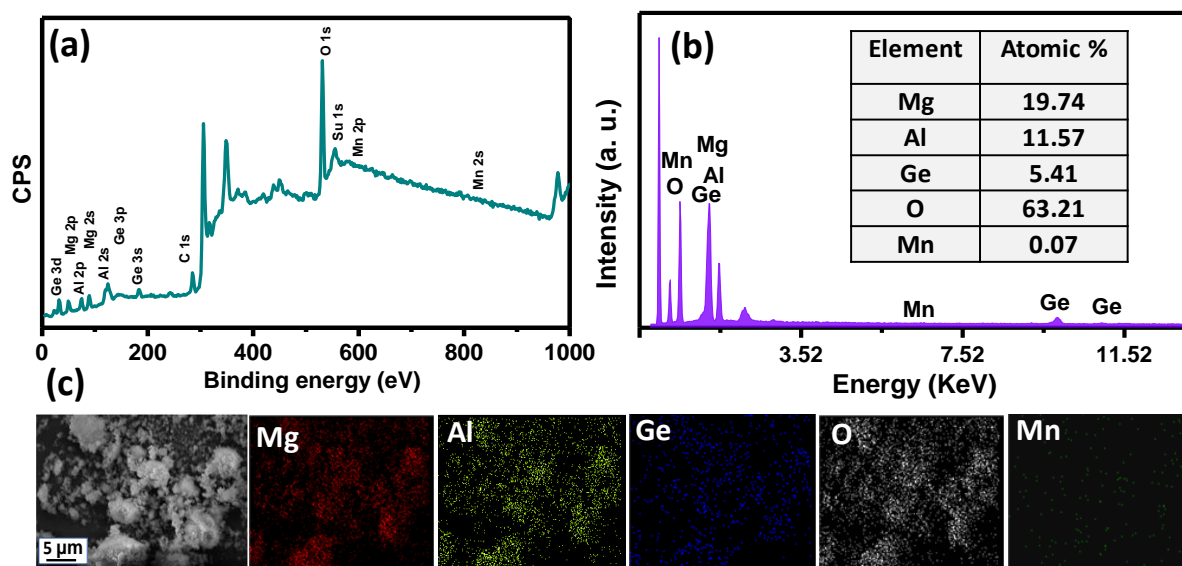


Fig.2.S1. (a) XPS survey spectra of $\text{MAG}:\text{Mn}^{4+}$ sample. (b) EDX compositional analysis, (c) SEM image and elemental mapping of Mg, Al, Ge, O, and Mn for $\text{MAG}:\text{Mn}^{4+}$.

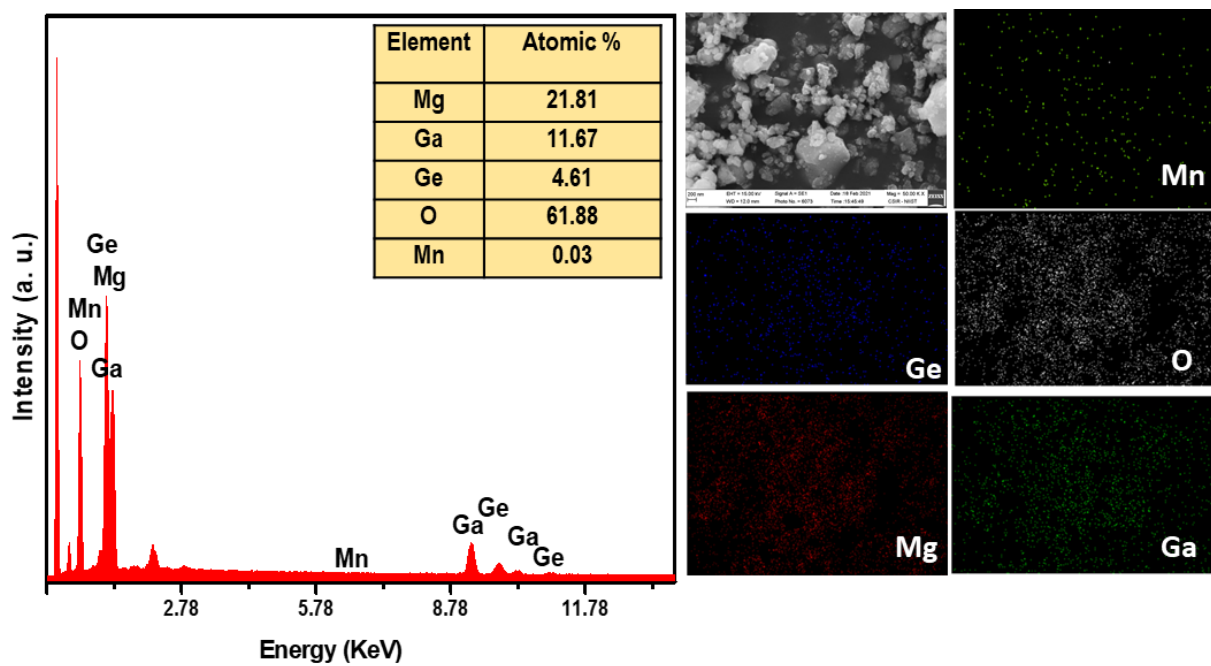


Fig.2.S2. EDX composition analysis and SEM image of MGG: Mn⁴⁺ with EDX elemental mapping images of Mg, Ga, Ge, O and Mn.

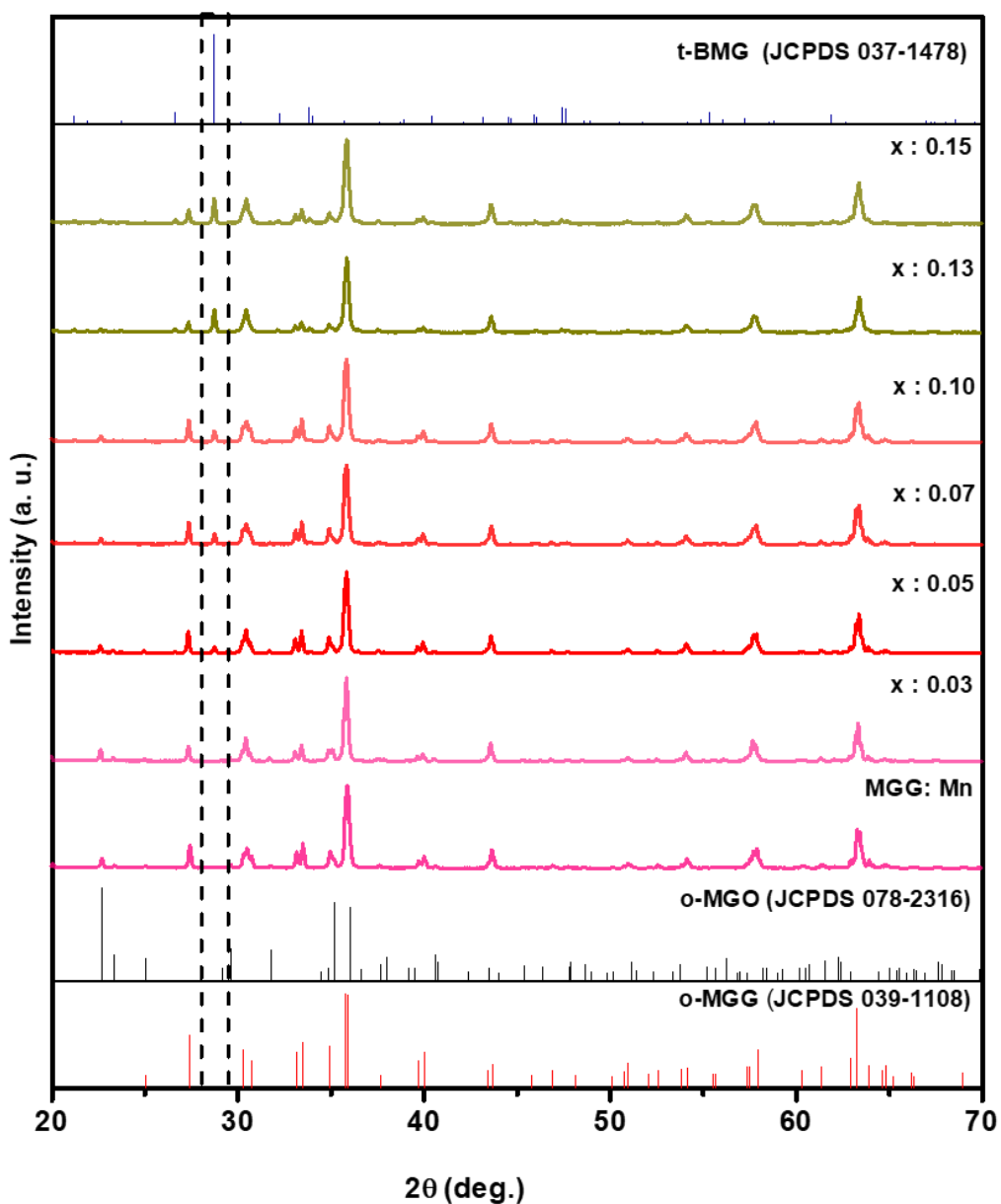


Fig.2.S3. XRD patterns of MGG, MGG: Mn⁴⁺, MGG: Mn⁴⁺, xBa²⁺ (x = 0.03 to 0.15) samples.

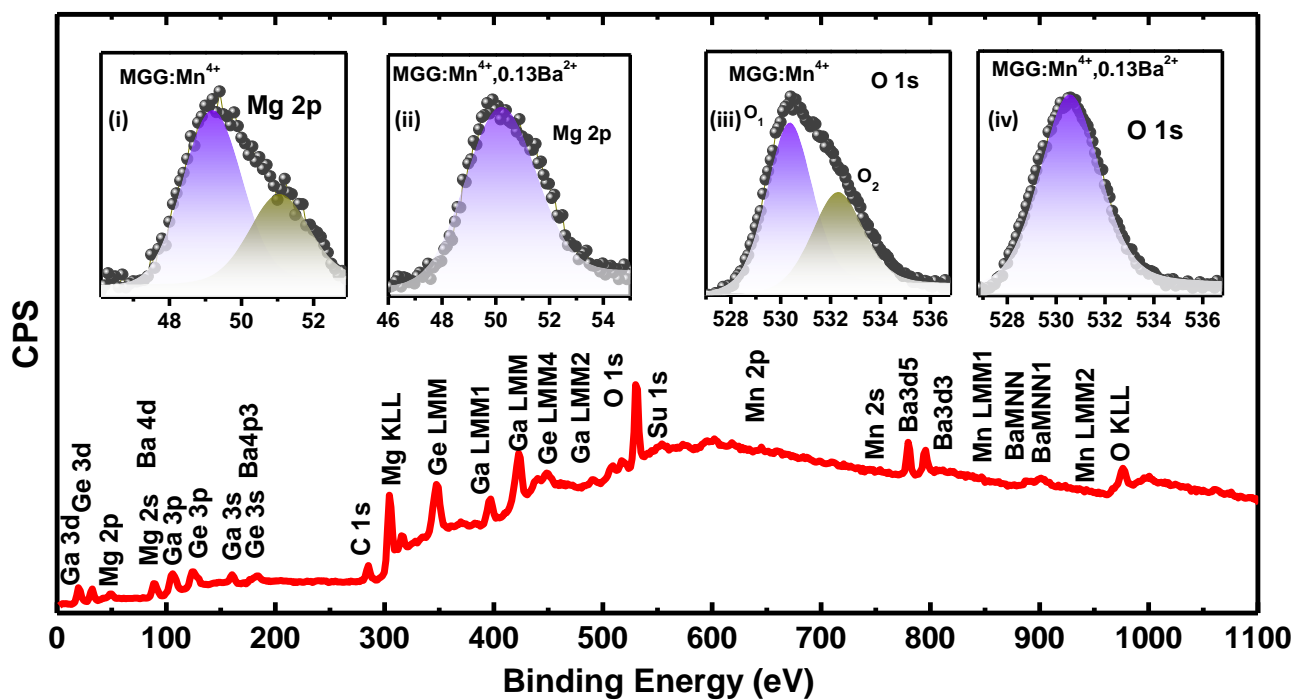


Fig.2.S4. XPS survey spectrum of the sample MGG: Mn⁴⁺, 0.13Ba²⁺. The inset shows the XPS core-level spectra of Mg 2p and O 1s for the samples MGG: Mn⁴⁺ and MGG: Mn⁴⁺, 0.13Ba²⁺.

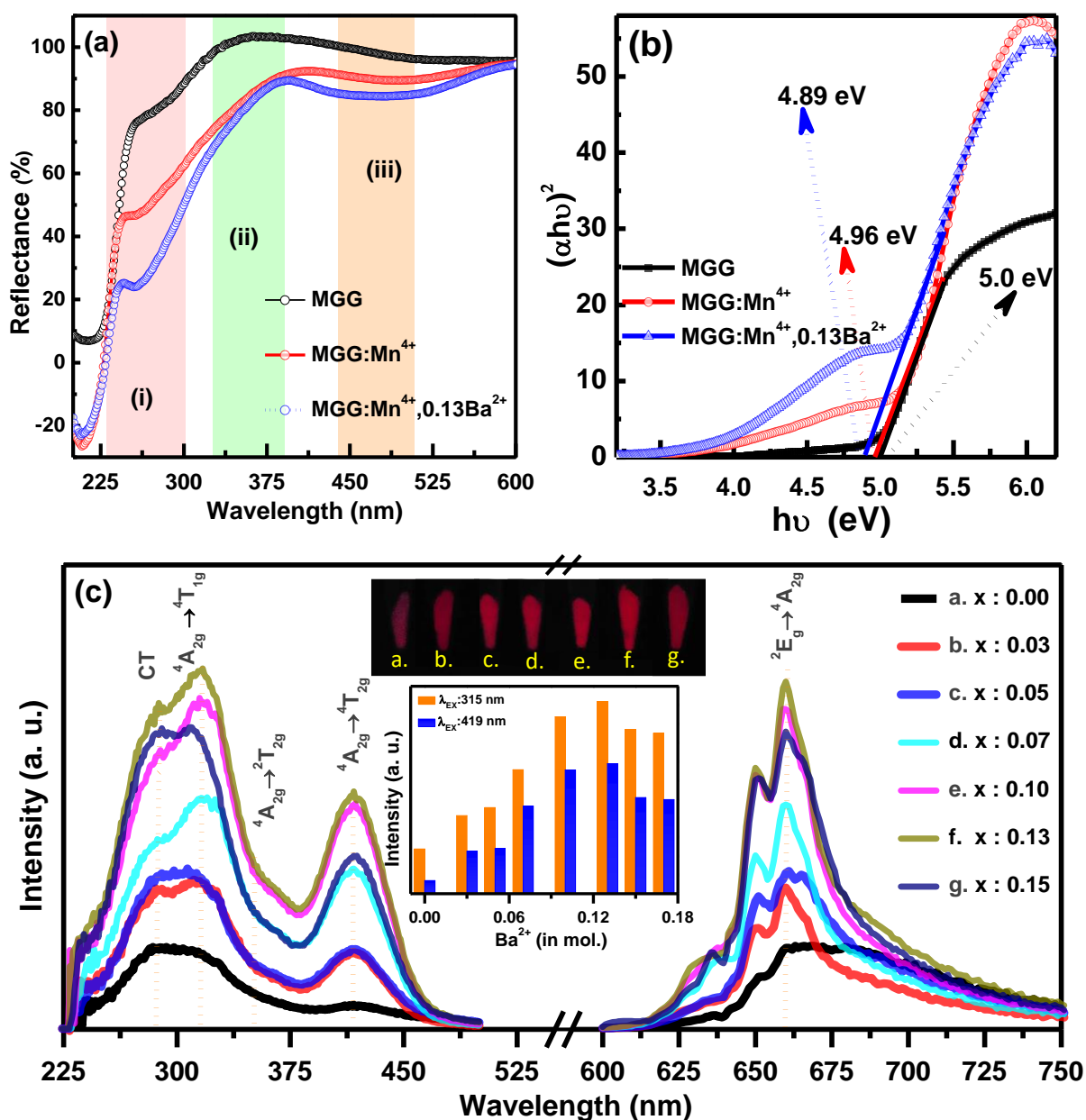


Fig.2.S5. (a) UV-DRS spectra of MGG and MGG: Mn^{4+} , $x\text{Ba}^{2+}$ ($x = 0.0, 0.13$), (i) Overlapping of the host absorption and the Mn^{4+} - O^{2-} CTB (ii) ${}^4\text{A}_{2g} \rightarrow {}^4\text{T}_{1g}$, and (iii) ${}^4\text{A}_{2g} \rightarrow {}^4\text{T}_{2g}$ transitions. (b) Tauc's plots for bandgap calculation (c) PLE spectra (λ_{em} : 659 nm) and PL emission spectra (λ_{ex} : 315 nm) of MGG: Mn^{4+} , $x\text{Ba}^{2+}$ ($x = 0.0$ to 0.15). Inset shows the variation of PL intensity with Ba^{2+} concentration under UV and blue excitation.

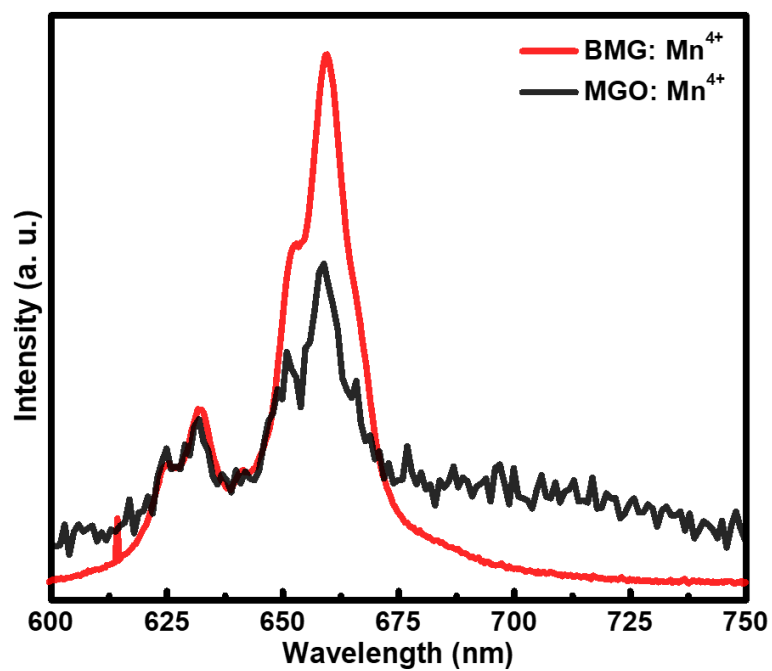


Fig.2.S6. PL emission spectra of BMG: Mn⁴⁺ and MGO: Mn⁴⁺ samples under the UV excitation of 284 nm.

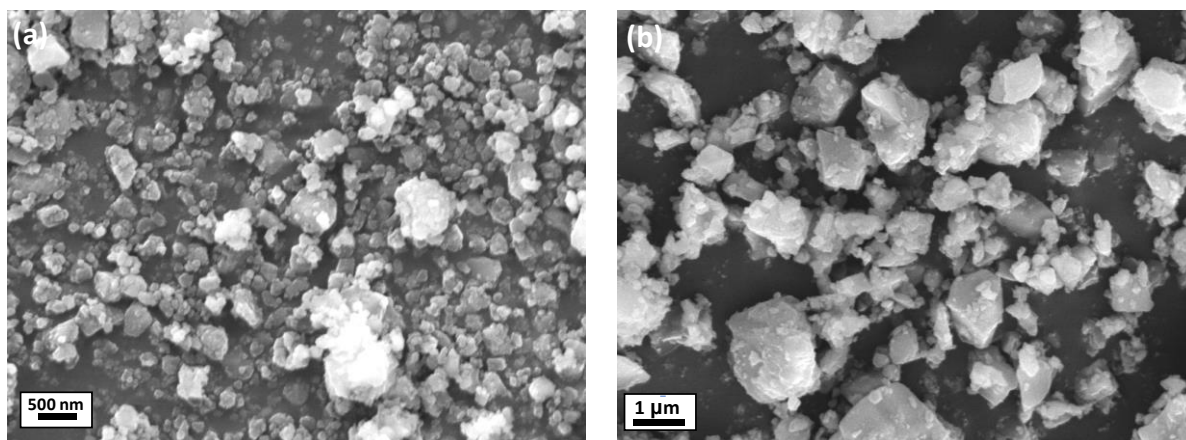


Fig.2.S7. SEM images of (a) MAG: Mn⁴⁺ and (b) MAG: Mn⁴⁺, 0.27Ba²⁺ samples.

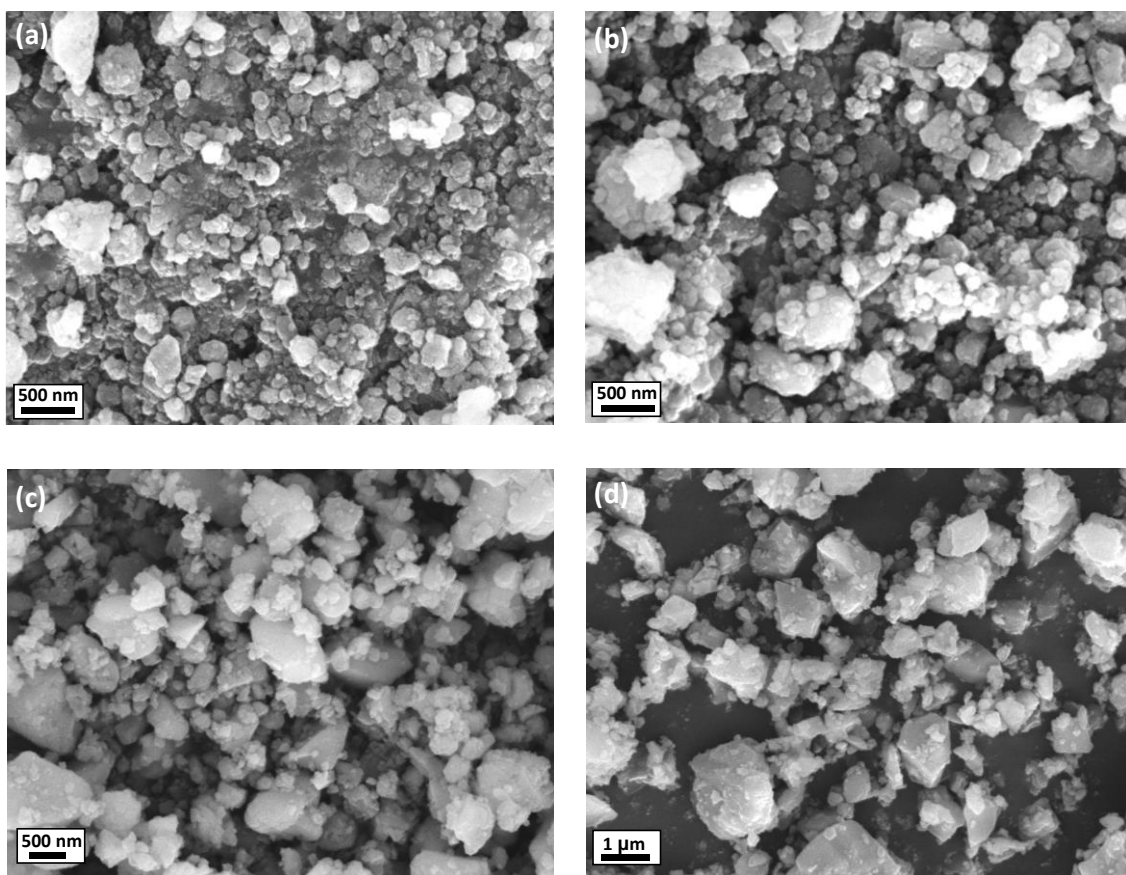


Fig.2.S8. SEM images of MAG: Mn⁴⁺, 0.27Ba²⁺ samples synthesized at various sintering temperatures (a) 700 °C (b) 800 °C (c) 900 °C and (d) 1300 °C.

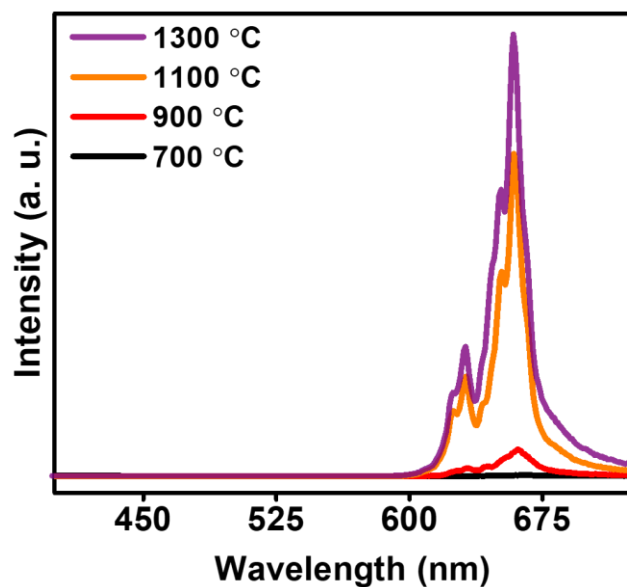


Fig.2.S9. PL emission spectra (λ_{ex} : 284) of MAG: Mn⁴⁺, 0.27Ba²⁺ samples synthesized at various sintering temperatures (700 °C, 800 °C, 900 °C and 1300 °C).

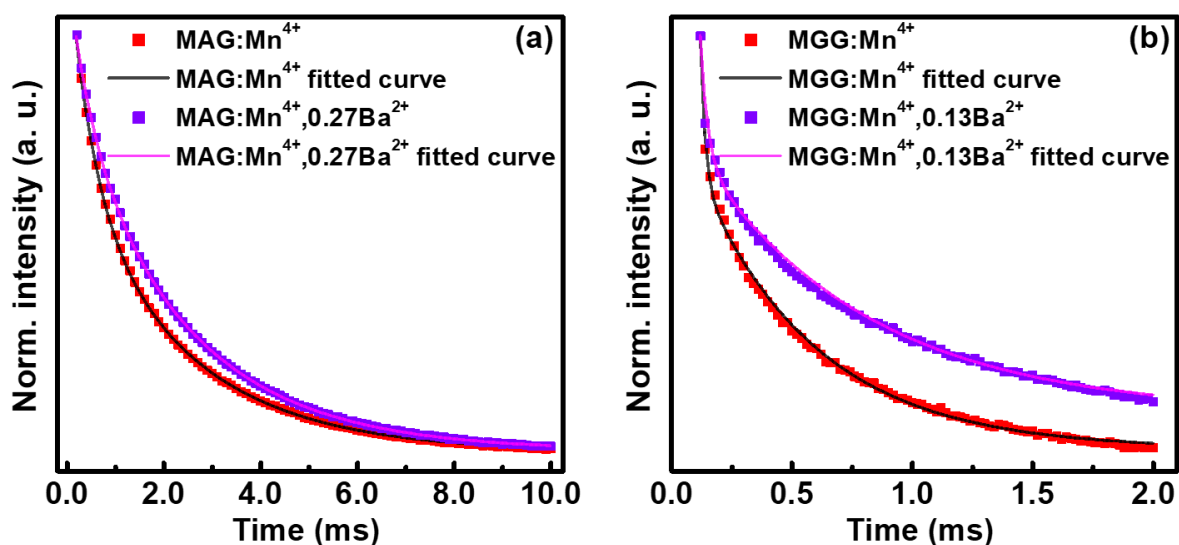


Fig.2.S10. PL emission decay curves of (a) MAG: Mn⁴⁺ and MAG: Mn⁴⁺, 0.27Ba²⁺ (b) MGG: Mn⁴⁺ and MGG: Mn⁴⁺, 0.13Ba²⁺ recorded at $\lambda_{Em} = 659$ nm and $\lambda_{Exc} = 284$ nm.

Table 2.S1: The lattice parameters of the following refined samples

Lattice parameters	MAG	MGG	MAG: Mn ⁴⁺ , 0.03Ba ²⁺	MGG: Mn ⁴⁺ , 0.1Ba ²⁺
a [Å]	5.741	5.8197	5.761	5.89
b [Å]	11.479	11.7646	11.499	11.797
c [Å]	8.104	8.3126	8.154	8.353
V[Å ³]	534.059	569.13	540.166	580.46
Rp (%)	3.3	4.1	2.88	3.8
Rwp (%)	4.6	5.68	4.14	5.45
GOF	2.0	2.0	2.43	2.12

Table 2.S2: Rietveld refined atomic coordinates and fraction of occupancies of MAG and MGG samples.

MAG					
Atoms	Sites	x	y	z	Fraction of occupancy
Mg	Mg1	0.00000	0.00000	0.00000	0.800
Al	Al1	0.00000	0.00000	0.00000	0.200
Mg	Mg2	0.00000	0.25000	0.97580	0.900
Al	Al2	0.00000	0.25000	0.97580	0.100
Mg	Mg3	0.25000	0.12460	0.25000	0.650
Al	Al3	0.25000	0.12460	0.25000	0.350
Al	Al4	0.00000	0.12020	0.61860	0.500
Ge	Ge4	0.00000	0.12020	0.61860	0.500
O	O1	0.00000	0.25000	0.22000	1.00
O	O2	0.00000	0.25000	0.72200	1.00
O	O3	0.00000	0.99970	0.25300	1.00
O	O4	0.25200	0.12700	0.99820	1.00
MGG					
Atoms	Sites	x	y	z	Fraction of occupancy
Mg	Mg1	0.00000	0.00000	0.00000	0.800
Ga	Ga1	0.00000	0.00000	0.00000	0.200
Mg	Mg2	0.00000	0.25000	0.97580	0.900
Ga	Ga2	0.00000	0.25000	0.97580	0.100
Mg	Mg3	0.25000	0.12460	0.25000	0.650
Ga	Ga3	0.25000	0.12460	0.25000	0.350
Ga	Ga4	0.00000	0.12020	0.61860	0.500
Ge	Ge4	0.00000	0.12020	0.61860	0.500
O	O1	0.00000	0.25000	0.22000	1.000
O	O2	0.00000	0.25000	0.72200	1.000
O	O3	0.00000	0.99970	0.25300	1.000
O	O4	0.25200	0.12700	0.99820	1.000

Table 2.S3: Rietveld refined atomic coordinates and fraction of occupancies of MAG:
0.03Ba²⁺ and MGG: Mn⁴⁺, 0.1Ba²⁺ samples.

MAG: Mn⁴⁺, 0.03Ba²⁺					
Atoms	Sites	X	Y	Z	Fraction of occupancy
Mg	Mg1	0.00000	0.00000	0.00000	0.790
Al	Al1	0.00000	0.00000	0.00000	0.200
Ba	Ba1	0.00000	0.00000	0.00000	0.010
Mg	Mg2	0.00000	0.25000	0.97580	0.890
Al	Al2	0.00000	0.25000	0.97580	0.100
Ba	Ba2	0.00000	0.25000	0.97580	0.010
Mg	Mg3	0.25000	0.12460	0.25000	0.640
Al	Al3	0.25000	0.12460	0.25000	0.345
Ba	Ba3	0.25000	0.12460	0.25000	0.010
Mn	Mn1	0.25000	0.12460	0.25000	0.005
Al	Al4	0.00000	0.12020	0.61860	0.500
Ge	Ge4	0.00000	0.12020	0.61860	0.500
O	O1	0.00000	0.25000	0.22000	1.000
O	O2	0.00000	0.25000	0.72200	1.000
O	O3	0.00000	0.99970	0.25300	1.000
O	O4	0.25200	0.12700	0.99820	1.000
MGG: Mn⁴⁺, 0.1Ba²⁺					
Mg	Mg1	0.00000	0.00000	0.00000	0.767
Ga	Ga1	0.00000	0.00000	0.00000	0.200
Ba	Ba1	0.00000	0.00000	0.00000	0.033
Mg	Mg2	0.00000	0.25000	0.97580	0.867
Ga	Ga2	0.00000	0.25000	0.97580	0.100
Ba	Ba2	0.00000	0.25000	0.97580	0.033
Mg	Mg3	0.25000	0.12460	0.25000	0.617
Ga	Ga3	0.25000	0.12460	0.25000	0.345
Ba	Ba3	0.25000	0.12460	0.25000	0.033
Mn	Mn1	0.25000	0.12460	0.25000	0.005
Ga	Ga4	0.00000	0.12020	0.61860	0.5000
Ge	Ge4	0.00000	0.12020	0.61860	0.5000
O	O1	0.00000	0.25000	0.22000	1.0000
O	O2	0.00000	0.25000	0.72200	1.0000
O	O3	0.00000	0.99970	0.25300	1.0000
O	O4	0.25200	0.12700	0.99820	1.0000

Table 2.S4: Calculated bond lengths (Å) and average bond lengths (Å) in the following samples.

Bond	MAG	MGG	MAG: Mn ⁴⁺ , 0.03Ba ²⁺	MGG: Mn ⁴⁺ , 0.1Ba ²⁺
Mg1/Al1/Ga1-O4	2.05393 (×4)	2.09365 (×4)	2.05928 (×4)	2.10907 (×4)
Mg1/Al1/Ga1-O3	2.05026 (×2)	2.10308 (×2)	2.06291 (×2)	2.11343 (×2)
Avg. Mg1/Al1/Ga1-O	2.0527	2.09679	2.06049	2.110523
Mg2/Al2/Ga2-O4	2.02968 (×4)	2.06868 (×4)	2.03508 (×4)	2.08418 (×4)
Mg2/Al2/Ga2-O1	1.97895	2.02993	1.99116	2.03992
Mg2/Al2/Ga2-O2	2.05674	2.10973	2.06943	2.12011
Avg. Mg2/Al2/Ga2-O	2.025735	2.06906	2.03348	2.08279
Mg3/Al3/Ga3-O4	2.04076 (×2)	2.09333 (×2)	2.05334 (×2)	2.10363 (×2)
Mg3/Al3/Ga3-O1	2.04724 (×2)	2.08697 (×2)	2.05269 (×2)	2.10231 (×2)
Mg3/Al3/Ga3-O3	2.02884 (×2)	2.06799 (×2)	2.03415 (×2)	2.0833 (×2)
Avg. Mg3/Al3/Ga3-O	2.038946	2.08276	2.046726	2.09641
Avg. Mg/Al/Ga-O	2.03913	2.08287	2.0469	2.09657
Ge4/Al4/Ga4- O4	1.71151 (×2)	1.7413 (×2)	1.71887 (×2)	1.75852 (×2)
Ge4/Al4/Ga4- O2	1.70941	1.75233	1.71421	1.75803
Ge4/Al4/Ga4- O3	1.72538	1.76888	1.73116	1.77512
Avg. Ge/Al/Ga- O	1.71444	1.75095	1.72077	1.76255

2.7 References

- [1] Huang, L.; Liu, Y.; Yu, J.; Zhu, Y.; Pan, F.; Xuan, T.; Brik, M. G.; Wang, C.; Wang, J. Highly Stable $\text{K}_2\text{SiF}_6:\text{Mn}^{4+}$ @ K_2SiF_6 Composite Phosphor with Narrow Red Emission for White LEDs. *ACS Appl. Mater. Interfaces* **2018**, *10* (21), 18082–18092. <https://doi.org/10.1021/acsami.8b03893>.
- [2] Zhu, H.; Lin, C. C.; Luo, W.; Shu, S.; Liu, Z.; Liu, Y.; Kong, J.; Ma, E.; Cao, Y.; Liu, R. S.; Chen, X. Highly Efficient Non-Rare-Earth Red Emitting Phosphor for Warm White Light-Emitting Diodes. *Nat. Commun.* **2014**, *5*, 1–10. <https://doi.org/10.1038/ncomms5312>.
- [3] Ming, H.; Liu, L.; He, S.; Peng, J.; Du, F.; Fu, J.; Yang, F.; Ye, X. An Ultra-High Yield of Spherical $\text{K}_2\text{NaScF}_6:\text{Mn}^{4+}$ Red Phosphor and Its Application in Ultra-Wide Color Gamut Liquid Crystal Displays. *J. Mater. Chem. C* **2019**, *7* (24), 7237–7248. <https://doi.org/10.1039/c9tc02295c>.
- [4] Singh, S. P.; Kim, M.; Park, W. B.; Lee, J. W.; Sohn, K. S. Discovery of a Red-Emitting $\text{Li}_3\text{RbGe}_8\text{O}_{18}:\text{Mn}^{4+}$ Phosphor in the Alkali-Germanate System: Structural Determination and Electronic Calculations. *Inorg. Chem.* **2016**, *55* (20), 10310–10319. <https://doi.org/10.1021/acs.inorgchem.6b01576>.
- [5] Li, P.; Wondraczek, L.; Peng, M.; Zhang, Q.; Setlur, A. Tuning Mn^{4+} Red Photoluminescence in $(\text{K,Rb})_2\text{Ge}_4\text{O}_9:\text{Mn}^{4+}$ Solid Solutions by Partial Alkali Substitution. *J. Am. Ceram. Soc.* **2016**, *99* (10), 3376–3381. <https://doi.org/10.1111/jace.14363>.
- [6] Hu, J.; Huang, T.; Zhang, Y.; Lu, B.; Ye, H.; Chen, B.; Xia, H.; Ji, C. Enhanced Deep-Red Emission from $\text{Mn}^{4+}/\text{Mg}^{2+}$ Co-Doped CaGdAlO_4 Phosphors for Plant Cultivation. *Dalt. Trans.* **2019**, *48* (7), 2455–2466. <https://doi.org/10.1039/c8dt04955f>.
- [7] Li, K.; Zhu, D.; Van Deun, R. Photoluminescence Properties and Crystal Field Analysis of a Novel Red-Emitting Phosphor $\text{K}_2\text{BaGe}_8\text{O}_{18}:\text{Mn}^{4+}$. *Dye. Pigment.* **2017**, *142*, 69–76. <https://doi.org/10.1016/j.dyepig.2017.03.007>.
- [8] Huang, X.; Zhang, P.; Liu, Z.; Ma, B.; Zhou, Y.; Tian, X. Fluorine Doping Induced Crystal Space Change and Performance Improvement of Single Crystalline $\text{LiNi}_{0.6}\text{Co}_{0.2}\text{Mn}_{0.2}\text{O}_2$ Layered Cathode Materials. *ChemElectroChem* **2022**, *9* (1), 1–7. <https://doi.org/10.1002/celec.202100756>.

- [9] Liang, S.; Shang, M.; Lian, H.; Li, K.; Zhang, Y.; Lin, J. An Efficient Rare-Earth Free Deep Red Emitting Phosphor for Improving the Color Rendering of White Light-Emitting Diodes. *J. Mater. Chem. C* **2017**, *5* (11), 2927–2935. <https://doi.org/10.1039/c6tc05499d>.
- [10] Dolgov, L.; Hong, J.; Zhou, L.; Li, X.; Li, J.; Djordjevic, V.; Dramicanin, M.; Shi, J.; Wu, M. Efficient Luminescence Enhancement of $\text{Mg}_2\text{TiO}_4:\text{Mn}^{4+}$ Red Phosphor by Incorporating Plasmonic $\text{Ag}@\text{SiO}_2$ Nanoparticles. *ACS Appl. Mater. Interfaces* **2019**, *11* (23), 21004–21009. <https://doi.org/10.1021/acsami.9b05781>.
- [11] Ding, X.; Zhu, G.; Geng, W.; Wang, Q.; Wang, Y. Rare-Earth-Free High-Efficiency Narrow-Band Red-Emitting $\text{Mg}_3\text{Ga}_2\text{GeO}_8:\text{Mn}^{4+}$ Phosphor Excited by Near-UV Light for White-Light-Emitting Diodes. *Inorg. Chem.* **2016**, *55* (1), 154–162. <https://doi.org/10.1021/acs.inorgchem.5b02048>.
- [12] Liang, S.; Shang, M.; Lian, H.; Li, K.; Zhang, Y.; Lin, J. Deep Red $\text{MGe}_4\text{O}_9:\text{Mn}^{4+}$ (M = Sr, Ba) Phosphors: Structure, Luminescence Properties and Application in Warm White Light Emitting Diodes. *J. Mater. Chem. C* **2016**, *4* (26), 6409–6416. <https://doi.org/10.1039/c6tc01813k>.
- [13] Huang, Q.; Ye, W.; Hu, G.; Liu, X. Strong Red Emission in Bi^{3+} and Mn^{4+} Codoped $\text{Mg}_{3.5}\text{Ge}_{1.25}\text{O}_6$ Phosphors Applied in Optical Agriculture. *J. Lumin.* **2019**, *210*, 89–95. <https://doi.org/10.1016/j.jlumin.2019.01.047>.
- [14] Liang, S.; Li, G.; Dang, P.; Wei, Y.; Lian, H.; Lin, J. Cation Substitution Induced Adjustment on Lattice Structure and Photoluminescence Properties of $\text{Mg}_{14}\text{Ge}_5\text{O}_{24}:\text{Mn}^{4+}$: Optimized Emission for w-LED and Thermometry Applications. *Adv. Opt. Mater.* **2019**, *7* (12), 1–15. <https://doi.org/10.1002/adom.201900093>.
- [15] Peng, L.; Chen, W.; Cao, S.; Liu, B.; Han, T.; Zhao, L.; Zhao, C.; Li, F.; Li, X. Enhanced Photoluminescence and Thermal Properties Due to Size Mismatch in $\text{Mg}_2\text{Ti}_x\text{Ge}_{1-x}\text{O}_4:\text{Mn}^{4+}$ Deep-Red Phosphors. *J. Mater. Chem. C* **2019**, *7* (8), 2345–2352. <https://doi.org/10.1039/c8tc05743e>.
- [16] Abraham, M.; Kunti, A. K.; K.K., T.; Amador-Mendez, N.; Gogneau, N.; K.G., N.; Tchernycheva, M.; Das, S. The Elevated Colour Rendering of White-LEDs by Microwave-Synthesized Red-Emitting $(\text{Li}, \text{Mg})_3\text{RbGe}_8\text{O}_{18}:\text{Mn}^{4+}$ nanophosphors. *Dalt. Trans.* **2021**, *50* (8), 3044–3059. <https://doi.org/10.1039/d0dt04309e>.

- [17] Wu, Y.; Zhuang, Y.; Xie, R. J.; Ruan, K.; Ouyang, X. Novel Mn⁴⁺ Doped Red Phosphors Composed of MgAl₂O₄ and CaAl₁₂O₁₉ Phases for Light-Emitting Diodes. *Dalt. Trans.* **2020**, *49* (11), 3606–3614. <https://doi.org/10.1039/d0dt00118j>.
- [18] Cao, R.; Ye, Y.; Peng, Q.; Zheng, G.; Ao, H.; Fu, J.; Guo, Y.; Guo, B. Synthesis and Luminescence Characteristics of Novel Red-Emitting Ba₂TiGe₂O₈:Mn⁴⁺ Phosphor. *Dye. Pigment.* **2017**, *146*, 14–19. <https://doi.org/10.1016/j.dyepig.2017.06.061>.
- [19] Chen, D.; Zhou, Y.; Zhong, J. A Review on Mn⁴⁺ Activators in Solids for Warm White Light-Emitting Diodes. *RSC Adv.* **2016**, *6* (89), 86285–86296. <https://doi.org/10.1039/c6ra19584a>.
- [20] Wang, Y.; Ding, F.; Wu, J.; Ke, J.; Yuan, X.; Wang, X.; Qiu, Z.; Zhou, W.; Zhang, J.; Lian, S. Site Preference-Driven Mn⁴⁺ Stabilization in Double Perovskite Phosphor Regulating Quantum Efficiency from Zero to Champion. *Inorg. Chem.* **2022**, *61* (8), 3631–3640. <https://doi.org/10.1021/acs.inorgchem.1c03756>.
- [21] Dong, L.; Zhang, L.; Jia, Y.; Shao, B.; Lü, W.; Zhao, S.; You, H. Site Occupation and Luminescence of Novel Orange-Red Ca₃M₂Ge₃O₁₂:Mn²⁺, Mn⁴⁺ (M = Al, Ga) Phosphors. *ACS Sustain. Chem. Eng.* **2020**, *8* (8), 3357–3366. <https://doi.org/10.1021/acssuschemeng.9b07281>.
- [22] Cao, R.; Luo, W.; Xiong, Q.; Liang, A.; Jiang, S.; Xu, Y. Synthesis and Luminescence Properties of Novel Red Phosphors LiRGe₂O₆:Mn⁴⁺ (R = Al or Ga). *J. Alloys Compd.* **2015**, *648*, 937–941. <https://doi.org/10.1016/j.jallcom.2015.07.080>.
- [23] Dai, D.; Wang, Z.; Xing, Z.; Li, X.; Liu, C.; Zhang, L.; Yang, Z.; Li, P. Broad Band Emission Near-Infrared Material Mg₃Ga₂GeO₈:Cr³⁺: Substitution of Ga-In, Structural Modification, Luminescence Property and Application for High Efficiency LED. *J. Alloys Compd.* **2019**, *806*, 926–938. <https://doi.org/10.1016/j.jallcom.2019.07.166>.
- [24] Lu, Z.; Fu, A.; Gao, F.; Zhang, X.; Zhou, L. Synthesis and Luminescence Properties of Double Perovskite Ba₂MgGe₂O₇:Mn⁴⁺ Deep Red Phosphor. *J. Lumin.* **2018**, *203* (June), 420–426. <https://doi.org/10.1016/j.jlumin.2018.06.061>.
- [25] Kaminskii, A. A.; Bohatý, L.; Becker, P.; Liebertz, J.; Held, P.; Eichler, H. J.; Rhee, H.; Hanuza, J. Tetragonal Ba₂MgGe₂O₇ - A Novel Multifunctional Optical Crystal with Numerous Manifestations of Nonlinear-Laser Effects: Almost Sesqui-Octave Stokes

- and Anti-Stokes Combs and Cascaded $\chi(3) \leftrightarrow \chi(2)$ Lasing with Involved Second and Third Harmonic Generation. *Laser Phys. Lett.* **2008**, *5* (12), 845–868. <https://doi.org/10.1002/lapl.200810089>.
- [26] Öztürk, E. The Effect of Ba/Mg Impurities on the Phase Formation and Photoluminescence Properties of $(\text{Sr}_{3-x}\text{M}_x)\text{Al}_2\text{O}_6:\text{Eu}^{3+},\text{Ho}^{3+}$ (M = Ba, Mg) Phosphors. *J. Therm. Anal. Calorim.* **2016**, *126* (2), 365–369. <https://doi.org/10.1007/s10973-016-5546-z>.
- [27] Shannon, R. D. Revised Effective Ionic Radii and Systematic Studies of Interatomic Distances in Halides and Chalcogenides BY. *Acta Crystallogr. Sect. A* **1976**, *32* (5), 751–766. <https://doi.org/10.1023/A:1018927109487>.
- [28] Zhang, R.; Wang, Z.; Meng, Y.; Jiao, S.; Jia, J.; Min, Y.; Liu, C. Quantitative Insight into Aluminum Structures in CaO–Al₂O₃–SiO₂ System via Raman and ²⁷Al MAS-NMR Spectroscopies. *J. Non. Cryst. Solids* **2021**, *573*, 121116. <https://doi.org/10.1016/j.jnoncrysol.2021.121116>.
- [29] Rudolph, W. W.; Irmer, G.; Hefter, G. T. Raman Spectroscopic Investigation of Speciation in MgSO₄(Aq). *Phys. Chem. Chem. Phys.* **2003**, *5* (23), 5253–5261. <https://doi.org/10.1039/b308951g>.
- [30] Alvarado-Rivera, J.; Rodríguez-Carvajal, D. A.; Acosta-Enríquez, M. del C.; Manzanares-Martínez, M. B.; Álvarez, E.; Lozada-Morales, R.; Díaz, G. C.; de Leon, A.; Zayas, M. E. Effect of CeO₂ on the Glass Structure of Sodium Germanate Glasses. *J. Am. Ceram. Soc.* **2014**, *97* (11), 3494–3500. <https://doi.org/10.1111/jace.13202>.
- [31] Hasegawa, T.; Tanaka, R.; Ueda, T.; Toda, K. Preparation of MGF Phosphor by O₂ Postannealing and Impact on Luminescence Properties and Crystal Lattice. *J. Am. Ceram. Soc.* **2020**, *103* (9), 5145–5156. <https://doi.org/10.1111/jace.17222>.
- [32] Fang, W.; Ao, L.; Tang, Y.; Li, J.; Xiang, H.; Zhang, Z.; Du, Q.; Fang, L. Phase Evolution and Microwave Dielectric Properties of the Li_{2(1+x)}ZnGe₃O₈ Spinel Oxides. *J. Mater. Sci. Mater. Electron.* **2020**, *31* (16), 13496–13502. <https://doi.org/10.1007/s10854-020-03904-8>.
- [33] Li, J.; Chou, K.; Shu, Q. Structure and Viscosity of CaO–Al₂O₃–B₂O₃ Based Mould Fluxes with Varying CaO/Al₂O₃ Mass Ratios. *ISIJ Int.* **2020**, *60* (1), 51–57.

- <https://doi.org/10.2355/isijinternational.ISIJINT-2019-234>.
- [34] Zhou, Y.; Zhuang, W.; Hu, Y.; Liu, R.; Jiang, Z.; Liu, Y.; Li, Y.; Zheng, Y.; Chen, L.; Zhong, J. A Broad-Band Orange-Yellow-Emitting $\text{Lu}_2\text{Mg}_2\text{Al}_2\text{Si}_2\text{O}_{12}:\text{Ce}^{3+}$ Phosphor for Application in Warm White Light-Emitting Diodes. *RSC Adv.* **2017**, *7* (74), 46713–46720. <https://doi.org/10.1039/c7ra08760h>.
- [35] Wood, D. L. Weak Absorption Tails in Amorphous Semiconductors. *Phys. Rev. B* **1972**, *5* (8), 3144–3151. <https://doi.org/https://doi.org/10.1103/PhysRevB.5.3144>.
- [36] Xia, M.; Gu, S.; Zhou, C.; Liu, L.; Zhong, Y.; Zhang, Y.; Zhou, Z. Enhanced Photoluminescence and Energy Transfer Performance of $\text{Y}_3\text{Al}_4\text{GaO}_{12}:\text{Mn}^{4+},\text{Dy}^{3+}$ Phosphors for Plant Growth LED Lights. *RSC Adv.* **2019**, *9* (16), 9244–9252. <https://doi.org/10.1039/c9ra00700h>.
- [37] Xue, J.; Ran, W.; Noh, H. M.; Choi, B. C.; Park, S. H.; Jeong, J. H.; Kim, J. H. Influence of Alkaline Ions on the Luminescent Properties of Mn^{4+} -Doped MGe_4O_9 ($\text{M} = \text{Li}_2, \text{LiNa}$ and K_2) Red-Emitting Phosphors. *J. Lumin.* **2017**, *192*, 1072–1083. <https://doi.org/10.1016/j.jlumin.2017.08.036>.
- [38] Xue, F.; Hu, Y.; Chen, L.; Wu, H.; Ju, G.; Wang, T.; Yang, L. A Novel Rare-Earth Free Red Long-Persistent Phosphor: $\text{Mg}_2\text{GeO}_4:\text{Mn}^{4+}$. *Ceram. Int.* **2017**, *43* (17), 15141–15145. <https://doi.org/10.1016/j.ceramint.2017.08.044>.
- [39] Feng, J.; Wang, Z.; Xu, H.; Jia, M.; Wei, Y.; Fu, Z. The Charge Transfer Band as a Key to Study the Site Selection Preference of Eu^{3+} in Inorganic Crystals. *Inorg. Chem.* **2021**, *60* (24), 19440–19447. <https://doi.org/10.1021/acs.inorgchem.1c03273>.
- [40] Ji, H.; Hou, X.; Molokeyev, M. S.; Ueda, J.; Tanabe, S.; Brik, M. G.; Zhang, Z.; Wang, Y.; Chen, D. Ultrabroadband Red Luminescence of Mn^{4+} in MgAl_2O_4 peaking at 651 Nm. *Dalt. Trans.* **2020**, *49* (17), 5711–5721. <https://doi.org/10.1039/d0dt00931h>.
- [41] Srivastava, A. M.; Brik, M.; Beers, W. W.; Cohen, W. On the Mn^{4+} R-Line Intensity and Energy in the Perovskite Layer of SrLaAlO_4 and Sr_2TiO_4 : A Comparative Study with LaAlO_3 and SrTiO_3 . *Opt. Mater. (Amst.)* **2020**, *109* (September). <https://doi.org/10.1016/j.optmat.2020.110372>.
- [42] Yan, W.; Yun, X.; Yang, H.; Wei, Y.; Li, G. A Novel Mn^{4+} -Activated $\text{Li}_3\text{CsGe}_8\text{O}_{18}$ Red Phosphor and Cation Substitution Induced Photoluminescence Improvement. *J. Lumin.*

- 2020, 225 (May), 117323. <https://doi.org/10.1016/j.jlumin.2020.117323>
- [43] Cao, R.; Lv, X.; Ran, Y.; Xu, L.; Chen, T.; Guo, S.; Ao, H.; Yu, X. Rare-Earth-Free $\text{Li}_5\text{La}_3\text{Ta}_2\text{O}_{12}:\text{Mn}^{4+}$ Deep-Red-Emitting Phosphor: Synthesis and Photoluminescence Properties. *J. Am. Ceram. Soc.* **2019**, *102* (10), 5910–5918. <https://doi.org/10.1111/jace.16447>.
- [44] Tao, C.; Li, P.; Li, Q.; Zhang, N.; Wang, D.; Zhao, J.; Yang, Z.; Wang, Z. Improvement of Thermal Stability and Photoluminescence in $\text{Mg}_2\text{Y}_2\text{Al}_2\text{Si}_2\text{O}_{12}:\text{Ce}^{3+}$ by the Cation Substitution of Ca^{2+} , Sr^{2+} and Ba^{2+} ions. *Dalt. Trans.* **2021**, *50* (37), 13138–13148. <https://doi.org/10.1039/d1dt02336e>.
- [45] Fang, S.; Han, T.; Lang, T.; Zhong, Y.; Liu, B.; Cao, S.; Peng, L.; Yakovlev, A. N.; Korepanov, V. I. Synthesis of a Novel Red Phosphor $\text{K}_{2x}\text{Ba}_{1-x}\text{TiF}_6:\text{Mn}^{4+}$ and Its Enhanced Luminescence Performance, Thermal Stability and Waterproofness. *J. Alloys Compd.* **2019**, *808*, 151697. <https://doi.org/10.1016/j.jallcom.2019.151697>.
- [46] Peng, M.; Yin, X.; Tanner, P. A.; Brik, M. G.; Li, P. Site Occupancy Preference, Enhancement Mechanism, and Thermal Resistance of Mn^{4+} Red Luminescence in $\text{Sr}_4\text{Al}_{14}\text{O}_{25}:\text{Mn}^{4+}$ for Warm WLEDs. *Chem. Mater.* **2015**, *27* (8), 2938–2945. <https://doi.org/10.1021/acs.chemmater.5b00226>.
- [47] Yang, D.; Li, G.; Kang, X.; Cheng, Z.; Ma, P.; Peng, C.; Lian, H.; Li, C.; Lin, J. Room Temperature Synthesis of Hydrophilic Ln^{3+} -Doped KGdF_4 ($\text{Ln} = \text{Ce}, \text{Eu}, \text{Tb}, \text{Dy}$) Nanoparticles with Controllable Size: Energy Transfer, Size-Dependent and Color-Tunable Luminescence Properties. *Nanoscale* **2012**, *4* (11), 3450–3459. <https://doi.org/10.1039/c2nr30338h>.
- [48] Huang, D.; Dang, P.; Lian, H.; Zeng, Q.; Lin, J. Luminescence and Energy-Transfer Properties in $\text{Bi}^{3+}/\text{Mn}^{4+}$ -Codoped $\text{Ba}_2\text{GdNbO}_6$ Double-Perovskite Phosphors for White-Light-Emitting Diodes. *Inorg. Chem.* **2019**, *58* (22), 15507–15519. <https://doi.org/10.1021/acs.inorgchem.9b02558>.
- [49] Li, X.; Chen, Z.; Wang, B.; Liang, R.; Li, Y.; Kang, L.; Liu, P. Effects of Impurity Doping on the Luminescence Performance of Mn^{4+} -Doped Aluminates with the Magnetoplumbite-Type Structure for Plant Cultivation. *Materials (Basel)*. **2018**, *12* (1), 1–11. <https://doi.org/10.3390/ma12010086>.

- [50] Wu, C.; Li, J.; Xu, H.; Wu, J.; Zhang, J.; Ci, Z.; Feng, L.; Cao, C.; Zhang, Z.; Wang, Y. Preparation, Structural and Photoluminescence Characteristics of Novel Red Emitting $\text{Mg}_7\text{Ga}_2\text{GeO}_{12}:\text{Mn}^{4+}$ Phosphor. *J. Alloys Compd.* **2015**, *646*, 734–740. <https://doi.org/10.1016/j.jallcom.2015.06.166>.
- [51] Thejas, K. K.; Abraham, M.; Kunti, A. K.; Tchernycheva, M.; Ahmad, S.; Das, S. Review on Deep Red-Emitting Rare-Earth Free Germanates and Their Efficiency as Well as Adaptability for Various Applications. *Appl. Mater. Today* **2021**, *24*, 101094. <https://doi.org/10.1016/j.apmt.2021.101094>.
- [52] Wang, Z.; Ji, H.; Xu, J.; Hou, X.; Ueda, J.; Tanabe, S.; Yi, S.; Zhou, Y.; Chen, D. Microsized Red Luminescent $\text{MgAl}_2\text{O}_4:\text{Mn}^{4+}$ Single-Crystal Phosphor Grown in Molten Salt for White LEDs. *Inorg. Chem.* **2020**, *59* (24), 18374–18383. <https://doi.org/10.1021/acs.inorgchem.0c03005>.
- [53] Gu, S.; Xia, M.; Zhou, C.; Kong, Z.; Molokeev, M. S.; Liu, L.; Wong, W. Y.; Zhou, Z. Red Shift Properties, Crystal Field Theory and Nephelauxetic Effect on Mn^{4+} -Doped $\text{SrMgAl}_{10-y}\text{Ga}_y\text{O}_{17}$ Red Phosphor for Plant Growth LED Light. *Chem. Eng. J.* **2020**, *396*, 125208. <https://doi.org/10.1016/j.cej.2020.125208>.
- [54] S Sun, Q.; Wang, S.; Devakumar, B.; Sun, L.; Liang, J.; Huang, X. Synthesis, Crystal Structure, and Photoluminescence Characteristics of High-Efficiency Deep-Red Emitting $\text{Ba}_2\text{GdTao}_6:\text{Mn}^{4+}$ Phosphors. *ACS Omega* **2019**, *4* (8), 13474–13480. <https://doi.org/10.1021/acsomega.9b01787>.
- [55] Li, K.; Van Deun, R. Novel Intense Emission-Tunable $\text{Li}_{1.5}\text{La}_{1.5}\text{WO}_6:\text{Mn}^{4+},\text{Nd}^{3+},\text{Yb}^{3+}$ Material with Good Luminescence Thermal Stability for Potential Applications in c-Si Solar Cells and Plant-Cultivation Far-Red-NIR LEDs. *ACS Sustain. Chem. Eng.* **2019**, *7* (19). <https://doi.org/10.1021/acssuschemeng.9b03308>.
- [56] Ji, H.; Ueda, J.; Brik, M. G.; Du, M. H.; Chen, D.; Tanabe, S. Intense Deep-Red Zero Phonon Line Emission of Mn^{4+} in Double Perovskite $\text{La}_4\text{Ti}_3\text{O}_{12}$. *Phys. Chem. Chem. Phys.* **2019**, *21* (45), 25108–25117. <https://doi.org/10.1039/c9cp04007b>.
- [57] Zhang, S.; Hu, Y. Photoluminescence Spectroscopies and Temperature-Dependent Luminescence of Mn^{4+} in BaGe_4O_9 Phosphor. *J. Lumin.* **2016**, *177*, 394–401. <https://doi.org/10.1016/j.jlumin.2016.05.020>.

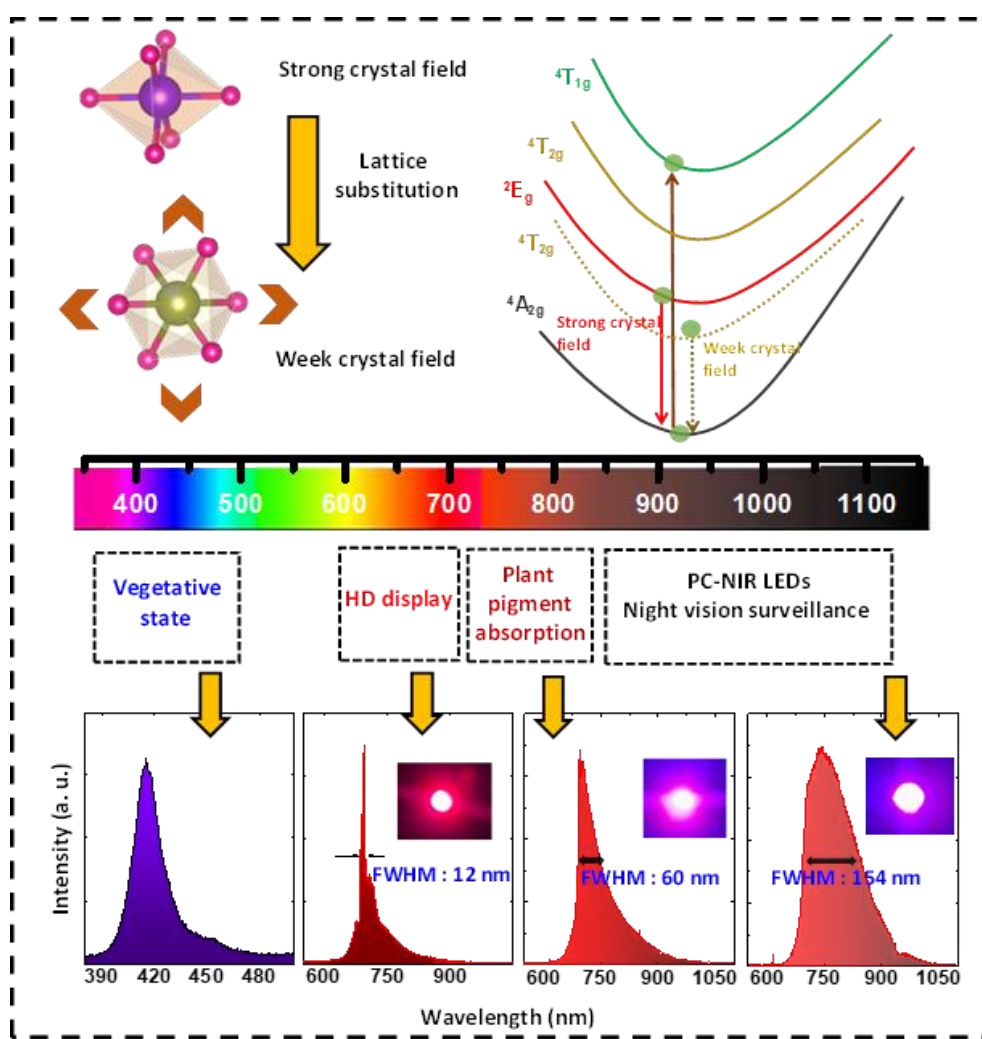
- [58] Song, Y.; Guo, N.; Li, J.; Xin, Y.; Lü, W.; Miao, Y. Dual-Emissive $\text{Ln}^{3+}/\text{Mn}^{4+}$ Co-Doped Double Perovskite Phosphor: Via Site-Beneficial Occupation. *Mater. Adv.* **2021**, 2 (4), 1402–1412. <https://doi.org/10.1039/d0ma00841a>.
- [59] Zhang, S.; Hu, Y.; Duan, H.; Chen, L.; Fu, Y.; Ju, G.; Wang, T.; He, M. Novel $\text{La}_3\text{GaGe}_5\text{O}_{16} : \text{Mn}^{4+}$ Based Deep Red Phosphor: A Potential Color Converter for Warm White Light. *RSC Adv.* **2015**, 5 (110), 90499–90507. <https://doi.org/10.1039/c5ra18163a>.
- [60] Hu, T.; Lin, H.; Cheng, Y.; Huang, Q.; Xu, J.; Gao, Y.; Wang, J.; Wang, Y. A Highly-Distorted Octahedron with a: C 2v Group Symmetry Inducing an Ultra-Intense Zero Phonon Line in Mn^{4+} -Activated Oxyfluoride $\text{Na}_2\text{WO}_2\text{F}_4$. *J. Mater. Chem. C* **2017**, 5 (40), 10524–10532. <https://doi.org/10.1039/c7tc03655h>.
- [61] Zhou, Y.; Zhang, S.; Wang, X.; Jiao, H. Structure and Luminescence Properties of Mn^{4+} -Activated $\text{K}_3\text{TaO}_2\text{F}_4$ Red Phosphor for White LEDs. *Inorg. Chem.* **2019**, 58 (7), 4412–4419. <https://doi.org/10.1021/acs.inorgchem.8b03577>.
- [62] Dierre, B.; Takeda, T.; Sekiguchi, T.; Suehiro, T.; Takahashi, K.; Yamamoto, Y.; Xie, R. J.; Hirosaki, N. Local Analysis of Eu^{2+} Emission in CaAlSiN_3 . *Sci. Technol. Adv. Mater.* **2013**, 14 (6). <https://doi.org/10.1088/1468-6996/14/6/064201>.
- [63] Liu, X. Y.; Guo, H.; Ye, S.; Peng, M. Y.; Zhang, Q. Y. Enhanced Tunable Color Emission in Transparent Ag/Mn^{2+} Codoped Zinc Borate Glasses for Broad Band Light Source. *J. Mater. Chem. C* **2015**, 3 (20), 5183–5191. <https://doi.org/10.1039/c5tc00641d>.
- [64] Wang, Q.; Ci, Z.; Wang, Y.; Zhu, G.; Wen, Y.; Shi, Y. Crystal Structure, Photoluminescence Properties and Energy Transfer of Ce^{3+} , Mn^{2+} Co-Activated $\text{Ca}_8\text{NaGd}(\text{PO}_4)_6\text{F}_2$ Phosphor. *Mater. Res. Bull.* **2013**, 48 (3), 1065–1070. <https://doi.org/10.1016/j.materresbull.2012.11.114>.
- [65] Shanshan, H.; Wanjun, T. Single-Phased White-Light-Emitting $\text{Sr}_3\text{NaLa}(\text{PO}_4)_3\text{F} : \text{Eu}^{2+}, \text{Mn}^{2+}$ Phosphor via Energy Transfer. *J. Lumin.* **2014**, 145, 100–104. <https://doi.org/10.1016/j.jlumin.2013.07.044>.
- [66] Kang, H.; Lee, K. N.; Unithrattil, S.; Kim, H. J.; Oh, J. H.; Yoo, J. S.; Im, W. Bin; Do, Y. R. Narrow-Band $\text{SrMgAl}_{10}\text{O}_{17} : \text{Eu}^{2+}, \text{Mn}^{2+}$ Green Phosphors for Wide-Color-Gamut Backlight for LCD Displays. *ACS Omega* **2020**, 5 (31), 19516–19524.

<https://doi.org/10.1021/acsomega.0c01798>.

- [67] Shea, L. E.; Mckittrick, J. Predicting and Modeling the Low-Voltage Cathodoluminescent Efficiency of Oxide Phosphors. *1998*, *145* (9), 3165–3170.
- [68] Xiao, F.; Xie, C.; Yi, R.; Yuan, H.; Zhou, Q. Luminescence and Interstitial-Defect-Related Self-Reduction in Mn²⁺ Activated Ba₃BP₃O₁₂ Phosphor. *Opt. Mater. (Amst)*. **2022**, *125* (February), 112131. <https://doi.org/10.1016/j.optmat.2022.112131>.
- [69] Zhu, Y.; Li, C.; Deng, D.; Chen, B.; Yu, H.; Li, H.; Wang, L.; Shen, C.; Jing, X.; Xu, S. A High-Sensitivity Dual-Mode Optical Thermometry Based on One-Step Synthesis of Mn²⁺:BaAl₁₂O₁₉–Mn⁴⁺:SrAl₁₂O₁₉ Solid Solution Phosphors. *J. Alloys Compd.* **2021**, *853*, 157262. <https://doi.org/10.1016/j.jallcom.2020.157262>.
- [70] Cao, R.; Luo, W.; Xiong, Q.; Jiang, S.; Luo, Z.; Fu, J. Synthesis and Photoluminescence Properties of Ba₂GeO₄:Mn⁴⁺ Novel Deep Red-Emitting Phosphor. *Chem. Lett.* **2015**, *44* (10), 1422–1424. <https://doi.org/10.1246/cl.150578>.
- [71] Singh, K.; Rajendran, M.; Devi, R.; Vaidyanathan, S. Narrow-Band Red-Emitting Phosphors with High Color Purity, Trifling Thermal and Concentration Quenching for Hybrid White LEDs and Li₃Y₃BaSr(MoO₄)₈:Sm³⁺, Eu³⁺-Based Deep-Red LEDs for Plant Growth Applications. *Inorg. Chem.* **2022**, *61* (6), 2768–2782. <https://doi.org/10.1021/acs.inorgchem.1c02836>.
- [72] Shi, L.; Han, Y. jie; Zhang, Z. gang; Ji, Z. xin; Shi, D. chen; Geng, X. yu; Zhang, H.; Li, M.; Zhang, Z. wei. Synthesis and Photoluminescence Properties of Novel Ca₂LaSbO₆:Mn⁴⁺ Double Perovskite Phosphor for Plant Growth LEDs. *Ceram. Int.* **2019**, *45* (4), 4739–4746. <https://doi.org/10.1016/j.ceramint.2018.11.166>.

Chapter 3

Compositionally engineered $(\text{Mg}, \text{Sr})_3(\text{Al}, \text{Ga})_2\text{GeO}_8: \text{Cr}^{3+}$ phosphors with tuned emission from ultra-sharp red to ultra-broad NIR band for LEDs and *in vitro* cell imaging applications



3.1 Abstract

Phosphor with deep red to near infrared emitting abilities have great application potentials in various fields. Here a multisite host capable of accommodating Cr^{3+} ions in different sites with different crystal field has been developed. Initially, a new $\text{Mg}_3\text{Al}_2\text{GeO}_8: 0.01\text{Cr}^{3+}$ phosphor with ultra-sharp emission band peaking at 693 nm having full width at half maximum (FWHM) of around 4 nm has been developed. The composition consists of three phases orthorhombic- $\text{Mg}_3\text{Ga}_2\text{GeO}_8$, orthorhombic- Mg_2GeO_4 , and cubic- MgAl_2O_4 . The emission intensity, as well as the FWHM of the phosphor, has been increased by the substitution of alkaline earth metal ions. The optimum $\text{Mg}_{2.9}\text{Al}_2\text{GeO}_8: 0.01\text{Cr}^{3+}, 0.1\text{Sr}^{2+}$ exhibits three times greater emission intensity than that of $\text{Mg}_3\text{Al}_2\text{GeO}_8: 0.01\text{Cr}^{3+}$ sample. The additional $[\text{MgO}_6]$ sites contributed from the newly generated Sr impurity phase and the structural distortion in the Cr^{3+} occupied sites are responsible for the emission enhancement. In addition, a series of Ga^{3+} co-doped $\text{Mg}_{2.9}(\text{Al}_{2-y}\text{Ga}_y)\text{GeO}_8: 0.01\text{Cr}^{3+}, 0.1\text{Sr}^{2+}$ samples have been developed. The partial Ga^{3+} substitution weakens the crystal field environment in $[\text{GaO}_6]$ that occupy Cr^{3+} ions. The combined emission from the multiple sites with strong and weak crystal field environments resulted in a broadband emission (630 nm to 1050 nm) with an FWHM of ~ 150 nm that cover the first biological window region effectively. Hence, the developed phosphors are suitable for bio-imaging applications. Finally, various phosphor-converted LEDs have been fabricated using commercial blue LEDs. The pc-LED produced by combining 410 nm LED with $\text{Mg}_{2.9}\text{Al}_2\text{GeO}_8: 0.01\text{Cr}^{3+}, 0.1\text{Sr}^{2+}$ phosphor having 100% colour purity could be used for display application. While the 410 nm LED combined with $\text{Mg}_{2.9}(\text{AlGa})\text{GeO}_8: 0.01\text{Cr}^{3+}, 0.1\text{Sr}^{2+}$ phosphor exhibited the potential for plant growth applications. Moreover, the NIR LEDs produced from $\text{Mg}_{2.9}(\text{Al}_{0.5}\text{Ga}_{1.5})\text{GeO}_8: 0.01\text{Cr}^{3+}, 0.1\text{Sr}^{2+}$ phosphor having increased FWHM can be used for night vision surveillance. Finally, the bio-imaging studies were carried out using a highly intense sample.

3.2 Introduction

The urge for highly efficient rare-earth free deep red-emitting as well as near infrared (NIR)-emitting phosphors has arisen owing to its application in various *in vitro* imaging, non-destructive analysis, night vision technologies, lighting, display, medical imaging, sensors and security.^{1,2,3} Particularly, NIR-emitting phosphor-converted light-emitting diodes (pc-LEDs), which can be used in common smart optoelectronic devices, exhibit notable advantages over

traditional NIR light sources such as halogen lamps and tungsten-halogen lamps because of their low price, high efficiency, compactness, and portability.³ The broadband NIR emitting phosphors are highly suitable for bioimaging rather than the sharp emitting systems owing to the deep tissue penetration abilities that can cover several optical windows. However, sharp deep red-emitting phosphors have high color purity which are suitable for elevating the color gamut in display systems.^{4,5,6}

Deep red to NIR range emission from the phosphors corresponds to the higher transmittance wavelength range of biological tissue (called biological optical window).^{2,7} Nowadays, up-converted nanoparticles (UCN) are used for bioimaging since UCN can be excited by NIR photons which have excellent tissue penetration depth. However, the widely used NaYF₄: Er³⁺, Yb³⁺ UCN for biomedical applications is not chemically stable and needs continuous pumping by NIR light, which can cause cell damage due to the generated heat by NIR photons. Also, the synthesis process of this composition is complicated.^{8,9,10} The uses of common rare earth activators including Pr³⁺, Nd³⁺, Tm³⁺, and Yb³⁺ are limited by their narrow-band NIR emission and relatively poor absorption.³ Recently, Eu²⁺, Bi³⁺ and Mn⁴⁺- based systems are also tried to explore, but these systems produce emission in the deep red regions and could not extend to the NIR region.³

The Cr³⁺-activated oxides, fluorides, and oxyfluorides can be considered as a better alternative for NaYF₄: Er³⁺, Yb³⁺ UCN system. The occupancy of Cr³⁺ activated phosphors in a weak crystal field environment can produce emission ranging from 650 nm to 1200 nm.^{11,12} In comparison with Mn⁴⁺ ions, Cr³⁺ ions in the d³ electronic configuration could exist in both weak and strong crystal field environments. In the strong crystal field environment, Cr³⁺ ions produce sharp emission (~ 700 nm) from the spin-forbidden ²E_g → ⁴A_{2g} transition. While their occupation in the weak crystal field environment can lead to broadband emission (650 nm to 1200 nm) due to the spin-allowed ⁴T_{2g} → ⁴A_{2g} transition.¹³ Compared to fluoride and sulphide phosphors, oxides are having greater advantages such as easy synthesis procedure and chemical stability.¹⁴ Also, the synthesis of some of the fluoride phosphors requires HF solutions (Cr³⁺-activated Na₃X₂Li₃F₁₂ (X = Al, Ga, or In)) garnet phosphors).¹⁵ To date, different Cr³⁺ activated oxide phosphors are produced, and some of them are the suitable candidates for bio imaging

applications on account of its emission in deep-red to NIR region, good stability, efficiency as well as economic and eco-friendly preparation methods.

The deep red to NIR emitting phosphors includes $\text{La}_3\text{Ga}_5\text{GeO}_{14}:\text{Cr}^{3+}$ (FWHM ~330 nm),^{16,17} $\text{La}_2\text{MgZrO}_6:\text{Cr}^{3+}$ (FWHM ~210 nm),¹¹ $\text{NaScGe}_2\text{O}_6:\text{Cr}^{3+}$ (FWHM ~162 nm),¹⁸ and $\text{ZnGa}_2\text{O}_4:\text{Cr}^{3+}$ (FWHM~ 35 nm) phosphors.^{19,20} Among these, $\text{ZnGa}_2\text{O}_4:\text{Cr}^{3+}$ phosphor gained attention owing to its persistence emission under UV excitation. Hence this phosphor has been efficiently used for *in vivo* bio imaging applications. However, the above phosphor shows less emission intensity under visible light excitation and the continuous UV exposure for bio imaging can cause damage in biological tissues. Meanwhile, the research focusing on the tuneable and excitation dependent deep red to NIR emitting phosphors are very less. The crystal field has a significant impact on the spin-allowed ${}^4\text{T}_{2g} \rightarrow {}^4\text{A}_{2g}$ transition (d-d transition) of Cr^{3+} ions. Hence, altering the local lattice environment via chemical unit substitution is one of the best method for tuning the PL properties.³

The present work focused on the advantages of various sites present in $\text{Mg}_3\text{Al}_2\text{GeO}_8$ (MAG) sample for Cr^{3+} ions and efficiently altered the local environment of Cr^{3+} ions by chemical unit co-substitution. The above substitution led to increased emission intensity and enhanced FWHM of this sample. At first, novel MAG: Cr^{3+} samples were synthesized and PL emission intensity was enhanced by alkaline earth metal ions' substitution. Later the FWHM of the sample were enhanced to ~150 nm from ~12 nm due to the efficient utilization of both strong and weak crystal field environment, respectively. Finally, the phosphors with various emission width were used for fabricating pc-LEDs with tuneable emission properties depending on the excitation wavelength of commercial LEDs. These fabricated pc-LEDs showed their potential for display and plant growth applications.

3.3 Experimental

3.3.1 Materials and Synthesis

The following raw materials were used to produce the $(\text{Mg}_{3-x}\text{Sr}_x)(\text{Al}_{2-y}\text{Ga}_y)\text{GeO}_8:0.01\text{Cr}^{3+}$ ($x = 0.0$ to 0.2 , $y = 0.0$ to 0.15) phosphor compositions: MgO (99.99%), SrCO_3 (99.9%), Al_2O_3 (99.6%), Ga_2O_3 (99.9%), GeO_2 (99.998%), and Cr_2O_3 (>99.9%) all of which

were acquired from Sigma-Aldrich. The raw materials were weighed and taken in a stoichiometric ratio for the synthesis of various compositions. In an agate mortar, these raw materials were combined with ethanol and ground for 30 minutes. After drying, white powder is obtained, which is warmed in an air furnace for two hours at 600 °C before being sintered for 6 h at 1300 °C with intermediate grinding. The heating rate used for calcination is 5 °C /min. The finished powder is milled and used for additional characterisation after cooling.

3.3.2 Sample characterization

The X-ray powder diffraction (XRD) of the prepared samples was carried out using the Malvern PANalytical B.V. EMPYREAN 3 diffractometer with Ni-filtered Cu-K α radiation ($\lambda = 1.54 \text{ \AA}$) and Rietveld refinement analysis of the samples are carried out using the GSAS2 software. The structural properties were determined using a high-resolution transmission electron microscope (HR-TEM), JEOL JEM-F200. The UV-Vis diffuse reflectance spectra (DRS) measurements were recorded using the Shimadzu UV-VIS-NIR spectrophotometer (UV 3600). The photoluminescence (PL) excitation, emission and quantum yield (QY) were investigated using a Yvon Fluorolog 3 spectrofluorimeter having a 450 W Xenon irradiation source. The electroluminescence spectra (EL) of the phosphor-converted LEDs (pc-LEDs) were measured using the CCD spectrophotometer (Ocean Optics Maya 2000 Pro).

3.3.3 In vitro cell imaging

3.3.3.1 Culturing of cells

Hela (Human cervical cancer cells) and HEPG2 cells (human hepato cellular carcinoma) were procured from National Centre for Cell Sciences (NCCS), Pune. Cells were cultured in Minimum Essential Media (MEM, GIBCO) supplemented with 10% Fetal Bovine Serum (FBS, Gibco) and 1% antibiotic antimycotic solution 100X (with Penicillin, Streptomycin and Amphotericin B-Himedia) and incubated at 5% CO₂ at 37 °C in incubator.

3.3.3.2 Assessment of cell viability

Single cell suspension of HeLa and HepG2 were prepared and seeded in flat bottom 96 well micro titre plates plates (1×10^4 cells/well) and were kept at 5 % CO₂ & 37 °C for 24 hours. Then, phosphor material was supplemented to the cells at variable concentrations ranging from 0-100 μM in serum free culture medium and further incubated for 24 hours. Afterwards, the compound containing culture medium was removed and the wells were rinsed with PBS. MTT (3-[4,5-dimethylthiazol-2-yl]-2,5-diphenyltetrazolium) reagent (0.5 mg/mL) was prepared in

Hanks balanced Salt solution (HBSS) and added to each well including the untreated control wells and kept in dark for 4 hours. The insoluble formazan crystals formed were dissolved in DMSO and the absorbance (Abs) was measured colorimetrically at 570 nm in a multimode plate reader (Synergy H1, Biotek) (2). Percentage cell viability was calculated using the formula.,

$$\% \text{ Cell viability} = [\text{Abs. sample} / \text{Abs. control}] \times 100$$

3.3.3.3 Cellular internalization studies

To evaluate the time dependent internalisation of the compound, HeLa cells were seeded in a flat bottom 96 well plate at a seeding density of 7×10^3 cells per well. After 24 hours of incubation, these cells were treated with a non-cytotoxic concentration (25 μM) of the compound for different time intervals like 1, 2, 3, 4 and 5 hours. After the corresponding incubation time, the wells were rinsed with PBS and visualised with the red channel filter (TRIT-C) of fluorescent microscope.

3.4 Results and discussion

3.4.1 Structural, compositional and morphological characterization

Fig. 3.1 (a) displays the Rietveld refinement of XRD patterns for the $\text{Mg}_3\text{Al}_{1.99}\text{GeO}_8: 0.01\text{Cr}^{3+}$ (MAG: Cr^{3+}) sample. In **Fig. 3.1 (a)**, it is evident that the undoped MAG: Cr^{3+} sample is composed of three phases namely o-MGG (orthorhombic- $\text{Mg}_3\text{Ga}_2\text{GeO}_8$), o-MGO (orthorhombic- Mg_2GeO_4) and c-MAO (cubic- MgAl_2O_4), which were used for the refinement process. The o-MGG phase is observed to be dominant, suggesting that MAG could be an analog of the o-MGG phase (**Fig.3.1 (c)**).²¹

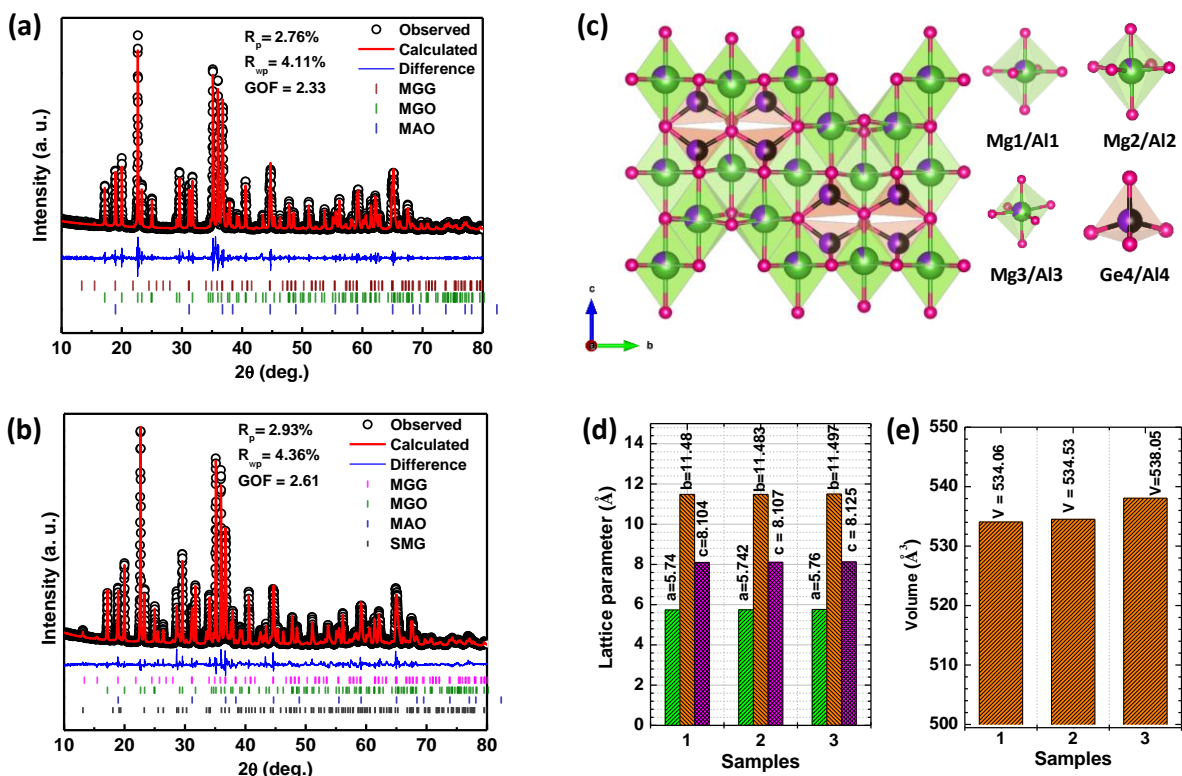


Fig.3.1 Rietveld refinement patterns of (a) MAG: Cr³⁺ and (b) MAG: Cr³⁺, 0.05Sr²⁺. (c) Representation of orthorhombic crystal structure for MAG sample and corresponding polyhedrons. (d) Bar diagram showing the variation in lattice parameter values and cell volume for sample 1 (MAG), Sample 2 (MAG: Cr³⁺) and Sample 3 (MAG: Cr³⁺, 0.1Sr²⁺).

The lattice volume and lattice parameters are found to be increased after Cr³⁺ doping since the ionic radius of a Cr³⁺ ion in an octahedral site (0.615 Å) is slightly higher than that of an octahedral Al³⁺ ion (0.535 Å). After adding 0.01 mol of Cr³⁺ doping, the lattice volume has increased from V = 534.06 Å to V = 534.53 Å. Some of the Cr³⁺ ions could have occupied the [MgO₆] octahedrons also due to the ionic size of the octahedral Mg²⁺ ion (0.72 Å). **Fig.3.1 (b)** displays the Rietveld refinement of the Sr²⁺ co-doped Mg_{2.95}Al_{1.99}GeO₈: 0.01Cr³⁺, 0.05Sr²⁺ (MAG: Cr³⁺, 0.05Sr²⁺) sample. In addition to the o-MGG, o-MGO, and c-MAO, a new monoclinic-SrMgGe₂O₆ (m-SMG) phase has been generated after Sr²⁺ co-doping. Herein, the larger Sr²⁺ ions might have replaced octahedral Mg²⁺ ions in the lattice. As a result, the lattice volume is observed to enhance from V = 534.53 Å to V = 538.05 Å. The variation in lattice parameter values and cell volume has been shown for the MAG, MAG: 0.01Cr³⁺ and MAG: 0.01Cr³⁺, 0.05Sr²⁺ samples in **Fig.3.1 (d)**.

More specifically, the increase in average [Mg/Al-O] bond length from 2.041 Å to 2.05 Å due to Sr²⁺ co-doping clearly indicated the substitution of Sr²⁺ ions in to the octahedral Mg²⁺ sites. Such increase in average Mg/Al-O bond length values after 0.05Sr²⁺ ions substitution causes severe structural distortion in the host lattice by changing both the bond angle and bond length. A schematic representation of the above structural distortion in [(Mg/Al)O₆] octahedrons after Sr²⁺ ions' doping is shown in **Fig.3.2 (a)**. Additionally, one new m-SMG phase is also generated.

In **Fig.3.2 (b)**, the XRD patterns for the different Sr²⁺ co-doped samples are displayed. The section of the XRD pattern between 2θ ~ 34 ° to 38 ° has been enlarged to show the shift towards the lower 2θ angle caused by the successful integration of Sr²⁺ ions in the Mg²⁺ sites [**Fig.3.2 (c)**]. However, some Sr²⁺ ions may not occupy Mg²⁺ sites, leading to the production of a new impurity phase known as m-SMG, as described earlier. This new phase could also contribute to the emission intensity since it is composed of [MgO₆] octahedrons.^{22,23} Interestingly, the increase in [Al-O] bond lengths after Sr²⁺ ions incorporation makes the Al³⁺ sites more favourable for Cr³⁺ due to the comparatively nearer ionic size of Al³⁺ ions.

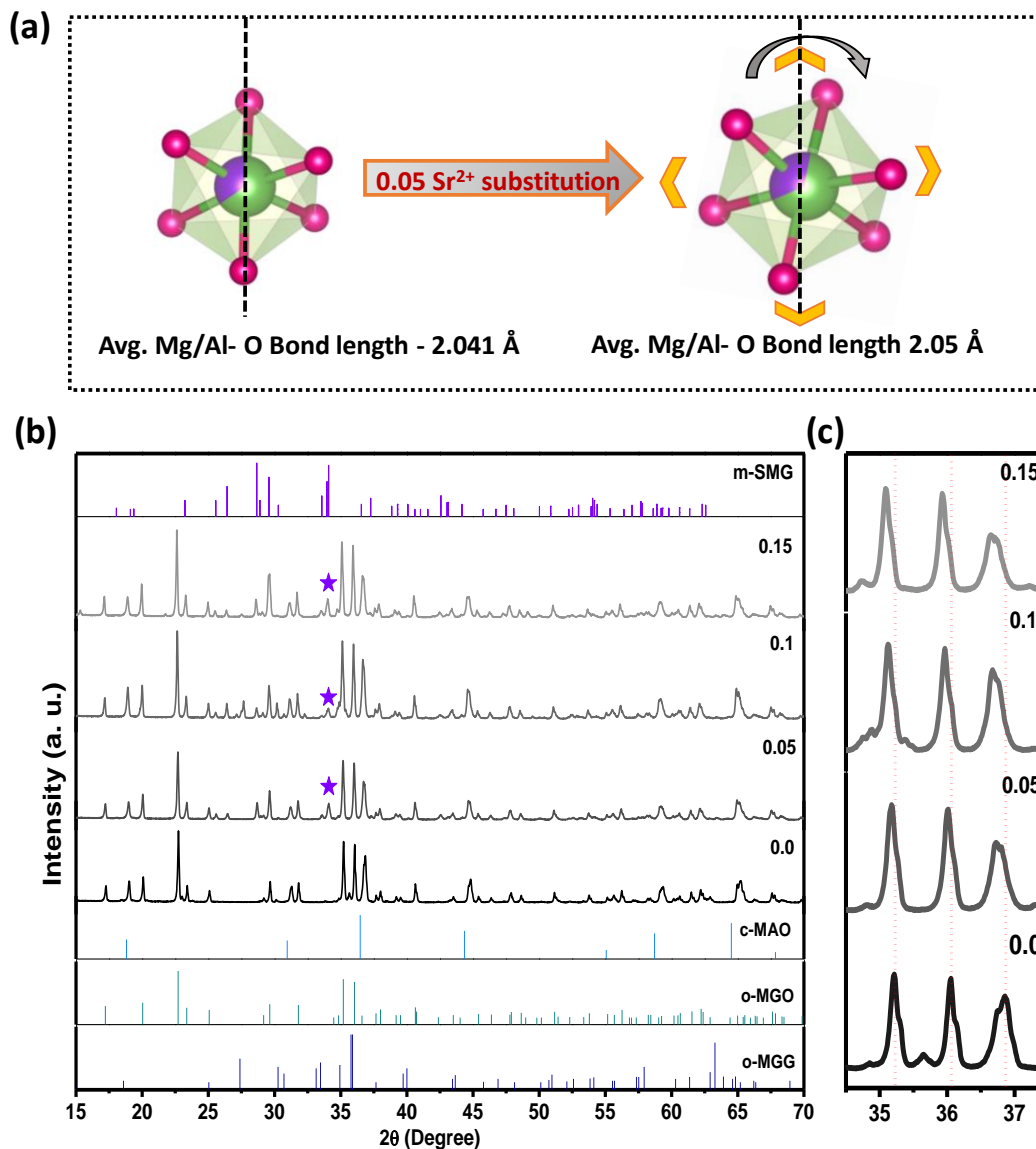


Fig. 3.2 (a) Schematic representation of structural distortion in $[(\text{Mg}/\text{Al})\text{O}_6]$ octahedrons after Sr^{2+} ions' doping (b) The powder XRD patterns of $\text{MAG}: 0.01\text{Cr}^{3+}, x\text{Sr}^{2+}$ ($x = 0.0$ to 0.15) samples and the (c) enlarged portion of the patterns between $2\theta \sim 34^\circ$ to 38° .

The HRTEM images of $\text{MAG}: \text{Cr}^{3+}, 0.1\text{Sr}^{2+}$, displayed in **Fig.3.3 (a) and (b)**, represent various planes which might correspond to existing phases. The magnified version of a small portion of the HRTEM and its associated reduced FFT (r-FFT), as represented in **Fig. 3.3 (a1)** and **(a11)**, respectively, estimates the interplanar distance $\sim 2.56 \text{ \AA}$, which probably corresponds to the (1 3 2) plane of the o-MGG phase (JCPDS 00-039-1108). Similarly, **Fig. 3.3 (a2)** and **(a3)** highlighted the magnified zonal visuals of additional small portions of the HRTEM, and their corresponding r-FFT patterns are depicted in **Fig. 3.3 (a22)** and **(a33)**,

respectively. From **Fig.3.3 (a2)** and **(a22)**, the (3 1 1) plane corresponding to the c-MAO phase (JCPDS 01-086-0096) has been identified, and the associated d value is estimated to be 2.46 Å. Likewise, the (3 0 1) plane of the o-MGO phase (JCPDS 01-078-2316) with a d value of 2.81 Å has been identified from **Fig.3.3 (a3)** and **(a33)**. Another scanned HRTEM image for the same sample is depicted **Fig.3.3 (b)**, from which the m-SMG phase has been identified. A small area in **Fig.3.3 (b)** has been marked and its magnified version is given in **Fig. 3.3 (b1)** along with the reduced FFT in **Fig.3.3 (b11)**, which confirmed the (0 0 2) plane of the m-SMG phase with d value 2.64 Å. Hence, all the four phases present in the MAG: Cr³⁺, 0.1Sr²⁺ sample has been identified since the obtained d values are in good agreement with theoretical values.¹¹

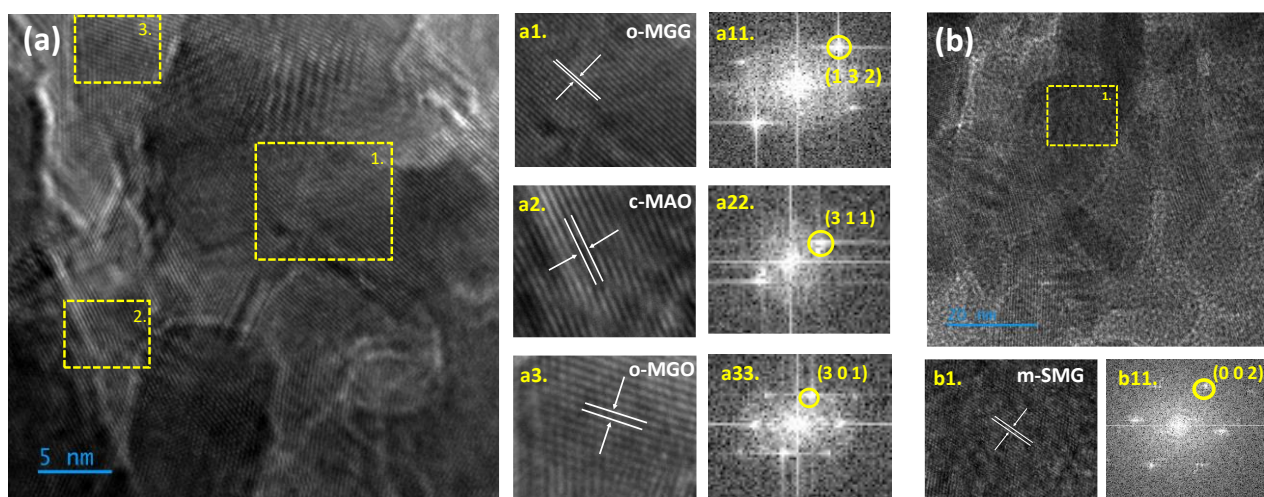


Fig.3.3 (a) and **(b)** HRTEM images of MAG: Cr³⁺, 0.1Sr²⁺ sample with a magnified version of four different regions and the corresponding reduced FFT.

The EDX analysis was performed to further analyse the composition of the sample. The EDX spectra and atomic percentage of MAG: Cr³⁺, 0.1Sr²⁺ sample were shown in **Fig.3.S1 (a)**. The atomic percentage of elements is found to be consistent with the stoichiometry of the sample. The elemental mapping of the TEM image (**Fig.3.S1 (b)**) shows the success in the Cr³⁺ doping and a uniform distribution of chemical elements.¹¹

3.4.2 UV-Vis DRS and photoluminescence studies of MAG: Cr³⁺ and effect of alkaline earth metal ions' substitution

The UV-Vis DRS spectra for the undoped MAG, MAG: 0.01Cr³⁺ and various alkaline earth metal ions co-doped MAG: 0.01Cr³⁺, 0.1M²⁺ (M = Ca²⁺, Sr²⁺ and Ba²⁺) samples were collected and plotted in **Fig.3.4 (a)**. The undoped MAG sample shows a dip around 250 nm due to the host absorption,²⁴ which overlaps with the excitation band due to the ⁴A₂ - ⁴T₁ (te²) transition of Cr³⁺.^{24, 25} Due to the respective ⁴A_{2g} → ⁴T_{1g} and ⁴A_{2g} → ⁴T_{2g} electronic transitions of Cr³⁺, the Cr³⁺-doped samples exhibit strong absorption in the blue and green zones of the visible spectrum.²⁶ In the Cr³⁺-doped samples, the dip in the UV region is found to be decreased, which might be due to the host-to-activator ions' transition. **Fig.3.4 (a)** broadly indicates that the alkaline earth metal ions' substitution could improve the absorption in the visible range, and the absorption is higher for MAG: Cr³⁺, 0.1Sr²⁺ sample. These results can be attributed to the reduction in the octahedral symmetry of [Mg/Al]O₆ octahedrons due to the already discussed structural distortion in the XRD section after Sr²⁺ ions' substitution (**Fig. 3.2(a)**) The above distortions can relax the selection rules for ⁴A_{2g} → ⁴T_{1g} and ⁴A_{2g} → ⁴T_{2g} transitions of Cr³⁺ thereby increasing the visible absorption.²⁷

Further, the bandgap values have been calculated using Tauc's plots,²⁸ as shown in **Fig.3.4 (b)**, and the bandgap values are found to be decreased after various alkaline earth metal ions substitution. This can be attributed to the lower electronegativity of the Sr²⁺, Ca²⁺ and Ba²⁺ compared to the Mg²⁺ ions.²⁹ Meanwhile, the UV-Vis spectrum of the MAG: 0.01Cr³⁺, 0.1Sr²⁺ sample has also been compared with the ZnGa₂O₄: Cr³⁺ sample prepared through solid state method.¹ **Fig.3.4 (c)** illustrates that the MAG: Cr³⁺, 0.1Sr²⁺ sample exhibits stronger absorption in the visible region compared to the ZnGa₂O₄: Cr³⁺ sample. Hence the MAG: Cr³⁺, 0.1Sr²⁺ phosphor can be excited effectively by the visible range rather than the UV range.

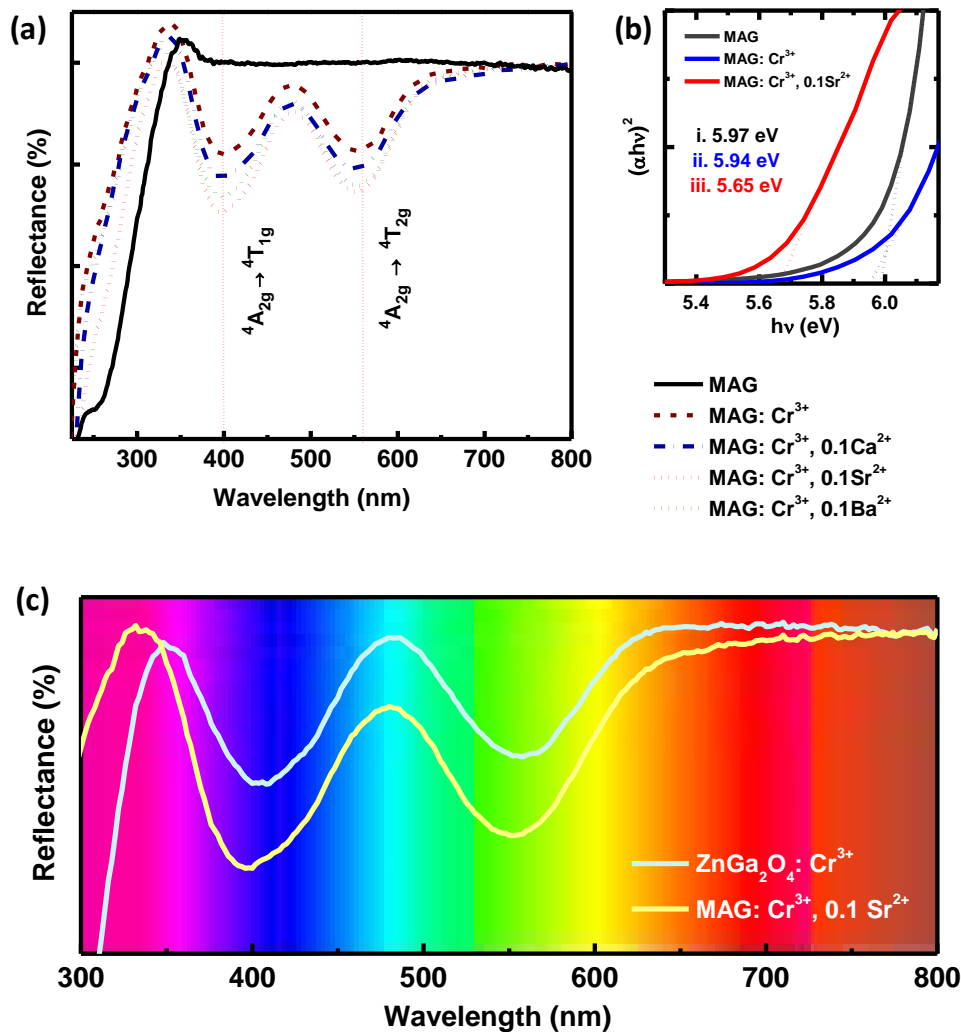


Fig. 3.4 (a) UV-Vis DRS spectra of the undoped MAG, MAG: Cr³⁺ and MAG: Cr³⁺, 0.1M²⁺ (M = Ca, Sr, Ba) and (b) Tauc's plot for bandgap calculation (c) UV-Vis DRS spectra of MAG: Cr³⁺, 0.1Sr²⁺ and ZnGa₂O₄: Cr³⁺.

The PLE and PL emission spectra of MAG: 0.01 Cr³⁺ samples without and with various alkaline earth metal ions' co-doping are shown in **Fig.3.5** (a). The PLE spectra recorded for 693 nm produce three broad excitation bands located around ~255 nm, ~400 nm, and ~555 nm, corresponding to the three different inner transition of d³ electronic configurations of Cr³⁺ ions, namely ⁴A₂→⁴T₁ (4P), ⁴A₂→⁴T₁ (4F) and ⁴A₂→⁴T₂ (4F) transitions.³⁰ Further, the sharp emission peak positioned at 693 nm can be attributed to the ²E_g → ⁴A_{2g} transition of Cr³⁺ ions in [AlO₆] octahedrons. Meanwhile, the peak at 687 nm is likely caused by the vibrational sidebands of the zero-phonon R-line, with phonon assistance.²⁵ A simplified energy level diagram of a Cr³⁺ ion in d³ electronic configuration with the possible transitions are displays in

Fig.3.5 (b).^{25,31} Herein, Cr³⁺ ions are occupying in strong crystal field environment and the transition from the ²E_g state to ⁴A_{2g} state results in sharp deep red emission (~ 693 nm). To confirm the emission from the various emission centres such as [Mg1/Al1-O₆], [Mg2/Al2-O₆] and [Mg3/Al3-O₆] in MAG sample the PL emission spectra were recorded under 280 nm and it is shown in **Fig.3.S2**. Three different peaks positioning at 693 nm, 704 nm, and 740 nm can be attributed to the above three different emission centers.^{32,33} The PL emission intensity of MAG: Cr³⁺ sample is enhanced after various alkaline earth metal ions' substitution (**Fig.3.5 (a)**), among which the Sr²⁺ co-doped shows maximum emission intensity.

Fig.3.5 (c) displays the PLE (λ_{em} : 693 nm) and PL (λ_{ex} : 400 nm) spectra of different Sr²⁺ co-doped MAG: Cr³⁺, 0.1Sr²⁺ (x = 0.0 to 0.2) samples. The emission intensity is found to be enhanced after Sr²⁺ ions' incorporation and it is maximized for x = 0.1. The emission intensity variations under blue (400 nm) and green (555 nm) excitations as a function of various Sr²⁺ concentrations are depicted in **Fig.3.5 (d)**. The increase in emission intensity can be attributed to the structural distortions (**Fig.3.2 (a)**) that occurred in the [(Mg/Al)O₆] octahedrons after larger ionic substitution as explained during interpreting the XRD results. The spectroscopic properties of the transition metal ions having d³ electronic configurations are largely determined by the lattice properties of the surrounding environment. Hence, the lattice distortion in the [Mg/Al-O₆] octahedrons can relax the optical transition selection rule including ²E_g → ⁴A_{2g} transition of Cr³⁺ leading to enhanced emission.²⁷ Other possible reasons are the improved crystallinity and greater Cr³⁺ ions' absorption (**Fig.3.4 (a)**). Hence, Cr³⁺ ions are situated in a stable and rigid octahedral environment with enhanced covalency due to Sr²⁺ ions' substitutions, which elevate Cr³⁺ luminescence intensity.³⁴ As previously discussed in the structural section, the introduction of Sr²⁺ ions in Mg²⁺ sites produces a new phase m-SMG. This new phase creates more [MgO₆] sites for Cr³⁺ ions to occupy, resulting in a stronger emission intensity.

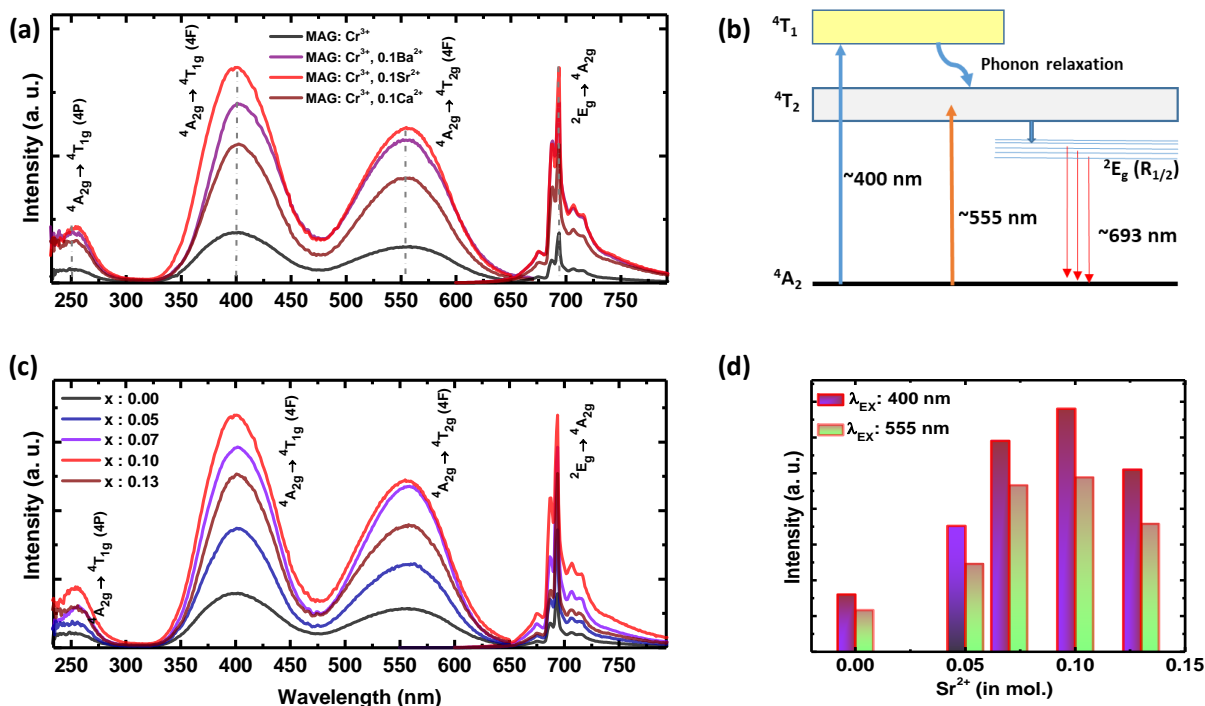


Fig.3.5 (a) PLE (λ_{em} : 693 nm) and emission (λ_{ex} : 400 nm) spectra of alkaline earth metal ions co-doped MAG: $0.01Cr^{3+}$, $0.1 M^{2+}$ ($M = Ca^{2+}$, Sr^{2+} , and Ba^{2+}) samples. (b) simplified energy level diagram of Cr^{3+} ions in d^3 electronic configuration (strong crystal field environment) (c) PLE (λ_{em} : 693 nm) and emission spectra (λ_{ex} : 400 nm) of MAG: $0.01Cr^{3+}$, xSr^{2+} ($x = 0.0$ to 0.13) (d) Bar diagram showing the variation of PL emission intensity under blue and green excitation.

To check the performance of the optimized Sr^{2+} codoped MAG: $0.01Cr^{3+}$, $0.1Sr^{2+}$ sample, its PLE and PL spectra are compared with the well-known $ZnGa_2O_4: 0.01Cr^{3+}$ sample. The PLE and PL emission spectra of MAG: $0.01Cr^{3+}$, $0.1Sr^{2+}$ and $ZnGa_2O_4: Cr^{3+}$ samples are displayed in **Fig.3.6 (a)** and **Fig.3.6 (b)**, respectively, where MAG: $0.01Cr^{3+}$, $0.1Sr^{2+}$ exhibits greater excitation intensity in the entire visible region ranging from 350 nm to 650 nm compared to $ZnGa_2O_4: 0.01Cr^{3+}$. Meanwhile, MAG: $0.01Cr^{3+}$, $0.1Sr^{2+}$ sample exhibits two folds' greater emission intensity than the $ZnGa_2O_4: Cr^{3+}$ upon 400 nm excitations. Moreover, MAG: $0.01Cr^{3+}$, $0.1Sr^{2+}$ sample exhibits broader emission width that covers the first biological window region more efficiently in comparison with the $ZnGa_2O_4: Cr^{3+}$ phosphors. The above results suggest the efficiency of the MAG: Cr^{3+} , $0.01Cr^{3+}$ for bio imaging applications.

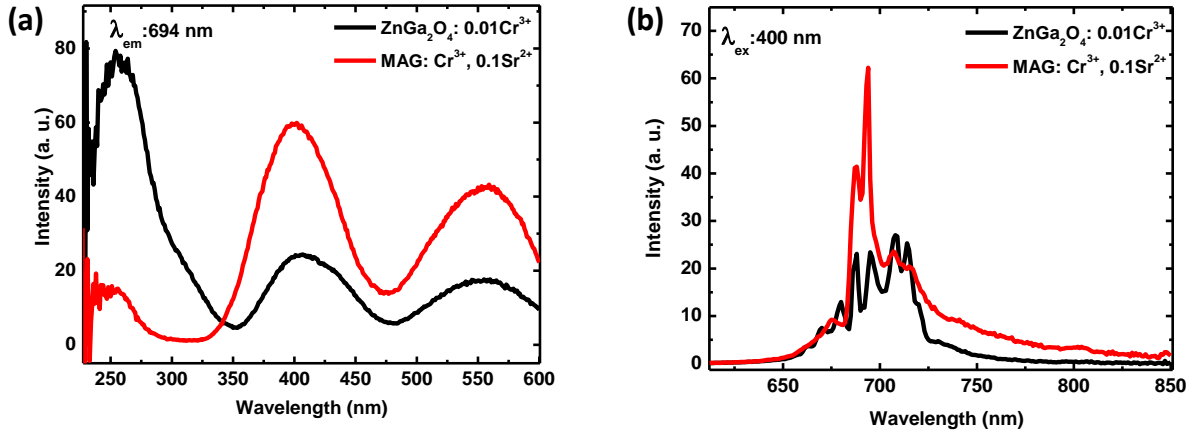


Fig. 3.6 The (a) PLE (λ_{em} : 693 nm) and (b) emission spectra of the MAG: Cr³⁺, 0.1Sr²⁺ and ZnGa₂O₄: 0.01Cr³⁺ sample.

3.4.3 Structural properties of Ga³⁺ co-doped MAG: Cr³⁺, 0.1Sr²⁺, yGa³⁺ samples

The XRD patterns of various Ga³⁺ co-doped samples are shown in **Fig.3.7 (a)**. Here, the XRD peak positioned at 36.4 ° corresponding to the o-MAO phase is found to be shifted towards the lower 2θ side due to higher ionic radii of Ga³⁺ ions compared to Al³⁺ ions. Furthermore, an incomplete phase transition from the co-existing c-MAO to cubic-MgGa₂O₄ [space group: *Fd3m*, JCPDS 00-010-0113] is observed after partial Ga³⁺ to Al³⁺ ionic substitutions. The above phase transition from c-MAO to cubic-MgGa₂O₄ is clearly observed in **Fig.3.7 (b)**. Hence additional [GaO₆] sites are developed after Ga³⁺ co-doping. After Ga³⁺ ions' incorporation, many of the [Mg1/Al1-O₆], [Mg2/Al2-O₆] and [Mg3/Al3-O₆] octahedrons might have transformed into [Mg1/Ga1-O₆], [Mg2/Ga2-O₆] and [Mg3/Ga3-O₆] octahedrons associated to the above phase transitions.

The EDAX spectrum shown in **Fig.3.S3** and elemental mapping represented in **Fig. 3.7 (c)** identifies the presence of all elements in MAG: Cr³⁺, 0.1Sr²⁺, 1.5 Ga³⁺ sample. Further, the TEM image depicts particles of irregular morphology ranging in 20 nm - 500 nm range (**Fig.3.7 (c)**). To confirm the presence of the cubic-MgGa₂O₄ phase, the HRTEM analysis were also carried for the MAG: Cr³⁺, 0.1Sr²⁺, 1.5 Ga³⁺ sample. The lattice plane corresponding to the cubic-MgGa₂O₄ phase were identified and depicted in **Fig.3.7 (d)**. From this figure, the interplanar distance is calculated to be 2.92 Å, which is corresponds to the (2 2 2) plane of cubic-MgGa₂O₄ (JCPDS 00-010-0113). The corresponding reduced FFT pattern for the above plane is shown in the inset of **Fig.3.7 (d)**, which is also confirmed the (2 2 2) plane.

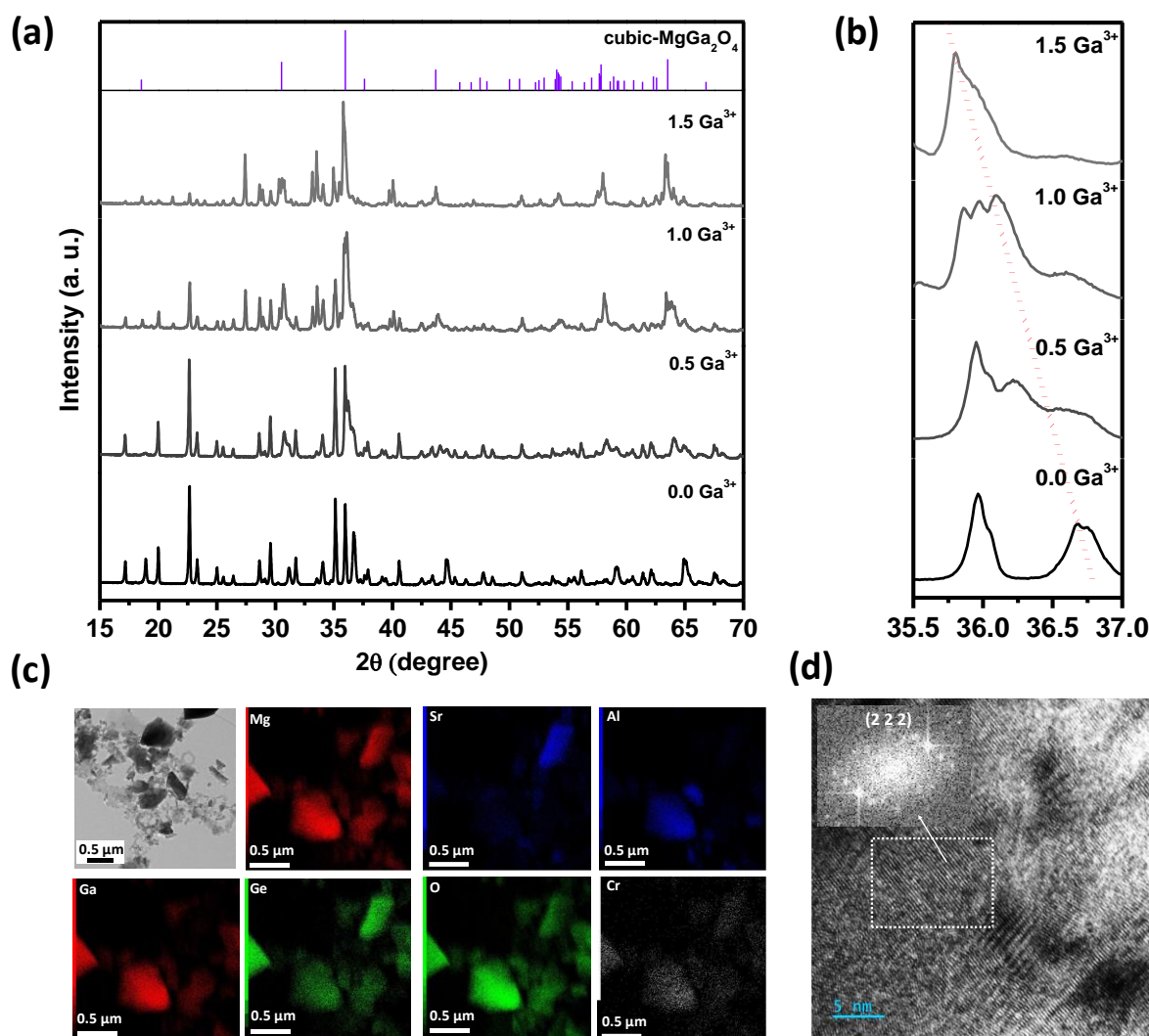


Fig.3.7 (a) Powder XRD patterns of MAG: Cr³⁺, 0.1Sr²⁺, yGa³⁺ (y = 0.0 to 1.5) samples and (b) enlarged portion of XRD pattern from 35.5 ° to 37 °. (c) TEM image and EDX elemental mapping of various elements in MAG: Cr³⁺, 0.1Sr²⁺, 1.5Ga³⁺ sample. (d) HRTEM image showing the lattice planes of MAG: Cr³⁺, 0.1Sr²⁺, 1.5 Ga³⁺ sample and the r-FFT of a small portion.

3.4.4 UV-Vis DRS and photoluminescence of Ga³⁺ co-doped MAG: Cr³⁺, 0.1Sr²⁺, yGa³⁺ samples

Fig.3.8 (a) displays the UV-Vis DRS spectra of various Ga³⁺ co-doped MAG: Cr³⁺, 0.1Sr²⁺, yGa³⁺ (y = 0.0 to 1.5) samples. A clear shift towards the higher wavelength region is

observed after Ga³⁺ ions' incorporation. The shift associated with the increase in Ga³⁺ content can be attributed to the weakening of the crystal field.²⁶

To accomplish higher FWHM and to increase the emission towards the NIR region, weak crystal field environment has been generated purposefully in the host lattice along with the existing strong crystal field environment. This targeted tailoring of the crystal field environment has been achieved by the partial incorporation of Ga³⁺ ions in Al³⁺ sites. **Fig.3.8 (b)** shows the PLE (λ_{em} : 693 nm) and PL emission spectra (λ_{ex} : 400 nm) of MAG: Cr³⁺, MAG: Cr³⁺, 0.1 Sr²⁺, and various Ga³⁺ co-doped MAG: Cr³⁺, 0.1Sr²⁺, yGa³⁺ samples. The peak at 687 nm corresponding to the o-MAO phase is found to be disappearing at higher concentrations of Ga³⁺ ions ($y > 1$), and a new peak around 703 nm is observed might be due to the formation of cubic-MgGa₂O₄ phase at higher concentration as disused in structural part.^{35,36}

To exploit the different emission peaks corresponding to various sites, the emission spectra were also recorded under 450 nm excitations, and it is shown in **Fig.3.8 (c)** separately. The PL emission spectra under 450 nm excitation show different emission behaviour than that recorded under 400 nm shown in **Fig.3.8 (b)**. The result indicates the larger contribution of Ga³⁺ ionic sites since the 450 nm excitation is capable of exciting Cr³⁺ ions occupying both Ga³⁺ and Al³⁺ sites with weaker crystal fields more effectively compared to 400 nm. From the UV-Vis DRS spectra (**Fig.3.8 (a)**), a clear red shift has been observed in Ga³⁺ co-doped samples, which mainly illustrates the increased absorption in the higher wavelength regions of blue and green. Similarly, the PLE peak (**Fig.3.8 (b)**) in the blue region (⁴A₂→⁴T₁ (4F)) has been enlarged from 470 nm to 490 nm with Ga³⁺ ions' co-doping. **Fig.3.8 (b)** also illustrates that the emission from the Ga³⁺ co-doped samples shows higher FWHM compared to that of the MAG: Cr³⁺, 0.1Sr²⁺ sample, and it is extended to the NIR region. The increased FWHM can be attributed to the generation of multiple sites and the existence of a weak crystal field environment due to Ga³⁺ ions' incorporation. Precisely, the crystal field strength (10D_q), that is the energy level difference between the ⁴A_{2g} and ⁴T_{2g} can be estimated using the following equation.³⁷

$$10D_q = K/R^n \quad (1)$$

where R is the bond length between the cation and the ligand, while n and K are the fitting parameters. The value of power 'n' depends on the nature of ligands, and the geometry of the complex, and varies depending upon the systems.

Since the crystal field strength is inversely proportional to bond length, the substitution with higher ionic sized Ga^{3+} ions into Al^{3+} sites with relatively lower size might have reduced the crystal field strength and led to the formation of a weak crystal field environment. This could result in a broader band emission. Moreover, the observed broad emission peak (${}^4\text{A}_2 \rightarrow {}^4\text{T}_2$) (**Fig.3.8 (b)**) is red-shifted from 703 nm to 708 nm due to the further increase in Ga^{3+} ions' co-doping. Since the Ga^{3+} ions' co-doping in Al^{3+} sites decreases the crystal field strength (Dq) in the vicinity of Cr^{3+} ions and decreases the energy of ${}^4\text{T}_{1g}$ and ${}^4\text{T}_{2g}$ states for the ground state ${}^4\text{A}_{2g}$.¹³

The corresponding energy level diagram showing the emission from both strong and weak crystal field environments and lowering of ${}^4\text{T}_1$ and ${}^4\text{T}_2$ state is shown schematically in **Fig.3.8 (e)**. It is worth noting that in octahedral coordination, Cr^{3+} takes the place of Al^{3+} , Ga^{3+} , and Mg^{2+} ions. Additionally, the strength of the crystal field experienced by the ion (i.e. whether it is strong, intermediate, or weak) is highly dependent on the crystal field environment of the host lattice.²⁵ The Ga^{3+} ions provide a weak crystal field environment and result in broadband emission. After Ga^{3+} incorporation many of the Mg1/Al1, Mg2/Al2 and Mg3/Al3 sites translate into Mg1/Ga1, Mg2/Ga2 and Mg3/Ga3. A new phase of cubic- MgGa_2O_4 also formed as seen in the structural part with $[\text{GaO}_6]$ octahedrons. Hence the multiple site occupancy after Ga^{3+} co-doping is also responsible for the higher FWHM and broad emission peaks.

The FWHM of the MAG: Cr^{3+} sample under 400 nm excitation is 4 nm and it is enhanced to 80 nm for MAG: Cr^{3+} , 0.1Sr^{2+} , 1.5Ga^{3+} sample. Meanwhile, under 450 nm excitation the FWHM of the emission peaks are relatively much higher since these excitations could efficiently exploit almost all possible octahedral sites of the hosts such as $[\text{MgO}_6]$, $[\text{AlO}_6]$, and $[\text{GaO}_6]$ sites. The variation of PL emission intensity and FWHM as a function of Ga^{3+} ion concentration under different excitations are represented in **Fig.3.8 (d)**. The FWHM of the MAG: Cr^{3+} under 450 nm excitation is ~10 nm and it is enhanced to ~150 nm for MAG: Cr^{3+} , 1.5Ga^{3+} . Compared to $\text{ZnGa}_2\text{O}_4: 0.01\text{Cr}^{3+}$ the Ga^{3+} -codoped samples are excitable with

450 nm and these LEDs are relatively cheap. Hence the Ga³⁺-codoped MAG: Cr³⁺, 0.1Sr²⁺ samples are economical in their commercial purpose.

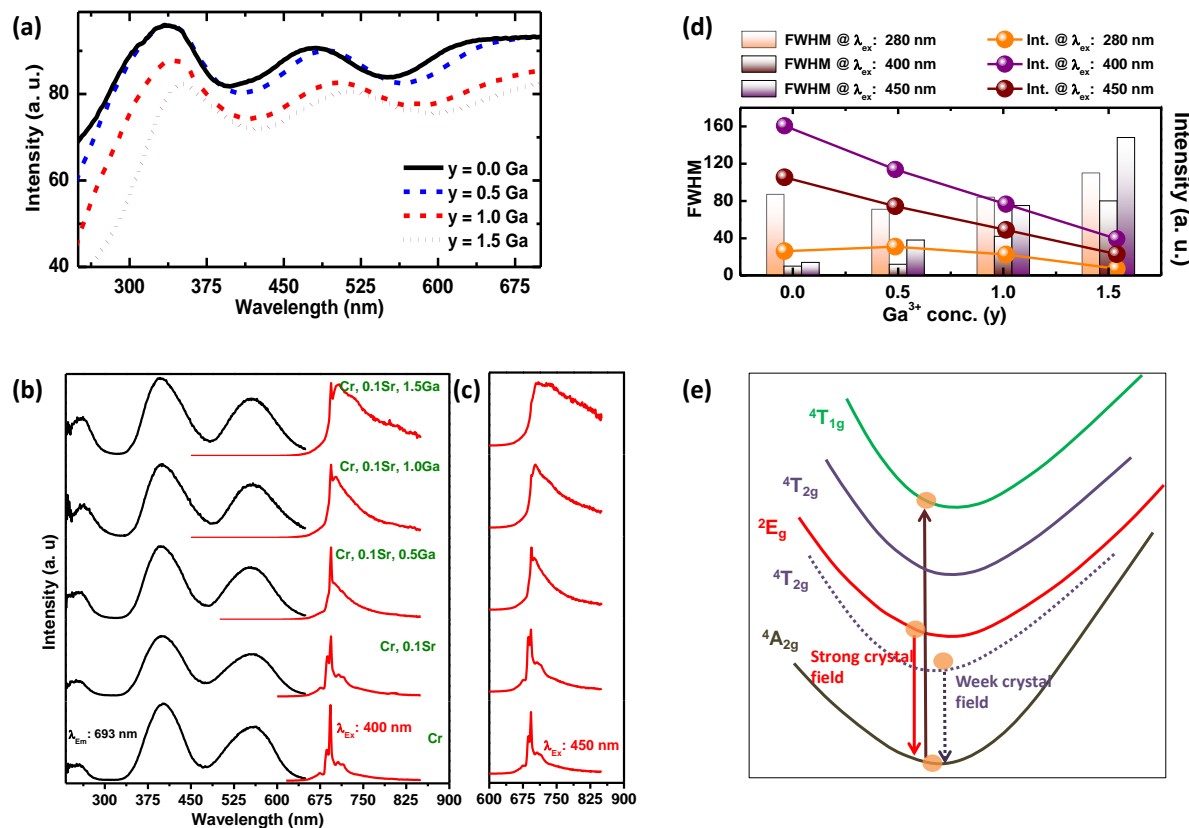


Fig.3.8 (a) UV-Vis spectra of MAG: Cr³⁺ and MAG: Cr³⁺, 0.1Sr²⁺, xGa³⁺ (x = 0.0 to 0.15) samples (b) PLE (λ_{em}: 693 nm) and emission (λ_{ex}: 400 nm) spectra of MAG: Cr³⁺ and MAG: Cr³⁺, 0.1Sr²⁺, xGa³⁺ (x = 0.0 to 0.15) samples and the corresponding (c) emission spectra under 450 nm excitation. (d) Graph showing the variation of FWHM and emission intensity for different Ga co-doped samples under different excitations. (e) Energy level diagram of Cr³⁺ ions in d³ electronic configuration showing emission from both weak and strong crystal field environments.

3.4.5 Temperature-dependent PL emission

Temperature-dependent PL emission spectra of MAG: Cr³⁺, 0.1Sr²⁺ and MAG: Cr³⁺, 0.1Sr²⁺, 1Ga³⁺ samples were recorded under 410 nm excitation by varying the temperature from 298 K to 433 K, and the results are shown in **Fig.3.9** (a) and (c), along with the corresponding contour plots represented in **Fig.3.9** (b) and (d), respectively.

The PL emission intensity of both the samples peaking at 693 nm (${}^2E_g \rightarrow {}^4A_{2g}$) and that of the broadband emission of MAG: Cr³⁺, 0.1Sr²⁺, 1.0Ga³⁺ (${}^4T_2 \rightarrow {}^4A_2$) are decreased with increasing temperature. However, the Stokes and anti-Stokes bands of MAG: Cr³⁺, 0.1Sr²⁺ show different emission behaviour with the temperature elevation. The Stokes bands at 693 nm (P1) and 687 nm (P2) are found to decrease with increasing temperature, whereas the anti-Stokes band at 675 nm (P3) is reduced. Wang *et al.* reported a similar kind of emission behaviour at higher temperatures for Zn₃Ga₂Ge₂O₁₀: Cr³⁺.³⁸ The decrease in the anti-Stokes band can be attributed to the participation of more restricted phonon vibrations at higher temperatures. Also, the intensity ratio of the anti-Stokes sideband to the Stokes vibronic sideband should agree with Boltzmann's law. At higher temperatures, the anti-Stokes sideband may become more intense as the population is lost from the Stokes sideband due to thermal depopulation. This happens as the system reaches thermal equilibrium.³⁹ The above contrasting behaviour of the Stokes and anti-Stokes bands is highly beneficial for thermometry applications.^{24, 40} Moreover, a slight red shift is observed while increasing the temperature, which is shown in the inset of **Fig.3.9 (a)** and **(c)**. This shift is in accordance with the Varshini equation mentioned elsewhere.⁴¹

The variation of emission intensity of different peaks as a function of temperatures for both the samples are depicted in the insets of **Fig.3.10 (a)** and **(b)**. At 423 K, the ${}^2E_g \rightarrow {}^4A_{2g}$ transition of Cr³⁺ ions in MAG: Cr³⁺, 0.1Sr²⁺ sample could retain 69 % of its room temperature intensity. Meanwhile the ${}^2E_g \rightarrow {}^4A_{2g}$ and ${}^4T_2 \rightarrow {}^4A_{2g}$ transitions of Cr³⁺ ions in MAG: Cr³⁺, 0.1Sr²⁺, 1.0Ga³⁺ samples are also exhibited 74 % at 423 K of the room temperature intensity. Hence the Ga³⁺ ions' co-doping makes some elevation in the thermal stability. The Arrhenius plots,⁴² drawn for MAG: Cr³⁺, 0.1Sr²⁺ and MAG: Cr³⁺, 0.1Sr²⁺, 1.0Ga³⁺ samples are shown in the insets of **Fig.3.10 (a)** and **(b)**, respectively. The activation energy for the MAG: Cr³⁺, 0.1Sr²⁺ sample is calculated to be 0.23 eV. Meanwhile the activation energies for the ${}^2E_g \rightarrow {}^4A_{2g}$ and ${}^4T_2 \rightarrow {}^4A_{2g}$ transitions of Cr³⁺ ions in MAG: Cr³⁺, 0.1Sr²⁺, 1.0Ga³⁺ sample are found to be $E_{a1} = 0.2$ eV and $E_{a2} = 0.18$ eV, respectively

The thermally excited electrons in the MAG: Cr³⁺, 0.1Sr²⁺ sample could reach the intersection point of ${}^4A_{2g}$ and 2E_g (cross-over point) and relax to the ground state (${}^4A_{2g}$) non-radiatively. The increase in the non-radiative transition leads to a decrease in emission intensity

in the case of MAG: Cr³⁺, 0.1Sr²⁺. There will be two cross-over points in the case of MAG: Cr³⁺, 0.1Sr²⁺, Ga³⁺ due to the intersection of (i) ⁴A_{2g} and ²E_g and (ii) ⁴A_{2g} and ⁴T_{2g}. The corresponding configuration coordinate diagram representing the above two cross-over points has been shown in **Fig. 3.10 (c)**.^{12, 43} The thermal stability is found to be enhanced after Ga³⁺ ions' incorporation due to the multiple site occupancy of Cr³⁺ ions. The energy transfer process from one excited state to another reduces the non-radiative transitions from the cross-over points. Hence the multisite occupancy enables higher thermal stability in Ga³⁺ co-doped samples.^{44, 45}

The emission intensity of various reported phosphors at 423 K is shown in **Fig. 3.10 (d)**. These reported values are comparable with the thermal stability of MAG: Cr³⁺, 0.1Sr²⁺ and MAG: Cr³⁺, 0.1Sr²⁺, 1Ga³⁺ samples. Further, the Internal quantum efficiency (IQE) values of the above samples are found to be 95 % and 92 %, respectively. These IQE values are found to be higher compared to the reported samples, as shown in **Fig. 3.10 (d)**.

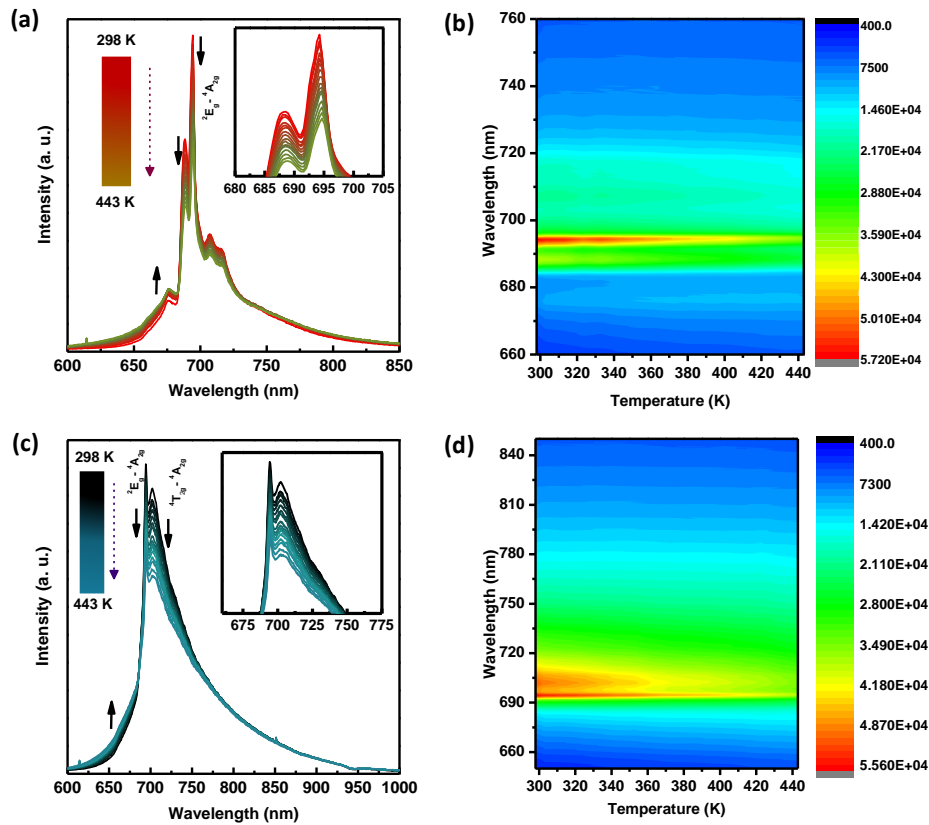


Fig. 3.9 Temperature-dependent PL emission spectra of (a) MAG: Cr³⁺, 0.1Sr²⁺ and corresponding (b) contour plot. Temperature-dependent PL emission spectra of (c) MAG: Cr³⁺, 0.1Sr²⁺, 1.0Ga³⁺, and (d) corresponding PL plot.

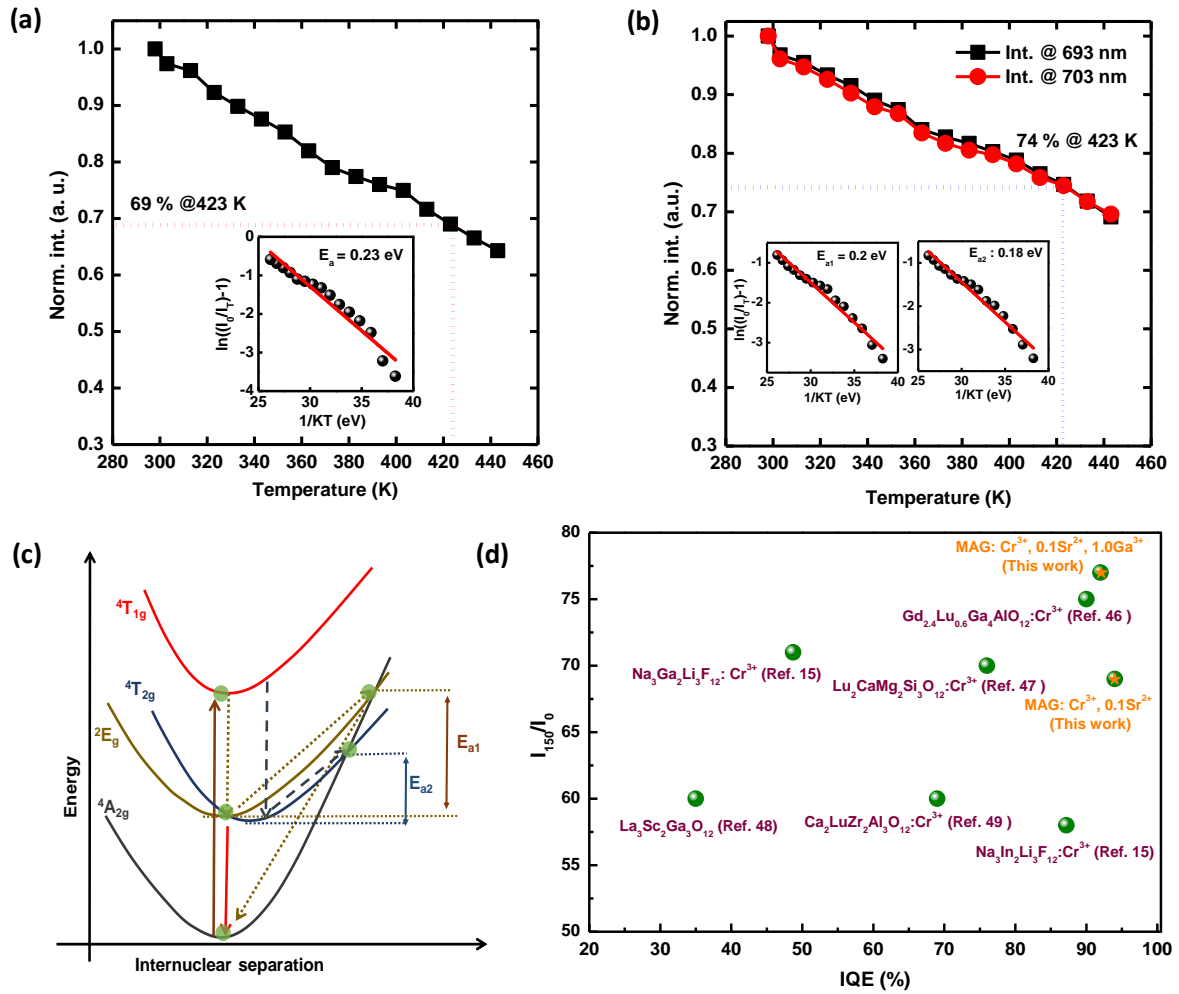


Fig. 3.10. Plots of normalized emission intensity vs temperature and Arrhenius plots for the samples (a) $\text{MAG: Cr}^{3+}, 0.1\text{Sr}^{2+}$ and (b) $\text{MAG: Cr}^{3+}, 0.1\text{Sr}^{2+}, 1\text{Ga}^{3+}$. (c) Configuration coordinate diagram for activation energy calculation (d) The comparison of luminescence thermal stability at 423 K and internal quantum efficiency (IQE)^{15,44,46,47,48,49}

3.4.6 Phosphor-converted LEDs for display, plant growth, and night vision surveillances

To gauge the effectiveness of the newly created phosphors with different emission width and ranging from deep red to NIR, a series of LEDs that have deep red to NIR light emitting properties were fabricated by pairing the respective phosphors with commercial 410 nm and 450 nm LEDs. The excitation-dependent emission properties of these phosphors due to vast absorption ranges enabled the production of multiple pc-LEDs having various emission ranges and FWHM.

Fig.3.11 (a) displays the electroluminescence (EL) spectrum of the pc-LED fabricated using the MAG: Cr³⁺, 0.1Sr²⁺ phosphor with a 410 nm LED. Here the FWHM of the fabricated red LED is found to be as narrow as ~ 12 nm. This ultra-sharp red emission has a color purity of 100 %. Further, the CIE value of the red LED is (0.63, 0.37), which is very close to the National Television Standard Committee (NTSC) CIE value for an ideal red phosphor (0.67, 0.33).^{50,51} The corresponding CIE diagram of the developed LED is represented in the insets of **Fig.3.11 (a)**.

Further, the Ga³⁺ co-doped MAG: Cr³⁺, 0.1Sr²⁺, Ga³⁺ sample has also been combined with the 410 nm LED for indoor plant growth applications. The corresponding EL spectra and the captured image for the above-fabricated LED are shown in **Fig.3.11 (b)**. This figure indicates the overlapping of absorption peaks an important pigment in plant (P_{fr}) with the fabricated pc-LED emission peaks.⁵² Since, this pigment is very crucial for the plant growth, hence, the developed LED can be effectively used for indoor plant cultivations.

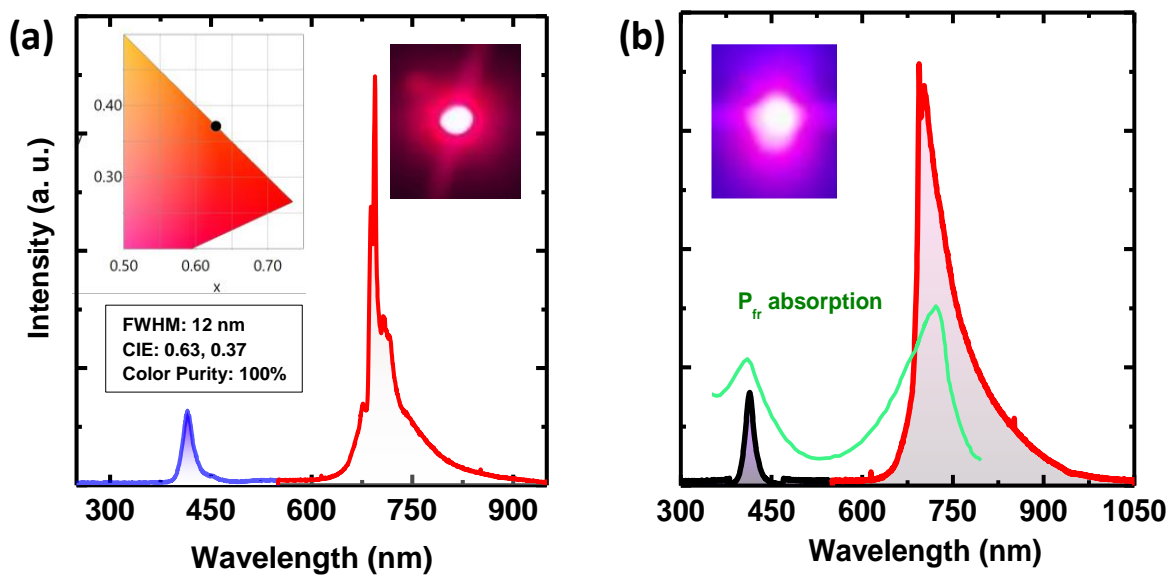


Fig.3.11 (a) The EL spectrum of the fabricated LED for display application by combing 410 nm LED with MAG: Cr³⁺, 0.1Sr²⁺. **(b)** The EL spectrum of the fabricated LED for plant growth application by combing 410 nm LED with MAG: Cr³⁺, 0.1Sr²⁺, 1.0Ga³⁺.

Meanwhile, the MAG: Cr³⁺, 0.1Sr²⁺, 1.5Ga³⁺ sample having higher FWHM in the deep red to NIR region has been used for the NIR pc-LED fabrication. The above phosphor has been combined with 410 nm LED and 450 nm LED separately, and two different NIR LEDs have been fabricated and denoted as NIR pc-LED1 and NIR pc-LED2, respectively. The corresponding EL spectra and LED images are shown in **Fig.3.12 (a)** and **(b)**. The NIR pc-LED2 fabricated using 450 nm commercial LED and MAG: Cr³⁺, 0.1Sr²⁺, 1.5Ga³⁺ sample exhibits a FWHM as broad as 151 nm with an the emission spectrum is ranging from 630 nm to 1050 nm. Meanwhile, the NIR pc-LED1, made with a 410 nm LED exhibits an FWHM of 132 nm. Hence the MAG: Cr³⁺, 0.1Sr²⁺, 1.5Ga³⁺ composition is capable of producing ultra-broad emitting NIR pc-LEDs. The power-dependent studies have also been carried out for the above two LEDs by varying the LED power from 600 mW to 1200 mW (**Fig. 3.12 (a) and (b)**). When the pumping power is increased, the EL intensity also increases significantly. This is because the enhanced current drives more electrons from the ground state to the excited state, which increases the population of the ²E_g and ⁴T_{2g} states of Cr³⁺ ions in MAG: Cr³⁺, 0.1Sr²⁺, 1.5Ga³⁺. Meanwhile, no saturation effect is observed even at high powers, which indicates the potential of these phosphors for high-power LED applications.

The pictures of an Institutional logo and a QR code were captured under the indoor light, and it is shown in **Fig. 3.12 (c)**. The same images are also taken under the developed NIR pc-LEDs and it is shown in **Fig. 3.12 (d)**. The logo and QR code are visible in the glow of the fabricated NIR pc-LEDs. The QR code can be scanned from the recorded image using NIR pc-LED, which can be read out as “CSIR NIIST”. Hence the developed NIR LEDs exhibit potential applications in night vision surveillance also.

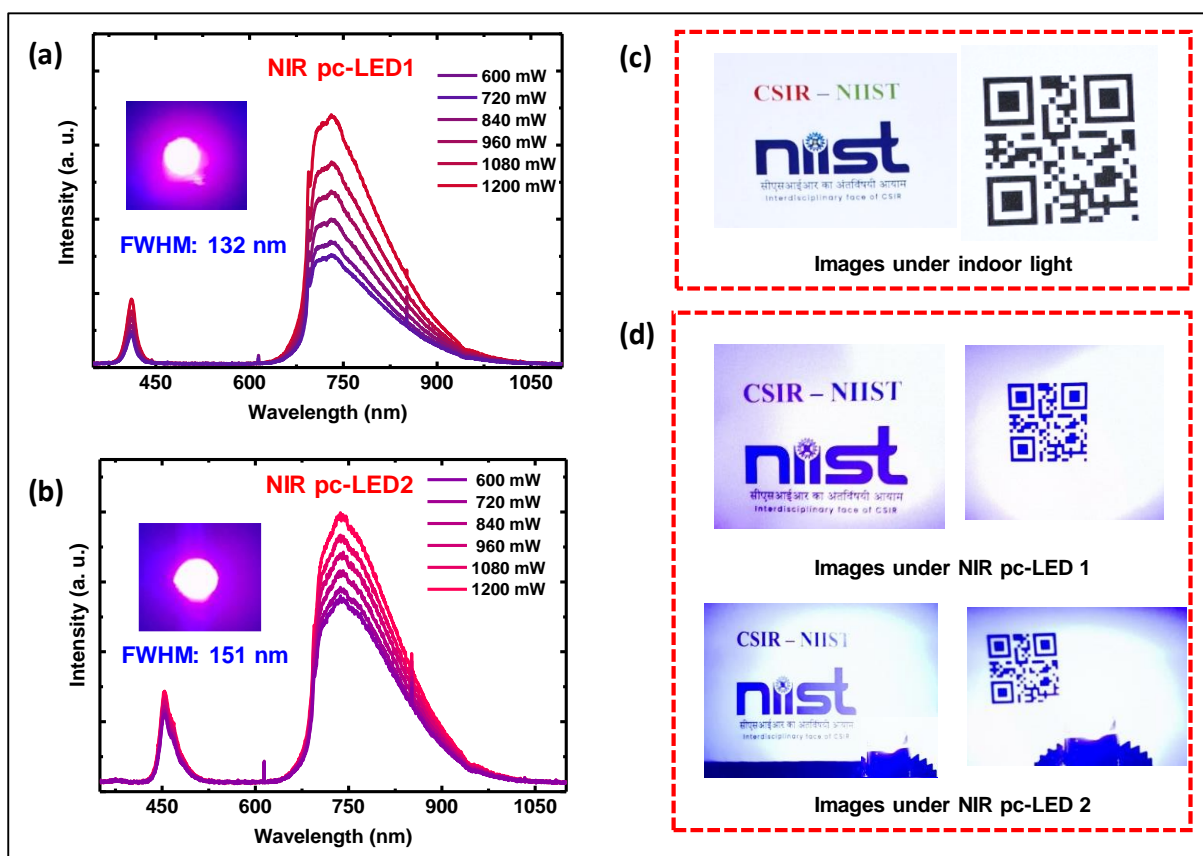


Fig. 3.12 EL spectra of (a) NIR pc-LED1 (fabricated using 410 nm LED with MAG: Cr³⁺, 0.1Sr²⁺, 1.5Ga³⁺) and (b) NIR pc-LED2 (fabricated using 450 nm LED with MAG: Cr³⁺, 0.1Sr²⁺, 1.5Ga³⁺). Images of CSIR NIIST logo and QR code (c) under indoor light and (d) under fabricated NIR LEDs.

3.4.7 *in vitro* cell imaging

Here, we have used the high-intense MAG: Cr³⁺, 0.1Sr²⁺ phosphor for the cell imaging application. It is crucial to analyse the effect of the test material on cell viability before going for any *in vitro* assays. MTT study portrays the extend of cellular metabolic response and thereby measuring the rate of cell proliferation.⁵³ Here, we analysed the effect of MAG: Cr³⁺, 0.1Sr²⁺ on the proliferation of HeLa cells. Upon 24 h of incubation, even the higher concentration of 100 μ M retained above 80 % cell viability in both the cell lines (**Fig. 3.13 (a) and (b)**) depicting the appropriateness of the compound for *in vitro* studies. Initial concentrations of 1 μ M to 10 μ M of MAG: Cr³⁺, 0.1Sr²⁺ was found to exhibit 100 % cell viability. Considering the cytotoxic pattern, we have selected 25 μ M concentration with a cell viability above 95 %, for further studies. **Fig. 3.13 (c)** represents the cellular uptake of MAG: Cr³⁺, 0.1Sr²⁺ by HeLa cells after

5 h incubation. The bright field image and fluorescent image are captured after treating the HeLa cells with 25 μM concentration of the MAG: Cr^{3+} , 0.1Sr^{2+} compound after 5h incubation. The compound is found to be internalised in the cells.

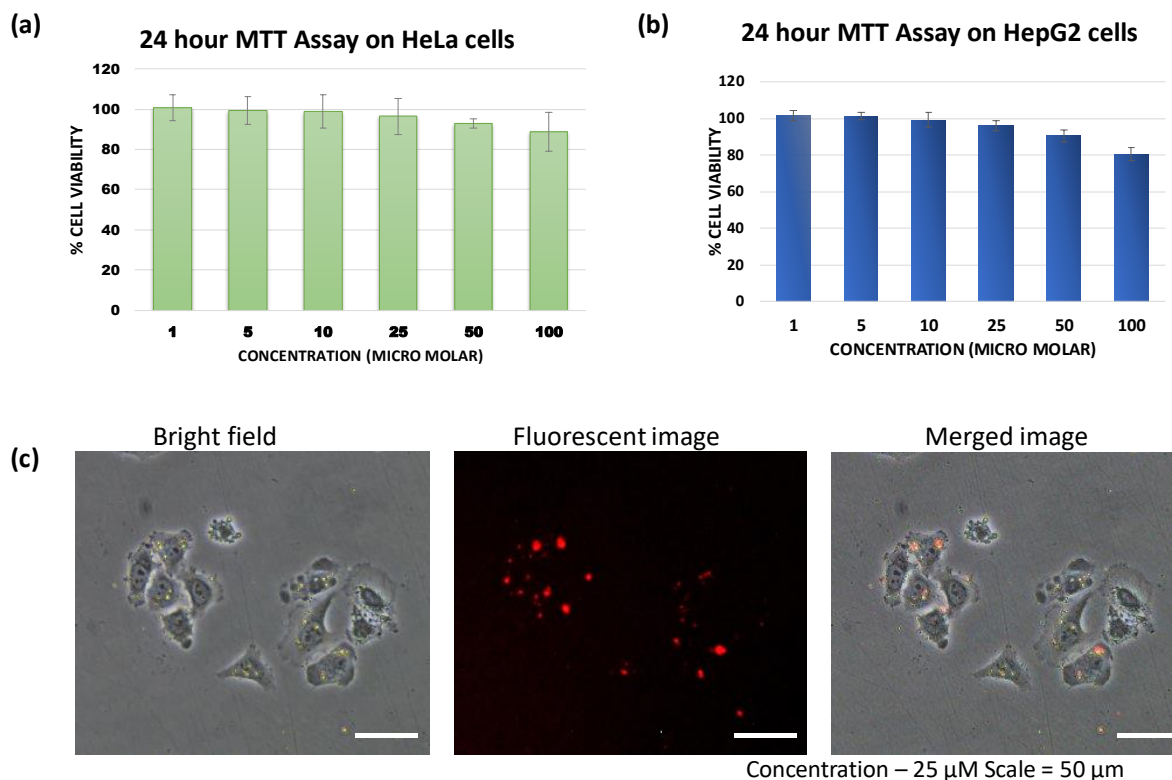


Fig. 3.13 Effect of MAG: Cr^{3+} , 0.1Sr^{2+} on cell viability of (a) HeLa cells and (b) HepG2 cells. (c) Cellular uptake of MAG: Cr^{3+} , 0.1Sr^{2+} by HeLa cells.

Subsequently, the time dependent internalisation study was conducted by tracking the fluorescence from the cells. After treating the HeLa cells with 25 μM concentration of the MAG: Cr^{3+} , 0.1Sr^{2+} compound for varying time points from 1 hour to 5 hours, it was noticed that the compound started to get internalized only after 2 hours. A noticeable fluorescence from the cells was able to get from 3 hours with the maximum intensity gained at 4 and 5 hours of incubation (**Fig. 3.14**). It was also perceptible that only the smaller sized particles were cell permeable whereas the larger particles retained on the background were removed upon PBS wash. Thus, it was concluded that the preparation methodology can be modified so as to get the uniform sized particles of sized below 200 nm for better cellular internalization.⁵⁴

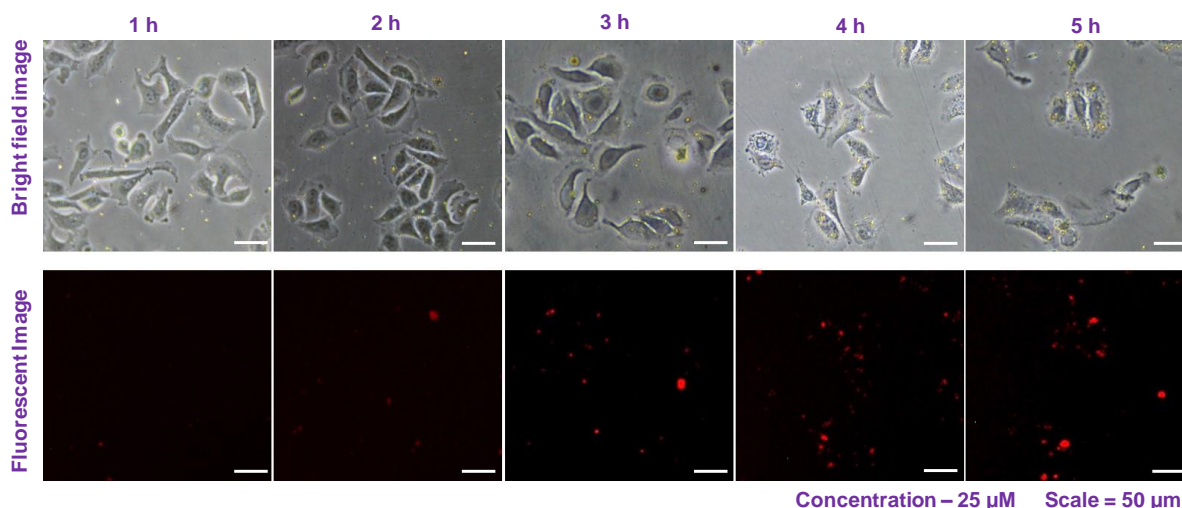


Fig. 3.14 Time dependent internalisation of MAG: Cr^{3+} , 0.1Sr^{2+} by HeLa cells.

3.5 Conclusions

A novel $\text{Mg}_3\text{Al}_2\text{GeO}_8: 0.01\text{Cr}^{3+}$ phosphor developed with ultra-sharp band emission peaking at 693 nm having a full width at half maximum (FWHM) of around 4 nm. Further the emission intensity and FWHM of the phosphor increased alkaline earth metal ions' substitution in Mg^{2+} sites. The $\text{Mg}_{2.9}\text{Al}_2\text{GeO}_8: 0.01\text{Cr}^{3+}, 0.1\text{Sr}^{2+}$ sample showed three times greater emission intensity than the $\text{Mg}_3\text{Al}_2\text{GeO}_8: 0.01\text{Cr}^{3+}$ sample and the FWHM increased to ~12 nm. The structural distortion in the Cr^{3+} occupied sites and the additional $[\text{MgO}_6]$ sites from the newly generated Sr impurity phase are responsible for the emission enhancement. The $\text{Mg}_3\text{Al}_2\text{GeO}_8: 0.01\text{Cr}^{3+}, 0.1\text{Sr}^{2+}$ sample showed greater emission intensity than the well-known $\text{ZnGa}_2\text{O}_4: \text{Cr}^{3+}$ sample under 400 nm excitation, showing its efficiency for bioimaging applications. Meanwhile, different Ga^{3+} co-doped $\text{Mg}_{2.9}(\text{Al}_{2-y}\text{Ga}_y)\text{GeO}_8: 0.01\text{Cr}^{3+}, 0.1\text{Sr}^{2+}$ ($y = 0, 0.5, 1, 1.5$) samples developed and the partial Ga^{3+} substitution reduced the crystal field strength and created weak crystal field environment $[\text{GaO}_6]$ suitable for Cr^{3+} ions to occupy. The combined emission from the strong and weak crystal field environment resulted in a broadband emission (630 nm to 1050 nm) with an FWHM of 148 nm covering the first biological window region effectively. Hence, the developed phosphors are suitable for bioimaging applications. Finally, various phosphor-converted LEDs were fabricated using commercial 410 nm and 450 nm LEDs. The sharp red emitting LED produced by combining 410 nm LED with $\text{Mg}_{2.9}\text{Al}_2\text{GeO}_8: 0.01\text{Cr}^{3+}, 0.1\text{Sr}^{2+}$ phosphor having 100% colour purity can be used for display application. The 410 nm LED combined with $\text{Mg}_{2.9}(\text{AlGa})\text{GeO}_8: 0.01\text{Cr}^{3+}, 0.1\text{Sr}^{2+}$ phosphor can be used for plant growth application since the absorption range of

phytochrome P_{fr} matches well with the emission range of the developed LED. Moreover, the NIR LEDs produced from $Mg_{2.9}(Al_{0.5}Ga_{1.5})GeO_8: 0.01Cr^{3+}, 0.1Sr^{2+}$ phosphor having increased FWHM can be used for night vision surveillance. Finally, the bio-imaging studies were carried out using a highly intense sample.

3.6 Supporting information

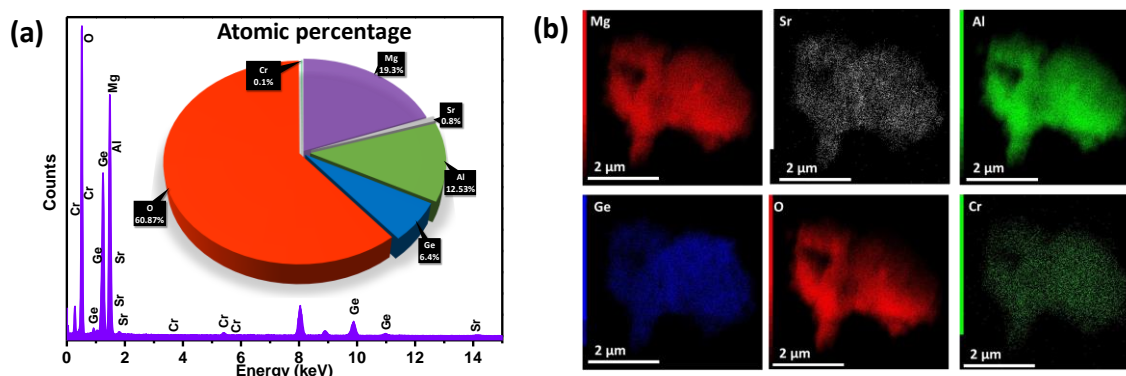


Fig.3.S1 (a) The EDX spectra and (b) EDX elemental mapping of Mg, Sr, Al, Ge, O and Cr for $MAG: Cr^{3+}, 0.1Sr^{2+}$ sample.

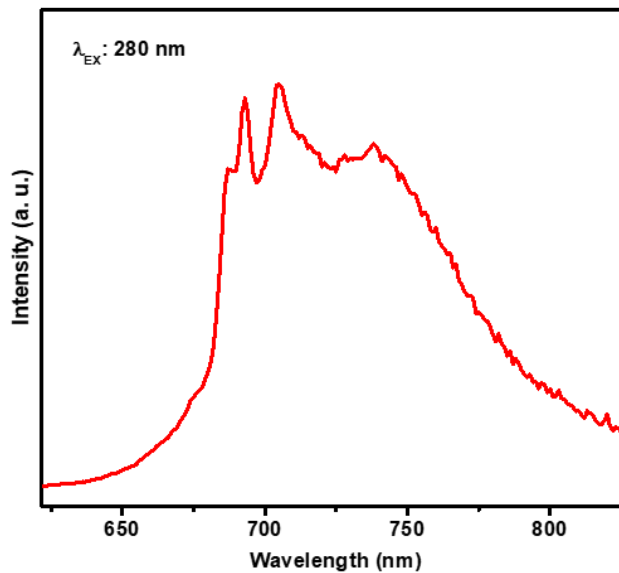


Fig.3.S2 PL emission spectra of $MAG: Cr^{3+}$ sample for under 280 nm excitation.

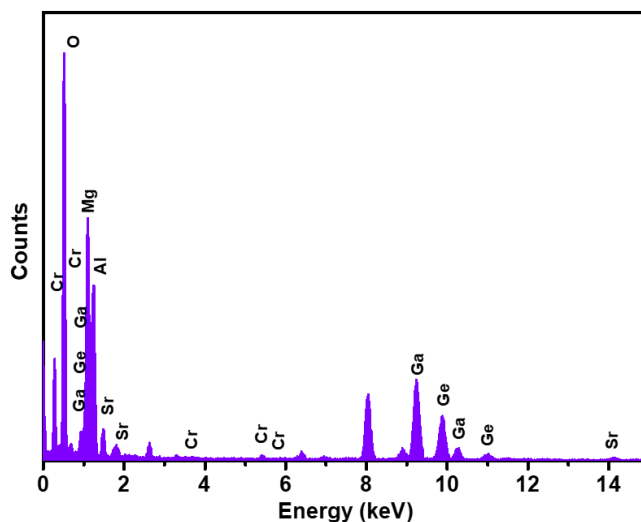


Fig.3.S3. The EDX spectra of MAG: Cr^{3+} , 1.5 Ga^{3+} , 0.1 Sr^{2+} sample showing the presence of Mg, Al, Ge, Ga, Sr and Cr elements in the sample.

3.7 References

- [1] Maldiney, T.; Bessière, A.; Seguin, J.; Teston, E.; Sharma, S. K.; Viana, B.; Bos, A. J. J.; Dorenbos, P.; Bessodes, M.; Gourier, D.; Scherman, D.; Richard, C. For Optical Imaging of Vascularization. Tumours. **2014**, *13* (April). <https://doi.org/10.1038/NMAT3908>.
- [2] Wang, S.; Pang, R.; Tan, T.; Wu, H.; Wang, Q.; Li, C.; Zhang, S.; Tan, T.; You, H.; Zhang, H. Achieving High Quantum Efficiency Broadband NIR $\text{Mg}_4\text{Ta}_2\text{O}_9:\text{Cr}^{3+}$ Phosphor through Lithium Ion Compensation. *Adv. Mater.* **2023**, *2300124*, 2300124. <https://doi.org/10.1002/adma.202300124>.
- [3] Liu, D.; Li, G.; Dang, P.; Zhang, Q.; Wei, Y.; Lian, H.; Shang, M.; Lin, C. C.; Lin, J. Simultaneous Broadening and Enhancement of Cr^{3+} Photoluminescence in $\text{LiIn}_2\text{SbO}_6$ by Chemical Unit Cosubstitution: Night-Vision and Near-Infrared Spectroscopy Detection Applications. *Angew. Chemie - Int. Ed.* **2021**, *60* (26), 14644–14649. <https://doi.org/10.1002/anie.202103612>.
- [4] Singh, S. P.; Kim, M.; Park, W. B.; Lee, J. W.; Sohn, K. S. Discovery of a Red-Emitting $\text{Li}_3\text{RbGe}_8\text{O}_{18}:\text{Mn}^{4+}$ Phosphor in the Alkali-Germanate System: Structural Determination and Electronic Calculations. *Inorg. Chem.* **2016**, *55* (20), 10310–10319. <https://doi.org/10.1021/acs.inorgchem.6b01576>.

- [5] Li, S.; Guo, Y.; Xie, R. J. Laser Phosphors for Next-Generation Lighting Applications. *Accounts Mater. Res.* **2022**, *3* (12), 1299–1308. <https://doi.org/10.1021/accountsmr.2c00193>.
- [6] Fabitha, K.; Ramachandra Rao, M. S. Ho³⁺-Doped ZnO Nano Phosphor for Low-Threshold Sharp Red Light Emission at Elevated Temperatures. *J. Opt. Soc. Am. B* **2017**, *34* (12), 2485. <https://doi.org/10.1364/josab.34.002485>.
- [7] Back, M.; Ueda, J.; Brik, M. G.; Lesniewski, T.; Grinberg, M.; Tanabe, S. Revisiting Cr³⁺-Doped Bi₂Ga₄O₉ Spectroscopy: Crystal Field Effect and Optical Thermometric Behavior of Near-Infrared-Emitting Singly-Activated Phosphors. *ACS Appl. Mater. Interfaces* **2018**, *10* (48), 41512–41524. <https://doi.org/10.1021/acsami.8b15607>.
- [8] Budijono, S. J.; Shan, J.; Yao, N.; Miura, Y.; Hoye, T.; Austin, R. H.; Ju, Y.; Prud'Homme, R. K. Synthesis of Stable Block-Copolymer-Protected NaYF₄:Yb³⁺,Er³⁺ up-Converting Phosphor Nanoparticles. *Chem. Mater.* **2010**, *22* (2), 311–318. <https://doi.org/10.1021/cm902478a>.
- [9] Zhou, J. C.; Yang, Z. L.; Dong, W.; Tang, R. J.; Sun, L. D.; Yan, C. H. Bioimaging and Toxicity Assessments of Near-Infrared Upconversion Luminescent NaYF₄:Yb, Tm Nanocrystals. *Biomaterials* **2011**, *32* (34), 9059–9067. <https://doi.org/10.1016/j.biomaterials.2011.08.038>.
- [10] Lisjak, D.; Vozlič, M.; Kostiv, U.; Horák, D.; Majaron, B.; Kralj, S.; Zajc, I.; Žiberna, L.; Ponikvar-Svet, M. NaYF₄-Based Upconverting Nanoparticles with Optimized Phosphonate Coatings for Chemical Stability and Viability of Human Endothelial Cells. *Methods Appl. Fluoresc.* **2022**, *10* (1). <https://doi.org/10.1088/2050-6120/ac41ba>.
- [11] Zeng, H.; Zhou, T.; Wang, L.; Xie, R. J. Two-Site Occupation for Exploring Ultra-Broadband Near-Infrared Phosphor - Double-Perovskite La₂MgZrO₆:Cr³⁺. *Chem. Mater.* **2019**, *31* (14), 5245–5253. <https://doi.org/10.1021/acs.chemmater.9b01587>.
- [12] Fang, L.; Zhang, L.; Wu, H.; Wu, H.; Pan, G.; Hao, Z.; Liu, F.; Zhang, J. Efficient Broadband Near-Infrared CaMgGe₂O₆:Cr³⁺ Phosphor for Pc-LED. *Inorg. Chem.* **2022**, *61* (23), 8815–8822. <https://doi.org/10.1021/acs.inorgchem.2c00798>.
- [13] Chen, K. C.; Fang, M. H.; Huang, W. T.; Kamiński, M.; Majewska, N.; Leśniewski, T.; Mahlik, S.; Leniec, G.; Kaczmarek, S. M.; Yang, C. W.; Lu, K. M.; Sheu, H. S.; Liu, R. S. Chemical and Mechanical Pressure-Induced Photoluminescence Tuning via Structural

Evolution and Hydrostatic Pressure. *Chem. Mater.* **2021**, *33* (10), 3832–3840. <https://doi.org/10.1021/acs.chemmater.1c01041>.

[14] Thejas, K. K.; Abraham, M.; Kunti, A. K.; Tchernycheva, M.; Ahmad, S.; Das, S. Review on Deep Red-Emitting Rare-Earth Free Germanates and Their Efficiency as Well as Adaptability for Various Applications. *Appl. Mater. Today* **2021**, *24*, 101094. <https://doi.org/10.1016/j.apmt.2021.101094>.

[15] Nie, W.; Li, Y.; Zuo, J.; Kong, Y.; Zou, W.; Chen, G.; Peng, J.; Du, F.; Han, L.; Ye, X. Cr³⁺-Activated Na₃X₂Li₃F₁₂ (X = Al, Ga, or In) Garnet Phosphors with Broadband NIR Emission and High Luminescence Efficiency for Potential Biomedical Application. *J. Mater. Chem. C* **2021**, *9* (42), 15230–15241. <https://doi.org/10.1039/d1tc03763c>.

[16] Rajendran, V.; Fang, M. H.; Guzman, G. N. De; Lesniewski, T.; Mahlik, S.; Grinberg, M.; Leniec, G.; Kaczmarek, S. M.; Lin, Y. S.; Lu, K. M.; Lin, C. M.; Chang, H.; Hu, S. F.; Liu, R. S. Super Broadband Near-Infrared Phosphors with High Radiant Flux as Future Light Sources for Spectroscopy Applications. *ACS Energy Lett.* **2018**, *3* (11), 2679–2684. <https://doi.org/10.1021/acsenerylett.8b01643>.

[17] Yan, W.; Liu, F.; Lu, Y.; Wang, X.; Yin, M.; Pan, Z. Near Infrared Long-Persistent Phosphorescence in La₃Ga₅GeO₁₄: Cr³⁺ Phosphor. **2010**, *18* (19), 103–104.

[18] Zhou, X.; Geng, W.; Li, J.; Wang, Y.; Ding, J.; Wang, Y. An Ultraviolet–Visible and Near-Infrared-Responded Broadband NIR Phosphor and Its NIR Spectroscopy Application. *Adv. Opt. Mater.* **2020**, *8* (8), 1–8. <https://doi.org/10.1002/adom.201902003>.

[19] Maldiney, T.; Doan, B. T.; Alloyeau, D.; Bessodes, M.; Scherman, D.; Richard, C. Gadolinium-Doped Persistent Nanophosphors as Versatile Tool for Multimodal in Vivo Imaging. *Adv. Funct. Mater.* **2015**, *25* (2), 331–338. <https://doi.org/10.1002/adfm.201401612>.

[20] Allix, M.; Chenu, S.; Véron, E.; Poumeyrol, T.; Kouadri-Boudjelthia, E. A.; Alahraché, S.; Porcher, F.; Massiot, D.; Fayon, F. Considerable Improvement of Long-Persistent Luminescence in Germanium and Tin Substituted ZnGa₂O₄. *Chem. Mater.* **2013**, *25* (9), 1600–1606. <https://doi.org/10.1021/cm304101n>.

[21] Kurunthatil Kuttat, T.; Abraham, M.; Kunti, A. K.; Amador-Mendez, N.; Tchernycheva, M.; Das, S. Enriching the Deep-Red Emission in (Mg, Ba)₃M₂GeO₈: Mn⁴⁺ (M = Al, Ga) Compositions for Light-Emitting Diodes. *ACS Appl. Mater. Interfaces* **2023**, *15* (5),

7083–7101. <https://doi.org/10.1021/acsami.2c20066>.

[22] Wei, X.; He, Y.; Liu, K.; Gao, P.; Chen, X.; Liu, X.; Zhou, H. Sintering Behavior, Crystal Structure, and Microwave Dielectric Properties of a Novel Diopside SrMgGe₂O₆ Ceramic and Adjustment of Its Tf Value. *Ceram. Int.* **2023**, *49* (9PA), 13807–13815. <https://doi.org/10.1016/j.ceramint.2022.12.259>.

[23] Peng, F.; Yuhua W.; Songsong D.; Theoretical calculations and investigation on properties and defect states in SrMgGe₂O₆: Mn²⁺, Sm³⁺ *Chem. Eng. J.* **2022**, *450*, 137820. <https://doi.org/10.1016/j.cej.2022.137820>.

[24] Xihui S.; Michele B.; Dongxun C.; Shihai M.; Ruiqi S.; Yanjie L.; A reliable and stable ratiometric luminescence thermometer based on dual near-infrared emission in a Cr³⁺-doped LaSr₂Ga₁₁O₂₀ phosphor. *J. Mater. Chem. C*, **2023**, *11*, 8952–8960. <https://doi.org/10.1039/d3tc01232h>.

[25] Li, Y.; Li, Y.; Chen, R.; Sharafudeen, K.; Zhou, S.; Gecevicius, M.; Wang, H.; Dong, G.; Wu, Y.; Qin, X.; Qiu, J. Tailoring of the Trap Distribution and Crystal Field in Cr³⁺-Doped Non-Gallate Phosphors with near-Infrared Long-Persistence Phosphorescence. *NPG Asia Mater.* **2015**, *7* (5). <https://doi.org/10.1038/am.2015.38>.

[26] Zhong, J.; Zhuo, Y.; Du, F.; Zhang, H.; Zhao, W.; Brgoch, J. Efficient and Tunable Luminescence in Ga_{2-x}In XO₃:Cr³⁺ for Near-Infrared Imaging. *ACS Appl. Mater. Interfaces* **2021**, *13* (27), 31835–31842. <https://doi.org/10.1021/acsami.1c05949>.

[27] Adachi, S. Review—Mn⁴⁺ vs Cr³⁺ : A Comparative Study as Activator Ions in Red and Deep Red-Emitting Phosphors . *ECS J. Solid State Sci. Technol.* **2020**, *9* (2), 026003. <https://doi.org/10.1149/2162-8777/ab6ea6>.

[28] Tauc J.; Optical properties and electronic structure of amorphous Ge and Si, *Mat. Res. Bull.* **1968**, *3*, 37-46.

[29] Xia, M.; Gu, S.; Zhou, C.; Liu, L.; Zhong, Y.; Zhang, Y.; Zhou, Z. Enhanced Photoluminescence and Energy Transfer Performance of Y₃Al₄GaO₁₂:Mn⁴⁺, Dy³⁺ Phosphors for Plant Growth LED Lights. *RSC Adv.* **2019**, *9* (16), 9244–9252. <https://doi.org/10.1039/c9ra00700h>.

[30] Zhang, S.; Hu, Y.; Chen, L.; Fu, Y.; Ju, G. La₃GaGe₅O₁₆:Cr³⁺ Phosphor: The near-Infrared Persistent Luminescence. *Opt. Mater. Express* **2016**, *6* (4), 1247.

<https://doi.org/10.1364/ome.6.001247>.

[31] Yorulmaz, I.; Beyatli, E.; Kurt, A.; Sennaroglu, A.; Demirbas, U. Efficient and Low-Threshold Alexandrite Laser Pumped by a Single-Mode Diode. *Opt. Mater. Express* **2014**, *4* (4), 776. <https://doi.org/10.1364/ome.4.000776>.

[32] Wang, C.; Wang, X.; Zhou, Y.; Zhang, S.; Li, C.; Hu, D.; Xu, L.; Jiao, H. An Ultra-Broadband Near-Infrared Cr³⁺-Activated Gallogermanate Mg₃Ga₂GeO₈ Phosphor as Light Sources for Food Analysis. *ACS Appl. Electron. Mater.* **2019**, *1* (6), 1046–1053. <https://doi.org/10.1021/acsaelm.9b00219>.

[33] Dai, D.; Wang, Z.; Xing, Z.; Li, X.; Liu, C.; Zhang, L.; Yang, Z.; Li, P. Broad Band Emission Near-Infrared Material Mg₃Ga₂GeO₈:Cr³⁺: Substitution of Ga-In, Structural Modification, Luminescence Property and Application for High Efficiency LED. *J. Alloys Compd.* **2019**, *806*, 926–938. <https://doi.org/10.1016/j.jallcom.2019.07.166>.

[34] Wang, J.; Han, X.; Zhou, Y.; Wu, Z.; Liu, D.; Zeng, C.; Cao, S.; Zou, B. Ion Substitution Strategy toward High-Efficiency Near-Infrared Photoluminescence of Cs₂KIn_{1- γ} Al γ F₆:Cr³⁺ Solid Solutions. *J. Phys. Chem. Lett.* **2023**, *14* (6), 1371–1378. <https://doi.org/10.1021/acs.jpcclett.3c00089>.

[35] Basavaraju, N.; Sharma, S.; Bessière, A.; Viana, B.; Gourier, D.; Priolkar, K. R. Red Persistent Luminescence in MgGa₂O₄: Cr³⁺; A New Phosphor for in Vivo Imaging. *J. Phys. D. Appl. Phys.* **2013**, *46* (37), 1–10. <https://doi.org/10.1088/0022-3727/46/37/375401>.

[36] Sharma, S. K.; Gourier, D.; Viana, B.; Maldiney, T.; Teston, E.; Scherman, D.; Richard, C. Persistent Luminescence of AB₂O₄:Cr³⁺ (A = Zn, Mg, B = Ga, Al) Spinel: New Biomarkers for in Vivo Imaging. *Opt. Mater. (Amst.)* **2014**, *36* (11), 1901–1906. <https://doi.org/10.1016/j.optmat.2014.06.020>.

[37] Brik, M. G.; Ogasawara, K. Microscopic Analysis of the Crystal Field Strength and Lowest Charge Transfer Energies in the Elpasolite Crystals Cs₂NaYX₆ (X = F, Cl, Br) Doped with Cr³⁺. *Phys. Rev. B - Condens. Matter Mater. Phys.* **2006**, *74* (4), 1–9. <https://doi.org/10.1103/PhysRevB.74.045105>.

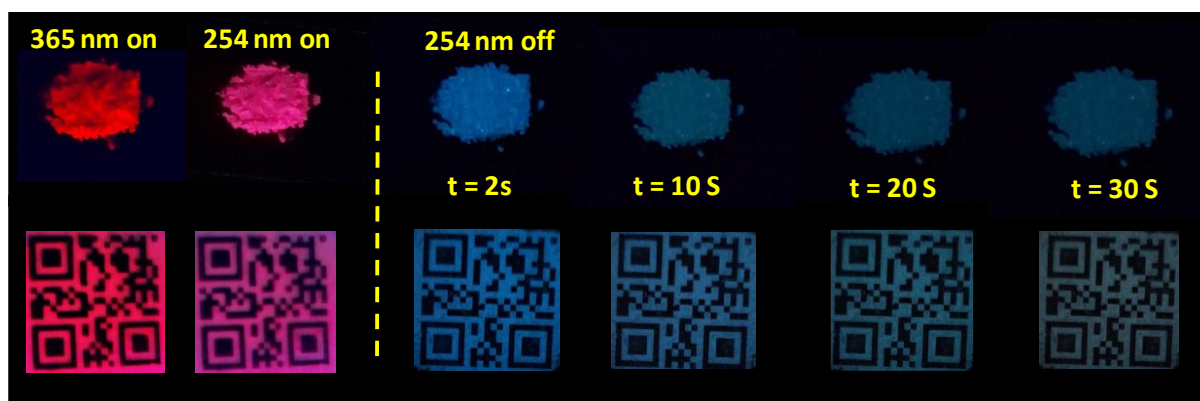
[38] Wang, Q.; Zhang, S.; Li, Z.; Zhu, Q. Near Infrared-Emitting Cr³⁺/Eu³⁺ Co-Doped Zinc Gallogermanate Persistence Luminescent Nanoparticles for Cell Imaging. *Nanoscale Res. Lett.* **2018**, *13*, 15–21. <https://doi.org/10.1186/s11671-018-2477-6>.

- [39] Peng, L.; Chen, W.; Cao, S.; Liu, B.; Han, T.; Zhao, L.; Zhao, C.; Li, F.; Li, X. Enhanced Photoluminescence and Thermal Properties Due to Size Mismatch in $\text{Mg}_2\text{Ti}_x\text{Ge}_{1-x}\text{O}_4:\text{Mn}^{4+}$ Deep-Red Phosphors. *J. Mater. Chem. C* **2019**, *7* (8), 2345–2352. <https://doi.org/10.1039/c8tc05743e>.
- [40] Liang, S.; Li, G.; Dang, P.; Wei, Y.; Lian, H.; Lin, J. Cation Substitution Induced Adjustment on Lattice Structure and Photoluminescence Properties of $\text{Mg}_{14}\text{Ge}_5\text{O}_{24}:\text{Mn}^{4+}$ Optimized Emission for w-LED and Thermometry Applications. *Adv. Opt. Mater.* **2019**. <https://doi.org/10.1002/adom.201900093>.
- [41] Shang, M.; Fan, J.; Lian, H.; Zhang, Y.; Geng, D.; Lin, J. Doped Garnet Phosphor for White LEDs. *Inorg. Chem.* **2014**, No. 1, 1–8.
- [42] Jensen, F. Activation energies and the Arrhenius. **1985**, *1* (September 1984), 1–5.
- [43] M. Szymczak, P. Woźny, M. Runowski, M. Pieprz, V. Lavín, L. Marciniak Temperature invariant ratiometric luminescence manometer based on Cr^{3+} ions emission. *Chem. Eng. J.* **2023**, 453, 139632
- [44] Liu, G.; Xia, Z. Modulation of Thermally Stable Photoluminescence in Cr^{3+} -Based Near-Infrared Phosphors. *J. Phys. Chem. Lett.* **2022**, *13* (22), 5001–5008. <https://doi.org/10.1021/acs.jpcclett.2c01143>.
- [45] Liu, S.; Wang, Z.; Cai, H.; Song, Z.; Liu, Q. Highly Efficient Near-Infrared Phosphor $\text{LaMgGa}_{11}\text{O}_{19}:\text{Cr}^{3+}$. *Inorg. Chem. Front.* **2020**, *7* (6), 1467–1473. <https://doi.org/10.1039/d0qi00063a>.
- [46] Zou, X.; Wang, X.; Zhang, H.; Kang, Y.; Yang, X.; Zhang, X.; Molokeyev, M. S.; Lei, B. A Highly Efficient and Suitable Spectral Profile Cr^{3+} -Doped Garnet near-Infrared Emitting Phosphor for Regulating Photomorphogenesis of Plants. *Chem. Eng. J.* **2022**, 428 (August 2021). <https://doi.org/10.1016/j.cej.2021.132003>.
- [47] Nie, W.; Yao, L.; Chen, G.; Wu, S. H.; Liao, Z.; Han, L.; Ye, X. A Novel Cr^{3+} -Doped $\text{Lu}_2\text{CaMg}_2\text{Si}_3\text{O}_{12}$ garnet Phosphor with Broadband Emission for near-Infrared Applications. *Dalt. Trans.* **2021**, 50 (24), 8446–8456. <https://doi.org/10.1039/d1dt01195b>.
- [48] Malysa, B.; Meijerink, A.; Jüstel, T. Temperature Dependent Cr^{3+} Photoluminescence in Garnets of the Type $\text{X}_3\text{Sc}_2\text{Ga}_3\text{O}_{12}$ ($X = \text{Lu}, \text{Y}, \text{Gd}, \text{La}$). *J. Lumin.* **2018**, 202, 523–531. <https://doi.org/10.1016/j.jlumin.2018.05.076>.

- [49] Zhang, L.; Zhang, S.; Hao, Z.; Zhang, X.; Pan, G. H.; Luo, Y.; Wu, H.; Zhang, J. A High Efficiency Broad-Band near-Infrared $\text{Ca}_2\text{LuZr}_2\text{Al}_3\text{O}_{12}:\text{Cr}^{3+}$ Garnet Phosphor for Blue LED Chips. *J. Mater. Chem. C* **2018**, *6* (18), 4967–4976. <https://doi.org/10.1039/c8tc01216d>.
- [50] Wang, S.; Xu, C.; Qiao, X. Synthesis and Photoluminescence Properties of the Novel Eu^{3+} -Activated $\text{CaNa}(\text{PO}_3)_3$ Phosphors. *J. Mater. Sci. Mater. Electron.* **2020**, *31* (12), 9605–9613. <https://doi.org/10.1007/s10854-020-03503-7>.
- [51] Pratapkumar, C.; Prashantha, S. C.; Nagabhushana, H.; Jnaneshwara, D. M. Photoluminescence and Photometric Studies of Low Temperature Prepared Red Emitting $\text{MgAl}_2\text{O}_4:\text{Cr}^{3+}$ Nanophosphors for Solid State Displays. *J. Sci. Adv. Mater. Devices* **2018**, *3* (4), 464–470. <https://doi.org/10.1016/j.jsamd.2018.09.002>.
- [52] Ye Wang, Zhijun Wang, Guohui Wei, Yuanbo Yang, Shaoxuan He, Jiehong Li, Yawei Shi, Rui Li, Jiawei Zhang, and Panlai Li Highly Efficient and Stable Near-Infrared Broadband Garnet Phosphor for Multifunctional Phosphor-Converted Light-Emitting Diodes. *Adv. Optical Mater.* **2022**, *10*, 2200415.
- [53] Ghasemi, M.; Turnbull, T.; Sebastian, S.; Kempson, I. The Mtt Assay: Utility, Limitations, Pitfalls, and Interpretation in Bulk and Single-Cell Analysis. *Int. J. Mol. Sci.* **2021**, *22* (23). <https://doi.org/10.3390/ijms222312827>.
- [54] Valsan, A.; Meenu, M. T.; Murali, V. P.; Malgija, B.; Joseph, A. G.; Nisha, P.; Radhakrishnan, K. V.; Maiti, K. K. Exploration of Phaeanthine: A Bisbenzylisoquinoline Alkaloid Induces Anticancer Effect in Cervical Cancer Cells Involving Mitochondria-Mediated Apoptosis. *ACS Omega* **2023**, *8* (16), 14799–14813. <https://doi.org/10.1021/acsomega.3c01023>.

Chapter 4

Inducing defects to boost the persistent luminescence in novel cyan emitting rare-earth free strontium zirconium silicate for dynamic anti-counterfeiting and plant growth LED applications



4.1 Abstract

Initially, a self-activated $\text{Sr}_2\text{Zr}(\text{SiO}_3)_4$ phosphor is developed by substituting Sr^{2+} for Ca^{2+} in the reported $\text{Ca}_2\text{Zr}(\text{SiO}_3)_4$. XRD pattern of the synthesized $\text{Sr}_2\text{Zr}(\text{SiO}_3)_4$ crystal matches with $m\text{-Sr}_3\text{Y}_2\text{Si}_6\text{O}_{18}$ having a cyclosilicate structure. This discovery led to the development of a novel self-activating cyan-emitting persistent luminescence $\text{Sr}_2\text{Zr}_2(\text{SiO}_3)_6$ phosphor. The XRD analysis identified the presence of a secondary orthorhombic- $\text{Sr}_3\text{Zr}_2\text{O}_7$ phase, along with some impurity peaks from precursor materials. The various phases and corresponding planes in the host lattice were confirmed from the HRTEM analysis. Under 284 nm excitation, the PL emission of the host exhibited broadband centred at 485 nm, originating from the Zr^{4+} ions and lattice defects. Additionally, the host shows a cyan persistent luminescence having a duration of 60s. The addition of NH_4Cl flux enhances persistent luminescence intensity and duration of the host material (>60s). Bi^{3+} doping and post-annealed vacuum treatment increased the oxygen vacancy compared to $\text{Sr}_2\text{Zr}_2(\text{SiO}_3)_6: 12\text{wt}\% \text{NH}_4\text{Cl}$ phosphor, as evidenced by the XPS analysis. After Bi^{3+} incorporation, an additional PL band centered at 620 nm is observed due to the oxygen-vacancy-induced electronic localisation around the Bi^{3+} ions. The optimised vacuum-treated $\text{Sr}_2\text{Zr}_2(\text{SiO}_3)_6: 12\text{wt}\% \text{NH}_4\text{Cl}, 0.02\text{Bi}^{3+}$ phosphor exhibits enhanced persistent luminescence intensity and duration (90s) due to the presence of additional shallow traps. The vacuum-treated phosphor has been used for dynamic anticounterfeiting application by mixing with the red-emitting $\text{Mg}_3\text{Al}_2\text{GeO}_8: 0.005 \text{Mn}^{4+}, 0.27\text{Ba}^{2+}$ phosphor. Vacuum-treated $\text{Sr}_2\text{Zr}_2(\text{SiO}_3)_6: 12\text{wt}\% \text{NH}_4\text{Cl}, 0.02\text{Bi}^{3+}$ is the first cyan emitting rare earth-free persistent luminescence phosphor used for anticounterfeiting and security ink applications. Furthermore, $\text{Sr}_2\text{Zr}_2(\text{SiO}_3)_6: 12\text{wt}\% \text{NH}_4\text{Cl}/\text{Mg}_3\text{Al}_2\text{GeO}_8: 0.005 \text{Mn}^{4+}, 0.27\text{Ba}^{2+}$ mixture is used to develop a plant growth LED, covering the absorption spectra of plant phytochrome (P_r) and chlorophylls.

4.2 Introduction

Persistent luminescence (PersL), also known as long-lasting luminescence or afterglow, is an optical phenomenon that continues for seconds to days after the cessation of optical excitation.¹⁻⁴ The long-lasting luminescence is possible due to the storage of excitation energy in trap centers (defects in the host lattice), which can be released by external thermal stimuli. Owing to their unique optical properties, materials exhibiting persistent luminescence find diverse applications in optical bioimaging, security and anticounterfeiting measures,

optical information and data storage, photocatalysis, latent fingerprint recognition, and light-emitting diodes.^{4–11}

The presently available commercial PersL phosphors are $\text{SrAl}_2\text{O}_4: \text{Eu}^{2+}, \text{Dy}^{3+}$ (green)¹², $\text{CaAl}_2\text{O}_4: \text{Eu}^{2+}, \text{Nd}^{3+}$ (blue)¹², and $\text{Y}_2\text{O}_2\text{S}: \text{Eu}^{3+}, \text{Ti}^{3+}, \text{Mg}^{2+}$ (red)¹³. However, these PersL materials have some drawbacks, such as low moisture resistance of aluminates and poor stability of sulphides.¹⁴ Therefore, it is essential to develop and characterize novel PersL phosphors to understand their intriguing applications. The most commonly used oxide hosts for achieving PersL include aluminates, silicates, germanates, gallates, and phosphates.^{12,15–20} Among these, silicates are particularly noteworthy due to their easy preparation, excellent stability, high brightness, long PersL duration, and adjustable luminous emission color, making them a focus of significant interest.¹⁵ The most renowned persistent luminescent silicate is the blue-emitting $\text{Sr}_2\text{MgSi}_2\text{O}_7: \text{Eu}^{2+}, \text{Dy}^{3+}$, first reported by Lin et al., with an PersL lasting over 10 hours.²¹ Another notable example is $\text{Ba}_2\text{MgSi}_2\text{O}_7: \text{Eu}^{2+}, \text{Tm}^{3+}$, which emits green light and has an PersL exceeding 5 hours.^{22,23} The family of alkaline earth akermanites materials $\text{M}_2\text{MgSi}_2\text{O}_7$ (M = Ca, Sr, Ba) are among the most extensively studied persistent luminescent silicates.²⁴ These materials are frequently used as models for explaining PersL mechanisms. PersL materials typically use rare-earth cations such as Eu^{2+} , Ce^{3+} , Tb^{3+} , Nd^{3+} , and Tm^{3+} as luminescent centers.²⁵ Due to the limited abundance of rare-earths, there has been significant interest in non-RE bismuth-activated phosphors, which exhibit intriguing optical properties and have potential applications in optical information storage, anticounterfeiting measures, biomedical imaging, x-ray imaging, stress sensing, and photocatalysis.²⁵ Bi^{3+} -activated phosphors have garnered attention for their ability to emit flexible colors under ultraviolet (UV) and near-ultraviolet excitation. Bi^{3+} ions can serve as multicolor luminescent centers by adjusting the crystal field, valence state and introducing structural defects into the host. Bi^{3+} has a $^1\text{S}_0$ ground state derived from the $6s^2$ configuration, with a singlet $^1\text{P}_1$ excited state and triplet $^3\text{P}_0$, $^3\text{P}_1$, and $^3\text{P}_2$ excited states derived from the $6s6p$ configuration. The strong absorption bands in the UV region correspond to the spin-allowed transitions from the $^1\text{S}_0$ ground state to the $^3\text{P}_1$ and $^1\text{P}_1$ excited states, while the emission of Bi^{3+} is attributed to the $^3\text{P}_1 \rightarrow ^1\text{S}_0$ transition. The outer 6s electrons of Bi^{3+} are highly sensitive to the crystal field of the host material.²⁵ Li *et al.* reported a super-long PersL material based on $\text{BaGa}_2\text{O}_4: \text{Bi}^{3+}$ with an PersL duration of 7 days.²⁶ Due to the rigid host network and defects introduced by doping, this material exhibits strong resistance to thermal quenching and superlong PersL. The orange-

red-emitting phosphor is employed in the development of a white LED with a high color rendering index (>90). Recently, Yuan *et al.* reported a new cyan emitting persistent $\text{BaLu}_2\text{Al}_2\text{Ga}_2\text{SiO}_{12}:\text{Ce}^{3+}, \text{Bi}^{3+}$ phosphors for AC-LEDs via defect modulation.¹¹ Various Bi^{3+} -activated PersL materials, such as $\text{Na}_4\text{CaSi}_3\text{O}_9:\text{Bi}^{3+}, \text{Eu}^{3+}$ ²⁷ with tunable blue-red emission, $\text{Ca}_2\text{LaTaO}_6:\text{Bi}^{3+}/\text{Mn}^{4+}$ ²⁸ emitting far-red light, and $\text{CaGdGaO}_4:\text{Bi}^{3+}$ ²⁹ emitting blue light, are also utilized for plant growth applications. Counterfeiting is a significant issue that poses a threat to economic security and violates intellectual property rights. This suggests the necessity of a high-level anticounterfeiting system. Persistent luminescence (PersL) phosphors, known for their tunable emissions, have gained attention for anticounterfeiting applications.⁶ For example, Tang *et al.* developed a multicolor-emitting phosphor, $\text{Ba}_{0.99}\text{Ga}_2\text{O}_4:0.01\text{Bi}^{3+}$, suitable for dynamic anticounterfeiting due to the varied emission centers of Bi ions and the presence of Ga vacancies.³⁰ The color of PersL in $\text{Ba}_{0.99}\text{Ga}_2\text{O}_4:0.01\text{Bi}^{3+}$ changes from yellow to green with increasing temperature. Wang *et al.* created multiple anticounterfeiting phosphors by incorporating Bi^{3+} and upconversion ion Er^{3+} into the NaYTiO_4 host, generating numerous trap levels.³¹ These phosphors exhibit promising applications in advanced anticounterfeiting measures due to the combination of their photochromic characteristics, upconversion, downshifted emissions, and PersL emission. Several silicate-based PersL materials are employed for dynamic anticounterfeiting applications. Tao *et al.* recently reported on a silicate composite, $\text{Zn}_2\text{SiO}_4/\text{CdSiO}_3:\text{Dy}^{3+}$, whose emission changes from white to yellow to orange and ultimately red over time, making it suitable for anticounterfeiting purposes.³² Another example of silicate $\text{Na}_3\text{LuSi}_3\text{O}_9:\text{Ce}^{3+}, \text{Eu}^{2+}$ demonstrated by Li *et al.* has the potential for multimode dynamic luminescence, as it is highly sensitive to dopant composition, excitation wavelength, and detection time.³³ The remarkable properties of this material make it practical for fingerprint identification and anticounterfeiting applications.

In 2015, Xiaochen *et al.* reported a novel phosphor consisting of un-doped $\text{SrZrSi}_2\text{O}_7$ material exhibiting blue long-lasting phosphorescence lasting for 5400 seconds.³⁴ It was found that both the emission centers and trap levels were associated with oxygen-deficient defects induced in a reducing atmosphere. Despite this, zirconate-based host materials have not been effectively utilized for PersL applications. In response, a new host, $\text{Sr}_2\text{Zr}_2(\text{SiO}_3)_6$ (SZSO6), was developed in which Zr^{4+} occupies three Sr^{2+} sites, creating more opportunities for oxygen deficiency and enhancing PersL. One major advantage of the prepared SZSO6 material is its

dynamic color changes, making it suitable for mixing with various red and green-emitting phosphors for anticounterfeiting applications. The $\text{Sr}_2\text{Zr}_2(\text{SiO}_3)_6$: 12wt% NH_4Cl (SZSO6: 12wt% NH_4Cl) phosphor has been effectively mixed with the reported red-emitting $\text{Mg}_3\text{Al}_2\text{GeO}_8$: 0.005 Mn^{4+} , 0.27 Ba^{2+} (MAG: Mn^{4+} , 0.27 Ba^{2+}) phosphor.³⁵ The above-mixed compositions have been successfully applied in plant growth applications. Meanwhile, the vacuum-treated $\text{Sr}_2\text{Zr}_2(\text{SiO}_3)_6$: 12wt% NH_4Cl , 0.02 Bi^{3+} (SZSO6: 12wt% NH_4Cl , 0.02 Bi^{3+}) sample also mixed with the above-mentioned MAG: Mn^{4+} , 0.27 Ba^{2+} red phosphor and used for dynamic anti-counterfeiting applications.

4.3 Experimental

4.3.1 Materials synthesis

The persistent luminescence materials $\text{Ca}_2\text{Zr}(\text{SiO}_3)_4$ (CZSO4), $\text{Sr}_2\text{Zr}(\text{SiO}_3)_4$ (SZSO4), $\text{Sr}_2\text{Zr}(\text{SiO}_3)_4$: x wt% NH_4Cl (SZSO4: x wt% NH_4Cl), $\text{Sr}_2\text{Zr}_2(\text{SiO}_3)_6$: (SZSO6), $\text{Sr}_2\text{Zr}_2(\text{SiO}_3)_6$: x wt% NH_4Cl (SZSO6: x wt% NH_4Cl) and $\text{Sr}_2\text{Zr}_2(\text{SiO}_3)_6$: x wt% NH_4Cl , y Bi^{3+} (SZSO6: x wt% NH_4Cl , y Bi^{3+}) samples were prepared through the conventional solid-state reaction route. CaCO_3 (99.9 %), SrCO_3 (99.9 %), ZrO_2 (99.99 %), SiO_2 (99.9%), NH_4Cl (99.99 %) and Bi_2O_3 (99.99%) were the raw material used for the synthesis. The reagents were weighed according to the stoichiometric ratio and ground for 30 minutes in ethanol using an agate-mortar. The dried sample were heated in air furnace for 1250 °C for 5 h. The optimized sample is post annealed in vacuum at 1000 °C for 2 h.

4.3.2 Characterization

The X-ray powder diffraction (XRD) patterns of the materials were collected using Malvern PANalytical B.V. EMPYREAN 3 diffractometer with Ni filtered $\text{Cu-K}\alpha$ radiation ($\lambda = 1.54 \text{ \AA}$). Rietveld refinement analysis of the XRD patterns were carried out using the GSAS2 software. The X-ray photoelectron spectroscopy (XPS) analysis was conducted using a PHI 5000 VersaProbe II equipped with a micro-focused (200 μm , 15 kV) monochromatic Al $\text{K}\alpha$ X-ray source (1486.6 eV). The crystal planes and various phases in the samples were identified using a high-resolution transmission electron microscope (HRTEM), JEOL JEM-F200. The elemental identification and morphological characteristics of the samples were analysed using scanning electron microscopy (JEOL JSM-5600 LV SEM). The UV–vis diffuse reflectance spectra (DRS) measurements were recorded using a Shimadzu UV–vis–NIR spectrophotometer (UV 3600). The photoluminescence (PLE) excitation, emission (PL),

and lifetime were investigated using a Horiba Yvon Fluorolog 3 spectrofluorimeter having a 450 W xenon irradiation source. PersL decay curves of the selected samples were recorded using Edinburgh FLS 1000 spectrophotometer. To obtain the PersL decay of the phosphors, the samples were illuminated under an excitation of 284 nm for 5 minutes by a Xenon source (450 W).

4.4 Results and discussion

4.4.1 Structural and optical properties of CZSO4 and SZSO4

Fig.4.S1 (a) in the supporting information shows the XRD pattern of $\text{Ca}_2\text{Zr}(\text{SiO}_3)_4$ (CZSO4) and $\text{Sr}_2\text{Zr}(\text{SiO}_3)_4$ (SZSO4). CZSO4 is reported to have a monoclinic structure belonging to space group $P2_1/m$.^{36,37} Ca^{2+} and Si^{4+} ions occupy two crystallographic sites each, while Zr^{4+} ions occupy one. The Ca atom has multiple coordination ([CaO8] and [CaO9]), whereas the Si atom forms a tetrahedron with four O atoms [SiO4], and the Zr atom is coordinated by six oxygen atoms [ZrO6], forming an octahedron. However, the XRD pattern of SZSO6 matches well with the JCPDS of monoclinic- $\text{Sr}_3\text{Y}_2\text{Si}_6\text{O}_{18}$ (m-SYSO, JCPDS 00-065-0204) rather than the JCPDS of monoclinic- $\text{Ca}_2\text{ZrSi}_4\text{O}_{12}$ (JCPDS 04-011-5399). Apart from the m-SYSO phase (alkaline-earth lanthanide cyclosilicates), some of the major peaks are matching with hexagonal SrSiO_3 (h-SrSiO₃, JCPDS 04-021-7867). Hence, the above h-SrSiO₃ phase can be considered as a secondary phase. Impurity peaks from the precursor material SiO₂ are also observed.

Since multiple secondary phases are observed, NH_4Cl is added as a flux during the synthesis procedure to enhance the crystallinity of SZSO4. The NH_4Cl , as a flux, is reported to enhance the PersL luminescence of $\text{Sr}_2\text{MgSi}_2\text{O}_7: \text{Eu}^{2+}, \text{Dy}^{3+}$, and $\text{CaSnO}_4: \text{Sm}^{3+}$ phosphors by forming crystals at lower temperatures with enhanced morphology.^{14,38} Flux controls the particle size, shape, and distribution of phosphors, thereby improving their luminescence properties. In $\text{CaSnO}_4: \text{Sm}^{3+}$, the addition of flux enhances the PersL duration by inducing more shallow traps in the crystal. The XRD pattern of various NH_4Cl added SZSO4 samples is displayed in **Fig.4.S1 (b)**. However, the XRD patterns are similar to the patterns obtained without flux, with the major phase being m-SYSO. While increasing the NH_4Cl concentration from 0 to 15 wt% the peaks corresponding to the secondary phases h-SrSiO₃ and SiO₂ are found to be enhanced. Thus, the NH_4Cl can be considered as an effective tool for regulating the phase fraction of h-SrSiO₃ and SiO₂ in this host.

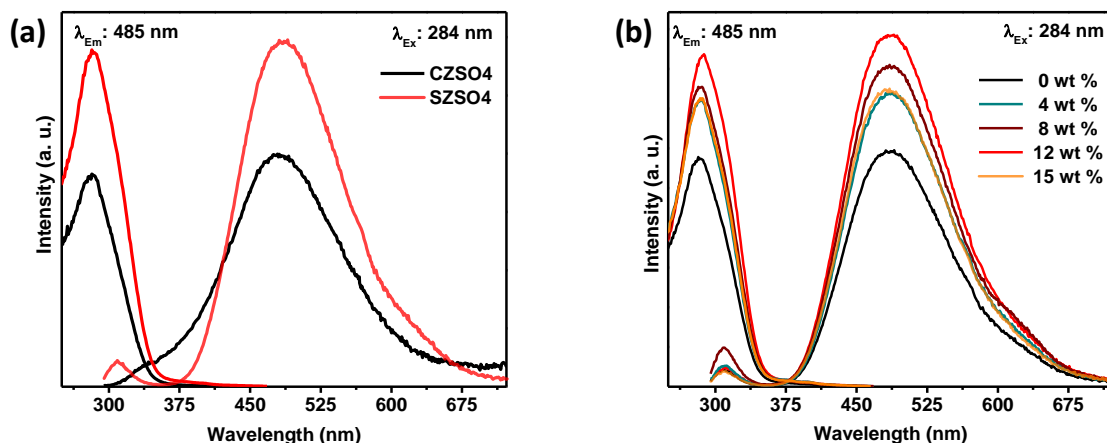


Fig.4.1. PLE and PL spectra of (a) CZSO4, SZSO4 and (b) SZSO4: x wt% NH₄Cl (x = 0 to 15 wt%).

The PLE and PL spectra of the undoped CZSO4 and multiphase SZSO4 (m-SYSO /h-SrSiO₃/SiO₂) are displayed in **Fig.4.1 (a)**. Monitored at 485 nm, the excitation spectrum of CZSO4 presents a PLE band in the range 260 nm to 375 nm centered at 284 nm due to the O²⁻ → Zr⁴⁺ charge transfer inside the [ZrO₆] group. Under 284 nm excitation, the PL spectrum exhibits a broadband in the range of 300 nm to 675 nm peaking at 485 nm (FWHM = 140 nm). The emission can be attributed to the metal to ligand (Zr⁴⁺ → O²⁻) charge transfer transition. The PL spectrum of CZSO4 is reported to consist of two bands: one broadband centered at 490 nm and a weak band centered at 375 nm. The two different bands arise due to the occupation of Zr⁴⁺ ions in different coordination environments. One possibility is Zr⁴⁺ ion occupies Ca²⁺ sites along with the octahedral [ZrO₆] site during synthesis at high temperatures, creating positive defects (Zr_{Ca})[•].^{36,37} The charge compensation, in this case, is achieved by cation vacancies or interstitial oxygen present in the compound. The distortion in the coordination environments affects the covalence of Zr⁴⁺ and O²⁻ ions, resulting in the long wavelength emission of Zr⁴⁺ ions. The SZSO4 sample with the same PLE and PL maximum as that of CZSO4 exhibits enhanced PLE and PL intensity; however, with a reduced FWHM of 132 nm. An additional peak centered at 310 nm is also observed in SZSO4 is due to the PL of Zr⁴⁺ ions in disordered coordination environments. The higher intensity of emission in SZSO4 can be attributed to the presence of the secondary phases present in the phosphor. The secondary phase, SiO₂ is reported to exhibit self-activated blue emission.³⁹ The PLE and PL spectra of various NH₄Cl doped phosphors are shown in **Fig.4.1 (b)**. The emission intensity gradually increases with the increase in NH₄Cl concentration up to 12 wt%. After 12 wt% NH₄Cl, the emission gets quenched, which might result from the agglomeration of particles

or the formation of a glass (amorphous) phase. The increase in intensity can be attributed to the enhanced crystallinity and increase in the SiO₂ phase with NH₄Cl, as suggested by the XRD patterns. At 15 wt% of NH₄Cl, the SiO₂ phase is also decreasing as evident from **Fig.4.S1 (b)**.

4.4.2 Structural, elemental and morphological characterization of SZSO6

4.4.2.1 XRD analysis

Since the XRD pattern of SZSO4 matches more with the m-SYSO cyclosilicate structure, a novel composition with stoichiometry Sr₂Zr₂(SiO₃)₆ (SZSO6) is developed by balancing the charge. The above materials consist of two phases, namely m-SYSO and orthorhombic-Sr₃Zr₂O₇ (o-SZO). The m-SYSO can be considered as a major phase, and the o-SZO is the secondary phase. Also, the impurity peaks of SiO₂ from the precursor material is also observed in the sample.

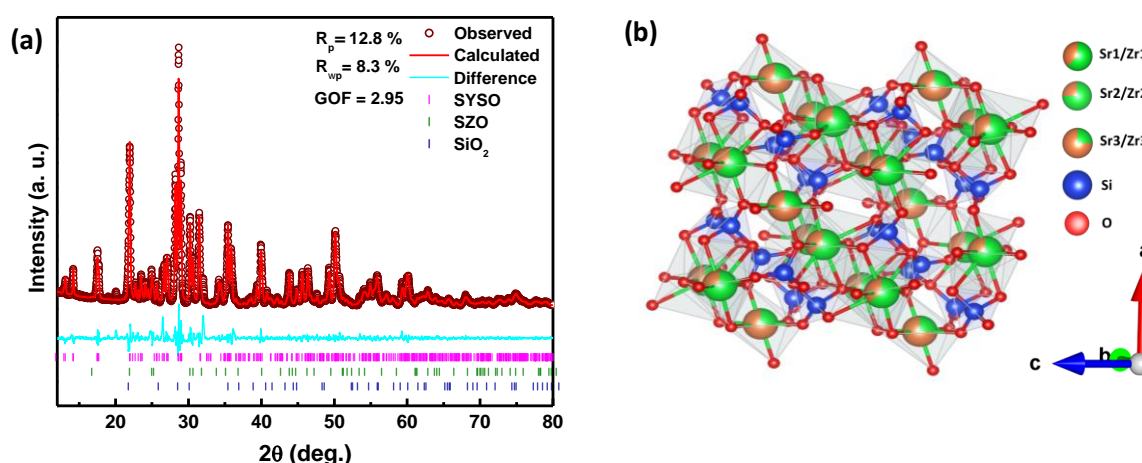


Fig.4.2 (a) Rietveld refinement pattern of SZSO6 phosphor and the corresponding **(b)** monoclinic crystal structure

Fig.4.2 (a) represents the Rietveld refinement pattern of SZSO6 using the above three phases. The refinement parameters are $R_p = 12.8\%$, $R_{wp} = 8.3\%$ and $GOF = 2.95$. The lattice parameters of the compound is obtained as $a = 13.41 \text{ \AA}$, $b = 7.88 \text{ \AA}$, $c = 14.67 \text{ \AA}$. The corresponding crystal structure of the above phosphor is shown in **Fig.4.2 (b)**. The m-SYSO phase is having monoclinic crystal structure belonging to the space group $C2/c$ (15). m-SYSO is a cyclosilicate crystal characterized by alternating layers of Sr/Y atoms and [Si₃O₉] ring

layers along the [101] direction. Each $[\text{Si}_3\text{O}_9]$ ring consists of three SiO_4 tetrahedra, with two oxygen atoms from each tetrahedron being shared. The Sr/Y atoms are located in the Sr/Y layer and exhibit eightfold (Sr1/Y1), sevenfold (Sr2/Y2), and sixfold (Sr3/Y3) coordination, occupying distinct sites. Within the Sr/Y layer, only 5/6 of the cation sites are filled with Sr or Y ions in various coordination geometries, leaving 1/6 of the sites vacant. When doped, ions preferentially occupy the eight-coordinated Sr/Y sites due to the high concentration of these sites.⁴⁰ In the case of the SZSO6 sample, the Zr^{4+} ions are replacing the Y^{3+} sites and occupying those sites. The corresponding crystal structure is represented in **Fig.4.2 (b)**. The XRD pattern of x wt% NH_4Cl doped SZSO6 (x = 0, 4, 8, 12, 15, 18) samples are shown in **Fig.4.S2 (a)**. The peaks corresponding to the secondary phase o-SZO are found to be increasing with an increase in NH_4Cl concentration, which is similar to the behaviour of the SrSiO_3 phase in the XRD patterns of NH_4Cl co-doped SZSO4. Further Bi^{3+} ions have been co-doped in the Sr^{2+} sites of optimum SZSO6: 12wt% NH_4Cl phosphor at four different concentrations ($y\text{Bi}^{3+}$; y = 0, 0.01, 0.02, 0.03, 0.04) and the corresponding changes in the XRD pattern are shown in **Fig.4.S2 (b)**. A slight shift towards a higher 2θ angle has been observed due to the lower ionic radii of Bi^{3+} ions compared to the Sr^{2+} ions.

4.4.2.2 HRTEM analysis

The HRTEM images for the undoped SZSO6 sample are displayed in **Fig.4.3 (a-b)** and the various planes corresponding to different phases were identified. The planes corresponding to the major phase m-SYSO can be identified from the inset of **Fig.4.3 (a)**, which is the magnified portion of a small area. The calculated inter-planar spacing in two different regions of the magnified portion is 3.10 Å and 2.247 Å, and it corresponds to the (0 2 3) and (-2 2 5) planes of the m-SYSO phase respectively. Further, the corresponding reduced 2D- fast Fourier transform (2D-FFT) of the magnified version is taken and shown in the inset of **Fig.4.3 (a)**, which further confirms the existing (0 2 3) and (-2 2 5) planes of m-SYSO. **Fig.4.3 (b)** represents the HRTEM images of the sample from a different region. Since the planes are overlapped in this region, a reduced FFT of the entire image is taken in order to identify the planes. From the reduced FFT, the calculated inter-planar distances are 6.23 Å and 3.07 Å, and it corresponds (1 1 1) and (3 1 3) planes the m-SYSO phase. Apart from this major phase, the (2 2 0) planes of the secondary phase o-SZO are also identified and the corresponding inter-planar distance is 2.06 Å.

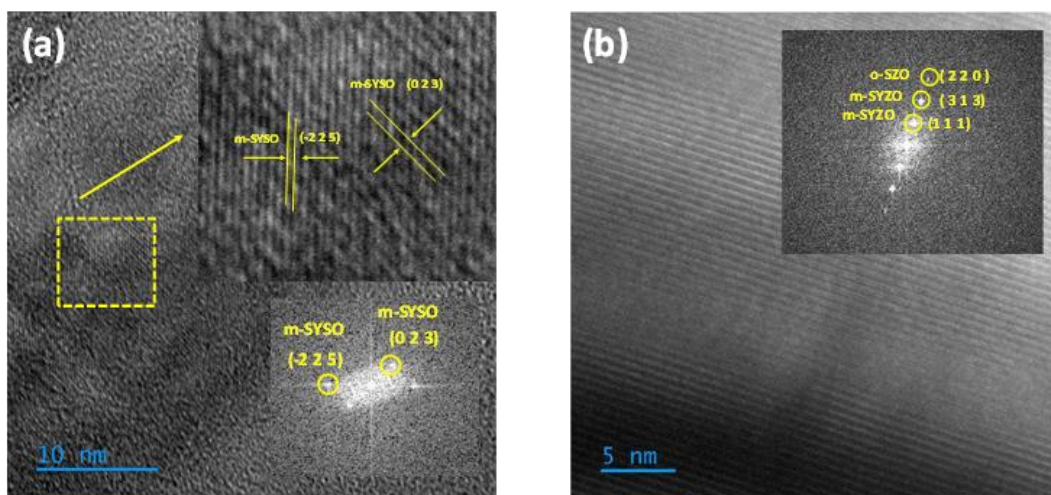


Fig.4.3 (a-b) HRTEM images of SZSO6 sample with magnified versions (inset) and reduced FFT (inset) showing the planes corresponding to different phases.

Fig.4.S3 (a) demonstrates $(-1\ 1\ 3)$ and $(0\ 2\ 3)$ planes of the m-SYSO phase having the d-spacing values of $4.02\ \text{\AA}$ and $3.1\ \text{\AA}$ respectively. **Fig.4.S3 (b)** also shows the overlapping of two planes as observed in **Fig.4.3 (b)**. Here, the $(1\ 1\ 1)$ plane of the major m-SYSO phase and the $(1\ 1\ 5)$ plane of the o-SZO are identified from the reduced FFT as shown in the inset of **Fig.4.S3 (b)** and the associated d values are $6.23\ \text{\AA}$ and $2.95\ \text{\AA}$ respectively. The phases identified from the HRTEM images match with the phases used for the Rietveld refinement of the XRD pattern of undoped SZSO6, confirming the existence of secondary phase o-SZO identified in SZSO6 phosphor.

4.4.2.3 Elemental and morphological studies of SZSO6: 12 wt% NH_4Cl , 0.02 Bi^{3+}

SEM image of SZSO6: 12 wt% NH_4Cl , 0.02 Bi^{3+} phosphor is shown in **Fig.4.S4 (a)**. The particles exhibit irregular granular morphology with sizes varying in the micrometre range. TEM images shown in **Fig.4.S4 (b)** also confirm the micrometer size of the particles. The EDAX spectrum shown in **Fig.4.S4 (c)** recorded for the SZSO6: 12wt% NH_4Cl , 0.02 Bi^{3+} sample demonstrates the presence of the elements Sr, Zr, Si, O, and Bi. Further, the atomic percentage of the elements represented in **Fig.4.S4 (c)** matches with the stoichiometry of the composition SZSO6: 12wt% NH_4Cl , 0.02 Bi^{3+} . The elemental mapping shown in **Fig.4.S4 (d)** suggests the uniform distribution of elements within the crystal.

4.4.2.4 XPS analysis of SZSO6: 12wt% NH₄Cl and SZSO6: 12 wt% NH₄Cl, 0.02 Bi³⁺

XPS survey spectrum of SZSO6:12wt% NH₄Cl phosphor is shown in **Fig.4.4 (a)**. The elements Sr, Zr, Si, and O are identified from the survey spectra. The high-resolution core level spectra for the above elements are recorded and shown in **Fig.4.4 (a1-a4)**. The high-resolution XPS spectra for Sr 3d and Zr 3d are deconvoluted into the 3d_{5/2} and 3d_{3/2} energy levels, which originate from the splitting of the 3d level due to spin-orbit coupling⁴¹ (**Fig.4.4 (a1)** and **(a2)**). The peak position of Si 2p observed at 102.98 eV confirms the 4+ oxidation state of Si (**Fig.4.4 (a3)**). The core level spectra for the O1s sample were deconvoluted into two peaks O_I and O_{II} (**Fig.4.4(a4)**). The O_I peak positioned at 531.4 eV corresponds to the lattice oxygen, and O_{II} peak positioned at 532.9 eV can be assigned to oxygen vacancy.⁴² The higher oxygen vacancy content in the sample can be attributed to the mixed phase formation as well as the high-temperature synthesis procedure.

The SZSO6 composition has a non-equivalent Zr⁴⁺ site instead of Y³⁺ in m-SYSO, and this also can lead to the formation of oxygen vacancies in SZSO6: 12wt% NH₄Cl. The XPS survey spectrum of the SZSO6: 12 wt% NH₄Cl, 0.02Bi³⁺ phosphors is shown in **Fig.4.4 (b)**. The presence of Bi indicates their successful incorporation in the SZSO6 host. The high-resolution core level spectra of the Sr 3d, Zr 3d, Si 2p, O 1s, and Bi 4f are displayed in **Fig.4.4 (b1-b5)**. The core level spectra of Sr 3d, Zr 3d, and Si 2p are similar to SZSO6. However, the slight changes in the core level spectra of Sr 3d might be attributed to the structural distortion in the Sr²⁺ sites due to Bi³⁺ incorporation. The O 1s core-level spectra of SZSO6:12 wt% NH₄Cl, 0.02Bi³⁺ phosphor has been deconvoluted into two peaks O_I (lattice oxygen) and O_{II} (oxygen vacancy) as shown in **Fig.4.4 (b4)**. While comparing the oxygen vacancy (O_{II}) content in SZSO6: 12 wt% NH₄Cl, 0.02Bi³⁺ phosphor (**Fig.4.4 (b4)**) with the undoped SZSO6: 12 wt% NH₄Cl (**Fig.4.4 (a4)**), the peak corresponds to the oxygen vacancy is found to be higher for the Bi³⁺ co-doped sample. Hence, the increased oxygen vacancy in the Bi³⁺ doped phosphor can be attributed to the non-equivalent Bi³⁺ doping in the Sr²⁺ sites.⁴³

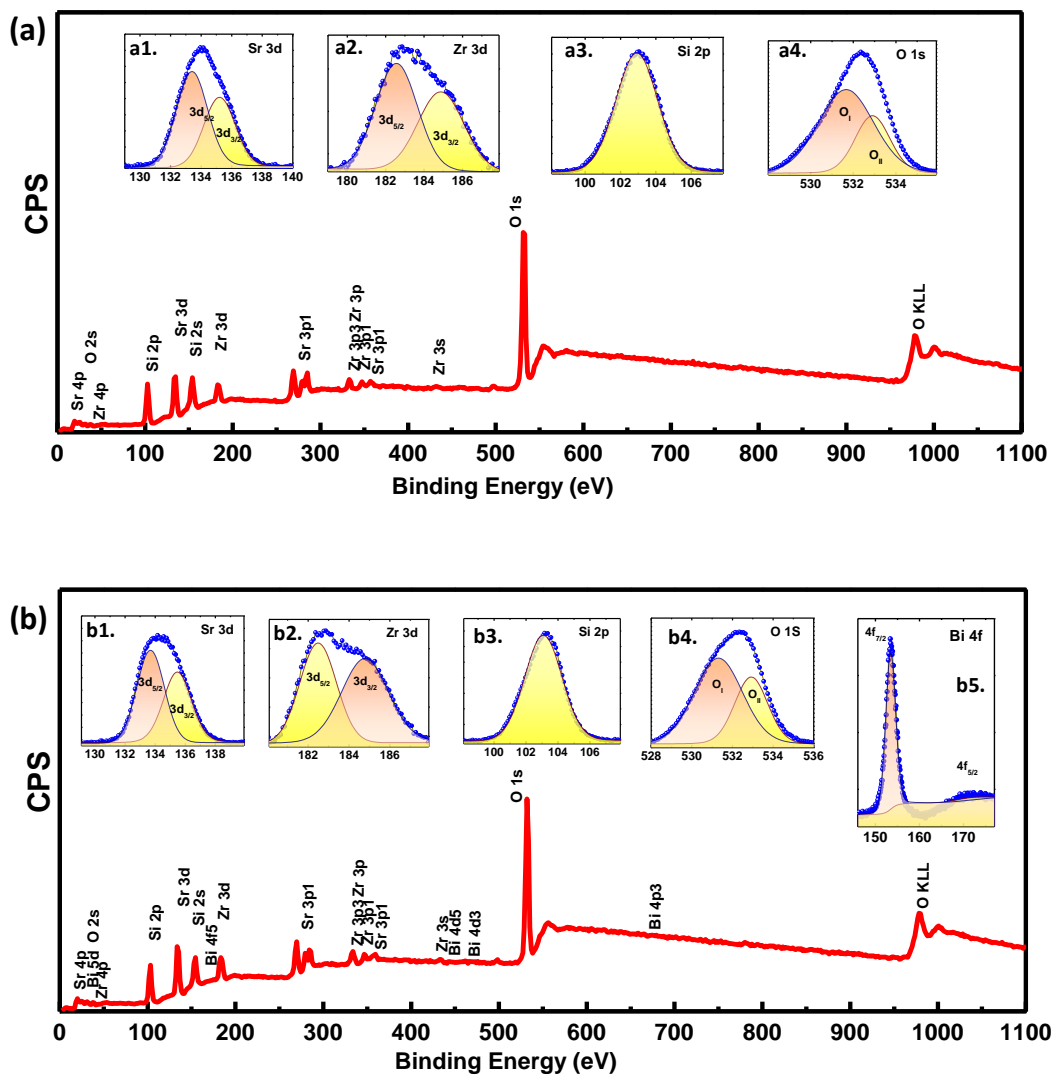


Fig.4.4 (a) XPS survey spectra of SZSO6: 12wt% NH₄Cl. Insets: core level XPS spectra of **(a1)** Sr 3d, **(a2)** Zr 3d, **(a3)** Si 2p and **(a4)** O 1s. **(b)** XPS survey spectra of the SZSO6: 12wt% NH₄Cl, 0.02Bi³⁺. Insets core level XPS spectra of **(b1)** Sr 3d, **(b2)** Zr 3d, **(b3)** Si 2p, **(b4)** O 1s and **(b5)** Bi 4f.

4.4.3 UV-Vis DRS and photoluminescence properties of SZSO6, SZSO6: 12wt% NH₄Cl and SZSO6: 12 wt% NH₄Cl, 0.02 Bi³⁺

4.4.3.1 UV-Vis DRS and bandgap

Fig.4.5 (a) presents the diffuse reflectance spectra of SZSO6, SZSO6: 12wt% NH₄Cl, and SZSO6: 12 wt% NH₄Cl, 0.02 Bi³⁺ in the range 200 nm to 450 nm. Two major absorption bands in the range 240 – 275 nm and 325 – 400 nm are observed in the spectra. The first band corresponds to O²⁻ → Zr⁴⁺ charge transfer transitions.^{36,37} The latter absorption is found to be

decreasing with NH_4Cl addition, suggesting that the absorption might be due to any additional phases present in the host. After NH_4Cl addition, the phase formation of crystalline SZSO6 becomes much better compared to the host before adding NH_4Cl . This can be validated by the increasing absorption of the host in the range of 240 – 275 nm, as shown in **Fig.4.5 (a)**. **Fig.4.5(b)** exhibits the tauc plot of SZSO6, SZSO6: 12wt% NH_4Cl , and SZSO6: 12 wt% NH_4Cl , 0.02 Bi^{3+} phosphors for finding the bandgap energy for direct- transitions. A slight increase in bandgap is observed after Bi^{3+} doping that can be attributed to the higher electronegativity of Bi^{3+} compared to Sr^{2+} .^{44,45} The introduction of Bi^{3+} might reduce the localized states within the bandgap.

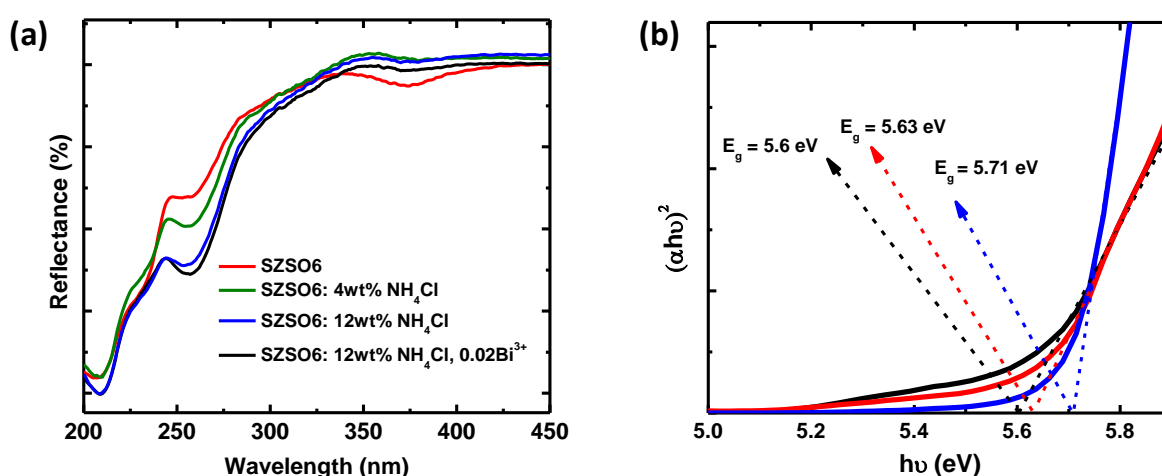


Fig.4.5 The (a) UV- vis diffuse reflectance spectra and (b) Tauc plots for SZSO6, SZSO6: 12wt% NH_4Cl and SZSO6: 12 wt% NH_4Cl , 0.02 Bi^{3+} .

4.4.3.2 Persistent Luminescence

4.4.3.2.1 PL and PersL properties of SZSO6 and effect of NH_4Cl addition

A comparison of PLE and PL spectra of SZSO4 and SZSO6 is shown in **Fig.4.6 (a)**. The two phosphors exhibit similar profiles with broad emission bands ranging from 390 nm to 620 nm, peaking at 484 nm. However, the SZSO6 phosphor shows slightly higher emission intensity than the SZSO4 phosphor. The PLE spectra recorded for the SZSO6 phosphor at an emission wavelength of 484 nm exhibit a broad excitation band peaking at 284 nm. The excitation band position matches with the absorption maximum of UV-Vis DRS spectra for the SZSO6 phosphor, as observed in **Fig.4.5 (a)**. The SZSO6 phosphor has a strong excitation band in the UV region ranging from 250 nm to 360 nm. This can be attributed to the host absorption band originating from the charge transfer from the oxygen ligands to the central

Zr^{4+} ions.^{36,37} This outcome implies that the SZSO6 host can effectively absorb the energy from UV irradiation and then transfer it to the emission centers for PL. The possible emission centers in the host are point defects formed by the substitution of Zr^{4+} in the Y^{3+} site of m-SYSO cyclosilicate structure, a stoichiometric defect due to Sr^{2+} vacancy (V_{sr}'') and oxygen vacancies (V_O) generated during the high-temperature synthesis procedure. Hence, the higher intensity of emission in SZSO6 can be explained by both $Zr^{4+} \rightarrow O^{2-}$ charge transfer transition and intrinsic defects such as oxygen vacancies present in the host lattice.⁴³

Further, the NH_4Cl concentration has been varied in the SZSO6 sample from 0 wt% to 20 wt% and the corresponding PLE and PL spectra are shown in **Fig.4.6 (b)**. The PL excitation and emission intensity increase with NH_4Cl addition and this can be attributed to the increased crystallinity and reduced non-radiative transitions within the crystal. Beyond 12 wt% of NH_4Cl , the intensity of emission in SZSO6 gradually decreases until the concentration of NH_4Cl reaches 20 wt%. However, the emission intensity of 20 wt% NH_4Cl added SZSO6 is still greater than SZSO6 sample without NH_4Cl . The CIE diagram of SZSO6: 12 wt% NH_4Cl phosphor is displayed in **Fig.4.6 (c)**. The chromaticity coordinates of (0.225, 0.321) suggest the emission color of SZSO6: 12 wt% NH_4Cl phosphor is cyan, as shown in the inset of **Fig.4.6 (c)**. The PL decay curves of SZSO6 and SZSO6: 12 wt% NH_4Cl are shown in **Fig.4.6 (d)** and their respective lifetimes are 64 ms and 70 ms. The emission decays faster in SZSO6 compared to SZSO6: 12 wt% NH_4Cl implies the enhanced crystallinity and reduced non-radiative PL quenching mechanisms after NH_4Cl addition.

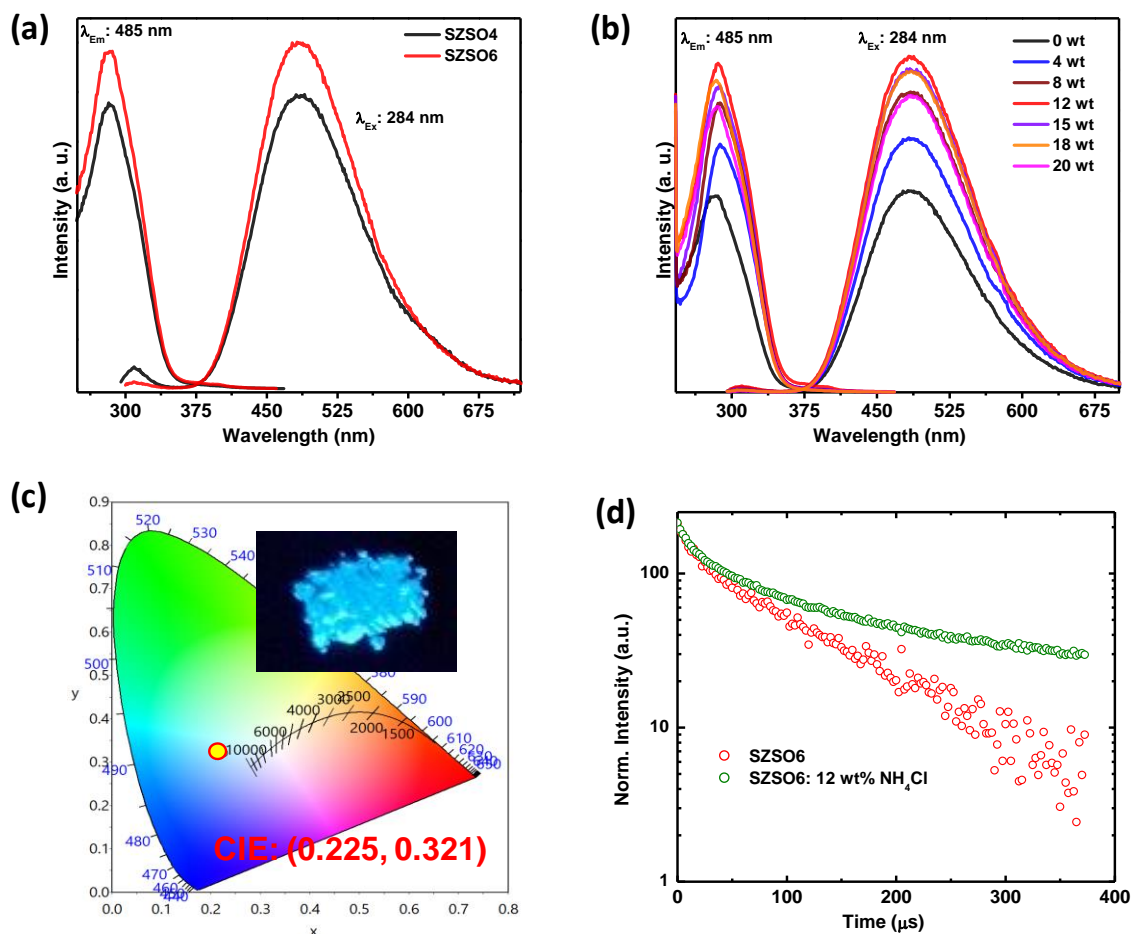


Fig.4.6 (a) A comparison of PLE and PL spectra of SZSO4 and SZSO6. (b) PLE and PL spectra of SZSO6: x wt% NH_4Cl (x = 0, 4, 8, 12, 15, 18, 20), (c) CIE diagram of SZSO6: 12 wt% NH_4Cl phosphor and (d) PL decay curves of SZSO6 and SZSO6: 12 wt% NH_4Cl .

The phosphors CZSO4, SZSO4, SZSO4: 12wt% NH_4Cl , SZSO6 and SZSO6: 12wt% NH_4Cl also demonstrate persistent luminescence, as shown in **Fig.4.7** (a) and (b). After irradiating with 254 nm for one minute, the prepared CZSO4 phosphor exhibits a PersL duration of 15s. As per the reported PersL properties of CZSO, the material has an PersL duration of 4800s (0.32 mcd m^{-2}) when irradiated at 254 nm for 10 minutes.³⁶ On the other hand, the PersL of SZSO4 lasts for 45s after the irradiation stops. In the case of SZSO6 the PersL lasts for 60s after stopping the illumination under 254 nm. The enhanced PersL in SZSO6 might be due to the different types of defects (traps) present in the phosphor (cation and oxygen vacancies).⁴ Interestingly, the PersL duration is enhanced with the addition of NH_4Cl in both SZSO4 and SZSO6, as shown in **Fig.4.7** (a) and (b), respectively. SZSO4: 12 wt% NH_4Cl shows a brighter PersL even at 45s compared to CZSO and SZSO. Even after

60s, the PersL of SZSO6: 12 wt% NH₄Cl glows brighter than SZSO6 at 60s. This might be due to the increase of shallow traps generated after adding the flux, which is evident from the XPS spectrum, as shown in Fig.4.4 (a). From the XPS spectra, it is clear that one of the major traps present in the SZSO6:12 wt% NH₄Cl is oxygen vacancies. PersL decay curves of SZSO6 and SZSO6: 12 wt% NH₄Cl are shown in Fig.4.7 (c). The PersL of SZSO6 decays faster compared to SZSO6: 12 wt% NH₄Cl, which supports the PersL images in Fig.4.7 (b).

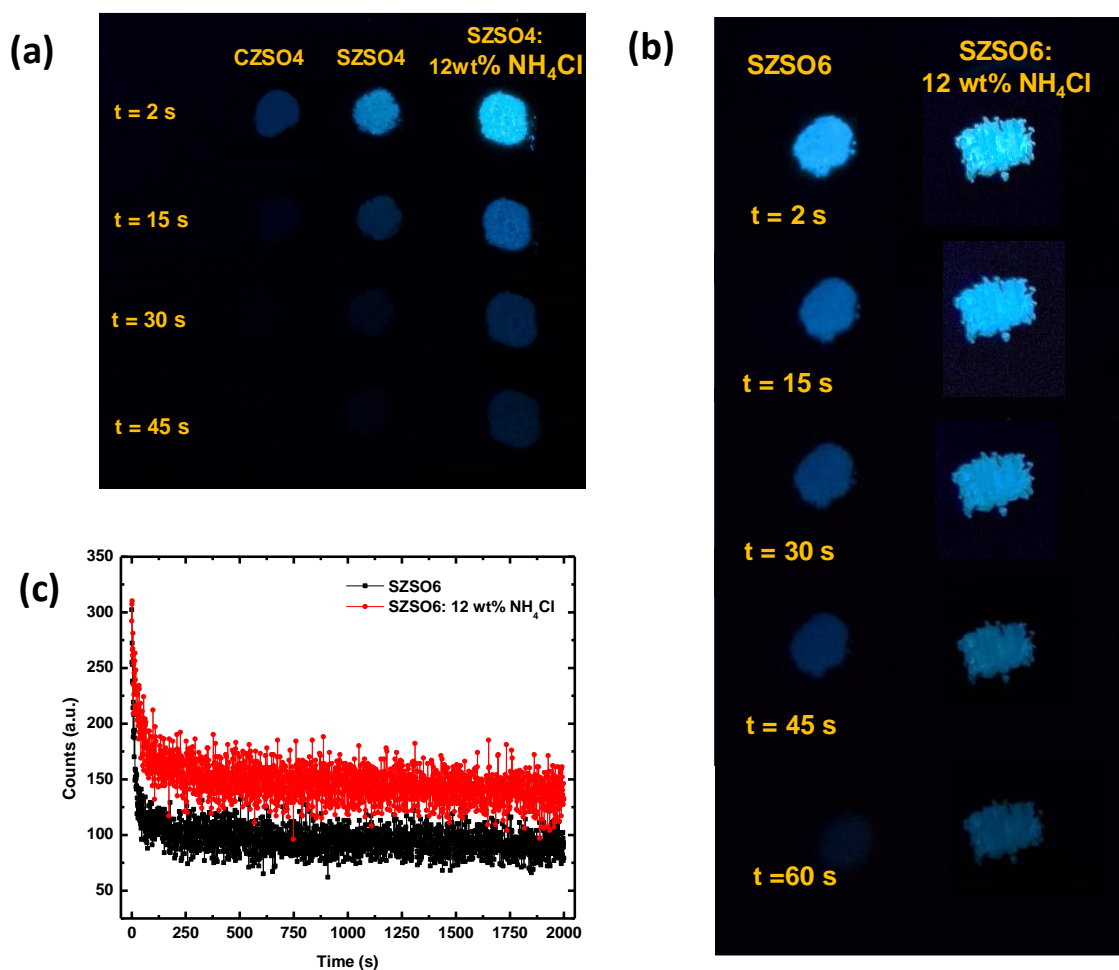


Fig.4.7 (a) PL images of CZSO₄, SZSO₄ and SZSO₄: 12 wt% NH₄Cl sample under 254 nm excitation. PersL images of **(b)** CZSO₄, SZSO₄, SZSO₄: 12 wt% NH₄Cl, and **(c)** SZSO₆ and SZSO₆: 12 wt% NH₄Cl samples after illuminating under 254 nm irradiation for one minute.

4.4.3.2.2 Enhancing the PersL via Bi³⁺ co-doping and post-annealed vacuum treatment.

There are several methods to improve the persistence luminescence of materials, such as creating oxygen vacancies, non-equivalent substitution, doping sensitizers, activator ions,

etc. Here, the Bi³⁺ ions are doped in the Sr²⁺ site of SZSO6: 12 wt% NH₄Cl phosphor to introduce defects. Since the Bi³⁺ ions prefer to occupy the Sr²⁺ sites due to the comparable ionic radii {Sr²⁺: r_A = 1.26Å, Bi³⁺: r_A = 1.17Å (eight-fold coordination)}, the cation defects may be formed due to this non-equivalent substitution.³⁶ This can be explained using the following equation.



In order to balance the charge, three Sr²⁺ cations are replaced by two Bi³⁺ ions, resulting in the formation of two positive defects (Bi_{Sr}[•]) and one Sr²⁺ vacancy. The first one is an electron trap, and the latter is a hole trap. Also, XPS of SZSO6: 12 wt% NH₄Cl, 0.02 Bi³⁺ shown in **Fig.4.4 (b)** predicts excess oxygen vacancy compared to SZSO6: 12 wt% NH₄Cl. The PLE and PL spectra of the yBi³⁺ doped SZSO6: 12 wt% NH₄Cl (y = 0.01, 0.02, 0.03 and 0.04) are shown in **Fig.4.8 (a)**. PL spectra present an additional band centred at 620 nm that can be attributed to the oxygen-vacancy-induced electronic localization around the Bi³⁺ ions. A similar kind of orangish-red emission due to Bi³⁺ ion substitution is reported by Yi Wei *et al.*⁴⁶ Here, the PL intensity centred at 486 nm is found to be reduced after Bi³⁺ co-doping. The decrease in emission intensity can be ascribed to the energy transfer from the host to Bi³⁺ ions. As can be seen from **Fig.4.8 (a)**, as the concentration of Bi³⁺ increases, the peak centred at 620 nm increases.

The PersL images of Bi³⁺ doped SZSO6: 12 wt% NH₄Cl s are shown in **Fig.4.8 (b)** after 1 min irradiation of the 254 nm UV lamp. From **Fig.4.8 (b)**, it can be observed that the PersL time is enhanced with the Bi³⁺ co-doping and lasts for more than 90s. The above increment in persistence luminescence time can be ascribed to the creation of extrinsic defects and cation vacancies after Bi³⁺ co-doping.^{19,20} The SZSO6: 12 wt% NH₄Cl, 0.02Bi³⁺ sample exhibits greater PersL duration in comparison with SZSO6: 12 wt% NH₄Cl. To further improve the PersL time, the SZSO6: 12 wt% NH₄Cl, 0.02Bi³⁺ phosphor has been post-annealed at 1000 °C for 2h in a vacuum atmosphere. The PLE and PL spectra of the vacuum-treated phosphor have been compared with the SZSO6:12 wt% NH₄Cl, 0.02Bi³⁺ phosphor prepared in air (**Fig.4.8 (c)**). The PL intensity has been reduced after vacuum treatment. The reduction in the intensity can be attributed to the formation of oxygen vacancies, which can act as electron-trapping centres. The PersL images of vacuum-treated SZSO6: 12 wt% NH₄Cl, 0.02Bi³⁺ are shown in **Fig.4.8 (b)**. The PersL intensity and duration are improved for the

vacuum-treated phosphor. Vacant oxygen and vacant metal sites are likely to form when exposed to high temperatures and an atmosphere that lacks oxygen. This is because atoms can move more easily to the surface and then be released into the external environment. The following defect equilibrium equation can be used to express the formation of oxygen vacancies, as per the Kröger–Vink notation.⁴⁷



The reaction shifts towards the right when exposed to a reducing atmosphere, which also enhances oxygen vacancy defects. Conversely, an oxidizing atmosphere produces the opposite outcome.

In order to confirm the creation of oxygen vacancies in the phosphor, the XPS analysis is carried out for the SZSO6: 12wt% NH₄Cl, 0.02 Bi³⁺ phosphor post-annealed in vacuum. **Fig.4.8 (d)** represents the deconvoluted core-level spectra of O 1s for the vacuum-treated SZSO6: 12wt%NH₄Cl, 0.02 Bi³⁺ phosphor. While comparing core-level XPS spectra of O 1s of the as-prepared SZSO6: 12wt%NH₄Cl, 0.02 Bi³⁺ (**Fig.4.4 (b)**) with the vacuum-treated phosphor, the peak corresponds to the oxygen vacancy (O_{II}) is found to be enhanced in the latter. Hence, the post-annealed vacuum treatment enhances oxygen vacancy content, thereby enhancing the PersL. The PersL decay curves of SZSO6: 12wt%NH₄Cl, 0.02 Bi³⁺, and vacuum-treated phosphor are shown in **Fig.4.8 (e)**. The as-prepared phosphor decays faster than the vacuum-treated phosphor, indicating the enhanced PersL of the phosphor after vacuum treatment.

A possible persistent luminescence mechanism of SZSO6: 12wt%NH₄Cl, 0.02 Bi³⁺ is as follows (**Fig.4.S5**). Under ultraviolet excitation at 284 nm, electrons in the valence band are excited to the conduction band. Some of these electrons recombine near the emission centres, creating excited levels for PL. The sequential trapping of these excited electrons into shallow traps (point defects and oxygen vacancies) occurs. The PersL occurring at room temperature indicates that the traps in this system are shallow. The trapped electrons are later released to the valence band, resulting in persistent luminescence.

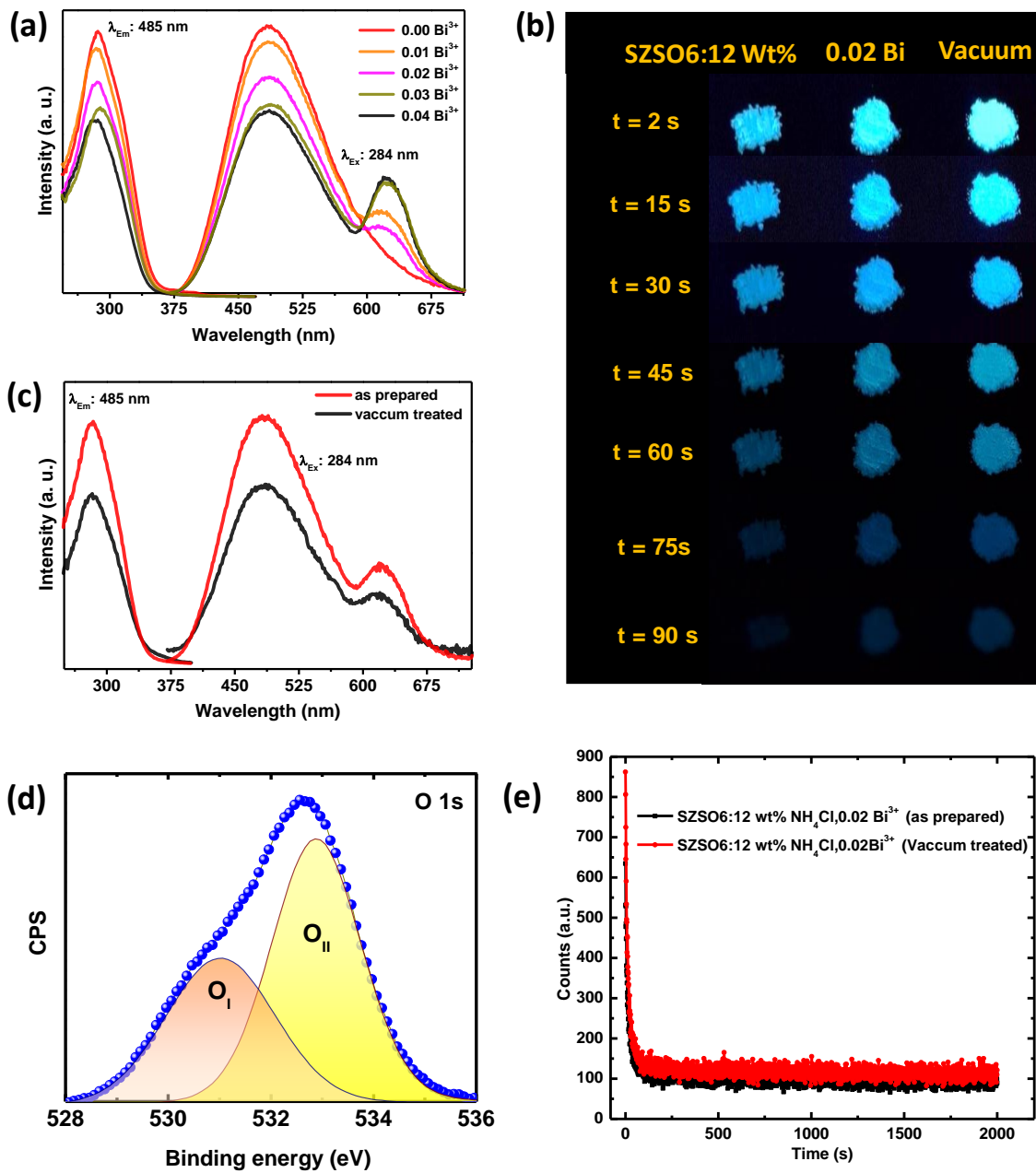


Fig.4.8 (a) PLE and PL spectra of the $x\text{Bi}^{3+}$ doped SZSO6: 12 wt% NH_4Cl ($x = 0.01, 0.02, 0.03$ and 0.04), (b) PersL images of the SZSO6:12 wt% NH_4Cl , SZSO6: 12 wt% NH_4Cl , 0.02Bi^{3+} and post annealed vacuum treated SZSO6: 12 wt% NH_4Cl , 0.02Bi^{3+} sample (c) PLE and PL spectra of the SZSO6: 12 wt% NH_4Cl , 0.02Bi^{3+} and post annealed vacuum treated SZSO6: 12 wt% NH_4Cl , 0.02Bi^{3+} sample (d) deconvoluted core-level spectra of O 1s for the post annealed vacuum treated SZSO6: 12 wt% NH_4Cl , 0.02Bi^{3+} phosphor and (e) PersL decay curves of SZSO6: 12 wt% NH_4Cl , 0.02Bi^{3+} and post annealed vacuum treated SZSO6: 12 wt% NH_4Cl , 0.02Bi^{3+} phosphor.

4.4.4 Anti-counterfeiting and plant-growth LED applications

A method involving handwritten security inks was used to assess the practical usability of the persistent blue phosphor in dynamic anti-counterfeiting marking. Here, the security inks were prepared by dispersing the phosphors in the PVA to make viscous solutions. The security ink is prepared using the mixture of cyan-emitting post annealed vacuum treated SZSO6: 12wt% NH_4Cl , 0.02Bi^{3+} and the deep red-emitting MAG: Mn^{4+} , 0.27Ba^{2+} phosphors. The PLE spectra of the MAG: Mn^{4+} , 0.27Ba^{2+} red phosphor and PL spectra of the persistent cyan phosphor are shown in **Fig.4.S6** of the supporting information. The overlapping region is found to be less in this case, and the photon reabsorption will be minimal for the security ink developed from the mixture of the above two samples.

The developed security inks were utilized to produce various writings on different surfaces, including currency notes and QR codes. Under daylight conditions, these phosphors do not emit any noticeable light. Under UV irradiation, at 254 nm, the mixture of cyan and red-emitting phosphors exhibits pink luminescence, and under 365 nm irradiation, the mixture exhibits red luminescence. After the irradiation is off, the phosphor mixture shows cyan luminescence. The digital photographs of dip pen writing on currency notes and QR code encoded the search word "CSIR-NIIST" under 254 nm and 365 nm UV light are shown in **Fig.4.9 (a)** and **Fig.4.9 (b)**. When the irradiation stops, the surfaces of the currency note and QR code demonstrate a cyan colour. Hence, the developed PersL phosphors can be used for dynamic anticounterfeiting applications. The above technique can prevent fraud by safeguarding documents from forgery and duplication. The duplication of logos, currency notes and documents can be prevented to a certain limit using this technique.⁴⁸

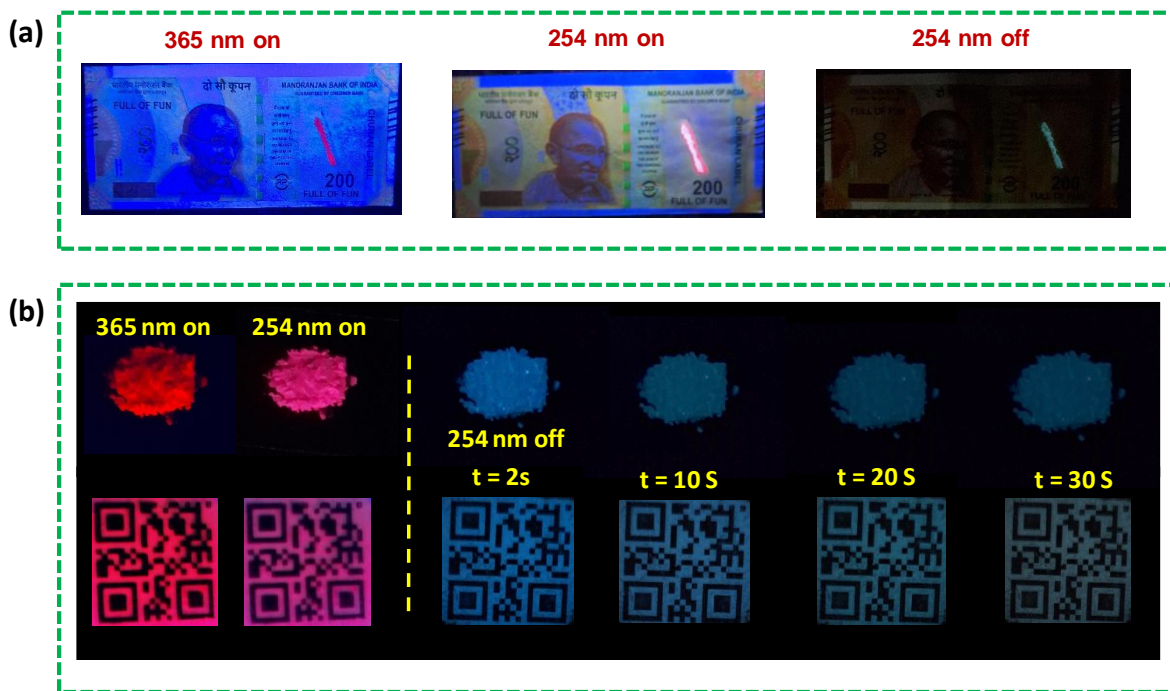


Fig.4.9 Digital photographs of dip pen writing on (a) currency note and (b) QR code under 365 nm, 254 nm and after irradiation stops.

Another application of the phosphor mixture developed is to use in plant growth LEDs. In vitro culture plays a crucial role in mass-producing plants with specific traits and has proven effective in conserving and rapidly propagating economically important rare and endangered plants. Various external and internal factors influence the growth and development of in vitro plants, with light being particularly significant. The lighting system used for in vitro culture must deliver light within the spectral range essential for photosynthesis and photomorphogenic responses. Employing light sources that emit photons across a wide spectral range typically fulfils these dual lighting requirements.^{49,50}

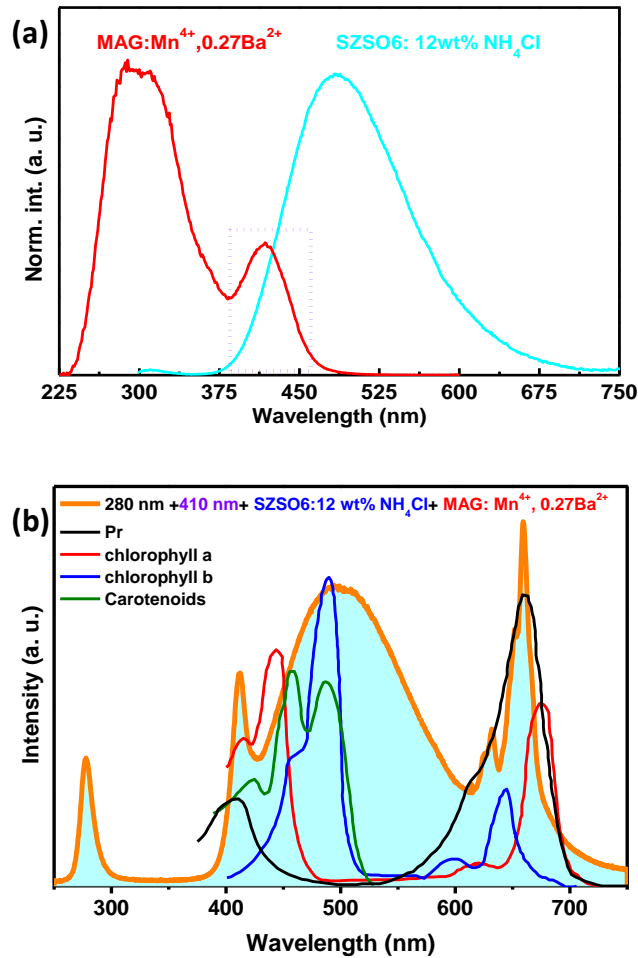


Fig.4.10 (a) PLE spectrum of MAG: Mn⁴⁺, 0.27Ba²⁺ and PL spectrum of SZSO6: 12wt% NH₄Cl and **(b)** EL spectrum of the MAG: Mn⁴⁺, 0.27Ba²⁺/ SZSO6: 12wt% NH₄Cl mixture and the absorption spectra of phytochrome (P_r) and Chlorophyll a, b, and carotenoids.

Fig.4.10 (a) shows the PLE spectrum of MAG: Mn⁴⁺, 0.27Ba²⁺ and the PL spectrum of SZSO6: 12wt% NH₄Cl. The overlap between the PLE and PL spectra is minimal, indicating that photon reabsorption in the MAG: Mn⁴⁺, 0.27Ba²⁺/ SZSO6: 12wt% NH₄Cl mixture will be less. Furthermore, both the phosphors can be simultaneously excited using a 280 nm UV LED. An LED is developed using the MAG: Mn⁴⁺, 0.27Ba²⁺/ SZSO6: 12wt% NH₄Cl mixture. The EL spectrum of the MAG: Mn⁴⁺, 0.27Ba²⁺/ SZSO6: 12wt% NH₄Cl mixture shows a broad emission in the range of 400 nm to 750 nm that matches the absorption spectrum of plant phytochrome (P_R) and chlorophyll (**Fig.4.10 (b)**).^{49,50} Hence, this mixture can be used for plant-growth LED applications.

4.5 Conclusions

A novel cyan emitting persistent luminescence material $\text{Sr}_2\text{Zr}_2(\text{SiO}_3)_6$ is synthesized by balancing the charge after identifying a major m- $\text{Sr}_3\text{Y}_2\text{Si}_6\text{O}_{18}$ phase in the initially developed $\text{Sr}_2\text{Zr}(\text{SiO}_3)_4$ by substituting Sr^{2+} for Ca^{2+} in the reported $\text{Ca}_2\text{Zr}(\text{SiO}_3)_4$. The additional phases identified from the Rietveld refinement of the XRD pattern are confirmed by HRTEM analysis. The self-activated phosphor exhibits PersL that lasts for 60s after irradiating with a 254 nm UV lamp for one minute. The addition of NH_4Cl flux enhances the intensity and duration of persistent luminescence by adding shallow traps (oxygen vacancies) as evident from the XPS analysis. The high-resolution core-level spectrum of O 1s shows an increase in oxygen vacancy with NH_4Cl addition. Further, the shallow traps in the $\text{Sr}_2\text{Zr}_2(\text{SiO}_3)_6$: 12 wt% NH_4Cl system are boosted by adding Bi^{3+} in the Sr^{2+} site followed by annealing the phosphor under vacuum. This process increases both cation defects and oxygen vacancies in the material, resulting in an enhanced PersL lasting 90s. The post-annealed vacuum-treated $\text{Sr}_2\text{Zr}_2(\text{SiO}_3)_6$: 12 wt% NH_4Cl , 0.02 Bi^{3+} phosphor with higher persistent time is used for dynamic anti-counterfeiting applications by mixing with the reported red-emitting $\text{Mg}_3\text{Al}_2\text{GeO}_8$: 0.005 Mn^{4+} , 0.27 Ba^{2+} phosphor. Meanwhile, the highly intense $\text{Sr}_2\text{Zr}_2(\text{SiO}_3)_6$: 12 wt% NH_4Cl sample has been used for plant growth LED applications.

4.6 Supporting Information

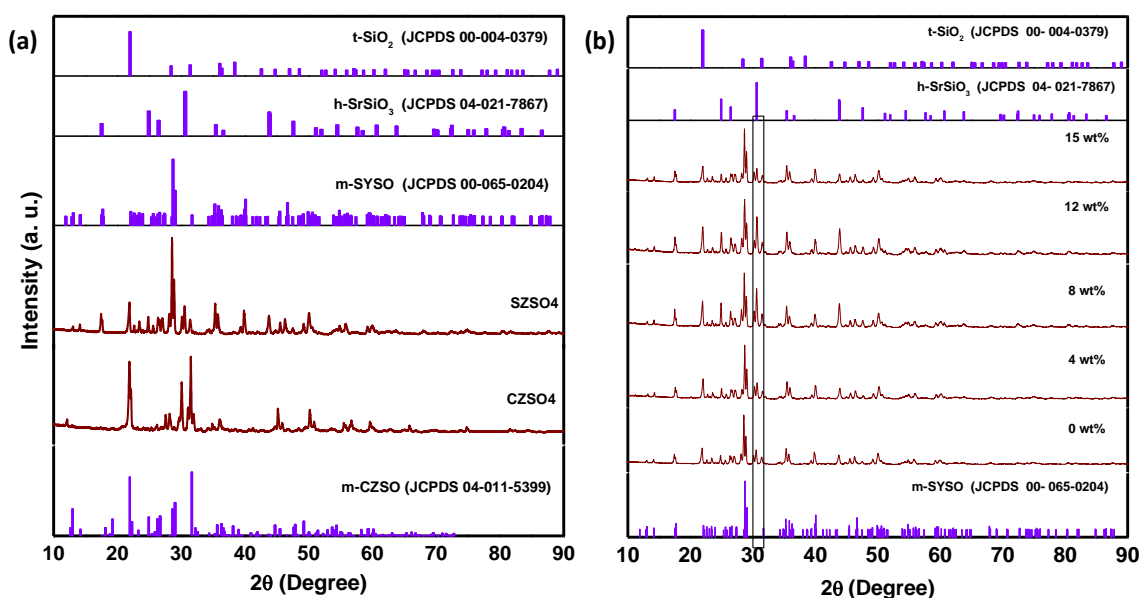


Fig.4.S1 (a) XRD pattern of CZSO4 and SZSO4 **(b)** XRD pattern of SZSO4: x wt% NH_4Cl (x = 0, 4, 8, 12, 15).

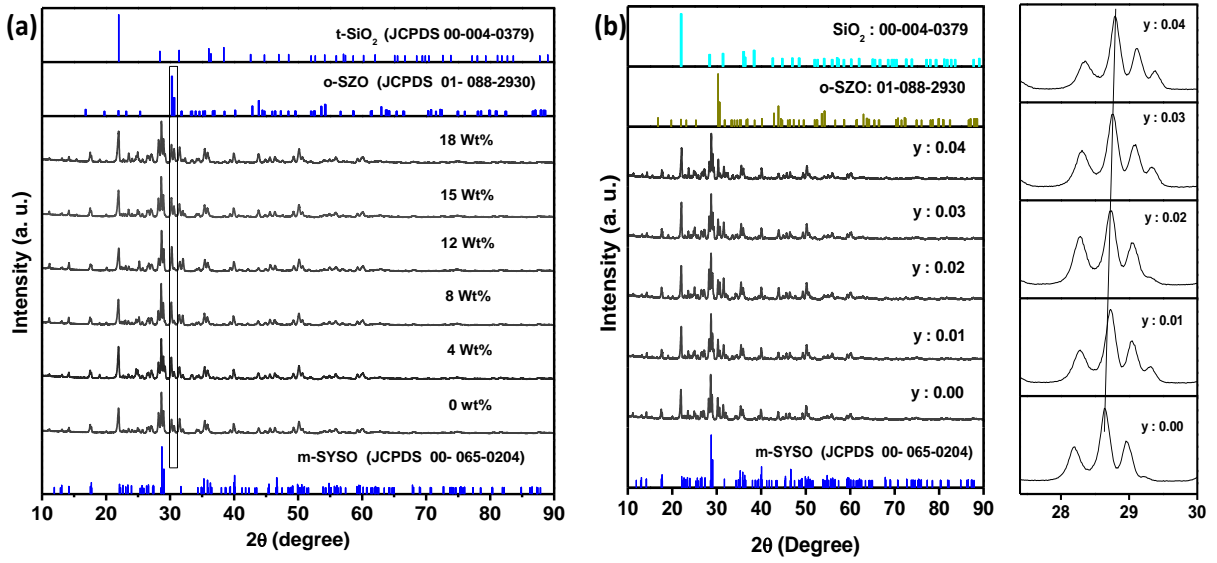


Fig.4.S2. XRD patterns of (a) SZSO6: x wt% NH₄Cl (x = 0, 4, 8, 12, 15, 18 wt%) samples and (b) SZSO6: 12 wt% NH₄Cl, yBi³⁺ (y = 0, 0.01, 0.02, 0.03, 0.04).

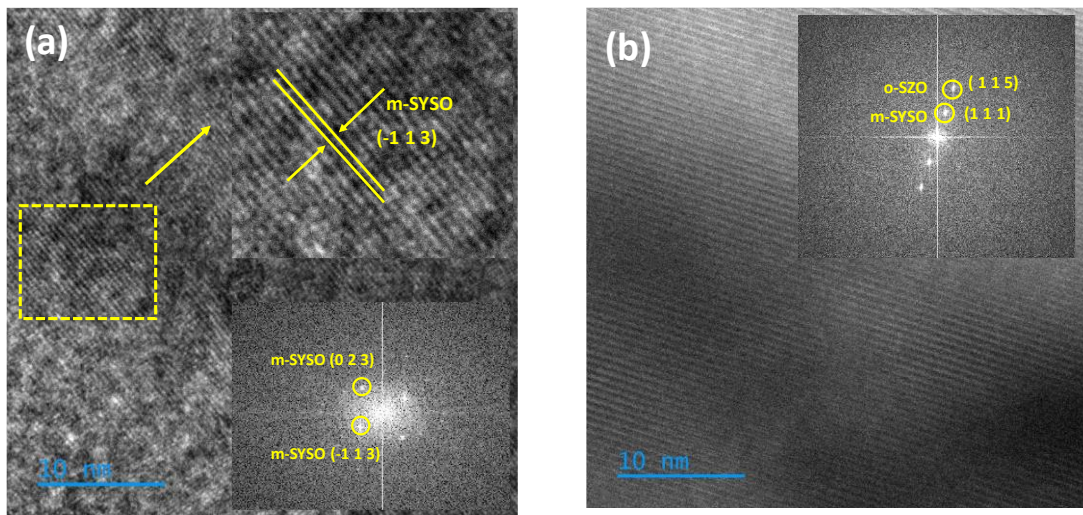


Fig.4.S3. (a-b) HRTEM images of undoped SZSO6 with magnified versions (inset) and reduced FFT (inset) showing the planes corresponds to different phases.

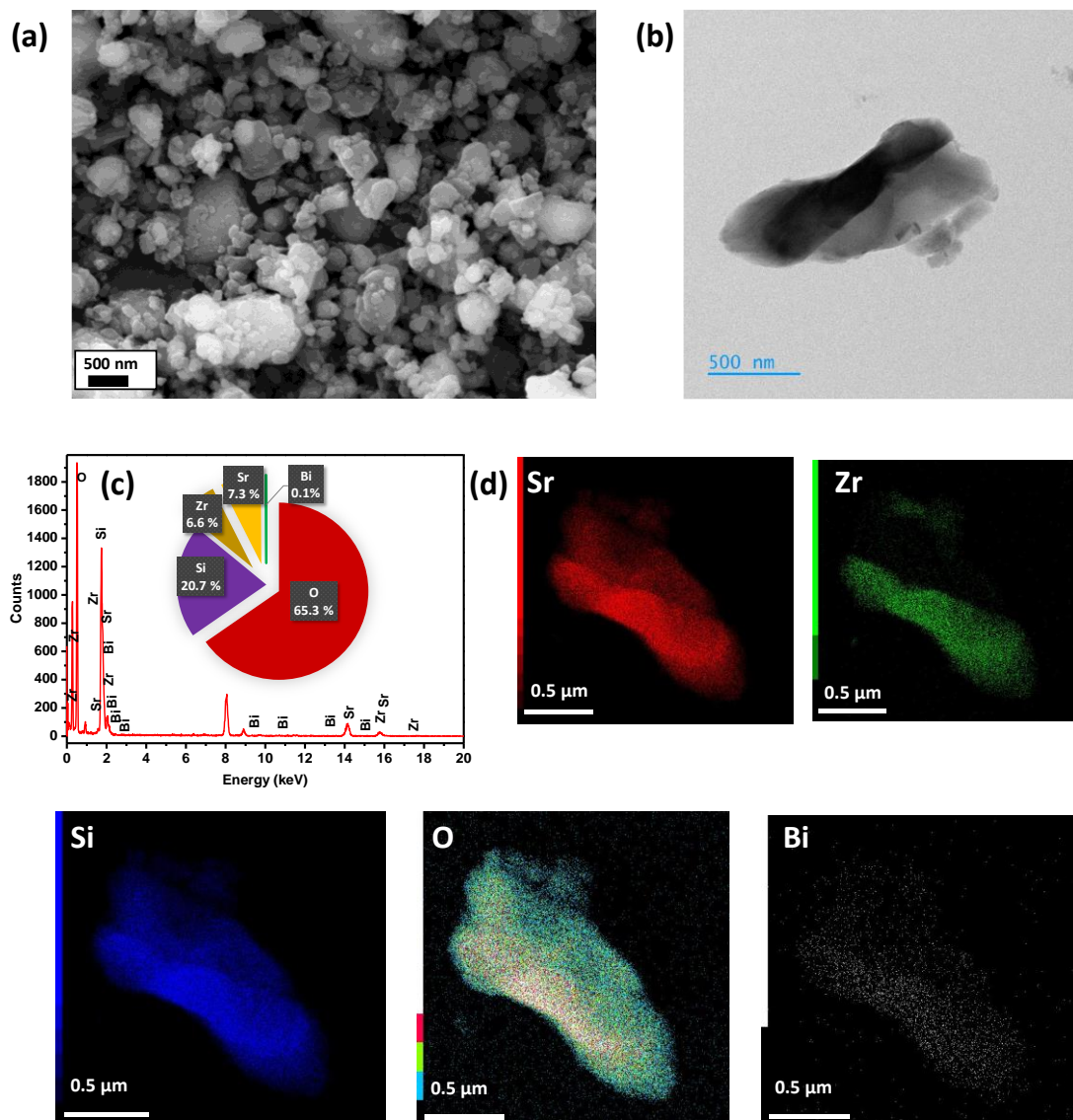


Fig.4.S4 (a) SEM image and (b) TEM image of SZSO6: 12wt% NH₄Cl, 0.02Bi³⁺ sample. (c) The EDAX spectrum and atomic percentage of elements in SZSO6: 12 wt% NH₄Cl, 0.02Bi³⁺. (d) EDAX elemental mapping of Sr, Zr, Si, O and Bi for SZSO6: 12 wt% NH₄Cl, 0.02Bi³⁺ phosphor.

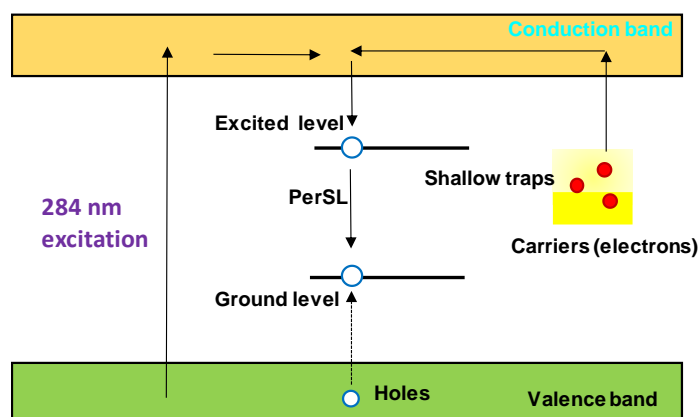


Fig.4.S5 Persistent luminescence mechanism of SZSO6: 12wt%NH₄Cl, 0.02 Bi³⁺.

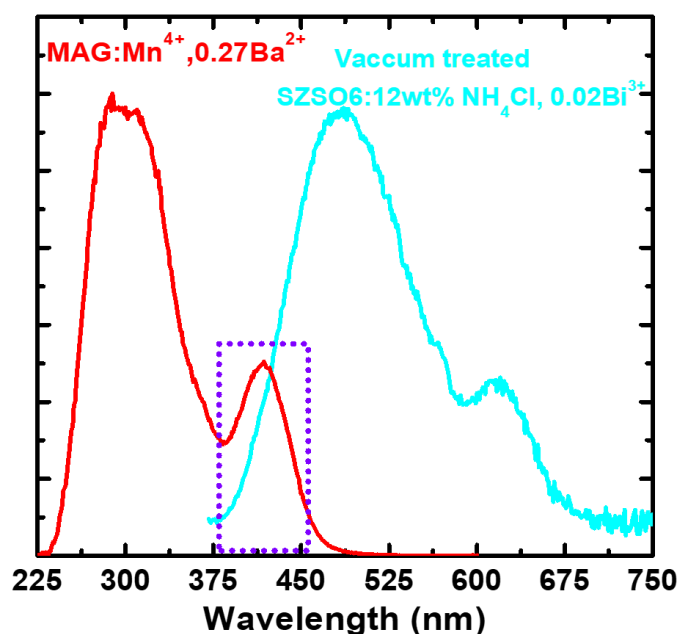


Fig.4.S6 PLE spectrum of MAG: Mn⁴⁺, 0.27Ba²⁺ (λ_{em} : 659 nm) and PL emission (λ_{ex} : 284 nm) spectrum of SZSO6: 12wt% NH₄Cl.

4.7 References

- [1] Tan, H.; Wang, T.; Shao, Y.; Yu, C.; Hu, L. Crucial Breakthrough of Functional Persistent Luminescence Materials for Biomedical and Information Technological Applications. *Front. Chem.* **2019**, *7*, 387. <https://doi.org/10.3389/fchem.2019.00387>.
- [2] Wang, T.; Liu, M.; Mao, J.; Liang, Y.; Wang, L.; Liu, D.; Wang, T.; Hu, W. Recent Advances in Long-Persistent Luminescence Materials Based on Host–Guest Architecture. *Chin. Chem. Lett.* **2024**, *35*, 108385. <https://doi.org/10.1016/j.ccllet.2023.108385>.

- [3] Chiatti, C.; Fabiani, C.; Pisello, A. L. Long Persistent Luminescence: A Road Map Toward Promising Future Developments in Energy and Environmental Science. *Annu. Rev. Mater. Res.* **2021**, *51*, 409-433. <https://doi.org/10.1146/annurev-matsci-091520>.
- [4] Yang, L.; Gai, S.; Ding, H.; Yang, D.; Feng, L.; Yang, P. Recent Progress in Inorganic Afterglow Materials: Mechanisms, Persistent Luminescent Properties, Modulating Methods, and Bioimaging Applications. *Adv. Opt. Mater.* **2023**, *11*, 2202382. <https://doi.org/10.1002/adom.202202382>.
- [5] Shi, J.; Sun, X.; Song, L.; Hong, M.; Yuan, Q.; Zhang, Y. Inorganic Persistent Luminescence Materials: Emerging Optical Theranostic Agents. *Prog. Mater. Sci.* **2024**, *142*, 101246. <https://doi.org/10.1016/j.pmatsci.2024.101246>.
- [6] Zhang, J.; Wang, Z.; Huo, X.; Meng, X.; Wang, Y.; Suo, H.; Li, P. Anti-Counterfeiting Application of Persistent Luminescence Materials and its Research Progress. *Laser Photon. Rev.* **2024**, *18*, 2300751. <https://doi.org/10.1002/lpor.202300751>.
- [7] Li, Z.; Xiang, J.; Chen, C.; Wu, Z.; Jin, M.; Zhao, X.; Zhao, L.; Guo, C. Stimulated-Source-Independent Persistent Luminescence Phosphor $\text{Sr}_2\text{Ta}_2\text{O}_7:\text{Tb}^{3+}, \text{Tm}^{3+}$ for Multi-Mode Anti-Counterfeiting Applications. *J. Mater. Chem. C* **2024**, <https://doi.org/10.1039/D4TC00732H> (accessed 2024-04-05)
- [8] Song, Y.; Zhang, Y.; Wang, Y.; Wu, M.; Yang, S.; Song, J.; Zhao, H.; Yu, J. Dynamic Optical Information Encoding Strategy of Flexible Thin Films Based on Ba_2SiO_4 Phosphor for Ultra-Long Storage Time. *Ceram. Int.* **2024**, <https://doi.org/10.1016/j.ceramint.2024.03.258> (accessed 2024-04-05).
- [9] Ding, Y.; Ye, Y.; Wang, C.; Pei, L.; Mao, Q.; Liu, M.; Zheng, R.; Bokhari, A.; Han, N.; Zhong, J. “Light Battery” Role of Long Afterglow Phosphor for Round-the-Clock Environmental Photocatalysis. *J. Clean Prod.* **2024**, *450*, 142041. <https://doi.org/10.1016/j.jclepro.2024.142041>.
- [10] Zhang, J.; Wang, Z.; Liu, P.; Huo, X.; Wang, Y.; Suo, H.; Li, L.; Li, P. Dual-Mode Luminous and Afterglow $\text{Ca}_3\text{Al}_2\text{Ge}_3\text{O}_{12}:\text{Yb}^{3+}, \text{Er}^{3+}$ Phosphors for Anti-Counterfeiting and Fingerprint Verification. *Ceram. Int.* **2024**, *50*, 2436–2442. <https://doi.org/10.1016/j.ceramint.2023.11.029>.

- [11] Yuan, W.; Pang, R.; Wang, S.; Tan, T.; Li, C.; Wang, C.; Zhang, H. Enhanced Blue-Light Excited Cyan-Emitting Persistent Luminescence of BaLu₂Al₂Ga₂SiO₁₂:Ce³⁺, Bi³⁺ Phosphors for AC-LEDs via Defect Modulation. *Light Sci. Appl.* **2022**, *11*, 184. <https://doi.org/10.1038/s41377-022-00868-8>.
- [12] Yamamoto, H.; Matsuzawa, T. Mechanism of Long Phosphorescence of SrAl₂O₄:Eu²⁺, Dy³⁺ and CaAl₂O₄:Eu²⁺, Nd³⁺. *J. Lumin.* **1997**, *72–74*, 287–289. [https://doi.org/10.1016/S0022-2313\(97\)00012-4](https://doi.org/10.1016/S0022-2313(97)00012-4).
- [13] Hölsä, J.; Laamanen, T.; Lastusaari, M.; Malkamäki, M.; Niittykoski, J.; Zych, E. Effect of Mg²⁺ and Ti^{IV} Doping on the Luminescence of Y₂O₂S:Eu³⁺. *Opt. Mater.* **2009**, *31*, 1791–1793. <https://doi.org/10.1016/j.optmat.2009.01.018>.
- [14] Zou, L.; Shi, Z.; Zhang, X.; Liao, C.; Chen, Z.; Liu, Y.; Sun, Y. Enhanced Long Afterglow Luminescence of Sr₂MgSi₂O₇: Eu²⁺, Dy³⁺ by NH₄Cl. *Inorg. Chem. Commun.* **2022**, *146*, 110151. <https://doi.org/10.1016/j.inoche.2022.110151>.
- [15] Fernández-Rodríguez, L.; Durán, A.; Pascual, M. J. Silicate-Based Persistent Phosphors. *Open Ceram.* **2021**, *7*, 100150. <https://doi.org/10.1016/j.oceram.2021.100150>.
- [16] Xu, J.; Tanabe, S. Persistent Luminescence Instead of Phosphorescence: History, Mechanism, and Perspective. *J. Lumin.* **2019**, *205*, 581–620. <https://doi.org/10.1016/j.jlumin.2018.09.047>.
- [17] Wang, X. J.; Jia, D.; Yen, W. M. Mn²⁺ Activated Green, Yellow, and Red Long Persistent Phosphors. *J. Lumin.* **2003**, *102–103*, 34–37. [https://doi.org/10.1016/S0022-2313\(02\)00541-0](https://doi.org/10.1016/S0022-2313(02)00541-0).
- [18] Pan, Z.; Lu, Y. Y.; Liu, F. Sunlight-Activated Long-Persistent Luminescence in the near-Infrared from Cr³⁺-Doped Zinc Gallogermanates. *Nat. Mater.* **2011**, *11*, 58–63. <https://doi.org/10.1038/nmat3173>.
- [19] Wang, S.; Wang, T.; Yu, X.; Li, Z.; Guo, L.; Chen, J.; Zhao, F.; Feng, W.; Xu, X.; Qiu, J. Tailored Luminescence Output of Bi³⁺-Doped BaGa₂O₄ Phosphors with the Assistance of the Introduction of Sr²⁺ Ions as Secondary Cations. *Inorg. Chem.* **2021**, *60*, 14467–14474. <https://doi.org/10.1021/acs.inorgchem.1c02271>.

- [20] Feng, Z.; Lou, B.; Yin, M.; Yeung, Y. Y.; Sun, H. T.; Duan, C. K. First-Principles Study of Bi³⁺-Related Luminescence and Electron and Hole Traps in (Y/Lu/La)PO₄. *Inorg. Chem.* **2021**, *60*, 4434–4446. <https://doi.org/10.1021/acs.inorgchem.0c03217>.
- [21] Lin, Y.; Tang, Z.; Zhang, Z.; Wang, X.; Zhang, J. Preparation of a New Long Afterglow Blue-Emitting Sr₂MgSi₂O₇-Based Photoluminescent Phosphor. *J. Mater. Sci. Lett.* **2001**, *20*, 1505–1506. <https://doi.org/10.1023/A:1017930630889>.
- [22] Aitasalo, T.; Hölsä, J.; Laamanen, T.; Lastusaari, M.; Lehto, L.; Niittykoski, J.; Pellé, F. Luminescence Properties of Eu²⁺ Doped Dibarium Magnesium Disilicate, *Ceram.-Silikit.* **2005**, *49*, 58 - 62.
- [23] Aitasalo, T.; Hreniak, D.; Hölsä, J.; Laamanen, T.; Lastusaari, M.; Niittykoski, J.; Pellé, F.; Streck, W. Persistent Luminescence of Ba₂MgSi₂O₇:Eu²⁺. *J. Lumin.* **2007**, *122–123*, 110–112. <https://doi.org/10.1016/j.jlumin.2006.01.112>.
- [24] Van den Eeckhout, K.; Smet, P. F.; Poelman, D. Persistent Luminescence in Eu²⁺-Doped Compounds: A Review. *Mater.* **2010**, *3* (4), 2536–2566. <https://doi.org/10.3390/ma3042536>.
- [25] Tang, Y.; Deng, M.; Wang, M.; Liu, X.; Zhou, Z.; Wang, J.; Liu, Q. Bismuth-Activated Persistent Phosphors. *Adv. Opt. Mater.* **2023**, *11*, 2201827. <https://doi.org/10.1002/adom.202201827>.
- [26] Li, H.; Cai, J.; Pang, R.; Liu, G.; Zhang, S.; Jiang, L.; Li, D.; Li, C.; Feng, J.; Zhang, H. A Strategy for Developing Thermal-Quenching-Resistant Emission and Super-Long Persistent Luminescence in BaGa₂O₄:Bi³⁺. *J. Mater. Chem. C* **2019**, *7* (42), 13088–13096. <https://doi.org/10.1039/C9TC04963K>.
- [27] Liu, M.; Yang, C.; Liu, W.; Zhou, X.; Liu, S.; You, Q.; Jiang, X. Synthesis of Bi³⁺ and Eu³⁺ Co-Doped Na₄CaSi₃O₉ Blue-Red Light Tunable Emission Phosphors for Inducing Plant Growth. *Ceram. Int.* **2024**, *50*, 9058–9069. <https://doi.org/10.1016/j.ceramint.2023.12.219>.
- [28] Liu, H.; Liu, J.; Sun, B.; Zhang, Z.; Jiao, C.; Sun, D.; Zhang, L. X.; Zhang, Y. Ca₂LaTaO₆:Bi³⁺/Mn⁴⁺ Phosphors with High Brightness Far-Red Emitting and Luminescence Enhancement for Plant Growth LED Lights and Temperature Sensor. *Inorg. Chem.* **2024**, *63*, 5365 - 5377. <https://doi.org/10.1021/acs.inorgchem.3c03939>.

- [29] Gai, S.; Gao, P.; Chen, K.; Tang, C.; Zhao, Y.; Wei, J.; Zhang, Y.; Molokeev, M. S.; Xia, M.; Zhou, Z.; Gai, S.; Zhou, Z.; Gao, P.; Chen, K.; Tang, C.; Zhao, Y.; Wei, J.; Zhang, Y.; Xia, M.; Molokeev, M. S. Superior Quantum Efficiency Blue-Emitting Phosphors with High Thermal Stability toward Multipurpose LED Applications. *Adv. Opt. Mater.* **2024**, Article ASAP. <https://doi.org/10.1002/adom.202302870>. (accessed 2024-04-05).
- [30] Tang, Y.; Deng, M.; Zhou, Z.; Wang, J.; Liu, Q. A Multicolor-Emitted Phosphor for Temperature Sensing and Multimode Dynamic Anti-Counterfeiting. *J. Am. Ceram. Soc.* **2022**, *105*, 6241–6251. <https://doi.org/10.1111/jace.18587>.
- [31] Wang, Y.; Yuan, X.; Cao, Y.; Ma, C. Multiple Anti-Counterfeiting Strategy by Integrating up-Conversion, down-Shifting Luminescence, Phosphorescence and Photochromism into NaYTiO₄: Bi/Er Phosphors. *J. Mater. Sci. Technol.* **2022**, *130*, 219 - 226. <https://doi.org/10.1016/j.jmst.2022.05.030>.
- [32] Tao, C.; Xie, F.; Guo, C.; Liu, L.; wei, ruilong; xu, mengxia; Mao, H.; Xu, H.; Zhong, S. Dynamic Color-Tunable Persistent Zinc-Cadmium Silicate Composites Phosphor: Design, Preparation and Application. **2024**. <https://doi.org/10.2139/ssrn.4685758>.
- [33] Li, X.; Chen, S.; Zhang, K.; Deng, S.; He, J.; Wang, B.; Zeng, Q. Color-Tunable Persistent Luminescence Phosphor for Multimode Dynamic Anti-Counterfeiting. *Mater. Today Chem.* **2023**, *30*, 101594. <https://doi.org/10.1016/j.mtchem.2023.101594>.
- [34] Li, X.; Zou, Z.; Wang, Z.; Wu, C.; Zhang, J.; Wang, Y. A Novel Un-Doped Long Lasting Phosphorescence Phosphor: SrZrSi₂O₇. *J. Rare Earth.* **2015**, *33*, 37–41. [https://doi.org/10.1016/S1002-0721\(14\)60380-X](https://doi.org/10.1016/S1002-0721(14)60380-X).
- [35] Kurunthatil Kuttiat, T.; Abraham, M.; Kunti, A. K.; Amador-Mendez, N.; Tchernycheva, M.; Das, S. Enriching the Deep-Red Emission in (Mg, Ba)₃M₂GeO₈: Mn⁴⁺ (M = Al, Ga) Compositions for Light-Emitting Diodes. *ACS Appl. Mater. Interfaces* **2023**, *15*, 7083–7101. <https://doi.org/10.1021/acsami.2c20066>.
- [36] Feng, P.; Zhang, J.; Wu, C.; Liu, X.; Wang, Y. Self-Activated Afterglow Luminescence of Un-Doped Ca₂ZrSi₄O₁₂ Material and Explorations of New Afterglow Phosphors in a Rare Earth Element-Doped Ca₂ZrSi₄O₁₂ System. *Mater. Chem. Phys.* **2013**, *141*, 495–501. <https://doi.org/10.1016/j.matchemphys.2013.05.049>.

- [37] Cao, R.; Su, L.; Cheng, X.; Chen, T.; Liao, C.; Guo, Y.; Liu, P.; Li, W. Ca₂ZrSi₄O₁₂: Eu³⁺, Bi³⁺ Phosphor: Synthesis, Tunable Emission, and Luminescence Properties. *J. Mater. Sci.: Mater. Electron.* **2019**, *30*, 7808 - 7814. <https://doi.org/10.1007/s10854-019-01097-3>.
- [38] Tian, W.; Zhang, L.; Chen, D.; Lin, S.; Zhou, Z.; Wang, H.; Streck, W.; Ren, Z.; Chen, H. Enhanced Afterglow Properties in Reddish-Orange Ca₂SnO₄:Sm³⁺ Phosphors by NH₄Cl or CaCl₂ Flux. *Opt. Mater.* **2024**, *147*, 114773. <https://doi.org/10.1016/j.optmat.2023.114773>.
- [39] Uma, K.; Chen, S. W.; Krishna Kumar, B.; Jeyaprabha, C.; Yang, T. C. K.; Lin, J. H. Enhanced Photocatalytic Activity of CdS Nanostar Decorated SiO₂/TiO₂ Composite Spheres and the Simulation Effect Using FDTD Model. *Ionics* **2021**, *27*, 397–406. <https://doi.org/10.1007/S11581-020-03795-Z>.
- [40] Wang, X. Design, Synthesis and Applications of Ultraviolet-C and Ultraviolet-B Persistent Phosphors. Ph.D. Thesis, University of Georgia, Athens, Georgia, 2020.
- [41] El-Ads, E. H.; Galal, A.; Atta, N. F. The Effect of A-Site Doping in a Strontium Palladium Perovskite and Its Applications for Non-Enzymatic Glucose Sensing. *RSC Adv* **2016**, *6* (20), 16183–16196. <https://doi.org/10.1039/c5ra24107c>.
- [42] Sreevalsa, S.; Ranjith, P.; Ahmad, S.; Sahoo, S. K.; Som, S.; Pandey, M. K.; Das, S. Host Sensitized Photoluminescence in Sr_{2.9-3x/2}Ln_xAlO₄F: 0.1Eu³⁺ (Ln = Gd, Y) for Innovative Flexible Lighting Applications. *Ceram. Int.* **2020**, *46*, 21448–21460. <https://doi.org/10.1016/j.ceramint.2020.05.243>.
- [43] Luo, L.; Liu, R.; Liu, Y.; Zhuang, W.; Li, Y.; Gao, T. Effects of Oxygen Vacancies on Luminescent Properties of Phosphor Sr₄Al₁₄O₂₅:Mn⁴⁺ Co-Doping with Alkali Metal Ion. *Inorg. Chem. Commun.* **2020**, *118*, 107972. <https://doi.org/10.1016/j.inoche.2020.107972>.
- [44] Hooge, F. N. Relation between Electronegativity and Energy Bandgap. *Z. fur Phys. Chem.* **1960**, *24*, 275–282. https://doi.org/10.1524/ZPCH.1960.24.3_4.275.
- [45] Om Kumar, A. S.; Shukla, V.; Srivastava, S. K. Role of Electronegativity on the Bulk Modulus, Magnetic Moment and Band Gap of Co₂MnAl Based Heusler Alloys. *J. Sci.: Adv. Mater. Devices* **2019**, *4*, 158–162. <https://doi.org/10.1016/J.JSAMD.2019.02.001>.
- [46] Wei, Y.; Xing, G.; Liu, K.; Li, G.; Dang, P.; Liang, S.; Liu, M.; Cheng, Z.; Jin, D.; Lin, J. New Strategy for Designing Orangish-Red-Emitting Phosphor via Oxygen-Vacancy-

Induced Electronic Localization. *Light Sci. Appl.* **2019**, *8*, 15. <https://doi.org/10.1038/s41377-019-0126-1>.

[47] Yang, T.; Jiang, H.; Hai, O.; Dong, Y.; Liu, S.; Gao, S. Effect of Oxygen Vacancies on the Persistent Luminescence of $\text{Y}_3\text{Al}_2\text{Ga}_3\text{O}_{12}:\text{Ce}^{3+}, \text{Yb}^{3+}$ Phosphors. *Inorg. Chem.* **2021**, *60*, 17797–17809. <https://doi.org/10.1021/acs.inorgchem.1c02420>.

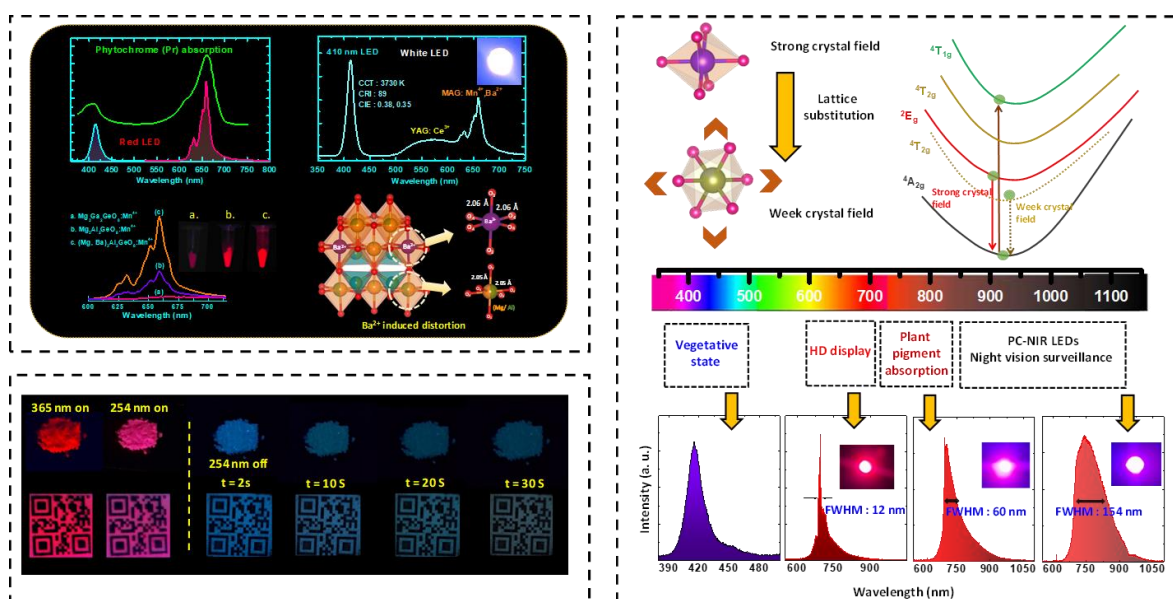
[48] Wang, J.; Ma, J.; Zhang, J.; Fan, Y.; Wang, W.; Sang, J.; Ma, Z.; Li, H. Advanced Dynamic Photoluminescent Material for Dynamic Anticounterfeiting and Encryption. *ACS Appl. Mater. Interfaces* **2019**, *11*, 35871–35878. <https://doi.org/10.1021/ACSAMI.9B10870>.

[49] Yeh, N.; Chung, J. P. High-Brightness LEDs-Energy Efficient Lighting Sources and Their Potential in Indoor Plant Cultivation. *Renew. Sustain. Energy Rev.* **2009**, *13*, 2175–2180. <https://doi.org/10.1016/j.rser.2009.01.027>.

[50] Dutta Gupta, S.; Jatothu, B. Fundamentals and Applications of Light-Emitting Diodes (LEDs) in in Vitro Plant Growth and Morphogenesis. *Plant Biotechnol. Rep.* **2013**, *7*, 211–220. <https://doi.org/10.1007/s11816-013-0277-0>.

Chapter 5

Summary and future scope of the thesis



The invention of various types of phosphor materials has been a game-changer in the world of technology. These materials have enabled the development of energy-efficient light-emitting diodes (LEDs), which have revolutionized the lighting industry. Additionally, phosphor materials have replaced many traditional functional materials, making them an indispensable component in various applications including optoelectronics, bioimaging, sensors, and security. However, there exists a scarcity of highly efficient non-rare earth-based inorganic oxide phosphors. The rare earth-free inorganic oxide materials are highly recommended due to their low cost and good chemical as well as thermal stability.

Hence, in Chapter 1, a detailed description of the deep red/NIR emitting non-rare earth-based inorganic phosphor activated by transition metal ions such as Mn⁴⁺ and Cr³⁺ is provided. Also detailed review of the structural and optical properties of the currently available phosphors is described in this chapter. This review provides structural dependent luminescence properties, different methods for amplification of luminescence intensity and potential applications of deep/NIR phosphors. Meanwhile, the mechanism, overview, and applications of the self-activated persistent phosphors are also described in Chapter 1.

In Chapter 2, a novel deep red-emitting (Mg, Ba)₃Al₂GeO₈: Mn⁴⁺ phosphor developed

from its analogue of $\text{Mg}_3\text{Ga}_2\text{GeO}_8: \text{Mn}^{4+}$. The replacement of Ga^{3+} by Al^{3+} yielded $\text{Mg}_3\text{Al}_2\text{GeO}_8: \text{Mn}^{4+}$, which showed more intense red emission than $\text{Mg}_3\text{Ga}_2\text{GeO}_8: \text{Mn}^{4+}$ due to the strong preference of Mn^{4+} to the $[\text{AlO}_6]$ octahedrons compared to $[\text{GaO}_6]$ octahedrons. The co-existing phases, MgAl_2O_4 and Mg_2GeO_4 in $\text{Mg}_3\text{Al}_2\text{GeO}_8$ also contributed to the Mn^{4+} luminescence by providing octahedral sites for Mn^{4+} occupancy. These sites reduced the natural reduction probability of Mn^{4+} to Mn^{2+} , which was confirmed by the low-temperature photoluminescence and cathodoluminescence studies. The partial substitution of larger Ba^{2+} ions in Mg^{2+} sites caused structural distortions and generated new Ba impurity phases, which improved the Mn^{4+} photoluminescence further. Under UV and violet-blue exposure, the optimum composition $\text{Mg}_{2.73}\text{Ba}_{0.27}\text{Al}_2\text{GeO}_8: \text{Mn}^{4+}$ exhibited deep red emission at 659 nm, which was 35 folds greater in intensity than the base composition of $\text{Mg}_3\text{Ga}_2\text{GeO}_8: \text{Mn}^{4+}$. The emission matched with the absorption of chlorophylls liable for plants' photosynthesis. The intense red emission with 100% colour purity of the optimised composition makes it a suitable red phosphor to enhance the colour rendering of commercial white LEDs.

In Chapter 3, $\text{Mg}_3\text{Al}_2\text{GeO}_8: 0.01\text{Cr}^{3+}$ phosphor developed with ultra-sharp emission band peaking at 693 nm having FWHM of around 4 nm. The emission intensity and the FWHM of the phosphor increased due to the substitution of alkaline earth metal ions. The optimum $\text{Mg}_{2.9}\text{Al}_2\text{GeO}_8: 0.01\text{Cr}^{3+}, 0.1\text{Sr}^{2+}$ showed three times greater emission intensity than that of $\text{Mg}_3\text{Al}_2\text{GeO}_8: 0.01\text{Cr}^{3+}$ sample. The additional $[\text{MgO}_6]$ sites from the newly generated Sr impurity phase and the structural distortion in the Cr^{3+} occupied sites are responsible for the emission enhancement. In addition, developed a series of Ga^{3+} co-doped $\text{Mg}_{2.9}(\text{Al}_{1-y}\text{Ga}_y)\text{GeO}_8: 0.01\text{Cr}^{3+}, 0.1\text{Sr}^{2+}$ samples. The partial Ga^{3+} substitution weakens the crystal field environment in $[\text{GaO}_6]$ that occupy Cr^{3+} ions. The partial Ga^{3+} co-doped sample could produce broadband emission (630 nm to 1050 nm) with an FWHM of ~150 nm due to the combined emission from the multiple sites with strong and weak crystal field environments. Meanwhile, this emission range could cover the first biological window region, showing the suitability for bio-imaging applications. Finally, various phosphor-converted LEDs are fabricated using commercial blue LEDs. The pc-LED produced by combining 410 nm LED with $\text{Mg}_{2.9}\text{Al}_2\text{GeO}_8: 0.01\text{Cr}^{3+}, 0.1\text{Sr}^{2+}$ phosphor having 100% colour purity could be used for display application. While the 410 nm LED combined with $\text{Mg}_{2.9}(\text{AlGa})\text{GeO}_8: 0.01\text{Cr}^{3+}, 0.1\text{Sr}^{2+}$ phosphor exhibited the potential for plant growth applications. Moreover, the NIR LEDs produced from $\text{Mg}_{2.9}(\text{Al}_{0.5}\text{Ga}_{1.5})\text{GeO}_8: 0.01\text{Cr}^{3+}, 0.1\text{Sr}^{2+}$ phosphor having increased FWHM can be used for night vision surveillance.

Chapter 4 reports a novel cyan-emitting persistent phosphor suitable for anti-counterfeiting and plant growth applications. Initially, a self-activated $\text{Sr}_2\text{Zr}(\text{SiO}_3)_4$ phosphor is developed from the reported $\text{Ca}_2\text{Zr}(\text{SiO}_3)_4$. The XRD pattern of the synthesised sample matches with monoclinic- $\text{Sr}_3\text{Y}_2\text{Si}_6\text{O}_{18}$ (JCPDS 00-065-0204), and this led to the development of a novel self-activating persistent cyan emitting $\text{Sr}_2\text{Zr}_2(\text{SiO}_3)_6$ phosphor. The XRD analysis revealed the presence of a secondary orthorhombic $\text{Sr}_3\text{Zr}_2\text{O}_7$ phase and the various planes in the host lattice were confirmed from the HRTEM analysis. The optimised $\text{Sr}_2\text{Zr}_2(\text{SiO}_3)_6$: 12 wt% NH_4Cl phosphor material with high intensity and persistent luminescence shows potential application in information storage due to its self-activated property. The presence of oxygen vacancies in these samples was identified from the XPS analysis. The Bi^{3+} co-doping and the vacuum treatment increased the cation vacancies and oxygen vacancies in the sample. The orange-red emission observed around 620 nm due to Bi^{3+} incorporation can have attributed to the oxygen-vacancy-induced electronic localisation around the Bi^{3+} ions. The optimised vacuum-treated $\text{Sr}_2\text{Zr}_2(\text{SiO}_3)_6$: 12 wt% NH_4Cl , 0.02Bi^{3+} sample with high persistence luminescence has been used for information storage. The designed QR code using the above phosphor mixed with rare earth-free deep red phosphor stores the information CSIR NIIST, which can be read out and found suitable for security applications. Further, the material is used for anti-counterfeiting applications. Here, the vacuum-treated $\text{Sr}_2\text{Zr}_2(\text{SiO}_3)_6$: 12 wt% NH_4Cl , 0.02Bi^{3+} material is incorporated with rare earth-free deep red phosphor. Meanwhile the high intense $\text{Sr}_2\text{Zr}_2(\text{SiO}_3)_6$: 12 wt% NH_4Cl phosphor has been mixed with deep red-emitting phosphor and combined with 280 nm LED and 410 nm LED for the plant growth applications. Overall, the thesis focuses on the development of non-rare-earth-based highly efficient oxide phosphors and the effective utilisation of the developed phosphors for various applications.

Future Scope

The current thesis could develop different types of phosphors with emissions in various ranges. These phosphors were effectively utilized in lighting, medical imaging, and security applications. However, the developed compositions can be used for some other important applications without any changes in their compositions. Meanwhile, the scope of the developed phosphor can be extended to various areas with slight modifications in the compositions. The scope for the three different working chapters are provided separately in this section.

In the second chapter $(\text{Mg, Ba})_3\text{M}_2\text{GeO}_8: \text{Mn}^{4+}$ ($\text{M} = \text{Al, Ga}$) phosphor has been developed and utilized for lighting and plant growth applications. In future, the fabricated red LEDs for plant growth can be used for indoor plant cultivations and we can observe the improvements in plant growth. Moreover, the CL spectra of the $(\text{Mg, Ba})_3\text{Al}_2\text{GeO}_8: \text{Mn}^{4+}$ ($\text{M} = \text{Al, Ga}$) phosphor shows emission in both red and green regions due to the presence of Mn^{2+} ions. Hence synthesizing samples in a reduction atmosphere may produce green and red emissions. The variation of both emissions with the temperature can be studied in detail and can be used for optical temperature sensing applications.

In the third chapter, Cr^{3+} -activated deep red to NIR emitting phosphors are developed and used for various applications. Instead of the carried out *in vitro* cell imaging, the application can be extended to *in vivo* bioimaging if the phosphor is capable of producing persistent emission in deep red to NIR region. Hence suitable cationic modification can be done to create trapping centres in the host for producing persistent emission. Moreover, introducing anionic/cationic vacancies by various methods can induce persistent emission in the Cr^{3+} sample. Hence the phosphor can be used for *in vitro* bio imaging applications in future. Also, the above phosphor finds scope in solar cell applications. Since the developed Cr^{3+} activated phosphor have a strong absorption band in the UV and blue region and is capable of producing emission in deep red to NIR region. The phosphors can convert the UV and blue light from the sunlight to deep red to NIR. The spectral mismatch between the bandgap of silicon solar cells and incident photon energy coming from sunlight that causes difficulty in converting the solar energy to electricity. The bandgap of the Si cell is appropriate for absorbing deep red and NIR regions, but the incident solar energy contains UV content. Hence the developed Cr^{3+} -activated phosphors are capable of collecting solar photons and converting them into matching bandgap energy of Si cells. Another important future scope for the developed activated phosphor is its utilization in Far red/NIR therapy. Since the developed phosphor has high quantum efficiency it can be easily and effectively used for the therapy treatment.

A cyan-emitting persistent $\text{Sr}_2\text{Zr}_2(\text{SiO}_3)_6$ is developed in the fourth chapter and it is effectively utilized for dynamic anti-counterfeiting applications and plant growth applications. The dynamic anti-counterfeiting can be extended by combining this phosphor with suitable green, blue or red-emitting persistent phosphors. Due to the persistent emission of the above phosphor, it can be used for the *in vivo* bio-imaging application after checking its cytotoxicity.

Name of the Student: Thejas K. K.	Registration No. 10PP19J39002
Faculty of Study: Physical Science	Year of Submission: 2024
CSIR Lab: National Institute for Interdisciplinary Science & Technology (CSIR-NIIST), TVM, Kerala	Name of supervisor: Dr. Subrata Das
Title of the thesis: <i>Non-rare earth-based new class of inorganic phosphors for lighting, medical imaging and security applications</i>	

ABSTRACT

The thesis focused on the development of various non-rare earth-based inorganic oxide phosphors for various human and eco-centric applications. Chapter 1 provides a detailed description of the currently available Mn^{4+} and Cr^{3+} activated deep red/NIR emitting phosphor, and the advantages of rare earth-free inorganic oxide phosphors are also elaborated. Further, the potential applications and various methods for red emission enhancements are also explained in detail. This introduction chapter also includes a brief idea of the current status, mechanism and various applications of self-activated persistent cyan-emitting phosphors. In Chapter 2, a novel a novel deep red-emitting $(\text{Mg}, \text{Ba})_3\text{Al}_2\text{GeO}_8: \text{Mn}^{4+}$ phosphor developed from $\text{Mg}_3\text{Ga}_2\text{GeO}_8: \text{Mn}^{4+}$. The larger Ba^{2+} ions' co-doping in Mg^{2+} sites caused structural distortions and generated new Ba impurity phases, which improved the Mn^{4+} photoluminescence further. The optimum composition $\text{Mg}_{2.73}\text{Ba}_{0.27}\text{Al}_2\text{GeO}_8: \text{Mn}^{4+}$ exhibited deep red emission at 659 nm having 35 folds greater emission intensity than the base composition of $\text{Mg}_3\text{Ga}_2\text{GeO}_8: \text{Mn}^{4+}$. The emission matched with the absorption of chlorophylls liable for plants' photosynthesis and the 100 % colour purity makes it a suitable red phosphor to enhance the colour rendering of commercial white LEDs. In Chapter 3, $\text{Mg}_3\text{Al}_2\text{GeO}_8: 0.01\text{Cr}^{3+}$ phosphors were developed with ultra-sharp emission band peaking at 693 nm having FWHM of around 4 nm. The emission intensity and the FWHM of the phosphor were increased by the substitution of alkaline earth metal ions and the $\text{Mg}_{2.9}\text{Al}_2\text{GeO}_8: 0.01\text{Cr}^{3+}, 0.1\text{Sr}^{2+}$ showed greater emission intensity. Further, developed a series of Ga^{3+} co-doped $\text{Mg}_{2.9}(\text{Al}_{2-y}\text{Ga}_y)\text{GeO}_8: 0.01\text{Cr}^{3+}, 0.1\text{Sr}^{2+}$ samples and the Ga^{3+} substitution weakens the crystal field environment in $[\text{GaO}_6]$ that occupies Cr^{3+} ions. The combined emission from the multiple sites with strong and weak crystal field environments resulted in a broadband emission (630 nm to 1050 nm) with an FWHM of ~150 nm that covers the first biological window region, showing the suitability for bio-imaging applications. Finally, various phosphor-converted LEDs are fabricated using commercial blue LEDs. The pc- LED produced by combining 410 nm LED with $\text{Mg}_{2.9}\text{Al}_2\text{GeO}_8: 0.01\text{Cr}^{3+}, 0.1\text{Sr}^{2+}$ phosphor having 100% colour purity could be used for display application. While the 410 nm LED combined with $\text{Mg}_{2.9}(\text{AlGa})\text{GeO}_8: 0.01\text{Cr}^{3+}, 0.1\text{Sr}^{2+}$ phosphor exhibited the potential for plant growth applications. In Chapter 4, a novel self-activating cyan-emitting persistent luminescence $\text{Sr}_2\text{Zr}_2(\text{SiO}_3)_6$ phosphor was developed. Under 284 nm excitation, the PL emission of the host exhibited broadband centred at 485 nm, originating from the Zr^{4+} ions and lattice defects. Additionally, the host shows a cyan persistent luminescence having a duration of 60s. The optimised vacuum-treated $\text{Sr}_2\text{Zr}_2(\text{SiO}_3)_6: 12\text{wt}\% \text{NH}_4\text{Cl}, 0.02\text{Bi}^{3+}$ phosphor exhibits enhanced persistent luminescence and has been used for dynamic anti-counterfeiting and security application by mixing with the red-emitting $\text{Mg}_3\text{Al}_2\text{GeO}_8: 0.005 \text{Mn}^{4+}, 0.27\text{Ba}^{2+}$ phosphor. Furthermore, $\text{Sr}_2\text{Zr}_2(\text{SiO}_3)_6: 12\text{wt}\% \text{NH}_4\text{Cl}/\text{Mg}_3\text{Al}_2\text{GeO}_8: 0.005 \text{Mn}^{4+}, 0.27\text{Ba}^{2+}$ mixture is used to develop a plant growth LED, covering the absorption spectra of plant pigments.

Thesis outcomes

List of Publications Emanating from Thesis Work

1. **Thejas K. K.**; Abraham M.; Kunti A. K.; Tchernycheva M.; Ahmad S; Das S. Review on Deep Red-Emitting Rare-Earth Free Germanates and Their Efficiency as Well as Adaptability for Various Applications. *Appl. Mater. Today* **2021**, *24*, 101094. (<https://doi.org/10.1016/j.apmt.2021.101094>)
2. **Thejas K. K.**; Abraham, M.; Kunti, A. K.; Amador-mendez, N.; Tchernycheva, M.; Das, S. Enriching the Deep-Red Emission in $(\text{Mg}, \text{Ba})_3\text{M}_2\text{GeO}_8 : \text{Mn}^{4+}$ ($\text{M} = \text{Al}, \text{Ga}$) Compositions for Light-Emitting Diodes. *ACS Appl. Mater. Interfaces* **2023**, *15*, 5, 7083–7101. (<https://doi.org/10.1021/acsami.2c20066>)
3. **Thejas K. K.**;; Vishnu Priya Murali;; Kaustabh Kumar Maiti;; Subrata Das. Compositionally engineered $(\text{Mg}, \text{Sr})_3(\text{Al}, \text{Ga})_2\text{GeO}_8 : \text{Cr}^{3+}$ phosphors with tuned emission from ultra-sharp red to ultra-broad NIR band for LEDs and *in vitro* cell imaging applications. (Manuscript to be communicated)
4. **Thejas K. K.**; Sariga C. Lal;; Subrata Das. Inducing defects to boost the persistent luminescence in novel cyan emitting rare-earth free strontium zirconium silicate for dynamic anti-counterfeiting and plant growth LED applications (Manuscript to be communicated)

List of Publications Not Related to Thesis Work

1. **Thejas K. K.**; Supin, K. K.; Akshay, V. R.; Arun, B.; Mandal, G.; Chanda, A.; Vasundhara, M. Effect of Annealing Time on Structural, Optical and Magnetic Properties of TiO_2 Nanoparticles. *Opt. Mater. (Amst)*. **2022**, *134* (PA), 113178. (<https://doi.org/10.1016/j.optmat.2022.113178>).
2. Abraham, M.; Kunti, A. K.; **Thejas K. K.**; Amador-mendez, N.; Gogneau, N.; Nishanth, K. G.; Tchernycheva, M.; Das, S. The Elevated Colour Rendering of White-LEDs by Microwave-Synthesized Red-Emitting $(\text{Li}, \text{Mg})_3\text{RbGe}_8\text{O}_{18} : \text{Mn}^{4+}$ Nanophosphors. *Dalton Trans.*, 2021, **50**, 3044–3059. (<https://doi.org/10.1039/d0dt04309e>.)
3. Gopal, R.; Nidhisha, V.; Amrutha, T. P.; Aswathi, A. A.; Midhila, P.; **Thejas K. K.**; Das, S.; Kizhakayil, R. N. Aggregation-Induced White Light Emission and Solvent-Induced Dual Mode Multi-Analyte Sensing by Highly Crystalline Single Component

- Derived N , S Co-Doped Carbon Nanodots. *ACS Appl. Opt. Mater.* **2023**, 1, 3, 701–714. (<https://doi.org/10.1021/acsaom.2c00170>).
4. Mukesh, M.; **Thejas K. K.**; Akshay, V. R.; Arun, B.; Vasundhara, M. Effect of Annealing Conditions on Particle Size , Magnetic and Optical Properties of Gd₂O₃ Nanoparticles Effect of Annealing Conditions on Particle Size , Magnetic and Optical Properties of Gd₂O₃ Nanoparticles. *AIP Conf. Proc.* **2019**, 2162, 020091. (<https://doi.org/10.1063/1.5130301>)
 5. Supin K K.; Anson George.; Y. Ranjith Kumar.; **Thejas K. K.**; Guruprasad Mandal, Anupama Chanda.; M. Vasundhara. Structural, optical and magnetic properties of pure and 3d metal dopant-incorporated SnO₂ nanoparticles. *RSC Adv.*, **2022**, 12, 26712. <https://doi.org/10.1039/D2RA03691F>.
 6. Abraham M.; **Thejas K. K.**; Kunti, A. K.; Roberto Hernandez.; J. Duras.; Nishanth K.G.; S. K. Sahoo.; Amador-mendez, N.; Tchernycheva, M.; Das, S. Strategically developed strong red-emitting oxyfluoride nanophosphors for next-generation lighting applications. (Manuscript communicated)

List of posters and oral presented

1. **Thejas K. K.**, Malini Abraham., Subrata Das. Enriching the deep red emission in (Mg, Ba)₃M₂GeO₈: Mn⁴⁺ (M = Al, Ga) compositions for light-emitting diodes, National Conference on Advanced Material and Manufacturing Technologies (AMMT 2023), 23-24 February, 2023, CSIR-NIIST, Thiruvananthapuram, Kerala, India. (Poster Presentation)
2. **Thejas K. K.**, Mukesh M, V R Akshay, B Arun, M Vasundhara. Tailoring the magnetic and optical properties of TiO₂ nanocrystals derived from sol-gel techniques via different annealing conditions. International Conference on Advanced Materials (ICAM 2019), 12–14 June, 2019, Nirmalagiri college, Kannur, Kerala, India. (Poster Presentation)

Abstracts for conference presentations

Enriching the deep red emission in $(\text{Mg}, \text{Ba})_3\text{M}_2\text{GeO}_8: \text{Mn}^{4+}$ ($\text{M} = \text{Al}, \text{Ga}$) compositions for light-emitting diodes

Thejas K. K.^{a,b}, Malini Abraham^{a,b}, Subrata Das^{a,b,*}

^aMaterials Science and Technology Division, CSIR-National Institute for Interdisciplinary Science and Technology (NIIST), Thiruvananthapuram 695019, India.

^bAcademy of Scientific and Innovative Research (AcSIR), Ghaziabad 201002, India.

*Corresponding author. Tel.: +91471 2515360

E-mail address: subratadas@niist.res.in

Abstract

The currently available commercial white LEDs (WLEDs) produce cool white light due to the deficiency of red components. Hence the red emission from Mn^{4+} -containing oxides inspired the development of high-colour rendering and cost-effective warm WLEDs. Aiming this fact, a series of new crystallographic site-modified $\text{Mg}_3(\text{Al}, \text{Ga})_2\text{GeO}_8: \text{Mn}^{4+}$ compositions were developed with strong deep red emission in reaction to UV and blue lights for the development of WLEDs. The co-existing phases present in this composition contributed to the Mn^{4+} luminescence by providing additional octahedrons for Mn^{4+} occupancy. Further, these sites reduced the natural reduction probability of Mn^{4+} to Mn^{2+} , which was confirmed using cathodoluminescence analysis. A cationic substitution strategy was employed on $\text{Mg}_3(\text{Al}, \text{Ga})_2\text{GeO}_8: \text{Mn}^{4+}$ to improve the luminescence. The optimum composition $\text{Mg}_{2.73}\text{Ba}_{0.27}\text{Al}_2\text{GeO}_8: 0.005\text{Mn}^{4+}$ shows 35 folds greater emission intensity than the reported $\text{Mg}_3\text{Ga}_2\text{GeO}_8: \text{Mn}^{4+}$. The optimum composition could retain 70% of its initial room temperature intensity at 450 K showing its higher thermal stability. A warm WLED with CCT of 3730 K and CRI of 89 was fabricated by combining the optimized red component with yellow emitting $\text{Y}_3\text{Al}_5\text{O}_{12}: \text{Ce}^{3+}$ and 410 nm blue-LED. Meanwhile, three red LEDs were also fabricated using the optimum red phosphor with commercial sources.

Acknowledgements: This research is financially supported by the Indo French Centre for the Promotion of Advanced Research (CEFIPRA), New Delhi, India to promote collaborative scientific research between India and France (Project No. 6008-1).

Tailoring the magnetic and optical properties of TiO₂ nanocrystals derived from sol-gel techniques via different annealing conditions

Thejas K K^{1,2}, Mukesh Murali¹, V R Akshay^{1,2}, B Arun^{1,2} and M Vasundhara^{1,2}**

¹ *Materials Science and Technology Division, CSIR-National Institute for Interdisciplinary Science and Technology, Trivandrum, India.*

² *Academy of Scientific and Innovative Research (AcSIR), CSIR-National Institute for Interdisciplinary Science and Technology, Trivandrum, India.*

**Corresponding author. Mobile: (+91) 9496445333; E-mail:mvas@niist.res.in

Abstract

TiO₂ is a non-toxic and an inexpensive wide-band-gap semiconductor which is having several practical applications such as dilute magnetic semiconductors, photo-catalysis, lithium-ion batteries and photo-electrochemical solar energy conversion [1]. It exists in three different crystal structures, namely anatase, rutile, and brookite and each structure has different physical properties. Among the three phases, rutile is the most stable phase under ambient conditions whereas anatase and brookite are metastable at all temperatures and will transform to rutile upon are heated. Some reports suggest that the stability of the different phases of TiO₂ depends on the particle size, i.e, anatase phase is found to be stable if particles sizes are lesser than 11 nm and rutile phase is stable if the particles sizes are greater than 35 nm while brookite is the most stable phase if the particles sizes are in between 11–35 nm. There also have been several results on TiO₂ nanocrystals with different magnetic behavior depending on the different synthesis conditions reported by several co-workers. A room temperature ferromagnetism (RTFM) is observed in TiO₂ nanoparticles whereas a perfect diamagnetism is observed in its bulk counterparts. However, the origin of RTFM is under debate because, some have reported the origin of RTFM is due to the intrinsic defects like oxygen vacancy or Ti interstitials while others have reported the nature as extrinsic arising from magnetic clusters due to the existence of mixed valance of Ti ions [2]. Very limited efforts have been made to compare the particle size as well as magnetic properties associated with the annealing temperature. Hence, in this work, we report variation of particle sizes with increase in reaction time of TiO₂ nanoparticles derived by sol-gel technique associated with different annealing temperature and studied their magnetic and optical properties. Detailed analysis of magnetic and optical properties associated with the particle size variation will also be demonstrated.

Keywords: TiO₂ nanocrystals ; bandgap; optical properties; magnetic properties

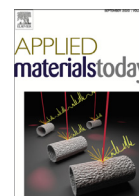
Acknowledgements

The authors would like to acknowledge CSIR, India granted project number MLP0031 for the financial support.

Reference:

H. Chen, C.E. Nanayakkara and V.H. Grassian, *Chem. Rev.*, 2012, **112**, 5919-5948.

M. Parras, A. Varela, R. C. Gil, K. Boulahya, A. Hernando and J. M. G. Calbet, *J. Phys. Chem. Lett.*, 2013, **4**, 2171



Review on deep red-emitting rare-earth free germanates and their efficiency as well as adaptability for various applications

K.K. Thejas^{a,b}, Malini Abraham^a, Arup K. Kunti^c, Maria Tchernycheva^c, Shahzad Ahmad^{d,*}, Subrata Das^{a,b,*}

^a Materials Science and Technology Division, CSIR – National Institute for Interdisciplinary Science and Technology, Thiruvananthapuram, Kerala, 695019, India

^b Academy of Scientific and Innovative Research (AcSIR), Ghaziabad, 201002, India

^c Centre de Nanosciences et de Nanotechnologies (C2N), Université Paris Saclay, UMR 9001 CNRS, 10 Boulevard Thomas, Gobert, 91120 Palaiseau, France

^d Department of Chemistry, Zakir Husain Delhi College, University of Delhi, Delhi, 110002, India

ARTICLE INFO

Article history:

Received 18 April 2021

Revised 4 June 2021

Accepted 9 June 2021

Keywords:

Deep-red emission

Germanates

Mn⁴⁺ and Cr³⁺

Octahedral site occupancy

Crystal engineering

ABSTRACT

Deep red-emitting phosphors are becoming the hot area of research during these times owing to their wide variety of applications in various fields, including lighting, display, imaging, and many others. The transition metal ions, especially Mn⁴⁺ and Cr³⁺ activated oxide phosphors possess admirable merits such as high chemical and thermal stability, eco-friendly preparation, and emission in the deep-red region. It is important to mention that Mn⁴⁺ doped germanates usually show emission spectra peaking above 650 nm. Thanks to this emissive property, germanates can be the best choice for display applications for providing a wide colour gamut in ultra-high-definition TV. Moreover, the emission of these phosphors can be extended to the near-infrared region with long persistence. Most of the reviews published on Mn⁴⁺ activated phosphors concentrate on the white light-emitting diode applications. Whereas the reviews on Cr³⁺ activated phosphors are focused on their persistent near-infrared emission. In this article, we mainly focused on the Mn⁴⁺ and Cr³⁺-activated deep red-emitting germanate phosphors since octahedral Ge⁴⁺ sites in germanates are ideal for accommodating these transition metal ions. We have thoroughly discussed the crystal structure-dependant luminescence behaviour of the reported germanates. In addition to that, we have also discussed various methods for improving the luminescence properties of these transition metal ions. Finally, we have presented possible potential applications of the reviewed phosphors. We believe that this article will give the insight to develop new deep red-emitting phosphors and it will be helping the researchers to improve the luminescence properties of different existing phosphors. After all, it will be good to make a better understanding of the reported work in this area in a short time.

© 2021 Elsevier Ltd. All rights reserved.

1. Introduction

Red emitting phosphors have crucial roles in the areas of solid-state lighting, field emission displays, thermal sensors, solar cells, plant cultivation, bio-imaging, and many others [1–6]. The activators used in the red-emitting phosphors can be sharp band red-emitting rare-earth ions (Eu³⁺, Pr³⁺, Sm³⁺), broad-band red-emitting rare-earth ions (Eu²⁺, Ce³⁺), and the sharp band deep red-emitting transition metals (Mn⁴⁺, Cr³⁺). The sharp-band red-emitting phosphors produce a red colour with high quantum efficiency, which is eye sensitive for humans. However, the absence of

a wide excitation band in the ultra-violet (UV) or blue region limits their applications in light-emitting diodes (LEDs) [7]. The broad-band red-emitting phosphors such as nitrides, oxynitrides, silicates, aluminates, which are mostly activated by Eu²⁺ ions, have better LED applications while comparing with that of Eu³⁺ doped phosphors. Nitrides hosts such as CaAlSiN₃:Eu²⁺ and Sr₂Si₅N₈:Eu²⁺ are known as efficient phosphors owing to their broad absorption band, high luminescence intensity, and low thermal quenching [8,9]. However, these broad red-emitting phosphors possess either harsh synthesis conditions, high production cost, toxicity, or poor chemical and thermal stability [10]. Moreover, the inability of Eu²⁺ ions in producing emissions beyond 650 nm in the visible region and non-radiative loss due to the re-absorption phenomena further restrict their practical utility in several fields including agriculture [11]. Eventually, the focus of the research community recently moved to the development of red-emitting phosphors acti-

* Corresponding authors.

E-mail addresses: shahzadncfm@gmail.com (S. Ahmad), subratadas@niist.res.in (S. Das).

vated by transition metal ions such as Mn^{4+} , Mn^{2+} , Cr^{3+} , and Bi^{2+} [12–15]. In addition, a strong interest is grown in producing phosphors, which exhibit broad absorption in the UV and blue regions and are able to emit sharp-band red or deep-red lights and emission [12,16,17].

Amongst all the transition metal ions, Mn^{4+} ions may be the better choice for red-emitting phosphors since the spectral position of the red emission (600–790 nm) can be tuned by appropriate modification in their crystal field environment as the position of their emission peaks depends upon the host employed [16,17]. The intense absorption band in the UV and blue region is attributed to the spin-allowed ${}^4A_{2g} \rightarrow {}^4T_{1g}$, ${}^4T_{2g}$ transitions. The excited electrons in the ${}^4T_{1g}$ and ${}^4T_{2g}$ states non-radiatively relax to the 2E_g state leading to a spin forbidden ${}^2E_g \rightarrow {}^4A_{2g}$ transition, which is responsible for the red emission. Generally, Mn^{4+} ions prefer to occupy the octahedral site as they possess strong crystal field stabilization energy in an octahedral environment [16,17]. The Mn^{4+} ions can be very well substituted for Ga^{3+} [18], Al^{3+} [11], Ge^{4+} [6], Ti^{4+} [19], Sb^{5+} [20], Si^{4+} [21], Sn^{4+} [22], Zr^{4+} [23], Ta^{5+} [24], Te^{6+} [25], Sc^{3+} [26], Nb^{5+} [27], W^{6+} [28] etc. in the unit cell, and thus, the covalency of Mn^{4+} -ligand bonding can be altered.

Another deep red-emitting transition metal under consideration is Cr^{3+} for synthesizing deep red-emitting phosphors. Although the Cr^{3+} ion has the essentially same electronic configuration as the Mn^{4+} ion (i.e., $3d^3$), their electronic transitions are quite different [29]. In fact, Mn^{4+} -doped oxide and fluoride phosphors emit only red light caused by the ${}^2E_g \rightarrow {}^4A_{2g}$ transitions (strong crystal field) [30], but Cr^{3+} -doped oxide phosphors can emit red light caused by the ${}^2E_g \rightarrow {}^4A_{2g}$ transitions or deep red/far-red light caused by the ${}^4T_2 \rightarrow {}^4A_2$ transitions (weak crystal field) [31]. Similarly, Cr^{3+} -doped fluoride phosphors emit only deep red or far-red light due to the ${}^4T_2 \rightarrow {}^4A_2$ transitions [32]. Comparing to Mn^{4+} activated hosts, Cr^{3+} activated hosts have some other merits such as emission in deep red and near-infrared (NIR) region, long persistence, etc. The long persistence of Cr^{3+} doped phosphors in the NIR region generates its applications in near-infrared bio-imaging, dark glow signage, photodynamic tumour therapy, night vision surveillance, etc. [33–35]. On the other hand, its emission in the deep-red region could facilitate the applications in solid-state lighting, plant photo-morphogenesis, solar concentrator, etc. [36–38].

Fluorides, oxides, and oxyfluorides are the three types of hosts where the Mn^{4+} ions can be doped efficiently. In particular, Mn^{4+} doped fluoride hosts are getting huge attention owing to their ability in producing intense red emission in the region of 600 to 640 nm, high colour purity, broad excitation bands in the UV and blue regions [39,40]. Because of the eye-sensitive red-emitting nature below 640 nm, these materials are promising candidates for improving the colour rendering index (CRI) of white light-emitting diodes (W-LEDs) [41]. Eventually, these phosphors can be efficiently used for the backlighting in liquid-crystal displays (LCDs) and LEDs since the transmittance spectrum of the optical filters matches well with that of the narrow red emission produced by these phosphors [42]. Amongst the various fluoride compositions having the empirical formula of $A_2MF_6:Mn^{4+}$ fluoride phosphors (A = alkali metal; M = Ge, Ti, Si, etc.), $K_2SiF_6:Mn^{4+}$ and $K_2TiF_6:Mn^{4+}$ are the popular phosphors for the W-LEDs application [43,44]. But the synthesis of these phosphors requires a highly corrosive HF solution. In addition, the obtained fluorides are suffering from low stability and have considerable moisture sensitivity, which makes them inadequate for high-temperature applications. Furthermore, the red emission from the Mn^{4+} -activated fluorides usually gets saturated at a certain excitation power, which restricts their commercial utility [39]. Eventually, the highly electronegative fluoride environment is also not favourable for tuning the red emission peak above 650 nm [45].

Meanwhile, the researchers have started to focus on oxyfluoride hosts, which combine the advantage of fluorides as well as oxides. In comparison with other hosts, oxyfluoride may possess non-centrosymmetric structures as the incorporation of the fluorine into the oxide sites will lead to a distortion of polyhedron coordination [46]. Furthermore, due to the similar ionic radii of the F^- and O^{2-} ions [47], the formation of a stable anionic sublattice is possible in oxyfluorides, owing to which, oxyfluorides show excellent absorption and emission properties. These phosphors are widely applicable in W-LEDs also in the areas of catalysis, batteries, UV shielding properties, etc. [48–51]. The most researched oxyfluoride material is Sr_3AlO_4F due to its easy synthesis, its better stability, and its excellent luminescence property. However, this host can be optically activated by Eu^{3+} ions only for producing red-orange emissions which have their own drawbacks including the lack of broadband absorption and emission nature, as mentioned earlier [49–51]. Hence the studies on Mn^{4+} doped oxyfluorides have gathered some attention for the last few years. Few red-emitting Mn^{4+} doped oxyfluorides phosphors such as $BaNbOF_5:Mn^{4+}$ [52], $Cs_2NbOF_5:Mn^{4+}$ [53], $Na_2WO_2F_4:Mn^{4+}$ [54], $Rb_2NbOF_5:Mn^{4+}$ [55], and $Cs_2WO_2F_4:Mn^{4+}$ [56] have been reported recently. Even though these phosphors exhibit satisfactory luminescence properties, they could not eliminate the usage of HF solution during their synthesis, make them imperfect in large-scale eco-friendly production.

The oxide hosts bear more advantages due to the excellent thermal and chemical stability and outstanding material properties including hardness, larger transparency, etc. [57]. Compared with the oxyfluoride hosts, the oxide hosts exhibit stronger covalence, weaker polarizability, and lesser thermal vibration which make them favourable for attaining intense red emission [58]. Chen et al. reported that the Mn^{4+} ions in fluoride hosts are associated with the 2E_g value ranging from 626 nm to 635 nm [17]. While in oxide hosts, its range becomes wider from 652 nm to 713 nm owing to the high covalency of oxides, and considerable shifting of energy levels due to the nephelauxetic effect [17,59,60]. Such a wide spectral range of Mn^{4+} ions in oxides can extend their application by taking the advantage of deep red emission. Furthermore, a solid-state synthesis is an easiest and adaptable method for synthesizing various Mn^{4+} -activated oxides since it includes simplified stoichiometric mixing, grinding, and high-temperature heating [10]. In the various oxide hosts, Mn^{4+} can easily be stabilized in aluminates, germanates, titanates, zirconates, niobates, arsenate, etc. [16]. Germanate-based phosphors are a promising host as they provide the most optimal octahedral sites for Mn^{4+} ions due to the same ionic radii and charge of Ge^{4+} and Mn^{4+} ions [47]. The recent rising of germanates as the suitable hosts of Mn^{4+} ions for producing deep red emission above 650 nm attracted our focus to accomplish a detailed review of their progress as the prominent deep red-emitting phosphor systems. The development scheme of deep red-emitting phosphors from nitrides to Mn^{4+}/Cr^{3+} activated germanates and gallates is represented in Fig. 1.

This review focuses on the Mn^{4+} and Cr^{3+} activated germanates with deep red emission above 650 nm. Such deep red emission systems are highly capable of providing a larger colour gamut and thereby accomplish the parameter values for ultra-high-definition television systems according to ITU-R BT.2020–2 recommendations [6]. So far, some interesting germanate host systems have been proposed from the formulas of $A-Ge-O$ and $M-Ge-O$ (A = Alkali metal; M = alkaline-earth metal), which can emit deep red emissions in the desired wavelength region under UV and blue excitation. Although these germanates are generated using the same chemical formula, however, their crystal arrangements are not similar. This is because of the fact that the crystal structure mainly depends on the size of the monovalent cations at the A or divalent cations at the M site as well as on the bond length of Ge–O.

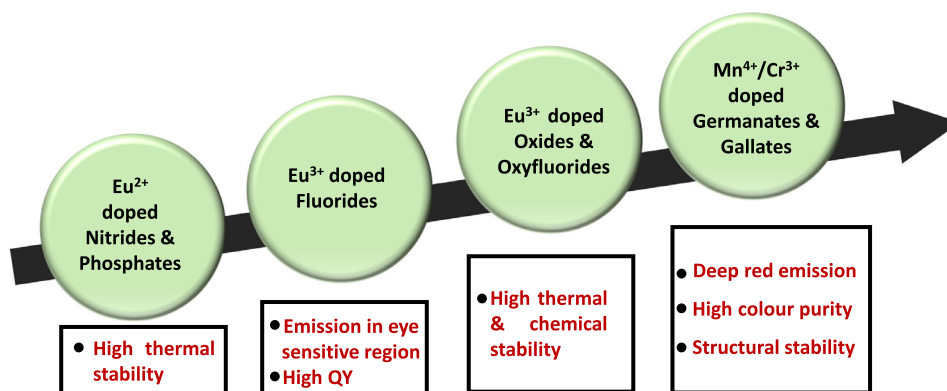


Fig. 1. Development scheme of deep red-emitting phosphors. (For interpretation of the references to colour in this figure legend, the reader is referred to the web version of this article.)

Hence, there are decent possibilities for finding new phosphors based on the alkali- or alkaline-earth germanate system depending upon a suitable search for one or a combination of alkali or alkaline-earth metal ions. Therefore, we emphasize the structural and spectroscopic properties of Mn⁴⁺ and Cr³⁺ activated deep-red emitting germanates for some of their special characteristic features, which are discussed in Sections 3 and 4 of this review article. Additionally, we have also discussed the various techniques employed to enhance the red emission like synthesis methodologies, crystal structure, the role of activator, dopant concentration, temperature, etc. Simultaneously, the electronic properties of transition metal ions of these germanate phosphors have also been presented. Also, some of the important applications and future perspectives of these germanate phosphors are discussed in the last part.

2. Basic ionic configurations of Mn⁴⁺ and Cr³⁺ ions

The general electronic configuration of both Mn⁴⁺ and Cr³⁺ is 1s²2s²2p⁶3s²3p⁶3d³, while their ground state valence electronic configuration in an octahedral environment is t_{2g}³e_g⁰. This half-filled t_{2g}³ orbital provides extra stability to manganese and chromium in their +4 and +3 oxidation state, respectively. Moreover, the fascinating electronic, magnetic, and spectroscopic properties of these metal ions are possible due to their favourable electronic configuration. There will be 8 LS terms originating from the Coulomb interaction that occurs between the electrons in the unfilled d orbitals and they were generally denoted by ^{2S+1}L. Here “L” represents the total angular momentum while “S” stands for the total spin. The eight LS terms denoted by ⁴F, ⁴P, ²G, ²P, ²D₍₁₎, ²F, ²D₍₂₎, and ²H are consisting of two spin quarters, and six spin doublets. According to Hund’s rule, the first term ⁴F corresponds to the ground state while the remaining terms correspond to the excited states [61,62]. Further, each term is found to be degenerate to (2S+1)(2L+1) states and the number of degenerate states for all the 8 terms will give rise to 120 possible combinations. Hence, the three electrons can be distributed in the 3d orbitals in 120 ways [61,62]. The energy values of the LS coupling terms in the d³ electronic configuration are provided in terms of the Racah parameters B and C in Table 1 [61,62]. By substituting the Racah parameter values of Cr³⁺, Mn⁴⁺, Fe⁵⁺, and V²⁺ free ions given in Table 2, the energy values for 8 LS terms for each of these ions having a d³ system are estimated and illustrated in an energy level diagram in Fig. 2. The splitting of LS terms and energy position of the split sublevels highly depend on the strength and symmetry of the crystal field. The splitting of LS terms of Mn⁴⁺, Cr³⁺, and all other ions having d³ or d⁷ electronic configuration is listed in Table 3 [62].

Table 1

Energies of eight electrostatic terms (LS terms) in the d³ system in terms of B and C taking the energy of ground-level ⁴F as zero. Adapted from Ref. [62].

Term(s)	Energy
⁴ F	0
⁴ P	15B
² P	9B+3C
² D ₍₁₎ , ² D ₍₂₎	20B+5C±√193B ² +8BC+4C ²
² F	24B+3C
² G	4B+3C
² H	9B+3C

Table 2

The Racah parameters values of free ions having d³ electronic configuration. Adapted from Ref. [62].

Ion	B (cm ⁻¹)	C (cm ⁻¹)
V ²⁺	766	2855
Cr ³⁺	918	3850
Mn ⁴⁺	1160	4303
Fe ⁵⁺	1210	5066

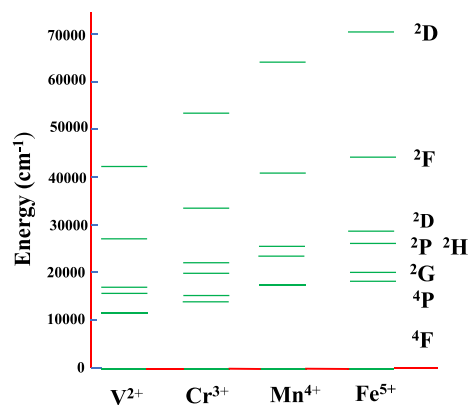


Fig. 2. Energy levels diagram of the free V²⁺, Cr³⁺, Mn⁴⁺, and Fe⁵⁺ ions by taking the energy of ground state energy as zero. Adapted from Ref. [62].

Table 3

Splitting of LS terms of the d³ (or d⁷) configuration in the O_h or T_d group. Adapted from Ref. [62].

The electrostatic terms	T _d or O _h groups irreducible representation
P-term (L = 1)	T ₁
D-term (L = 2)	T ₂ +E
F-term (L = 3)	A ₂ +T ₁ +T ₂
G-term (L = 4)	A ₁ +E + T ₁ +T ₂
H-term (L = 5)	E + 2T ₁ +T ₂

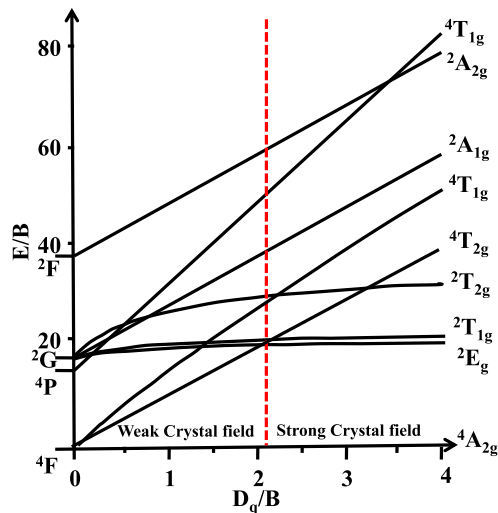


Fig. 3. Simplified T-S diagram in the octahedral crystal field for ions having d^3 electronic configuration. Adapted from Ref. [57].

2.1. Simplified Tanabe-Sugano (T-S) energy level diagrams of Mn^{4+} and Cr^{3+}

The simplified T-S diagram shown in Fig. 3 represents the splitting of the energy levels of Mn^{4+} and Cr^{3+} ions in an ideal octahedral environment. The energy difference between the ground state $^4A_{2g}$ and the excited state $^4T_{2g}$ is $10D_q$ (D_q is the crystal field intensity). For a D_q/B value less than 2.1, the first excited state is $^4T_{2g}$, and after that 2E_g becomes the first excited state, as represented in Fig. 3. The strong and weak crystal fields can be distinguished in the T-S diagram by a point at which the $^4T_{2g}$ and 2E_g levels intersect, as marked in Fig. 3. The separation between the $^4A_{2g}$ ground state and the 2E_g and $^2T_{1g}$ states is practically independent of crystal field strength D_q . While Cr^{3+} ion can experience both strong as well as weak field environments, Mn^{4+} ion, on the other hand, experiences only a strong field environment because of its larger positive charge [62,63]. A general energy level diagram of Mn^{4+} and Cr^{3+} in a strong field environment is shown in Fig. 4(a). The bands arising from the ground state, $^4A_{2g} \rightarrow ^2E_g$, $^2T_{1g}$, $^4T_{2g}$, $^2T_{2g}$, $^4T_{1g}$ are called R line, R' line, U band, B, line, and Y band, respectively. The ions from the higher excited states come down to 2E_g excited state through non-radiative transition, and then their transition from the 2E_g state to the ground state results in emission [63]. In the case of Mn^{4+} ion, as already discussed, the sharp emission peak corresponds to the spin forbidden $^2E_g \rightarrow ^4A_{2g}$ transition. Depending upon the crystal field environment, the spectral position of this transition can vary over a wide range of 620 to 723 nm. Also, the two broad excitation bands correspond to the spin-allowed transitions of $^4A_{2g} \rightarrow ^4T_{1g}$ (4F) and $^4A_{2g} \rightarrow ^4T_{2g}$. Another spin allowed transition is $^4A_{2g} \rightarrow ^4T_{1g}$ (4P), however, it is generally covered by the host absorption as well as the charge transfer [17,59,60]. For a case study, we used Mn^{4+} doped $NaMgGdTeO_6$ phosphor [64], and the energy level diagram consisting of all possible transitions in Mn^{4+} is shown in Fig. 4(b). Here the electrons from the higher excited $^4T_{1g}$, $^2T_{2g}$, and $^4T_{2g}$ states may relax to the lower excited 2E_g state through a non-radiative transition and then completely transfer to the ground state resulting in a deep red emission [17,64]. Similarly, for Cr^{3+} ion, let us consider an example of Cr^{3+} -doped $ZnGa_2O_4$ phosphor with the energy level diagram consisting of all possible transitions in Cr^{3+} shown in Fig. 5 [65]. Here the substitution of Al^{3+} ions in the Ga sites does not make any changes in the diagram except a slight upward shift in the conduction band (represented in green

colour). The excitation of electrons from the ground state to excited states or 4T_1 (4P) in the conduction band leads to its trapping which facilitates the persistence in these phosphors. The non-radiative relaxation occurs to the 2E_g state and the transition from this state to the ground state results in a red emission [65].

2.2. Crystal field analysis

As we already discussed, the Racah parameters B and C are the characteristics of an oxide ion within a metal oxide compound. The introduction of the Mn^{4+} and Cr^{3+} ions in the crystal field results in the formation of the chemical bond between the metal 3d orbitals and the ligands resulting in the nephelauxetic effect. Subsequently, the hybridization between these metal ions and ligands becomes maximized resulting in the reduction of the Racah parameters. Irrespective of the same Mn^{4+} and/or Cr^{3+} ionic doping, the reduction in the Racah parameters are found to be different for each host, causing a wide variation in the energy value of their emission peak [59]. Considering the case of Mn^{4+} -activated fluoride phosphors, the emission peak lies in the range of 620–640 nm owing to the comparatively weak hybridisation effect [66]. However, in the case of oxides, the emission peak lies above 650 nm due to a strong hybridisation effect [66]. Hence, it can be concluded that the position of the 2E_g level of Mn^{4+} and Cr^{3+} highly depends on the covalency, nature of ligands, and bond angle in chemical bonds [59,60,67,68]. The energy level difference between $^4A_{2g}$ and $^4T_{2g}$ of Mn^{4+} and Cr^{3+} is $10D_q$, which can be represented as follows [67],

$$10D_q = \frac{K}{R^n} \quad (1)$$

here R is the bond length between the cation and the ligand, while n and K are the fitting parameters. The value of power ' n ' depends on the nature of ligands, the geometry of the complex, etc. Depending upon the systems, it varies from 3.5 to 7.3 – as was shown by many quantum-chemical calculations [67,69–71]. Ogasawara et al. estimated the value of n and K for CrO_6 and MnO_6 clusters and observed that the value ' n ' for Cr^{3+} is greater than Mn^{4+} showing that the $10D_q$ value of Cr^{3+} ions is more sensitive to bond length in comparison with Mn^{4+} ions [63]. The nephelauxetic ratio (β_1) can be introduced for predicting the position of the emission spectrum since the 2E_g level (generally for Mn^{4+}) can be written as the linear function of this parameter. The nephelauxetic ratio can be estimated using the following equation [59,72,73],

$$\beta_1 = \sqrt{\left(\frac{B}{B_0}\right)^2 + \left(\frac{C}{C_0}\right)^2} \quad (2)$$

where B_0 and C_0 represent the values of Racah parameters of free Mn^{4+} ions.

The value of D_q can also be estimated from the absorption spectrum using the equation,

$$D_q = E(^4A_{2g} \rightarrow ^4T_{2g})/10 \quad (3)$$

The Racah parameter B can be obtained from the absorption spectra by considering the peak energy difference between the two transitions $^4A_{2g} \rightarrow ^4T_{1g}$ and $^4A_{2g} \rightarrow ^4T_{2g}$. The equation used for calculation [64,73]

$$\frac{D_q}{B} = \frac{15(x-8)}{x^2-10x} \quad (4)$$

where the parameter x is given by

$$x = \left[E(^4A_{2g} \rightarrow ^4T_{1g}) - E(^4A_{2g} \rightarrow ^4T_{2g}) \right] / D_q \quad (5)$$

The Racah parameter C can also be calculated from the emission spectrum using the peak energy value from the $^2E_g \rightarrow ^4A_{2g}$ transition and the obtained B value [64,73].

$$E(^2E_g \rightarrow ^4A_{2g})/B = 3.05C/B + 7.9 - 1.8B/D_q \quad (6)$$

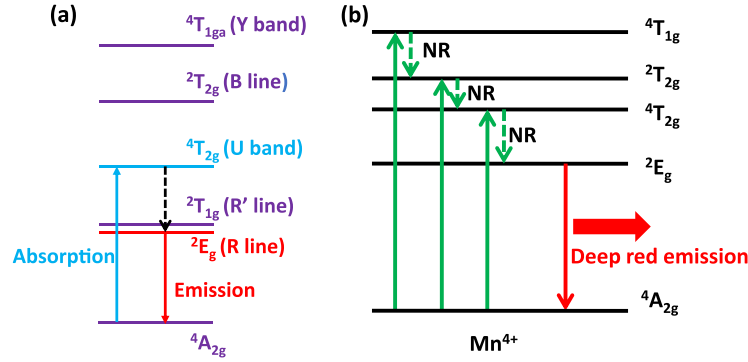


Fig. 4. (a) General energy level diagram for Mn⁴⁺ and Cr³⁺. Adapted from Ref. [63]; (b) Typical energy level diagram of Mn⁴⁺ showing excitation and emission (NR representing non-radiative transition). Adapted from Ref. [64].

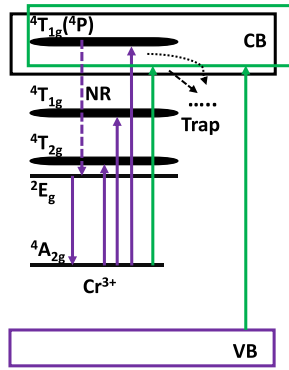


Fig. 5. Typical energy level diagram for Cr³⁺. (NR representing non-radiative transition) Adapted from Ref. [65].

The T-S diagram is used for interpreting the optical spectra and the splitting of energy levels however it is not applicable for crystal fields having lower symmetry than cubic. Hence a method can be used by finding the eigenvalues of the crystal field Hamiltonian. The eigenvalues of the following crystal field Hamiltonian can be used for representing the energy levels of impurity ions with the *D*-electron shell ($p = 2, 4$) and *f*-electron shell ($p = 2, 4, 6$) (in our case, Mn⁴⁺ and Cr³⁺ ions having *d*³ electronic configuration) in a crystal field of arbitrary symmetry [74].

$$H = \sum_{p=2} \sum_{k=-p}^p B_p^k O_p^k \quad (7)$$

where the B_p^k represents the crystal field parameters which are obtained from the crystal structure data and the O_p^k is the linear combination of appropriately selected tensor operators which were acting on the angular part of the dopant ion's wave function. Thus, it can be concluded that these parameters include all the geometrical and structural characteristics of the host lattice. The crystal field parameters B_p^k , with reference to the Exchange Charge Model (ECM), can be written as [75],

$$B_p^k = B_{p,q}^k + B_{p,s}^k \quad (8)$$

$$B_{p,q}^k = -K_p^k e^2 (r^p) \sum_i q_i \frac{V_p^k(\theta_i, \varphi_i)}{R_i^{p+1}} \quad (9)$$

$$B_{p,s}^k = K_p^k e^2 \frac{2(2p+1)}{5} \sum_i (G_s S(s)_i^2 + G_\sigma S(\sigma)_i^2 + \gamma_p G_\pi S(\pi)_i^2) \frac{V_p^k(\theta_i, \varphi_i)}{R_i} \quad (10)$$

The term $B_{p,q}^k$ describes the electrostatic interaction between the dopant valence electrons and the host metal ions while the term $B_{p,s}^k$ represents the overlap integral of wave functions of the dopant ion and the ligands. The summations are performed over the lattice ions i with charge q_i . R_i , θ_i , and φ_i denote the spherical polar coordinates of the i^{th} ion of the crystal lattice in the reference system centred at the dopant ion. Here, the average $\langle r^p \rangle$ of the p^{th} power of electron radial coordinate (r) can be calculated using the radial parts of the wave function of 3d orbitals. The values of the various constants like K_p^k , γ_p , and V_p^k are provided in reference [75]. The overlapping integrals between *D*-functions of the dopant ion, and the *s*- and *p*-functions of the ligands having different ' l ' and ' m ' quantum numbers are defined in terms of S_s , S_σ , and S_π ; where (in $|lm\rangle, |m'\rangle$ notation) $S_s = \langle d0|s0\rangle$, $S_\sigma = \langle d0|p0\rangle$ and $S_\pi = \langle d1|p1\rangle$. G_s , G_σ , and G_π represent the dimensionless adjustable parameters obtained from the positions of the first three absorption bands of the given crystal. It is possible to approximate $G_s = G_\sigma = G_\pi = G$, thereby reducing the number of parameters which is a key feature of the ECM approach. The value of G could be obtained by fitting the position of the calculated first absorption band to the observed first absorption band. The superiority of the ECM is that if the G parameter is determined to fit the first absorption band, the other higher energy levels will also fit experimental spectra quite well [74]. Brik et al. carried out the crystal field analysis for $\text{KAl}(\text{MoO}_4)_2:\text{Cr}^{3+}$ [74]. Here the Cr³⁺ ion is entering into the octahedral Al³⁺ site. The energy value obtained for 2E_g (2G) from ECM is 13,516 cm⁻¹ which is very close to the experimental value (13,512 cm⁻¹). All other energy values obtained using ECM are also well matching with the experimental data [74].

2.3. Configuration coordinate model

The electron-phonon interaction of Cr³⁺ and Mn⁴⁺ ions with the lattice vibrations can very well be analysed using the configurational coordinate model. The model assumes that the local environment of Cr³⁺ and Mn⁴⁺ ions vibrate harmonically about their mean position. Fig. 6 shows the potential energies of the electronic states expressed as a function of the vibrational coordinate for the case of a strong crystal field. The electron-phonon interaction plays a vital role in the absorption and emission processes taking place at the impurity centre. Consequently, the photoluminescence excitation (PLE) and photoluminescence (PL) spectra of Cr³⁺ and Mn⁴⁺ in solids can be explained using Frank-Condon analysis with the configurational coordinate model. Here the positions of excitation and emission lines are given as [57,76,77],

$$h\nu_{\text{ex}} = E_{\text{ZPL}} + kh\nu_{\text{p,ex}} \quad (11)$$

$$h\nu_{\text{em}} = E_{\text{ZPL}} - lh\nu_{\text{p,em}} \quad (12)$$

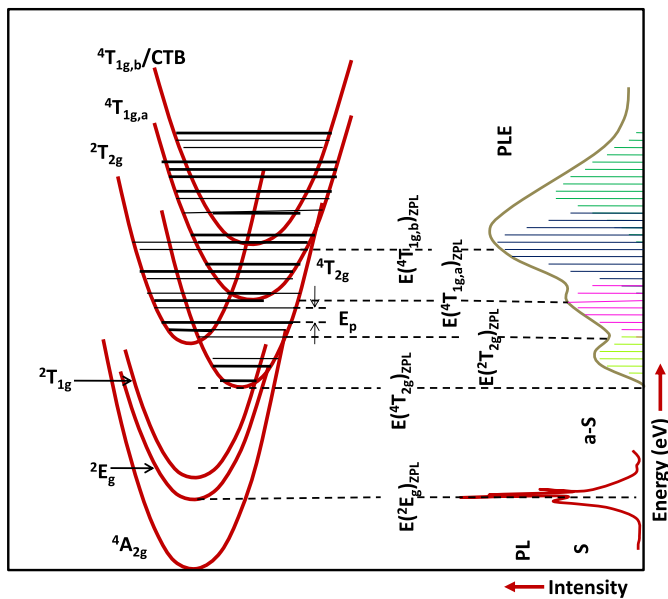


Fig. 6. Configuration coordinate model representing typical PL emission and absorption transition along with the schematic representation for the PL and PLE spectra of the Mn^{4+} -activated oxide phosphor (S = Stokes; a-S = anti-Stokes). Adapted from Ref. [57].

where, $h\nu_{p,ex}$ and $h\nu_{p,em}$ represent the lattice vibrational quanta for the excited and ground state, respectively. The absorption and emission bands could be considered as consisting of several lines representing the transitions between the vibrational levels, for example, the vibrational level l of the ground electronic state, and k of the excited electronic state. Using the Configurational Coordinate model, the spectral distribution of the excitation and emission spectra could be illustrated as [57],

$$I_{PLE}(E) = \sum_n I_n^{ex}(n) \exp\left[-\frac{(E - E_{ZPL} - nh\nu_{p,ex})^2}{2\sigma_{ex}^2}\right] \quad (13)$$

$$I_{PL}(E) = \sum_n I_n^{em}(n) \exp\left[-\frac{(E - E_{ZPL} + nh\nu_{p,em})^2}{2\sigma_{em}^2}\right] \quad (14)$$

where,

$$I_n^{ex}(n) = I_0^{ex} \exp(-S) \frac{S^n}{n!} \quad (15)$$

$$I_n^{em}(n) = I_0^{em} \exp(-S) \frac{S^n}{n!} \quad (16)$$

where, I_0^{ex} and I_0^{em} represent the ZPL intensity, S , the mean local vibrational number, and σ_{ex} and σ_{em} represent the broadening energy of each Gaussian component [57].

3. Mn^{4+} -activated deep red-emitting germanate phosphors

The literature available on different Mn^{4+} -activated hosts is represented in Fig. 7(a). Since the red-emitting fluoride host has some unavoidable drawbacks (mentioned earlier), the search for a new efficient phosphor ends up with Mn^{4+} -activated red-emitting oxide hosts. Nowadays, major studies on oxides are taking place in between aluminates [11], titanites [61], germanates [6], pyrosilicates [61], Perovskites [28], double perovskites [24,57], etc. (Fig. 7(b)). Amongst the different oxide hosts, aluminates, titanates, and germanates are getting more research interests because of the similar ionic radii of Al^{3+} (Al^{VI} : 0.535 Å), Ti^{4+} (Ti^{VI} : 0.605 Å), and

Ge^{4+} (Ge^{VI} : 0.530 Å) with that of Mn^{4+} (Mn^{VI} : 0.530 Å) in an octahedral environment [47]. In an octahedral environment, the d -orbital splits into three-fold degenerate t_{2g} and two-fold degenerate e_g states, and the three valence electrons of Mn^{4+} occupy the lower t_{2g} energy level. The crystal field splitting creates a large energy splitting between t_{2g} and e_g states leading to the crystal field stabilization of Mn^{4+} in the octahedral environment [78]. Fig. 8 shows the trigonal crystal structure considering the occupation of Mn^{4+} in the tetrahedral and octahedral environments. Here Ge^{4+} ions coordinate with four oxygen atoms to form a tetrahedron and coordinates with six oxygen atoms to form the octahedron. Mostly Mn^{4+} occupies the octahedral sites provided by the Ge^{4+} .

Comparing to titanites, aluminates, and even other Mn^{4+} doped oxide hosts, germanates are even more superior due to their structural stability. Even though the octahedral sites of Mn^{4+} can be easily replaced by the Al^{3+} ions, these systems require the use of a charge compensator owing to the ionic mismatch between Al^{3+} and Mn^{4+} ions. The charge imbalance between these two ions promotes some electronic defects which not only reduce the intensity of emission but also affect the emission profile of Mn^{4+} . Considering aluminates, their covalency is higher (greater than germanates) which leads to the decrease of interactions amongst electrons and results in the spread out of electrons over wide orbitals [80]. Since charge defects are unfavourable for luminescence intensity, high temperature and long calcination time are required during their synthesis although it is not economically favourable [80,81]. On the other hand, Mn^{4+} and Ti^{4+} have the same ionic charges, and this charge equivalency helps in eliminating electronic defects as well as the incorporation of charge compensator. However, small differences in their ionic sizes (0.065 Å) are sufficient to perturb the symmetry distortion in their crystal lattice thereby lowering the stability of the titanium host. In comparison with the Al^{3+} and Ti^{4+} , Ge^{4+} ion has the same ionic radii and charge as that of Mn^{4+} ion, and thus doping of Mn^{4+} does not make any charge imbalance and symmetry distortion of the crystal lattice. This charge equivalency helps in eliminating electronic defects as well as the incorporation of charge compensator. Further, the use of energy-consuming experimental conditions can also be avoided due to the lack of these charge defects. To confirm the site suitability in germanates mathematically, a parameter called effective compensating factor can be used in six coordinated environments which can be defined as $\varphi = z/r$ where z is the ionic charge, and the r is the ionic radius in that octahedral environment. This value for Mn^{4+} and Ge^{4+} is found to be the same (7.54) [47,81]. The emission intensity of Mn^{4+} -activated phosphors highly depends upon its local symmetry, that is presence or absence of an inversion centre at the Mn^{4+} site [82]. Ji et al. reported Mn^{4+} -activated double-perovskite structural $La_4Ti_3O_{12}$, which possesses a slightly- and highly-distorted $Ti(1)O_6$ and $Ti(2)O_6$ octahedra, respectively [83]. The Mn^{4+} ion occupying $Ti(1)$ site possesses a centre of inversion with symmetry of C_{3i} , while the Mn^{4+} ion occupying $Ti(2)$ site has a reduced symmetry of C_3 . High distortion in $Ti(2)O_6$ octahedra makes $MnTi(2)$ less stable than the $MnTi(1)$ by 0.09 eV as calculated from the density functional theory (DFT). As a result, the ratio of the zero-phonon line (ZPL) with vibronic emission intensity of $MnTi(2)$ is larger than those of $MnTi(1)$ [83]. The list of synthesis parameters, crystal structure and space groups of most of the recently reported germanates are tabulated in Table 4, and their spectroscopic parameters are tabulated in Table 5.

3.1. Alkali metal-based germanate system

The alkali germanate systems can be represented as $A-Ge-O$, where A represents the alkali metals such as Li, K, and Rb. Initially, the studies were concentrated on the $A_2Ge_4O_9$ alkali germanate system. In 2015, Kunitomo and co-workers synthesized

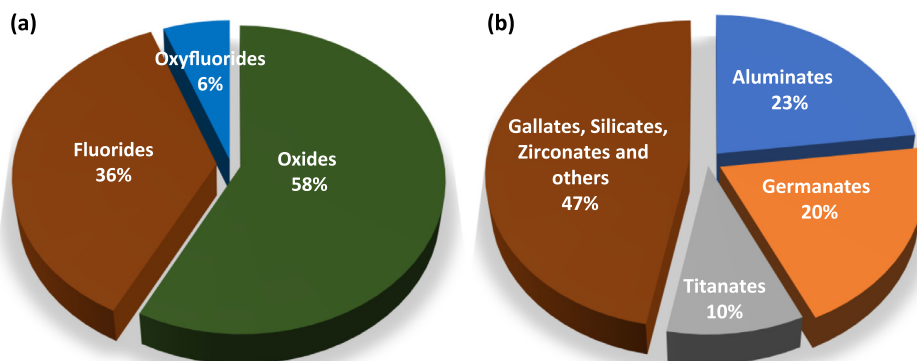


Fig. 7. Chart showing the available literature on different Mn^{4+} activated (a) hosts and (b) oxide hosts. (Based on the literature collected from the Web of Science published during January 2000-December 2020).

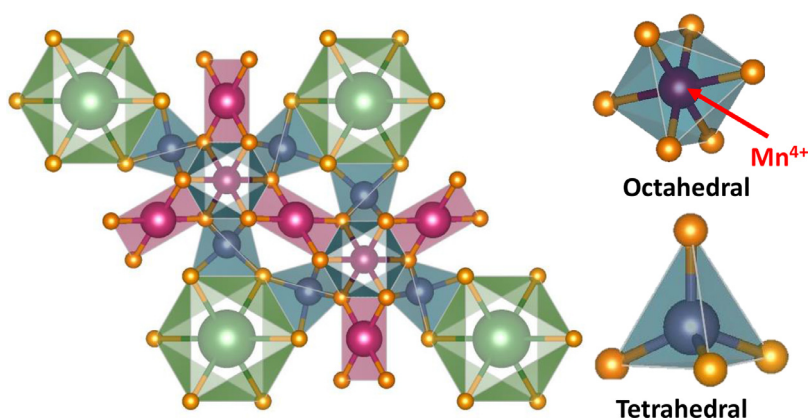


Fig. 8. Structure of trigonal crystal structure with the occupation of Mn^{4+} in octahedral and tetrahedral sites drawn using the VESTA software [79].

Table 4

Synthesis parameters, crystal structure and space groups of Mn^{4+} -doped germanate phosphors.

Germanates	Temp.(°C)	Holding time(h)	Optimal Mn conc.(mol%)	Crystal structure	Space group	Ref
$K_2BaGe_8O_{18}$	1050	6	0.2	Hexagonal	P3c1	[66,151]
$BaAl_2Ge_2O_8$	1200	2	0.1	Monoclinic	12/C	[105]
$BaGe_4O_9$	1100	10	2	Trigonal	P321	[107]
$BaGe_4O_9$	1100	6	0.5	Trigonal	P321	[106]
Ba_2GeO_4	1400	4	0.6	Orthorhombic	Pnma	[102]
$Ba_2MgGe_2O_7$	1000	6	1.3	Tetragonal	P42m	[104]
$Ba_2TiGe_2O_8$	1050	6	0.6	Orthorhombic	Cmm2	[103]
$K_2Ge_4O_9$	850	4	0.08	Trigonal	P3c1	[91]
$K_2Ge_4O_9$	800	4	0.4	Trigonal	P3c1	[94]
$K_2Ge_4O_9$	900	6	0.1	Trigonal	P3c1	[90]
$K_2Ge_4O_9$	900	6	0.2	Trigonal	P3c1	[93]
K_2MgGeO_4	920	8	0.4	Orthorhombic	Pnma	[95]
$La_3GaGe_5O_{16}$	1300	12	0.25	Triclinic	$p2_1/c$	[110]
La_2MgGeO_6	1400	6	0.2	Hexagonal	R3H	[109]
$LiAlGe_2O_6$	900	8	0.6	Trigonal	P-3m1	[112]
$LiGaGe_2O_6$	900	8	0.6	Monoclinic	P21/c	[112]
Li_2MgGeO_4	920	8	0.4	Orthorhombic	Pnma	[95]
$Li_2Ge_4O_9$	900	6	0.2	Orthorhombic	P21ca	[93]
$Li_2Ge_4O_9$	800	6	0.3	Orthorhombic	Pcca	[86]
$LiNaGe_4O_9$	900	6	0.2	Orthorhombic	Pcca	[93]
$Li_3RbGe_8O_{18}$	800	4	0.5	Trigonal	P31m	[6]
$Mg_3Ga_2GeO_8$	1300	6	0.5	Orthorhombic	Imma	[111]
$Mg_7Ga_2GeO_{12}$	1400	10	0.5	Orthorhombic	Cmmm	[113]
Mg_2GeO_4	1250	5	0.1	Orthorhombic	Pnma	[98]
$Mg_{14}Ge_5O_{24}$	1300	8	1	Orthorhombic	Pbam	[80]
$Mg_{3.5}Ge_{1.25}O_6$	1000	3	0.5	Orthorhombic	Pbam	[132]
$Mg_3Y_2Ge_3O_{12}$	1350	6	1	Cubic	$Ia\bar{3}d$	[115]
$Mg_6ZnGa_2GeO_{12}$	1400	5	1	Orthorhombic	Cmmm	[114]
$Rb_2Ge_4O_9$	800	4	0.4	Trigonal	P3C1	[94]
$SrGe_4O_9$	1100	6	0.5	Trigonal	P321	[106]

Table 5
Spectroscopic properties of some of the important germanates.

Germanates	CIE	QE (%)	$\lambda_{em}(nm)$	$\lambda_{exc}(nm)$	${}^2E_g(cm^{-1})$	${}^4T_{2g}(cm^{-1})$	${}^4T_{1g}(cm^{-1})$	$D_q(cm^{-1})$	$B(cm^{-1})$	$C(cm^{-1})$	Ref
$K_2BaGe_8O_{18}$	(0.702, 0.298)	32.9	666	468	15,015	21,645	28,571	2164	654	3345	[66]
$BaAl_2Ge_2O_8$	(0.720, 0.279)	28	668	288	15,345	19,443	26,543	1945	690	3390	[105,151]
$BaGe_4O_9$	–	61	666	335,465	15,015	20,408	29,411	2040	740	2980	[107]
Ba_2GeO_4	0.7187, 0.281	22.5	667	290	14,990	19,847	26,624	1985	650	3360	[102,151]
$Ba_2MgGe_2O_7$	(0.721, 0.279)	14.3	660	289	15,563	22,025	30,255	2205	805	3190	[104,151]
$Ba_2TiGe_2O_8$	(0.719, 0.281)	35.6	666	300	14,990	20,492	25,414	2050	445	3820	[103,151]
$K_2Ge_4O_9$	(0.719, 0.280)	57.8	664	300,450	15,060	22,271	31,250	2227	900	2821	[93]
K_2MgGeO_4	–	–	667	310,470	15,232	18,556	24,365	1855	545	3675	[95]
$La_3GaGe_5O_{16}$	–	68	660	330	15,151	21,413	30,303	2141	856	2947	[110]
La_2MgGeO_6	–	–	708	320	14,124	21,551	29,761	2155	807	2719	[109]
$LiAlGe_2O_6$	(0.72, 0.27)	32	671	289	14,885	18,879	23,558	1890	425	3840	[112,151]
$LiGaGe_2O_6$	(0.72, 0.27)	15	669	289	14,942	18,395	23,881	1840	510	3660	[112,151]
$Li_2Ge_4O_9$	(0.723, 0.277)	30.7	669	330,450	14,947	22,522	29,069	2252	608	3423	[93]
Li_2MgGeO_4	(0.699, 0.300)	–	671	323,470	15,167	17,749	21,783	1775	365	4080	[95,151]
$LiNaGe_4O_9$	(0.723, 0.278)	58.9	661	330,450	15,128	22,371	28,571	2237	571	3566	[93]
$Li_3RbGe_8O_{18}$	–	–	667	460	14,998	19,201	23,558	1920	390	3950	[6,151]
$Mg_3Ga_2GeO_8$	(0.295, 0.677)	64.7	659	419	15,401	21,138	25,817	2115	420	4015	[111,151]
$Mg_7Ga_2GeO_{12}$	(0.713, 0.287)	28.1	660	420	15,426	20,815	24,920	2080	365	4150	[113,151]
Mg_2GeO_4	–	–	659	303,420	15,635	20,654	25,252	2065	415	4110	[98,151]
$Mg_{14}Ge_5O_{24}$	(0.62, 0.29)	81	659	422	15,603	20,331	24,607	2035	380	4170	[80,151]
$Mg_{3.5}Ge_{1.25}O_6$	–	–	660	405,450	15,522	20,573	25,414	2055	435	4015	[132,151]
$Mg_3Y_2Ge_3O_{12}$	–	64	658	288,421	15,595	21,944	27,269	2195	480	3930	[115,151]
$Mg_6ZnGa_2GeO_{12}$	(0.717, 0.283)	–	660	420	15,385	21,380	25,978	2140	410	4030	[114,151]
$Rb_2Ge_4O_9$	–	–	657	345	15,240	18,475	23,800	1850	495	3800	[94]
$SrGe_4O_9$	(0.71, 0.29)	46	670	430	15,240	19,766	26,785	1975	680	3380	[106,151]

red-emitting orthorhombic $Li_2Ge_4O_9:Mn^{4+}$ using a glass-ceramic route [84]. It has a slightly distorted GeO_6 octahedron connected with $[GeO_3]_n$ -chains to form a three-dimensional framework and shows a sharp emission peak at a wavelength of 670 nm [84]. But the thermal quenching even below 100 °C makes $Li_2Ge_4O_9:Mn^{4+}$ inappropriate for several practical applications. Odawara et al. prepared nanocrystals of $Li_2Ge_4O_9:Mn^{4+}$ by employing a modified glass-ceramic route wherein they used YAG laser irradiation operated at 1064 nm [85]. Cao et al. used a conventional solid-state method with the usage of flux to synthesize this $Li_2Ge_4O_9:0.003Mn^{4+}$ phosphor for W-LED application with a high quantum yield and deep red emission [86]. All the raw materials along with the flux were taken in the stoichiometric ratio and grounded and heated at a temperature of 800 °C for 6 h. The obtained phosphor has a quantum yield of 80.3%, and good thermal stability better than the $K_2SiF_6:Mn^{4+}$ sample. At 300 °C, $Li_2Ge_4O_9:0.003Mn^{4+}$ could maintain 42% of its initial room temperature intensity. But at the same temperature, the emission intensity of $K_2SiF_6:Mn^{4+}$ dropped to 18% of its initial intensity [86]. Further, they have also studied the water resistance property of $Li_2Ge_4O_9:0.003Mn^{4+}$ and compared the outcomes with $K_2SiF_6:Mn^{4+}$. Under the same experimental condition, the red emission of $K_2SiF_6:Mn^{4+}$ reduced from 100% to 32% but no change in intensity is reported in the case of $Li_2Ge_4O_9:0.003Mn^{4+}$ showing its superior moisture resistance [86].

The luminescence spectrum of tetra germanate $LiNaGe_4O_9:Mn^{4+}$ phosphor is initially studied by Omel'chenko and co-workers wherein they observed a strong red and weak yellow-green emission [87]. Later, Suzuki et al. studied the effect of Na substitution on the luminescence properties of $LiNaGe_4O_9:Mn^{4+}$ phosphors [88]. They have prepared $Li_{2-x}Na_xGe_4O_9:Mn^{4+}$ samples using a glass-ceramic technique by melting the raw materials in the required stoichiometric ratio at 1200 °C for 30 min. The substitution of Na at the Li site helps in improving the quenching temperature as well as the quantum yield of the obtained phosphor. The same research group has also prepared $LiNaGe_4O_9:Mn^{4+}$ by the solid-state method which shows greater quantum yield and better colour purity [88]. This might be due to the suppression of crystal defects when prepared through solid-state synthesis

at high temperatures resulting in the reduction of non-radiative transition [88]. Solid-state synthesized $LiNaGe_4O_9:0.05Mn^{4+}$ with a high quantum yield of 78% has been reported by Li and co-workers [89]. To get the best performance of the phosphor they optimised synthesis condition at 850 °C for 3 h with 0.05% Mn^{4+} . The emission peak consists of the strongest peak at 661 nm in the deep-red region along with some shoulder peaks centred at 666, 676, 682, and 687 nm. These peaks are attributed to the ${}^2E_g \rightarrow {}^4A_{2g}$ transition of Mn^{4+} ions in the octahedral environment and its vibronic sidebands. The broad excitation spectrum is observed in the UV and blue region and peaks were centred at 295 nm due to the spin allowed ${}^4A_{2g} \rightarrow {}^4T_{1g}$ and 462 nm due to spin allowed ${}^4A_{2g} \rightarrow {}^4T_{2g}$ transitions, respectively. The emission intensity of this phosphor is about four times higher than that of commercially available $3.5MgO \cdot 0.5MgF_2 \cdot GeO_2:Mn^{4+}$ [MFG: Mn^{4+}]. The main reason behind its better emission intensity is its crystal structure which is shown in Fig. 9(a) and (b). The PL plots of $LiNaGe_4O_9:Mn^{4+}$ and MFG: Mn^{4+} samples are shown in Fig. 9(c). Here Mn^{4+} is efficiently doped into the GeO_6 octahedra. The layer of the GeO_6 group is separated by the layer of GeO_4 and each GeO_6 is connected to the three GeO_4 polyhedra by sharing common corners. Also, none of the GeO_6 is connected to each other showing the good isolation of the GeO_6 octahedra. Since Mn^{4+} ions are occupying these octahedral sites, the interactions between these Mn^{4+} ions are weakened or blocked leading to stronger luminescence and higher quantum yield [89].

Ding et al. reported novel trigonal $K_2Ge_4O_9:0.001Mn^{4+}$ (KGO: Mn^{4+}) prepared using solid-state reaction [90]. The unit cell of trigonal $K_2Ge_4O_9$ is composed of both octahedral and tetrahedral sites wherein the octahedral site is preferred by the Mn^{4+} . Here the concentration of Mn^{4+} is optimised to be 0.1 mol% and the concentration quenching mechanism of the sample is explained by the energy transfer mechanism involved between the Mn^{4+} ions. The emission spectrum of the sample under blue excitation is centred at 663 nm and the corresponding *commission internationale de l'éclairage* (CIE) values are found to be (0.702, 0.296) which is close to that of commercialised MFG: Mn^{4+} . This phosphor could be applied in W-LEDs owing to its satisfactory luminescence intensity and CIE values. But the major problem

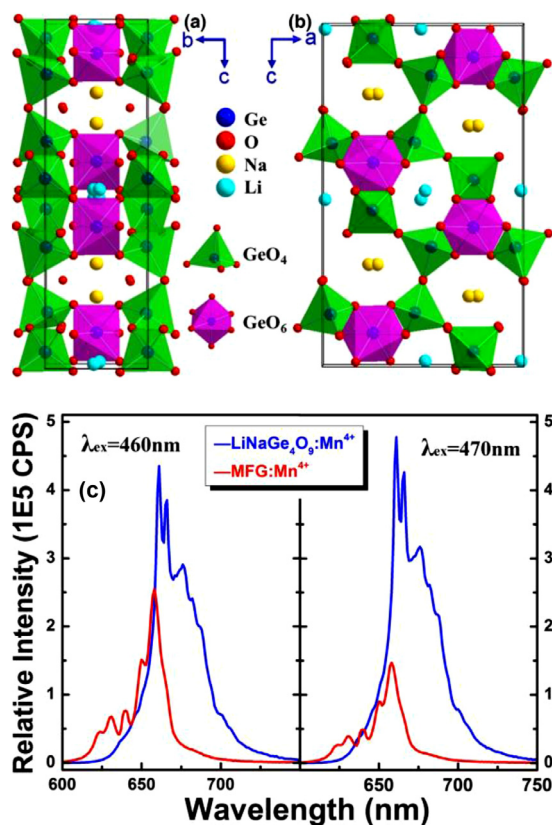


Fig. 9. (a) and (b) Crystal structure of $\text{LiNaGe}_4\text{O}_9:0.05\%\text{Mn}^{4+}$ (orthorhombic- $Pcca$) viewed along a and b ; (c) Comparison of PL emission intensities of $\text{LiNaGe}_4\text{O}_9:\text{Mn}^{4+}$ and $\text{MFG}:\text{Mn}^{4+}$. Reproduced with permission from Ref. [89].

depicted for this phosphor is its low thermal quenching. The thermal quenching property has been explained using the configurational coordinate diagram, where at high temperature the electrons absorb an energy from the lattice vibration and come back to the ground state through a non-radiative transition. The easy path provided by the charge transfer band $\text{Mn}^{4+}-\text{O}^{2-}$ is the main reason for the lower thermal stability of the sample [90].

Li et al. predicted the energy levels of Mn^{4+} ion in the same phosphor by crystal field calculation based on the ECM which is well matching with the phosphor prepared using similar experimental conditions [91]. The calculation result shows the red emission peak at 663 nm and 450–470 nm wavelength range of blue absorption. From the calculation, both $\text{Ge}1$ and $\text{Ge}2$ octahedral sites are found to be favourable for the Mn^{4+} . Here an important observation made from the structural analysis is that there are two octahedral germanium sites and that the mean bond lengths of $\text{Ge}-\text{O}$ are 1.8937 Å and 1.8988 Å [91,92]. These shorter bond lengths indicate the higher covalence around Mn^{4+} , which is favourable for longer emission and excitation wavelength and this is also matching with the experimental results [91].

Li et al. prepared partial alkali substituted $\text{K}_x\text{Rb}_{2-x}\text{Ge}_4\text{O}_9:0.02\%\text{Mn}^{4+}$ to enhance its photoluminescent properties [45]. Structural analysis of $\text{Rb}_2\text{Ge}_4\text{O}_9:\text{Mn}^{4+}$ suggested that Mn^{4+} ions prefer to occupy GeO_6 octahedral sites, which are surrounded by GeO_4 tetrahedrons. Surrounding GeO_4 tetrahedrons can favour structural isolation of Mn^{4+} from local perturbations and also it can weaker interaction amongst Mn^{4+} ions. Due to the partial substitution of K for Rb , a slight shifting of X-ray diffraction (XRD) peaks towards a higher diffraction angle and a decrease in interplanar spacing have also been observed. The contraction of crystal lattice upon the substitution of K^+ ion indicates the

presence of higher crystal field strength. From the PL analysis, it is observed that $\text{Rb}_2\text{Ge}_4\text{O}_9:\text{Mn}^{4+}$ shows a comparatively lower intensity than $\text{K}_2\text{Ge}_4\text{O}_9:\text{Mn}^{4+}$ but the partial substitution of K in this compound helps to increase the luminous intensity. It is observed that the $\text{K}_{1.5}\text{Rb}_{0.5}\text{Ge}_8\text{O}_{18}:\text{Mn}^{4+}$ sample shows a significantly larger intensity than the $\text{K}_2\text{Ge}_4\text{O}_9:\text{Mn}^{4+}$ sample. The blue excitation peak observed for $\text{Rb}_2\text{Ge}_4\text{O}_9:\text{Mn}^{4+}$ shifts gradually from 480 nm to 462 nm with the increase of potassium content but no change in the UV excitation peak indicates that the incorporation of potassium content affects the ${}^4\text{T}_2$ energy level but not the ${}^4\text{T}_1$ energy level. This effect can be efficiently used for designing a new material having tailored blue excitation. The strongest emission peak of Mn^{4+} is shifted from 666 nm to 663 nm while moving from $\text{Rb}_2\text{Ge}_4\text{O}_9:\text{Mn}^{4+}$ to $\text{K}_{1.5}\text{Rb}_{0.5}\text{Ge}_8\text{O}_{18}:\text{Mn}^{4+}$. The presence of potassium increases the energy of the ${}^2\text{E}_g$ level because of the decreased covalency of the $\text{Mn}-\text{O}$ bond in MnO_6 octahedra since potassium ion possesses lower polarizability than Rb^+ ion. The emission lifetime is observed to increase gradually with potassium substitution. The quantum yield value of $\text{K}_{1.5}\text{Rb}_{0.5}\text{Ge}_8\text{O}_{18}:\text{Mn}^{4+}$ is higher than that of $\text{K}_2\text{Ge}_4\text{O}_9:\text{Mn}^{4+}$, and it is much greater than $\text{Rb}_2\text{Ge}_4\text{O}_9:\text{Mn}^{4+}$. The emission lifetime and thermal stability are also much shorter in $\text{Rb}_2\text{Ge}_4\text{O}_9:\text{Mn}^{4+}$ and it is found to be enhanced with the partial K^+ substitution [45].

A detailed study on the influence of alkali ions on the luminescence property of Mn^{4+} -activated $\text{MGe}_4\text{O}_9:\text{Mn}^{4+}$ ($M = \text{Li}_2, \text{Li Na}$, and K_2) as a function of various alkali ions has been carried out by Xue and co-workers [93]. They have also adopted a similar milder solid-state methodology for the syntheses of these samples. Apart from the already discussed results, the calculated D_q/B values for these three phosphors are found to be greater than 2.2 indicating that Mn^{4+} is experiencing a stronger crystal field. As the energy of the emission spectrum is mainly influenced by the nephelauxetic effect, their obtained β_1 value is found to be distinct for the three different phosphors showing that the nephelauxetic effect is varying with different phosphors according to the type of host. As expected, the phosphor having smaller ${}^2\text{E}_g$ value has smaller β_1 indicating the host experiencing comparatively strong nephelauxetic and emit lights in the lower wavelength region [93].

Another study on $\text{K}_2\text{Ge}_4\text{O}_9:\text{Mn}^{4+}$ and $\text{Rb}_2\text{Ge}_4\text{O}_9:\text{Mn}^{4+}$ phosphors has been carried out in order to get a clear insight on the dependence of their optical properties on the chemical compositions and the temperature [94]. In these germanates, Mn^{4+} ions occupy two germanate octahedral sites, but the $\text{Mn}-\text{O}$ bond length is dissimilar for these two sites. Usually, Mn^{4+} ions occupying $\text{Ge}-\text{O}$ sites with larger bond length experience smaller crystal field splitting and the corresponding ${}^4\text{T}_{2g}$ band locates at a lower energy region. Owing to the smaller $\text{Mn}-\text{O}$ distance in $\text{K}_2\text{Ge}_4\text{O}_9$ comparing to $\text{Rb}_2\text{Ge}_4\text{O}_9$ results in stronger crystal field splitting for $\text{K}_2\text{Ge}_4\text{O}_9$. Meanwhile, Mn^{4+} ions occupying a site with a smaller $\text{Mn}-\text{O}$ bond length show a higher thermal quenching temperature. As we know, the Racah parameter, B , is the measure of inter electronic repulsion in $3d$ orbitals, and the maximum value is achieved for free Mn^{4+} ions, which is equal to 1160 cm^{-1} . The redshift observed in the emission spectrum with increasing temperature may be due to the decrease of D_q , B , or C . But the magnitude of these parameters with temperature clearly shows that the value of B increases with the temperature while the decrease in D_q value is minor. These results strongly suggest that the redshift in the spectrum is due to the considerable decrease of C value with an increase in temperature. This shows the strong influence of Racah parameter C on the luminescent properties of these phosphors. The Racah parameters B and C can be related through the Slater-Condon parameters F_2 and F_4 [94].

$$B = F_2 - 5F_4 \quad \text{and} \quad C = 35F_4 \quad (17)$$

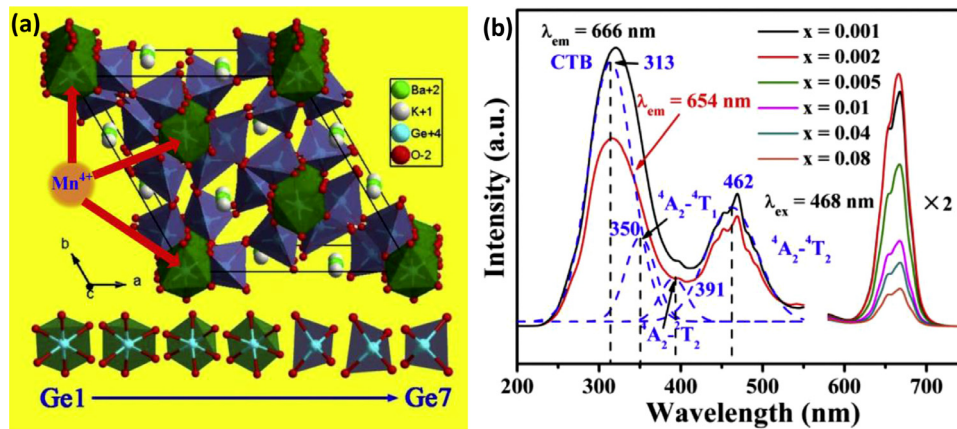


Fig. 10. (a) Crystal structure of $K_2BaGe_8O_{18}:Mn^{4+}$ (hexagonal-P3c1); (b) PL excitation and emission spectra of $K_2BaGe_8O_{18}:0.002Mn^{4+}$. Reproduced with permission from Ref. [66].

Here the parameters F_2 and F_4 describe the electrostatic interaction between the electrons in the unfilled shell of Mn^{4+} ions. Therefore, the covalent character of M–O bonds mainly affects the parameter F_2 . These two equations indicate that the decrease in F_4 is the reason for the decrease in the C value and the increase in the B value. However, it is quite difficult to generate a simple relation between B and C , which hinders the exact prediction of the position of the emission wavelength of these phosphors. In fact, the bond angle $Mn^{4+}-O-M^{n+}$ (M stands for neighbouring cations) has a strong influence on the parameter C and less effect on B . Brik et al. demonstrated a correlation between the energy position of the Mn^{4+} and the $Mn^{4+}-O^{2-}-M^{n+}$ bond angle in the materials possessing a perovskite structure [59]. A bond angle close to 180° results in a small value for C . Hence, a highly ionic host with a bond angle that deviates more from 180° B as well as C coefficients should have larger values resulting in a blue shift. In $K_2Ge_4O_9$ and $Rb_2Ge_4O_9$, the decrease in crystal field strength and increase in B value with the increase in temperature is due to the thermal expansion of the host which results in a reduction in the covalent interaction between Mn^{4+} and O^{2-} [94].

Li et al. reported a novel red-emitting $K_2BaGe_8O_{18}:0.002Mn^{4+}$ for W-LEDs application with an emission spectrum centred at 666 nm [66]. They adopted the conventional solid-state method for synthesis with a calcination temperature of $1050^\circ C$ for 6 h. The crystal structure of this compound consists of four octahedral Ge^{4+} sites ($Ge1-Ge4$) and three tetrahedral Ge^{4+} sites ($Ge5-Ge7$) (Fig. 10(a)). However, the PL origin is only due to the occupancy of Mn^{4+} at octahedral Ge sites. Here the obtained excitation spectrum is deconvoluted into four Gaussian curves centred at 313 nm, 350 nm, 391 nm, and 462 nm and these are attributed to the $Mn^{4+}-O^{2-}$ charge transfer band, spin allowed ${}^4A_2 \rightarrow {}^4T_1$, spin forbidden ${}^4A_2 \rightarrow {}^2T_2$, and spin allowed ${}^4A_2 \rightarrow {}^4T_2$ transitions, respectively (Fig. 10(b)). To understand the energy transfer mechanism involved in the concentration quenching, critical distance has been calculated to 35.75 Å. As the exchange interaction plays a significant role only when the critical distance value is less than 5 Å, further evaluation was carried out wherein the dominant energy transfer mechanism is caused by the electric dipole-dipole interactions. While increasing the Mn^{4+} concentrations from the optimum leads to the reduction of emission lifetime, which implies the faster decay of the emission because of the energy transfer amongst the $Mn^{4+}-Mn^{4+}$ pairs. The crystal field analysis is also carried out and the obtained value of Dq/B (3.31) is high enough since Mn^{4+} ions experience a stronger crystal field in the GeO_6 octahedra compared to other germanates. As the ${}^2E_g \rightarrow {}^4A_{2g}$ transition depends mainly on the nephelauxetic effect rather than on

the strength of the crystal, the nephelauxetic ratio (0.9604) was also estimated [66].

Cao et al. introduced two red-emitting phosphors $Li_2MgGeO_4:0.004Mn^{4+}$ and $K_2MgGeO_4:0.004Mn^{4+}$ and found that the former one has greater intensity while the latter one easily deliquesces at room temperature [95,96]. The shift in the emission position between these phosphors may be attributed to the difference in the ionic radii of Li^+ and K^+ [95]. Another novel deep red-emitting phosphor $Li_3RbGe_8O_{18}:0.005Mn^{4+}$ was reported by Singh and co-workers which shows better emission intensity greater than other available alkali tetra germanate hosts [6]. Here a combinatorial chemistry approach is used for finding the best emitting phosphors amongst A–Ge–O systems where A can be alkali metals such as Li, Rb, K, or their combination. At first, the ratio between A:Ge was fixed as 2:4, then 21 compositions based on this ratio were prepared as shown in Fig. 11(a) and studies were extended with four other ratios (A: Ge = 2.25:4, 2.5:4, 2.75:4, 3:4). Then out of the total 105 prepared samples, the sample $Li_3RbGe_8O_{18}:Mn^{4+}$ was found to show maximum emission intensity Fig. 11(b). The crystal structure of $Li_3RbGe_8O_{18}:Mn^{4+}$ shown in Fig. 11(c) consists of GeO_4 tetrahedra and GeO_6 octahedra. While the bond length of all Ge–O bonds in the GeO_6 octahedra are identical, two values are observed for the bond length of Ge–O bonds in the GeO_4 tetrahedra.

Although its emission intensity is observed to be lower than $K_2SiF_6:Mn^{4+}$ as shown in Fig. 11(d), its PL spectrum falls in the deep-red region [6]. Recently a novel deep red-emitting phosphor $Li_3Cs_{1-y}Rb_yGe_8O_{18}:0.01Mn^{4+}$ was also prepared using a similar methodology as described for the $Li_3RbGe_8O_{18}:0.005Mn^{4+}$ sample [97]. The PL intensity of $Li_3Cs_{1-y}Rb_yGe_8O_{18}:0.01Mn^{4+}$ phosphor increased to about 1.75 times compared to its corresponding rubidium phosphor, while its internal quantum efficiency is also increased by 1.57 times [97].

3.2. Alkaline-earth metal-based germanate systems

Xue and co-workers discovered a long persistent phosphor $Mg_2GeO_4:0.001Mn^{4+}$ and reported its long glow luminescence properties [98]. The emission of the $Mg_2GeO_4:0.001Mn^{4+}$ lasted for 30 min, which can be observed with the naked eye. This phosphor is a well-suited deep red long-lasting or storage phosphor for many applications. The persistence luminescence of this phosphor is enhanced by the substitution of Ln^{3+} ions ($Ln^{3+} = Pr^{3+}, Er^{3+}, Yb^{3+},$ and Nd^{3+}) at the Mg^{2+} sites. The addition of these Ln^{3+} ions with larger ionic radii (as compared to the Mg^{2+}) caused cationic distortions which create some additional defects. Amongst the var-

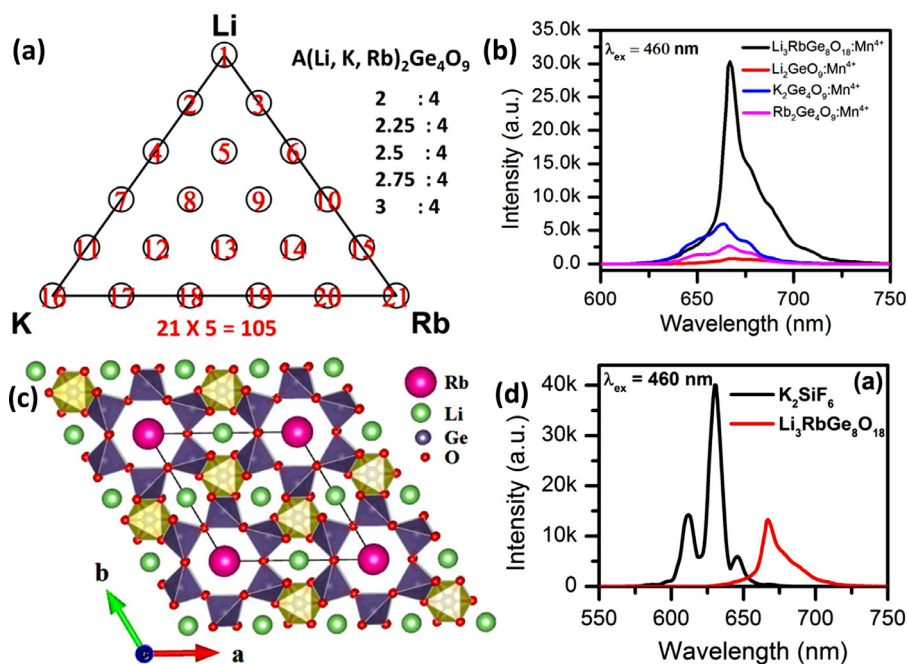


Fig. 11. (a) Design of the phosphor-composition search space; (b) Comparison of PL emission spectra of $\text{Li}_3\text{RbGe}_8\text{O}_{18}:\text{0.005Mn}^{4+}$ with $\text{Li}_2\text{Ge}_4\text{O}_9:\text{Mn}^{4+}$, $\text{K}_2\text{Ge}_4\text{O}_9:\text{Mn}^{4+}$ and $\text{Rb}_2\text{Ge}_4\text{O}_9:\text{Mn}^{4+}$; (c) Crystal structure of $\text{Li}_3\text{RbGe}_8\text{O}_{18}$ (trigonal-P31m); (d) Comparison of PL emission spectra of $\text{Li}_3\text{RbGe}_8\text{O}_{18}:\text{0.005Mn}^{4+}$ with $\text{K}_2\text{SiF}_6:\text{Mn}^{4+}$. Reproduced with permission from Ref. [6].

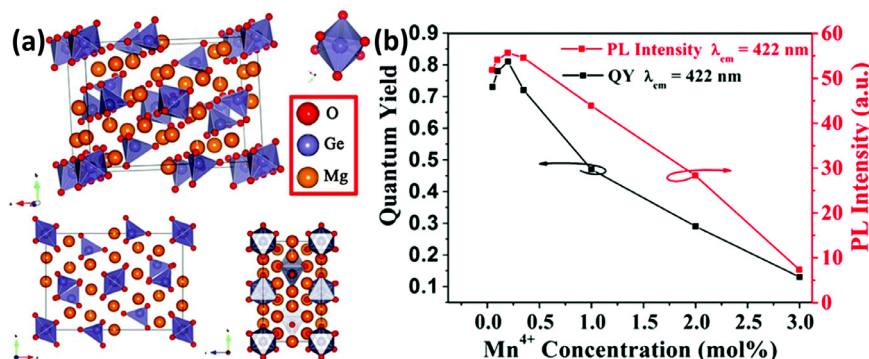


Fig. 12. (a) Crystal structure of $\text{Mg}_{14}\text{Ge}_5(1-0.2\%)\text{O}_{24}:\text{0.2\%Mn}^{4+}$ (orthorhombic-Pbam); (b) The change of emission intensity and quantum yields as a function of Mn^{4+} concentration. Reproduced with permission from Ref. [80].

ious co-doped samples, the afterglow emission from the phosphor composition of $\text{Mg}_2\text{GeO}_4:\text{0.001Mn}^{4+},\text{0.005Yb}^{3+}$ lasts for 2 h. The performance of the persistent or afterglow emission depends highly on the carriers captured in the trapping centres. Compare to other co-doped samples, the trapping centres introduced by Yb^{3+} ions in $\text{Mg}_2\text{GeO}_4:\text{0.001Mn}^{4+},\text{0.005Yb}^{3+}$ significantly enhanced the persistence behaviour of this composition, and making this material good for room temperature long afterglow (LAG) performance. Here the substitution of Yb^{3+} ions in the Mg^{2+} sites may lead to the formation of defects and the positive defects are acting as the electron traps whereas the negative defects act as the hole traps [98].

Liang et al. reported $\text{Mg}_{14}\text{Ge}_5(1-0.2\%)\text{O}_{24}:\text{0.2\%Mn}^{4+}$ phosphor having a high quantum yield of 81% [80]. Crystal structure analysis of this compound revealed that the Ge^{4+} ions occupied two tetrahedral and one octahedral site. The octahedral site occupies the centre of lattice faces as well as the vertex of the crystal lattice (Fig. 12(a)). Further, these octahedrons are connected to each other by sharing the same vertices, and Mn^{4+} ions occupy these six coordinated octahedral sites and act as the luminescence centres. As seen from Fig. 12(b), the highest PL intensity, as well as

quantum yield is reported for 1 mol% Mn^{4+} -doped $\text{Mg}_{14}\text{Ge}_5\text{O}_{24}$ phosphor. This is because of the fact that this composition possesses high crystallinity without any defects and negligible lattice distortion due to well-matched ionic radii and the charge between Ge^{4+} and Mn^{4+} . Meanwhile, this composition also exhibited appreciable emission intensity at elevated temperatures as it maintained 64% PL intensity at 60 °C relative to the PL intensity at 20 °C [80].

The emission intensity of this phosphor is enhanced by Zn^{2+} substitution in the Mg^{2+} site since this substitution makes some ionic rearrangement in the crystal. The difference in ionic radii between Zn^{2+} and Mg^{2+} leads to the lattice distortion of the crystal [99]. Q. Huang et al. reported Bi^{3+} and Mn^{4+} co-doped $\text{Mg}_{14}\text{Ge}_5\text{O}_{24}$ phosphor for optical agriculture application [100]. Comparing with the single Mn^{4+} doped phosphor, the Bi^{3+} co-doped one has enhanced emission because of the energy transfer mechanism involved between Bi^{3+} and Mn^{4+} [100]. Another detailed study on this phosphor was carried out by Liang and co-workers who substituted cations such as Ti^{4+} , Sn^{4+} , and Si^{4+} for the Ge^{4+} site since the cation substitution is the better way to tune or enhance the emission in matrix sensitive activator such as Mn^{4+} doped phosphors [101]. In the PL emission spec-

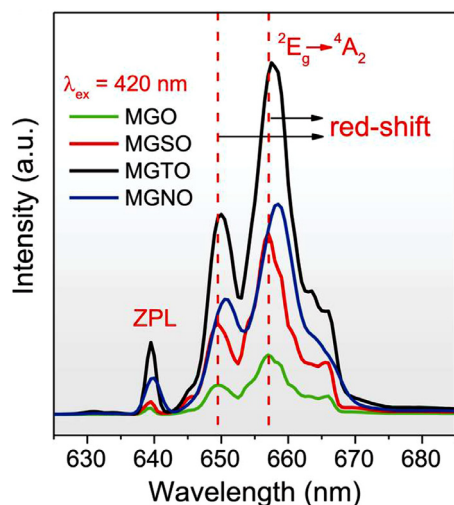


Fig. 13. Low-temperature PL emission spectra of MGO ($\text{Mg}_{14}\text{Ge}_5\text{O}_{24}:\text{Mn}^{4+}$) and cation substituted MGSO ($\text{Mg}_{14}\text{Ge}_5\text{O}_{24}:\text{Mn}^{4+}, \text{Si}^{4+}$), MGTO ($\text{Mg}_{14}\text{Ge}_5\text{O}_{24}:\text{Mn}^{4+}, \text{Ti}^{4+}$), and MGNO ($\text{Mg}_{14}\text{Ge}_5\text{O}_{24}:\text{Mn}^{4+}, \text{Sn}^{4+}$) samples. Reproduced with permission from Ref. [101].

tra, the peak located at 639 nm is identified as the ZPL. The peaks located at lower energy (above 639 nm) are the Stokes shift emission peak whereas the peak located at higher energy (below 639 nm) is the anti-Stokes shift emission peak. The Ti^{4+} substituted $\text{Mg}_{14}\text{Ge}_4.5\text{Ti}_{0.5}\text{O}_{24}:\text{Mn}^{4+}$ has higher emission intensity which is about 2.49 times greater than the $\text{Mg}_{14}\text{Ge}_5\text{O}_{24}:\text{Mn}^{4+}$. The addition of these cations leads to the formation of energy or electron trapping defects which helps in increasing the emission intensity. The change in the intensity of the ZPL is also observed with the cationic substitution. The ZPL is very sensitive to lattice distortion hence, the degree of lattice distortion is calculated by the polyhedron distortion index. The quantum yield of the optimized $\text{Mg}_{14}\text{Ge}_4.5\text{Ti}_{0.5}\text{O}_{24}:\text{Mn}^{4+}$ sample is 94% which could maintain up to 85% of the initial intensity at 473 K.

The low-temperature emission spectrum of $\text{Mg}_{14}\text{Ge}_5\text{O}_{24}:\text{Mn}^{4+}$ with cation substitution and without cation substitution was carried out at 6.9 K (Fig. 13). Here the emission intensity gets significantly increased manifolds with Ti^{4+} and Sn^{4+} substitution while comparing with PL spectra recorded at room temperature. Moreover, the substitution of the three cations (Ti^{4+} , Sn^{4+} , and Si^{4+}) leads to a slight redshift in their emission peaks, and the shifting increases with the increase in ionic radii of cations since these substitutions weaken the crystal field strength. The crystal field strength Dq has an inverse relation ($Dq = Ze^2r^4/6R^5$) between the bond length (R) of the central ion with the ligand [101]. Here the XRD refinement result indicates that with an increase in ionic radii of cations, the bond length is also found to be increased which weakens the crystal field strength resulting in a slight shift (red-shift) in their emission peaks [101].

Another class of alkaline-earth based germanate material is $\text{Ba}_2\text{GeO}_4:0.006\text{Mn}^{4+}$ [102]. Owing to its deep red-emitting ability peaking at 667 nm, $\text{Ba}_2\text{GeO}_4:0.006\text{Mn}^{4+}$ can be used as a red LED for indoor plant cultivation. This wavelength range is very close to the absorption peaks of the chlorophyll, and therefore suitable for the photosynthesis and photoperiodic effects of indoor plants. A novel thermally stable red-emitting $\text{Ba}_2\text{TiGe}_2\text{O}_8:0.006\text{Mn}^{4+}$ is also reported by Cao and co-workers for plant growth application [103]. In this phosphor structure, a Ba^{2+} ion combines with the eight oxygens to form the BaO_8 polyhedral, whereas a Ti^{4+} ion combines with the five oxygens to form the TiO_5 polyhedral. On the other hand, a Ge^{4+} ion combines with four oxygens as well as with six oxygens to form GeO_4 tetrahedra and GeO_6 octahedra, respectively.

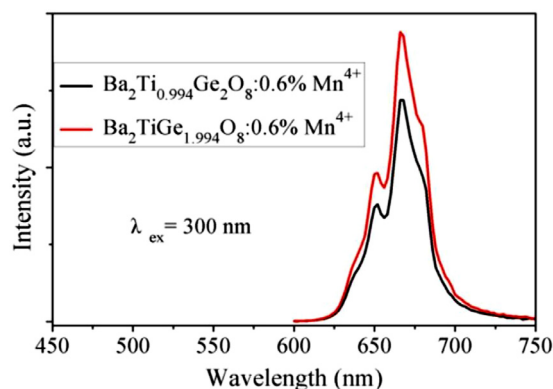


Fig. 14. Comparison of PL emission spectra of $\text{Ba}_2\text{Ti}_{0.994}\text{Ge}_2\text{O}_8:0.006\text{Mn}^{4+}$ and $\text{Ba}_2\text{TiGe}_{1.994}\text{O}_8:0.006\text{Mn}^{4+}$. Reproduced with permission from Ref. [103].

Importantly, Mn^{4+} ions are expected to occupy the Ge^{4+} site in the GeO_6 octahedra. To confirm this, Mn^{4+} has been doped into two different sites Ge^{4+} and Ti^{4+} separately. It is observed that Mn^{4+} ions occupied the Ge^{4+} sites have greater intensity showing the site suitability of Mn^{4+} in GeO_6 octahedra (Fig. 14) [103].

Lu et al. reported deep red-emitting double perovskite $\text{Ba}_2\text{MgGe}_2\text{O}_7:0.013\text{Mn}^{4+}$ phosphors prepared by a conventional solid-state methodology [104]. These phosphors show a strong red emission band centred at 660 nm, while the maximum emission intensity is observed at 0.013 mol of Mn^{4+} concentration. The dipole-dipole interaction amongst the Mn^{4+} ions led to luminescence quenching [104]. Fu et al. reported $\text{BaAl}_2\text{Ge}_2\text{O}_8:0.001\text{Mn}^{4+}$ phosphors for the plant growth application [105]. In this composition, Mn^{4+} ions occupy either Al^{3+} or Ge^{4+} sites in the AlO_4 and GeO_4 tetrahedra. The results of temperature-dependence emission spectra and the calculated activation energy ($\Delta E = 0.36$ eV) suggested that this phosphor composition is thermally stable [105].

Two alkaline-earth metal-based materials, $\text{SrGe}_4\text{O}_9:0.005\text{Mn}^{4+}$ and $\text{BaGe}_4\text{O}_9:0.005\text{Mn}^{4+}$ have been reported by Liang and co-workers for W-LED applications [106]. The crystal structure of these hosts has a great impact on their luminescence properties. Both BaGe_4O_9 and SrGe_4O_9 matrices are isostructural and consist of three different types of coordination environments: BaO_8 polyhedral, GeO_4 tetrahedral, and GeO_6 octahedral. The GeO_4 tetrahedra and GeO_6 octahedra are connected, and Mn^{4+} ions are occupying the Ge^{4+} sites of GeO_6 octahedra. As observed from the PL analysis, the emission intensity of $\text{BaGe}_4\text{O}_9:0.005\text{Mn}^{4+}$ is higher than that of the $\text{SrGe}_4\text{O}_9:0.005\text{Mn}^{4+}$ sample. Even though SrGe_4O_9 and BaGe_4O_9 are isostructural, the excitation peak position and shape of their emission spectra are different. This observation can be attributed to the change in the microstructure around Mn^{4+} ions, which might be occurred due to the difference in ionic radii between Ba^{2+} and Sr^{2+} . Hence the crystal field strength and nephelauxetic effect may also be different for these two phosphors leading to the aforementioned difference in their spectra. Meanwhile, the PL emission intensities of $\text{BaGe}_4\text{O}_9:0.005\text{Mn}^{4+}$ and $\text{SrGe}_4\text{O}_9:0.005\text{Mn}^{4+}$ are observed to reduce half of the room temperature PL intensity at 180 °C and 100 °C, respectively, indicated that both phosphors have appreciable thermal stability. However, the absolute quantum efficiency of these phosphors is not even higher than 50 [106].

Zhang et al. carried out the detailed crystal field studies on $\text{BaGe}_4\text{O}_9:0.005\text{Mn}^{4+}$, and the obtained $Dq/B = 2.7$ value indicates that Mn^{4+} ions experience a strong crystal field in this host [107]. The temperature-dependant PL analysis, including the low-temperature PL studies, is also carried out (Fig. 15). The change in the PL excitation spectra at a temperature greater than 300 K is

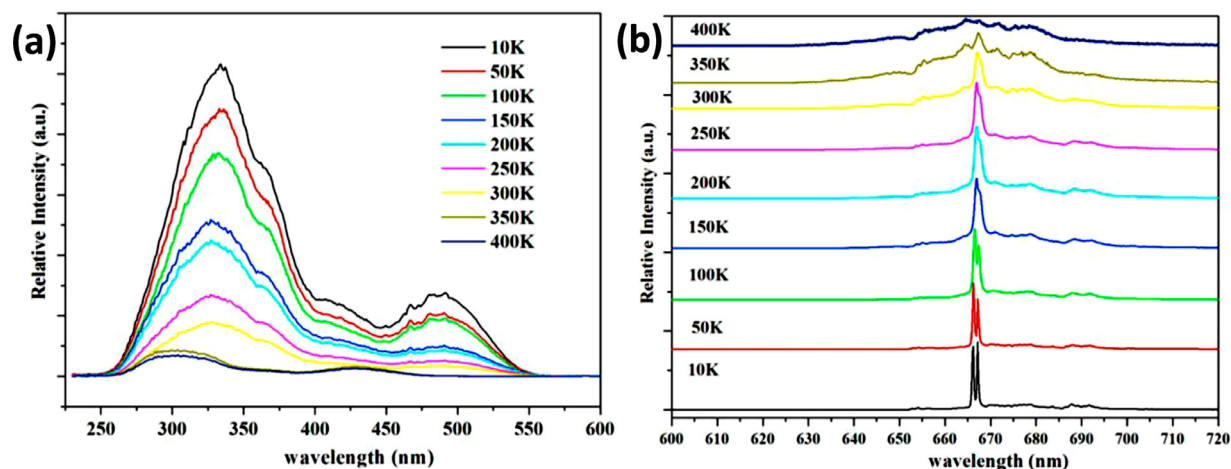


Fig. 15. The temperature dependent PL (a) excitation, and (b) emission spectra of BaGe₄O₉:0.005Mn⁴⁺. Reproduced with permission from Ref. [107].

attributed to the activation of vibronic modes in the luminescence centres. While the PL intensity is found to be increasing with the decrease in temperatures. From the PL emission spectra, surprisingly, the ZPL identified at 666 nm has a relatively strong intensity over the temperature range of 10–300 K. No spectral shift is observed with temperature variation, but the peaks get broadened while increasing the temperature from 10 to 400 K. The broadening of peaks with temperature manifests the involvement of phonon in these transitions. The visibility of the ZPL is very much sensitive to the local symmetry of Mn⁴⁺ ions. The peak centred at 666 nm can be ascribed to the ZPL of the transition at the C₃ site since this transition is much stronger than the ZPL of the transition at the centrosymmetric D₃ site. At an ultra-low temperature of 10 K, the emission peak at 666 nm split into two peaks which may be appeared due to the formation of Kramer's doublets since Mn⁴⁺ ion belongs to the d³ system [107].

Another Sr-based novel Sr₂MgGe₂O₇:0.007Mn⁴⁺ phosphor is reported by Chen and co-workers [108]. The crystal structure of this phosphor consists of MgO₄ tetrahedra and Ge₂O₇ double tetrahedra which are connected through oxygen. It is believed that Mn⁴⁺ ions occupy the Ge⁴⁺ sites in Ge₂O₇ double tetrahedra. The crystal field studies show that the Dq/B value is approximately equal to 2.86 showing that Mn⁴⁺ experiences a strong crystal field, and the calculated nephelauxetic ratio is 0.9747. Also, Sr₂MgGe₂O₇:0.007Mn⁴⁺ phosphor could maintain 60.3% of the room temperature emission intensity at 145 °C [108].

3.3. Lanthanum-based germanate systems

The reports on lanthanum-based germanate phosphors are comparatively less numerous. The double perovskite La₂MgGeO₆:Mn⁴⁺ is a long persisting germanate producing deep red emission centred at 708 nm under UV excitation [109]. The crystal structural analysis of this compound reveals that a La³⁺ ion is coordinated with 12 oxygen atoms. Although there exist both GeO₆ and MgO₆ octahedral, Mn⁴⁺ ions prefer GeO₆ octahedral sites mostly. The alternatively arranged GeO₆ and MgO₆ octahedral help in increasing the distance between Mn⁴⁺ ions, owing to which intense deep red emission is observed. Based on the value of Dq/B (2.67), it is concluded that Mn⁴⁺ ions are experiencing a strong crystal field in the above host [109].

Another lanthanum-based germanate system is La₃GaGe₅O₁₆:0.0025Mn⁴⁺, which can also be efficiently used in phosphor-converted W-LEDs [110]. The crystal structure of this phosphor consists of GeO₆ octahedral, GeO₄ tetrahedra, and GaO₄ tetrahedra (Fig. 16(a)). Each octahedron is connected to six tetra-

hedrons while each tetrahedron is connected to two octahedrons, thereby forming the chains of composition [Ge(GaGeO₄)₃]. The PLE spectrum recorded at 659 nm shows three excitation bands originating from ⁴A_{2g} → ⁴T_{1g}, ²T_{2g}, ⁴T_{2g} transitions of Mn⁴⁺, while the PL spectrum recorded at 330 nm shows one sharp peak corresponds to the ²E_g → ⁴A_{2g} transitions of Mn⁴⁺ (Fig. 16(b)). From the low-temperature PL analysis (Fig. 16(c)), two sharper peaks named B and D with one shoulder peak C, are observed at a temperature of 10 K. The intensity of these peaks gets reduced with the increase in temperature. However, the intensity of the anti-Stokes shoulder peak A gets increased with the increase in temperature. This abnormality is due to the thermal vibration in the host. Since the ²E_g → ⁴A_{2g} transition is spin forbidden, therefore, the ²E_g state life time is rather long. Because of the increase in temperature and the thermal vibration, the electrons are coupled to the lattice. The electrons can jump from the lower vibrational energy level to higher and thereby making the balance in electron distribution in these two levels [110]. Because of this, the shoulder peak appears and grows with the increase in temperature. But the PL intensity of other peaks decreases with an increase in temperature.

3.4. Non-Ge⁴⁺ site occupancy of germanates

There are some other germanate phosphors where the Ge sites may not accommodate Mn⁴⁺ ions. Mg₃Ga₂GeO₈:0.005Mn⁴⁺ is one of the best examples of such phosphors [111]. Since Mn⁴⁺ ions stabilized in the octahedral environment. Herein, Mn⁴⁺ ions prefer to occupy octahedral sites provided by Mg²⁺ and Ga³⁺ ions instead of the tetrahedral sites of Ge⁴⁺ ions (Fig. 17(a)). The variation in PL emission intensity with different Mn⁴⁺ sources doped in different sites is shown in Fig. 17(b), which ascertained the occupancy of the Mn⁴⁺ at Mg²⁺/Ga³⁺ sites [111]. In addition, maximum emission intensity is seen when the source of the activator ion is MnO₂. This observation reveals the octahedral preference of Mn⁴⁺ ions, and also indicates that Mn⁴⁺ ions have high crystal field stabilization energy in the octahedral environment. Cao et al. reported a deep red-emitting LiRGe₂O₆:0.006Mn⁴⁺ (R = Al or Ga) composition where Mn⁴⁺ ions occupy the octahedral sites provided by Al³⁺ and Ga³⁺ ions. The emission intensity of the LiAlGe₂O₆:0.006Mn⁴⁺ and LiGaGe₂O₆:0.006Mn⁴⁺ are found to be different. After the occupation of the Mn⁴⁺ ions in Al³⁺ and Ga³⁺ sites of the host lattice, the bond of Mn-O in the GaO₆ octahedral is become stronger than that in the AlO₆ octahedral due to the different ionic radii of Al³⁺ and Ga³⁺ ions. Due to this, the PL in-

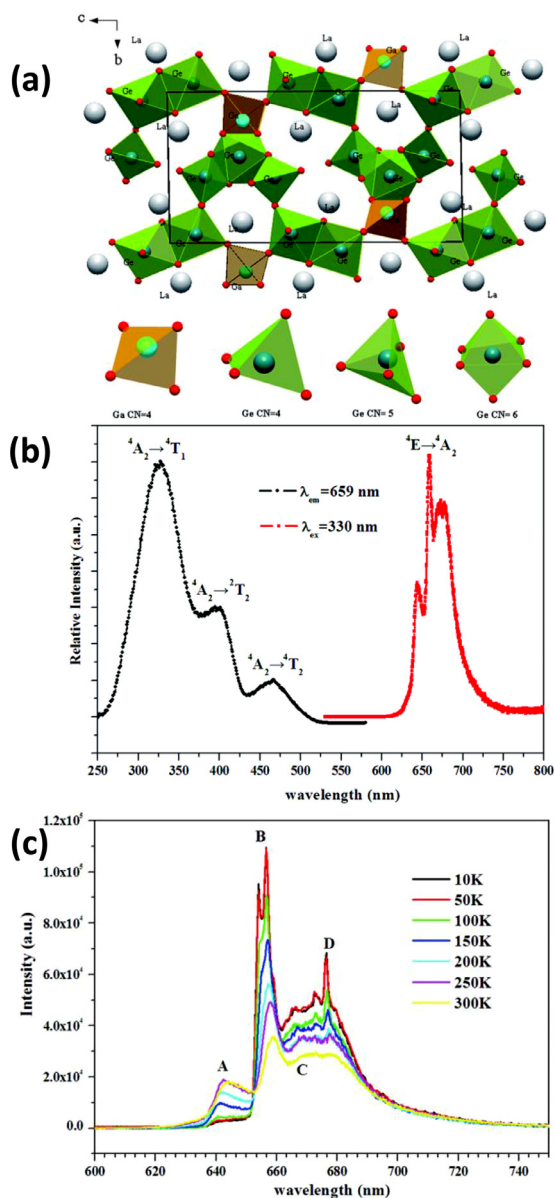


Fig. 16. (a) Crystal structure of $\text{La}_3\text{GaGe}_5\text{O}_{16}:0.0025\text{Mn}^{4+}$ (trigonal-P321); (b) PL excitation and emission spectra; (c) Low temperature PL of $\text{La}_3\text{GaGe}_5\text{O}_{16}:0.0025\text{Mn}^{4+}$ phosphor. Reproduced with permission from Ref. [110].

tensity of $\text{LiAlGe}_2\text{O}_6:0.006\text{Mn}^{4+}$ is found to be greater than that of $\text{LiGaGe}_2\text{O}_6:0.006\text{Mn}^{4+}$ under UV excitations [112].

Another reported germanate is $\text{Mg}_7\text{Ga}_2\text{GeO}_{12}:\text{Mn}^{4+}$, where Mn^{4+} ions prefer Ga^{3+} sites [113]. In this host, Mn^{4+} ions conveniently occupy Mg^{2+} , Ga^{3+} and Ge^{4+} sites of $\text{Mg}_7\text{Ga}_2\text{GeO}_{12}:0.005\text{Mn}^{4+}$ and it was found that Mn^{4+} doped in the Ga^{3+} site has higher emission intensity as compared to when it is doped at the Mg^{2+} site. Further, this phosphor can be efficiently excited by blue light. In the case of $\text{Mg}_6\text{ZnGeGa}_2\text{O}_{12}:0.01\text{Mn}^{4+}$ phosphor, the XRD, as well as PL analysis reveals that Mn^{4+} ions occupy the octahedral ($\text{Mg}^{2+}/\text{Zn}^{2+}/\text{Ga}^{3+}$) sites [114]. This phosphor is a promising red-emitting candidate excited by near ultra-violet (NUV) chips [114]. Jansen et al. reported a novel $\text{Mg}_3\text{Y}_2\text{Ge}_3\text{O}_{12}:0.01\text{Mn}^{4+}, 0.015\text{Li}^+$ phosphor prepared by a sol-gel method [115]. Here, Mn^{4+} ions occupy the Mg^{2+} sites, and Li^+ is incorporated for charge compensation. This phosphor shows extraordinary thermal quenching behaviour since its $T_{1/2}$ value is above 800 K, which is greater than the thermal quenching temperature $T_{1/2}$ of red-emitting $\text{Mg}_{14}\text{Ge}_5\text{O}_{24}:\text{Mn}^{4+}$. Because of these properties, this phosphor is a potential red candidate in phosphor blends of high-power W-LEDs [115].

Dong et al. reported novel orange red-emitting $\text{Ca}_3\text{M}_2\text{Ge}_3\text{O}_{12}:\text{Mn}^{2+}, \text{Mn}^{4+}$ ($M = \text{Al}, \text{Ga}$) [116]. Here, Mn^{2+} ions occupying Ca^{2+} sites produce the orange emission, whereas Mn^{2+} and Mn^{4+} ions occupying $\text{Al}^{3+}/\text{Ga}^{3+}$ sites produce red and deep red emission [116]. Lingling et al. reported the PL of $\text{Mg}_2\text{Ti}_{0.65}\text{Ge}_{0.35}\text{O}_4:0.001\text{Mn}^{4+}$ by substituting Ge^{4+} ions in Ti^{4+} sites [117]. The incorporation of Ge^{4+} ions enhances the emission intensity. When Ge^{4+} is incorporated, there are two sites for Mn^{4+} to occupy and it is believed that replacement of Ge^{4+} by Ti^{4+} accelerates the translation of a greater number of TiO_6 octahedral to contorted GeO_6 octahedral and separation of adjacent TiO_6 octahedral. As a result of this, the distance between isolated Mn^{4+} ions as well as the $\text{Mn}^{4+}-\text{Mn}^{4+}$ distance enhanced, which can decrease the energy transfer rate in the host thereby increasing the PL intensity. The PL emission spectra and the crystal structure are shown in Fig. 18 [117].

4. Cr^{3+} -activated deep red-emitting germanate phosphors

Detailed description on the ionic configuration of Cr^{3+} ion and its related luminescence properties in the various host materials can be found in Refs. [31] and [32]. As we have already discussed in the introduction part, the studies on Cr^{3+} -activated phosphors are mainly taking place in oxide hosts owing to their admirable merits comparing to fluorides. In comparison with Mn^{4+} activated phosphors, the Cr^{3+} activated phosphors have some ad-

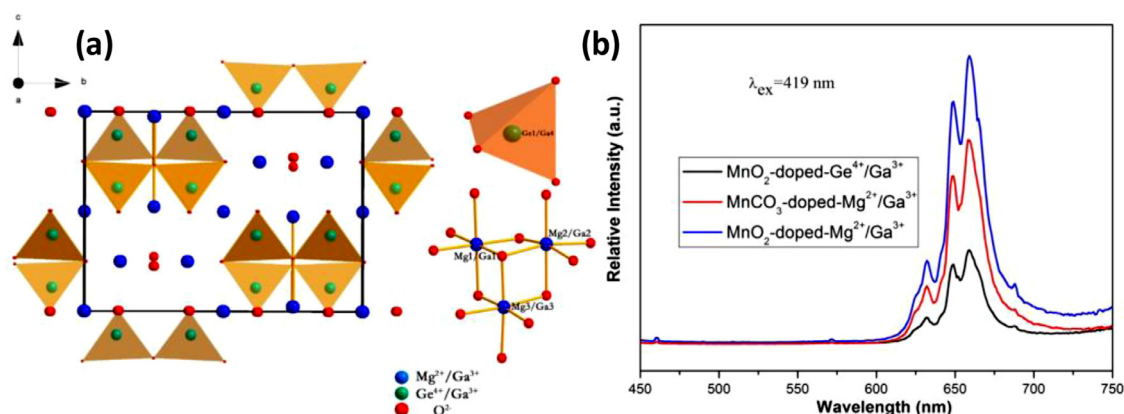


Fig. 17. (a) Crystal structure of $\text{Mg}_3\text{Ga}_2\text{GeO}_8$ (orthorhombic- Imma); (b) PL emission spectra of $\text{Mg}_3\text{Ga}_2\text{GeO}_{12}:0.005\text{Mn}^{4+}$ with different Mn^{4+} sources and different dopant sites. Reproduced with permission from Ref. [111].

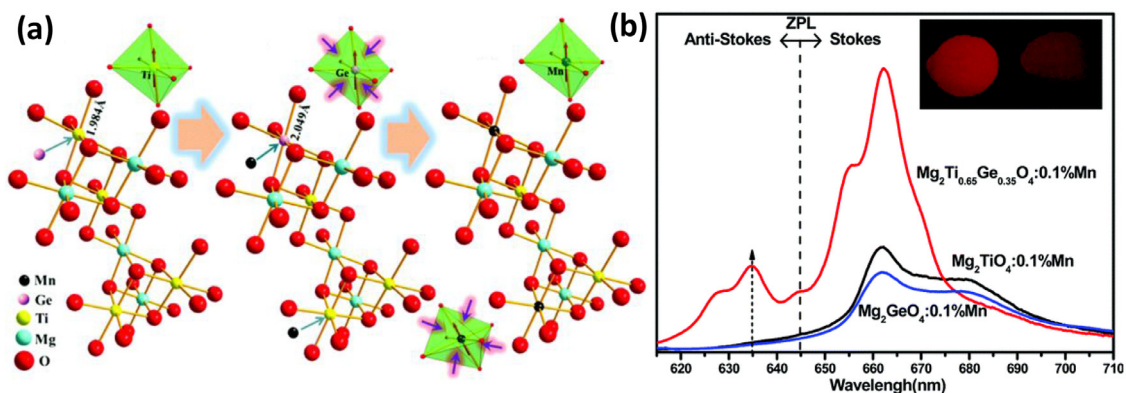


Fig. 18. (a) Crystal structure of $\text{Mg}_2\text{Ti}_{0.65}\text{Ge}_{0.35}\text{O}_4:0.001\text{Mn}^{4+}$ (cubic-Fd3m); (b) PL emission spectra showing the effect of Ge substitution. Reproduced with permission from Ref. [117].

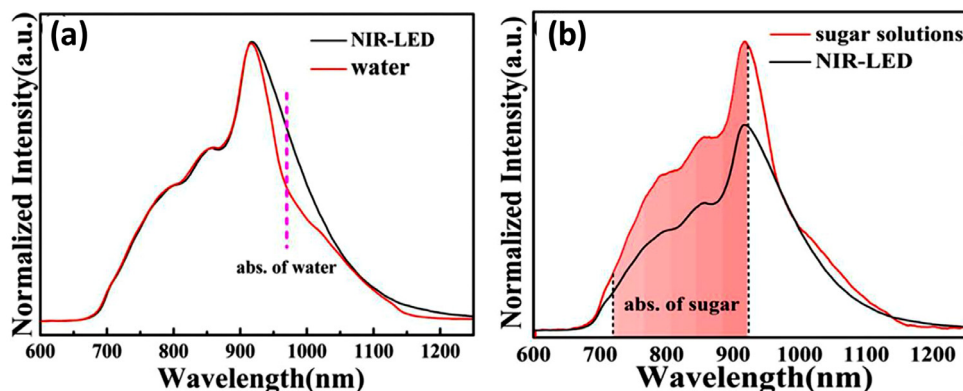


Fig. 19. (a) Normalized transmission spectra of NIR light after penetrating water and (b) sugar solutions. Reproduced with permission from Ref. [124].

vantages such as their capability in producing light in deep red and NIR region, long persistence, etc. Hence apart from the various display applications, these phosphors can extend their use in sensors, biomedical imaging, decoration, night vision surveillance, dark glow signage, security, etc. [118]. Most of the studies on Cr^{3+} -doped phosphors are based on gallates since Ga^{3+} can efficiently provide the octahedral site for Cr^{3+} because of their similar ionic radii and charge. The ionic radius of Cr^{3+} (Cr^{VI} : 0.615 Å) is quite close to the ionic radius of Ga^{3+} (Ga^{VI} : 0.620 Å) in an octahedral environment [47]. Although our area of consideration in this article is deep red-emitting phosphors, however, it is noteworthy to discuss the Cr^{3+} -doped NIR emitting phosphors. Some of the important NIR emitting gallates and gallo-germanates are $\text{Zn}_3\text{Ga}_2\text{GeO}_8:\text{Cr}^{3+}$ [119], $\text{ZnGa}_2\text{O}_4:0.005\text{Cr}^{3+}$ [120], $\text{Mg}_4\text{Ga}_4\text{Ge}_3\text{O}_{16}:0.005\text{Cr}^{3+}$ [121], and $\text{Ca}_3\text{Ga}_2\text{Ge}_3\text{O}_{12}:0.01\text{Cr}^{3+}$ [122].

Zhou et al. reported Cr^{3+} -doped NIR emitting gallo-germanate garnet $\text{La}_3\text{GaGe}_5\text{O}_{16}:0.03\text{Cr}^{3+}$ for the luminescent solar concentrator, which can convert the photons from sunlight to the required deep or NIR radiation [123]. Wang et al. reported Cr^{3+} -doped NIR emitting $\text{Mg}_3\text{Ga}_2\text{GeO}_8:0.05\text{Cr}^{3+}$ phosphor for light source application in food analysis [124]. This phosphor exhibits a broad emission band in the range of 650–1200 nm, which is matching with the overtones of vibration of molecules present in the food components, hence the details of water content or sugar content, as well as the damages in food materials, can be analysed by making use of these phosphors in the light source of food analyser (Fig. 19) [124].

Besides these NIR emitting phosphors, some of the efficient Cr^{3+} -activated deep red-emitting phosphors are $\text{MgY}_2\text{Al}_4\text{SiO}_{12}:0.02\text{Cr}^{3+}$ [125], $\text{Zn}(\text{GaAl})_2\text{O}_4:0.005\text{Cr}^{3+}, 0.01\text{Bi}^{3+}$

[65], $\text{MgGa}_2\text{O}_4:\text{Cr}^{3+}$ [126], etc. Chi et al. synthesized $\text{MgAl}_2\text{O}_4:0.012\text{Cr}^{3+}$ by co-precipitation method which produces deep red emission centred at 687 nm [14]. Further, a W-LED has fabricated by combining this phosphor with blue InGaN chip commercial $\text{YAG}:\text{Ce}^{3+}$, and the produced W-LED exhibited a CRI value of 3481 K and a CRI value of 78 [14]. Katayama et al. reported long persisting Cr^{3+} -doped deep red-emitting phosphor $\text{LaAlO}_3:0.005\text{Cr}^{3+}$ having emission band centred at 734 nm for *in-vivo* imaging application [127]. The intensity of this phosphor is found to be greater than Cr^{3+} -doped persistent phosphor $\text{ZnGa}_2\text{O}_4:\text{Cr}^{3+}$, which shows an emission peak at 694 nm. The afterglow properties and luminescence intensity of $\text{LaAlO}_3:0.005\text{Cr}^{3+}$ phosphors are found to increase with Sm^{3+} -doping [127]. There are different reports on the various types of Cr^{3+} activated phosphors but the focus of our review is deep red-emitting Cr^{3+} activated germanate phosphors. The reports on these categories of phosphors are comparatively less in number. Bai et al. prepared $\text{Ca}_3\text{Al}_2\text{Ge}_2\text{O}_{10}:0.07\text{Cr}^{3+}$ phosphor by a solid-state method and it shows a broad emission band in the range of 650–750 nm peaking at 697 nm [38]. The optimum concentration for Cr^{3+} in this phosphor is 0.07 mol. Bai et al. synthesized $\text{Zn}_3\text{Al}_2\text{Ge}_2\text{O}_{10}:0.01\text{Cr}^{3+}$ phosphor by using a solid-state methodology [128]. The heating condition required for the preparation of this sample in a box furnace is 1200 °C for 2.5 h. The phosphor can produce deep red emission in the range of 650–750 nm with an emission peak centred at 694 nm under the excitation of 400 nm (Fig. 20). Further, the introduction of Ca^{2+} ions in the Zn^{2+} sites of this phosphor could induce long afterglow properties and bluish-white light emission [128].

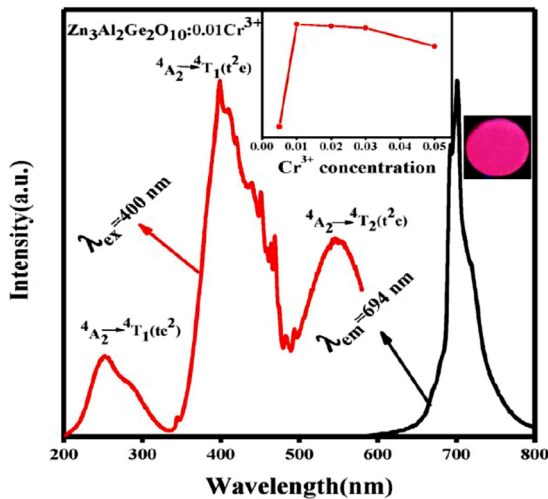


Fig. 20. PL excitation and emission spectrum of $\text{Zn}_3\text{Al}_2\text{Ge}_2\text{O}_{10}:0.01\text{Cr}^{3+}$. Reproduced with permission from Ref. [128].

5. Amplification of deep red emission

5.1. Effect of synthesis methods and particle morphology

Methods adopted for the synthesis of phosphors have a great impact on their luminescence properties and potential applications. Phosphors prepared through different methods can produce different structures such as spherical, core-shell, nanoflakes, etc., and these may have pure or tuneable emission properties [129]. As we already discussed the glass-ceramic routes were used for the synthesis of nanocrystals of $\text{Li}_2\text{Ge}_4\text{O}_9:\text{Mn}^{4+}$ and $\text{LiNaGe}_4\text{O}_9:\text{Mn}^{4+}$ [84,85,88]. Even though they could make samples even in the nano range, the phosphor $\text{LiNaGe}_4\text{O}_9:\text{Mn}^{4+}$ prepared by the solid-state reaction possesses greater colour purity as well as quantum yield compared to the sample prepared through the glass-ceramic route. The tetragermanate phase obtained for $\text{LiNaGe}_4\text{O}_9:\text{Mn}^{4+}$ through the glass-ceramic route contains more defects than the solid-state sample [88]. Suppression of defects that are acting as non-radiative centres during solid-state synthesis is the reason for improved quantum yield [84,85,88,97–102].

While discussing the effect of synthesis on deep red-emitting phosphor, the Mn^{4+} and Cr^{3+} sources have some relevance. The phosphor $\text{Mg}_3\text{Ga}_2\text{GeO}_8:0.005\text{Mn}^{4+}$ is prepared by using two different sources of Mn, which are MnCO_3 and MnO_2 . Then it is observed that phosphor prepared using MnO_2 has better intensity. In the MnCO_3 compound, Mn is divalent, and after calcination, many of the Mn^{2+} ions will not oxidize to Mn^{4+} , some may be just oxidized to Mn^{3+} . Hence the actual contribution of Mn^{4+} from MnCO_3 is less than MnO_2 . (Fig. 17(b)) [111]. In solid-state synthesis, fluxes can be used for lowering the sintering and reaction time along with improved crystallinity without making any reaction with raw materials. The lower melting point of flux compared to final calcination temperature can assure the liquid face during sintering which can further increase the mobility and homogeneity of solid reactants. The cationic radius of flux is large enough to avoid atomic substitution. The luminescence intensity and morphology of $\text{Sr}_2\text{MgAl}_{22}\text{O}_{36}:0.012\text{Mn}^{4+}$ phosphor are increased with the usage of flux H_3BO_3 since the addition of flux stimulate the ionic diffusion inducing enhanced red emission [130,131]. Most of the germanates mentioned in this article are prepared through the solid-state method. But this method requires higher calcination temperature, and the chances for forming impurity phases are relatively high. The red emission of these phosphors and their morphology can be improved by implementing the sol-gel technique with a

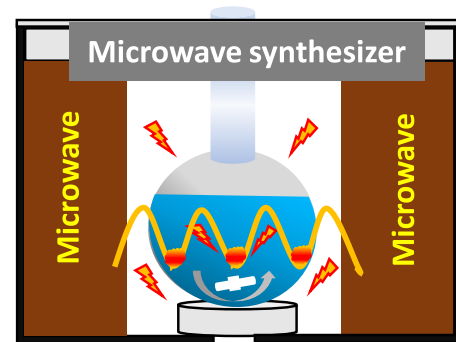


Fig. 21. Schematic representation of microwave-assisted sol-gel synthesis. Adapted from Ref. [133].

lower calcination time. $\text{Mg}_2\text{TiO}_4:\text{Mn}^{4+}$ is one of the best examples that we can provide since the sample prepared through the sol-gel technique shows 2.24-fold emission enhancement in comparison with the solid-state sample [129,132]. The microwave-assisted sol-gel technique is one method that we can suggest for red emission enhancement and nanoscale production of germanates. Our research group used the microwave-assisted sol-gel method efficiently to enhance the red emission of $\text{Li}_3\text{RbGe}_8\text{O}_{18}:0.005\text{Mn}^{4+}$ nanophosphor [133]. Here the raw materials were taken in the stoichiometric ratio. The carbonates (Li_2CO_3 , Rb_2CO_3 , and MnCO_3) were dissolved in HNO_3 to obtain their corresponding nitrates and then separate solutions of GeO_2 and citric acid were mixed into this solution. The obtained resultant solution was placed in a microwave at different temperatures and microwave power for optimization (Fig. 21). The microwave energy in the microwave-assisted method couples directly with the ions in the reaction medium. This results in effective internal volumetric heating, rapid and homogeneous heating of reaction medium, with minimal thermal variations. This method leads to uniform nucleation, producing uniform-sized crystalline nanoparticles with better performance.

Morphology has a great influence on photoluminescence property, and it is very important for some specific applications. Phosphor with spherical size can minimize the scattering, thereby elevating the luminescence properties. Also, phosphors with nanosize are highly desirable since particle with smaller size is preferred for higher resolution [80]. But the greater surface effects of the nanoparticle may reduce the luminescence efficiency since the unsaturated bonds on the surfaces are capable to quench the luminescence centres on or near the surface. Hence, a method that can be adapted for red emission enhancement for germanate, that we can suggest is the synthesis of nano phosphor with a core-shell structure. Here surface coating with the non-metals can be used for reducing the surface effects, or metal shells can be used to coat over the nanoparticle for metal enhanced luminescence. In the former case if we are using sensitizers in the shell additional luminescence enhancement may be visible. In the latter case, there may be an increased radiative transition and enhanced luminescence only if the distance between luminescence species and the metal surface is between 5 and 20 nm [134]. A combination of noble metal nanoparticles with luminescence species is collectively called plasmons. The oscillation of surface electrons in the nanoparticle can interact with the incident light leading to increased light absorption cross-section. Dolgov and co-workers prepared $\text{Mg}_2\text{TiO}_4:\text{Mn}^{4+}$ with core-shell $\text{Ag}@\text{SiO}_2$ nanoparticles, and the luminescence intensity is observed to increase due to the core-shell structure (Fig. 22) [135]. This approach can be used in the case of germanates.

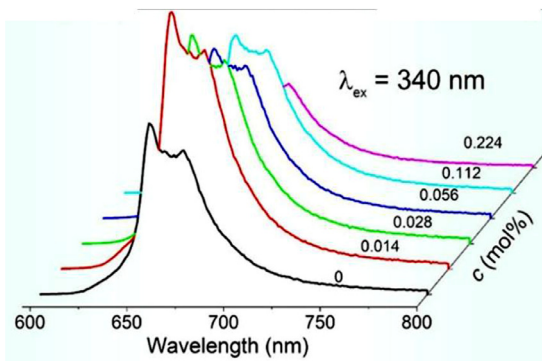


Fig. 22. Emission spectrum of $\text{Mg}_2\text{TiO}_4:\text{Mn}^{4+}$ for different concentration of $\text{Ag}@\text{SiO}_2$ nanoparticles having 40 nm Ag cores. Reproduced with permission from Ref. [135].

5.2. Cationic modifications and co-doping

It is known that Cr^{3+} and Mn^{4+} ions are host-sensitive activators and the phosphors activated by these ions include $3d-3d$ transitions. Hence, the cationic substitution is one of the most efficient methods utilized for improving and modulating the emission intensity of these phosphors [101]. It is already mentioned that partial substitution of K^+ in the Rb^+ site of $\text{Rb}_2\text{Ge}_4\text{O}_9:\text{Mn}^{4+}$ phosphor can lead to emission enhancement [45]. Also, the partial substitution of Rb^+ ions in the Cs^+ sites of $\text{Li}_3\text{CsGe}_8\text{O}_{18}:0.01\text{Mn}^{4+}$ phosphor improved its quantum efficiency from 37% to 55% [97]. The optimized sample with the most efficient optical properties is $\text{Li}_3\text{Cs}_{0.5}\text{Rb}_{0.5}\text{Ge}_8\text{O}_{18}:0.01\text{Mn}^{4+}$. Also, a slight red shift is observed in the emission spectra with Rb substitution which can be attributed to the local crystal structure variation and stronger crystal field strength with Rb substitution. Structural rigidity has a great role in luminescence property. Phosphor having greater structural rigidity shows greater emission. The substitution of Rb^+ in the Cs^+ site can alter the degree of distortion of $\text{Ge}(1)\text{O}_6$ octahedra where Mn^{4+} ions are going to be incorporated [97]. The change in the degree of distortion occurs because of the difference in the ionic radii of Rb^+ and Cs^+ . From the calculation of the degree of distortion of $\text{Ge}(1)\text{O}_6$ octahedra for different Rb substituted samples, the optimized sample $\text{Li}_3\text{Cs}_{0.5}\text{Rb}_{0.5}\text{Ge}_8\text{O}_{18}:0.01\text{Mn}^{4+}$ has the smallest value showing its high structural rigidity thus greater emission [97]. While discussing how cationic modification enhancing red emission, the Ti^{4+} , Sn^{4+} , and Si^{4+} substituted $\text{Mg}_{14}\text{Ge}_5\text{O}_{24}:\text{Mn}^{4+}$ phosphor is worth mentioning even though it is mentioned in the alkali earth metal-based germanates in Section 3.2. Here the substitution of Ti^{4+} at the Ge^{4+} site could enhance the emission intensity by 2.49 times. The enhancement of PL emission in the Ti^{4+} substituted phosphors can be attributed to the resonance effect. As we know the emission spectrum of Mn^{4+} is dominated by energy differences of some vibronic bands which involved allowed transition. During their vibronic transitions, the energy waves travelling in the lattice obey the periodic function given by [101],

$$I = 4I_0 \cos^2\left(\frac{\pi d}{\lambda}\right) \quad (18)$$

where I represent the relative intensity and d is the distance between Mn^{4+} ions. The increase in d value due to the cation substitution can alter the intensities of emission. In addition, the intensity of the emission peak will be higher when d is an integral multiple of λ . This phenomenon is called the resonance emission enhancement effect, which plays a significant role in the enhancement of emission intensity in Ti^{4+} ions substituted $\text{Mg}_{14}\text{Ge}_5\text{O}_{24}:\text{Mn}^{4+}$ phosphor [101].

Although in some cases, co-doping is carried out for charge compensation, this compensation is also found to be one of the efficient ways to tune the optical properties. In the case of $\text{Mg}_3\text{Ga}_2\text{GeO}_8:0.005\text{Mn}^{4+}$ phosphor, the emission intensity gets increased with the co-doping of Li^+ ions [111]. Here as already discussed Mn^{4+} ions are substituting at $\text{Mg}^{2+}/\text{Ga}^{3+}$ sites. If Mn^{4+} ions are substituting at the Mg^{2+} sites, then the extra positive charges developed could be balanced by co-doping of Li^+ ions at the Mg^{2+} sites leading to charge compensation as well as emission enhancement [111]. The persistent red luminescence of the Cr^{3+} activated $\text{ZnGa}_2\text{O}_4:0.005\text{Cr}^{3+}$ phosphor is enhanced by substituting the codopant Bi^{3+} at the Zn^{2+} site [120]. Similarly, the Sm^{3+} co-doping in $\text{LaAlO}_3:0.005\text{Cr}^{3+}$ could also enhance the persistent red emission [127]. Consequently, it can be concluded that co-doping and cationic modification is an efficient way of enhancing persistence and luminescence in Cr^{3+} and Mn^{4+} doped phosphors.

5.3. Energy transfer mechanisms

The energy transfer mechanism involved between the codopant and the activator-like Cr^{3+} and Mn^{4+} can also alter the intensity of red emission. In some cases, the codopant is found to act as a sensitizer. One of the best examples for the red emission enhancement via sensitizer is Bi^{3+} and Mn^{4+} co-doped $\text{Mg}_{14}\text{Ge}_5\text{O}_{24}$. Usually, Bi^{3+} ion is known for its metal-to-metal charge transfer (MMCT) character between its outer $6s^2$ orbital and host metal cations with d^0 or d^{10} system. The energy transfer mechanism involved between Bi^{3+} and Mn^{4+} is represented schematically (Fig. 23(a)). Under the excitation of UV light, the electrons in the $^1\text{S}_0$ state get excited to MMCT, $^1\text{P}_1$ or $^3\text{P}_1$ states. After that, these electrons may relax to lower excited $^3\text{P}_{1,0}$ states of Bi^{3+} by the non-radiative process, followed by energy transfer to excited state $^2\text{E}_g$ of Mn^{4+} ion, as shown in Fig. 23(a). Under UV and blue excitations, electrons in the ground state of Mn^{4+} get excited to $^4\text{T}_{1,2}$ states. After that, these electrons may relax to a lower excited $^2\text{E}_g$ state and produce amplified deep red emission about 10.6 times greater than without Bi^{3+} sample [100]. Xu et al. enhanced the red emission $\text{CaAl}_{12}\text{O}_{19}:\text{Cr}^{3+}$ by Sm^{3+} co-doping. Here the energy transfer mechanism is involved between the Sm^{3+} and Cr^{3+} (Fig. 23(b)). Hence the energy transfer mechanism is one of the efficient methods for enhancing red emission [136].

6. Thermal stability enhancement

Thermal stability is an important requirement of phosphors during their practical applications in particular, in solid-state lighting. Taking the LED application of phosphor as an example, the operating temperature of LED can exceed 150 °C due to the high input power density imparted in the chip. This heat may transfer to the phosphor [137]. Thermal stability of the efficient germanate $\text{Mg}_{14}\text{Ge}_5\text{O}_{24}:\text{Mn}^{4+}$ which is capable of maintaining 75% of its initial intensity at 473 K is increased by the substitution of Ti^{4+} cations to 85% at 473 K of its room-temperature emission intensity. Here, cation substitution leads to an increase in lattice distortion which can induce traps (defects acting as electron trapping centres). These traps may be able to capture and store the phonon energy at room temperature from the excited state, and it will release the captured phonons to maintain the emission loss at high temperatures. The increased activation energy due to cation substitution can suppress the non-radiative transition and enhance thermal stability [101]. An alternative to a cationic substitution for enhancing thermal stability that can be suggested is the preparation of core-shell morphology to protect the phosphor particles via shell. Already some graphite-like carbon nitride has been used

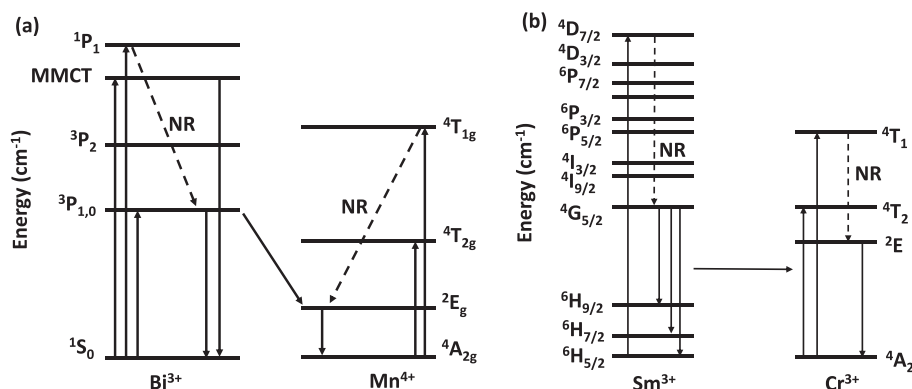


Fig. 23. Energy level diagrams and energy transfer process between (a) Bi³⁺ and Mn⁴⁺. Adapted from Ref. [100] (b) Sm³⁺ and Cr³⁺ Adapted from Ref. [136]. [(NR representing non-radiative relaxation).

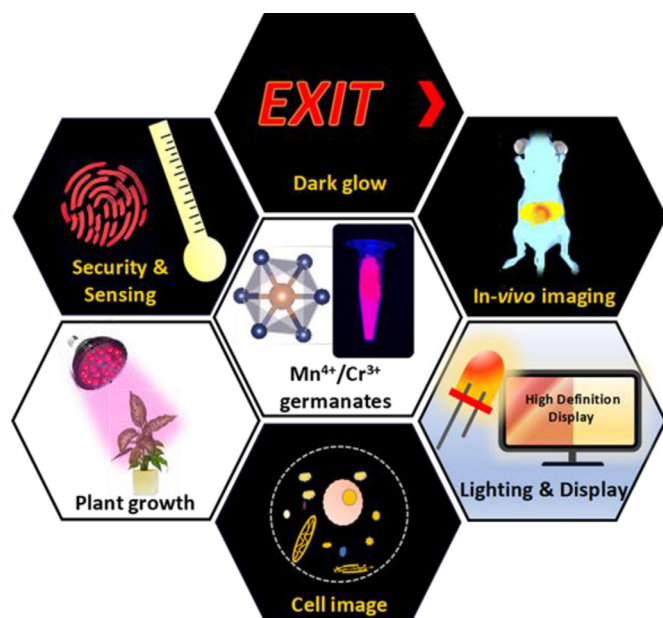


Fig. 24. Representation of different applications of Mn⁴⁺ and Cr³⁺ activated phosphors.

as a coating shell on Y₂O₃:Eu³⁺,Tb³⁺ and Ca_{9.5}Na₂(PO₄)₇:Eu²⁺. At the elevated temperature, the outer shell can be able to isolate the luminescence centres from external effects (moisture, temperature, etc.) and significantly reduce the surface defects. The coating layer combined with the phosphor favours the decrease of dangling bonds and defects on the surface of Y₂O₃:Eu³⁺ thereby modifying the surface micro-structure effectively leading to enhanced thermal stability [138].

7. Potential applications

In this section, the important present and some future applications of Mn⁴⁺ and Cr³⁺ activated deep red-emitting phosphors including W-LEDs, plant growth, security, night vision surveillance, decoration, *in-vivo* imaging, display, biomarking, etc. (illustrated in Fig. 24) have been highlighted. Some of the applications can be achieved only if these phosphors exhibit long persistent nature. Even though these wide varieties of applications are available for Cr³⁺ and Mn⁴⁺ activated phosphors, we are focusing mainly on deep red-emitting Mn⁴⁺ and Cr³⁺ germanate phosphors.

7.1. W-LED applications

Most of the reports on Mn⁴⁺-activated germanates are aiming for providing an efficient red component for the commercial W-LEDs. A famous commercialized method to produce white light is to combine broad yellow emitting Y₃Al₅O₁₂:Ce³⁺ (YAG:Ce³⁺) phosphor along with blue InGaN LED. However, due to the deficiency of the red component and higher correlated colour temperature (CCT) value, this commercially available W-LED faces a severe CRI problem [48]. To resolve the colour rendering issue of this system, Mn⁴⁺-activated phosphors perhaps are a good solution as Mn⁴⁺ ions can be activated by the blue excitations. Li et al. used optimized LiNaGe₄O₉:0.05Mn⁴⁺ for warm W-LED fabrication [89]. They fabricated a W-LED by combining blue InGaN LED chip, LiNaGe₄O₉:0.05Mn⁴⁺, and YAG:Ce³⁺ and able to produce warm white light with a CCT value of 3353 K and CRI value of 69.2. But these systems do not have competing luminous efficiency, which shows the urge for another Mn⁴⁺-doped phosphor for this application [89]. Ding et al. fabricated a W-LED using 455 nm InGaN LED chip, YAG:Ce³⁺, and K₂Ge₄O₉:0.001Mn⁴⁺ phosphor in various empirical ratios. While increasing the weight ratio of K₂Ge₄O₉:Mn⁴⁺, the CCT values decrease from 6343 K to 3119 K, while the CRI value increases from 65.4 to 84.1. After tuning the weight ratio, the optimized white LED has a CIE value of (0.405, 0.356), and a CCT value of 3119 K, and a CRI of 84.1 [90].

Yan et al. fabricated three W-LEDs using the three different deep red-emitting phosphors (Li₃RbGe₈O₁₈:0.01Mn⁴⁺, Li₃CsGe₈O₁₈:0.01Mn⁴⁺, and Li₃Cs_{0.5}Rb_{0.5}Ge₈O₁₈:0.01Mn⁴⁺) by combining each one of them separately with the blue-emitting InGaN chip, and the yellow emitting YAG:Ce³⁺ [97]. Amongst these W-LEDs, the W-LED fabricated using Li₃Cs_{0.5}Rb_{0.5}Ge₈O₁₈ phosphor has good CRI (90.8) and CCT (4474 K) values. Our research group recently reported W-LEDs by combining the red-emitting Mn⁴⁺, Mg²⁺ co-doped Li₃RbGe₈O₁₈:Mg²⁺,0.005Mn⁴⁺ nanophosphor and YAG:Ce³⁺ using blue InGaN chip [133]. The electroluminescence (EL) spectra of W-LED for various mixing ratio of YAG:Ce³⁺ yellow phosphor and red nanophosphor along with their digital images and CIE plots are depicted in Fig. 25(a)-(c). The transition of cool white light (with a CCT of 6952 and CRI of 71) to the natural white light (with CCT of 5025 and CRI of 92) with the increment in red phosphor component can be easily identified from the digital images [133], as well as from the CIE diagram, as shown in Fig. 25.

Liang et al. fabricated W-LED by combining the blue InGaN chip with the yellow emitting YAG:Ce³⁺ and Mg₁₄Ge₅O₂₄:0.002Mn⁴⁺ [80]. The CCT, CRI, and CIE values of the fabricated W-LED are observed to be 2864 K, 80.6, and (0.36, 0.38), respectively. These results are found to be much better than the LED fabricated with-

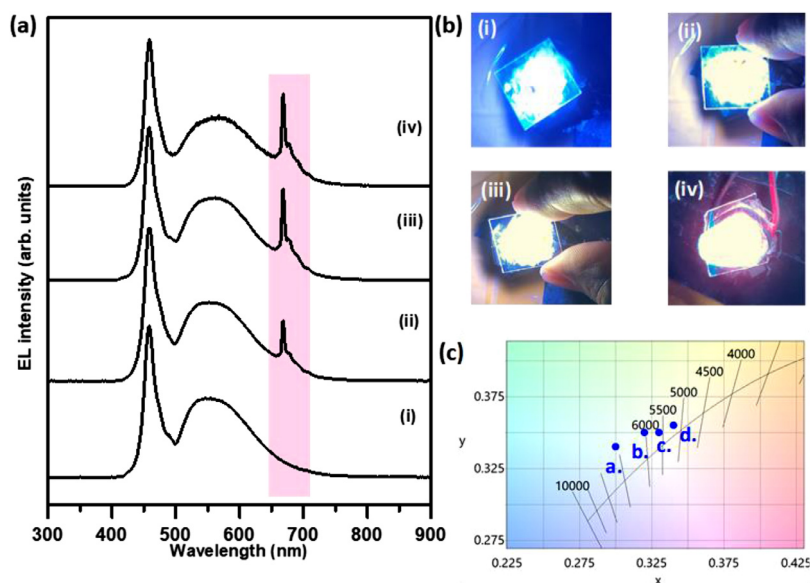


Fig. 25. (a) EL spectra of the W-LEDs fabricated with the various mixing ratios of YAG:Ce³⁺ and Li₃RbGe₅O₁₈:0.005Mn⁴⁺,Mg²⁺ ((i) 1:0, (ii) 1:1, (iii) 2:3, and (iv) 3:7), combined with 460 nm blue InGaN chip. (b) The digital images of the W-LEDs ((i) 1:0, (ii) 1:1, (iii) 2:3, and (iv) 3:7). (c) CIE plot showing the change in CCT values for different mixing ratio. Reproduced with permission from Ref. [133]. (For interpretation of the references to colour in this figure legend, the reader is referred to the web version of this article.)

out the Mg₁₄Ge₅O₂₄:0.002Mn⁴⁺ phosphor suggesting its suitability for solving the deficiency of red component in W-LEDs [80]. As cationic substitution in this phosphor (Mg₁₄Ge₅O₂₄:Mn⁴⁺) could increase the emission intensity, the W-LED is also fabricated using the optimized cationic substituted Mg₁₄Ge_{4.5}Ti_{0.5}O₂₄:Mn⁴⁺ 440 nm blue chip, and YAG:Ce³⁺ [101]. The CCT value, CRI value, and CIE coordinate of the optimized cationic substituted W-LED are 3566 K, 87.3, and (0.45, 0.35), respectively. Moreover, the luminescence efficiency and the R_a value of this optimized W-LED are 109.42 lm/W and 93, respectively, showing the enhanced red spectral saturation [101].

Other important phosphors used for the fabrication of W-LED are SrGe₄O₉:0.005Mn⁴⁺ and BaGe₄O₉:0.005Mn⁴⁺ [106]. W-LED was fabricated by combining the blue InGaN chip with YAG and the respective phosphors. The obtained CRI and CCT values for W-LED fabricated using BaGe₄O₉:Mn⁴⁺ is 92.1 and 3082 K, respectively, whereas these values for W-LED fabricated using SrGe₄O₉:Mn⁴⁺ is 89.1 and 3440 K. Thus, based on the obtained results, BaGe₄O₉:0.005Mn⁴⁺ provides a better deep red component for W-LED than SrGe₄O₉:0.005Mn⁴⁺ [106]. Mg₃Ga₂GeO₈:0.005Mn⁴⁺ is another phosphor that can be efficiently used for W-LED. Here the ratio of the blue-emitting BaMgAl₁₀O₁₇:Eu²⁺ (BAM:Eu²⁺), green-emitting Sr₂SiO₄:Eu²⁺, and red-emitting Mg₃Ga₂GeO₈:0.005Mn⁴⁺ are tuned and combined with the GaN NUV chip to fabricate W-LED. The optimized fabricated W-LED produces white light with a CIE value of (0.316,0.375) and a CCT value of 3340 K [111]. Likewise, Mn⁴⁺ ions, Cr³⁺ activated red-emitting phosphors are also used for W-LED application. A W-LED was fabricated by combining the red-emitting Y₃Al₅O₁₂:Cr³⁺ with the blue InGaN chip and YAG:Ce³⁺. The fabricated W-LED has a CRI value of 76.4 and a CCT value of 5236 K [139].

7.2. Long-glow applications

The long glow or dark glow phosphors have crucial applications in the areas of optical memory, decoration, *in-vivo* imaging, traffic signs, imaging storage, etc. Deep red-emitting phosphor plays a crucial role in traffic signs and other important dark glow applications due to its higher wavelength emission. Ac-

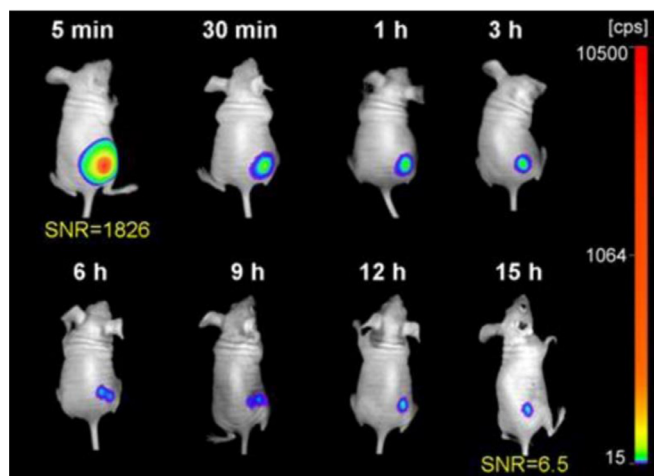


Fig. 26. *In-vivo* images of the mouse after injection of Zn_{2.94}Ga_{1.96}Ge₂O₁₀:Cr³⁺,Pr³⁺ phosphor. Reproduced with permission from Ref. [140].

cording to Rayleigh scattering, the scattering of light is inversely proportional to the fourth power of wavelength. Deep red light greater than 650 nm undergoes the least scattering during the cloudy atmosphere, fog time, and translucent situation. Generally, Cr³⁺-activated phosphors serve the purpose of long red afterglow emission. Few Mn⁴⁺-activated red afterglow phosphors including Mg₂GeO₄:0.001Mn⁴⁺ are also reported [98]. Previously mentioned ZnGa₂O₄:0.005Cr³⁺-Bi³⁺ [120], Zn(Ga_{1-x}Al_x)₂O₄:0.005Cr³⁺,0.01Bi³⁺ [65], and LaAlO₃:0.005Cr³⁺ perovskite [127] are the best examples for long persistent phosphors emitting deep red light. Some of these phosphors are also found to be used *in-vivo* imaging. Deep red to NIR range corresponds to the higher transmittance wavelength range of biological tissue called biological optical window [127]. The Cr³⁺ activated NIR emitting Zn_{2.94}Ga_{1.96}Ge₂O₁₀:Cr³⁺,Pr³⁺ phosphor is successfully used for *in-vivo* imaging, and its *in-vivo* images are shown in Fig. 26. Before injecting the phosphor into the body of the mouse, it is irradiated with a 254 nm UV lamp. After that *in-vivo* images were collected

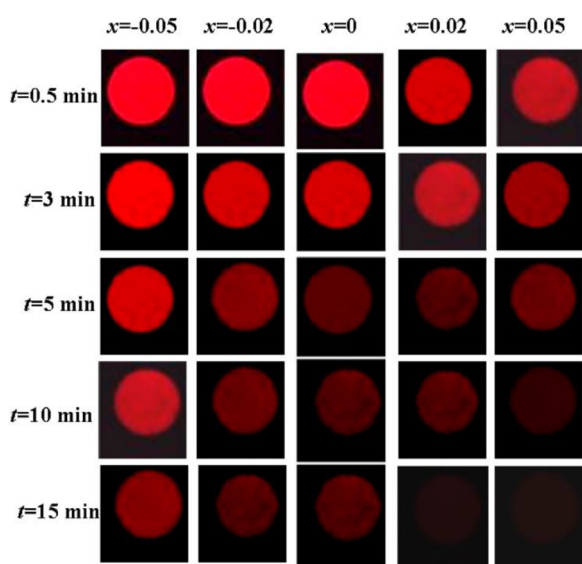


Fig. 27. Red emission images of $\text{La}_3\text{GaGe}_{5+x}\text{O}_{16-x}:\text{0.01Cr}^{3+}$ ($-0.005 < x < 0.05$) at different afterglow time with same exposure time. Reproduced with permission from Ref. [141]. (For interpretation of the references to colour in this figure legend, the reader is referred to the web version of this article.)

for more than 450 min without any excitation [140]. Eventually, $\text{La}_3\text{GaGe}_5\text{O}_{16}:\text{0.01Cr}^{3+}$ can also be used for *in-vivo* imaging, medical imaging, night vision due to its emission range (650–750 nm) and better afterglow time (more than 30 min) [141]. The red emission images of this phosphor for different afterglow time by varying Ge/O content is shown in Fig. 27 and it clearly shows that Ge/O content deficiency can improve the persistent luminescence and afterglow time. This observation can be attributed to the close relationship between persistent luminescence of this phosphor with oxygen or germanium deficiency in the host [141].

7.3. Security applications

$\text{Mn}^{4+}/\text{Cr}^{3+}$ activated deep red-emitting phosphors have a significant role in security and forensic applications, including latent fingerprint visualisation. The development of fluorescent nanomaterials for the detection of latent fingerprints requires good contrast with minimal background interference. Pavitra et al. reported $\text{Ba}_2\text{LaNbO}_6:\text{0.25Mn}^{4+}$ nanophosphor to visualize all the features such as to individualize the minute fingerprint details such as termination, bifurcation, core, and ridge clearly and to identify partial or damaged fingerprints on various nonporous surfaces [142]. The $\text{Ba}_2\text{LaNbO}_6:\text{0.25Mn}^{4+}$ nanorod-like particles exhibited good adhesion with the fingerprint ridges on all the nonporous surfaces without any background staining and displayed a well-defined pattern, which is clearly visible to the naked eye [142]. Yang et al. reported $\text{Mg}_2\text{TiO}_4:\text{Mn}^{4+}$ for the same application [129]. Fluorescent images of latent fingerprints stained using this phosphor on glass and other substrates are shown in Fig. 28 [129].

King and co-workers used NIR emitting persistent $\text{Zn}_3\text{Ga}_2\text{Ge}_2\text{O}_{10}:\text{0.5\%Cr}^{3+}$ phosphor activated by sunlight for fingerprint visualization. Since the background patterns and textures make no transmission at higher wavelengths imaging of substrates in the NIR region of the spectra can mute these background patterns and textures [143]. Most of the $\text{Mn}^{4+}/\text{Cr}^{3+}$ activated germanates are having emissions above 650 nm but in the visible region. So that these deep red-emitting phosphors can take the advantage of its higher wavelength for muting the background and textures. At the same time, it can use its emission in the eye sensitive region for latent fingerprint visualization.

7.4. Display applications

Apart from lighting applications, deep red-emitting phosphors can be efficiently used for various display applications. Recently Mn^{4+} activated fluoride phosphor K_2NaScF_6 with narrow-band red emission peaking at 630 nm were reported [144]. But phosphor with deep-red emission 650 nm or greater are highly preferred for providing a wide colour gamut in UHD TV according to ITU-R BT.2020–2 recommendations [6]. Reportedly, $\text{Li}_3\text{RbGe}_8\text{O}_{18}:\text{0.005Mn}^{4+}$ phosphor with emission spectra peaking at 667 nm (Fig. 11(b)) is one of the best examples for display application that can be used for providing a wide colour gamut in UHD TV [6]. Another efficient Mn^{4+} doped phosphor showing application as wide gamut backlight is $\text{Mg}_{14}\text{Ge}_{4.5}\text{Ti}_{0.5}\text{O}_{16}:\text{Mn}^{4+}$ [101]. Amongst different Cr^{3+} activated phosphors, $\text{MgAl}_2\text{O}_4:\text{0.05Cr}^{3+}$ finds potential applications in solid-state displays and lasers due to its suitable CCT and CIE value. The CIE coordinates ($x = 0.633$, $y = 0.366$) of this phosphor is very much close to the standard value given by NSTC (National television standard committee) and its CCT value is 2109 K (Fig. 29) [145].

7.5. Plant growth applications

Comparing to the traditional horticulture lighting available for plant growth, LEDs possess greater advantages owing to their durability, compact size, and long liveness. Many of the reported germanate phosphors show their promising application in optical agriculture and indoor planting as these deep red-emitting phosphors can convert the unwanted UV light to deep red light. The wavelength of deep red light emitted by germanates matches with the absorption range of chlorophylls responsible for photosynthesis in plants and thus this range of wavelengths helps in the photoperiodic effects in plants. Consequently, germanates are potential candidates for agriculture sunlight spectrum converter and LEDs, which can be used for indoor plant cultivation [100,102,105]. Some of the reported Mn^{4+} -activated germanates for plant growth applications are $\text{Mg}_{3.5}\text{Ge}_{1.25}\text{O}_6:\text{0.0125 Bi}^{3+}, \text{0.01Mn}^{4+}$ [100], $\text{Ba}_2\text{GeO}_4:\text{0.006Mn}^{4+}$ [102], $\text{Ba}_2\text{TiGe}_2\text{O}_8:\text{0.006Mn}^{4+}$ [103], and $\text{BaAl}_2\text{Ge}_2\text{O}_8:\text{0.001Mn}^{4+}$ [105]. The emission wavelength of these phosphors is matching well with the absorption spectrum of chlorophylls. The PL emission spectrum of $\text{Ba}_2\text{TiGe}_2\text{O}_8:\text{0.006Mn}^{4+}$ [103] and its potential application in plant growth is illustrated in Fig. 30. This phosphor has a CIE value of (0.7188, 0.2811) which is in the deep-red region [103]. One of the potential Cr^{3+} activated red-emitting phosphors that can be used for plant growth LEDs is $\text{BaMgAl}_{10}\text{O}_{17}:\text{0.01Cr}^{3+}$ [146].

7.6. Thermometry applications

Luminescence temperature sensors are grasping more attention during these times owing to their fast response, better spatial resolution, and comparatively low perturbation of sample temperature during measurement [147]. Germanates phosphors can effectively be used for optical thermometry applications. The currently available phosphor-converted optical thermometry has some disadvantages such as narrow temperature range, energy loss in multiple activators due to the energy transfer process and relatively low sensitivity, etc. A single activator doped phosphor with high sensitivity and relatively high-temperature range is required for thermometry application. Reportedly, $\text{Mg}_{14}\text{Ge}_{4.5}\text{Ti}_{0.5}\text{O}_{24}:\text{Mn}^{4+}$ finds potential application in optical thermometry as it shows an abnormal variation in the intensity of Stokes and anti-Stokes lines with temperature [101]. The lattice distortion induced by the cation ($\text{Ti}^{4+} \rightarrow \text{Ge}^{4+}$) substitution has a significant effect on temperature-dependant luminescence. Here the emission spectrum

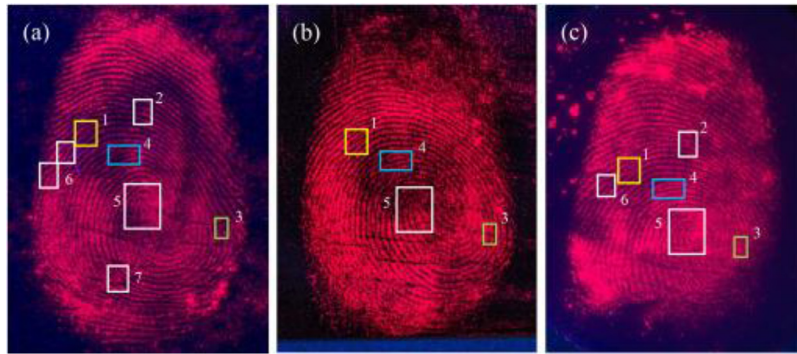


Fig. 28. Images of latent fingerprints stained with $Mg_2TiO_4:Mn^{4+}$ phosphor on (a) glass, (b) Si wafer, and (c) plastic; regions squared in images, 1: termination; 2: bridge; 3: eyes; 4: island; 5: whorl; 6: bifurcation; 7: hook. Reproduced with permission from Ref. [129].

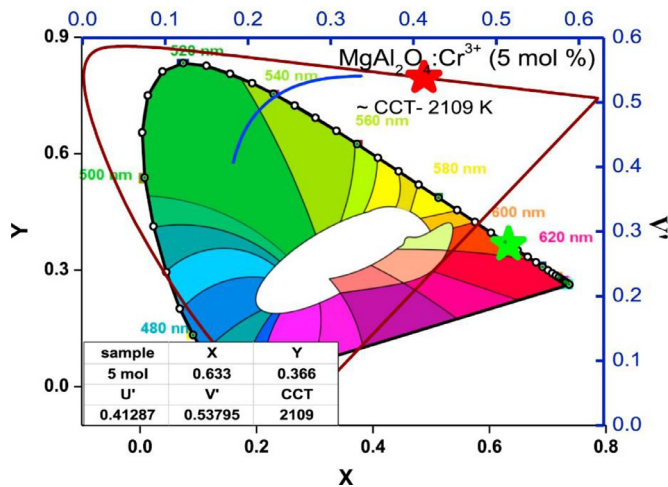


Fig. 29. CIE and CCT diagram of $MgAl_2O_4:0.05Cr^{3+}$. Reproduced with permission from Ref. [145].

of the sample is recorded by varying the temperature from 6.9–303 K and 303–473 K.

It is observed that the emission intensity of Stokes lines increases with the increase in temperature whereas the intensity of anti-Stokes lines decreases with an increase in temperature (Fig. 31). This high-temperature dependence behaviour makes this phosphor a potential candidate for optical thermometry. To evaluate the performance of this phosphor as a thermometer the absolute sensitivity (S_a) as well as relative sensitivity (S_r) were calculated in the temperature range 6.9 K to 303 K. The maximum

S_r value is $2.71\% K^{-1}$ and the maximum S_a value is $0.00152 K^{-1}$ which are calculated at temperatures 97 K and 215 K, respectively. This maximum S_r value is comparatively greater than that of most of the reported optical thermometry materials. The converse change in Stokes and anti-Stokes peaks, broad temperature range, and higher relative sensitivity make this phosphor suitable for thermometry application [101].

One of the best examples of Cr^{3+} -activated phosphor for the thermometry application is $LaGaO_3:0.005Cr^{3+}$ phosphor [148]. It can be used as an optical nano thermometer for sensing temperature below room temperature as well as at above room temperature. Here the temperature-dependant peak intensity, as well as the lifetime changes with the temperature, are used for sensing [148]. Another important phosphor coming under this category is Cr^{3+} -activated $Sr_2MgAl_{22}O_{36}:0.02Cr^{3+}$ phosphor [149].

7.7. Solar energy applications

Fig. 32(a) represents the spectral mismatch between the bandgap of silicon solar cell and incident photon energy coming from sunlight that causes difficulty in converting the solar energy to electricity. The bandgap of the Si cell is appropriate for absorbing deep red and NIR region, but the incident solar energy contains the UV content. Hence luminescent solar concentrator or a downconverter capable of collecting solar photons and converting them into matching bandgap energy of Si cells is highly required [123]. The Solar spectrum showing a potential gain from the downconversion of UV rays for a silicon solar cell is represented in Fig. 32(a). As seen from Fig. 32(b), a transparent layer of downconverters is situated on the top of the solar cell. They are used for converting UV photons to a red-rich spectrum [150].

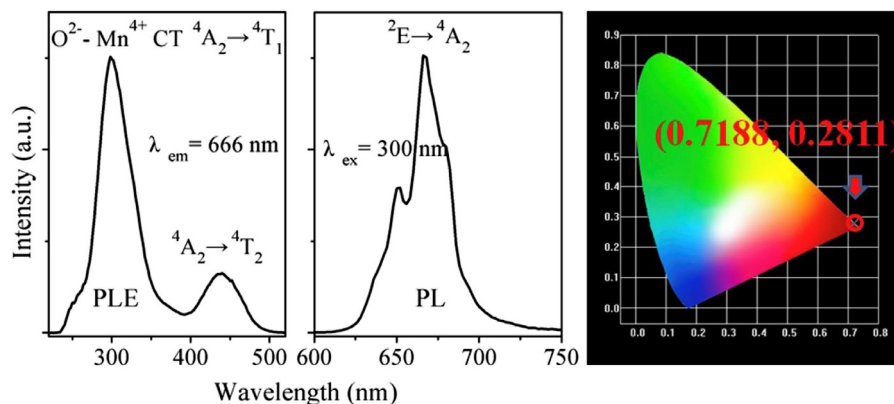


Fig. 30. The PL emission, excitation spectra and CIE diagram of $Ba_2TiGe_2O_8:0.006Mn^{4+}$. Reproduced with permission from Ref. [103].

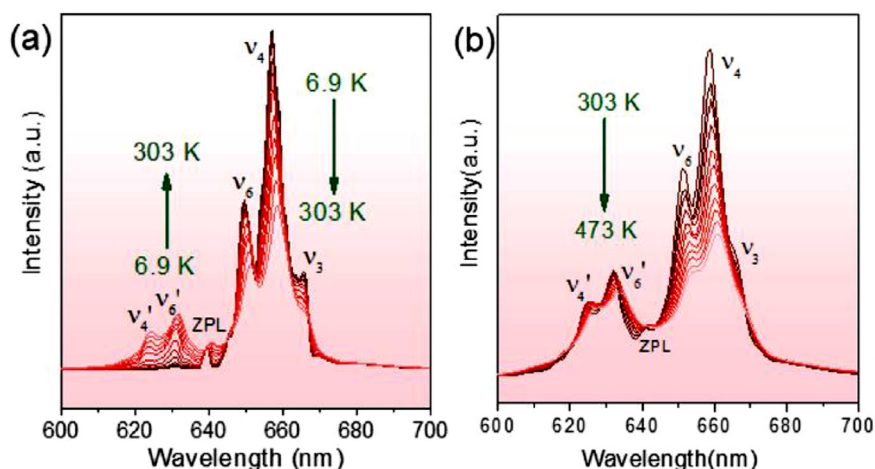


Fig. 31. PL emission spectrum of $\text{Mg}_{14}\text{Ge}_{4.5}\text{Ti}_{0.5}\text{O}_{24}:\text{Mn}^{4+}$ by varying temperature from (a) 6.9–303 K and (b) 303–473 K. Reproduced with permission from Ref. [101].

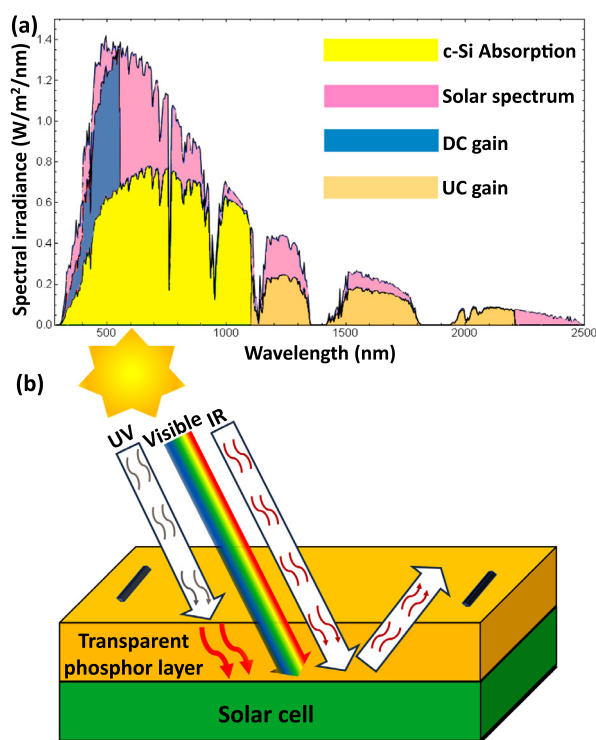


Fig. 32. Schematic representation of (a) a potential gain for down- and upconversion for a silicon solar cell; (b) solar cell with down converter. Adapted from Ref. [150].

Mn^{4+} doped germanates are suitable for down-converting applications. Comparing to fluorides these phosphors are accomplished with emission in the deep-red region (greater than 650 nm) and strong absorption in UV. J. Zhou et al. reported that Cr^{3+} -activated $\text{La}_3\text{GaGe}_5\text{O}_{16}:0.03\text{Cr}^{3+}$ phosphor in luminescence solar concentrator can significantly enhance the efficiency of Si cell due to its UV absorption as well as deep red and NIR emission [123]. The emission peak of this phosphor is centred at 700 nm (Fig. 33) [123].

8. Summary, future and perspective

In this review article, we have reviewed the spectroscopic properties of the $\text{Mn}^{4+}/\text{Cr}^{3+}$ activated deep red-emitting oxide phosphors, in particular germanates. According to our literature re-

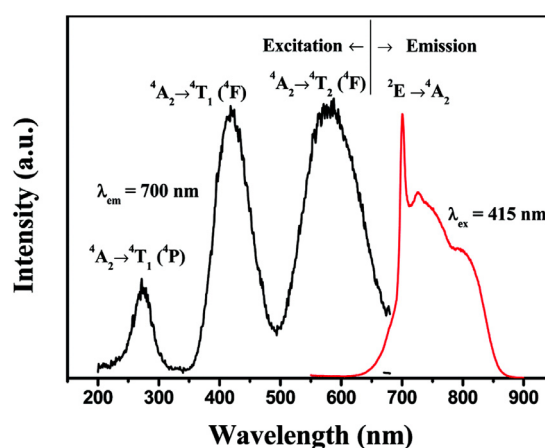


Fig. 33. Excitation and emission spectrum of $\text{La}_3\text{GaGe}_5\text{O}_{16}:0.03\text{Cr}^{3+}$ phosphor applicable in luminescence solar concentrator. Reproduced with permission from Ref. [123].

view, Mn^{4+} activated germanates can be classified into three categories: alkali metal-based germanates, alkaline-earth metal-based germanates, and lanthanum-based germanates. Further, a study on the crystal structure-dependant luminescence behaviour of these $\text{Mn}^{4+}/\text{Cr}^{3+}$ deep red-emitting phosphors is also discussed. From the detailed analysis of the crystal structures, it is concluded that for the efficient optical properties, Mn^{4+} ions should possess a well isolated octahedral geometry. The Cr^{3+} activated phosphors are capable of giving long persistent character. However, it is difficult for Mn^{4+} activated phosphors to produce the same. Most of the germanate phosphors discussed here do not possess good morphology. Phosphor with spherical morphology is highly needed in practical applications since it enables dense packing of luminescence layer, and it can minimize the loss due to scattering. Eventually, there is a lack of efficient germanate phosphors having a particle size in the nano range, which is mainly arising due to the problems associated with the synthesis techniques. Phosphors with nano-size are highly desirable since particle with smaller size is preferred for the high resolution display and imaging applications. The majority of the phosphors discussed here have comparatively low quantum efficiency. Consequently, good synthetic methods that can simultaneously improve the morphology, as well as red emission, are required. The microwave-assisted sol-gel method is one of the efficient methods that we can suggest for solving this problem. Moreover, a detailed description of various other methods that can

be used for enhancing the red emission as well as the thermal stability of red-emitting phosphor is discussed. We have presented the possible and potential application of these phosphors in the last part of the review. Most of the reports discussed here focus on the W-LED application. The next generation of oxide phosphors will be Cr^{3+} and Mn^{4+} activated deep red to NIR emitting phosphors. So that in addition to W-LEDs, the applications can be extended to wide areas including medical diagnosis, *in-vivo* imaging, night vision surveillance, security, etc.

Declaration of Competing Interest

The authors announce zero competing interest.

Acknowledgement

This work was financially supported by the Indo-French Centre for the Promotion of Advanced Research (IFC-PAR/CEFIPRA) (Project no. 6008–1). Thejas K. K. acknowledges Council of Scientific & Industrial Research, Govt. of India, for the award of Junior Research Fellowship.

References

- Z. Yang, Q. Wei, M. Rong, Z. Yang, Z. Wang, Q. Zhou, Q. Wang, Novel red-emitting phosphors $\text{A}_2\text{HfF}_6:\text{Mn}^{4+}$ ($\text{A} = \text{Rb}^+, \text{Cs}^+$) for solid-state lighting, *Dalt. Trans.* 46 (2017) 9451–9456, doi:10.1039/c7dt01842h.
- P. Du, X. Huang, J.S. Yu, Facile synthesis of bifunctional Eu^{3+} -activated NaBiF_4 red-emitting nanoparticles for simultaneous white light-emitting diodes and field emission displays, *Chem. Eng. J.* 337 (2018) 91–100, doi:10.1016/j.cej.2017.12.063.
- X. Wang, Q. Liu, Y. Bu, C.S. Liu, T. Liu, X. Yan, Optical temperature sensing of rare-earth ion doped phosphors, *RSC Adv.* 5 (2015) 86219–86236, doi:10.1039/c5ra16986k.
- X. Min, Z. Huang, M. Fang, Y.G. Liu, C. Tang, X. Wu, Energy transfer from Sm^{3+} to Eu^{3+} in red-emitting phosphor $\text{LaMgAl}_{11}\text{O}_{19}:\text{Sm}^{3+}, \text{Eu}^{3+}$ for solar cells and near-ultraviolet white light-emitting diodes, *Inorg. Chem.* 53 (2014) 6060–6065, doi:10.1021/ic500412r.
- J. Liang, L. Sun, B. Devakumar, S. Wang, Q. Sun, H. Guo, B. Li, X. Huang, Novel Mn^{4+} -activated LiLaMgWO_6 far-red emitting phosphors: high photoluminescence efficiency, good thermal stability, and potential applications in plant cultivation LEDs, *RSC Adv.* 8 (2018) 27144–27151, doi:10.1039/c8ra05669b.
- S.P. Singh, M. Kim, W.B. Park, J.W. Lee, K.S. Sohn, Discovery of a red-emitting $\text{Li}_3\text{RbGe}_3\text{O}_{18}:\text{Mn}^{4+}$ phosphor in the alkali-germanate system: structural determination and electronic calculations, *Inorg. Chem.* 55 (2016) 10310–10319, doi:10.1021/acs.inorgchem.6b01576.
- Y. Li, S. Qi, P. Li, Z. Wang, Research progress of Mn doped phosphors, *RSC Adv.* 7 (2017) 38318–38334, doi:10.1039/c7ra06026b.
- X. Piao, K.I. Machida, T. Horikawa, H. Hanzawa, Y. Shimomura, N. Kijima, Preparation of $\text{CaAlSi}_3\text{Eu}^{2+}$ phosphors by the self-propagating high-temperature synthesis and their luminescent properties, *Chem. Mater.* 19 (2007) 4592–4599, doi:10.1021/cm070623c.
- R.J. Xie, N. Hirotsaki, T. Suehiro, F.F. Xu, M. Mitomo, A simple, efficient synthetic route to $\text{Sr}_2\text{Si}_5\text{N}_8:\text{Eu}^{2+}$ -based red phosphors for white light-emitting diodes, *Chem. Mater.* 18 (2006) 5578–5583, doi:10.1021/cm061010n.
- S. Shisina, S. Das, S. Som, S. Ahmad, V. Vinudja, P. Merin, K.G. Nishanth, P. Kumari, M.K. Pandey, Structure and optoelectronic properties of palmierite structured $\text{Ba}_2\text{Y}_{0.67}\text{δ}_{0.33}\text{V}_2\text{O}_8:\text{Eu}^{3+}$ red phosphors for n-UV and blue diode based warm white light systems, *J. Alloys Compd.* 802 (2019) 723–732, doi:10.1016/j.jallcom.2019.05.355.
- J. Hu, T. Huang, Y. Zhang, B. Lu, H. Ye, B. Chen, H. Xia, C. Ji, Enhanced deep-red emission from $\text{Mn}^{4+}/\text{Mg}^{2+}$ co-doped CaGdAlO_4 phosphors for plant cultivation, *Dalt. Trans.* 48 (2019) 2455–2466, doi:10.1039/c8dt04955f.
- E. Song, J. Wang, J. Shi, T. Deng, S. Ye, M. Peng, J. Wang, L. Wondraczek, Q. Zhang, Highly efficient and thermally stable $\text{K}_3\text{AlF}_6:\text{Mn}^{4+}$ as a red phosphor for ultra-high-performance warm white light-emitting diodes, *ACS Appl. Mater. Interfaces* 9 (2017) 8805–8812, doi:10.1021/acsami.7b00749.
- Z. Zhang, C. Ma, R. Gautier, M.S. Molokeev, Q. Liu, Z. Xia, Structural confinement toward giant enhancement of red emission in Mn^{2+} -based phosphors, *Adv. Funct. Mater.* 28 (2018) 2–8, doi:10.1002/adfm.201804150.
- N.T.K. Chi, N.V. Quang, N.T. Tuan, N.D.T. Kien, D.Q. Trung, P.T. Huy, P.D. Tam, D.H. Nguyen, Deep red emitting $\text{MgAl}_2\text{O}_4:\text{Cr}^{3+}$ phosphor for solid state lighting, *J. Electron. Mater.* 48 (2019) 5891–5899, doi:10.1007/s11664-019-07358-5.
- R. Cao, Y. Cao, T. Fu, S. Jiang, W. Li, Z. Luo, J. Fu, Synthesis and luminescence properties of novel red-emitting $\text{R}_3\text{PaO}_{13}:\text{Bi}^{2+}$ ($\text{R}=\text{Sr}$ and Ba) phosphors, *J. Alloys Compd.* 661 (2016) 77–81, doi:10.1016/j.jallcom.2015.11.176.
- R. Cao, X. Lv, Y. Ran, L. Xu, T. Chen, S. Guo, H. Ao, X. Yu, Rare-earth-free $\text{Li}_5\text{La}_3\text{Ta}_2\text{O}_{12}:\text{Mn}^{4+}$ deep-red-emitting phosphor: synthesis and photoluminescence properties, *J. Am. Ceram. Soc.* 102 (2019) 5910–5918, doi:10.1111/jace.16447.
- D. Chen, Y. Zhou, J. Zhong, A review on Mn^{4+} activators in solids for warm white light-emitting diodes, *RSC Adv.* 6 (2016) 86285–86296, doi:10.1039/c6ra19584a.
- Y. Zhong, S. Gai, M. Xia, S. Gu, Y. Zhang, X. Wu, J. Wang, N. Zhou, Z. Zhou, Enhancing quantum efficiency and tuning photoluminescence properties in far-red-emitting phosphor $\text{Ca}_{14}\text{Ga}_{10}\text{Zn}_6\text{O}_{35}:\text{Mn}^{4+}$ based on chemical unit engineering, *Chem. Eng. J.* 374 (2019) 381–391, doi:10.1016/j.cej.2019.05.201.
- M. Zhang, M. Jia, T. Sheng, Z. Fu, Multifunctional optical thermometer based on the transition metal ions doped down-conversion $\text{Gd}_2\text{ZnTiO}_6:\text{Bi}^{3+}, \text{Mn}^{4+}$ phosphors, *J. Lumin.* 229 (2021) 117653–117658, doi:10.1016/j.jlumin.2020.117653.
- J. Liang, B. Devakumar, L. Sun, S. Wang, Q. Sun, H. Guo, X. Huang, Deep-red-emitting $\text{Ca}_2\text{LuSbO}_6:\text{Mn}^{4+}$ phosphors for plant growth LEDs: synthesis, crystal structure, and photoluminescence properties, *J. Alloys Compd.* 804 (2019) 521–526, doi:10.1016/j.jallcom.2019.06.312.
- A. Fu, L. Zhou, S. Wang, Y. Li, Preparation, structural and optical characteristics of a deep red-emitting $\text{Mg}_2\text{Al}_4\text{Si}_5\text{O}_{18}:\text{Mn}^{4+}$ phosphor for warm w-LEDs, *Dye. Pigment.* 148 (2018) 9–15, doi:10.1016/j.dyepig.2017.08.050.
- R. Cao, X. Liu, K. Bai, T. Chen, S. Guo, Z. Hu, F. Xiao, Z. Luo, Photoluminescence properties of red-emitting $\text{Li}_2\text{ZnSn}_2\text{O}_7:\text{Mn}^{4+}$ phosphor for solid-state lighting, *J. Lumin.* 197 (2018) 169–174, doi:10.1016/j.jlumin.2018.01.023.
- R. Cao, Z. Shi, G. Quan, T. Chen, S. Guo, Z. Hu, P. Liu, Preparation and luminescence properties of $\text{Li}_2\text{MgZrO}_4:\text{Mn}^{4+}$ red phosphor for plant growth, *J. Lumin.* 188 (2017) 577–581, doi:10.1016/j.jlumin.2017.05.002.
- R. Cao, T. Chen, Y. Ren, T. Chen, H. Ao, W. Li, G. Zheng, Synthesis and photoluminescence properties of $\text{Ca}_2\text{LaTaO}_6:\text{Mn}^{4+}$ phosphor for plant growth LEDs, *J. Alloys Compd.* 780 (2019) 749–755, doi:10.1016/j.jallcom.2018.12.027.
- K. Li, H. Lian, R. Van Deun, M.G. Brik, A far-red-emitting $\text{NaMgLaTeO}_6:\text{Mn}^{4+}$ phosphor with perovskite structure for indoor plant growth, *Dye. Pigment.* 162 (2019) 214–221, doi:10.1016/j.dyepig.2018.09.084.
- R. Cao, X. Ouyang, Y. Jiao, X. Wang, Q. Hu, T. Chen, C. Liao, Y. Li, Deep-red-emitting $\text{SrLa}_2\text{Sc}_2\text{O}_7:\text{Mn}^{4+}$ phosphor: synthesis and photoluminescence properties, *J. Alloys Compd.* 795 (2019) 134–140, doi:10.1016/j.jallcom.2019.04.220.
- R. Cao, Y. Jiao, X. Wang, X. Ouyang, H. Wan, T. Chen, G. Zheng, S. Xie, Far-red emitting $\text{Mg}_2\text{La}_3\text{NbO}_9:\text{Mn}^{4+}$ powder phosphor: synthesis and luminescence properties, *Adv. Powder Technol.* 31 (2020) 4045–4052, doi:10.1016/j.apt.2020.08.009.
- R. Cao, W. Zhang, T. Chen, Y. Zheng, H. Ao, Z. Luo, S. Xie, H. Wan, Perovskite tungstate $\text{Ba}_2\text{La}_2\text{ZnW}_2\text{O}_{12}:\text{Mn}^{4+}$ phosphor: synthesis, energy transfer and tunable emission, *Mater. Res. Bull.* 137 (2021) 111200–111206, doi:10.1016/j.materresbull.2020.111200.
- S. Adachi, Review— Mn^{4+} vs Cr^{3+} : a comparative study as activator ions in red and deep red-emitting phosphors, *ECS J. Solid State Sci. Technol.* 9 (2020) 026003–026014, doi:10.1149/2162-8777/ab6ea6.
- S. Adachi, Crystal-field and Racah parameters of Mn^{4+} ion in red and deep red-emitting phosphors: fluoride versus oxide phosphor, *J. Lumin.* 218 (2020) 116829–116827, doi:10.1016/j.jlumin.2019.116829.
- S. Adachi, Review—photoluminescence properties of Cr^{3+} -activated oxide phosphors, *ECS J. Solid State Sci. Technol.* 10 (2021) 026001–026021, doi:10.1149/2162-8777/abdc01.
- S. Adachi, Review—photoluminescence properties of Cr^{3+} -activated fluoride phosphors, *ECS J. Solid State Sci. Technol.* 10 (2021) 036001–036020, doi:10.1149/2162-8777/abdfb7.
- J. Shi, X. Sun, S. Zheng, L. Song, F. Zhang, T. Madl, Y. Zhang, H. Zhang, M. Hong, Tin-doped near-infrared persistent luminescence nanoparticles with considerable improvement of biological window activation for deep tumor photodynamic therapy, *ACS Appl. Bio Mater.* 3 (2020) 5995–6004, doi:10.1021/acsabm.0c00644.
- J. Shi, X. Sun, J. Li, H. Man, J. Shen, Y. Yu, H. Zhang, Multifunctional near infrared-emitting long-persistence luminescent nanoprobes for drug delivery and targeted tumor imaging, *Biomaterials* 37 (2015) 260–270, doi:10.1016/j.biomaterials.2014.10.033.
- S. Pan, Y.Y. Lu, F. Liu, Sunlight-activated long-persistent luminescence in the near-infrared from Cr^{3+} -doped zinc gallogermanates, *Nat. Mater.* 11 (2012) 58–63, doi:10.1038/nmat3173.
- C. Pratap Kumar, S.C. Prashantha, H. Nagabhushana, D.M. Jnaneshwara, Photoluminescence and photometric studies of low temperature prepared red emitting $\text{MgAl}_2\text{O}_4:\text{Cr}^{3+}$ nanophosphors for solid state displays, *J. Sci. Adv. Mater. Devices.* 3 (2018) 464–470, doi:10.1016/j.jsamd.2018.09.002.
- D. Yu, Y. Zhou, C. Ma, J.H. Melman, K.M. Baroudi, M. LaCapra, R.E. Riman, Non-rare-earth $\text{Na}_3\text{AlF}_6:\text{Cr}^{3+}$ phosphors for far-red light-emitting diodes, *ACS Appl. Electron. Mater.* 1 (2019) 2325–2333, doi:10.1021/acsaelm.9b00527.
- Q. Bai, Z. Wang, P. Li, T. Li, S. Xu, Z. Yang, Luminescence properties of novel deep-red-emitting $\text{Ca}_3\text{Al}_2\text{Ge}_2\text{O}_{10}:\text{Cr}^{3+}$ phosphors, *Luminescence* 31 (2016) 1277–1282, doi:10.1002/bio.3103.
- T. Senden, R.G. Geitenbeek, A. Meijerink, Co-precipitation synthesis and optical properties of Mn^{4+} -doped hexafluoroaluminate w-LED phosphors, *Materials (Basel)* 10 (2017) 1322–1335, doi:10.3390/ma1011322.
- Y. Jin, M.H. Fang, M. Grinberg, S. Mahlik, T. Lesniewski, M.G. Brik, G.Y. Luo, J.G. Lin, R.S. Liu, Narrow red emission band fluoride phosphor $\text{KNaSiF}_6:\text{Mn}^{4+}$ for warm white light-emitting diodes, *ACS Appl. Mater. Interfaces* 8 (2016) 11194–11203, doi:10.1021/acsami.6b01905.

- [41] C.C. Lin, A. Meijerink, R.S. Liu, Critical red components for next-generation white LEDs, *J. Phys. Chem. Lett.* 7 (2016) 495–503, doi:10.1021/acs.jpclett.5b02433.
- [42] Z. Wang, N. Wang, Z. Yang, Z. Yang, Q. Wei, Q. Zhou, H. Liang, Luminescent properties of novel red-emitting phosphor Na_3TaF_6 with non-equivalent doping of Mn^{4+} for LED backlighting, *J. Lumin.* 192 (2017) 690–694, doi:10.1016/j.jlumin.2017.07.064.
- [43] L. Huang, Y. Liu, J. Yu, Y. Zhu, F. Pan, T. Xuan, M.G. Brik, C. Wang, J. Wang, Highly Stable $\text{K}_2\text{SiF}_6:\text{Mn}^{4+}/\text{K}_2\text{SiF}_6$ composite phosphor with narrow red emission for white LEDs, *ACS Appl. Mater. Interfaces* 10 (2018) 18082–18092, doi:10.1021/acsami.8b03893.
- [44] D. Huang, H. Zhu, Z. Deng, Q. Zou, H. Lu, X. Yi, W. Guo, C. Lu, X. Chen, Moisture-resistant Mn^{4+} -doped core-shell-structured fluoride red phosphor exhibiting high luminous efficacy for warm white light-emitting diodes, *Angew. Chemie.* 131 (2019) 3883–3887, doi:10.1002/ange.201813363.
- [45] P. Li, L. Wondraczek, M. Peng, Q. Zhang, A. Setlur, Tuning Mn^{4+} red photoluminescence in $(\text{K,Rb})_2\text{Ge}_4\text{O}_9:\text{Mn}^{4+}$ solid solutions by partial alkali substitution, *J. Am. Ceram. Soc.* 99 (2016) 3376–3381, doi:10.1111/jace.14363.
- [46] Z. Xia, M.S. Molokeev, A.S. Oreshonkov, V.V. Atuchin, R.S. Liu, C. Dong, Crystal and local structure refinement in $\text{Ca}_2\text{Al}_3\text{O}_6\text{F}$ explored by X-ray diffraction and Raman spectroscopy, *Phys. Chem. Chem. Phys.* 16 (2014) 5952–5957, doi:10.1039/c3cp53816h.
- [47] R.D. Shannon, Revised effective ionic radii and systematic studies of interatomic distances in halides and chalcogenides, *Acta Crystallogr. Sect. A.* 32 (1976) 751–766, doi:10.1023/a:1018927109487.
- [48] P. Ranjith, S. Sreevalsa, J. Tyagi, K. Jayanthi, G. Jagannath, P. Patra, S. Ahmad, K. Annapurna, A.R. Allu, S. Das, Elucidating the structure and optimising the photoluminescence properties of $\text{Sr}_2\text{Al}_3\text{O}_6\text{F}:\text{Eu}^{3+}$ oxyfluorides for cool white-LEDs, *J. Alloys Compd.* 826 (2020) 154015–154025, doi:10.1016/j.jallcom.2020.154015.
- [49] V.R. Bandi, B.K. Grandhe, H.J. Woo, K. Jang, D.S. Shin, S.S. Yi, J.H. Jeong, Luminescence and energy transfer of Eu^{3+} or/and Dy^{3+} co-doped in $\text{Sr}_3\text{AlO}_4\text{F}$ phosphors with NUV excitation for WLEDs, *J. Alloys Compd.* 538 (2012) 85–90, doi:10.1016/j.jallcom.2012.05.057.
- [50] M. Shang, G. Li, X. Kang, D. Yang, D. Geng, J. Lin, Tunable luminescence and energy transfer properties of $\text{Sr}_3\text{AlO}_4\text{F}:\text{RE}^{3+}$ (RE=Tm/Tb, Eu, Ce) phosphors, *ACS Appl. Mater. Interfaces* 3 (2011) 2738–2746, doi:10.1021/am200534u.
- [51] W. Chen, Effect of composition on the luminescence of Ce^{3+} activated $\text{Sr}_3\text{AlO}_4\text{F}$ phosphor for light-emitting diode, *J. Alloys Compd.* 550 (2013) 320–325, doi:10.1016/j.jallcom.2012.10.159.
- [52] X. Dong, Y. Pan, D. Li, H. Lian, J. Lin, A novel red phosphor of Mn^{4+} ion-doped oxyfluoroniobate BaNbOF_5 for warm WLED applications, *Cryst. Eng. Comm.* 20 (2018) 5641–5646, doi:10.1039/c8ce01304g.
- [53] H. Ming, J. Zhang, L. Liu, J. Peng, F. Du, X. Ye, Y. Yang, H. Nie, A novel $\text{Cs}_2\text{NbOF}_5:\text{Mn}^{4+}$ oxyfluoride red phosphor for light-emitting diode devices, *Dalt. Trans.* 47 (2018) 16048–16056, doi:10.1039/c8dt02817f.
- [54] T. Hu, H. Lin, Y. Cheng, Q. Huang, J. Xu, Y. Gao, J. Wang, Y. Wang, A highly-distorted octahedron with a C 2v group symmetry inducing an ultra-intense zero phonon line in Mn^{4+} -activated oxyfluoride $\text{Na}_2\text{WO}_2\text{F}_4$, *J. Mater. Chem. C.* 5 (2017) 10524–10532, doi:10.1039/c7tc03655h.
- [55] Z. Wang, Z. Yang, Z. Yang, Q. Wei, Q. Zhou, L. Ma, X. Wang, Red Phosphor $\text{Rb}_2\text{NbOF}_5:\text{Mn}^{4+}$ for warm white light-emitting diodes with a high color-rendering index, *Inorg. Chem.* 58 (2019) 456–461, doi:10.1021/acs.inorgchem.8b02676.
- [56] P. Cai, L. Qin, C. Chen, J. Wang, H.J. Seo, Luminescence, energy transfer and optical thermometry of a novel narrow red emitting phosphor: $\text{Cs}_2\text{WO}_2\text{F}_4:\text{Mn}^{4+}$, *Dalt. Trans.* 46 (2017) 14331–14340, doi:10.1039/c7dt02751f.
- [57] S. Adachi, Photoluminescence properties of Mn^{4+} -activated oxide phosphors for use in white-LED applications: a review, *J. Lumin.* 202 (2018) 263–281, doi:10.1016/j.jlumin.2018.05.053.
- [58] L. Chen, S. Xue, X. Chen, A. Bahader, X. Deng, E. Zhao, Y. Jiang, S. Chen, T.S. Chan, Z. Zhao, W. Zhang, The site occupation and valence of Mn ions in the crystal lattice of $\text{Sr}_4\text{Al}_{14}\text{O}_{25}$ and its deep red emission for high color-rendering white light-emitting diodes, *Mater. Res. Bull.* 60 (2014) 604–611, doi:10.1016/j.materresbull.2014.08.055.
- [59] M.G. Brik, S.J. Camardello, A.M. Srivastava, Influence of covalency on the $\text{Mn}^{4+}E_g \rightarrow {}^4A_{2g}$ emission energy in crystals, *ECS J. Solid State Sci. Technol.* 4 (2015) R39–R43, doi:10.1149/2.0031503jss.
- [60] M.G. Brik, A.M. Srivastava, On the optical properties of the Mn^{4+} ion in solids, *J. Lumin.* 133 (2013) 69–72, doi:10.1016/j.jlumin.2011.08.047.
- [61] Q. Zhou, L. Dolgov, A.M. Srivastava, L. Zhou, Z. Wang, J. Shi, M.D. Dramićanin, M.G. Brik, M. Wu, Mn^{2+} and Mn^{4+} red phosphors: synthesis, luminescence and applications in WLEDs. A review, *J. Mater. Chem. C.* 6 (2018) 2652–2671, doi:10.1039/c8tc00251g.
- [62] M.G. Brik, A.M. Srivastava, Critical Review—A review of the electronic structure and optical properties of ions with d^3 electron configuration (V^{2+} , Cr^{3+} , Mn^{4+} , Fe^{5+}) and main related misconceptions, *ECS J. Solid State Sci. Technol.* 7 (2018) R3079–R3085, doi:10.1149/2.0041801jss.
- [63] K. Ogasawara, F. Alluqmani, H. Nagoshi, Multiplet energy level diagrams for Cr^{3+} and Mn^{4+} in oxides with O_h site symmetry based on first-principles calculations, *ECS J. Solid State Sci. Technol.* 5 (2016) R3191–R3196, doi:10.1149/2.0231601jss.
- [64] K. Li, H. Lian, R. Van Deun, Site occupancy and photoluminescence properties of a novel deep-red-emitting phosphor $\text{NaMgGdTeO}_6:\text{Mn}^{4+}$ with perovskite structure for w-LEDs, *J. Lumin.* 198 (2018) 155–162, doi:10.1016/j.jlumin.2018.02.035.
- [65] Y. Zhuang, J. Ueda, S. Tanabe, Tunable trap depth in $\text{Zn}(\text{Ga}_{1-x}\text{Al}_x)_2\text{O}_4:\text{Cr}$, Bi red persistent phosphors: considerations of high-temperature persistent luminescence and photostimulated persistent luminescence, *J. Mater. Chem. C.* 1 (2013) 7849–7855, doi:10.1039/c3cc31462f.
- [66] K. Li, D. Zhu, R. Van Deun, Photoluminescence properties and crystal field analysis of a novel red-emitting phosphor $\text{K}_2\text{BaGe}_8\text{O}_{18}:\text{Mn}^{4+}$, *Dye. Pigment.* 142 (2017) 69–76, doi:10.1016/j.dyepig.2017.03.007.
- [67] M.G. Brik, K. Ogasawara, Microscopic analysis of the crystal field strength and lowest charge transfer energies in the elpasolite crystals Cs_2NaYX_6 (X=F, Cl, Br) doped with Cr^{3+} , *Phys. Rev. B - Condens. Matter Mater. Phys.* 74 (2006) 045105–045113, doi:10.1103/PhysRevB.74.045105.
- [68] D.T. Sviridov, R.K. Sviridova, N. Kulik, V.B. Glasko, Optical spectra of the iso-electronic ions V^{2+} , Cr^{3+} , and Mn^{4+} in an octahedral coordination, *J. Appl. Spectrosc.* 30 (1979) 334–337, doi:10.1007/BF00608274.
- [69] M. Moreno, B.M. T., J.A. Aramburu, The Huang-Rhys factor S (a_{1g}) for transition-metal impurities: a microscopic insight, *J. Phys. Condens. Matter.* 4 (1992) 9481–9488, doi:10.1088/0953-8984/4/47/027.
- [70] M. Moreno, M.T. Barriuso, J.A. Aramburu, The dependence of $10Dq$ upon the metal–ligand distance, R , for transition-metal complexes. What is its microscopic origin? *Int. J. Quantum Chem.* 52 (1994) 829–835, doi:10.1002/qua.56052041.
- [71] K. Wissing, J.A. Aramburu, M.T. Barriuso, M. Moreno, Optical properties due to Cr^{4+} in oxides: density functional study, *Solid State Commun.* 108 (1998) 1001–1005, doi:10.1016/S0038-1098(98)00479-7.
- [72] A.M. Srivastava, M.G. Brik, Crystal field studies of the Mn^{4+} energy levels in the perovskite, LaAlO_3 , *Opt. Mater. (Amst)* 35 (2013) 1544–1548, doi:10.1016/j.optmat.2013.03.021.
- [73] M.G. Brik, A.M. Srivastava, Electronic energy levels of the Mn^{4+} ion in the perovskite, CaZrO_3 , *ECS J. Solid State Sci. Technol.* 2 (2013) R148–R152, doi:10.1149/2.020307jss.
- [74] M.G. Brik, C.N. Avram, Exchange charge model and analysis of the microscopic crystal field effects in $\text{KAl}(\text{MoO}_4)_2:\text{Cr}^{3+}$, *J. Lumin.* 131 (2011) 2642–2645, doi:10.1016/j.jlumin.2011.06.034.
- [75] B.Z. Malkin, R.M. Macfarlane, A.A. Kaplyanski, *Spectroscopy of Solids Containing Rare-earth Ions*, Elsevier Science Publishers B.V., North-Holland, Amsterdam, 1987.
- [76] D.B. Fitchen, W.B. F. (Eds.), *Physics of Color Centers*, Academic, New York, 1968.
- [77] M.G. Brik, Crystal field analysis, electron-phonon coupling and spectral band shape modeling in $\text{MgO}:\text{Cr}^{3+}$, *Zeitschrift Für Naturforsch. A.* 60 (2005) 437–443, doi:10.1515/zna-2005-0609.
- [78] M.H. Du, Chemical trends of Mn^{4+} emission in solids, *J. Mater. Chem. C.* 2 (2014) 2475–2481, doi:10.1039/c4tc00031e.
- [79] K. Momma, F. Izumi, VESTA: a three-dimensional visualization system for electronic and structural analysis, *J. Appl. Crystallogr.* 44 (2011) 1272–1276.
- [80] S. Liang, M. Shang, H. Lian, K. Li, Y. Zhang, J. Lin, An efficient rare-earth free deep red emitting phosphor for improving the color rendering of white light-emitting diodes, *J. Mater. Chem. C.* 5 (2017) 2927–2935, doi:10.1039/c6tc05499d.
- [81] Y. Zhang, Z. Wu, D. Geng, X. Kang, M. Shang, X. Li, H. Lian, Z. Cheng, J. Lin, Full color emission in ZnGa_2O_4 : simultaneous control of the spherical morphology, luminescent, and electric properties via hydrothermal approach, *Adv. Funct. Mater.* 24 (2014) 6581–6593, doi:10.1002/adfm.201402092.
- [82] M.G. Brik, W.W. Beers, W. Cohen, S.A. Payne, N.J. Cherepy, M. Piasecki, A.M. Srivastava, On the Mn^{4+} R-line emission intensity and its tunability in solids, *Opt. Mater. (Amst)* 91 (2019) 338–343, doi:10.1016/j.optmat.2019.03.046.
- [83] H. Ji, J. Ueda, M.G. Brik, M.H. Du, D. Chen, S. Tanabe, Intense deep-red zero phonon line emission of Mn^{4+} in double perovskite $\text{La}_4\text{Ti}_3\text{O}_{12}$, *Phys. Chem. Chem. Phys.* 21 (2019) 25108–25117, doi:10.1039/c9cp04007b.
- [84] J. Kunitomo, R. Suzuki, Y. Takahashi, T. Miyazaki, N. Terakado, T. Fujiwara, Red-emissive Mn-doped $\text{Li}_2\text{Ge}_4\text{O}_9$ phase synthesized via glass-ceramic route, *J. Ceram. Soc. Japan* 122 (2014) 725–727, doi:10.2109/jcersj2.122.725.
- [85] Y. Odawara, Y. Takahashi, Y. Yamazaki, N. Terakado, T. Fujiwara, Synthesis of nanocrystals from glass-ceramics by YAG-laser irradiation: Mn^{4+} -doped $\text{Li}_2\text{Ge}_4\text{O}_9$ deep-red nanophosphor, *J. Lumin.* 125 (2017) 378–381.
- [86] Y. Cao, Y. Fang, G. Zhang, G. Zhao, Y. Liu, J. Zou, N. Vainos, J. Hou, High quantum yield red-emission phosphor $\text{Li}_2\text{Ge}_4\text{O}_9:\text{Mn}^{4+}$ for WLEDs application, *Opt. Mater. (Amst)* 98 (2019) 109442–109447, doi:10.1016/j.optmat.2019.109442.
- [87] K.S. Omel'chenko, O.V. Khmelenko, T.V. Panchenko, M.D. Volnyanski, Photoluminescence of manganese-doped $\text{LiNaGe}_4\text{O}_9$ crystals, *Phys. Solid State* 56 (2014) 751–756, doi:10.1134/S1063783414040246.
- [88] R. Suzuki, J. Kunitomo, Y. Takahashi, K. Nakamura, M. Osada, N. Terakado, T. Fujiwara, Mn-doped $\text{LiNaGe}_4\text{O}_9$ as a rare-earth free phosphor: impact of Na-substitution on emission in tetragrammatic phase, *J. Ceram. Soc. Japan* 123 (2015) 888–891, doi:10.2109/jcersj2.123.888.
- [89] P. Li, L. Tan, L. Wang, J. Zheng, M. Peng, Y. Wang, Synthesis, structure, and performance of efficient red phosphor $\text{LiNaGe}_4\text{O}_9:\text{Mn}^{4+}$ and its application in warm WLEDs, *J. Am. Ceram. Soc.* 99 (2016) 2029–2034, doi:10.1111/jace.14168.
- [90] X. Ding, Q. Wang, Y. Wang, Rare-earth-free red-emitting $\text{K}_2\text{Ge}_4\text{O}_9:\text{Mn}^{4+}$ phosphor excited by blue light for warm white LEDs, *Phys. Chem. Chem. Phys.* 18 (2016) 8088–8097, doi:10.1039/c6cp00168h.

- [91] P. Li, M.G. Brik, L. Li, J. Han, X. Li, M. Peng, Prediction on Mn⁴⁺-doped germanate red phosphor by crystal field calculation on basis of exchange charge model: a case study on K₂Ge₄O₉:Mn⁴⁺, *J. Am. Ceram. Soc.* 99 (2016) 2388–2394, doi:10.1111/jace.14236.
- [92] H. Vollenkle, A. Wittmann, Die Kristallstruktur des Kaliumtetragermanats K₂[Ge₄O₉], *Monatsh. Chem.* 102 (1971) 1245–1254, doi:10.1007/BF00917178.
- [93] J. Xue, W. Ran, H.M. Noh, B.C. Choi, S.H. Park, J.H. Jeong, J.H. Kim, Influence of alkaline ions on the luminescent properties of Mn⁴⁺-doped MGe₄O₉ (M = Li₂, LiNa and K₂) red-emitting phosphors, *J. Lumin.* 192 (2017) 1072–1083, doi:10.1016/j.jlumin.2017.08.036.
- [94] F. Baur, T. Jüstel, Dependence of the optical properties of Mn⁴⁺ activated A₂Ge₄O₉ (A=K, Rb) on temperature and chemical environment, *J. Lumin.* 177 (2016) 354–360, doi:10.1016/j.jlumin.2016.04.046.
- [95] R. Cao, D. Ceng, X. Yu, S. Guo, Y. Wen, G. Zheng, Synthesis and luminescence properties of novel deep red emitting phosphors Li₂MgGeO₄:Mn⁴⁺, *Funct. Mater. Lett.* 8 (2015) 1550046–1550049, doi:10.1142/S1793604715500460.
- [96] H. Zhu, C.C. Lin, W. Luo, S. Shu, Z. Liu, Y. Liu, J. Kong, E. Ma, Y. Cao, R.S. Liu, X. Chen, Highly efficient non-rare-earth red emitting phosphor for warm white light-emitting diodes, *Nat. Commun.* 5 (2014) 1–10, doi:10.1038/ncomms5312.
- [97] W. Yan, X. Yun, H. Yang, Y. Wei, G. Li, A novel Mn⁴⁺-activated Li₃CsGe₈O₁₈ red phosphor and cation substitution induced photoluminescence improvement, *J. Lumin.* 225 (2020) 117323–117333, doi:10.1016/j.jlumin.2020.117323.
- [98] F. Xue, Y. Hu, L. Chen, H. Wu, G. Ju, T. Wang, L. Yang, A novel rare-earth free red long-persistent phosphor: Mg₂GeO₄:Mn⁴⁺, *Ceram. Int.* 43 (2017) 15141–15145, doi:10.1016/j.ceramint.2017.08.044.
- [99] Q. Huang, W. Ye, G. Hu, X. Jiao, X. Liu, Deep red emission enhancement in Mg₂₈Ge₁₀O₄₈:Mn⁴⁺ phosphor by Zn substitution, *J. Lumin.* 194 (2018) 557–564, doi:10.1016/j.jlumin.2017.08.049.
- [100] Q. Huang, W. Ye, G. Hu, X. Liu, Strong red emission in Bi³⁺ and Mn⁴⁺ codoped Mg_{3.5}Ge_{1.25}O₆ phosphors applied in optical agriculture, *J. Lumin.* 210 (2019) 89–95, doi:10.1016/j.jlumin.2019.01.047.
- [101] S. Liang, G. Li, P. Dang, Y. Wei, H. Lian, J. Lin, Cation Substitution Induced Adjustment on Lattice Structure and Photoluminescence Properties of Mg₁₄Ge₅O₂₄:Mn⁴⁺: optimized Emission for w-LED and Thermometry Applications, *Adv. Opt. Mater.* 7 (2019) 1900093–1900107, doi:10.1002/adom.201900093.
- [102] R. Cao, W. Luo, Q. Xiong, S. Jiang, Z. Luo, J. Fu, Synthesis and photoluminescence properties of Ba₂GeO₄:Mn⁴⁺ novel deep red-emitting phosphor, *Chem. Lett.* 44 (2015) 1422–1424, doi:10.1246/cl.150578.
- [103] R. Cao, Y. Ye, Q. Peng, G. Zheng, H. Ao, J. Fu, Y. Guo, B. Guo, Synthesis and luminescence characteristics of novel red-emitting Ba₂TiGe₂O₈:Mn⁴⁺ phosphor, *Dye. Pigment.* 146 (2017) 14–19, doi:10.1016/j.dyepig.2017.06.061.
- [104] Z. Lu, A. Fu, F. Gao, X. Zhang, L. Zhou, Synthesis and luminescence properties of double perovskite Ba₂MgGeO₇:Mn⁴⁺ deep red phosphor, *J. Lumin.* 203 (2018) 420–426, doi:10.1016/j.jlumin.2018.06.061.
- [105] S. Fu, L. Tian, A novel deep red emission phosphor BaAl₂Ge₂O₈:Mn⁴⁺ for plant growth LEDs, *Optik (Stuttg)* 183 (2019) 635–641, doi:10.1016/j.ijleo.2019.02.131.
- [106] S. Liang, M. Shang, H. Lian, K. Li, Y. Zhang, J. Lin, Deep red MGe₄O₉:Mn⁴⁺ (M = Sr, Ba) phosphors: structure, luminescence properties and application in warm white light emitting diodes, *J. Mater. Chem. C* 4 (2016) 6409–6416, doi:10.1039/c6tc01813k.
- [107] S. Zhang, Y. Hu, Photoluminescence spectroscopies and temperature-dependent luminescence of Mn⁴⁺ in BaGe₄O₉ phosphor, *J. Lumin.* 177 (2016) 394–401, doi:10.1016/j.jlumin.2016.05.020.
- [108] W. Chen, Y. Cheng, L. Shen, C. Shen, X. Liang, W. Xiang, Red-emitting Sr₂MgGe₂O₇:Mn⁴⁺ phosphors: structure, luminescence properties, and application in warm white light emitting diodes, *J. Alloys Compd.* 762 (2018) 688–696, doi:10.1016/j.jallcom.2018.05.264.
- [109] X. Zhang, J. Nie, S. Liu, Y. Li, J. Qiu, Deep-red photoluminescence and long persistent luminescence in double perovskite-type La₂MgGeO₆:Mn⁴⁺, *Int. J. Lab. Hematol.* 101 (2018) 1576–1584, doi:10.1111/ijlh.12426.
- [110] S. Zhang, Y. Hu, H. Duan, L. Chen, Y. Fu, G. Ju, T. Wang, M. He, Novel La₃GaGe₅O₁₆:Mn⁴⁺ based deep red phosphor: a potential color converter for warm white light, *RSC Adv.* 5 (2015) 90499–90507, doi:10.1039/c5ra18163a.
- [111] X. Ding, G. Zhu, W. Geng, Q. Wang, Y. Wang, Rare-earth-free high-efficiency narrow-band red-emitting Mg₃Ga₂GeO₈:Mn⁴⁺ phosphor excited by near-UV light for white-light-emitting diodes, *Inorg. Chem.* 55 (2016) 154–162, doi:10.1021/acs.inorgchem.5b02048.
- [112] R. Cao, W. Luo, Q. Xiong, A. Liang, S. Jiang, Y. Xu, Synthesis and luminescence properties of novel red phosphors LiRGe₂O₆:Mn⁴⁺ (R = Al or Ga), *J. Alloys Compd.* 648 (2015) 937–941, doi:10.1016/j.jallcom.2015.07.080.
- [113] C. Wu, J. Li, H. Xu, J. Wu, J. Zhang, Z. Ci, L. Feng, C. Cao, Z. Zhang, Y. Wang, Preparation, structural and photoluminescence characteristics of novel red emitting Mg₇Ga₂GeO₁₂:Mn⁴⁺ phosphor, *J. Alloys Compd.* 646 (2015) 734–740, doi:10.1016/j.jallcom.2015.06.166.
- [114] X. Ding, Y. Wang, Structure and photoluminescence properties of rare-earth free narrow-band red-emitting Mg₆ZnGeGa₂O₁₂:Mn⁴⁺ phosphor excited by NUV light, *Opt. Mater. (Amst)* 64 (2017) 445–452, doi:10.1016/j.optmat.2017.01.003.
- [115] T. Jansen, J. Gorobez, M. Kirm, M.G. Brik, S. Vielhauer, M. Oja, N.M. Khaidukov, V.N. Makhov, T. Jüstel, Narrow band deep red photoluminescence of Y₂Mg₃Ge₃O₁₂:Mn⁴⁺, Li⁺ inverse garnet for high power phosphor converted LEDs, *ECS J. Solid State Sci. Technol.* 7 (2018) R3086–R3092, doi:10.1149/2.0121801jss.
- [116] L. Dong, L. Zhang, Y. Jia, B. Shao, S. Zhao, H. You, Site occupation and luminescence of novel orange-red Ca₃M₂Ge₃O₁₂:Mn²⁺, Mn⁴⁺ (M = Al, Ga) phosphors, *ACS Sustain. Chem. Eng.* 8 (2020) 3357–3366, doi:10.1021/acssuschemeng.9b07281.
- [117] L. Peng, W. Chen, S. Cao, B. Liu, T. Han, L. Zhao, C. Zhao, F. Li, X. Li, Enhanced photoluminescence and thermal properties due to size mismatch in Mg₂Ti_xGe_{1-x}O₄: Mn⁴⁺ deep-red phosphors, *J. Mater. Chem. C* 7 (2019) 2345–2352, doi:10.1039/c8tc05743e.
- [118] K. Van den Eckhout, D. Poelman, P.F. Smet, Persistent luminescence in Non-Eu²⁺-doped compounds: a review, *Materials (Basel)* 6 (2013) 2789–2818, doi:10.3390/ma6072789.
- [119] F. Liu, Y. Chen, Y. Liang, Z. Pan, Phonon-assisted upconversion charging in Zn₃Ga₂GeO₈:Cr³⁺ near-infrared persistent phosphor, *Opt. Lett.* 41 (2016) 954–957, doi:10.1364/ol.41.000954.
- [120] Y. Zhuang, J. Ueda, S. Tanabe, Enhancement of red persistent luminescence in Cr³⁺-doped ZnGa₂O₄ phosphors by Bi₂O₃ codoping, *Appl. Phys. Express.* 6 (2013) 052602–052605, doi:10.7567/APEX.6.052602.
- [121] Y. Zhan, Y. Jin, H. Wu, L. Yuan, G. Ju, Y. Lv, Y. Hu, Cr³⁺-doped Mg₄Ga₂Ge₃O₁₆ near-infrared phosphor membrane for optical information storage and recording, *J. Alloys Compd.* 777 (2019) 991–1000, doi:10.1016/j.jallcom.2018.11.065.
- [122] H. Lin, G. Bai, T. Yu, M.K. Tsang, Q. Zhang, J. Hao, Site Occupancy and near-infrared luminescence in Ca₃Ga₂Ge₃O₁₂:Cr³⁺ Persistent Phosphor, *Adv. Opt. Mater.* 5 (2017) 1700227–1700235, doi:10.1002/adom.201700227.
- [123] J. Zhou, Z. Xia, Synthesis and near-infrared luminescence of La₃GaGe₅O₁₆:Cr³⁺ phosphors, *RSC Adv.* 4 (2014) 46313–46318, doi:10.1039/c4ra09793a.
- [124] C. Wang, X. Wang, Y. Zhou, S. Zhang, C. Li, D. Hu, L. Xu, H. Jiao, An ultra-broadband near-infrared Cr³⁺-activated gallogermanate Mg₃Ga₂GeO₈ phosphor as light sources for food analysis, *ACS Appl. Electron. Mater.* 1 (2019) 1046–1053, doi:10.1021/acsaem.9b00219.
- [125] I.W. Kim, S. Kaur, A. Yadav, A.S. Rao, S. Saravanakumar, J.L. Rao, V. Singh, Structural, luminescence and EPR properties of deep red emitting Mg₇Al₄SiO₁₂:Cr³⁺ garnet phosphor, *J. Lumin.* 220 (2020) 116975–116981, doi:10.1016/j.jlumin.2019.116975.
- [126] N. Basavaraju, S. Sharma, A. Bessière, B. Viana, D. Gourier, K.R. Priolkar, Red persistent luminescence in MgGa₂O₄:Cr³⁺: A new phosphor for in vivo imaging, *J. Phys. D: Appl. Phys.* 46 (2013) 375401–375405, doi:10.1088/0022-3727/46/37/375401.
- [127] Y. Katayama, H. Kobayashi, S. Tanabe, Deep-red persistent luminescence in Cr³⁺-doped LaAlO₃ perovskite phosphor for in vivo imaging, *Appl. Phys. Express.* 8 (2015) 0121010–0121023, doi:10.7567/APEX.8.012102.
- [128] Q. Bai, P. Li, Z. Wang, T. Li, S. Xu, Z. Wang, Using Ca²⁺ ions to induce the long afterglow and bluish white emission of red emitting phosphor Zn₉Al₂Ge₂O₁₀:Cr³⁺, *Mater. Des.* 91 (2016) 28–36, doi:10.1016/j.matdes.2015.11.061.
- [129] S.H. Yang, Y.C. Hung, P.C. Tseng, H.Y. Lee, Versatile deep-red Mg₂TiO₄:Mn⁴⁺ phosphor for photoluminescence, thermometry, and latent fingerprint visualization, *J. Alloys Compd.* 801 (2019) 394–401, doi:10.1016/j.jallcom.2019.06.028.
- [130] X. Zhao, X. Wang, B. Chen, Q. Meng, W. Di, G. Ren, Y. Yang, Novel Eu³⁺-doped red-emitting phosphor Gd₂Mo₃O₉ for white-light-emitting-diodes (WLEDs) application, *J. Alloys Compd.* 433 (2007) 352–355, doi:10.1016/j.jallcom.2006.06.096.
- [131] H. Zhang, H. Zhang, J. Zhuang, H. Dong, Y. Zhu, X. Ye, Y. Liu, B. Lei, Effect of H₂BO₃ flux on the morphology and optical properties of Sr₇MgAl₂₂O₃₆:Mn⁴⁺ red phosphors for agricultural light conversion films, *Ceram. Int.* 42 (2016) 13011–13017, doi:10.1016/j.ceramint.2016.05.076.
- [132] S.J. Lee, J. Jung, J.Y. Park, H.M. Jang, Y.R. Kim, J.K. Park, Application of red light-emitting diodes using Mg_{3.5}Ge_{1.25}O₆:Mn⁴⁺ phosphor, *Mater. Lett.* 111 (2013) 108–111, doi:10.1016/j.matlet.2013.08.098.
- [133] M. Abraham, A.K. Kunti, K.K. Thejas, N. Amador-Mendez, N. Gogneau, K.G. Nishanth, M. Tchernycheva, S. Das, The elevated colour rendering of white-LEDs by microwave-synthesized red-emitting (Li, Mg)3RbGe8O18:Mn⁴⁺ nanophosphors, 50 (2021) 3044–3059. <https://doi.org/10.1039/d0dt04309e>.
- [134] D. Xie, H. Peng, S. Huang, F. You, Core-shell structure in doped inorganic nanoparticles: approaches for optimizing luminescence properties, *J. Nanomater.* 2013 (2013) 1–10, doi:10.1155/2013/891515.
- [135] L. Dolgov, J. Hong, L. Zhou, X. Li, J. Li, V. Djordjevic, M. Dramicanin, J. Shi, M. Wu, Efficient luminescence enhancement of Mg₂TiO₄:Mn⁴⁺ red phosphor by incorporating plasmonic Ag@SiO₂ nanoparticles, *ACS Appl. Mater. Interfaces* 11 (2019) 21004–21009, doi:10.1021/acami.9b05781.
- [136] Y. Xu, Y. Zhang, L. Wang, M. Shi, L. Liu, Y. Chen, Red emission enhancement for CaAl₁₂O₁₉:Cr³⁺ and CaAl₁₂O₁₉:Mn⁴⁺ phosphors, *J. Mater. Sci. Mater. Electron.* 28 (2017) 12032–12038, doi:10.1007/s10854-017-7014-3.
- [137] G.B. Nair, S.J. Dhoble, Fundamentals of LEDs, *Fundam. Appl. Light. Diodes.* (2020) 35–57, doi:10.1016/b978-0-12-819605-2.00002-1.
- [138] Y. Zhu, X. Li, B. Zhu, Y. Liang, Design of core-shell phosphors with tunable luminescence and improved thermal stability by coating with g-C₃N₄, *Inorg. Chem. Front.* 7 (2020) 3126–3135, doi:10.1039/d0qi00498g.
- [139] T. Xu, L. Yuan, Y. Chen, Y. Zhao, L. Ding, J. Liu, W. Xiang, X. Liang, Y₃Al₅O₁₂:Ce³⁺ single crystal and red-emitting Y₃Al₅O₁₂:Cr³⁺ single crystal for high power W-LEDs, *Opt. Mater. (Amst)* 91 (2019) 30–34, doi:10.1016/j.optmat.2019.03.010.
- [140] A. Abdulkayum, J.T. Chen, Q. Zhao, X.P. Yan, Functional near infrared-emitting Cr³⁺/Pr³⁺ Co-doped zinc gallogermanate persistent luminescent nanoparticles with superlong afterglow for in vivo targeted bioimaging, *J. Am. Chem. Soc.* 135 (2013) 14125–14133, doi:10.1021/ja404243v.

- [141] S. Zhang, Y. Hu, L. Chen, Y. Fu, G. Ju, $\text{La}_3\text{GaGe}_5\text{O}_{16}:\text{Cr}^{3+}$ phosphor: the near-infrared persistent luminescence, *Opt. Mater. Express*. 6 (2016) 1247–1255, doi:[10.1364/ome.6.001247](https://doi.org/10.1364/ome.6.001247).
- [142] E. Pavitra, G.S.R. Raju, J.Y. Park, S.K. Hussain, N.R. Chodankar, G.M. Rao, Y.K. Han, Y.S. Huh, An efficient far-red emitting $\text{Ba}_2\text{LaNbO}_6:\text{Mn}^{4+}$ nanophosphor for forensic latent fingerprint detection and horticulture lighting applications, *Ceram. Int.* 46 (2020) 9802–9809, doi:[10.1016/j.ceramint.2019.12.253](https://doi.org/10.1016/j.ceramint.2019.12.253).
- [143] R.S.P. King, D.A. Skros, Sunlight-activated near-infrared phosphorescence as a viable means of latent fingerprint visualisation, *Forensic Sci. Int.* 276 (2017) e35–e39, doi:[10.1016/j.forsciint.2017.04.012](https://doi.org/10.1016/j.forsciint.2017.04.012).
- [144] H. Ming, L. Liu, S. He, J. Peng, F. Du, J. Fu, F. Yang, X. Ye, An ultra-high yield of spherical $\text{K}_2\text{NaScF}_6:\text{Mn}^{4+}$ red phosphor and its application in ultra-wide color gamut liquid crystal displays, *J. Mater. Chem. C* 7 (2019) 7237–7248, doi:[10.1039/c9tc02295c](https://doi.org/10.1039/c9tc02295c).
- [145] C. Pratapkumar, S.C. Prashantha, H. Nagabhushana, D.M. Jnaneshwara, Photoluminescence and photometric studies of low temperature prepared red emitting $\text{MgAl}_2\text{O}_4:\text{Cr}^{3+}$ nanophosphors for solid state displays, *J. Sci. Adv. Mater. Devices* 3 (2018) 464–470, doi:[10.1016/j.jsamd.2018.09.002](https://doi.org/10.1016/j.jsamd.2018.09.002).
- [146] N.T. Huyen, N. Tu, D.T. Tung, D.Q. Trung, D.D. Anh, T.T. Duc, T.T.T. Nga, P.T. Huy, Photoluminescent properties of red-emitting phosphor $\text{BaMgAl}_{10}\text{O}_{17}:\text{Cr}^{3+}$ for plant growth LEDs, *Opt. Mater. (Amst)* 108 (2020) 110207–110213, doi:[10.1016/j.optmat.2020.110207](https://doi.org/10.1016/j.optmat.2020.110207).
- [147] M.N. Getz, O. Nilsen, P.A. Hansen, Sensors for optical thermometry based on luminescence from layered $\text{YVO}_4:\text{Ln}^{3+}$ ($\text{Ln} = \text{Nd, Sm, Eu, Dy, Ho, Er, Tm, Yb}$) thin films made by atomic layer deposition, *Sci. Rep.* 9 (2019) 1–11, doi:[10.1038/s41598-019-46694-8](https://doi.org/10.1038/s41598-019-46694-8).
- [148] A. Mondal, J. Manam, Structural, optical and temperature dependent photoluminescence properties of Cr^{3+} -activated LaGaO_3 persistent phosphor for optical thermometry, *Ceram. Int.* 46 (2020) 23972–23984, doi:[10.1016/j.ceramint.2020.06.174](https://doi.org/10.1016/j.ceramint.2020.06.174).
- [149] Q. Wang, Z. Liang, J. Luo, Y. Yang, Z. Mu, X. Zhang, H. Dong, F. Wu, Ratiometric optical thermometer with high sensitivity based on dual far-red emission of Cr^{3+} in $\text{Sr}_2\text{MgAl}_{22}\text{O}_{36}$, *Ceram. Int.* 46 (2020) 5008–5014, doi:[10.1016/j.ceramint.2019.10.241](https://doi.org/10.1016/j.ceramint.2019.10.241).
- [150] W.G.J.H.M. van Sark, A. Meijerink, R.E.I. Schropp, Solar spectrum conversion for photovoltaics using nanoparticles, in: V. Fthenakis (Ed.), *Third Gener. Photovoltaics*, InTechOpen, Croatia, 2012, pp. 1–28, doi:[10.1201/9781420076752](https://doi.org/10.1201/9781420076752).
- [151] S. Adachi, Review— Mn^{4+} -activated red and deep red-emitting phosphors, *ECS J. Solid State Sci. Technol.* 9 (2020) 016001–016034, doi:[10.1149/2.0022001jss](https://doi.org/10.1149/2.0022001jss).

Enriching the Deep-Red Emission in $(\text{Mg}, \text{Ba})_3\text{M}_2\text{GeO}_8: \text{Mn}^{4+}$ ($\text{M} = \text{Al}, \text{Ga}$) Compositions for Light-Emitting Diodes

Thejas Kurunthatil Kuttia, Malini Abraham, Arup K. Kunti, Nuño Amador-Mendez, Maria Tchernycheva, and Subrata Das*



Cite This: *ACS Appl. Mater. Interfaces* 2023, 15, 7083–7101



Read Online

ACCESS |

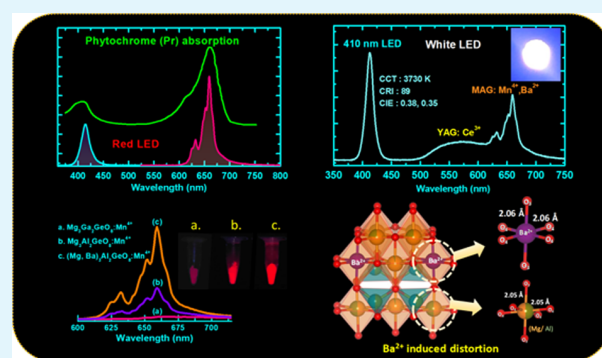
Metrics & More

Article Recommendations

Supporting Information

ABSTRACT: Red emission from Mn^{4+} -containing oxides inspired the development of high color rendering and cost-effective white-light-emitting diodes (WLEDs). Aiming at this fact, a series of new crystallographic site modified $(\text{Mg}, \text{Ba})_3\text{M}_2\text{GeO}_8: \text{Mn}^{4+}$ ($\text{M} = \text{Al}, \text{Ga}$) compositions were developed with strong deep-red emission in the reaction to UV and blue lights. The $\text{Mg}_3\text{Al}_2\text{GeO}_8$ host is composed of three phases: orthorhombic- $\text{Mg}_3\text{Ga}_2\text{GeO}_8$, orthorhombic- Mg_2GeO_4 , and cubic- MgAl_2O_4 . However, $\text{Mg}_3\text{Ga}_2\text{GeO}_8$ secured an orthorhombic crystal structure. Interestingly, $\text{Mg}_3\text{Al}_2\text{GeO}_8: \text{Mn}^{4+}$ showed a 13-fold more intense emission than $\text{Mg}_3\text{Ga}_2\text{GeO}_8: \text{Mn}^{4+}$ since Mn^{4+} occupancy was preferable to $[\text{AlO}_6]$ sites compared to $[\text{GaO}_6]$. The coexisting phases of MgAl_2O_4 and Mg_2GeO_4 in $\text{Mg}_3\text{Al}_2\text{GeO}_8: \text{Mn}^{4+}$ contributed to Mn^{4+} luminescence by providing additional $[\text{AlO}_6]$ and $[\text{MgO}_6]$ octahedrons for Mn^{4+} occupancy. Further, these sites reduced the natural reduction probability of Mn^{4+} to Mn^{2+} in $[\text{AlO}_4]$ tetrahedrons, which was confirmed using cathodoluminescence analysis for the first time. A cationic substitution strategy was employed on $\text{Mg}_3\text{M}_2\text{GeO}_8: \text{Mn}^{4+}$ to improve the luminescence, and $\text{Mg}_{3-x}\text{Ba}_x\text{M}_2\text{GeO}_8: \text{Mn}^{4+}$ ($\text{M} = \text{Al}, \text{Ga}$) phosphors were synthesized. Partial substitution of larger Ba^{2+} ions in Mg^{2+} sites caused structural distortions and generated a new Ba impurity phase, which improved the photoluminescence. Compositionally tuned $\text{Mg}_{2.73}\text{Ba}_{0.27}\text{Al}_{1.993}\text{GeO}_8: 0.005\text{Mn}^{4+}$ exhibited a 35-fold higher emission than that of $\text{Mg}_3\text{Ga}_{1.993}\text{GeO}_8: 0.005\text{Mn}^{4+}$. Additionally, this could retain 70% of its ambient emission intensity at 453 K. A warm WLED with a correlated color temperature (CCT) of 3730 K and a CRI of 89 was fabricated by combining the optimized red component with $\text{Y}_3\text{Al}_5\text{O}_{12}: \text{Ce}^{3+}$ and 410 nm blue LED. By tuning the ratio of blue ($\text{BaMgAl}_{10}\text{O}_{17}: \text{Eu}^{2+}$), green ($\text{Ce}_{0.63}\text{Tb}_{0.37}\text{MgAl}_{11}\text{O}_{19}$), and red ($\text{Mg}_{2.73}\text{Ba}_{0.27}\text{Al}_2\text{GeO}_8: 0.005\text{Mn}^{4+}$) phosphors, another WLED was developed using a 280 nm UV-LED chip. This showed natural white emission with a CRI of 79 and a CCT of 5306 K. Meanwhile, three red LEDs were also fabricated using the $\text{Mg}_{2.73}\text{Ba}_{0.27}\text{Al}_{1.993}\text{GeO}_8: 0.005\text{Mn}^{4+}$ phosphor with commercial sources. These could be potential pc-LEDs for plant growth applications.

KEYWORDS: Mn^{4+} emission enrichment, cationic substitutions, distorted lattice, photo- and cathode-luminescence, light-emitting diodes



1. INTRODUCTION

Deep-red-emitting Mn^{4+} -activated oxides are gathering extensive attention as suitable replacements for expensive rare-earth-based phosphors for potential applications in white-light-emitting diodes (WLEDs), security, sensing, plant growth, detectors, etc. Several Mn^{4+} -doped fluorides have recently been commercialized due to their eye-sensitive red peak at ~ 630 nm.^{1–3} Regrettably, these phosphors are unstable and require the use of highly corrosive HF for synthesis.^{1–3} However, Mn^{4+} -activated oxide phosphors have advantages such as eco-friendly preparation, higher thermal as well as chemical stability, and deep-red emission ($\lambda_{\text{em}} > 650$ nm). Moreover, Mn^{4+} ions can be stabilized in the Al^{3+} ($r_{\text{AlO}_6} = 0.535$ Å) and Ge^{4+} ($r_{\text{GeO}_6} = 0.53$ Å) octahedrons due to close ionic sizes with Mn^{4+} ($r_{\text{MnO}_6} = 0.53$ Å).^{3–8} Recently reported potential hosts such as $\text{Li}_3\text{RbGe}_8\text{O}_{18}$,

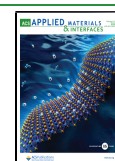
$\text{Mg}_{14}\text{Ge}_5\text{O}_{24}$,⁹ Mg_2TiO_4 ,¹⁰ $\text{Mg}_3\text{Ga}_2\text{GeO}_8$,¹¹ BaGe_4O_9 ,¹², etc. are observed to be suitable for Mn^{4+} ions to generate a deep-red emission. However, the red emission intensity of these samples needs to be enhanced further for commercial lighting and display applications.

Huang et al. intensified the deep-red emission of $\text{Mg}_{14}\text{Ge}_5\text{O}_{24}: \text{Mn}^{4+}$ by Bi^{3+} coactivation,¹³ which sensitized Mn^{4+} ions effectively. Liang et al. boosted the deep-red emission of this phosphor by 2.49 times via substituting Ti^{4+} and Sn^{4+} in the Ge^{4+}

Received: November 8, 2022

Accepted: January 6, 2023

Published: January 26, 2023



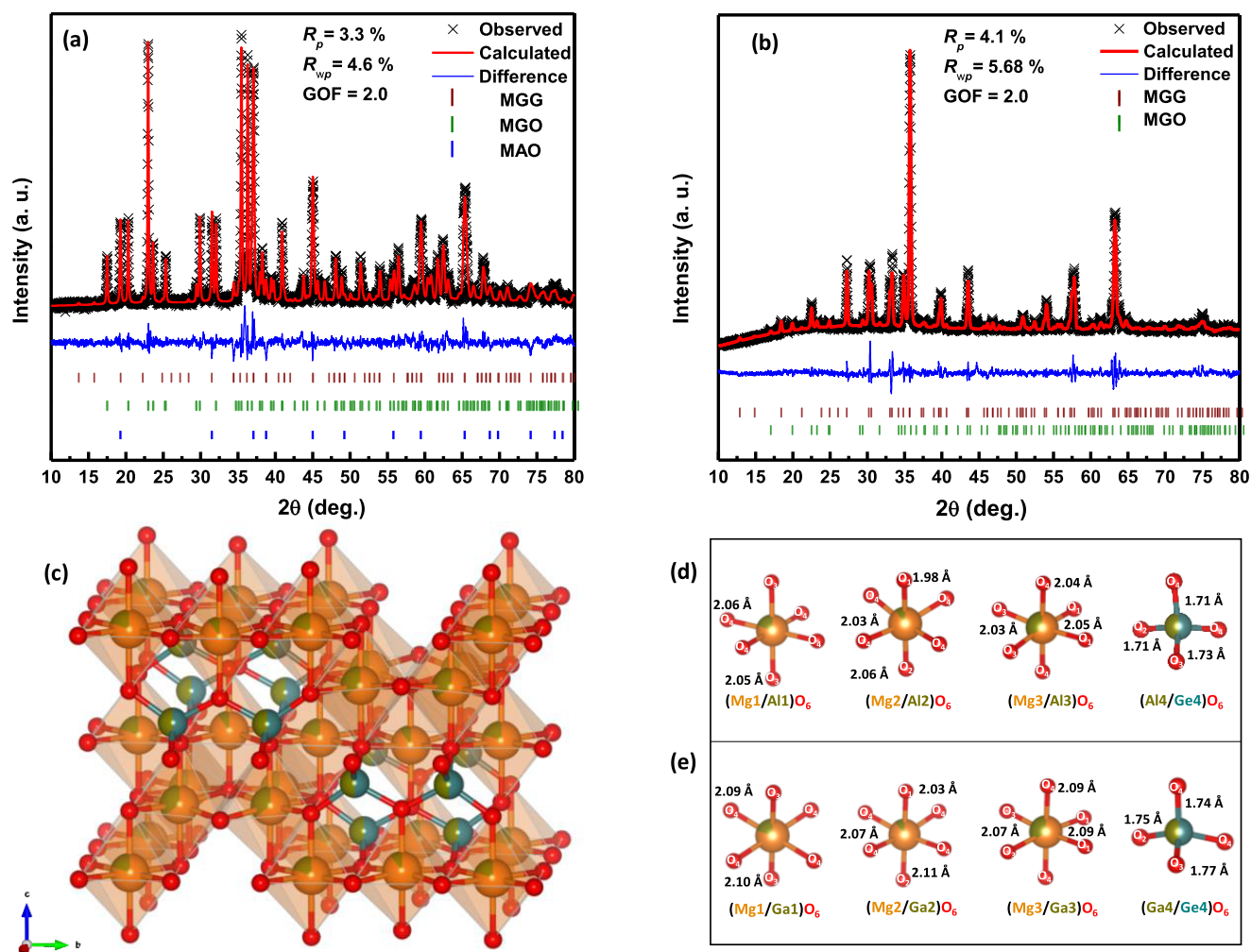


Figure 1. Rietveld refinement patterns of (a) MAG and (b) MGG. (c) Representation of an orthorhombic crystal arrangement for $\text{Mg}_3\text{M}_2\text{GeO}_8$ ($\text{M} = \text{Al}, \text{Ga}$) with the corresponding polyhedrons of (d) MAG and (e) MGG.

octahedrons, and it introduced some resonance effects due to the multiple luminescence centers.¹⁴ Likewise, the emission intensity of $\text{Mg}_2\text{TiO}_4: \text{Mn}^{4+}$ was immensely improved via Ge^{4+} -ion substitution in Ti^{4+} sites. Such a replacement enhanced the conversion of more $[\text{TiO}_6]$ octahedrons to $[\text{GeO}_6]$, which separated adjacent Mn^{4+} ions and interrupted the energy migrations among Mn^{4+} ionic pairs within the lattice.¹⁵ Recently, Mg^{2+} codoping in Li sites was employed to increase the emission intensity of $\text{Li}_3\text{RbGe}_8\text{O}_{18}: \text{Mn}^{4+}$ by reducing surface defects (conversion of surface oxygen to lattice oxygen).¹⁶

Since Mn^{4+} is a matrix-sensitive activator, cation substitution can induce a considerable impact on luminescence properties. Due to this fact, Mn^{4+} -activated $\text{Mg}_3\text{Ga}_2\text{GeO}_8$ ¹¹ was chosen for a case study and the emission intensity could be intensified via suitable cationic modifications. A major advantage of this phosphor is its multiple luminescence centers. According to Ding et al., Mn^{4+} ions can occupy both $[\text{MgO}_6]$ and $[\text{GaO}_6]$ octahedrons and produce a deep-red emission at 659 nm. Synthesizing mixed-phased hosts could be another promising strategy for improving luminescence efficiency. Wu et al. developed Mn^{4+} -activated red phosphor composed of $\text{CaAl}_{12}\text{O}_{19}$ and MgAl_2O_4 phases,¹⁷ where the coexisting phase

MgAl_2O_4 acted as a flux throughout the sintering process and increased the crystallinity and red emission intensity.

Herein, a new class of deep-red-emitting $\text{Mg}_3\text{M}_2\text{GeO}_8: \text{Mn}^{4+}$ ($\text{M} = \text{Al}, \text{Ga}$) compositions were developed. In particular, the $\text{Mg}_3\text{Al}_2\text{GeO}_8: \text{Mn}^{4+}$ emission is higher than that of $\text{Mg}_3\text{Ga}_2\text{GeO}_8: \text{Mn}^{4+}$. The substitution of Ba^{2+} ions in the Mg^{2+} sites enhanced the deep-red emission substantially. The presence of a new impurity-phase tetragonal- $\text{Ba}_2\text{MgGe}_2\text{O}_7$ was identified with Ba^{2+} substitution in $\text{Mg}_3\text{Al}_2\text{GeO}_8: \text{Mn}^{4+}$ and $\text{Mg}_3\text{Ga}_2\text{GeO}_8: \text{Mn}^{4+}$ samples. The emission intensity of the compositionally tuned $\text{Mg}_{2.73}\text{Ba}_{0.27}\text{Al}_2\text{GeO}_8: 0.005\text{Mn}^{4+}$ was found to be 3- and 35-fold greater than $\text{Mg}_3\text{Al}_2\text{GeO}_8: \text{Mn}^{4+}$ and $\text{Mg}_3\text{Ga}_2\text{GeO}_8: \text{Mn}^{4+}$, respectively. The optimized $\text{Mg}_{2.73}\text{Ba}_{0.27}\text{Al}_2\text{GeO}_8: 0.005\text{Mn}^{4+}$ phosphor showed an extensive choice of absorption features reaching from UV to blue and emitting intense red light maxima at 659 nm. This emission wavelength matches well with the chlorophylls' absorption choice accountable for plants' photosynthesis, and accordingly, it could be effective for indoor plant cultivation.¹⁸ Moreover, the intense red emission with 100% color purity of the optimized composition makes it a suitable red phosphor candidate to enhance the color rendering index (CRI) and reduce the correlated color temperature (CCT) of commercial phosphor-based white LEDs.

2. EXPERIMENTAL SECTION

2.1. Material Synthesis. The phosphors $\text{Mg}_3\text{Al}_{(2-4/3 \times 0.005)}\text{GeO}_8$: 0.005Mn^{4+} (MAG: Mn^{4+}), $\text{Mg}_3\text{Ga}_{(2-4/3 \times 0.005)}\text{GeO}_8$: 0.005Mn^{4+} (MGG: Mn^{4+}), and a series of Ba^{2+} -substituted $\text{Mg}_{3-x}\text{Al}_{(2-4/3 \times 0.005)}\text{GeO}_8$: 0.005Mn^{4+} , $x\text{Ba}^{2+}$ (MAG: Mn^{4+} , $x\text{Ba}^{2+}$) and $\text{Mg}_{3-x}\text{Ga}_{(2-4/3 \times 0.005)}\text{GeO}_8$: 0.005Mn^{4+} , $x\text{Ba}^{2+}$ (MGG: Mn^{4+} , $x\text{Ba}^{2+}$) compositions were prepared via the solid-state synthesis method. MgO (99.99%), Ga_2O_3 (99.99%), Al_2O_3 (99.6%), GeO_2 (99.998%), MnO_2 (>99%), BaCO_3 (99.8%), and 0.25 wt % H_3BO_3 (99.999%) are the raw materials (purchased from Sigma-Aldrich) used for synthesis. Required raw materials for the synthesis of different compositions are weighed and taken in a stoichiometric ratio. These raw materials were mixed with ethanol in an agate mortar and ground for 30 min. After drying, a white powder was obtained, and it is preheated in an air furnace at 600 °C for 2 h followed by sintering at 1300 °C for 6 h with intermediate grinding. The heating rate applied for calcination was 5 °C/min. After cooling, the final powder was ground and used for further characterization.

2.2. Characterization. The crystal structures of the obtained samples were analyzed by collecting the X-ray powder diffraction (XRD) patterns using a Malvern PANalytical B.V. EMPYREAN 3 diffractometer with Ni-filtered $\text{Cu K}\alpha$ radiation ($\lambda = 1.54 \text{ \AA}$). Rietveld refinement analysis was carried out using GSAS2 software. Micro-Raman spectroscopy was performed using an Alpha 300 R, WITec Spectra PRO Raman spectrometer using a laser power of 10 W. The X-ray photoelectron spectroscopy (XPS) analysis was accomplished with a PHI 5000 VersaProbe II equipped with a micro-focused (200 μm , 15 kV) monochromatic Al $\text{K}\alpha$ X-ray source (1486.6 eV). The structural properties were identified using a high-resolution transmission electron microscope (HRTEM), JEOL JEM-F200. The morphology, including elemental investigation of the prepared samples, was examined using scanning electron microscopy (JEOL JSM-5600 LV SEM). The UV–vis diffuse reflectance spectra (DRS) measurements were recorded using a Shimadzu UV–vis–NIR spectrophotometer (UV 3600). The photoluminescence (PL) excitation, emission, quantum efficiency (QE), and lifetime were investigated using a Yvon Fluorolog 3 spectrofluorimeter having a 450 W xenon irradiation source. The cathodoluminescence (CL) spectral analysis was performed by an Attolight Chronos CL-scanning electron microscope. The CL spectra were achieved with an achromatic reflective objective (numerical aperture 0.72) that delivers persistent recording capacity over a diameter field view of $\sim 150 \mu\text{m}$. The electron beam acceleration voltage and current were fixed at 6 kV and 2 nA, respectively. The CL emission spectra were dispersed with a Horiba diffraction grating (150 grooves/mm) and taken with an Andor Newton charge-coupled device (CCD) camera (1024 \times 256 pixels, pixel width 26 μm). The resultant spectral dispersion was 0.53 nm/pixel.

For evaluating the device performances, the optimum red component was mixed with $\text{Y}_3\text{Al}_5\text{O}_{12}$: Ce^{3+} (YAG: Ce^{3+}), and the mixture was incorporated with poly(methyl methacrylate) (PMMA; Sigma-Aldrich). With the above mixture, acralyn cold-curing liquid (Asian Acrylates, India) was added during stirring to make a thick paste. The paste was then deposited on a 410 nm violet-blue InGaN LED, which functioned at 300 mA. The electroluminescence (EL) behaviors of the phosphor-LED system were recorded using a CCD spectrophotometer (Ocean Optics Maya 2000 Pro). Another WLED was fabricated by mixing the optimum red component with the commercial blue and green components in an appropriate ratio. The EL spectra for these WLEDs and red LEDs were measured using the same spectrophotometer with 280 nm LEDs at a 1 A current.

3. RESULTS AND DISCUSSION

3.1. Elucidation of Structural Information. The XRD pattern of the inactivated $\text{Mg}_3\text{Al}_2\text{GeO}_8$ (MAG) was Rietveld-refined with three phases, viz. orthorhombic- $\text{Mg}_3\text{Ga}_2\text{GeO}_8$ (o-MGG, space group *Imma*), orthorhombic Mg_2GeO_4 (o-MGO, space group *Pnma*), and cubic- MgAl_2O_4 (c-MAO, space group *Fd-3m*). The refinement pattern of this mixed-phase composi-

tion is shown in Figure 1a, where MAG, an analog of the orthorhombic $\text{Mg}_3\text{Ga}_2\text{GeO}_8$ phase (space group *Imma*), appears as the main phase. The refinement results are tabulated in the Supporting Information (Tables S1 and S2), and the corresponding crystal structure, drawn using Vesta software, is shown in Figure 1c. The crystal assembly of the MAG phase consists of octahedral and tetrahedral units captured by the $\text{Mg}^{2+}/\text{Al}^{3+}$ ions and $\text{Ge}^{4+}/\text{Al}^{3+}$ ions, respectively. Here, Mn^{4+} ions preferentially occupy any of the three octahedrons provided by (Mg1/Al1), (Mg2/Al2), and (Mg3/Al3) sites, as shown in Figure 1c, due to the strong ligand field stabilization energy of Mn^{4+} ions in the octahedral sites.^{19,20} Meanwhile, the Rietveld analysis of $\text{Mg}_3\text{Ga}_2\text{GeO}_8$ (MGG) indicated that this host is crystallized in the orthorhombic arrangement with the space group of *Imma* (Figure 1b). A small fraction of impurity-phase o-MGO is also observed in this structure. According to Ding and co-workers, the activator Mn^{4+} ions can reliably occupy the $[\text{MgO}_6]$ and $[\text{GaO}_6]$ octahedrons rather than the $[\text{GeO}_4]$ or $[\text{GaO}_4]$ tetrahedrons in this host.¹¹

The calculated lattice parameters of MAG and MGG samples are listed in Table S1, and the obtained metal–oxygen bond lengths for their structures are presented in Table S4. The lower value of the lattice volume of the MAG host (534.06 \AA^3) in comparison with that of MGG (569.13 \AA^3) can be attributed to the smaller ionic radii of Al^{3+} ($r_{\text{AlO}_6} = 0.53 \text{ \AA}$) ions compared to Ga^{3+} ($r_{\text{GaO}_6} = 0.62 \text{ \AA}$) ions in the subsequent octahedral coordination. The $[(\text{Mg}/\text{Al})\text{O}_6]$ octahedrons and $[\text{AlO}_4]$ tetrahedrons in the MAG sample are found to be more contracted and distorted relative to the $[(\text{Mg}/\text{Ga})\text{O}_6]$ octahedrons and $[\text{GaO}_4]$ tetrahedrons in the MGG sample, as can be seen in Figure 1d,e, respectively.¹⁵ Such a contraction can be ascribed to the smaller Al–O bond lengths of the MAG compared to Ga–O bond lengths in the MGG (Table S4). Similar kinds of lattice volume reduction and bond-length contraction have been reported previously for $\text{Ca}_3\text{Ga}_2\text{Ge}_3\text{O}_{12}$ and $\text{LiGaGe}_2\text{O}_6$ hosts due to Al substitution in Ga sites.^{21,22}

The high-resolution microscopic analysis was also carried out for the samples MAG and MGG to verify the presence of different phases present in both samples by identifying the interplanar spacing of adjacent lattice fringes. Figure 2a,b depicts the HRTEM images of MAG and MGG host matrices, respectively. Figure 2a-i presents the magnified version of a region of the HRTEM image of MAG. The interplanar distance of the fringe pattern of this section is calculated to be 2.56 \AA , which is attributed to the (1 3 2) lattice planes of the orthorhombic-MGG phase (JCPDS 039-1108). Likewise, the other two insets, Figure 2a-ii, and Figure 2a-iii depict the two different regions of the HRTEM image of MAG. The interplanar distances of the fringe arrangements in these two magnified regions are calculated to be 2.88 and 3.06 \AA , respectively, which correspond to the (2 2 0) and (2 1 1) planes of the cubic-MAO (JCPDS 086-0096) and orthorhombic-MGO (JCPDS 078-2316) phases, respectively. However, only one existing phase has been identified in the HRTEM image of the MGG host, in which the interplanar distances of 4.77 and 2.67 \AA (Figure 2b-i,ii, respectively) correspond to the (1 0 1) and (2 1 1) planes of the orthorhombic-MGG phase (JCPDS 039-1108).

Existence of all of the major elements in the MAG: Mn^{4+} sample including Mg, Al, Ge, O, and Mn^{4+} is confirmed by the XPS survey spectra, as revealed in Figure S1a. The energy-dispersive X-ray (EDX) spectra (Figure S1b) and elemental mapping (Figure S1c) further confirmed the existence of the

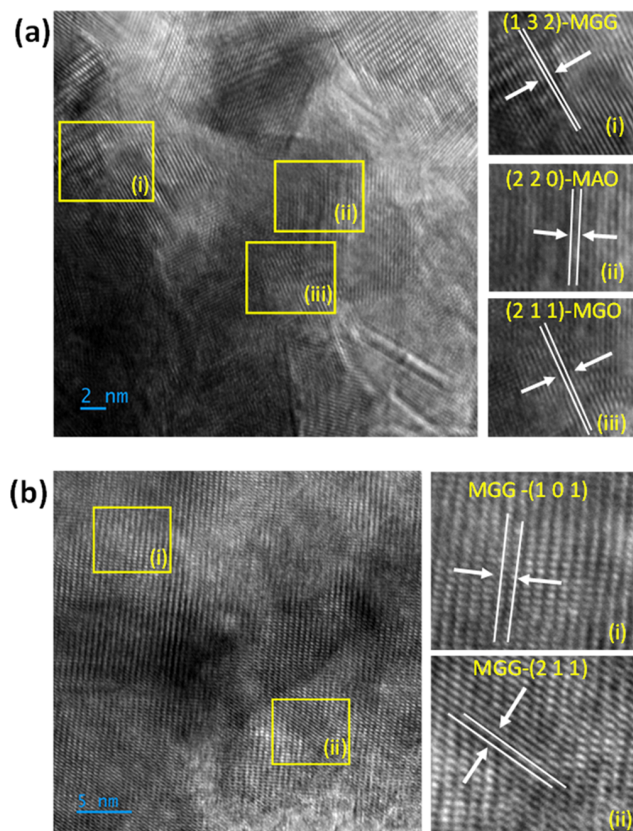


Figure 2. HRTEM images of the (a) MAG sample with a magnified version of three different regions denoted as (i), (ii), and (iii), and (b) MGG sample with a magnified version of two different regions denoted as (i) and (ii).

above elements with stoichiometric homogeneity. Meanwhile, the SEM images of MAG: Mn⁴⁺, shown in Figure S1c, exhibited an irregular granular morphology, and the sizes are in the micron range. The XPS and EDX results of the MGG: Mn⁴⁺ sample are also presented in the Supporting Information (Figure S2).

3.2. Effect of Ba²⁺ Doping on the Crystal Structure of Mg₃M₂GeO₈ (M = Al, Ga). The recorded XRD patterns of MAG: 0.005Mn⁴⁺ and MGG: 0.005Mn⁴⁺ samples including their structural parameters cannot be differentiated from the respective patterns and parameters of MAG and MGG samples. Because of this reason, the Rietveld refinement analysis of MAG: 0.005Mn⁴⁺ and MGG: 0.005Mn⁴⁺ samples are not included. However, to realize the effect of cationic substitution by larger-sized Ba²⁺ ions ($r_{\text{BaO}_6} = 1.35 \text{ \AA}$) on the crystal structure of Mg₃M₂GeO₈ (M = Al, Ga), the Rietveld refinement analysis of MAG: Mn⁴⁺, 0.03Ba²⁺ and MGG: Mn⁴⁺, 0.1Ba²⁺ samples were carried out, and the resultant plots are given in Figure 3a,b, respectively. The XRD pattern of MAG: Mn⁴⁺, 0.03Ba²⁺ was Rietveld-refined using four reference phases, *viz.* o-MGG, o-MGO, c-MAO, and tetragonal-Ba₂MgGe₂O₇ (t-BMG, space group *P*-421*m*), whereas the refinement of MGG: Mn⁴⁺, 0.1Ba²⁺ was carried out with three phases, *viz.* o-MGG, o-MGO, and t-BMG. The calculated refinement parameters are tabulated in Tables S1 and S3 of the Supporting Information. Due to the doping of 0.03Ba²⁺ in the MAG: Mn⁴⁺ sample, the cell volume was observed to be increased from 534.06 to 540.17 Å³ (Table S1). The values of the estimated metal–oxygen bond lengths are also listed in Table S4 of the Supporting Information.

Eventually, the increment in the metal–oxygen bond lengths (Table S4) in the various octahedral coordinations supports the above cell volume extension after Ba²⁺ ions' incorporation in the MAG: Mn⁴⁺ sample. Such a probable expansion due to the Ba²⁺ ions' substitution in the various [(Mg/Al)O₆] octahedral sites has been elaborated schematically in Figure 3c. Among the different octahedral coordinations, the volume enhancement of [(Mg1/Al1)O₆] sites is comparatively higher after Ba²⁺ ions' doping (Table S4). This might be due to the increased suitability of the (Mg1/Al1) sites for the larger-sized Ba²⁺ ions' occupation.²³

Meanwhile, the changes in [(Mg/Al)–O] bond lengths also indicate that the incorporation of larger Ba²⁺ ions caused structural distortion in the symmetry of [(Mg/Al)O₆] octahedrons. A slight variation in the bond lengths of adjacent [(Al/Ge)O₄] tetrahedrons has also been observed (Figure 3d). In the case of the MGG: Mn⁴⁺, 0.1Ba²⁺ sample, the Ba²⁺ ions' substitution in the [(Mg/Ga)O₆] octahedral sites caused an increase in the cell volume from 569.13 to 580.46 Å³ and similar types of changes in the metal–oxygen bond lengths, as depicted schematically in Figure 3d. The detailed structural parameters evaluated for the MGG: Mn⁴⁺, 0.1Ba²⁺ sample are provided in the Supporting Information in Tables S1, S3, and S4.

The XRD plots of a series of MAG: Mn⁴⁺, *x*Ba²⁺ (*x* = 0.0–0.3) samples are presented in Figure 4a. As can be seen from Figure 4a, the XRD patterns of MAG: Mn⁴⁺, *x*Ba²⁺ are not much altered below a certain amount of Ba²⁺ concentration (*x* < 0.1). With the further increase in Ba²⁺ ions' concentration to *x* = 0.1 and above, the XRD peaks of Mg impurity-phase o-MGO (at $2\theta = 22.6$ and 35.1°) and o-MGG (at $2\theta = 36^\circ$) are observed to decrease gradually. Eventually, a new peak at $2\theta = 28.7^\circ$, attributed to t-BMG,^{24,25} is generated with the Ba²⁺ doping, which becomes prominent when the Ba²⁺ ions' concentration reached *x* = 0.10. According to Ozturk, the major structure could tolerate the size mismatch between Ba²⁺ and Mg²⁺ up to a certain limit of Ba²⁺ substitution into the Mg²⁺ sites.²⁶ Hence, at higher Ba²⁺ ionic concentrations (*x* > 0.1), the substitution of Ba²⁺ ions in Mg²⁺ sites becomes ineffective owing to the large dissimilarity in the ionic radii of Mg²⁺ ($r_{\text{MgO}_6} = 0.72 \text{ \AA}$) and Ba²⁺ ($r_{\text{BaO}_6} = 1.35 \text{ \AA}$) in their octahedral coordination.²⁷ Because of this reason, a new Ba compound phase (t-BMG) was generated.^{24,25}

The t-BMG phase consists of [MgO₄] tetrahedrons, [Ge₂O₇] double tetrahedrons, and [BaO₈] dodecahedrons.²⁵ The higher concentration of Ba²⁺ ions could form more [BaO₈] dodecahedrons and utilized Mg²⁺ and Ge⁴⁺ ions from the respective octahedral and tetrahedral sites belonging to MGG and MGO phases for the formation of the t-BMG phase. Because of this reason perhaps, the MGG and MGO phases are suppressed significantly at higher Ba²⁺ concentrations. The newly generated t-BMG might also cause severe structural distortion in the host. To confirm the above prediction, the identified impurity phases such as o-MGO and t-BMG samples have been chosen and synthesized further via the solid-state method, and their XRD patterns are illustrated in Figure 4b along with the XRD of MAG: Mn⁴⁺, *x*Ba²⁺ (*x* = 0.1 and 0.27) samples. From Figure 4b, the existence of both o-MGO and t-BMG phases in MAG: Mn⁴⁺, 0.1Ba²⁺ samples can be easily identified by the corresponding JCPDS data included in the figure. Moreover, a higher amount of Ba²⁺ ions' doping (MAG: Mn⁴⁺, 0.27Ba²⁺) led to intensified XRD peaks of the t-BMG phase, while the main XRD peaks of MGO and MGG phases decreased significantly. The XRD analysis was also carried out

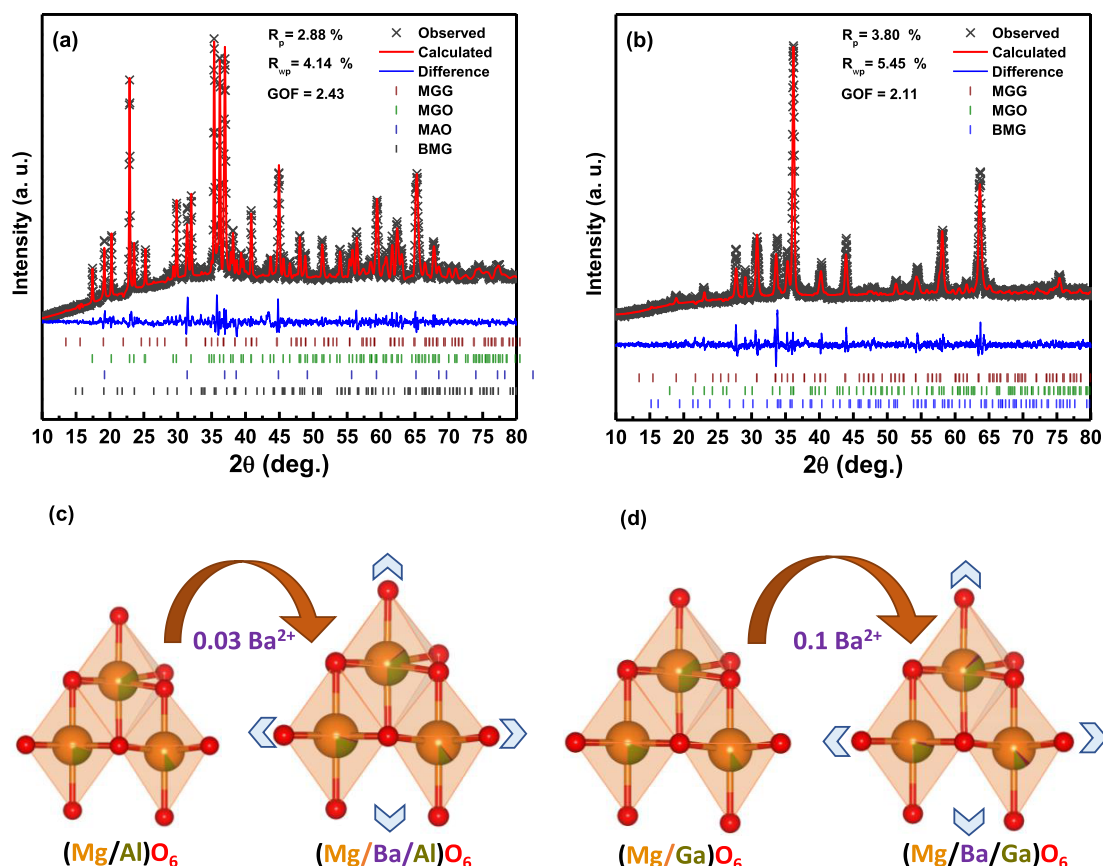


Figure 3. Refinement patterns of (a) MAG: Mn^{4+} , 0.03Ba^{2+} and (b) MGG: Mn^{4+} , 0.10Ba^{2+} . Schematic representation of variation in the octahedrons of (c) MAG and (d) MGG after Ba^{2+} incorporation.

for a series of MGG: Mn^{4+} , $x\text{Ba}^{2+}$ ($x = 0.0-0.15$), which are given in Figure S3 of the Supporting Information. Here also, the same impurity-phase t-BMG is identified to be prominent at the higher doping concentration of Ba^{2+} ions (Figure S3).

The change in the microstructure of MAG: Mn^{4+} due to the Ba^{2+} ions' incorporation could also be realized from the Raman analyses of MAG: Mn^{4+} and MAG: Mn^{4+} , $x\text{Ba}^{2+}$ ($x = 0.03, 0.27$) samples. In the obtained Raman spectra of the above samples, as illustrated in Figure 5a, the main band that appeared at $\sim 645\text{ cm}^{-1}$ can be attributed to the stretching vibration of $[\text{AlO}_6]$ bonds corresponding to $[\text{AlO}_6]$ octahedrons.²⁸ Meanwhile, the band at around 358 cm^{-1} could be attributed to the stretching vibrations of $[\text{MgO}_6]$ octahedrons.²⁹ The stretching vibrations corresponding to the above octahedrons become stronger in Ba^{2+} codoped MAG: Mn^{4+} , $x\text{Ba}^{2+}$ ($x = 0.03, 0.27$) samples. This might be because of the reduced symmetry of structurally distorted $[(\text{Mg}/\text{Al})\text{O}_6]$ octahedrons and increased $[(\text{Mg}/\text{Al})-\text{O}]$ bond lengths due to Ba^{2+} codoping as discussed in the XRD analysis of MAG: Mn^{4+} and MAG: Mn^{4+} , 0.03Ba^{2+} samples previously.²⁰ The average $[(\text{Mg}/\text{Al})-\text{O}]$ bond lengths are calculated to be 2.039 and 2.047 Å for MAG: Mn^{4+} and MAG: Mn^{4+} , 0.03Ba^{2+} samples, respectively (Table S4). Wang et al.²⁰ also reported a similar kind of larger ionic substitution in Ca_2MgWO_6 , which resulted in increased $[\text{W}-\text{O}]$ bond lengths of $[\text{WO}_6]$ octahedrons. The stretching vibration corresponds to the $[\text{WO}_6]$ octahedrons reportedly becoming stronger due to the above substitution, as visible in the present case also. The other peaks in Figure 5a located around 450,³⁰ 793,³¹ and 813 cm^{-1} ³² can be assigned to the stretching vibration of $[\text{GeO}_4]$

tetrahedrons and the peak at $\sim 830\text{ cm}^{-1}$ ³³ can be attributed to the stretching vibration of $[\text{AlO}_4]$ tetrahedrons.

Figure 5b presents the XPS survey spectrum of MAG: Mn^{4+} , 0.27Ba^{2+} , which confirmed the peaks of Ba, Mg, Al, Ge, O, and Mn exactly where they were predicted to be. The Mg 2p core spectrum of MAG: Mn^{4+} is deconvoluted into two peaks at 49.86 and 51.37 eV (Figure 5b(i)). The higher binding energy peak (51.37 eV) corresponding to Mg^{2+} ions disappeared in MAG: Mn^{4+} , 0.27Ba^{2+} (Figure 5b(ii)), indicating that Ba^{2+} might have created some structural distortion in the Mg^{2+} sites. The core-level spectra of O 1s for the samples MAG: Mn^{4+} and MAG: Mn^{4+} , 0.27Ba^{2+} are deconvoluted into O_1 (lattice oxygen) and O_2 (surface oxygen), which are positioned at 531 and 532.8 eV (Figure 5b(iii),(iv)). The content of surface oxygen (O_2) in MAG: Mn^{4+} , 0.27Ba^{2+} is reduced compared to that in MAG: Mn^{4+} . Moreover, the lattice oxygen content (O_1) is found to be higher in the MAG: Mn^{4+} , 0.27Ba^{2+} sample compared to that in the MAG: Mn^{4+} sample.

The formation t-BMG phase at a higher concentration ($x > 0.1$ mol) of Ba^{2+} ions might be responsible for the conversion of more nonlattice oxygen to lattice oxygen for the formation of Ba–O bonds. The enhanced lattice oxygen (O_1) content for the MAG: Mn^{4+} , 0.27Ba^{2+} sample might help to create additional octahedral sites for occupying Mn^{4+} ions. Moreover, due to the higher lattice oxygen content, the structural stability should be increased.⁸ The enhanced structural stability and octahedral sites due to the Ba^{2+} ions' substitution could be effective in intensifying Mn^{4+} ions' emission.¹⁶ The XPS spectra of MGG: Mn^{4+} , $x\text{Ba}^{2+}$ ($x = 0.0, 0.13$) are shown in Figure S4. In this case

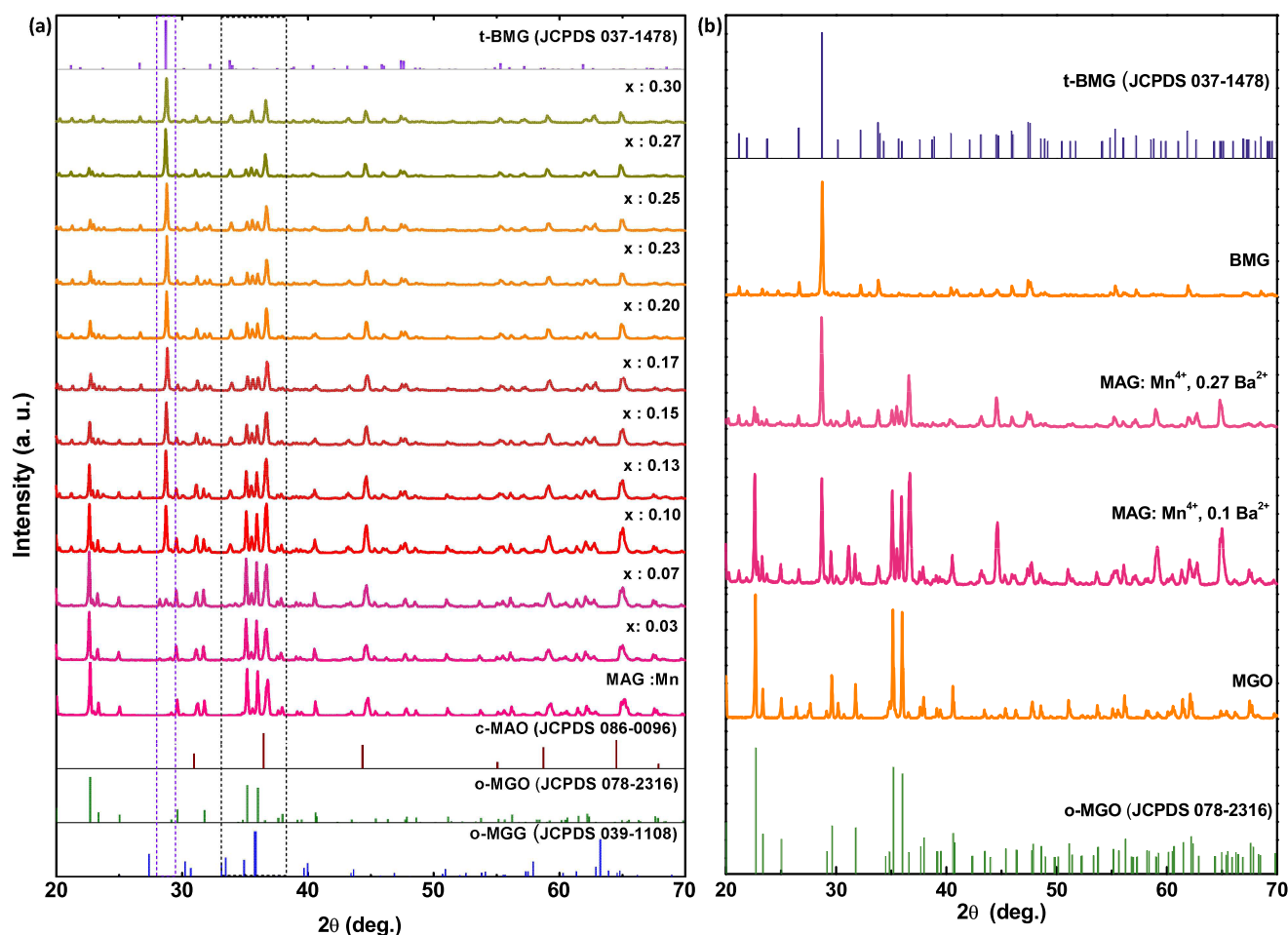


Figure 4. (a) XRD patterns of MAG: Mn⁴⁺, xBa²⁺ ($x = 0.0–0.3$) samples. (b) XRD patterns of synthesized MGO: Mn⁴⁺, BMG: Mn⁴⁺, MAG: Mn⁴⁺, 0.1Ba²⁺, and MAG: Mn⁴⁺, 0.27Ba²⁺ with corresponding JCPDS.

also, reduction of the Mg²⁺ content is observed because of Ba²⁺ inclusion (Figure S4i,ii). Meanwhile, the substitution of Ba²⁺ ions in the Mg²⁺ sites led to a substantial reduction in the surface oxygen peak (O₂), with the coinciding increase in the lattice oxygen peak (O₁) being observed (Figure S4iii,iv).

3.3. UV–Vis Absorption, Photoluminescence, and Cathodoluminescence Properties of (Mg, Ba)₃M₂GeO₈: Mn⁴⁺ (M = Al, Ga). The UV–DRS spectra of undoped MAG, MAG: Mn⁴⁺, and MAG: Mn⁴⁺, 0.27Ba²⁺ samples are shown in Figure 6a. The MAG host showed optical absorption at ~250 nm owing to the host absorption ((i) of Figure 6a).³⁴ In the MAG: Mn⁴⁺ and MAG: Mn⁴⁺, 0.27Ba²⁺ samples, the absorption peak at 250 nm becomes more prominent owing to the overlapping of the O²⁻-Mn⁴⁺ charge transfer band (CTB) and the host absorption. In addition, two more absorption deeps are observed at ~300 and 421 nm because of the ⁴A_{2g} → ⁴T_{1g} and ⁴A_{2g} → ⁴T_{2g} transitions of Mn⁴⁺ ions ((ii) and (iii) of Figure 6a). Eventually, the mentioned Mn⁴⁺ absorption peaks are intensified owing to the Ba²⁺ codoping in the MAG: Mn⁴⁺ sample (Figure 6a). The band-gap values obtained for MAG, MAG: Mn⁴⁺, and MAG: Mn⁴⁺, 0.27Ba²⁺ samples are calculated using Tauc plots³⁵ (Figure 6b), and the resultant values are 5.97, 5.91, and 5.67 eV, respectively. Because of the lower electronegativity of Mn⁴⁺ ions than Al³⁺ ions, the required energy for the band-to-band transitions is reduced after Mn⁴⁺ doping. The band-gap energy

further decreasing in MAG: Mn⁴⁺, 0.27Ba²⁺ might be due to the lower electronegativity of Ba²⁺ ions than Mg²⁺ ions.³⁶

The UV–vis DRS spectra of MGG and MGG: Mn⁴⁺, xBa²⁺ ($x = 0.0, 0.13$) samples are also analyzed as supporting evidence (Figure S5 of the Supporting Information). Broad absorption bands are observed in the UV and blue regions for the MGG: Mn⁴⁺ and MGG: Mn⁴⁺, 0.13Ba²⁺ samples. The absorption is higher in the case of the MGG: Mn⁴⁺, 0.13Ba²⁺ sample for all transitions. The obtained band-gap values for MGG, MGG: Mn⁴⁺, and MGG: Mn⁴⁺, 0.13Ba²⁺ samples (5.0, 4.96, and 4.89 eV, respectively) followed a similar trend with undoped and doped MAG compositions. It is worth mentioning that Mn⁴⁺ ions have strong ligand field stabilization energy in the octahedral sites.^{19,37} In the MAG host, both Mg²⁺ and Al³⁺ ions provide octahedral sites for Mn⁴⁺ ions due to matching ionic radii. Also, some of the Mn⁴⁺ ions can occupy [MgO₆] and [AlO₆] octahedrons provided by the o-MGO and c-MAO phases,³⁸ respectively, which could elevate the Mn⁴⁺ emission.

The photoluminescence excitation (PLE, λ_{em}: 659 nm) and emission (λ_{ex}: 284 nm) spectra of MAG: Mn⁴⁺, xBa²⁺ ($x = 0.0–0.37$) samples are shown in Figure 6c. The PLE spectrum of all of these samples exhibits broad excitation bands having peaks at 284 and 419 nm. The excitation band ranging from 230 to 380 nm, which is identical to the UV chips, can be ascribed to Mn⁴⁺-O²⁻ CTB and ⁴A_{2g} → ⁴T_{1g}, ²T_{2g} transitions of Mn⁴⁺ (as assigned in Figure 6c). The excitation band in the blue region (380–480

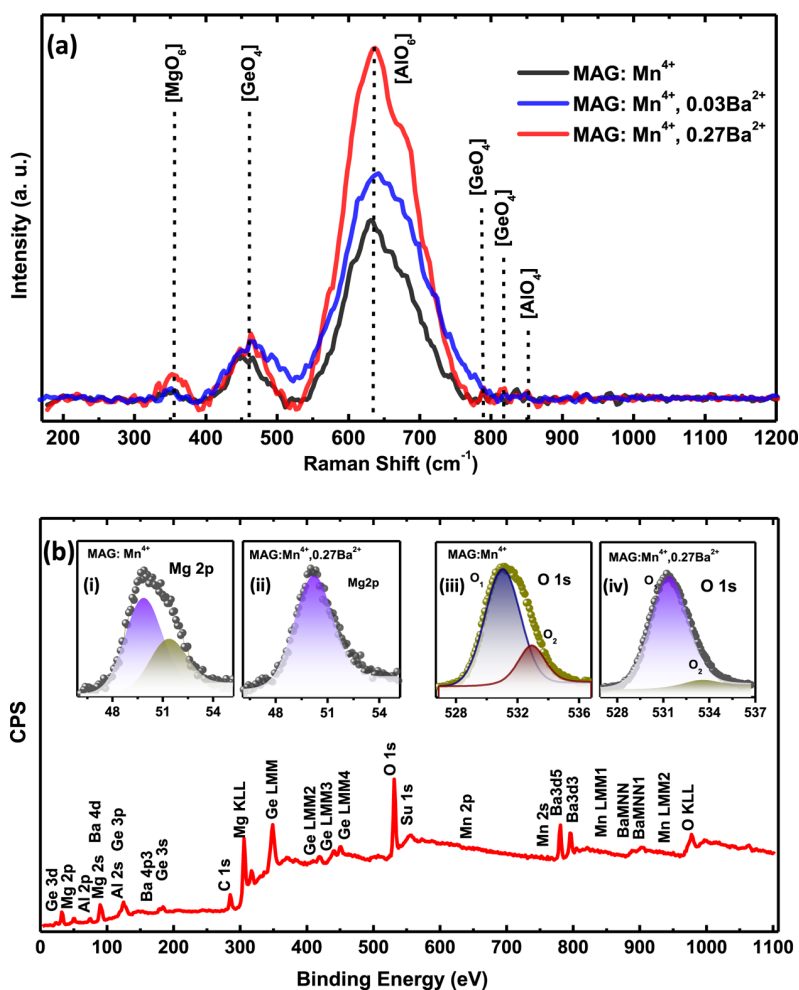


Figure 5. (a) Raman spectra of MAG: Mn^{4+} and MAG: Mn^{4+} , $x\text{Ba}^{2+}$ ($x = 0.03, 0.27$) samples. (b) XPS survey spectrum of the sample MAG: Mn^{4+} , 0.27Ba^{2+} . Inset figures show the XPS core-level spectra of Mg 2p and O 1s for the samples MAG: Mn^{4+} and MAG: Mn^{4+} , 0.27Ba^{2+} .

nm) is well-fitted with the commercial blue chip, which can be attributed to the spin-allowed ${}^4\text{A}_{2g} \rightarrow {}^4\text{T}_{2g}$ transition of Mn^{4+} ions.¹⁶ A slight red shift appeared in the spectra due to the addition of Ba^{2+} in MAG: Mn^{4+} since Ba^{2+} incorporation increases the bond length between the Mn^{4+} and the ligands, thereby decreasing the energy of the $\text{Mn}^{4+}\text{-O}^{2-}$ CTB.³⁹ Further, PL spectra for each sample resulted in a sharp emission peak at 659 nm due to the ${}^2\text{E}_g \rightarrow {}^4\text{A}_{2g}$ transition and the other weak emissions arise due to vibrational sidebands.⁴⁰ The emission intensity of the phosphors gets increased due to partial Ba^{2+} ions' substitutions and maximized at $x\text{Ba}^{2+} = 0.27$ mol, which is 3-fold greater than that of the MAG: Mn^{4+} sample. The external quantum efficiency (EQE) value obtained for the MAG: Mn^{4+} sample is 29.44%; however, it is calculated to be 49.35% for the MAG: Mn^{4+} , 0.27Ba^{2+} sample. Further increase in Ba^{2+} ions' concentration quenched the PL intensity. The variations in the emission intensity as a function of Ba^{2+} ions' concentrations can be understood via the PL images of these samples (Figure 6d), which are arranged in the increasing order of Ba^{2+} content.

The possible reasons for the red emission enhancement due to the Ba^{2+} ions' incorporation can be explained using three different aspects as follows: (i) structural distortion occurred in the MAG: Mn^{4+} sample due to larger-sized Ba^{2+} ionic substitution and contribution of luminescent centers provided by the newly generated barium phase, (ii) increase in the particle

sizes of the MAG: Mn^{4+} sample due to the inclusion of Ba^{2+} ions, and (iii) replacement of $\text{Mn}^{4+}\text{-Mn}^{4+}$ pairs by the $\text{Ba}^{2+}\text{-Mn}^{4+}$ pairs in Ba^{2+} codoped samples.

- (i) The most probable reason for the enhanced red emission intensity could be the structural distortion that occurred due to the Ba^{2+} ions' substitution in the MAG: Mn^{4+} sample. At lower Ba^{2+} -doping concentrations ($<0.1\text{Ba}^{2+}$), smaller Mg^{2+} ions might be substituted by larger Ba^{2+} ions, which resulted in a distorted lattice, as explained during interpreting the XRD results. Such lattice distortion, created due to the substitution of larger Ba^{2+} ions, possibly further reduced the site symmetry of $[(\text{Mg}/\text{Al})\text{O}_6]$ octahedrons, which are preferably accommodating Mn^{4+} ions and thereby enhanced the red emission.^{14–16,41–43} Since the 3d–3d forbidden transition probability of Mn^{4+} ions with the $3d^3$ configurations is largely determined by the local symmetry of $[\text{MnO}_6]$ octahedrons, the decrease of octahedral symmetry usually leads to the relaxation of the selection rule of Mn^{4+} ions occupied at these octahedral sites. Similar results are reported by Wang et al.²⁰ Here, the luminous intensity of $\text{Ca}_2\text{MgWO}_6: \text{Mn}^{4+}$ is reported to be increased by the larger cation pair ($\text{Na}^+\text{-La}^{3+}$) substitution in Ca^{2+} sites. This substitution makes severe lattice distortion in the $[\text{WO}_6]$ sites (preferential for Mn^{4+} occupation) by changing the $[\text{W-O}]$ bond

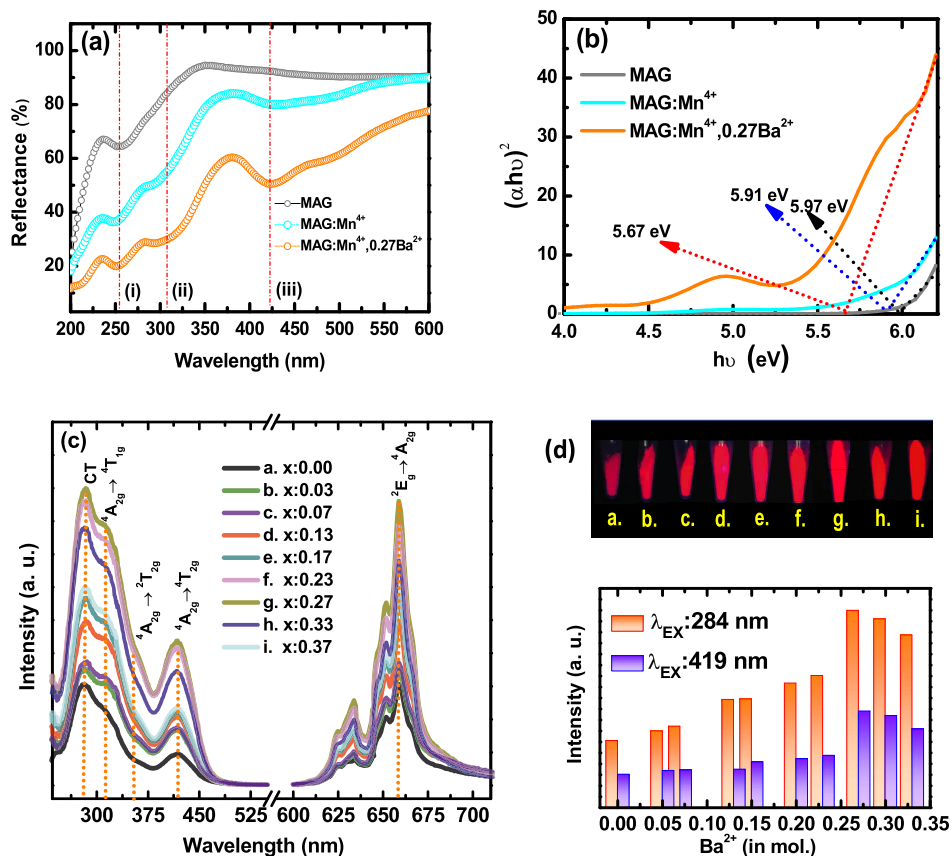


Figure 6. (a) UV–DRS spectra of MAG and MAG: Mn⁴⁺, xBa²⁺ (x = 0.0 and 0.27). (i) Overlapping of the host absorption and the Mn⁴⁺-O²⁻ CTB, (ii) ⁴A_{2g} → ⁴T_{1g} and (iii) ⁴A_{2g} → ⁴T_{2g} transitions. (b) Tauc's plots for band-gap calculation. (c) Photoluminescence excitation (PLE) (λ_{em}: 659 nm) and PL emission spectra (λ_{ex}: 284 nm) of MAG: Mn⁴⁺, xBa²⁺ (x = 0.0–0.37). (d) Corresponding PL images under UV excitation, and bar diagram showing the variation of PL intensity with Ba²⁺ concentration under UV and blue excitation.

length, which led to a higher emission. Recently, Wang and co-workers also introduced Ba²⁺ in the Mg²⁺ sites of Mg₂Y₂Al₂Si₂O₁₂: Ce³⁺ for increasing its emission intensity.⁴⁴ Fang et al. reported enhanced Mn⁴⁺ emission by introducing larger K⁺ ions in the Ba²⁺ sites of BaTiF₆: Mn⁴⁺, which led to the increase of [Ba/K-F] bond lengths and distortion in the [TiF₆] octahedral sites preferred for Mn⁴⁺ ions' occupation.⁴⁵

Meanwhile, after a certain amount of Ba²⁺ ions' doping (>0.1Ba²⁺), a new phase tetragonal-Ba₂MgGe₂O₇ (t-BMG) was observed in the Ba²⁺ codoped MAG: Mn⁴⁺ samples. This newly generated phase might have supplied the additional luminescent centers for Mn⁴⁺ ions, owing to which the emission of MAG: Mn⁴⁺, Ba²⁺ could be intensified further. Lu et al.²⁴ have reported the emission properties of Mn⁴⁺-doped t-BMG synthesized via the solid-state route. Herein, Mn⁴⁺ ions are reported to be substituted at the Ge⁴⁺ sites of t-BMG. The t-BMG crystal structure consists of [MgO₄] tetrahedrons, [Ge₂O₇] double tetrahedrons, and [BaO₈] dodecahedrons.^{24,25} Substituting Mn⁴⁺ ions in the Ge⁴⁺ sites of t-BMG exhibited a red emission at 660 nm due to the Mn⁴⁺: ²E_g → ⁴A_{2g} transitions.²⁴ The optimized composition of Ba₂MgGe₂O₇: 0.013Mn⁴⁺, reported by Lu et al.,²⁴ has been resynthesized to confirm the reported red emission from the Mn⁴⁺ ions located at the Ge-tetrahedral sites. The PL emission spectrum of the Ba₂MgGe₂O₇: 0.013Mn⁴⁺ sample is shown in the Supporting Informa-

tion in Figure S6. The PL emission spectrum of the UV-irradiated Ba₂MgGe₂O₇: 0.013Mn⁴⁺ sample shows identical emission features as reported in ref 24. Meanwhile, the peak position was noted at 660 nm, which well matches with that of MAG: Mn⁴⁺, xBa²⁺ (x = 0.0–0.3) samples. Since the structure of MAG: Mn⁴⁺, xBa²⁺ samples contains the t-BMG phase, it can be predicted that the t-BMG phase could supply additional luminescent centers for intensifying the Mn⁴⁺ ions' emission. Peng et al. recently reported an enhancement in the PL intensity of the Sr₄Al₁₄O₂₅: Mn⁴⁺ sample due to the additional luminescent centers contributed by the supplementary phases such as SrAl₂O₄ and SrAl₁₂O₁₉.⁴⁶ However, some advanced studies are still required to establish this phenomenon.

- (ii) The increase in phosphor particle size due to the Ba²⁺ ions' incorporation could be another probable reason for the observed PL enhancement in MAG: Mn⁴⁺, xBa²⁺ samples. To observe the effect of Ba²⁺ codoping on the morphology, SEM analyses were carried out for MAG: Mn⁴⁺ and MAG: Mn⁴⁺, 0.27Ba²⁺ samples (Figure S7, Supporting Information). It is detected that because of the inclusion of Ba²⁺ ions, the particle sizes are found to be increased, as can be seen in the SEM results of MAG: Mn⁴⁺ and MAG: Mn⁴⁺, 0.27Ba²⁺ samples (Figure S7). Generally, the surface-associated defects decrease with the increase in particle size, which may also be able to reduce the nonradiative transitions and enhance the

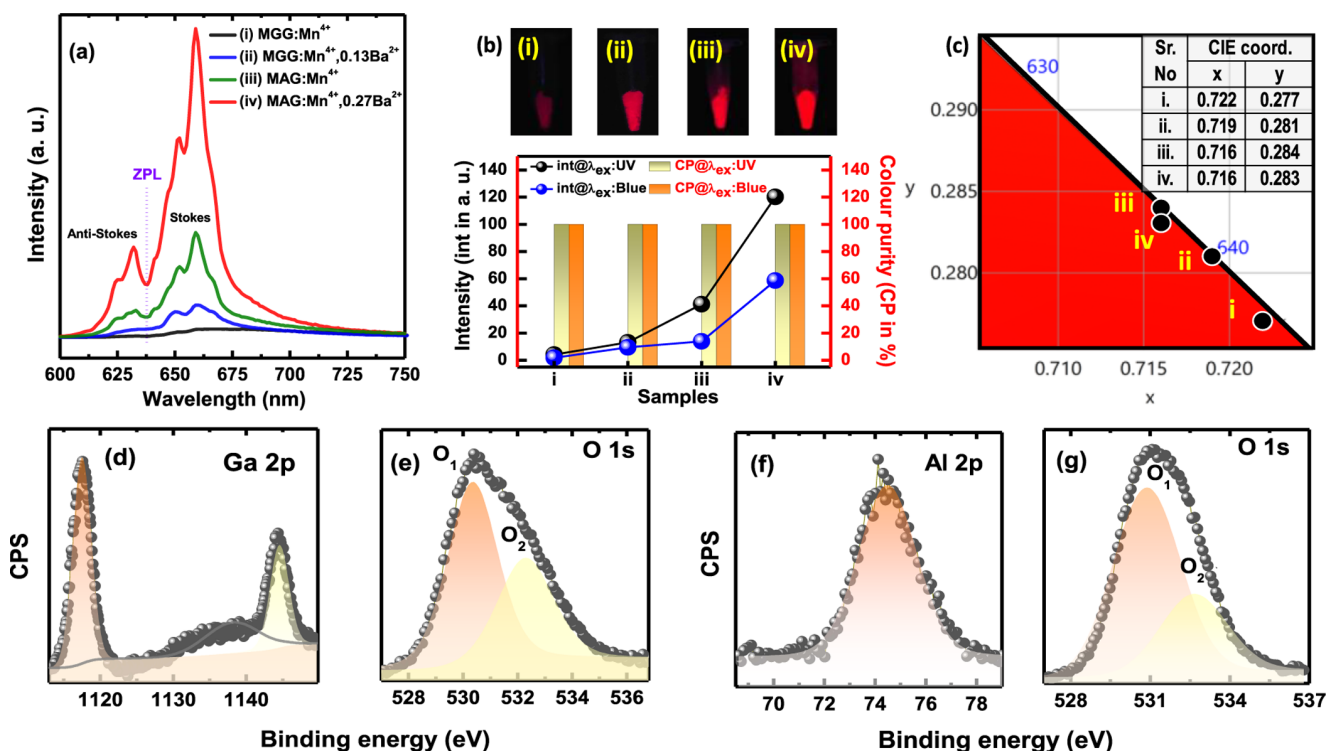


Figure 7. (a) Comparison of PL emission spectra ($\lambda_{\text{ex}} = 284$ nm) of (i) MGG: Mn⁴⁺, (ii) MGG: Mn⁴⁺, 0.13Ba²⁺, (iii) MAG: Mn⁴⁺, and (iv) MAG: Mn⁴⁺, 0.27Ba²⁺ samples with the (b) corresponding PL images, PL intensity (line with symbol), and color purity (bar). (c) CIE diagram and the color coordinates of the above four samples. XPS spectra of (d) Ga 2p and (e) O 1s for MGG: Mn⁴⁺. XPS spectra of (f) Al 2p and (g) O 1s for MAG: Mn⁴⁺.

emission subsequently.⁴⁷ Similar interpretations have been reported recently, where the K⁺ ions' substitution in the Ba²⁺ sites of Ba₂TiF₆:Mn⁴⁺⁴⁵ and the Mg²⁺ doping at the Sr²⁺ sites of Sr₄Al₁₄O₂₅: Mn⁴⁺⁴⁶ enhanced the particle sizes as well as the PL intensity of the respective phosphors. In the present case, the precursor material BaCO₃ melted earlier (melting point ~811 °C) and might act as a flux throughout the sintering process, thereby increasing the crystallinity and particle sizes.^{17,46} To reconfirm the effect of particle sizes of the MAG: Mn⁴⁺, 0.27Ba²⁺ sample on its emission intensity, this sample was also synthesized at various sintering temperatures (700, 900, 1100, and 1300 °C). The corresponding SEM images and PL emission spectra are given in Figures S8 and S9, respectively, of the Supporting Information. The PL intensity, as well as the particle sizes of the samples, was found to have increased with increasing annealing temperature.⁴⁷ The increase in PL emission intensity with the increase of particle size could be ascribed to the already explained reduction in nonradiative transition for the larger-sized particle.⁴⁷

- (iii) To verify the role of Mn⁴⁺–Ba²⁺ pairs in enhancing the PL emission intensity in Ba²⁺ codoped samples, PL emission decay lifetime measurements were also performed by monitoring the emission at 659 nm upon the UV excitation of 284 nm. The resultant PL decay curves for the samples MAG: Mn⁴⁺ and MAG: Mn⁴⁺, 0.27Ba²⁺ are shown in Figure S10a of the Supporting Information. All of the curves were well-fitted with a second-order exponential function, and the average lifetime values were calculated by following the procedures reported elsewhere.^{11,46,48} Most importantly, the double exponen-

tial fitting indicates the presence of multiple luminescence centers in these hosts. The average lifetime values for MAG: Mn⁴⁺ and MAG: Mn⁴⁺, 0.27Ba²⁺ are calculated to be 2.14 and 2.27 ms, respectively. The slightly higher emission lifetime value for MAG: Mn⁴⁺, 0.27Ba²⁺ is related to its brighter emission compared to that of the MAG: Mn⁴⁺ sample.⁴⁶ This elongation of emission lifetime because of the Ba²⁺ ions' doping in the MAG: Mn⁴⁺ sample might also indicate a possible reduction in the content of Mn⁴⁺–Mn⁴⁺ pairs due to the formation of Mn⁴⁺–Ba²⁺ pairs. Such newly formed Mn⁴⁺–Ba²⁺ pairs might reduce the nonradiative energy migration probabilities between two neighboring Mn⁴⁺ ions by reducing the nonradiative depopulation in the ²E_g level of Mn⁴⁺ and thereby enhancing the PL emission intensity.^{46,49}

The photoluminescence of a series of MGG: Mn⁴⁺, xBa²⁺ ($x = 0.0$ – 0.15) samples is also recorded to confirm the effectiveness of larger ionic substitution to enhance the Mn⁴⁺ ions' emission, as shown in Figure S5c of the Supporting Information. Also, in this case, a similar kind of luminescence behavior is observed with the Ba²⁺ ions' incorporation as seen in MAG: Mn⁴⁺, xBa²⁺ due to their isomorphic structure. The PL intensity is maximum when the Ba²⁺ concentration is 0.13 mol, which is 5-fold greater than the emission intensity of MGG: Mn⁴⁺. The PL images captured as a function of various Ba²⁺ ions' concentrations are shown in the inset of Figure S5c. The XRD of MGG: Mn⁴⁺, xBa²⁺ ($x = 0.0$ – 0.15) samples, shown in Figure S3 of the Supporting Information, indicated an impurity phase of t-BMG due to Ba²⁺ ions' substitution, which possibly helped to enhance the Mn⁴⁺ ions' emission in MGG: Mn⁴⁺, xBa²⁺ as in the case of MAG: Mn⁴⁺, xBa²⁺. The average lifetime values obtained (from Figure S10b) for MGG: Mn⁴⁺ and MGG: Mn⁴⁺, 0.13Ba²⁺

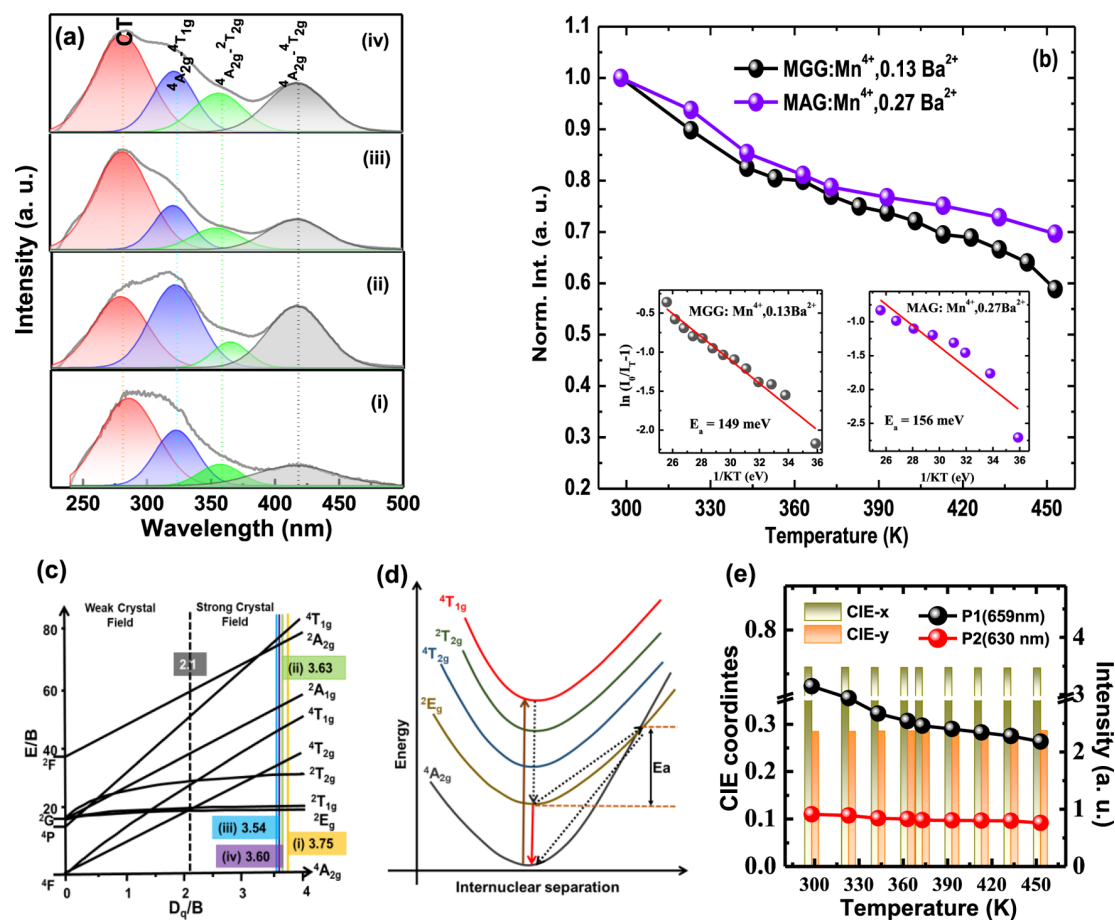


Figure 8. (a) Deconvoluted PL excitation spectra of (i) MGG: Mn⁴⁺, (ii) MGG: Mn⁴⁺, 0.13Ba²⁺, (iii) MAG: Mn⁴⁺, and (iv) MAG: Mn⁴⁺, 0.27Ba²⁺. (b) Plots of normalized emission intensity vs temperature and Arrhenius plots for the samples MGG: Mn⁴⁺, 0.13Ba²⁺ and MAG: Mn⁴⁺, 0.27Ba²⁺. (c) Tanabe–Sugano energy illustration of Mn⁴⁺ ions in an octahedron and representation of D_q/B values of MGG: Mn⁴⁺, x Ba²⁺ ($x = 0.0, 0.13$) and MAG: Mn⁴⁺, x Ba²⁺ ($x = 0.0, 0.27$). (d) Configuration coordinate diagram for activation energy calculation. (e) Bar diagram showing variation of CIE coordinates with temperature along with variation of peak intensities (positioning at 659 and 630 nm) with temperature for the sample MAG: Mn⁴⁺, 0.27Ba²⁺.

samples are 0.48 and 0.70 ms, respectively. However, these values are much smaller than the lifetime values of the MAG: Mn⁴⁺, 0.27Ba²⁺ sample.^{46,49,50}

3.3.1. Comparative PL Analysis. From the comparative photoluminescence emission spectra of MAG: Mn⁴⁺, x Ba²⁺ ($x = 0.0, 0.27$) and MGG: Mn⁴⁺, x Ba²⁺ ($x = 0.0, 0.13$) samples, shown in Figure 7a, it has been observed that replacing Ga³⁺ by Al³⁺ enhanced the PL intensity by 13-fold. The PL intensity of MAG: Mn⁴⁺ was further enhanced 3 times by the Ba²⁺ ions' substitution (Figure 7b), which effectively created a more appropriate crystal environment for Mn⁴⁺ occupancy in the MAG host. The preferential sites for Mn⁴⁺ occupancy in MGG are [MgO₆] ($r_{\text{MgO}_6} = 0.72 \text{ \AA}$) and [GaO₆] ($r_{\text{GaO}_6} = 0.62 \text{ \AA}$), whereas that for MAG are [MgO₆] and [AlO₆] ($r_{\text{AlO}_6} = 0.535 \text{ \AA}$). However, the ionic size of Al³⁺ in MAG is more closer to that of Mn⁴⁺ ($r_{\text{MnO}_6} = 0.53 \text{ \AA}$) than that of Ga³⁺ in MGG, which indicates that [AlO₆] octahedrons could be more favorable than [GaO₆] for Mn⁴⁺ ions' occupancy. To know the site suitability, a parameter known as the effective compensating factor ($\varphi = z/r$) can be employed in octahedral surroundings, where z and r are the charge and radius of an ion located in that octahedron. The z/r ratios of Mg²⁺, Ga³⁺, Al³⁺, and Mn⁴⁺ in octahedral sites are 2.77, 4.84, 5.607, and 7.547, respectively.⁵¹ From these values, it is clear

that the z/r ratio of Al³⁺ is closer to Mn⁴⁺ in comparison with other sites. Hence, MAG is expected to provide more suitable [AlO₆] sites for Mn⁴⁺ ions, leading to the greater intensity of MAG: Mn⁴⁺. Some Mn⁴⁺ ions could replace divalent Mg²⁺ ions at [MgO₆] octahedrons because of which Mn⁴⁺ valance could reduce to Mn²⁺ valance to account for the charge compensation.

However, the more preferential [AlO₆] sites in MAG efficiently reduce the probability of Mn⁴⁺ ions' occupancy in [MgO₆] sites. Hence, the natural reduction probability of Mn⁴⁺ to Mn²⁺ for charge compensation is lesser in the MAG host compared to the MGG host. This prediction is also supported by the cathodoluminescence studies (discussed later in this paper) for the first time for any Mn⁴⁺-activated sample.

In addition to the ionic similarities, the detailed XRD and HRTEM analyses of the MAG sample confirmed the presence of the coexisting phases such as o-MGO and c-MAO. The intense red emission identified in MAG: Mn⁴⁺ might be due to the additional luminescence centers of Mn⁴⁺ ions provided by the above coexisting phases. Xue et al. synthesized the Mg₂GeO₄: 0.001Mn⁴⁺ sample through the high-temperature solid-state method and observed the deep-red emission peaking at 659 nm due to the Mn⁴⁺ ions' occupancy in the [MgO₆] sites.³⁸ The emission spectrum of the UV-irradiated Mg₂GeO₄: Mn⁴⁺ sample, which was synthesized via adopting the method as

Table 1. Spectroscopic Parameter Values Obtained from PL Emission and Excitation Spectra

phosphor	4T_1 (cm $^{-1}$)	4T_2 (cm $^{-1}$)	2E_g (cm $^{-1}$)	D_q	D_q/B	B	C
MGG: Mn $^{4+}$	30,960	24,038	15,175	2404	3.75	642	3414
MGG: Mn $^{4+}$, 0.13Ba $^{2+}$	31,153	24,038	15,175	2404	3.63	662	3367
MAG: Mn $^{4+}$	31,153	23,923	15,175	2392	3.54	676	3338
MAG: Mn $^{4+}$, 0.27Ba $^{2+}$	31,055	23,923	15,175	2392	3.60	664	3362

reported by Xue et al., is shown in Figure S6 of the Supporting Information.

Another coexisting phase observed in the MAG host is c-MAO, which also contains octahedral coordination for accommodating Mn $^{4+}$ ions. Wang et al. described the luminescence performance of the MgAl $_2$ O $_4$: Mn $^{4+}$ sample prepared via the molten salt method.⁵² According to this report, Mn $^{4+}$ ions occupy the [AlO $_6$] octahedrons and produce a deep-red emission at 651 nm. Analogous emission properties of MgAl $_2$ O $_4$: Mn $^{4+}$ prepared through the coprecipitation method are also reported by Ji et al.⁴⁰ Nonetheless, no report so far has illustrated the photoluminescence of the MgAl $_2$ O $_4$: Mn $^{4+}$ sample prepared via the high-temperature solid-state route. Therefore, we have synthesized MgAl $_2$ O $_4$: Mn $^{4+}$ through the solid-state method at a sintering temperature of 1300 °C. However, the solid-state synthesized sample did not show any Mn $^{4+}$ ions' emission. In the present case, the MgAl $_2$ O $_4$ phase probably acted as a flux and helped in enhancing the red emission intensity by improving the crystallinity. Recently, various studies have been published by studying the advantages of coexisting phases on the red emission enhancement of Mn $^{4+}$ -activated oxide phosphors. For example, Wu et al. improved the emission intensity of CaAl $_2$ O $_9$: Mn $^{4+}$ by introducing the coexisting MgAl $_2$ O $_4$ phase as a flux.¹⁷ Similarly, Gu et al. also reported the advantages of the coexisting nonluminescent MgAl $_2$ O $_4$ phase on the increased red emission intensity of SrMgAl $_{10-y}$ Ga $_y$ O $_{17}$: Mn $^{4+}$.⁵³ Meanwhile, the coexisting phases SrAl $_2$ O $_4$ and SrAl $_2$ O $_9$ are reported to be helpful for improvising the emission intensity of Sr $_4$ Al $_4$ O $_{25}$: Mn $^{4+}$.⁴⁶

The average [Al–O] bond length (2.06 Å) in the octahedral sites of MAG: Mn $^{4+}$ is found to be less than the average [Ga–O] bond length in the octahedral sites of MGG: Mn $^{4+}$ (2.08 Å). These structural changes may also be the root cause for the higher red emission of MAG: Mn $^{4+}$ compared to MGG: Mn $^{4+}$.¹⁵ The digital PL images, the plots of emission intensity, and the color purity for MGG: Mn $^{4+}$, xBa $^{2+}$ ($x = 0.0, 0.13$) and MAG: Mn $^{4+}$, xBa $^{2+}$ ($x = 0.0, 0.27$) samples are revealed in Figure 7b. All four samples exhibit excellent red-color purity of ~100% under the response of both UV and blue irradiations. The CIE coordinates for these samples are in the deep-red zone (shown in Figure 7c). The CIE coordinates obtained for the brighter red-emitting MAG: Mn $^{4+}$, 0.27Ba $^{2+}$ sample are situated in the deeper red region (0.716, 0.283).

An effort has been made to support the above justifications for enhanced red emission in the MAG: Mn $^{4+}$ sample compared to the MGG: Mn $^{4+}$ sample with the help of XPS analysis. The core-level XPS spectra (Figure 7d,f) measured for Ga and Al strongly suggest their 3+ oxidation states in MGG: Mn $^{4+}$ and MAG: Mn $^{4+}$, respectively. While comparing the O 1s spectra recorded for MGG: Mn $^{4+}$ and MAG: Mn $^{4+}$ samples (Figure 7e,g), the lattice oxygen (O $_l$) content is higher in the case of MAG: Mn $^{4+}$. The higher lattice oxygen content in MAG: Mn $^{4+}$ may help to form more octahedral bonds in MAG: Mn $^{4+}$ compared to MGG: Mn $^{4+}$. Also, the structural stability will be higher in MAG: Mn $^{4+}$

due to the higher lattice oxygen content.⁸ These factors can lead to the higher emission intensity of MAG: Mn $^{4+}$.

3.3.2. Estimation of the Mn $^{4+}$ Energy-Level Diagram and Evaluation of Spectroscopic Parameters. The PLE spectra of MGG: Mn $^{4+}$, xBa $^{2+}$ ($x = 0.0, 0.13$) and MAG: Mn $^{4+}$, xBa $^{2+}$ ($x = 0.0, 0.27$) samples can be deconvoluted into four Gaussian peaks (Figure 8a).^{54,55} The peaks located around 280, 320, 360, and 420 nm resemble the Mn $^{4+}$ -O $^{2-}$ CTB, ${}^4A_{2g} \rightarrow {}^4T_{1g}$, ${}^4A_{2g} \rightarrow {}^2T_{2g}$, and ${}^4A_{2g} \rightarrow {}^4T_{2g}$ transitions of Mn $^{4+}$ ions, respectively. The Tanabe–Sugano energy-level illustration of Mn $^{4+}$ ions in an octahedron is displayed in Figure 8c. The strong and weak crystal fields are differentiated by a line passing through the intersection of ${}^4T_{2g}$ and 2E_g . The ratio of the octahedral field strength (D_q) and the Racah parameter (B) for MGG: Mn $^{4+}$, xBa $^{2+}$ ($x = 0.0, 0.13$) and MAG: Mn $^{4+}$, xBa $^{2+}$ ($x = 0.0, 0.27$) samples is greater than 2.1, indicating that Mn $^{4+}$ experiences a strong crystal field in all of these hosts. To compare the effect of the host structure, crystal field splitting energy value ($10D_q$) and Racah parameter values B and C for the samples MGG: Mn $^{4+}$, xBa $^{2+}$ ($x = 0.0, 0.13$) and MAG: Mn $^{4+}$, xBa $^{2+}$ ($x = 0.0, 0.27$) are also calculated and listed in Table 1. It is obvious from Figure 8a that the Mn $^{4+}$ -O $^{2-}$ CTB of MAG: Mn $^{4+}$ is slightly blue-shifted compared to the MGG: Mn $^{4+}$ since Mn $^{4+}$ ions in the smaller Al $^{3+}$ sites require a larger charge transfer (CT) energy than for the Mn $^{4+}$ in the Ga $^{3+}$ sites.³⁹ The slight reduction in the D_q/B values of MAG: Mn $^{4+}$ compared to MGG: Mn $^{4+}$ can be attributed to the lower average Al–O bond length of MAG: Mn $^{4+}$.⁴⁹

High-temperature PL analysis was carried out for the two compositions MAG: Mn $^{4+}$, 0.27Ba $^{2+}$ and MGG: Mn $^{4+}$, 0.13Ba $^{2+}$. The temperature was varied from 300 to 453 K, and the PL emission spectra were recorded under UV excitation. Even at 453 K, the MAG: Mn $^{4+}$, 0.27Ba $^{2+}$ sample could retain 70% of its initial room-temperature intensity. However, the MGG: Mn $^{4+}$, 0.13Ba $^{2+}$ sample could retain less than 60% of its room-temperature intensity (Figure 8b). The quenching temperature increases when Ga $^{3+}$ is replaced with Al $^{3+}$ in the MAG: Mn $^{4+}$, 0.27Ba $^{2+}$ sample. The ionic size of the Mn $^{4+}$ ion in the octahedral coordination is 0.53 Å, which is closer to that of Al $^{3+}$ ($r_{AlO_6} = 0.535$ Å) in MAG: Mn $^{4+}$ samples rather than that of Ga $^{3+}$ ($r_{GaO_6} = 0.62$ Å) in MGG: Mn $^{4+}$ samples. Using the Arrhenius plot,¹⁵ the activation energies were calculated for both samples, which were calculated to be 156 meV for MAG: Mn $^{4+}$, 0.27Ba $^{2+}$ and 149 meV for MGG: Mn $^{4+}$, 0.13Ba $^{2+}$.

The higher activation energy in the MAG: Mn $^{4+}$, 0.27Ba $^{2+}$ sample than that in MGG: Mn $^{4+}$, 0.13Ba $^{2+}$ can be explained by the configuration coordinate diagram, as presented in Figure 8d. With UV excitation, free electrons jump first from the ${}^4A_{2g}$ ground state to the excited states (2E_g , ${}^4T_{1g}$, or ${}^4T_{2g}$) and then nonradiatively relax to the 2E_g states. The radiative emission toward the ${}^4A_{2g}$ state from the 2E_g state results in a deep-red emission. While increasing the temperature, the number of electrons in the 2E_g state increases and gains more energy. The thermally excited electrons could reach the intersection point of ${}^4A_{2g}$ and 2E_g (crossover point) and relax to the ground state

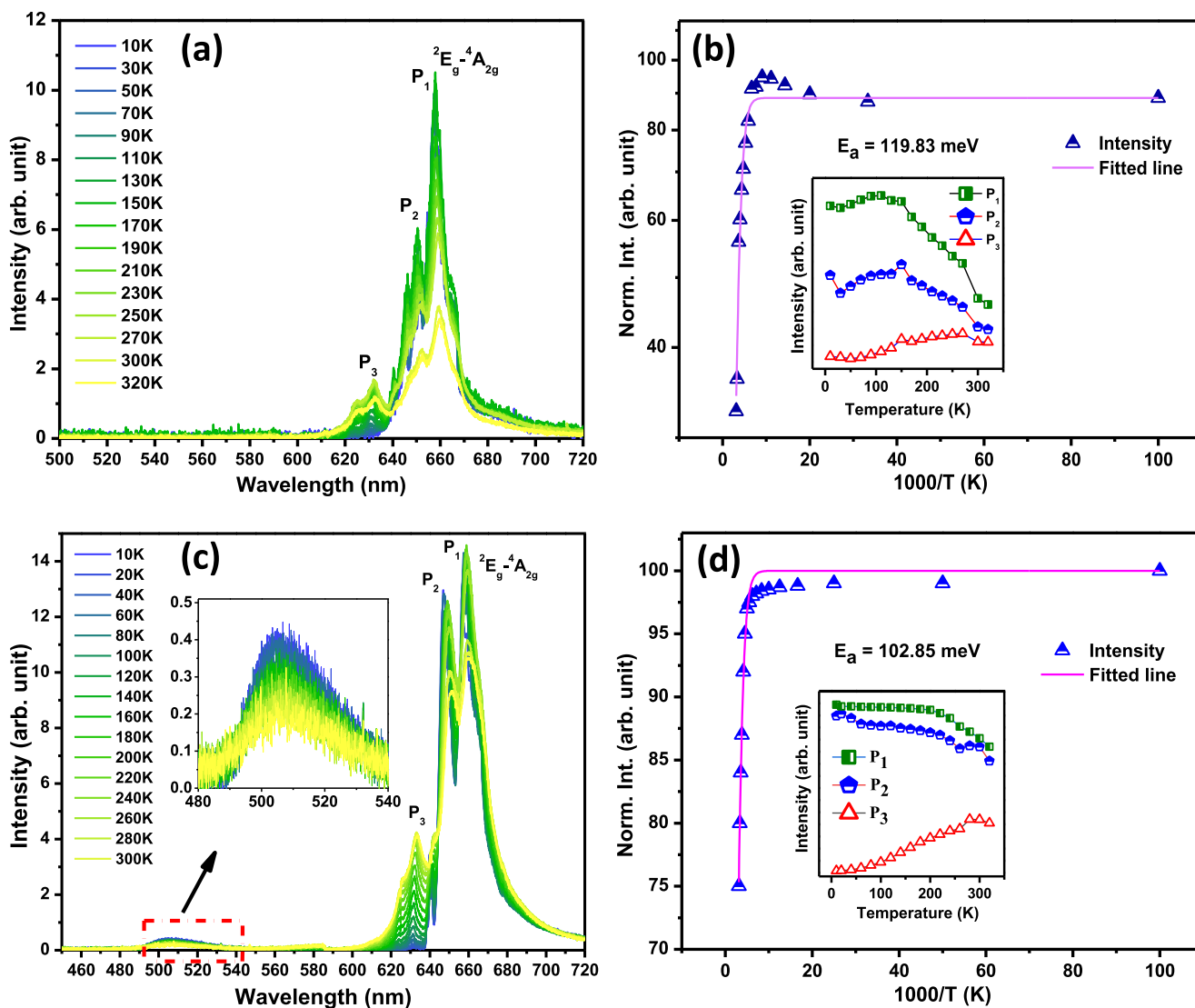


Figure 9. (a) Low-temperature PL spectra of MAG: Mn^{4+} , 0.27Ba^{2+} and corresponding (b) Arrhenius plot (inset shows the variation of peak intensities with temperature). (c) Low-temperature PL spectra of MGG: Mn^{4+} , 0.13Ba^{2+} (inset shows the enlarged portion of the green emission) and corresponding (d) Arrhenius plot (inset shows the variation of peak intensities with temperature).

(${}^4\text{A}_{2g}$) nonradiatively. The position of crossover points may be different for these two samples, and MAG: Mn^{4+} , 0.27Ba^{2+} might require more energy for reaching this point, leading to its higher activation energy. Hence, the different activation energy is due to the fact that Mn^{4+} in the above two samples experiences different quenching barriers considering the structural difference as well as the ${}^4\text{T}_{1g}$ and ${}^2\text{T}_{2g}$ energies and the $\text{Mn}^{4+}\text{-O}^{2-}$ CTB energy.⁵⁶ The variation of peak intensities (positioning at 659 and 630 nm) with temperature for MAG: Mn^{4+} , 0.27Ba^{2+} is shown in Figure 8e. The absorbed energy in this process is called the activation energy.^{57,58} Meanwhile, the CIE coordinates are not affected much due to the increase in temperature, indicating a strong ligand field stabilization energy in the octahedral sites of MAG: Mn^{4+} , 0.27Ba^{2+} where Mn^{4+} ions are situated (Figure 8e).

3.3.3. Low-Temperature Photoluminescence of MAG: Mn^{4+} , 0.27Ba^{2+} and MGG: Mn^{4+} , 0.13Ba^{2+} . Low-temperature PL spectra for the two optimum samples MAG: Mn^{4+} , 0.27Ba^{2+} and MGG: Mn^{4+} , 0.13Ba^{2+} are investigated with the excitation of a 266 nm laser source operated at 10 mW to compare the activation energy of these phosphors. To elucidate the influence

of $[\text{AlO}_6]$ octahedra in activation energy and photoluminescence, the PL spectra of these two samples were probed by varying the temperature from 10 to 300 K (Figure 9a). The activation energy was calculated from the low-temperature PL spectra using the Arrhenius plot, as revealed in Figure 9b for MAG: Mn^{4+} , 0.27Ba^{2+} .

Generally, electronic transitions between ${}^2\text{E}_g$ and ${}^4\text{A}_{2g}$ states of Mn^{4+} ions are forbidden because of the same parity. In these phosphors, Mn^{4+} ions occupy the $\text{Al}^{3+}/\text{Ga}^{3+}$ octahedral sites without inversion symmetry, which helps partially break the selection rules for this transition. The PL spectra of the ${}^2\text{E}_g \rightarrow {}^4\text{A}_{2g}$ transition show several emissions bands between 600 and 700 nm. The zero phonon line (ZPL) at 639 nm and sidebands are prominently observable at 10 K. The Stokes bands are highly intense, whereas the anti-Stokes bands are less intense. As the temperature increased, the intensity of the Stokes bands at 659 nm (P1) and 647 nm (P2) and the ZPL decrease, whereas that of the anti-Stokes band at 630 nm (P3) increased. This can be attributed to the participation of more restricted phonon vibrations at higher temperatures.¹⁵ On increasing the temper-

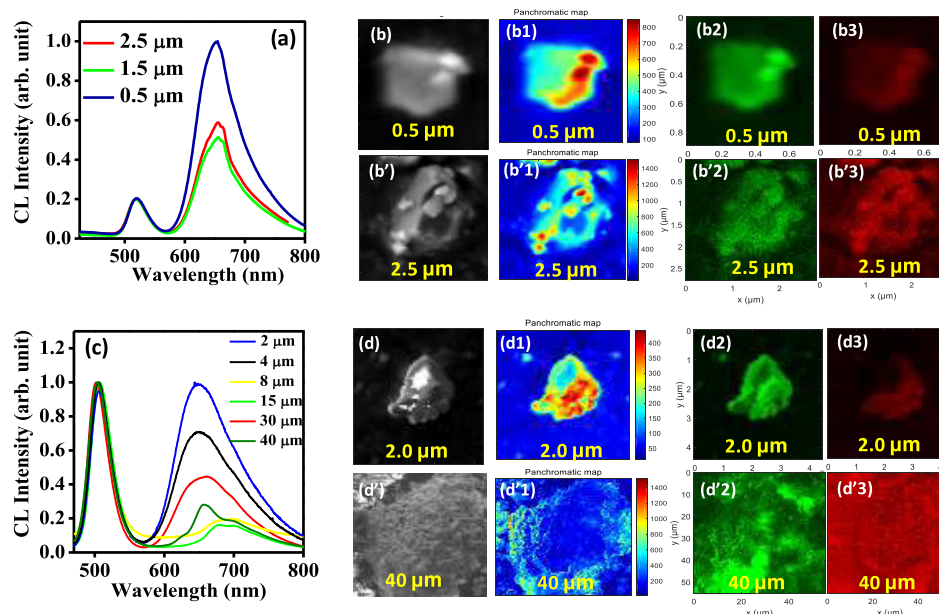


Figure 10. (a) Normalized CL spectra with respect to the green emission peak of the MAG: Mn^{4+} , 0.27Ba^{2+} sample. (b, b') SEM images, (b1, b'1) panchromatic overall intensity mapping, and filtered maps for the (b2, b'2) green (from 450 to 570 nm) and (b3, b'3) red emissions (from 570 to 800 nm) recorded for different-sized particles in the MAG: Mn^{4+} , 0.27Ba^{2+} sample. (c) Normalized CL spectra with respect to the green emission peak of the MGG: Mn^{4+} , 0.13Ba^{2+} sample. (d, d') SEM images, (d1, d'1) panchromatic overall intensity mapping, and filtered maps for the (d2, d'2) green (from 450 to 570 nm) and (d3, d'3) red emission (from 570 to 800 nm) bands recorded for different-sized particles in the MGG: Mn^{4+} , 0.13Ba^{2+} sample.

ature, the anti-Stokes bands are thermally depopulated from the Stokes bands until thermal equilibrium is reached. This substantiates the increase in intensity with the rise in temperature. Also, Boltzmann's law should be obeyed in the intensity ratio of anti-Stokes and Stokes bands as phonon-coupled sidebands are considered a couple of adjacent levels.¹⁵

The variation of peak intensities with temperature is shown in the inset of Figure 9b. This can be attributed to the thermal vibration developed in the host.⁵⁹ The temperature-dependent emission spectra show a typical trend of spectral broadening and a red shift of the emission band. As the temperature increases, the emission bands become broader and the peaks are shifted to higher-wavelength regions because of photon reabsorption and increased acoustic electron interaction following the Varshni equation. The red shift of the emission bands with increasing temperature is due to the expansion of the activator–ligand distance leading to a lower crystal field splitting. Furthermore, the ZPL intensity decreases with increasing temperature, which can be ascribed to the loss of phonon energy via nonradiative transition.¹⁶

The low-temperature PL spectra and intensity variations of P1, P2, and P3 with temperature and Arrhenius plots of MGG: Mn^{4+} , 0.13Ba^{2+} are shown in Figure 9c,d, respectively. A similar kind of temperature-dependent emission behavior is observed for P1 (~659 nm), P2 (~650 nm), and P3 (~631 nm) peaks in the MGG: Mn^{4+} , 0.13Ba^{2+} sample (inset of Figure 9d).

While comparing the low-temperature PL spectra for these two optimum samples, the shape of the emission spectra changed due to the replacement of Ga^{3+} with Al^{3+} . This might be due to the preferential occupancy of Mn^{4+} in $[\text{AlO}_6]$ octahedrons (in MAG: Mn^{4+} , 0.27Ba^{2+}) rather than $[\text{GaO}_6]$ octahedra (in MGG: Mn^{4+} , 0.13Ba^{2+}). The shape of the emission spectra depends on the coordination environment of Mn^{4+} . The activation energy obtained for MAG: Mn^{4+} , 0.27Ba^{2+}

is 119.83 meV, which is greater than the calculated activation energy of MGG: Mn^{4+} , 0.13Ba^{2+} (102.85 meV). The Mn–O bond in $[\text{AlO}_6]$ octahedrons is weaker than the same situated in $[\text{GaO}_6]$ octahedrons due to the smaller size of Al^{3+} ions than Ga^{3+} ions. These differences in their bond length cause differences in the energies of ${}^4\text{T}_{1g}$ and $\text{Mn}^{4+}\text{-O}^{2-}$ CTB. Hence, these two samples experience different quenching barriers, and it could be the reason for the higher activation energy of MAG: Mn^{4+} , 0.27Ba^{2+} compared to MGG: Mn^{4+} , 0.13Ba^{2+} .^{22,56,60} The ZPL (P2) intensity mainly depends on the Mn^{4+} ions' coordination environment. Therefore, the increased sharpness and higher intensity of the ZPL in MAG: Mn^{4+} , 0.27Ba^{2+} compared to MGG: Mn^{4+} , 0.13Ba^{2+} might be due to the lower symmetry of the $[\text{AlO}_6]$ octahedrons than the $[\text{GaO}_6]$ octahedrons.⁶¹

An interesting fact to note is that a very weakly intense broad green emission band that peaked at 505 nm is observed for the MGG: Mn^{4+} , 0.13Ba^{2+} sample at lower temperatures, which is however not seen in the low-temperature PL of MAG: Mn^{4+} , 0.27Ba^{2+} . The magnified portion below 600 nm of the low-temperature PL spectra of the MGG: Mn^{4+} , 0.13Ba^{2+} sample is shown in the insets of Figure 9c. To predict the origin of such a broad peak, cathodoluminescence analyses of MAG: Mn^{4+} , 0.27Ba^{2+} and MGG: Mn^{4+} , 0.13Ba^{2+} samples are carried out further.

3.3.4. Cathodoluminescence Properties of Optimum MAG: Mn^{4+} , 0.27Ba^{2+} and MGG: Mn^{4+} , 0.13Ba^{2+} . Apart from the ${}^2\text{E}_g \rightarrow {}^4\text{A}_{2g}$ transitions of Mn^{4+} ions, a weakly intense broad green emission is observed at 505 nm in low-temperature PL spectra of the MGG: Mn^{4+} , 0.13Ba^{2+} sample (Figure 9c). However, no such green emission is observed for the MAG: Mn^{4+} , 0.27Ba^{2+} sample (Figure 9a). To investigate the origin of the green emission, the cathodoluminescence (CL) spectra, as well as the spectral maps, are collected for MAG: Mn^{4+} , 0.27Ba^{2+} and

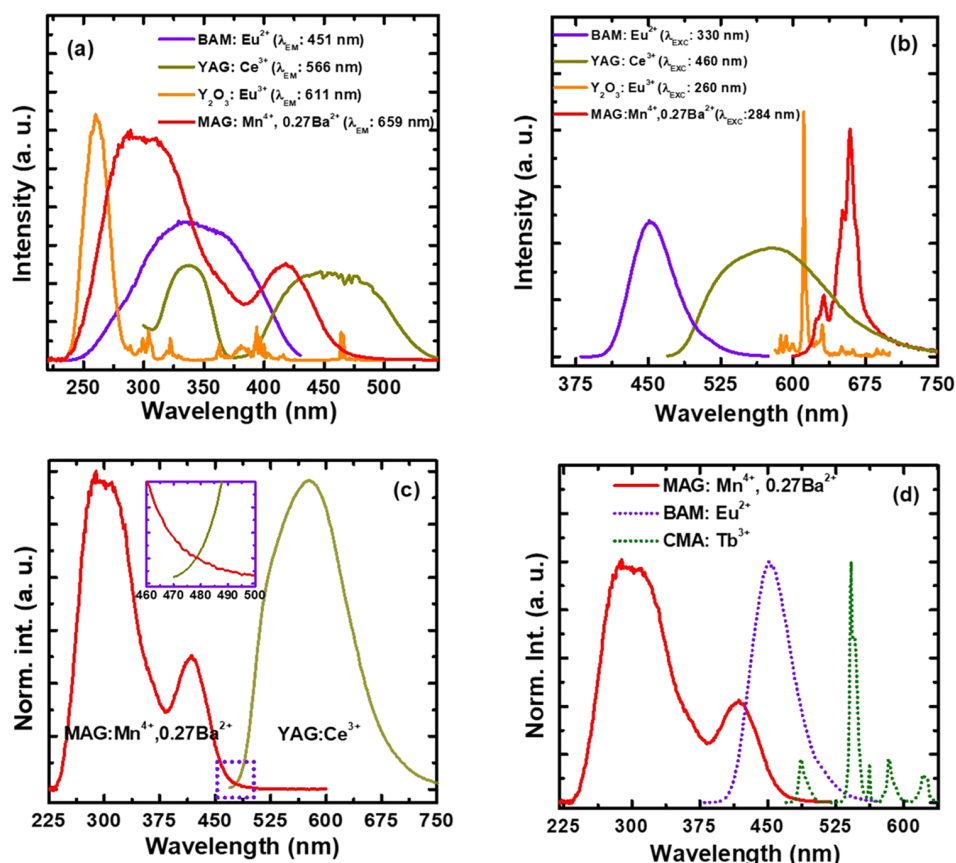


Figure 11. Comparative (a) PLE and (b) PL spectra of the optimum MAG: Mn⁴⁺, 0.27Ba²⁺ sample with commercial BAM: Eu²⁺ (blue), YAG: Ce³⁺ (yellow), and Y₂O₃: Eu³⁺ (red) phosphors. (c) PLE spectra of MAG: Mn⁴⁺, 0.27Ba²⁺ and emission spectra of YAG: Ce³⁺ showing spectral overlap. (d) PLE spectra of MAG: Mn⁴⁺, 0.27Ba²⁺ with the PL spectra of BAM: Eu²⁺ and CMA: Tb³⁺ showing spectral overlap.

MGG: Mn⁴⁺, 0.13Ba²⁺ samples. Unlike the UV photons' excitation in PL, the excitation with high-energy electrons in CL can produce almost all of the possible transitions to the higher energy state. Hence, it could be more useful to identify the various emission centers in any kind of luminescent materials.⁶²

The CL spectra are recorded at room temperature for MAG: Mn⁴⁺, 0.27Ba²⁺ and MGG: Mn⁴⁺, 0.13Ba²⁺ samples focusing on individual grains having different sizes (Figure 10a,c). Compared to the sharp PL emission spectra, the CL spectra of these samples show a broader emission band centered at 650 nm, which might be attributed to the red emission originating from the emission centers of both Mn⁴⁺ and Mn²⁺ ions since the occupancy of Mn²⁺ ions in the [MgO₆] octahedrons can also produce a broad orange-red emission.⁶³ Interestingly, broad green emission bands centered at 518 and 504 nm are observed for MAG: Mn⁴⁺, 0.27Ba²⁺ and MGG: Mn⁴⁺, 0.13Ba²⁺, respectively, which are attributed to the d–d transitions of Mn²⁺ ions. Unlike the PL spectra, the green emission band in both samples is observed to be prominent in their CL spectra. Since the d–d transitions of Mn²⁺ ions are forbidden in view of spin and parity, it requires high energy pumping or the help of sensitizers (Ce³⁺, Eu²⁺) to be intensified.^{64–66} In the present case, the high energy electronic irradiations during the CL spectral measurements could effectively pump the d–d transitions of Mn²⁺ ions owing to which broad Mn²⁺ emission bands are detected. The CL spectra normalized with respect to the intensity of the green emission bands observed in various-

sized grains in both of these samples are presented in Figure 10a,c. These could be helpful to observe the effect of particle sizes on the emission features of manganese ions having 2+ and 4+ valance.

The relative intensity of the red emission of MAG: Mn⁴⁺, 0.27Ba²⁺ and MGG: Mn⁴⁺, 0.13Ba²⁺ samples varies with the particle sizes, as can be seen in Figure 10a,c, respectively. Meanwhile, the red emission is dominant in the case of the MAG: Mn⁴⁺, 0.27Ba²⁺ sample irrespective of the particle size. However, no consistent trend of CL emission variation with particle size could be identified in both of these samples. A similar kind of result showing the independency of particle size on CL efficiency has been reported by Shea et al.⁶⁷ Although the variations appear to be uncorrelated with the particle size, interestingly, in the present case, the red-to-green emission proportion is seen to be dependent on the compositions of the materials. The red-to-green CL peak ratio in MGG: Mn⁴⁺, 0.13Ba²⁺ particles is lower than that observed in MAG: Mn⁴⁺, 0.27Ba²⁺ particles.

The existence of sharp red (from Mn⁴⁺) and broad red (from Mn²⁺) as well as broad green (from Mn²⁺) emission bands can be identified from the spectrally filtered SEM micrographs of different particles having different sizes in these two samples. Figure 10b,b',d,d' represents the general SEM images of different-sized particles to be studied in MAG: Mn⁴⁺, 0.27Ba²⁺ and MGG: Mn⁴⁺, 0.13Ba²⁺ samples, respectively. However, Figure 10b1,b'1,d1,d'1 represents the overall panchromatic intensity maps of the respective particles shown in Figure

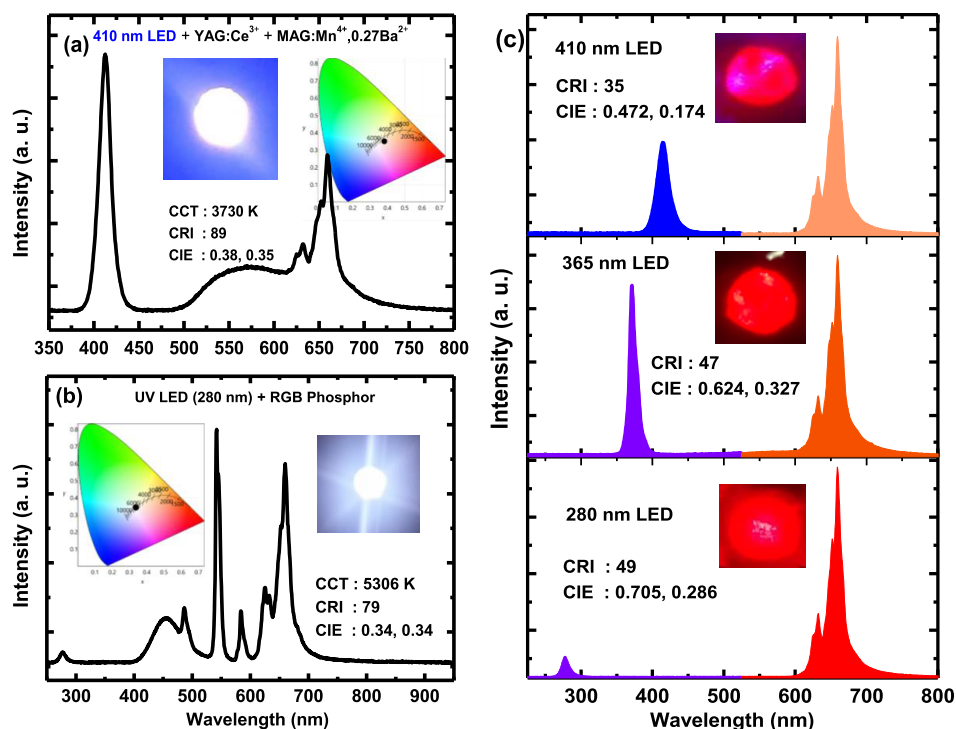
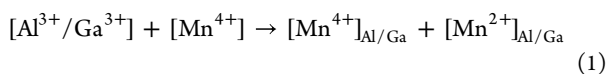


Figure 12. (a) EL spectra for the WLED fabricated by combining blue LED chip with YAG: Ce³⁺ and MAG: Mn⁴⁺, 0.27Ba²⁺. (b) EL spectra for the WLED fabricated by combining red MAG: Mn⁴⁺, 0.27Ba²⁺ phosphor with commercial green and blue phosphors using a 280 nm UV-LED chip. (c) EL spectra for the red LED fabricated using LED chips of different wavelengths with MAG: Mn⁴⁺, 0.27Ba²⁺ red phosphor.

10b,b',d,d'. In the illustrated panchromatic intensity maps, the CL signal is averaged over all visible wavelengths that fall within the specific detection range. The red and green emission regions can be easily visualized from the respective panchromatic maps of both samples. The spectrally filtered maps of the small and big particles in MAG: Mn⁴⁺, 0.27Ba²⁺ and MGG: Mn⁴⁺, 0.13Ba²⁺ samples are also presented in Figure 10b2,b3,b'2,b'3 and Figure 10d2,d3,d'2,d'3, respectively. These filtered maps are further helpful for the precise visualization and the spatial distribution of the green emission (from 450 to 570 nm) and the red emission (from 570 to 800 nm) intensities observed in the overall panchromatic maps.

The origin of green emissions can be attributed to the reduction of Mn⁴⁺ ions to Mn²⁺ ions and their occupancy in tetrahedral sites.⁶³ The reduction can be explained in two ways. One is self-reduction resulting from site occupation, and the other is caused by the electron beam during CL measurement. Here, the generated Mn²⁺ ions (r_{MnO_4} : 0.66 Å) can occupy the Al³⁺ (r_{AlO_4} : 0.39 Å) and Ga³⁺ (r_{GaO_4} : 0.47 Å) tetrahedral sites of MAG: Mn⁴⁺, 0.27Ba²⁺ and MGG: Mn⁴⁺, 0.13Ba²⁺, respectively. When a tetravalent ion is doped at the trivalent site, a divalent ion can be generated to maintain charge neutrality. In this case, a Mn⁴⁺ ion can substitute one Al³⁺ (or Ga³⁺) ion at the octahedrons, and other Mn⁴⁺ ions might be reduced to Mn²⁺ and occupy Al³⁺ (or Ga³⁺) tetrahedrons to maintain charge neutrality²¹ according to the following equation



If some of the Mn⁴⁺ ions are substituted in the [MgO₆] sites instead of Al³⁺ (or Ga³⁺) octahedral sites, the self-reduction of Mn⁴⁺ to Mn²⁺ may enhance. The number of Mn⁴⁺ ions going to [MgO₆] sites of MAG: Mn⁴⁺, 0.27Ba²⁺ is less due to the

availability of more suitable [AlO₆] sites of the MAG host for Mn⁴⁺ ions' occupancy. Hence, the self-reduction of Mn⁴⁺ to Mn²⁺ is expected to be lesser in MAG: Mn⁴⁺, 0.27Ba²⁺ compared to MGG: Mn⁴⁺, 0.13Ba²⁺.^{68,69} Also, compared to [AlO₄] tetrahedrons, [GaO₄] tetrahedrons are more suitable for Mn²⁺ to occupy. Therefore, the Mn²⁺ green emission is relatively lower in MAG: Mn⁴⁺, 0.27Ba²⁺ compared to MGG: Mn⁴⁺, 0.13Ba²⁺. Moreover, the full width at half-maximum (FWHM) of the electrons' irradiated red emission in MGG: Mn⁴⁺, 0.13Ba²⁺ is much higher due to more contribution of Mn²⁺ ions in the red emission. Further studies are required for the exact confirmation of these observations.

3.4. Applications in WLEDs and Red LEDs. The PLE and PL emission intensities of the optimum MAG: Mn⁴⁺, 0.27Ba²⁺ phosphor have been compared with commercial blue-emitting BaMgAl₁₀O₁₇: Eu²⁺ (BAM: Eu²⁺), yellow-emitting Y₃Al₅O₁₂: Ce³⁺ (YAG: Ce³⁺), and red-emitting (Y₂O₃: Eu³⁺) phosphors, as displayed in Figure 11a,b, respectively. The emission intensity of the optimum red phosphor is higher than that of the commercial blue and yellow phosphors. It exhibited almost the same emission intensity but more width (FWHM ~ 18 nm) than the commercial red phosphor (FWHM ~ 2 nm) (Figure 11b). Figure 11c represents the excitation spectrum of MAG: Mn⁴⁺, 0.27Ba²⁺ and emission spectra of YAG: Ce³⁺. The trivial overlapping of the emission spectra of YAG: Ce³⁺ and excitation spectra of MAG: Mn⁴⁺, 0.27Ba²⁺ indicates that the probability of photons' reabsorption is negligible. Therefore, MAG: Mn⁴⁺, 0.27Ba²⁺ composition can be a suitable red component to enhance the color rendering (CRI) and to reduce the correlated color temperature (CCT) of YAG: Ce³⁺-based WLEDs. Likewise, Figure 11d represents the excitation spectra of MAG: Mn⁴⁺, 0.27Ba²⁺ with the emission spectra of blue-emitting BAM: Eu²⁺ and green-emitting CeMgAl₁₁O₁₉: Tb³⁺

(CMA: Tb^{3+}) phosphors. In this case, the overlapping region between excitation spectra of the MAG: Mn^{4+} , 0.27Ba^{2+} phosphor and emission spectra of the green phosphor (CMA: Tb^{3+}) is negligible. Also, the overlapping between the excitation spectra and emission spectra of MAG: Mn^{4+} , 0.27Ba^{2+} and BAM: Eu^{2+} phosphors, respectively, is marginal. This result supports the suitability of MAG: Mn^{4+} , 0.27Ba^{2+} composition as a red component for the tricolor phosphor-based WLEDs.

Therefore, WLEDs have been fabricated by two different approaches. At first, MAG: Mn^{4+} , 0.27Ba^{2+} phosphor has been mixed with YAG: Ce^{3+} with a ratio of 6:4. This phosphor mixture is then incorporated with poly(methyl methacrylate) by grinding. Then, the mixture is stirred thoroughly with acryline to make a thick paste. The resulting paste has been coated on a blue InGaN chip of 410 nm wavelength to produce WLED. The EL spectrum and the corresponding digital image of the resultant WLED are shown in Figure 12a. This combination produces warm white light with a CCT of 3730 K, CRI of 89, and CIE coordinates of (0.38, 0.35). Using a 280 nm UV-LED chip, another WLED has been fabricated by mixing optimum MAG: Mn^{4+} , 0.27Ba^{2+} red phosphor with commercial blue (BAM: Eu^{2+}) and green (CMA: Tb^{3+}) phosphors with a mixing ratio of 7:3:2. This combination produces natural white light with a CCT of 5306 K, a CRI of 79, and a CIE coordinate of (0.34, 0.34). The EL spectrum and the corresponding digital image of the fabricated WLED are shown in Figure 12b. The obtained values of CCT and CRI strongly suggest that MAG: Mn^{4+} , 0.27Ba^{2+} is a promising red component for blue and UV-based phosphor-converted WLEDs used in indoor lighting.

Furthermore, three red LEDs are developed by combining the red phosphor with 280 nm, 365 nm UV-LED, and 410 nm blue LED chips. The corresponding EL spectra with the direct red LED images are shown in Figure 12c. The emission peak centered at 659 nm matches well with the absorption peaks of chlorophyll A and chlorophyll B responsible for photosynthesis and photoperiodic effects in plant leaves.^{18,70} The red LED developed by combining red phosphors with blue LED has two emission bands at 410 and 659 nm. Hence, this LED can cover the absorption spectrum of phytochrome Pr since its absorption spectrum exhibits major bands at 405 and 655 nm.⁷¹ Shi et al. developed red LED for plant growth application by combining $\text{Ca}_2\text{LaSbO}_6$: Mn^{4+} with a near-UV-LED chip, and it showed an emission peak at 695 nm with a CRI of 26.6.⁷² Gu et al. developed red LEDs by combining the $\text{SrMgAl}_{10-9}\text{Ga}_y\text{O}_{17}$: Mn^{4+} phosphor with blue LEDs, and its CIE coordinate values vary from (0.146, 0.036) to (0.578, 0.229).⁵³ Here, we fabricated three red LEDs, and the corresponding CRI (35, 47, and 49) and CIE values (0.472, 0.174), (0.624, 0.327), and (0.705, 0.286) are found to be suitable for artificial lighting for plant growth.^{18,70}

4. CONCLUSIONS

In the present research, the innovative deep-red-emitting (Mg , Ba) $_3\text{Al}_2\text{GeO}_8$: Mn^{4+} phosphor was evaluated from its analogue of $\text{Mg}_3\text{Ga}_2\text{GeO}_8$: Mn^{4+} . Initial replacement of Ga^{3+} by Al^{3+} yielded $\text{Mg}_3\text{Al}_2\text{GeO}_8$: Mn^{4+} , which showed a much more intense red emission than $\text{Mg}_3\text{Ga}_2\text{GeO}_8$: Mn^{4+} due to the strong preference of Mn^{4+} to the $[\text{AlO}_6]$ octahedrons compared to $[\text{GaO}_6]$ octahedrons. The coexisting phases of MgAl_2O_4 and Mg_2GeO_4 in $\text{Mg}_3\text{Al}_2\text{GeO}_8$: Mn^{4+} also contributed to the Mn^{4+} luminescence by providing more preferable octahedral sites for Mn^{4+} occupancy. These sites reduced the natural reduction probability of Mn^{4+} to Mn^{2+} in the tetrahedral sites, which was

confirmed by the low-temperature photoluminescence and cathodoluminescence studies for the first time. Eventually, the partial substitution of larger Ba^{2+} ions in Mg^{2+} sites caused structural distortions and generated new Ba impurity phases, which improved the Mn^{4+} photoluminescence further. Under UV and violet-blue exposure, the optimum composition $\text{Mg}_{2.73}\text{Ba}_{0.27}\text{Al}_2\text{GeO}_8$: Mn^{4+} exhibited a deep-red emission at 659 nm, which was 35-fold greater in intensity than the base composition of $\text{Mg}_3\text{Ga}_2\text{GeO}_8$: Mn^{4+} . The emission matched the absorption of chlorophylls liable for plants' photosynthesis. The intense red emission with 100% color purity of the optimized composition makes it a suitable red phosphor to enhance the color rendering of commercial white LEDs.

■ ASSOCIATED CONTENT

Supporting Information

The Supporting Information is available free of charge at <https://pubs.acs.org/doi/10.1021/acsami.2c20066>.

XPS survey spectra, EDX compositional analysis, and elemental mapping for MAG: Mn^{4+} (Figure S1); EDX composition analysis and elemental mapping images for MGG: Mn^{4+} (Figure S2); XRD patterns of MGG, MGG: Mn^{4+} , and MGG: Mn^{4+} , $x\text{Ba}^{2+}$ ($x = 0.03$ – 0.15) (Figure S3); XPS survey spectrum of MGG: Mn^{4+} , 0.13Ba^{2+} and core-level spectra of Mg 2p and O 1s for MGG: Mn^{4+} and MGG: Mn^{4+} , 0.13Ba^{2+} (Figure S4); UV–DRS spectra and Tauc's plots for MGG and MGG: Mn^{4+} , $x\text{Ba}^{2+}$ ($x = 0.0$, 0.13), and PLE and PL emission spectra of MGG: Mn^{4+} , $x\text{Ba}^{2+}$ ($x = 0.0$ – 0.15) (Figure S5); PL emission spectra of BMG: Mn^{4+} and MGO: Mn^{4+} (Figure S6); SEM images of MAG: Mn^{4+} and MAG: Mn^{4+} , 0.27Ba^{2+} (Figure S7); SEM images (Figure S8) and PL of MAG: Mn^{4+} , 0.27Ba^{2+} synthesized at various temperatures (Figure S9); PL decay curves of MAG: Mn^{4+} , MAG: Mn^{4+} , 0.27Ba^{2+} , MGG: Mn^{4+} , and MGG: Mn^{4+} , 0.13Ba^{2+} (Figure S10); lattice parameters of MAG, MAG: Mn^{4+} , 0.03Ba^{2+} , MGG, and MGG: Mn^{4+} , 0.1Ba^{2+} (Table S1); Rietveld-refined atomic coordinates and fraction of occupancies of MAG and MGG (Table S2); Rietveld-refined atomic coordinates and fraction of occupancies of MAG: 0.03Ba^{2+} and MGG: Mn^{4+} , 0.1Ba^{2+} (Table S3); calculated and average bond lengths in MAG, MAG: Mn^{4+} , 0.03Ba^{2+} , MGG, and MGG: Mn^{4+} , 0.1Ba^{2+} (Table S4) (PDF)

■ AUTHOR INFORMATION

Corresponding Author

Subrata Das – Materials Science and Technology Division, CSIR-National Institute for Interdisciplinary Science and Technology, Thiruvananthapuram, Kerala 695019, India; Academy of Scientific and Innovative Research (AcSIR), Ghaziabad 201002, India; orcid.org/0000-0003-0467-0872; Email: subratadas@niist.res.in

Authors

Thejas Kurunthatil Kuttit – Materials Science and Technology Division, CSIR-National Institute for Interdisciplinary Science and Technology, Thiruvananthapuram, Kerala 695019, India; Academy of Scientific and Innovative Research (AcSIR), Ghaziabad 201002, India; orcid.org/0000-0002-5092-1209

Malini Abraham – Materials Science and Technology Division, CSIR-National Institute for Interdisciplinary Science and Technology, Thiruvananthapuram, Kerala 695019, India; Academy of Scientific and Innovative Research (AcSIR), Ghaziabad 201002, India

Arup K. Kunti – Centre de Nanosciences et de Nanotechnologies (C2N), Univ. Paris-Sud, Univ. Paris-Saclay, UMR 9001 CNRS, Gobert, Palaiseau 91120, France; orcid.org/0000-0002-9340-1107

Nuño Amador-Mendez – Centre de Nanosciences et de Nanotechnologies (C2N), Univ. Paris-Sud, Univ. Paris-Saclay, UMR 9001 CNRS, Gobert, Palaiseau 91120, France

Maria Tchernycheva – Centre de Nanosciences et de Nanotechnologies (C2N), Univ. Paris-Sud, Univ. Paris-Saclay, UMR 9001 CNRS, Gobert, Palaiseau 91120, France; orcid.org/0000-0003-4144-0793

Complete contact information is available at: <https://pubs.acs.org/10.1021/acsami.2c20066>

Notes

The authors declare no competing financial interest.

ACKNOWLEDGMENTS

This work was financially supported by the Indo-French Centre for the Promotion of Advanced Research (CEFIPRA, Project no. 6008-1). Maria Tchernycheva acknowledges support from GANEX (ANR-11-LABX-0014). GANEX belongs to the public-funded “Investissements d’Avenir” program managed by the French ANR agency. T.K.K. acknowledges the Council of Scientific & Industrial Research, Govt. of India, for the award of Junior Research Fellowship. The authors are thankful to Dr. Kaustabh Kumar Maiti for facilitating the Raman spectrometer.

REFERENCES

- Huang, L.; Liu, Y.; Yu, J.; Zhu, Y.; Pan, F.; Xuan, T.; Brik, M. G.; Wang, C.; Wang, J. Highly Stable $K_2SiF_6:Mn^{4+}@K_2SiF_6$ Composite Phosphor with Narrow Red Emission for White LEDs. *ACS Appl. Mater. Interfaces* **2018**, *10*, 18082–18092.
- Zhu, H.; Lin, C. C.; Luo, W.; Shu, S.; Liu, Z.; Liu, Y.; Kong, J.; Ma, E.; Cao, Y.; Liu, R. S.; Chen, X. Highly Efficient Non-Rare-Earth Red Emitting Phosphor for Warm White Light-Emitting Diodes. *Nat. Commun.* **2014**, *5*, No. 4312.
- Ming, H.; Liu, L.; He, S.; Peng, J.; Du, F.; Fu, J.; Yang, F.; Ye, X. An Ultra-High Yield of Spherical $K_2NaSF_6:Mn^{4+}$ Red Phosphor and Its Application in Ultra-Wide Color Gamut Liquid Crystal Displays. *J. Mater. Chem. C* **2019**, *7*, 7237–7248.
- Singh, S. P.; Kim, M.; Park, W. B.; Lee, J. W.; Sohn, K. S. Discovery of a Red-Emitting $Li_3RbGe_8O_{18}:Mn^{4+}$ Phosphor in the Alkali-Germanate System: Structural Determination and Electronic Calculations. *Inorg. Chem.* **2016**, *55*, 10310–10319.
- Li, P.; Wondraczek, L.; Peng, M.; Zhang, Q.; Setlur, A. Tuning Mn^{4+} Red Photoluminescence in $(K,Rb)_2Ge_4O_9:Mn^{4+}$ Solid Solutions by Partial Alkali Substitution. *J. Am. Ceram. Soc.* **2016**, *99*, 3376–3381.
- Hu, J.; Huang, T.; Zhang, Y.; Lu, B.; Ye, H.; Chen, B.; Xia, H.; Ji, C. Enhanced Deep-Red Emission from Mn^{4+}/Mg^{2+} Co-Doped $CaGdAlO_4$ Phosphors for Plant Cultivation. *Dalton Trans.* **2019**, *48*, 2455–2466.
- Li, K.; Zhu, D.; Van Deun, R. Photoluminescence Properties and Crystal Field Analysis of a Novel Red-Emitting Phosphor $K_2BaGe_8O_{18}:Mn^{4+}$. *Dyes Pigm.* **2017**, *142*, 69–76.
- Huang, X.; Zhang, P.; Liu, Z.; Ma, B.; Zhou, Y.; Tian, X. Fluorine Doping Induced Crystal Space Change and Performance Improvement of Single Crystalline $LiNi_{0.6}Co_{0.2}Mn_{0.2}O_2$ Layered Cathode Materials. *ChemElectroChem* **2022**, *9*, 1–7.
- Liang, S.; Shang, M.; Lian, H.; Li, K.; Zhang, Y.; Lin, J. An Efficient Rare-Earth Free Deep Red Emitting Phosphor for Improving the Color Rendering of White Light-Emitting Diodes. *J. Mater. Chem. C* **2017**, *5*, 2927–2935.
- Dolgov, L.; Hong, J.; Zhou, L.; Li, X.; Li, J.; Djordjevic, V.; Dramicanin, M.; Shi, J.; Wu, M. Efficient Luminescence Enhancement of $Mg_2TiO_4:Mn^{4+}$ Red Phosphor by Incorporating Plasmonic $Ag@SiO_2$ Nanoparticles. *ACS Appl. Mater. Interfaces* **2019**, *11*, 21004–21009.
- Ding, X.; Zhu, G.; Geng, W.; Wang, Q.; Wang, Y. Rare-Earth-Free High-Efficiency Narrow-Band Red-Emitting $Mg_3Ga_2GeO_8:Mn^{4+}$ Phosphor Excited by Near-UV Light for White-Light-Emitting Diodes. *Inorg. Chem.* **2016**, *55*, 154–162.
- Liang, S.; Shang, M.; Lian, H.; Li, K.; Zhang, Y.; Lin, J. Deep Red $MGe_3O_9:Mn^{4+}$ ($M = Sr, Ba$) Phosphors: Structure, Luminescence Properties and Application in Warm White Light Emitting Diodes. *J. Mater. Chem. C* **2016**, *4*, 6409–6416.
- Huang, Q.; Ye, W.; Hu, G.; Liu, X. Strong Red Emission in Bi^{3+} and Mn^{4+} Codoped $Mg_{3.5}Ge_{1.25}O_6$ Phosphors Applied in Optical Agriculture. *J. Lumin.* **2019**, *210*, 89–95.
- Liang, S.; Li, G.; Dang, P.; Wei, Y.; Lian, H.; Lin, J. Cation Substitution Induced Adjustment on Lattice Structure and Photoluminescence Properties of $Mg_{14}Ge_5O_{24}:Mn^{4+}$: Optimized Emission for w-LED and Thermometry Applications. *Adv. Opt. Mater.* **2019**, *7*, No. 1900093.
- Peng, L.; Chen, W.; Cao, S.; Liu, B.; Han, T.; Zhao, L.; Zhao, C.; Li, F.; Li, X. Enhanced Photoluminescence and Thermal Properties Due to Size Mismatch in $Mg_2Ti_xGe_{1-x}O_4:Mn^{4+}$ Deep-Red Phosphors. *J. Mater. Chem. C* **2019**, *7*, 2345–2352.
- Abraham, M.; Kunti, A. K.; Thejas, K. K.; Amador-Mendez, N.; Gogneau, N.; Nishanth, K. G.; Tchernycheva, M.; Das, S. The Elevated Colour Rendering of White-LEDs by Microwave-Synthesized Red-Emitting $(Li, Mg)_3RbGe_8O_{18}:Mn^{4+}$ nanophosphors. *Dalton Trans.* **2021**, *50*, 3044–3059.
- Wu, Y.; Zhuang, Y.; Xie, R. J.; Ruan, K.; Ouyang, X. Novel Mn^{4+} Doped Red Phosphors Composed of $MgAl_2O_4$ and $CaAl_2O_9$ Phases for Light-Emitting Diodes. *Dalton Trans.* **2020**, *49*, 3606–3614.
- Cao, R.; Ye, Y.; Peng, Q.; Zheng, G.; Ao, H.; Fu, J.; Guo, Y.; Guo, B. Synthesis and Luminescence Characteristics of Novel Red-Emitting $Ba_2TiGe_2O_8:Mn^{4+}$ Phosphor. *Dyes Pigm.* **2017**, *146*, 14–19.
- Chen, D.; Zhou, Y.; Zhong, J. A Review on Mn^{4+} Activators in Solids for Warm White Light-Emitting Diodes. *RSC Adv.* **2016**, *6*, 86285–86296.
- Wang, Y.; Ding, F.; Wu, J.; Ke, J.; Yuan, X.; Wang, X.; Qiu, Z.; Zhou, W.; Zhang, J.; Lian, S. Site Preference-Driven Mn^{4+} Stabilization in Double Perovskite Phosphor Regulating Quantum Efficiency from Zero to Champion. *Inorg. Chem.* **2022**, *61*, 3631–3640.
- Dong, L.; Zhang, L.; Jia, Y.; Shao, B.; Lü, W.; Zhao, S.; You, H. Site Occupation and Luminescence of Novel Orange-Red $Ca_3M_2Ge_3O_{12}:Mn^{2+},Mn^{4+}$ ($M = Al, Ga$) Phosphors. *ACS Sustainable Chem. Eng.* **2020**, *8*, 3357–3366.
- Cao, R.; Luo, W.; Xiong, Q.; Liang, A.; Jiang, S.; Xu, Y. Synthesis and Luminescence Properties of Novel Red Phosphors $LiRGe_2O_6:Mn^{4+}$ ($R = Al$ or Ga). *J. Alloys Compd.* **2015**, *648*, 937–941.
- Dai, D.; Wang, Z.; Xing, Z.; Li, X.; Liu, C.; Zhang, L.; Yang, Z.; Li, P. Broad Band Emission Near-Infrared Material $Mg_3Ga_2GeO_8:Cr^{3+}$: Substitution of Ga-In, Structural Modification, Luminescence Property and Application for High Efficiency LED. *J. Alloys Compd.* **2019**, *806*, 926–938.
- Lu, Z.; Fu, A.; Gao, F.; Zhang, X.; Zhou, L. Synthesis and Luminescence Properties of Double Perovskite $Ba_2MgGe_2O_7:Mn^{4+}$ Deep Red Phosphor. *J. Lumin.* **2018**, *203*, 420–426.
- Kaminskii, A. A.; Bohatý, L.; Becker, P.; Liebertz, J.; Held, P.; Eichler, H. J.; Rhee, H.; Hanuza, J. Tetragonal $Ba_2MgGe_2O_7$ —A Novel Multifunctional Optical Crystal with Numerous Manifestations of Nonlinear-Laser Effects: Almost Sesqui-Octave Stokes and Anti-Stokes Combs and Cascaded $\chi(3) \leftrightarrow \chi(2)$ Lasing with Involved Second and Third Harmonic Generation. *Laser Phys. Lett.* **2008**, *5*, 845–868.

- (26) Öztürk, E. The Effect of Ba/Mg Impurities on the Phase Formation and Photoluminescence Properties of $(\text{Sr}_{3-x}\text{M}_x)\text{-Al}_2\text{O}_6\text{:Eu}^{3+},\text{Ho}^{3+}$ ($\text{M} = \text{Ba}, \text{Mg}$) Phosphors. *J. Therm. Anal. Calorim.* **2016**, *126*, 365–369.
- (27) Shannon, R. D. Revised Effective Ionic Radii and Systematic Studies of Interatomic Distances in Halides and Chalcogenides BY. *Acta Crystallogr., Sect. A: Cryst. Phys., Diffraction, Theor. Gen. Crystallogr.* **1976**, *32*, 751–766.
- (28) Zhang, R.; Wang, Z.; Meng, Y.; Jiao, S.; Jia, J.; Min, Y.; Liu, C. Quantitative Insight into Aluminum Structures in $\text{CaO-Al}_2\text{O}_3\text{-SiO}_2$ System via Raman and ^{27}Al MAS-NMR Spectroscopies. *J. Non-Cryst. Solids* **2021**, *573*, No. 121116.
- (29) Rudolph, W. W.; Irmer, G.; Hefter, G. T. Raman Spectroscopic Investigation of Speciation in $\text{MgSO}_4(\text{Aq})$. *Phys. Chem. Chem. Phys.* **2003**, *5*, 5253–5261.
- (30) Alvarado-Rivera, J.; Rodríguez-Carvajal, D. A.; Acosta-Enriquez, M.; del, C.; Manzanares-Martínez, M. B.; Alvarez, E.; Lozada-Morales, R.; Díaz, G. C.; de Leon, A.; Zayas, M. E. Effect of CeO_2 on the Glass Structure of Sodium Germanate Glasses. *J. Am. Ceram. Soc.* **2014**, *97*, 3494–3500.
- (31) Hasegawa, T.; Tanaka, R.; Ueda, T.; Toda, K. Preparation of MGF Phosphor by O_2 Postannealing and Impact on Luminescence Properties and Crystal Lattice. *J. Am. Ceram. Soc.* **2020**, *103*, 5145–5156.
- (32) Fang, W.; Ao, L.; Tang, Y.; Li, J.; Xiang, H.; Zhang, Z.; Du, Q.; Fang, L. Phase Evolution and Microwave Dielectric Properties of the $\text{Li}_{2(1+x)}\text{ZnGe}_3\text{O}_8$ Spinel Oxides. *J. Mater. Sci. Mater. Electron.* **2020**, *31*, 13496–13502.
- (33) Li, J.; Chou, K.; Shu, Q. Structure and Viscosity of $\text{CaO-Al}_2\text{O}_3\text{-B}_2\text{O}_3$ Based Mould Fluxes with Varying $\text{CaO/Al}_2\text{O}_3$ Mass Ratios. *ISIJ Int.* **2020**, *60*, 51–57.
- (34) Zhou, Y.; Zhuang, W.; Hu, Y.; Liu, R.; Jiang, Z.; Liu, Y.; Li, Y.; Zheng, Y.; Chen, L.; Zhong, J. A Broad-Band Orange-Yellow-Emitting $\text{Lu}_2\text{Mg}_2\text{Al}_2\text{Si}_2\text{O}_{12}\text{:Ce}^{3+}$ Phosphor for Application in Warm White Light-Emitting Diodes. *RSC Adv.* **2017**, *7*, 46713–46720.
- (35) Wood, D. L.; Tauc, J. Weak Absorption Tails in Amorphous Semiconductors. *Phys. Rev. B* **1972**, *5*, 3144–3151.
- (36) Xia, M.; Gu, S.; Zhou, C.; Liu, L.; Zhong, Y.; Zhang, Y.; Zhou, Z. Enhanced Photoluminescence and Energy Transfer Performance of $\text{Y}_3\text{Al}_4\text{GaO}_{12}\text{:Mn}^{4+},\text{Dy}^{3+}$ Phosphors for Plant Growth LED Lights. *RSC Adv.* **2019**, *9*, 9244–9252.
- (37) Xue, J.; Ran, W.; Noh, H. M.; Choi, B. C.; Park, S. H.; Jeong, J. H.; Kim, J. H. Influence of Alkaline Ions on the Luminescent Properties of Mn^{4+} -Doped MGe_4O_9 ($\text{M} = \text{Li}_2, \text{LiNa}$ and K_2) Red-Emitting Phosphors. *J. Lumin.* **2017**, *192*, 1072–1083.
- (38) Xue, F.; Hu, Y.; Chen, L.; Wu, H.; Ju, G.; Wang, T.; Yang, L. A Novel Rare-Earth Free Red Long-Persistent Phosphor: $\text{Mg}_2\text{GeO}_4\text{:Mn}^{4+}$. *Ceram. Int.* **2017**, *43*, 15141–15145.
- (39) Feng, J.; Wang, Z.; Xu, H.; Jia, M.; Wei, Y.; Fu, Z. The Charge Transfer Band as a Key to Study the Site Selection Preference of Eu^{3+} in Inorganic Crystals. *Inorg. Chem.* **2021**, *60*, 19440–19447.
- (40) Ji, H.; Hou, X.; Molokeev, M. S.; Ueda, J.; Tanabe, S.; Brik, M. G.; Zhang, Z.; Wang, Y.; Chen, D. Ultrabroadband Red Luminescence of Mn^{4+} in MgAl_2O_4 peaking at 651 Nm. *Dalton Trans.* **2020**, *49*, 5711–5721.
- (41) Srivastava, A. M.; Brik, M.; Beers, W. W.; Cohen, W. On the Mn^{4+} R-Line Intensity and Energy in the Perovskite Layer of SrLaAlO_4 and Sr_2TiO_4 : A Comparative Study with LaAlO_3 and SrTiO_3 . *Opt. Mater.* **2020**, *109*, No. 110372.
- (42) Yan, W.; Yun, X.; Yang, H.; Wei, Y.; Li, G. A Novel Mn^{4+} -Activated $\text{Li}_3\text{CsGe}_3\text{O}_{18}$ Red Phosphor and Cation Substitution Induced Photoluminescence Improvement. *J. Lumin.* **2020**, *225*, No. 117323.
- (43) Cao, R.; Lv, X.; Ran, Y.; Xu, L.; Chen, T.; Guo, S.; Ao, H.; Yu, X. Rare-Earth-Free $\text{Li}_3\text{La}_3\text{Ta}_2\text{O}_{12}\text{:Mn}^{4+}$ Deep-Red-Emitting Phosphor: Synthesis and Photoluminescence Properties. *J. Am. Ceram. Soc.* **2019**, *102*, 5910–5918.
- (44) Tao, C.; Li, P.; Li, Q.; Zhang, N.; Wang, D.; Zhao, J.; Yang, Z.; Wang, Z. Improvement of Thermal Stability and Photoluminescence in $\text{Mg}_2\text{Y}_2\text{Al}_2\text{Si}_2\text{O}_{12}\text{:Ce}^{3+}$ by the Cation Substitution of $\text{Ca}^{2+}, \text{Sr}^{2+}$ and Ba^{2+} ions. *Dalton Trans.* **2021**, *50*, 13138–13148.
- (45) Fang, S.; Han, T.; Lang, T.; Zhong, Y.; Liu, B.; Cao, S.; Peng, L.; Yakovlev, A. N.; Korepanov, V. I. Synthesis of a Novel Red Phosphor $\text{K}_2\text{Ba}_{1-x}\text{TiF}_6\text{:Mn}^{4+}$ and Its Enhanced Luminescence Performance, Thermal Stability and Waterproofness. *J. Alloys Compd.* **2019**, *808*, No. 151697.
- (46) Peng, M.; Yin, X.; Tanner, P. A.; Brik, M. G.; Li, P. Site Occupancy Preference, Enhancement Mechanism, and Thermal Resistance of Mn^{4+} Red Luminescence in $\text{SrAl}_{14}\text{O}_{25}\text{:Mn}^{4+}$ for Warm WLEDs. *Chem. Mater.* **2015**, *27*, 2938–2945.
- (47) Yang, D.; Li, G.; Kang, X.; Cheng, Z.; Ma, P.; Peng, C.; Lian, H.; Li, C.; Lin, J. Room Temperature Synthesis of Hydrophilic Ln^{3+} -Doped KGdF_4 ($\text{Ln} = \text{Ce}, \text{Eu}, \text{Tb}, \text{Dy}$) Nanoparticles with Controllable Size: Energy Transfer, Size-Dependent and Color-Tunable Luminescence Properties. *Nanoscale* **2012**, *4*, 3450–3459.
- (48) Huang, D.; Dang, P.; Lian, H.; Zeng, Q.; Lin, J. Luminescence and Energy-Transfer Properties in $\text{Bi}^{3+}/\text{Mn}^{4+}$ -Codoped $\text{Ba}_2\text{GdNbO}_6$ Double-Perovskite Phosphors for White-Light-Emitting Diodes. *Inorg. Chem.* **2019**, *58*, 15507–15519.
- (49) Li, X.; Chen, Z.; Wang, B.; Liang, R.; Li, Y.; Kang, L.; Liu, P. Effects of Impurity Doping on the Luminescence Performance of Mn^{4+} -Doped Aluminates with the Magnetoplumbite-Type Structure for Plant Cultivation. *Materials* **2019**, *12*, 1–11.
- (50) Wu, C.; Li, J.; Xu, H.; Wu, J.; Zhang, J.; Ci, Z.; Feng, L.; Cao, C.; Zhang, Z.; Wang, Y. Preparation, Structural and Photoluminescence Characteristics of Novel Red Emitting $\text{Mg}_2\text{Ga}_2\text{GeO}_{12}\text{:Mn}^{4+}$ Phosphor. *J. Alloys Compd.* **2015**, *646*, 734–740.
- (51) Thejas, K. K.; Abraham, M.; Kunti, A. K.; Tchernycheva, M.; Ahmad, S.; Das, S. Review on Deep Red-Emitting Rare-Earth Free Germanates and Their Efficiency as Well as Adaptability for Various Applications. *Appl. Mater. Today* **2021**, *24*, No. 101094.
- (52) Wang, Z.; Ji, H.; Xu, J.; Hou, X.; Ueda, J.; Tanabe, S.; Yi, S.; Zhou, Y.; Chen, D. Microsized Red Luminescent $\text{MgAl}_2\text{O}_4\text{:Mn}^{4+}$ Single-Crystal Phosphor Grown in Molten Salt for White LEDs. *Inorg. Chem.* **2020**, *59*, 18374–18383.
- (53) Gu, S.; Xia, M.; Zhou, C.; Kong, Z.; Molokeev, M. S.; Liu, L.; Wong, W. Y.; Zhou, Z. Red Shift Properties, Crystal Field Theory and Nephelauxetic Effect on Mn^{4+} -Doped $\text{SrMgAl}_{10}\text{YGa}_3\text{O}_{17}$ Red Phosphor for Plant Growth LED Light. *Chem. Eng. J.* **2020**, *396*, No. 125208.
- (54) Sun, Q.; Wang, S.; Devakumar, B.; Sun, L.; Liang, J.; Huang, X. Synthesis, Crystal Structure, and Photoluminescence Characteristics of High-Efficiency Deep-Red Emitting $\text{Ba}_2\text{GdTao}_6\text{:Mn}^{4+}$ Phosphors. *ACS Omega* **2019**, *4*, 13474–13480.
- (55) Li, K.; Van Deun, R. Novel Intense Emission-Tunable $\text{Li}_{1.5}\text{La}_{1.5}\text{WO}_6\text{:Mn}^{4+},\text{Nd}^{3+},\text{Yb}^{3+}$ Material with Good Luminescence Thermal Stability for Potential Applications in c-Si Solar Cells and Plant-Cultivation Far-Red-NIR LEDs. *ACS Sustainable Chem. Eng.* **2019**, *7*, 16284–16294.
- (56) Ji, H.; Ueda, J.; Brik, M. G.; Du, M. H.; Chen, D.; Tanabe, S. Intense Deep-Red Zero Phonon Line Emission of Mn^{4+} in Double Perovskite $\text{La}_4\text{Ti}_3\text{O}_{12}$. *Phys. Chem. Chem. Phys.* **2019**, *21*, 25108–25117.
- (57) Zhang, S.; Hu, Y. Photoluminescence Spectroscopies and Temperature-Dependent Luminescence of Mn^{4+} in BaGe_4O_9 Phosphor. *J. Lumin.* **2016**, *177*, 394–401.
- (58) Song, Y.; Guo, N.; Li, J.; Xin, Y.; Lü, W.; Miao, Y. Dual-Emissive $\text{Ln}^{3+}/\text{Mn}^{4+}$ Co-Doped Double Perovskite Phosphor: Via Site-Beneficial Occupation. *Mater. Adv.* **2021**, *2*, 1402–1412.
- (59) Zhang, S.; Hu, Y.; Duan, H.; Chen, L.; Fu, Y.; Ju, G.; Wang, T.; He, M. Novel $\text{La}_3\text{GaGe}_3\text{O}_{16}\text{:Mn}^{4+}$ Based Deep Red Phosphor: A Potential Color Converter for Warm White Light. *RSC Adv.* **2015**, *5*, 90499–90507.
- (60) Hu, T.; Lin, H.; Cheng, Y.; Huang, Q.; Xu, J.; Gao, Y.; Wang, J.; Wang, Y. A Highly-Distorted Octahedron with a: C 2v Group Symmetry Inducing an Ultra-Intense Zero Phonon Line in Mn^{4+} -Activated Oxyfluoride $\text{Na}_2\text{WO}_2\text{F}_4$. *J. Mater. Chem. C* **2017**, *5*, 10524–10532.

(61) Zhou, Y.; Zhang, S.; Wang, X.; Jiao, H. Structure and Luminescence Properties of Mn⁴⁺-Activated K₃TaO₂F₄ Red Phosphor for White LEDs. *Inorg. Chem.* **2019**, *58*, 4412–4419.

(62) Dierre, B.; Takeda, T.; Sekiguchi, T.; Suehiro, T.; Takahashi, K.; Yamamoto, Y.; Xie, R. J.; Hirotsuki, N. Local Analysis of Eu²⁺ Emission in CaAlSiN₃. *Sci. Technol. Adv. Mater.* **2013**, *14*, No. 064201.

(63) Liu, X. Y.; Guo, H.; Ye, S.; Peng, M. Y.; Zhang, Q. Y. Enhanced Tunable Color Emission in Transparent Ag/Mn²⁺ Codoped Zinc Borate Glasses for Broad Band Light Source. *J. Mater. Chem. C* **2015**, *3*, 5183–5191.

(64) Wang, Q.; Ci, Z.; Wang, Y.; Zhu, G.; Wen, Y.; Shi, Y. Crystal Structure, Photoluminescence Properties and Energy Transfer of Ce³⁺, Mn²⁺ Co-Activated Ca₃NaGd(PO₄)₆F₂ Phosphor. *Mater. Res. Bull.* **2013**, *48*, 1065–1070.

(65) Shanshan, H.; Wanjun, T. Single-Phased White-Light-Emitting Sr₃NaLa(PO₄)₃F:Eu²⁺,Mn²⁺ Phosphor via Energy Transfer. *J. Lumin.* **2014**, *145*, 100–104.

(66) Kang, H.; Lee, K. N.; Unithrattil, S.; Kim, H. J.; Oh, J. H.; Yoo, J. S.; Im, W. B.; Do, Y. R. Narrow-Band SrMgAl₁₀O₁₇:Eu²⁺, Mn²⁺ Green Phosphors for Wide-Color-Gamut Backlight for LCD Displays. *ACS Omega* **2020**, *5*, 19516–19524.

(67) Shea, L. E.; Mckittrick, J. Predicting and Modeling the Low-Voltage Cathodoluminescent Efficiency of Oxide Phosphors. *J. Electrochem. Soc.* **1998**, *145*, 3165–3170.

(68) Xiao, F.; Xie, C.; Yi, R.; Yuan, H.; Zhou, Q. Luminescence and Interstitial-Defect-Related Self-Reduction in Mn²⁺ Activated Ba₃BP₃O₁₂ Phosphor. *Opt. Mater.* **2022**, *125*, No. 112131.

(69) Zhu, Y.; Li, C.; Deng, D.; Chen, B.; Yu, H.; Li, H.; Wang, L.; Shen, C.; Jing, X.; Xu, S. A High-Sensitivity Dual-Mode Optical Thermometry Based on One-Step Synthesis of Mn²⁺:BaAl₁₂O₁₉–Mn⁴⁺:SrAl₁₂O₁₉ Solid Solution Phosphors. *J. Alloys Compd.* **2021**, *853*, No. 157262.

(70) Cao, R.; Luo, W.; Xiong, Q.; Jiang, S.; Luo, Z.; Fu, J. Synthesis and Photoluminescence Properties of Ba₂GeO₄:Mn⁴⁺ Novel Deep Red-Emitting Phosphor. *Chem. Lett.* **2015**, *44*, 1422–1424.

(71) Singh, K.; Rajendran, M.; Devi, R.; Vaidyanathan, S. Narrow-Band Red-Emitting Phosphors with High Color Purity, Trifling Thermal and Concentration Quenching for Hybrid White LEDs and Li₃Y₃BaSr(MoO₄)₈:Sm³⁺, Eu³⁺-Based Deep-Red LEDs for Plant Growth Applications. *Inorg. Chem.* **2022**, *61*, 2768–2782.

(72) Shi, L.; Han, Y. j.; Zhang, Z. g.; Ji, Z. x.; Shi, D. c.; Geng, X. y.; Zhang, H.; Li, M.; Zhang, Z. w. Synthesis and Photoluminescence Properties of Novel Ca₂LaSbO₆:Mn⁴⁺ Double Perovskite Phosphor for Plant Growth LEDs. *Ceram. Int.* **2019**, *45*, 4739–4746.

Recommended by ACS

Anionic Regulation toward Bi³⁺ Selective Occupation for Full-Spectrum White Light Emission

Sheng Wu, Yinzen Wang, *et al.*

MARCH 14, 2023

INORGANIC CHEMISTRY

READ 

Broadband UV-Excitation and Red/Far-Red Emission Materials for Plant Growth: Tunable Spectrum Conversion in Eu³⁺,Mn⁴⁺ Co-doped LaAl_{0.7}Ga_{0.3}O₃ Phosphors

Fan Ding, Shixun Lian, *et al.*

FEBRUARY 09, 2023

INORGANIC CHEMISTRY

READ 

Impact of Negative Thermal Expansion on Thermal Quenching of Luminescence of Sc₂Mo₃O₁₂:Eu³⁺

Forough Jahanbazi and Yuanbing Mao

NOVEMBER 15, 2022

CHEMISTRY OF MATERIALS

READ 

Bismuth Vacancy-Induced Enhancement of Luminescence Intensity and Irradiation Resistance for Bi₄Ge₃O₁₂

Mingxue Deng, Jiacheng Wang, *et al.*

APRIL 14, 2023

THE JOURNAL OF PHYSICAL CHEMISTRY LETTERS

READ 

Get More Suggestions >